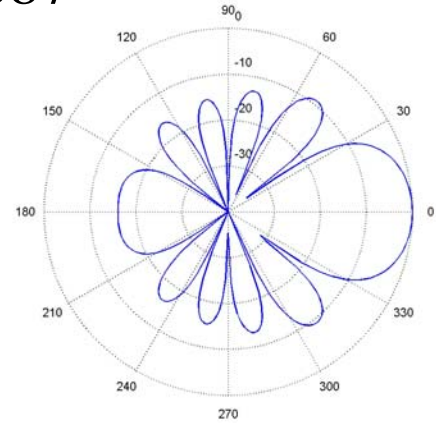


Applied Computational Electromagnetics Society Journal

Special Issue on
ACES 2006 Conference

Editor-in-Chief
Atef Z. Elsherbeni

March 2007
Vol. 22 No. 1
ISSN 1054-4887



GENERAL PURPOSE AND SCOPE: The Applied Computational Electromagnetics Society (*ACES*) Journal hereinafter known as the *ACES Journal* is devoted to the exchange of information in computational electromagnetics, to the advancement of the state-of-the art, and the promotion of related technical activities. A primary objective of the information exchange is the elimination of the need to “re-invent the wheel” to solve a previously-solved computational problem in electrical engineering, physics, or related fields of study. The technical activities promoted by this publication include code validation, performance analysis, and input/output standardization; code or technique optimization and error minimization; innovations in solution technique or in data input/output; identification of new applications for electromagnetics modeling codes and techniques; integration of computational electromagnetics techniques with new computer architectures; and correlation of computational parameters with physical mechanisms.

SUBMISSIONS: The *ACES Journal* welcomes original, previously unpublished papers, relating to applied computational electromagnetics. Typical papers will represent the computational electromagnetics aspects of research in electrical engineering, physics, or related disciplines. However, papers which represent research in applied computational electromagnetics itself are equally acceptable.

Manuscripts are to be submitted through the upload system of *ACES* web site <http://aces.ee.olemiss.edu> See “Information for Authors” on inside of back cover and at *ACES* web site. For additional information contact the Editor-in-Chief:

Dr. Atef Elsherbeni

Department of Electrical Engineering
The University of Mississippi
University, MS 386377 USA
Phone: 662-915-5382 Fax: 662-915-7231
Email: atef@olemiss.edu

SUBSCRIPTIONS: All members of the Applied Computational Electromagnetics Society who have paid their subscription fees are entitled to receive the *ACES Journal* with a minimum of three issues per calendar year and are entitled to download any published journal article available at <http://aces.ee.olemiss.edu>.

Back issues, when available, are \$15 each. Subscriptions to *ACES* is through the web site. Orders for back issues of the *ACES Journal* and changes of addresses should be sent directly to *ACES* Executive Officer:

Dr. Richard W. Adler

ECE Department, Code ECAB
Naval Postgraduate School
833 Dyer Road, Room 437
Monterey, CA 93943-5121 USA
Fax: 831-649-0300
Email: rwa@attglobal.net

Allow four week’s advance notice for change of address. Claims for missing issues will not be honored because of insufficient notice or address change or loss in mail unless the Executive Officer is notified within 60 days for USA and Canadian subscribers or 90 days for subscribers in other countries, from the last day of the month of publication. For information regarding reprints of individual papers or other materials, see “Information for Authors”.

LIABILITY. Neither *ACES*, nor the *ACES Journal* editors, are responsible for any consequence of misinformation or claims, express or implied, in any published material in an *ACES Journal* issue. This also applies to advertising, for which only camera-ready copies are accepted. Authors are responsible for information contained in their papers. If any material submitted for publication includes material which has already been published elsewhere, it is the author’s responsibility to obtain written permission to reproduce such material.

APPLIED COMPUTATIONAL ELECTROMAGNETICS SOCIETY JOURNAL

Special Issue on
ACES 2006 Conference

Editor-in-Chief
Atef Z. Elsherbeni

March 2007
Vol. 22 No. 1
ISSN 1054-4887

The ACES Journal is abstracted in INSPEC, in Engineering Index, DTIC, Science Citation Index Expanded, the Research Alert, and to Current Contents/Engineering, Computing & Technology.

The first, fourth, and sixth illustrations on the front cover have been obtained from the Department of Electrical Engineering at the University of Mississippi.

The third and fifth illustrations on the front cover have been obtained from Lawrence Livermore National Laboratory.

The second illustration on the front cover has been obtained from FLUX2D software, CEDRAT S.S. France, MAGSOFT Corporation, New York.

THE APPLIED COMPUTATIONAL ELECTROMAGNETICS SOCIETY

<http://aces.ee.olemiss.edu>

ACES JOURNAL EDITORS

EDITOR-IN-CHIEF/ACES/JOURNAL

Atef Elsherbeni

University of Mississippi, EE Dept.
University, MS 38677, USA

ASSOCIATE EDITOR-IN-CHIEF

Erdem Topsakal

Mississippi State University, EE Dept.
Mississippi State, MS 39762, USA

MANAGING EDITOR

Richard W. Adler

833 Dyer Rd, Rm 437 EC/AB
NPS, Monterey, CA 93943-5121, USA

EDITORIAL ASSISTANT

Mohamed Al Sharkawy

University of Mississippi, EE Dept.
University, MS 38677, USA

EDITORIAL ASSISTANT

Matthew J. Inman

University of Mississippi, EE Dept.
University, MS 38677, USA

ASSOCIATE EDITOR-IN-CHIEF,
EMERITUS

Alexander Yakovlev

University of Mississippi, EE Dept.
University, MS 38677, USA

EDITOR-IN-CHIEF, EMERITUS

Allen Glisson

University of Mississippi, EE Dept.
University, MS 38677, USA

EDITOR-IN-CHIEF, EMERITUS

Ahmed Kishk

University of Mississippi, EE Dept.
University, MS 38677, USA

EDITOR-IN-CHIEF, EMERITUS

Robert M. Bevensee

Box 812
Alamo, CA 94507-0516, USA

EDITOR-IN-CHIEF, EMERITUS

Ducan C. Baker

EE Dept. U. of Pretoria
0002 Pretoria, South Africa

EDITOR-IN-CHIEF, EMERITUS

David E. Stein

USAF Scientific Advisory Board
Washington, DC 20330, USA

ACES JOURNAL ASSOCIATE EDITORS

Giandomenico Amendola

John Beggs

John Brauer

Magda El-Shenawee

Pat Foster

Cynthia M. Furse

Christian Hafner

Michael Hamid

Andy Harrison

Chun-Wen Paul Huang

Todd H. Hubing

Nathan Ida

Yasushi Kanai

Leo C. Kempel

Andrzej Krawczyk

Stanley Kubina

Samir F. Mahmoud

Ronald Marhefka

Edmund K. Miller

Krishna Naishadham

Giuseppe Pelosi

Vicente Rodriguez

Harold A. Sabbagh

John B. Schneider

Abdel Razek Sebak

Amr M. Sharawee

Norio Takahashi

MARCH 2007 REVIEWERS

Natalia K. Nikolova

Rajeev Bansal

Francisco Jose Ares ARes

Shirook Ali

Mohamed Al-Sharkawy

Erdem Topsakal

Amir I. Zaghloul

Apisak Ittipiboon

Werner Wiesbeck

John H. Beggs

Veysel Demir

C. J. Reddy

David Chen

Todd H. Hubing

Magda Elshenawee

Magdalena Salazar

Michael Hamid

Poman So

Fan Yang

Nihad Dib

Hassan A. Kalhor

Matt Inman

Mohamed H. Bakr

Naftali (Tuli) Herscovici

Ali Gharsallah

Harvey Schuman

Robert J. Burkholder

Nathan Ida

Joe LoVetri

Michiko Kuroda

Andy Harrison

Ahmed Sharkawy

THE APPLIED COMPUTATIONAL ELECTROMAGNETICS SOCIETY

JOURNAL

SPECIAL ISSUE ON ACES 2006 CONFERENCE

Vol. 22 No. 1

March 2007

TABLE OF CONTENTS

“A Perspective on the 40-Year History of FDTD Computational Electrodynamics” A. Taflove.....	1
“Miniature Antennas and Arrays Embedded within Magnetic Photonic Crystals and Other Novel Materials” J. L. Volakis, K. Sertel, and C. Chen.....	22
“Estimation of Blockage Effects of Complex Structures on the Performance of the Spacecraft Reflector Antennas by a Hybrid PO/NF-FF Method” K. Bahadori and Y. Rahmat-Samii.....	31
“Enhanced Functionality for Hardware-Based FDTD Accelerators” P. F. Curt, J. P. Durbano, M. R. Bodnar, S. Shi, and M. S. Mirotznic.....	39
“MoM Solution to Scattering from Three-Dimensional Inhomogeneous Magnetic and Dielectric Bodies” M. Hasanovic, C. Mei, J. R. Mautz, and E. Arvas.....	47
“Surface Impedance Boundary Conditions of High Order of Approximation for the Finite Integration Technique” L. Di Rienzo, N. Ida, and S. Yuferev.....	53
“An Adaptive Basis Function Solution to the 1D and 2D Inverse Scattering Problems using DBIM and the BIM” I. Jeffrey, V. I. Okhmatovski, J. LoVetri, and C. Gilmore.....	60
“High-Order FVTD on Unstructured Grids using an Object-Oriented Computational Engine” D. Firsov, J. LoVetri, I. Jeffrey, V. Okhmatovski, C. Gilmore, and W. Chammaa.....	71
“Improved Smart Antenna Design Using Displaced Sensor Array Configuration” R. M. Shubair.....	83
“Development of Wideband L-Probe Coupled Patch Antenna” K. M. Luk, K. F. Lee, and H. W. Lai.....	88

“Novel Broadband Dielectric Resonator Antennas Fed Through Double-Bowtie-Slot Excitation Scheme” G. Almpanis, C. Fumeaux, and R. Vahldieck.....	97
“Approximated Method Neglecting Coupling for Conformal Array” F. Chauvet, R. Guinvarc’h, and M. Hélier.....	105
“Two Element Phased Array Dipole Antenna” M. Taguchi, K. Era, and K. Tanaka.....	112
“Mixed Order Tangential Vector Finite Elements (TVFEs) for Tetrahedra and Applications to Multi-Functional Automotive Antenna Design” T. Karacolak and E. Topsakal.....	117
“Modeling and Analysis of a Dual-Band Dual-Polarization Radiator Using FEKO” Amir I. Zaghloul, C. Babu Ravipati, and M. T. Kawser.....	125
“Polymorphic Time Domain Computational Electromagnetics” P. So.....	134
“Simulation of Non Linear Circuits by the Use of a State Variable Approach in the Wavelet Domain” S. Barmada, A. Musolino, and M. Raugi.....	147
“Monochromatic Scattering from Three-Dimensional Gyrotropic Bodies Using the TLM Method” A. F. Yagli, J. K. Lee, and E. Arvas.....	155
“High Frequency Phase Variable Model of Electric Machines from Electromagnetic Field Computation” O. A. Mohammed, S. Ganu, N. Abed, S. Liu, and Z. Liu.....	164
“Cascading Optical Negative Index Metamaterials” A. V. Kildishev and U. K. Chettiar.....	172
“Characterizing Infrared Frequency Selective Surfaces on Dispersive Media” J. Ginn, B. Lail, D. Shelton, J. Tharp, W. Folks, and G. Boreman.....	184

A Perspective on the 40-Year History of FDTD Computational Electrodynamics

Allen Taflove

Department of Electrical Engineering and Computer Science
 Northwestern University
 Evanston, IL 60208

Abstract — This paper arises from an invited plenary talk by the author at the 2006 Applied Computational Electromagnetics Society Symposium in Miami, FL (The 71 original slides can be downloaded at http://www.ece.northwestern.edu/ecefaculty/taflove/ACES_talk.pdf). This paper summarizes the author’s perspectives on the history and future prospects of finite-difference time-domain (FDTD) computational electrodynamics on the occasion of the fortieth anniversary of the publication of Kane Yee’s seminal Paper #1. During these four decades, advances in basic theory, software realizations, and computing technology have elevated FDTD techniques to the top rank of computational tools for engineers and scientists studying electrodynamic phenomena and systems.

I. INTRODUCTION

In May 1966, Kane Yee published the first paper to delineate the space and time discretizations of Maxwell’s equations which form the basis of the finite-difference time-domain (FDTD) method [1]. As of March 7, 2006, according to a search conducted by the author on the ISI Web of Science®, Yee’s paper had been cited 2441 times since its publication. This large number of citations is a quantitative measure of the seminal nature of Yee’s insights, which opened the door to an entirely novel approach to computational electrodynamics relative to the other techniques being used by engineers and scientists in 1966. As shown in Fig. 1, the growth in FDTD-related publications continues unabated to the present time.

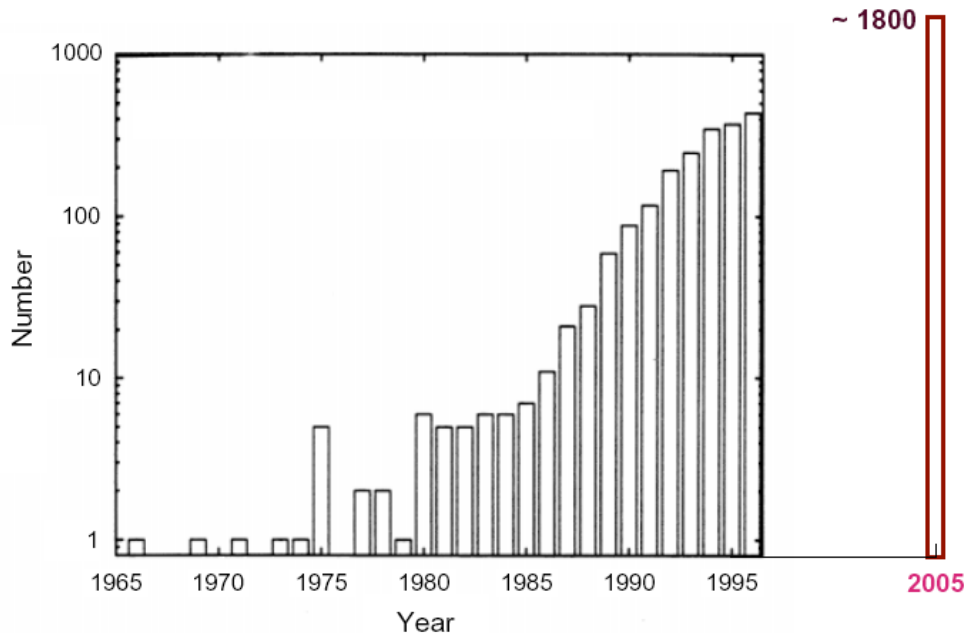


Fig. 1. Yearly FDTD-related publications. Data source for years 1966–96: Shlager and Schneider [2]. The 2005 data point is an estimate based upon a Web of Science® search by the author.

II. HISTORY OF FDTD TECHNIQUES FOR MAXWELL'S EQUATIONS

We can begin to develop an appreciation of the basis, technical development, and possible future of FDTD numerical techniques for Maxwell's equations by first considering their history. Table 1 lists some of the key initial publications in this area, starting with Yee's seminal paper [1].

Table 1
Partial History of FDTD and Related Techniques

1966	Yee [1] introduced the basic FDTD space grid and time-stepping algorithm.
1975	Taflove and Brodwin reported the correct numerical stability criterion for Yee's algorithm [3]; sinusoidal steady-state Yee-based solutions of 2-D and 3-D electromagnetic wave interactions with material structures [3, 4]; and Yee-based bioelectromagnetics models [4].
1977	Holland [5] and Kunz and Lee [6] applied Yee's algorithm to EMP problems.
1977, 1980	Engquist and Majda [7] and Bayliss and Turkel [8] reported second-order accurate absorbing boundary conditions (ABCs) for grid-based time-domain wave-propagation schemes
1980	Taflove coined the FDTD acronym and published validated models of sinusoidal steady-state electromagnetic wave penetration into a 3-D metal cavity [9].
1981	Mur reported a second-order accurate ABC for Yee's grid [10] based upon the Engquist-Majda theory.
1982, 3	Taflove and Umashankar [11, 12] reported a phasor-domain near-to-far field transformation which permits calculating the far fields and radar cross-section of 2-D and 3-D structures.
1984	Liao et al. [13] reported a novel space-time extrapolation ABC that is less reflective than Mur's ABC.
1985	Gwarek introduced an lumped equivalent-circuit formulation [14].
1986	Choi and Hoefer modeled waveguide structures [15].
1987, 8	Kriegsmann et al. and Moore et al. published the first articles on ABC theory in <i>IEEE Trans. Antennas and Propagation</i> [16, 17].
1987, 8, 1992	Contour-path subcell techniques were introduced by Umashankar et al. to model thin wires and wire bundles [18]; by Taflove et al. to model penetration through cracks in metal screens [19]; and by Jurgens et al. to conformally model smoothly curved surfaces [20].
1987, 1990	Finite-element time-domain (FETD) and finite-volume time-domain (FVTD) meshes were introduced by Cangellaris et al. [21], Shankar et al. [22], and Madsen and Ziolkowski [23].
1988	Sullivan et al. published a 3-D model of sinusoidal steady-state electromagnetic wave absorption by a complete human body [24].
1988	Zhang et al. modeled microstrips [25].
1989	Fang [26] introduced higher-order spatial derivatives.
1990, 1	Kashiwa and Fukai [27], Luebbers et al. [28], and Joseph et al. [29] modeled frequency-dependent dielectric permittivity.
1990, 1	Maloney et al. [30], Katz et al. [31], and Tirkas and Balanis [32] modeled antennas.
1990	Sano and Shibata [33] and El-Ghazaly et al. [34] modeled picosecond optoelectronic switches.
1991	Luebbers et al. [35] introduced the time-domain near-to-far field transformation.
1991-4	Optical pulse propagation in nonlinear media was reported, including temporal solitons by Goorjian and Taflove [36]; beam self-focusing by Ziolkowski and Judkins [37]; and spatial solitons by Joseph and Taflove [38].
1991-8	Digital processing of windowed FDTD time-waveforms was introduced by several groups [39-43] to allow extracting the underlying resonant frequencies and quality factors.
1992	Sui et al. modeled lumped circuit elements [44].
1993	Toland et al. modeled tunnel diodes and Gunn diodes exciting cavities and antennas [45].
1994	Thomas et al. [46] reported SPICE subgrid models of embedded electronic components.
1994	Berenger introduced the extraordinarily effective perfectly matched layer (PML) ABC for 2-D grids [47], which was later extended to 3-D grids by Katz et al. [48] and to dispersive waveguide terminations by Reuter et al. [49].
1995, 6	Sacks et al. [50] and Gedney [51] introduced a physically realizable, uniaxial perfectly matched layer (UPML) ABC.

Table 1 (continued)
 Partial History of FDTD Techniques for Maxwell's Equations

1995, 8	Hybrid FDTD-quantum mechanics models of two-level and four-level atoms were introduced by several groups [52-55] to model ultrafast optical interactions and lasing phenomena.
2002, 4	
1996	Krumpholz and Katehi [56] introduced the multiresolution time-domain (MRTD) technique based upon wavelet expansion functions.
1996, 7	Liu [57, 58] introduced the pseudospectral time-domain (PSTD) method, which permits coarse spatial sampling approaching the Nyquist limit.
1997	Ramahi [59] introduced complementary operators method (COM) analytical ABCs.
1997	Dey and Mittra [60] introduced a simple, stable, accurate contour-path technique to model curved metal surfaces.
1998	Maloney and Kesler [61] introduced several novel means to analyze periodic structures.
1999	Schneider and Wagner [62] reported a rigorous analysis of grid dispersion.
1999, 2000	Namiki [63] and Zheng, Chen, and Zhang [64] introduced 3-D alternating-direction implicit (ADI) FDTD algorithms with provable unconditional numerical stability.
2000	Roden and Gedney introduced the convolutional PML (CPML) ABC [65].
2000	Rylander and Bondeson introduced a provably stable FDTD-FE hybrid technique [66].
2002-6	Hayakawa et al. [67] and Simpson and Taflove [68, 69] reported models of the entire Earth-ionosphere waveguide for extremely low-frequency geophysical phenomena.
2003	DeRaedt introduced the unconditionally stable, "one-step" FDTD technique [70].

III. TECHNOLOGY DEVELOPMENT THEMES

In addition to the chronological summary provided in Table 1, it is useful to organize the past 40 years of FDTD developments according to their primary technology-development themes. These are summarized in Table 2, referencing the key initial publications listed in Table 1.

Table 2
 Primary FDTD Technology Development Themes

<ul style="list-style-type: none"> • Absorbing boundary conditions <ul style="list-style-type: none"> – Engquist-Majda one-way wave equation, 1977 [7] – Bayliss-Turkel outgoing wave annihilators, 1980 [8] – Liao et al. extrapolation of outgoing waves in space and time, 1984 [13] – Berenger perfectly matched layer, 1994 [47] – Uniaxial perfectly matched layer, 1995-6 [50, 51] – Roden and Gedney convolutional perfectly matched layer, 2000 [65] • Digital signal processing <ul style="list-style-type: none"> – Umashankar and Taflove, phasor-domain near-to-far field transformation, 1982, 83 [11, 12] – Luebbers et al. time-domain near-to-far field transformation, 1991 [35] – Extraction of underlying resonant frequencies and quality factors from windowed FDTD time-waveforms 1991-8 [39-43]. 	<ul style="list-style-type: none"> • Numerical dispersion <ul style="list-style-type: none"> – Fang higher-order spatial derivatives, 1989 [26] – Krumpholz and Katehi MRTD, 1996 [56] – Q. H. Liu PSTD, 1996-7 [57, 58] – Schneider and Wagner analysis for Yee FDTD, 1999 [62] • Numerical stability <ul style="list-style-type: none"> – Taflove and Brodwin analysis, 1975 [3] – Unconditionally stable ADI techniques, 1999-2000 [63, 64] – DeRaedt "one-step" FDTD technique, 2003 [70]. • Conforming grids <ul style="list-style-type: none"> – Locally conforming contour-path subcell techniques, 1987, 88, 92, 97 [18-20, 60] – Globally conforming grids, 1990 [22, 23] – Rylander and Bondeson stable hybrid FETD / FDTD, 2000 [66]
---	---

Table 2 (continued)
Primary FDTD Technology Development Themes

- | | |
|---|---|
| <ul style="list-style-type: none"> • Dispersive and nonlinear materials <ul style="list-style-type: none"> – Linear dispersions, 1990,91 [27-29] – Nonlinearities, yielding self-focusing and temporal and spatial solitons, 1991-4 [36-38] | <ul style="list-style-type: none"> • Multiphysics coupling to Maxwell's equations <ul style="list-style-type: none"> – Charge generation, recombination, and transport in semiconductors, 1990 [33, 34] – Electron transitions between multiple energy levels of atoms, modeling pumping, emission, and stimulated emission processes, 1995, 1998, 2002, 2004 [52-55] |
|---|---|

IV. CURRENT AND EMERGING FDTD APPLICATIONS

This section illustrates current and emerging FDTD computational electrodynamics modeling applications over the frequency range from about 1 Hz to 6×10^{14} Hz (i.e., extremely low frequencies to daylight).

A. Extremely Low Frequency Models of the Earth-Ionosphere Waveguide

FDTD has been recently applied to model extremely low frequency (ELF) electromagnetic wave propagation within the Earth-ionosphere waveguide. Fig. 2 illustrates the most advanced gridding technique used in such studies, and sample results for antipodal wave propagation around the Earth calculated using a high-resolution grid with space cells spanning only about 40 km over the entire surface of the planet.

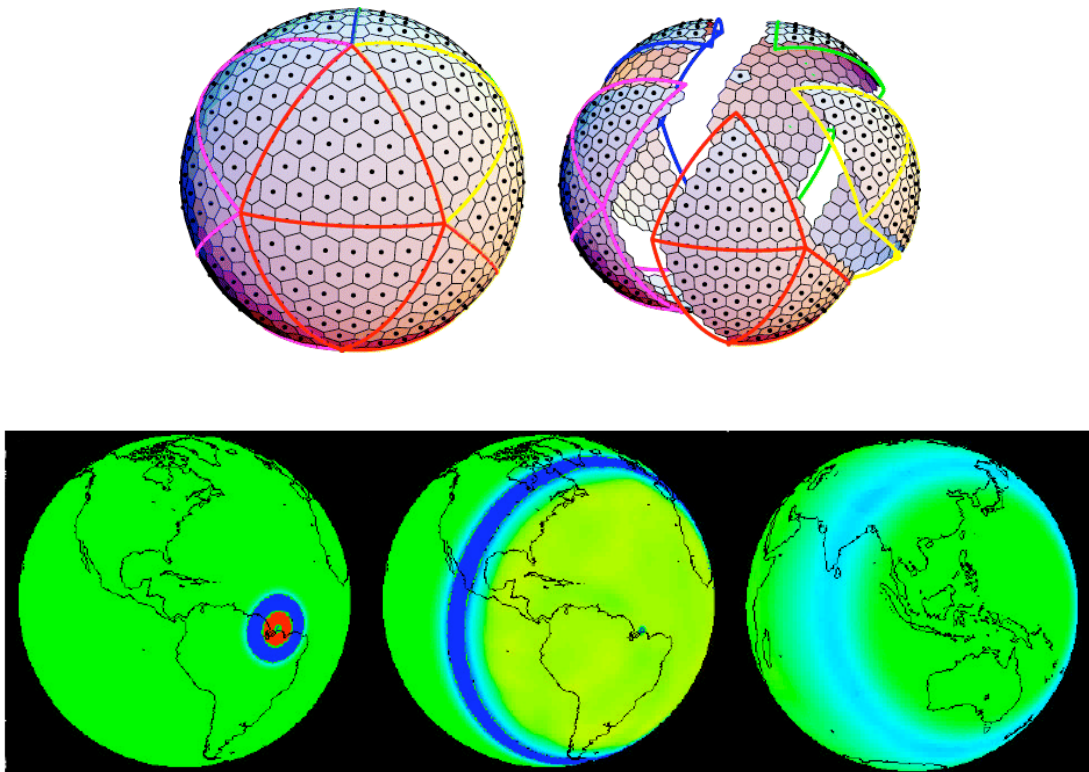
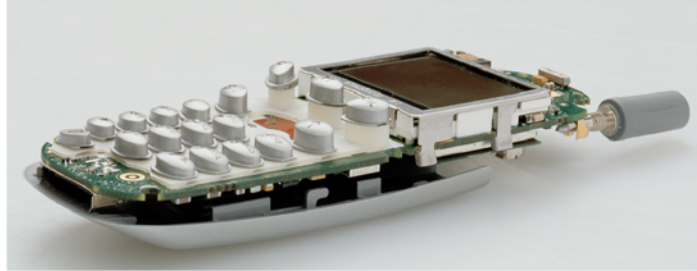


Fig. 2. FDTD model of the Earth-ionosphere waveguide. Top: geodesic grid [69]. Bottom: snapshots of impulsive wave propagation around the Earth (the complete video can be downloaded at <http://www.ece.northwestern.edu/ecefaculty/taflove/3Dmovidetext.gif.avi>)

B. Wireless Personal Communications Devices

Figs. 3-5 illustrate how FDTD has been applied to provide accurate, high-resolution models of cellphones [71]. Here, the grid-cell size is as fine as 0.1 mm to resolve fine geometrical details.

Physical phone



Phone model within CAD environment

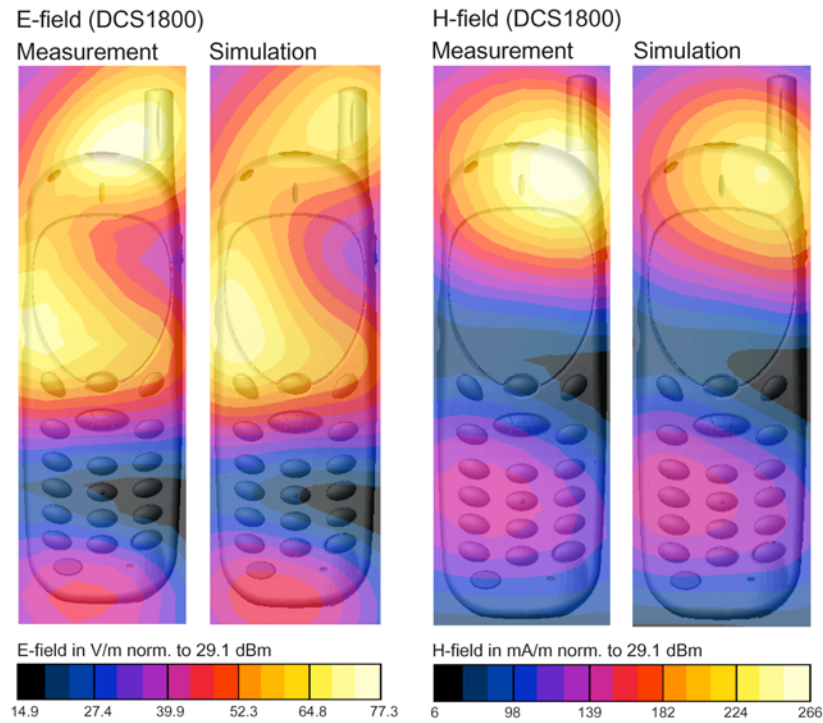
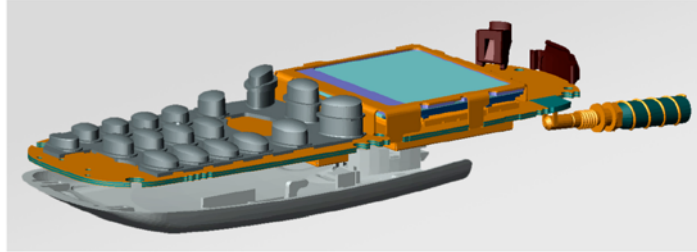


Fig. 3. FDTD model of the Motorola T250 cellphone [71]. Top: physical phone and the FDTD CAD model. Bottom: agreement of measured and FDTD-calculated near-surface electromagnetic fields at 1.8 GHz.

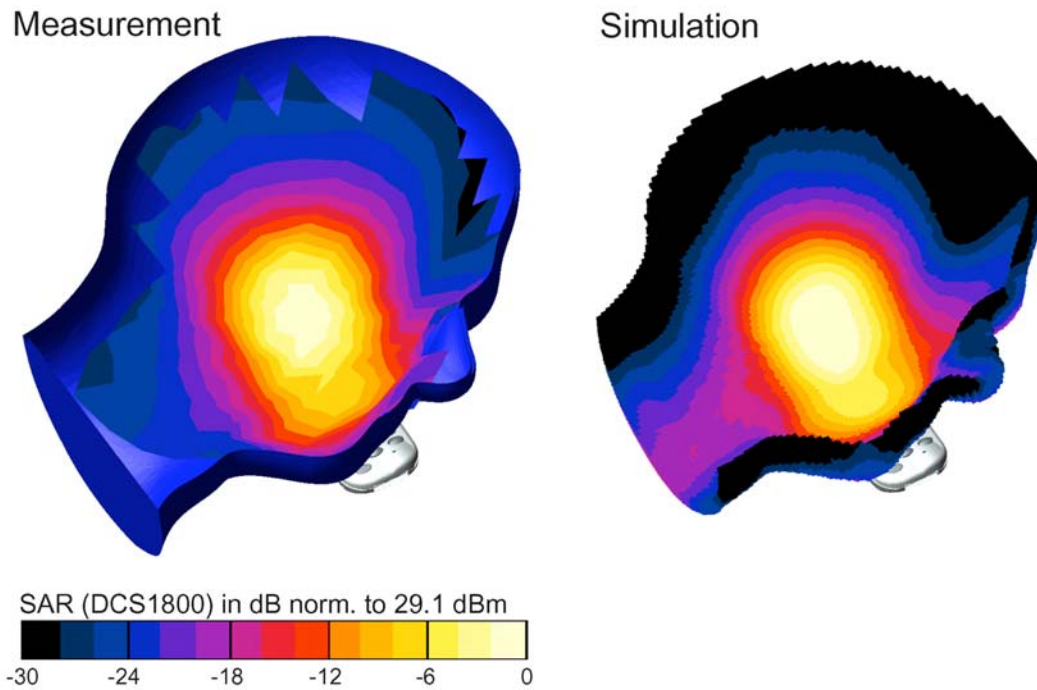


Fig. 4. Agreement of the measured and FDTD-calculated specific absorption rate (SAR) at 1.8 GHz for the cellphone of Fig. 3 positioned adjacent to a standard phantom head model [71].

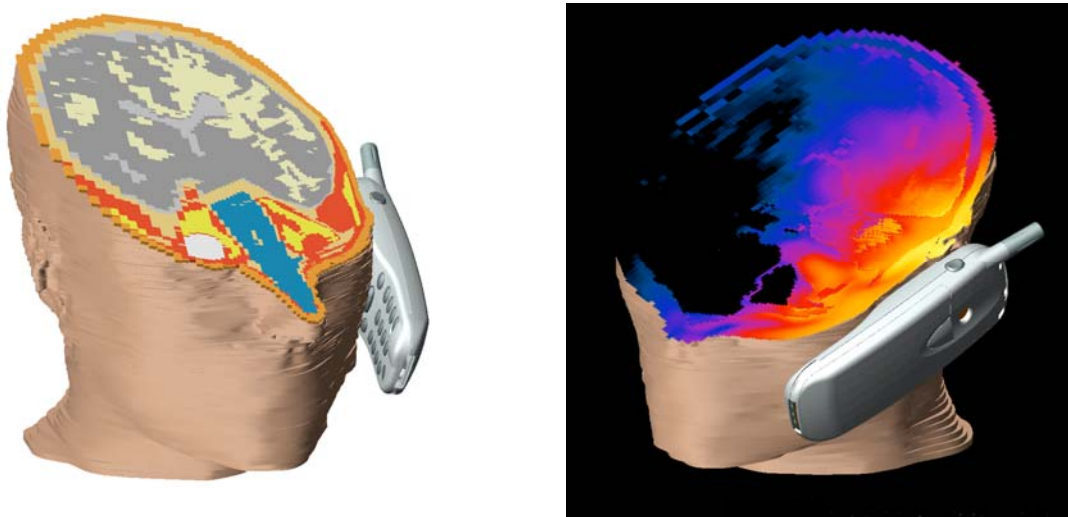


Fig. 5. FDTD-calculated SAR at 1.8 GHz for the cellphone of Fig. 3 positioned adjacent to a realistic head model derived from tomographic scans of a volunteer subject [71]. The head model has 121 slices (1 mm thick in the ear region, 3 mm thick elsewhere), wherein each slice has a transverse resolution of 0.2 mm.

C. Ultrawideband Microwave Detection of Early-Stage Breast Cancer

Fig. 6 illustrates how FDTD has been applied to model a proposed ultrawideband (UWB) microwave technique for early detection of breast cancer [72]. Here, FDTD was used to model the breast tissues and an antenna system consisting of impulsive sources and receptors located at the surface of the breast. In the case shown, a 2-mm diameter malignant tumor was assumed to be embedded 3 cm within a realistic breast model derived from tomographic scans of a volunteer subject. The impulsive excitation had spectral components primarily in the 1-10 GHz range. FDTD-calculated data for the backscattering response observed at the antenna was post-processed to derive the image shown. From Fig. 6, we see that the proposed UWB microwave technique yields a cancer signature which should be readily detectable, i.e., 15 dB to 30 dB stronger than the clutter due to the surrounding normal tissues. This is very encouraging, since a small malignancy of this type would almost certainly not be detectable using x-ray mammography.

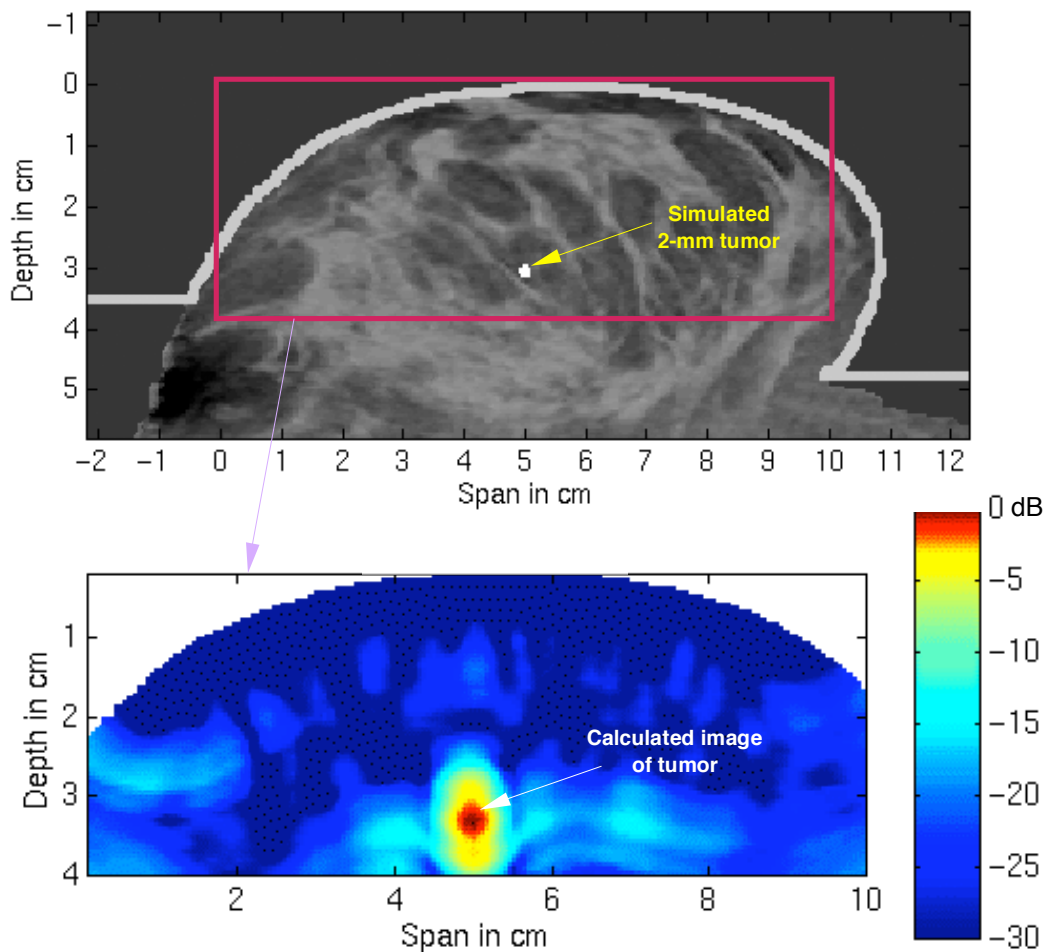


Fig. 6. Calculated image of a 2-mm diameter malignant tumor embedded 3 cm below the surface of a model of the female human breast [72]. This image was derived by post-processing FDTD data for the backscattering of ultrawideband electromagnetic wave pulses radiated by an antenna system located at the surface of the breast. The breast model was assembled from tomographic scans of a volunteer subject. The presence and location of the small tumor is easily discerned. Such a cancer would almost certainly not be detectable using x-ray mammography.

D. Ultrahigh-Speed Bandpass Digital Interconnects

Fig. 7 illustrates how FDTD has been applied to model proposed ultrahigh-speed substrate integrated waveguide (SIW) interconnects for digital circuits [73]. Each SIW would be implemented in a multilayer circuit board by inserting two parallel rows of vias to connect adjacent ground planes. With no center conductor required, high-characteristic-impedance operation is possible and copper losses can be significantly reduced relative to stripline interconnects. Furthermore, sharp bends up to 90° are possible with negligible reflections and little overall impact on the signal transmission. Fig. 7(top) is a photograph of a prototype straight SIW constructed and tested at Intel Corporation in summer 2005 [73]. Measurements confirmed the FDTD predictions (Fig. 7(bottom)) that both straight and bent SIWs exhibit 100% bandwidths with negligible multimoding, for this prototype, 27 GHz – 81 GHz. In ongoing work, half-width folded SIWs are predicted by FDTD to have even larger (115%) bandwidths. Board-level interconnects using this technology could stream digital data at rates 10 – 50 times greater than possible today, which would satisfy Intel's needs for the next decade.

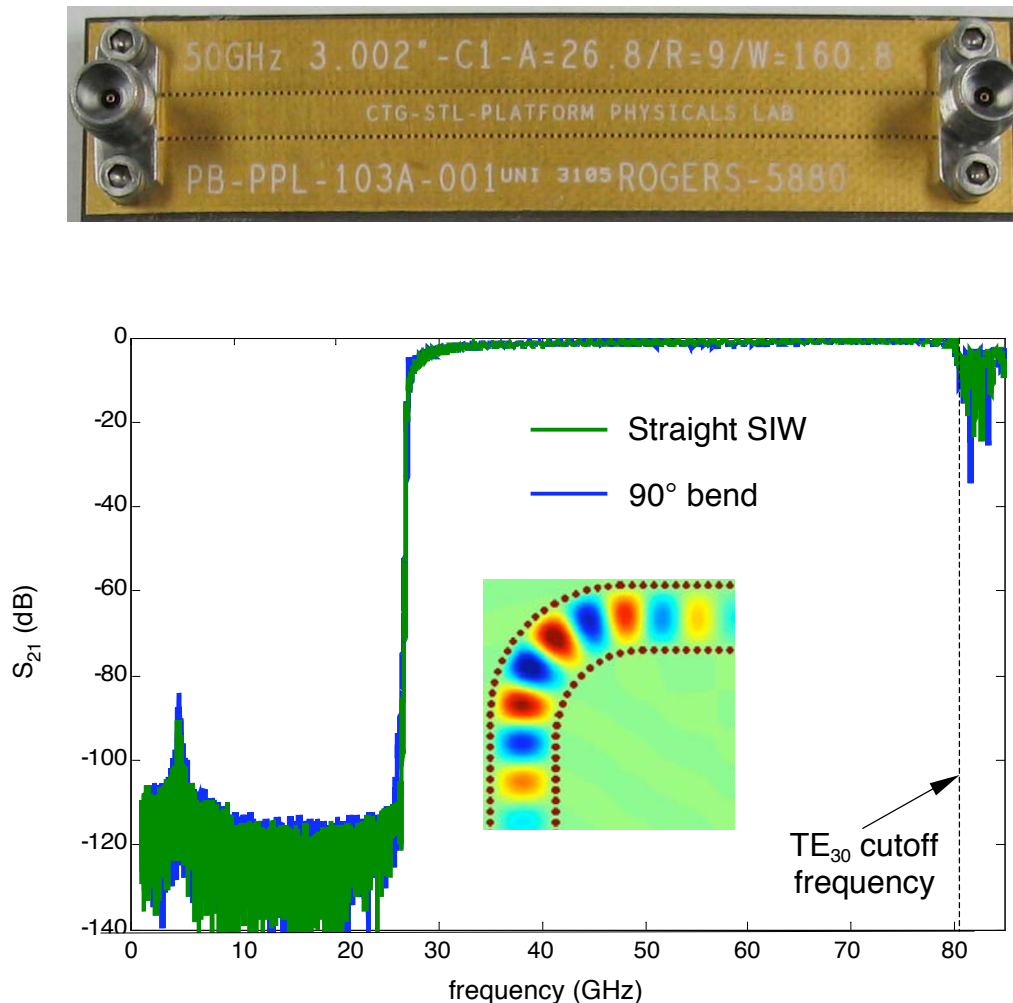


Fig. 7. FDTD-calculated S_{21} transmission versus frequency for the prototype substrate integrated waveguide board-level digital interconnect shown at the top [73]. FDTD predicts little difference in the S_{21} characteristic over the entire 100% bandwidth if a 90° bend is inserted (see inset for a snapshot visualization of the electric field within the bend, showing a clean pattern with no multimoding).

E. Micron/Nanometer Scale Photonic Devices: Category 1 (Linear)

Currently, FDTD is routinely applied by the photonics community to analyze and design micron- and nanometer-scale devices operating at infrared through visible-light wavelengths. Fig. 8 illustrates one recent application of 3-D linear FDTD modeling to design a microcavity laser [74]. This electrically driven, single-mode device employs a photonic bandgap defect-mode cavity and operates at room temperature with a low threshold current. The physics of electromagnetic wave confinement by the cavity is properly simulated.

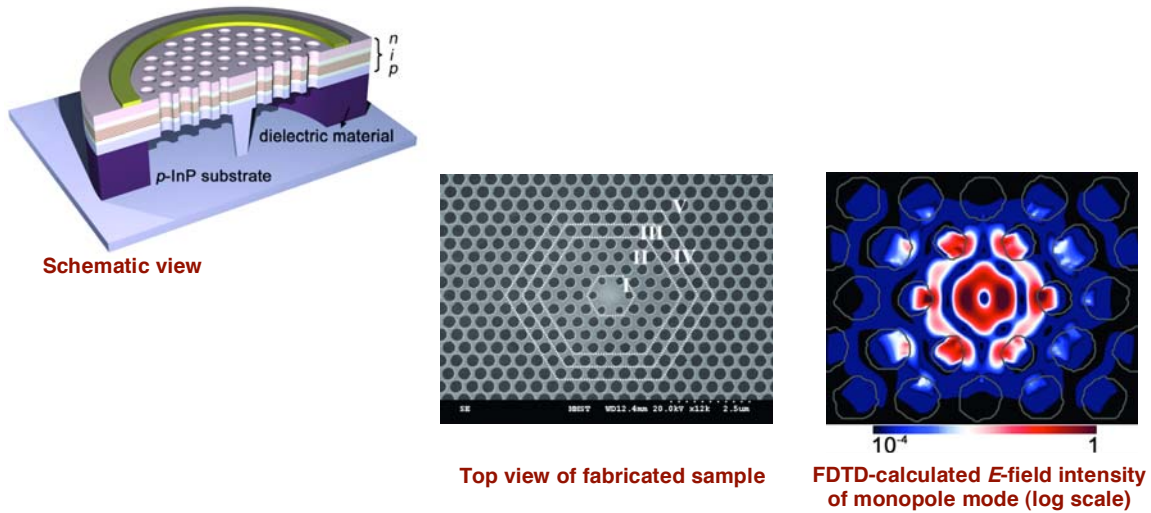


Fig. 8. Application of 3-D FDTD modeling to design a photonic bandgap defect-mode microcavity laser [74].

Fig. 9 illustrates a recent application of 3-D linear FDTD modeling to analyze the transmission of 532-nm wavelength light through a 200-nm diameter hole in a 100-nm thick gold film [75]. This illustrates the capability of a dispersive FDTD algorithm to properly model the formation of a plasmon mode at the surface of the gold film, which enhances the transmission of the normally incident light through the small hole.

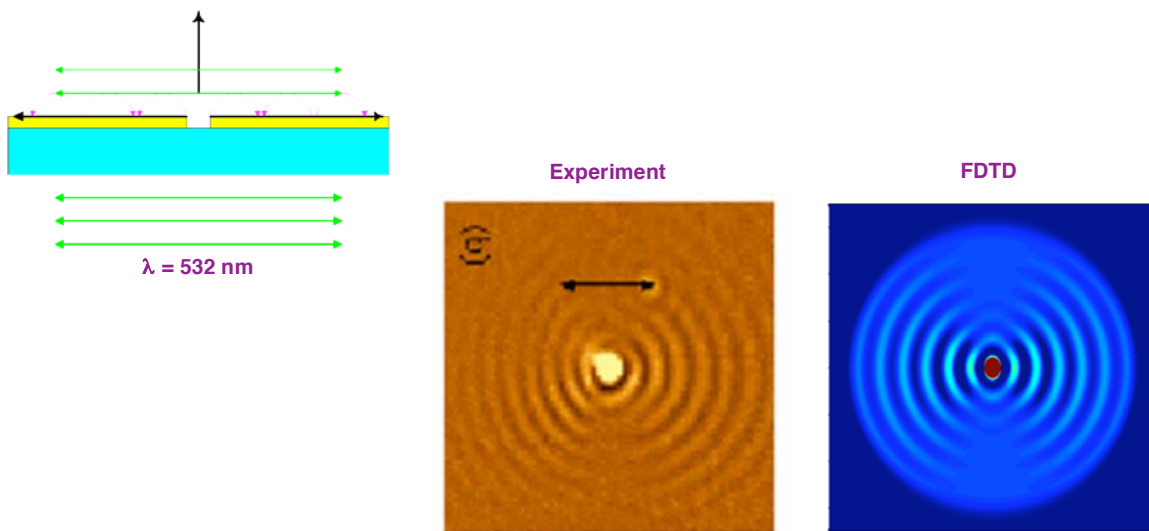


Fig. 9. Application of 3-D FDTD modeling to analyze enhanced light transmission through a sub-micron hole in a gold film due to the formation of a plasmon mode at the surface of the film [75].

F. Micron/Nanometer Scale Photonic Devices: Category 2 (Macroscopic Nonlinearity and Gain)

The incorporation of material nonlinearity and gain is an emerging area in FDTD modeling of micron- and nanometer-scale photonic devices. One approach incorporates nonlinearity and/or gain in the macroscopic description of the dielectric polarization or the index of refraction. Such nonlinearity and gain can be either independent or dependent upon the optical wavelength. Fig. 10 illustrates the first reported application of nonlinear FDTD modeling to simulate the propagation and interaction of spatial optical solitons [38]. Here, parallel, co-propagating, equal-amplitude spatial solitons having a dielectric wavelength of 528 nm in a glass medium exhibit a periodic coalescence or “braiding” if the optical carriers are assumed to be in phase. If the optical carriers are assigned a relative phase of π , FDTD modeling shows that the spatial solitons either immediately diverge to infinite separation or coalesce once before diverging. Such phenomena can form the basis of an ultrafast all-optical switch.

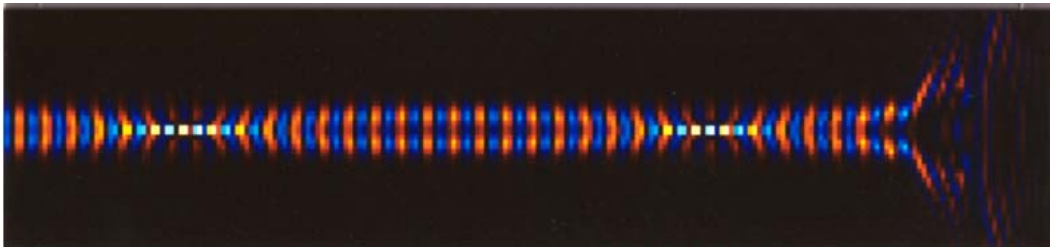
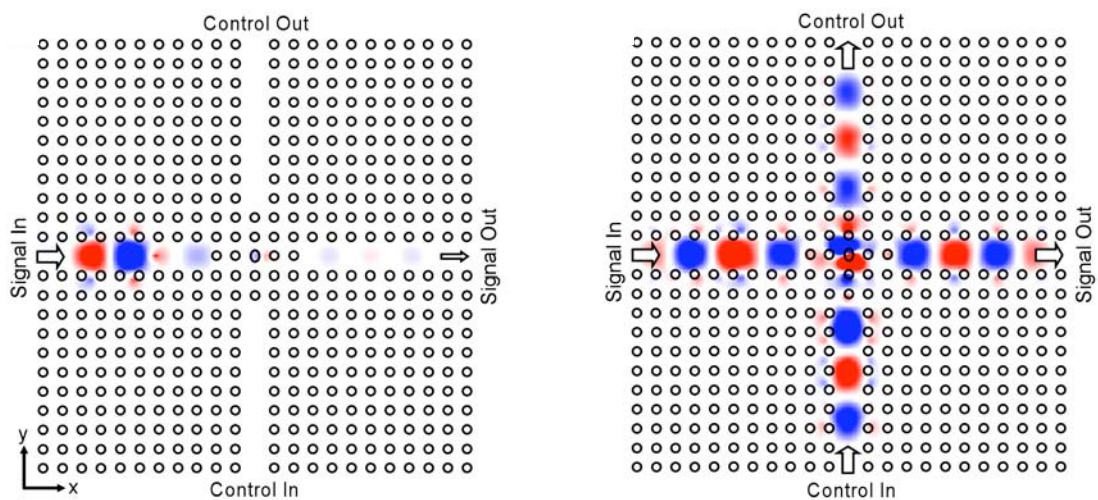


Fig. 10. Application of 2-D nonlinear FDTD modeling to analyze the periodic “braiding” of co-phased spatial optical solitons in glass [38]. The solitons propagate from left to right.

Fig. 11 illustrates an interesting recent application of 2-D nonlinear FDTD modeling to analyze the operation of a proposed low-power all-optical switch implemented in the crossing junction of photonic crystal defect-mode waveguides [76]. Here, the control signal perturbs the refractive index (and thereby the resonant frequency) of a defect-mode cavity at the intersection of the waveguides. This flips the cavity’s transmission of the signal from stopband to passband, permitting the signal to reach the output port.



(a) control input is absent, yielding low signal output

(b) control input is present, yielding high signal output

Fig. 11. Application of 2-D nonlinear FDTD modeling to analyze a proposed all-optical switch [76].

G. Micron/Nanometer Scale Photonic Devices: Category 3 (Semiclassical Models)

A second, more rigorous and more flexible approach to incorporate nonlinearity and gain in optical media involves time-stepping concurrently with the normal FDTD field updates a set of auxiliary differential equations which describes the behavior of individual atoms and their electrons. Phenomena of interest here include electron transitions between multiple energy levels of atoms that involve pumping, emission, and stimulated emission processes [52-55]. With this technique, quantum phenomena are coupled to the classical Maxwell's equations, yielding what may be called a semiclassical model.

Fig. 12 illustrates recent modeling results for electron population inversion and lasing output vs. time obtained using the semiclassical four-level-atom FDTD model reported in [55]. This laser is assumed to have a one-dimensional, optically pumped, single-defect, distributed Bragg reflector cavity with three layers of refractive indices alternating between $n = 1.0$ and 2.0 , with thickness 375 nm and 187.5 nm, respectively.

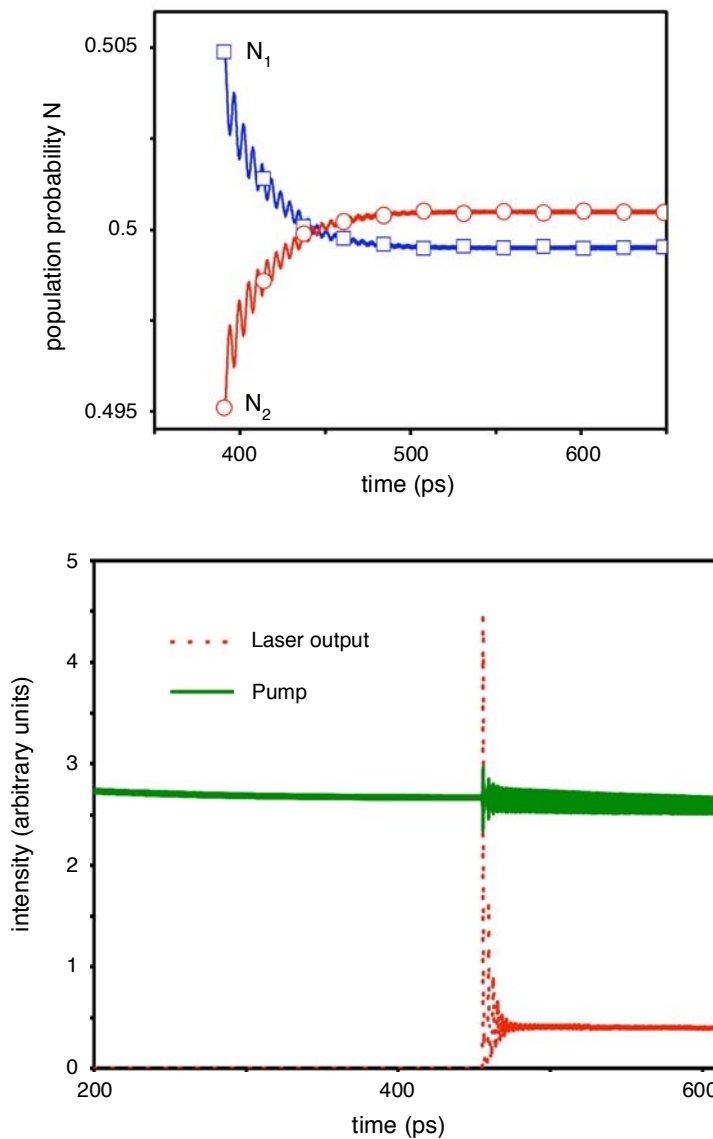


Fig. 12. Top: electron population density probability showing the inversion between Levels 1 and 2; Bottom: intensity output of the pump and laser output signals [55].

H. Biophotonics: Category 1 (Optical Interactions with Small Numbers of Living Cells)

Another important emerging application for FDTD modeling involves analyzing optical scattering by human biological cells and tissues. Such analyses are currently playing a key role in developing novel medical techniques for detecting precancerous conditions in the cervix and colon, with potential additional early detection applications for pancreatic, esophageal, and lung cancers. Fig. 13 illustrates the goal: to unambiguously distinguish normal cells from distressed cells when conventional optical microscopy fails.

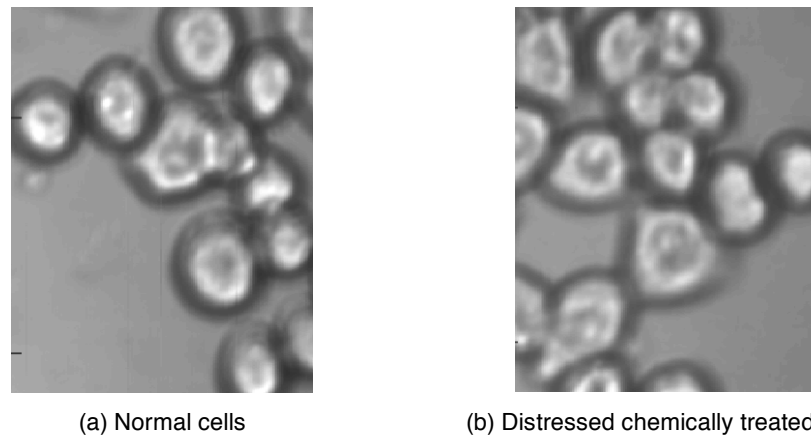


Fig. 13. Similar conventional microscope images: (a) normal HT-29 cells; (b) distressed chemically treated cells.

Fig. 14 illustrates applying FDTD to evaluate the sensitivity of optical backscattering and forward-scattering to small, random, refractive-index fluctuations spanning nanometer length scales [77]. Here, the spectral / angular distribution of scattered light from a randomly (and weakly) inhomogeneous dielectric sphere is compared to that for the homogeneous sphere of the same size and average refractive index.

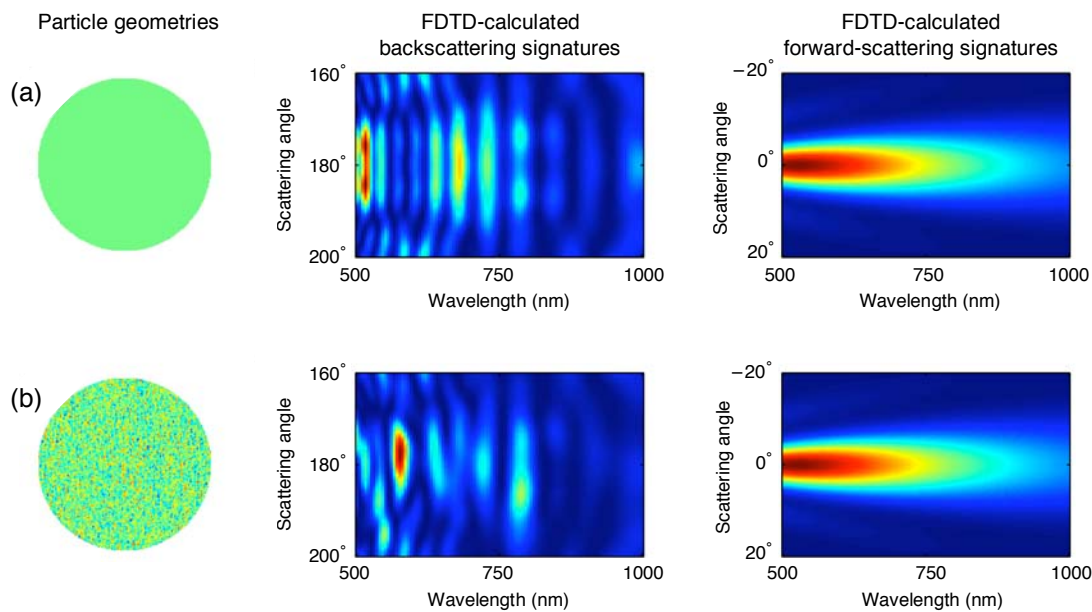


Fig. 14. FDTD-computed optical scattering signatures of a 4- μm -diameter sphere with average refractive index $n_{\text{avg}} = 1.1$: (a) homogeneous sphere; (b) random index fluctuations ($\Delta n = \pm 0.03$; ~ 50 nm) within sphere.

From Fig. 14, we see that there exists distinctive features of the backscattering spectral / angular distribution for the inhomogeneous case of Fig. 14(b) despite the fact that the inhomogeneities for this case are weak (only 3%) and much smaller (only about 50 nm) than the diffraction limit at the illuminating wavelengths. In contrast, the forward-scattering signature in Fig. 14(b) exhibits no distinctive features.

These FDTD models have supported laboratory optical backscattering measurements of rat colon tissues treated with the carcinogen AOM [78]. As shown in Fig. 15, only two weeks after application of the AOM, the treated colon tissues exhibited perturbed backscattering spectra apparently caused by the formation of subdiffraction tissue inhomogeneities akin to those in Fig. 14(b). Note that these could *not* be seen under a microscope. In fact, *these precancerous changes could not be detected by any existing pathology technique*. These findings led to the development of a preclinical instrument which has shown excellent sensitivity and specificity in initial trials with several hundred human subjects [79]. Currently, these trials are being greatly expanded.

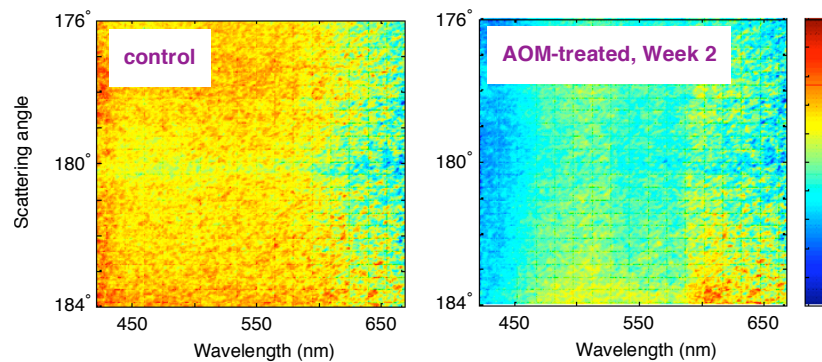


Fig. 15. Typical measured backscattering spectral / angular distributions for rat colon tissues [78].

Current FDTD modeling work in this area has shifted toward spectral analysis of individual backscattered pixels so that highly localized changes *within a single biological cell* can be investigated. First, as illustrated in Fig. 16, the near-to-far field transformation was augmented to yield a backscattered amplitude *image* [80].

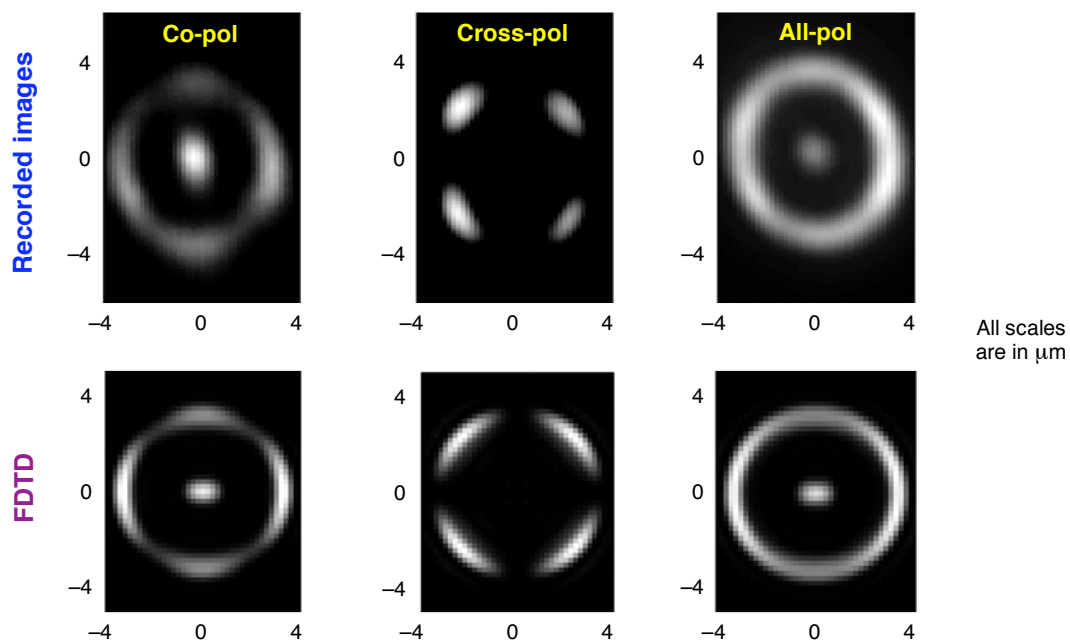


Fig.16. Agreement of measured / FDTD-calculated backscattered amplitude images of 6- μm dielectric sphere [80].

Next, assuming a normally incident plane wave, FDTD was used to calculate the optical spectra of individual pixels within the backscattered amplitude image of a rectangular layered material slab. Referring to Fig. 17, each layer of the slab was assumed to have a thickness in the order of 25 nanometers, with sub-micron lateral “checkerboard” inhomogeneities near the diffraction limit. As shown in this figure, it was determined that the backscattered spectra at pixels centered within each checkerboard square were highly correlated with those for a material slab having the same nanometer-scale layering, but no lateral variations (i.e., a 1-D illumination geometry) [81]. This yields additional evidence that nanometer-scale inhomogeneities can cause pronounced alterations of backscattering spectra. Furthermore, it suggests means to deduce the local layering of an inhomogeneous material structure (such as a living cell) by analyzing the spectra of individual pixels within its backscattered amplitude image.

Finally, exploiting the insights developed via FDTD modeling, a microscope system was constructed to acquire pixel-by-pixel backscattering spectra of individual living cells [81]. As shown in Fig. 18, this system was readily able to distinguish the normal HT-29 cells of Fig. 13 from their distressed, chemically treated counterparts.

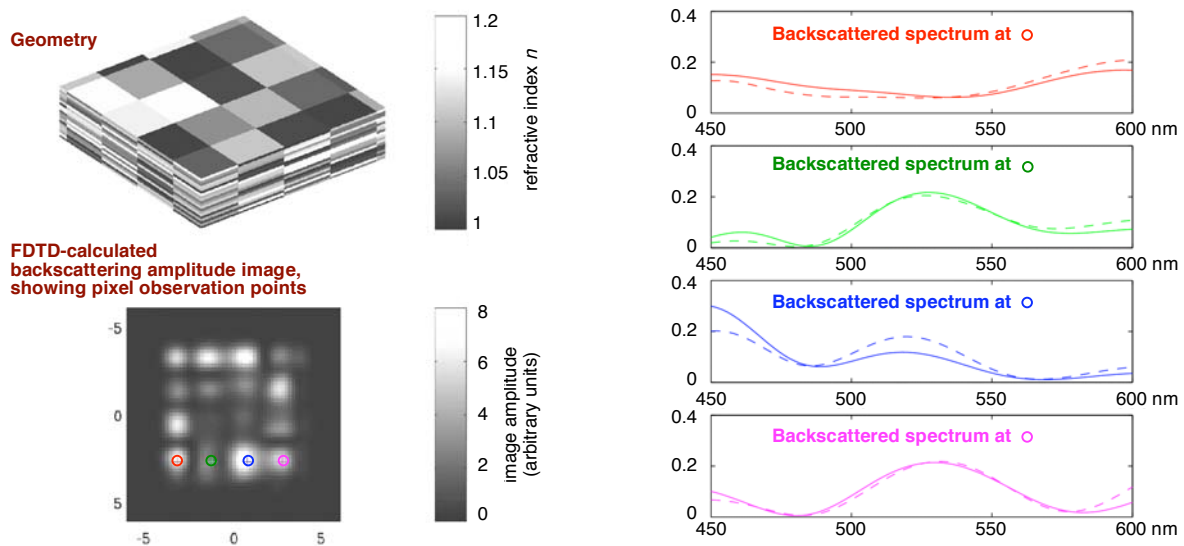


Fig. 17. FDTD-calculated spectra of four distinct pixels within the backscattered amplitude image of a layered material slab [81].

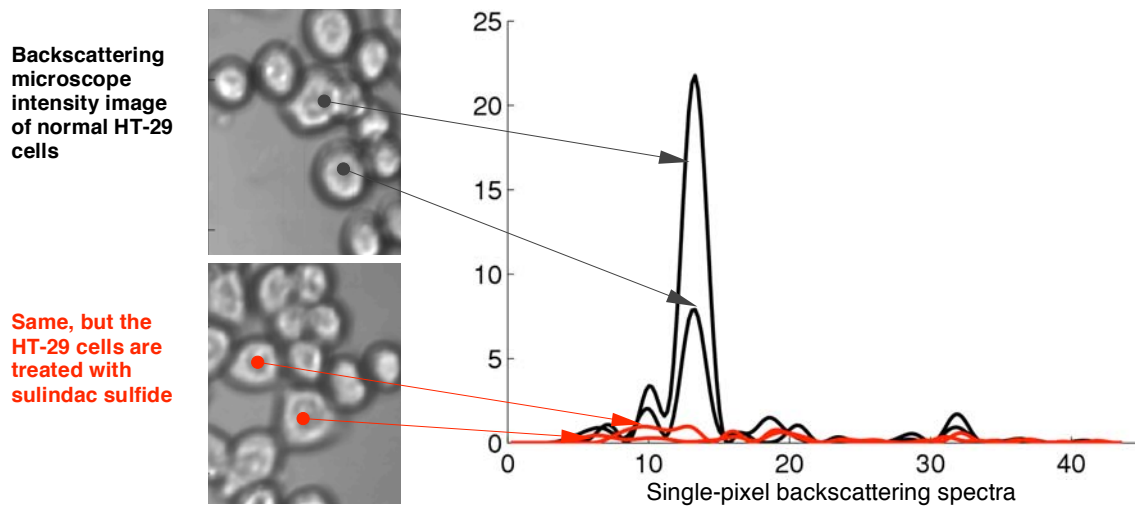


Fig. 18. Normal HT-29 cells have different pixel backscattering spectra than those chemically treated [81].

I. Biophotonics: Category 2 (Optical Interactions with Large Numbers of Living Cells)

Pseudospectral time-domain (PSTD) computational solutions of Maxwell's equations introduced by Liu [57, 58] permit coarse spatial sampling approaching the Nyquist limit. This characteristic of PSTD techniques permits modeling electromagnetic wave interactions in 3-D spatial regions spanning many tens of wavelengths. As a consequence, an important emerging biophotonics application of PSTD modeling involves analyzing light propagation through, and scattering by, large clusters of living cells; in fact, much larger clusters than possible using traditional FDTD techniques. Obtained directly from Maxwell's equations, PSTD solutions are more rigorous than many approximate techniques that are widely used by the biophotonics community. Hence, PSTD modeling affords new opportunities to advance a wide range of medical diagnoses and treatments that are based upon interactions of light with biological tissues.

Fig. 19 illustrates the accuracy of the Fourier-basis 3-D PSTD technique in calculating the differential scattering cross-section of a single dielectric sphere (diameter $d = 8 \mu\text{m}$, refractive index $n = 1.2$) [82]. The PSTD solution (wavelength $\lambda_0 = 750 \text{ nm}$, grid resolution $\Delta = 83.3 \text{ nm}$, staircased surface) agrees very well with the Mie series over a range of about $10^5:1$. Fig. 20 illustrates the accuracy of this technique in calculating the total scattering cross-section (TSCS) of a 20- μm cluster of 19 randomly positioned dielectric spheres (each $d = 6 \mu\text{m}$, $n = 1.2$) [82]. Here, the PSTD solution ($\Delta = 167 \text{ nm}$, staircased surfaces) agrees well with the results of a multi-sphere series expansion.

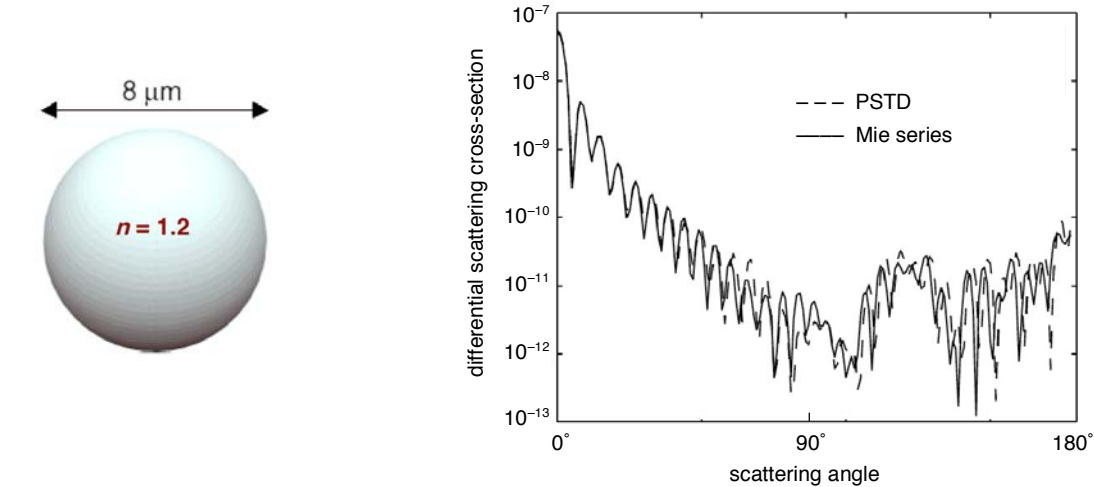


Fig. 19. Validation of Fourier-basis PSTD for scattering by a single sphere [82].

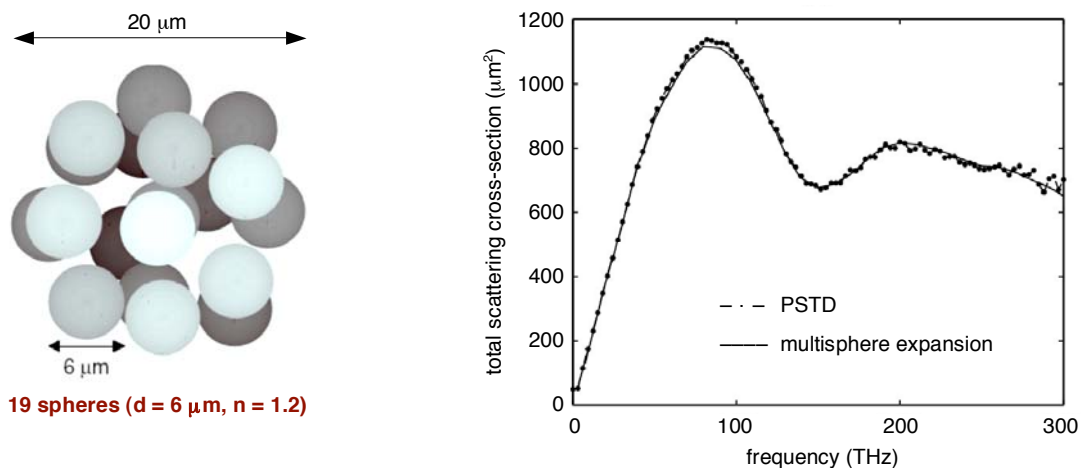


Fig. 20. Validation of Fourier-basis PSTD for scattering by a 20- μm cluster of 19 dielectric spheres [82].

The capability of the Fourier-basis 3-D PSTD technique to accurately solve the full-vector Maxwell's equations for closely coupled, electrically large objects opens up possibilities for accurately modeling optical interactions with clusters of biological cells. Fig. 21 illustrates a generic example wherein information regarding the diameter of individual particles within a cluster is obtained from its PSTD-computed TSCS [82]. Fig. 21(top) graphs versus frequency the PSTD results (grid resolution $\Delta = 167$ nm, staircased surfaces) for the TSCS of a 25- μm cluster of 192 randomly positioned dielectric spheres (each $d = 3$ μm , $n = 1.2$). Now, we perform a cross-correlation of this data set with the TSCS-versus-frequency characteristic of a single "trial" dielectric sphere of refractive index $n = 1.2$ and adjustable diameter d . We hypothesize that the maximum cross-correlation is achieved when the diameter of the trial sphere equals the diameter of the individual spheres comprising the cluster. Indeed, Fig. 21(bottom) shows that the peak cross-correlation occurs when the diameter of the trial sphere is 3.25 μm , within 10% of the actual 3 μm diameter. Similar results have been reported for a variety of clusters of dielectric spheres [82].

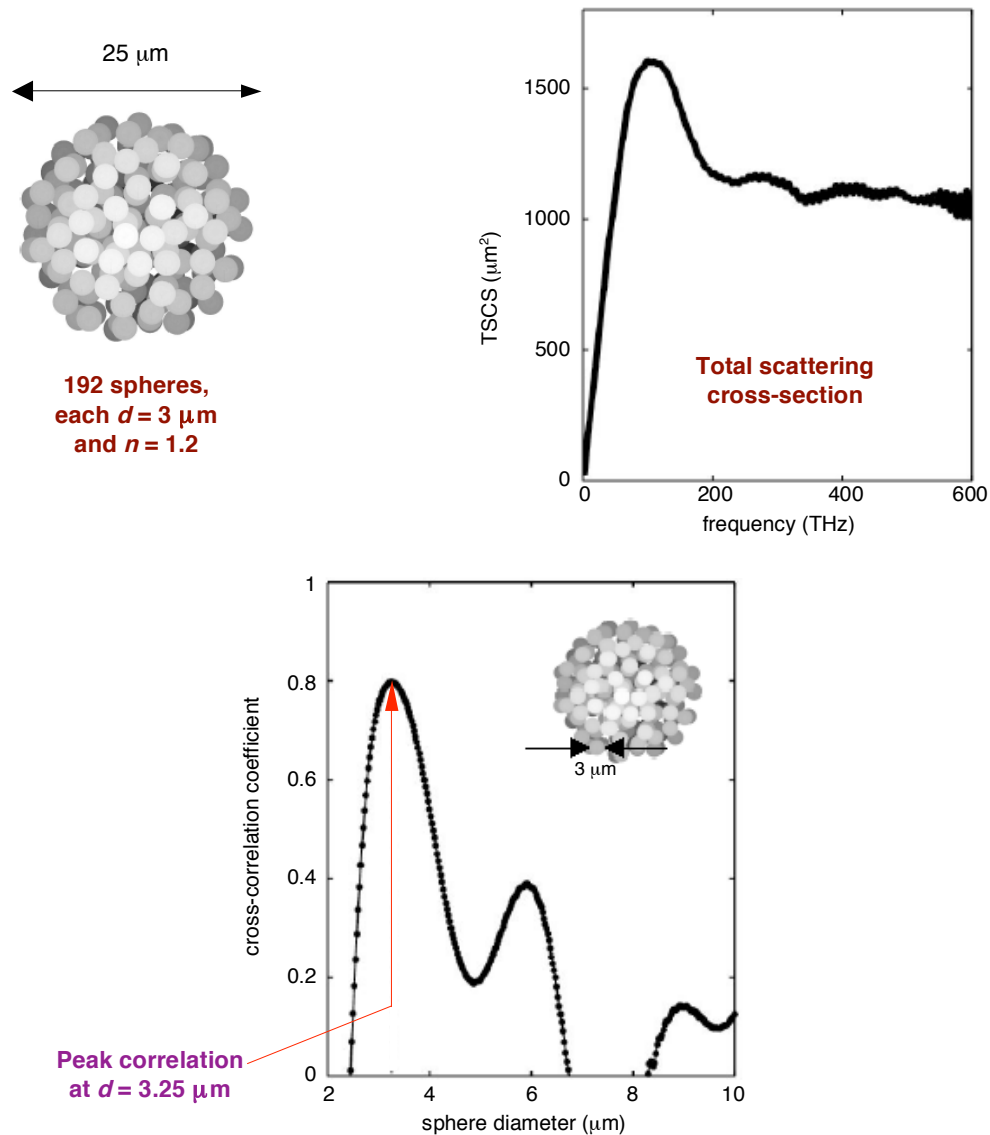


Fig. 21. Top: PSTD-calculated TSCS vs. frequency of a 25- μm cluster of 192 dielectric spheres ($d = 3$ μm , $n = 1.2$). Bottom: Cross-correlation of the top TSCS data set with the TSCS-vs.-frequency characteristic of a single trial dielectric sphere of the same refractive index ($n = 1.2$) but adjustable diameter [82].

V. FUTURE PROSPECTS

During the past 40 years since Yee's Paper #1, advances in FDTD theory and software and in general computing technology have elevated FDTD techniques to the top rank of computational tools for engineers and scientists studying electrodynamic phenomena and systems. There is every reason to believe that the steady pace of these advances will continue.

In particular, the author believes that a large expansion of FDTD and related techniques will occur in four research areas which cover the frequency spectrum from ELF past visible light: (1) geophysics and related remote sensing of the Earth and its atmosphere; (2) biophotonics; (3) nanometer-scale physics, especially interfacing with quantum electrodynamics; and (4) inverse scattering. Impacting these disparate areas is made possible by the extraordinary flexibility and robustness of FDTD and related grid-based time-domain solutions of Maxwell's equations, which arguably involve computational techniques which are the closest to how Mother Nature "solves" her electrodynamic problems.

ACKNOWLEDGEMENTS

The author recognizes the marvelous collaboration and warm friendship provided by Prof. Korada Umashankar during his all-too-brief lifetime. The author also says a hearty "thanks!" to all of his undergraduate and graduate research students over the years; to his project sponsors; and to his current collaborators, Profs. Vadim Backman and Xu Li of Northwestern University.

REFERENCES

- [1] K. S. Yee, "Numerical solution of initial boundary value problems involving Maxwell's equations in isotropic media," *IEEE Trans. Antennas Propagat.*, vol. 14, pp. 302–307, 1966.
- [2] K. L. Shlager and J. B. Schneider, "A Survey of the Finite-Difference Time-Domain Literature," Chap. 1 in *Advances in Computational Electrodynamics: The Finite-Difference Time-Domain Method*, A. Taflove, ed., Norwood, MA: Artech House, 1998.
- [3] A. Taflove and M. E. Brodwin, "Numerical solution of steady-state electromagnetic scattering problems using the time-dependent Maxwell's equations," *IEEE Trans. Microwave Theory Tech.*, vol. 23, pp. 623–630, 1975.
- [4] A. Taflove and M. E. Brodwin, "Computation of the electromagnetic fields and induced temperatures within a model of the microwave-irradiated human eye," *IEEE Trans. Microwave Theory Tech.*, vol. 23, pp. 888–896, 1975.
- [5] R. Holland, "Threde: a free-field EMP coupling and scattering code," *IEEE Trans. Nuclear Sci.*, vol. 24, pp. 2416–2421, 1977.
- [6] K. S. Kunz and K. M. Lee, "A three-dimensional finite-difference solution of the external response of an aircraft to a complex transient EM environment I: The method and its implementation," *IEEE Trans. Electromagn. Compat.*, vol. 20, pp. 328–333, 1978.
- [7] B. Engquist and A. Majda, "Absorbing boundary conditions for the numerical simulation of waves," *Mathematics of Computation*, vol. 31, pp. 629–651, 1977.
- [8] A. Bayliss and E. Turkel, "Radiation boundary conditions for wave-like equations," *Comm. Pure Appl. Math.*, vol. 23, pp. 707–725, 1980.
- [9] A. Taflove, "Application of the finite-difference time-domain method to sinusoidal steady-state electromagnetic penetration problems," *IEEE Trans. Electromagn. Compat.*, vol. 22, pp. 191–202, 1980.
- [10] G. Mur, "Absorbing boundary conditions for the finite-difference approximation of the time-domain electromagnetic field equations," *IEEE Trans. Electromagn. Compat.*, vol. 23, pp. 377–382, 1981.
- [11] K. R. Umashankar and A. Taflove, "A novel method to analyze electromagnetic scattering of complex objects," *IEEE Trans. Electromagn. Compat.*, vol. 24, pp. 397–405, 1982.
- [12] A. Taflove and K. R. Umashankar, "Radar cross section of general three-dimensional scatterers," *IEEE Trans. Electromagn. Compat.*, vol. 25, pp. 433–440, 1983.
- [13] Z. P. Liao, H. L. Wong, B. P. Yang, and Y. F. Yuan, "A transmitting boundary for transient wave analyses," *Scientia Sinica (series A)*, vol. XXVII, pp. 1063–1076, 1984.

- [14] W. Gwarek, "Analysis of an arbitrarily shaped planar circuit — A time-domain approach," *IEEE Trans. Microwave Theory Tech.*, vol. 33, pp. 1067–1072, 1985.
- [15] D. H. Choi and W. J. Hofer, "The finite-difference time-domain method and its application to eigenvalue problems," *IEEE Trans. Microwave Theory Tech.*, vol. 34, pp. 1464–1470, 1986.
- [16] G. A. Kriegsmann, A. Taflove, and K. R. Umashankar, "A new formulation of electromagnetic wave scattering using an on-surface radiation boundary condition approach," *IEEE Trans. Antennas Propagat.*, vol. 35, pp. 153–161, 1987.
- [17] T. G. Moore, J. G. Blaschak, A. Taflove, and G. A. Kriegsmann, "Theory and application of radiation boundary operators," *IEEE Trans. Antennas Propagat.*, vol. 36, pp. 1797–1812, 1988.
- [18] K. R. Umashankar, A. Taflove, and B. Beker, "Calculation and experimental validation of induced currents on coupled wires in an arbitrary shaped cavity," *IEEE Trans. Antennas Propagat.*, vol. 35, pp. 1248–1257, 1987.
- [19] A. Taflove, K. R. Umashankar, B. Beker, F. A. Harfoush, and K. S. Yee, "Detailed FDTD analysis of electromagnetic fields penetrating narrow slots and lapped joints in thick conducting screens," *IEEE Trans. Antennas Propagat.*, vol. 36, pp. 247–257, 1988.
- [20] T. G. Jurgens, A. Taflove, K. R. Umashankar, and T. G. Moore, "Finite-difference time-domain modeling of curved surfaces," *IEEE Trans. Antennas Propagat.*, vol. 40, pp. 357–366, 1992.
- [21] A. C. Cangellaris, C.-C. Lin, and K. K. Mei, "Point-matched time-domain finite element methods for electromagnetic radiation and scattering," *IEEE Trans. Antennas Propagat.*, vol. 35, pp. 1160–1173, 1987.
- [22] V. Shankar, A. H. Mohammadian, and W. F. Hall, "A time-domain finite-volume treatment for the Maxwell equations," *Electromagnetics*, vol. 10, pp. 127–145, 1990.
- [23] N. K. Madsen and R. W. Ziolkowski, "A three-dimensional modified finite volume technique for Maxwell's equations," *Electromagnetics*, vol. 10, pp. 147–161, 1990.
- [24] D. M. Sullivan, O. P. Gandhi, and A. Taflove, "Use of the finite-difference time-domain method in calculating EM absorption in man models," *IEEE Trans. Biomed. Engrg.*, vol. 35, pp. 179–186, 1988.
- [25] X. Zhang, J. Fang, K. K. Mei, and Y. Liu, "Calculation of the dispersive characteristics of microstrips by the time-domain finite-difference method," *IEEE Trans. Microwave Theory Tech.*, vol. 36, pp. 263–267, 1988.
- [26] J. Fang, *Time-Domain Finite Difference Computations for Maxwell's Equations*, Ph.D. dissertation, EECS Dept., Univ. of California, Berkeley, CA, 1989.
- [27] T. Kashiwa and I. Fukai, "A treatment by FDTD method of dispersive characteristics associated with electronic polarization," *Microwave Optics Tech. Lett.*, vol. 3, pp. 203–205, 1990.
- [28] R. Luebbers, F. Hunsberger, K. Kunz, R. Standler, and M. Schneider, "A frequency-dependent finite-difference time-domain formulation for dispersive materials," *IEEE Trans. Electromagn. Compat.*, vol. 32, pp. 222–229, 1990.
- [29] R. M. Joseph, S. C. Hagness, and A. Taflove, "Direct time integration of Maxwell's equations in linear dispersive media with absorption for scattering and propagation of femtosecond electromagnetic pulses," *Optics Lett.*, vol. 16, pp. 1412–1414, 1991.
- [30] J. G. Maloney, G. S. Smith, and W. R. Scott, Jr., "Accurate computation of the radiation from simple antennas using the finite-difference time-domain method," *IEEE Trans. Antennas Propagat.*, vol. 38, pp. 1059–1065, 1990.
- [31] D. S. Katz, A. Taflove, M. J. Piket-May, and K. R. Umashankar, "FDTD analysis of electromagnetic wave radiation from systems containing horn antennas," *IEEE Trans. Antennas Propagat.*, vol. 39, pp. 1203–1212, 1991.
- [32] P. A. Tirkas and C. A. Balanis, "Finite-difference time-domain technique for radiation by horn antennas," *Proc. 1991 IEEE Antennas Propagat. Soc. Intl. Symp.*, vol. 3, pp. 1750–1753, 1991.

- [33] E. Sano and T. Shibata, "Fullwave analysis of picosecond photoconductive switches," *IEEE J. Quantum Electron.*, vol. 26, pp. 372–377, 1990.
- [34] S. M. El-Ghazaly, R. P. Joshi, and R. O. Grondin, "Electromagnetic and transport considerations in subpicosecond photoconductive switch modeling," *IEEE Trans. Microwave Theory Tech.*, vol. 38, pp. 629–637, 1990.
- [35] R. J. Luebbers, K. S. Kunz, M. Schneider, and F. Hunsberger, "A finite-difference time-domain near zone to far zone transformation," *IEEE Trans. Antennas Propagat.*, vol. 39, pp. 429–433, 1991.
- [36] P. M. Goorjian and A. Taflove, "Direct time integration of Maxwell's equations in nonlinear dispersive media for propagation and scattering of femtosecond electromagnetic solitons," *Optics Lett.*, vol. 17, pp. 180–182, 1992.
- [37] R. W. Ziolkowski and J. B. Jerkins, "Full-wave vector Maxwell's equations modeling of self-focusing of ultra-short optical pulses in a nonlinear Kerr medium exhibiting a finite response time," *J. Optical Soc. America B*, vol. 10, pp. 186–198, 1993.
- [38] R. M. Joseph and A. Taflove, "Spatial soliton deflection mechanism indicated by FDTD Maxwell's equations modeling," *IEEE Photonics Tech. Lett.*, vol. 2, pp. 1251–1254, 1994.
- [39] W. L. Ko and R. Mittra, "A combination of FDTD and Prony's methods for analyzing microwave integrated circuits," *IEEE Trans. Microwave Theory Tech.*, vol. 39, pp. 2176–2181, 1991.
- [40] J. A. Pereda, L. A. Vielva, and A. Prieto, "Computation of resonant frequencies and quality factors of open dielectric resonators by a combination of the finite-difference time-domain (FDTD) and Prony's methods," *IEEE Microwave Guided Wave Lett.*, vol. 2, pp. 431–433, 1992.
- [41] J. Chen, C. Wu, T. K. Y. Lo, K.-L. Wu, and J. Litva, "Using linear and nonlinear predictors to improve the computational efficiency of the FDTD algorithm," *IEEE Trans. Microwave Theory Tech.*, vol. 42, pp. 1992–1997, 1994.
- [42] V. Jandhyala, E. Michielssen, and R. Mittra, "FDTD signal extrapolation using the forward-backward autoregressive (AR) model," *IEEE Microwave Guided Wave Lett.*, vol. 4, pp. 163–165, 1994.
- [43] S. Dey and R. Mittra, "Efficient computation of resonant frequencies and quality factors of cavities via a combination of the finite-difference time-domain technique and the Padé approximation," *IEEE Microwave Guided Wave Lett.*, vol. 8, pp. 415–417, 1998.
- [44] W. Sui, D. A. Christensen, and C. H. Durney, "Extending the two-dimensional FDTD method to hybrid electromagnetic systems with active and passive lumped elements," *IEEE Trans. Microwave Theory Tech.*, vol. 40, pp. 724–730, 1992.
- [45] B. Toland, B. Houshmand, and T. Itoh, "Modeling of nonlinear active regions with the FDTD method," *IEEE Microwave Guided Wave Lett.*, vol. 3, pp. 333–335, 1993.
- [46] V. A. Thomas, M. E. Jones, M. J. Picket-May, A. Taflove, and E. Harrigan, "The use of SPICE lumped circuits as sub-grid models for FDTD high-speed electronic circuit design," *IEEE Microwave Guided Wave Lett.*, vol. 4, pp. 141–143, 1994.
- [47] J. P. Berenger, "A perfectly matched layer for the absorption of electromagnetic waves," *J. Comp. Phys.*, vol. 114, pp. 185–200, 1994.
- [48] D. S. Katz, E. T. Thiele, and A. Taflove, "Validation and extension to three dimensions of the Berenger PML absorbing boundary condition for FDTD meshes," *IEEE Microwave Guided Wave Lett.*, vol. 4, pp. 268–270, 1994.
- [49] C. E. Reuter, R. M. Joseph, E. T. Thiele, D. S. Katz, and A. Taflove, "Ultrawideband absorbing boundary condition for termination of waveguiding structures in FDTD simulations," *IEEE Microwave Guided Wave Lett.*, vol. 4, pp. 344–346, 1994.
- [50] Z. S. Sacks, D. M. Kingsland, R. Lee, and J. F. Lee, "A perfectly matched anisotropic absorber for use as an absorbing boundary condition," *IEEE Trans. Antennas Propagat.*, vol. 43, pp. 1460–1463, 1995.

- [51] S. D. Gedney, "An anisotropic perfectly matched layer absorbing media for the truncation of FDTD lattices," *IEEE Trans. Antennas Propagat.*, vol. 44, pp. 1630–1639, 1996.
- [52] R. W. Ziolkowski, J. M. Arnold, and D. M. Gogny, "Ultrafast pulse interactions with two-level atoms," *Phys. Rev. A*, vol. 52, pp. 3082–3094, 1995.
- [53] A. S. Nagra and R. A. York, "FDTD analysis of wave propagation in nonlinear absorbing and gain media," *IEEE Trans. Antennas Propagat.*, vol. 46, pp. 334–340, 1998.
- [54] Y. Huang, *Simulation of Semiconductor Materials Using FDTD Method*, M.S. thesis, Northwestern University, Evanston, IL, 2002.
- [55] S.-H. Chang and A. Taflove, "Finite-difference time-domain model of lasing action in a four-level two-electron atomic system," *Optics Express*, vol. 12, pp. 3827–3833, 2004.
- [56] M. Krumpholz and L. P. B. Katehi, "MRTD: New time-domain schemes based on multiresolution analysis," *IEEE Trans. Microwave Theory Tech.*, vol. 44, pp. 555–572, 1996.
- [57] Q. H. Liu, *The PSTD Algorithm: A Time-Domain Method Requiring Only Two Grids Per Wavelength*, New Mexico State Univ., Las Cruces, NM, Tech. Rept. NMSU-ECE96-013, 1996.
- [58] Q. H. Liu, "The pseudospectral time-domain (PSTD) method: A new algorithm for solutions of Maxwell's equations," *Proc. 1997 IEEE Antennas Propagat. Soc. Intl. Symp.*, vol. 1, pp. 122–125, 1997.
- [59] O. M. Ramahi, "The complementary operators method in FDTD simulations," *IEEE Antennas Propagat. Mag.*, vol. 39, pp. 33–45, Dec. 1997.
- [60] S. Dey and R. Mittra, "A locally conformal finite-difference time-domain algorithm for modeling three-dimensional perfectly conducting objects," *IEEE Microwave Guided Wave Lett.*, vol. 7, pp. 273–275, 1997.
- [61] J. G. Maloney and M. P. Kesler, "Analysis of Periodic Structures," Chap. 6 in *Advances in Computational Electrodynamics: The Finite-Difference Time-Domain Method*, A. Taflove, (ed.), Norwood, MA: Artech House, 1998.
- [62] J. B. Schneider and C. L. Wagner, "FDTD dispersion revisited: Faster-than-light propagation," *IEEE Microwave Guided Wave Lett.*, vol. 9, pp. 54–56, 1999.
- [63] T. Namiki, "3-D ADI-FDTD method — Unconditionally stable time-domain algorithm for solving full vector Maxwell's equations," *IEEE Trans. Microwave Theory Tech.*, vol. 48, pp. 1743–1748, 2000.
- [64] F. Zheng, Z. Chen, and J. Zhang, "Toward the development of a three-dimensional unconditionally stable finite-difference time-domain method," *IEEE Trans. Microwave Theory Tech.*, vol. 48, pp. 1550–1558, 2000.
- [65] J. A. Roden and S. D. Gedney, "Convolutional PML (CPML): An efficient FDTD implementation of the CFS-PML for arbitrary media," *Microwave Optical Tech. Lett.*, vol. 27, pp. 334–339, 2000.
- [66] T. Rylander and A. Bondeson, "Stable FDTD-FEM hybrid method for Maxwell's equations," *Comput. Phys. Comm.*, vol. 125, pp. 75–82, 2000.
- [67] M. Hayakawa and T. Otsuyama, "FDTD analysis of ELF wave propagation in inhomogeneous subionospheric waveguide models," *ACES J.*, vol. 17, pp. 239–244, 2002.
- [68] J. J. Simpson and A. Taflove, "Three-dimensional FDTD modeling of impulsive ELF propagation about the Earth-sphere," *IEEE Trans. Antennas Propagat.*, vol. 52, pp. 443–451, 2004.
- [69] J. J. Simpson, R. P. Heikes, and A. Taflove, "FDTD modeling of a novel ELF radar for major oil deposits using a three-dimensional geodesic grid of the Earth-ionosphere waveguide," *IEEE Trans. Antennas Propagat.*, vol. 54, pp. 1734–1741, 2006.
- [70] H. De Raedt, K. Michielsen, J. S. Kole, and M. T. Figge, "Solving the Maxwell equations by the Chebyshev method: A one-step finite difference time-domain algorithm," *IEEE Trans. Antennas Propagat.*, vol. 51, pp. 3155–3160, 2003.
- [71] N. Chavannes, R. Tay, N. Nikoloski, and N. Kuster, "Suitability of FDTD-based TCAD tools for RF design of mobile phones," *IEEE Antennas Propagat. Magazine*, vol. 45, pp. 52–66, Dec. 2003.

- [72] E. J. Bond, X. Li, S. C. Hagness, and B. D. Van Veen, "Microwave imaging via space-time beamforming for early detection of breast cancer," *IEEE Trans. Antennas Propagat.*, vol. 51, pp. 1690–1705, 2003.
- [73] J. J. Simpson, A. Taflove, J. A. Mix, and H. Heck, "Substrate integrated waveguides optimized for ultrahigh-speed digital interconnects," *IEEE Trans. Microwave Theory Tech.*, vol. 54, pp. 1983–1990, 2006.
- [74] H.-G. Park, S.-H. Kim, S.-H. Kwon, Y.-G. Ju, J.-K. Yang, J.-H. Baek, S.-B. Kim, and Y.-H. Lee, "Electrically driven single-cell photonic crystal laser," *Science*, vol. 305, pp. 1444–1447, 2004.
- [75] L. Yin, V. K. Vlasko-Vlasov, A. Rydh, J. Pearson, U. Welp, S.-H. Chang, S. K. Gray, G. C. Schatz, D. B. Brown, and C. W. Kimball, "Surface plasmons at single nanoholes in Au films," *Applied Physics Lett.*, vol. 85, pp. 467–469, 2004.
- [76] M. F. Yanik, S. Fan, M. Soljacic, and J. D. Joannopoulos, "All-optical transistor action with bistable switching in a photonic crystal cross-waveguide geometry," *Optics Lett.*, vol. 28, pp. 2506–2508, 2003.
- [77] X. Li, A. Taflove, and V. Backman, "Recent progress in exact and reduced-order modeling of light-scattering properties of complex structures," *IEEE J. Selected Topics in Quantum Electronics, Special Issue on Biophotonics*, vol. 11, pp. 759–765, 2005.
- [78] H. K. Roy, Y. Liu, R. Wali, Y. L. Kim, A. K. Kromine, M. J. Goldberg, and V. Backman, "Four-dimensional elastic light-scattering fingerprints as preneoplastic markers in the rat model of colon carcinogenesis," *Gastroenterology*, vol. 126, pp. 1071–1081, 2004.
- [79] H. K. Roy, Y. L. Kim, Y. Liu, R. K. Wali, M. J. Goldberg, V. Turhitsky, J. Horwitz, and V. Backman, "Risk-stratification of colon carcinogenesis through enhanced backscattering (EBS) spectroscopy analysis of the uninvolved colonic mucosa," *Clinical Cancer Research*, vol. 19, pp. 961–968, 2006.
- [80] X. Li, "Synthesis of backscattering microscope amplitude images from FDTD-computed near fields," manuscript in preparation.
- [81] Y. Liu, P. Pradhan, X. Li, Y. L. Kim, R. K. Wali, H. K. Roy, A. Taflove, and V. Backman, "Alteration of intracellular mesoscopic light transport in the earliest stage of carcinogenesis demonstrated by single-cell partial-wave spectroscopy," manuscript in preparation.
- [82] S. H. Tseng, A. Taflove, D. Maitland, and V. Backman, "Pseudospectral time-domain simulations of multiple light scattering in three-dimensional macroscopic random media," *Radio Science*, vol. 41, RS4009, doi:10.1029/2005RS003408, 2006.



Allen Taflove is a professor in Northwestern University's EECS Department. He has helped to pioneer FDTD algorithms and applications since 1971. His publications include more than 115 journal papers and three editions (1995, 2000, and 2005) of the book *Computational Electrodynamics: The Finite-Difference Time-Domain Method*, which has become a standard reference in the FDTD field. He is listed by the Institute for Scientific Information as one of the most cited technical authors in the world.

Miniature Antennas and Arrays Embedded within Magnetic Photonic Crystals and Other Novel Materials

John L. Volakis, Kubilay Sertel, and Chi-Chih Chen

ElectroScience Laboratory, Electrical and Computer Engineering Dept.
The Ohio State University
1320 Kinnear Rd., Columbus, OH 43212 USA; Email: volakis@ece.osu.edu

Abstract — Engineered materials, such as new composites, electromagnetic bandgap and periodic structures have been of strong interest in recent years due to their extraordinary and unique electromagnetic behaviors. This paper will address how modified materials, inductive/capacitive lumped loads and low loss magnetic materials/crystals are impacting antenna design with the goal of overcoming miniaturization challenges (viz. bandwidth and gain reduction, multi-functionality etc.). Dielectric design and texturing for impedance matching has, for example, led to significant size reduction and higher bandwidth low frequency antennas. Examples showing a factor of 2 or more reduction in ultrawideband antennas will be shown and operating down to nearly 100MHz using a 6" aperture. A recently introduced new class of magnetic photonic crystals (MPCs) and Degenerate Band Edge (DBE), displaying spectral nonreciprocity are also introduced. Studies of these crystals have demonstrated that MPCs exhibit the interesting phenomena of (a) drastic incoming wave slow down, coupled with (b) significant amplitude growth while (c) maintaining minimal reflection at the interface with free space. The phenomena are associated with diverging frozen modes that occur around the stationary inflection points within the band diagram. Taking advantage of the frozen mode phenomena, we demonstrate that individual antenna elements and linear or volumetric arrays embedded within the MPC and DBE structures allow for supergain effects that can lead to novel miniature (high sensitivity and high gain antennas and sensors) array configurations.

I. INTRODUCTION

Engineered materials, such as new composites, electromagnetic bandgap [1], [2], and periodic structures have attracted considerable interest in recent years due to their remarkable and unique electromagnetic behavior. As a result, an extensive literature on the theory and application of artificially modified materials has risen. Already photonic crystals have been utilized in RF applications such as waveguides, filters, and cavities due to their extraordinary propagation characteristics [3]-[8].

One of the most interesting properties associated with photonic crystals relates to their high Q resonances, achieved when a defect is introduced within the periodic structure. When an antenna element is placed within the high Q cavity, it is then possible to harness the high fields and generate exceptional gain. Experiments have already demonstrated this enhanced gain by placing small radiating elements into a cavity built around a photonic crystal. Specifically, Temelkuran, et.al. [7] and Biswas, et.al. [8] reported a received power enhancement by a factor of 180 at the resonant frequency of the cavity.

More recently, computations using double-negative materials [9] illustrate that extraordinary gain can also be achieved when small dipoles are placed inside other exotic materials that exhibit resonance at specific frequencies [10]. However, an issue with the double negative and left-handed materials is their practical realization. In this paper, we present a new class photonic crystals [9]-[18] fabricated from available material structures such as rutile, alumina, titanates and CVGs. Of importance is that these crystals exhibit much larger gain without requiring excessive volume. As such, they may be applicable for hand held devices. Of importance is also their greater bandwidth and improved matching (due to their resonance away from the band edge). Specifically (see Fig. 1), they combine the two unique properties of (i) minimal reflection at the interface of the periodic assembly forming the crystal, implying impedance matching, and (ii) wave slow down leading to miniaturization, and concurrently causing large amplitude growths within the material. The latter is of importance in realizing high gain antennas using smaller volumes. Recent computational examples have demonstrated a gain increase of as much as 15 dB for a small dipole placed within the crystal [14]. Experiments using periodic assemblies of FSS that realize the desirable band-diagram have also validated this gain increase.

The paper discusses some of these successes and proceeds with a discussion on the challenges of fabricating high contrast materials, their loss properties, and their integration with printed antennas.

In contrast to standard photonic crystals, the MPC crystals

- Exhibit little reflection from the interface (nearly perfect matching)
- Exhibit dramatic wave slow down since higher order derivatives in the k - ω curve vanish, flattening the k - ω curve

and

- Wave slow down implies inherent miniaturization and high field concentration leading to very high gains
- Minimal reflection at the interface using high contrast materials implies further miniaturization, good impedance matching, higher radiation efficiency

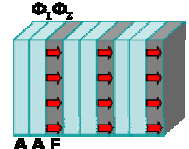
Stationary Inflection Point

$$\frac{\partial \omega}{\partial k} = 0, \frac{\partial^2 \omega}{\partial k^2} = 0, \frac{\partial^3 \omega}{\partial k^3} \neq 0$$

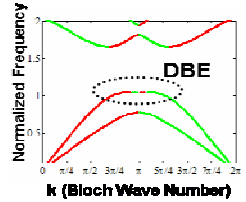
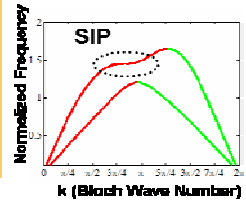
Degenerate Band Edge

$$\frac{\partial \omega}{\partial k} = 0, \frac{\partial^2 \omega}{\partial k^2} = 0, \frac{\partial^3 \omega}{\partial k^3} = 0, \frac{\partial^4 \omega}{\partial k^4} \neq 0$$

Magnetic Photonic Crystals & Degenerate Band Edge Crystals



- **A** : Anisotropic Dielectrics
- **F** : Ferromagnetic Material



Frozen Mode

Fig. 1. Properties of the magnetic photonic crystals (MPC) and their related Degenerate Band Edge (DBE) crystals formed by a periodic array of 3-layer unit cells. MPCs require at least one layer of magnetic materials whereas the DBEs are non-magnetic and therefore easily realizable. Both, MPCs and DBEs require the presence of anisotropy to realize their unique band diagrams.

The potential of fabricating printed microstrip lines that exhibit the same band diagram is a recent discovery that could lead to a variety of miniature microwave components as well as high sensitivity sensors. We begin below by noting that even properly designed materials with embedded inductive loadings can have significant impact in reducing antenna size and improving bandwidth properties. These modifications can be easily done and can be integrated into existing systems without much increase in cost for their adaptation.

II. MINIATURE ULTRAWIDEBAND ANTENNAS USING INDUCTIVE AND MATERIAL LOADING

Novel inductive loading within polymer structures has shown to be extremely effective in reducing antenna size, with particular emphasis on conformal installations. The motivation for using inductive loading comes from the need to emulate magnetic materials [21], [22]. By introducing inductive loading (capacitive loading is typically inherent to the structure), the antenna impedance can be matched as the antenna is miniaturized by increasing the dielectric loading. Our initial approach to implementing inductive loading was based on the artificial transmission line (ATL) miniaturization technique [21], [23]. The ATL concept of implementing inductive loading utilized distributed serial inductor elements to increase the inductance of the antenna. Avoiding use of chip inductors is critical since we need to suppress inherent losses. An alternative way to implement inductive loading is by coiling the spiral arm such that it resembles a helix as shown in Fig. 2 for a 6 inch diameter spiral antenna. Here, the coiled section of the spiral arm has a rectangular cross section which

allows us to control the inductance of the coil using the pitch, width and thickness of the coil separately. In this case, the thickness remains constant while the width and pitch are varied to create a smooth transition from the untreated portion to the inductive section of the spiral arm.

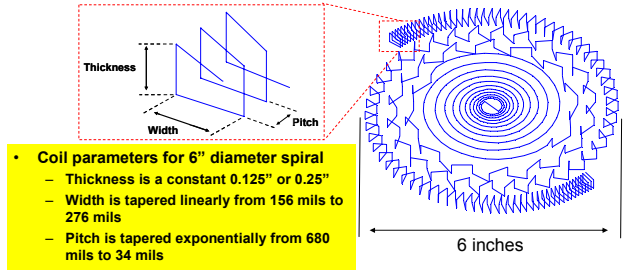


Fig. 2. Implementing inductive loading within a spiral antenna by coiling the conductor as it concurrently spirals away from the center.

We proceeded to use the concept of volumetric inductive loading via coiling [23], [24] to implement the wave slow down and miniaturization. The performance improvement is shown in Fig. 3, and shows that we have indeed achieved a 6'' design that operates down to 130 MHz (-15 dBic gain) that is only $\lambda/15$ in size, and 7.5 times smaller than the nominal $\lambda/2$ dipole. Of importance is that the frequency has shifted from 320 MHz down to 130 MHz with the same performance (nearly a factor of 2.5 reduction in frequency performance). Remarkably, we are also seen to approach the theoretical limit of miniaturization for a given aperture size [23], [25], [26].

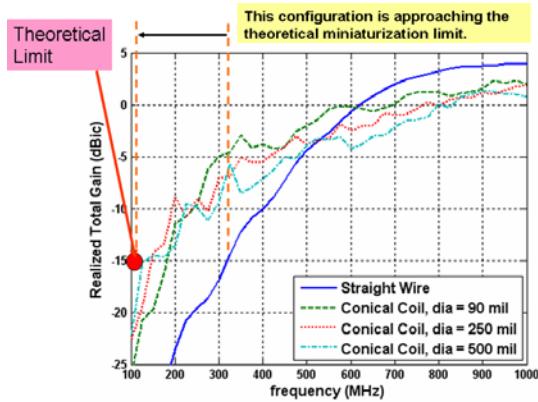
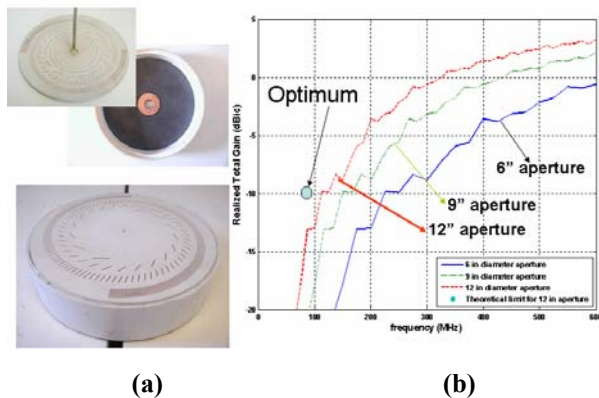


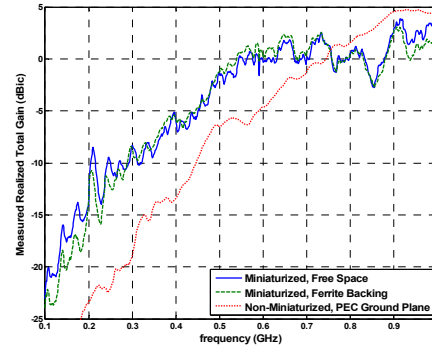
Fig. 3. Using coiling to shift antenna performance to lower frequencies.

The inductively loaded 6” spiral shown in Fig. 2 was also manufactured and measured along with a composite metal-magnetic ground plane. The assembled antenna is shown in Fig. 4(a) and has a total thickness of 1.5”. The 6” spiral was fabricated on a 0.25 inch thick Roger’s TMM4 substrate ($\epsilon_r = 4.5$) using standard printed circuit board manufacturing technology. The measured realized gain is shown in Fig. 4(c) along with the measured gain of a non-miniaturized spiral antenna backed by a metallic ground plane. This plot clearly demonstrates the superior performance of the miniaturized spiral below 600 MHz. For these frequencies, the miniaturized spiral with ferrite backing is able to achieve 5-10 dBi more gain than the non-miniaturized spiral. Because the spiral is a frequency independent antenna, the antenna can be scaled to any aperture size to meet the desired specifications. For instance, Fig. 4 (b) also shows the analytical performance (free space) of the 6” aperture in addition to two scaled versions that are 9” and 12” in diameter. From Fig. 4(b), the 12” aperture is seen to operate down to 80 MHz at the -15 dBic gain and to 110 MHz at the -10 dBic gain point. Again, we also show the theoretical limit point for the 12” aperture, and note that it is close to the achieved performance.



(a)

(b)



(c)

Fig. 4. Display of fabricated antenna articles incorporating volumetric coiling within dielectric loading and over a magnetic-PEC ground plane; Top left: 6” fabricated antenna 1.5” thick; Bottom: measurement results with and without ferrite backing.

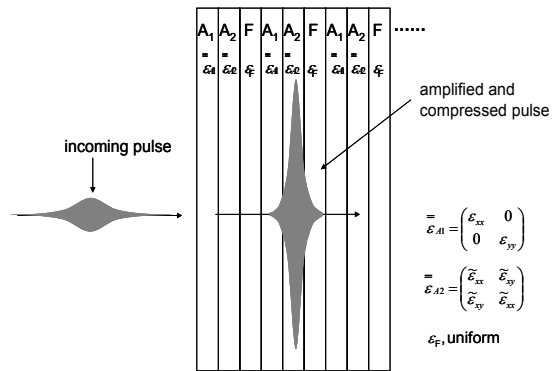


Fig. 5. Field compression within the MPC crystal: An incident pulse propagating towards right couples into the MPC and excites the frozen mode within the crystal.

III. VOLUMETRIC CRYSTALS FOR HIGH GAIN NARROW BAND ANTENNAS

MPC and DBE crystals have been pursued because they allow for further miniaturization and higher gains. However, so far, their promise has only been demonstrated for narrowband antennas. In [14], we demonstrated that the so-called *frozen mode* can indeed be realized in finite thickness magnetic photonic assemblies (MPCs) using a practical combination of materials. This mode is shown in Fig. 5. As displayed, the incoming pulse enters the periodic assembly (crystal) with very little reflection (15% of the field is typically reflected). Once in the crystal, it shows down, while it concurrently increases in amplitude by more than a factor of 10 for material with nominal losses.

A realization of the MPC and DBE crystal is shown in Fig. 6 using two misaligned anisotropic dielectric layers and an isotropic layer built into a unit cell. It was shown in [18] that it is possible to achieve a four-fold amplitude increase in the coupled electric field amplitude using 20 such unit cells to form a degenerate band edge (DBE) crystal which does not even require magnetic materials. As a direct consequence of this spatial focusing, the directivity and gain of a simple dipole antenna placed within the MPC crystal (see Fig. 7) was shown [14] to increase by 12.7 dB (~20 fold). Also shown in Fig. 7 is the effect of material loss on the overall gain of the dipole embedded within. A very slight loss of $\tan \delta = 10^{-5}$ reduces antenna gain by only 2 dB, and this gives much promise for the practical realization of those materials.

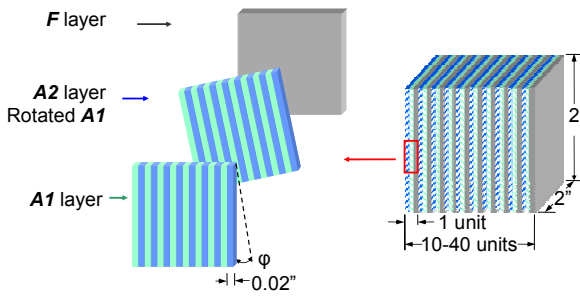


Fig. 6. MPA design: A1, A2 are two of the same anisotropic dielectric layers with ϕ being the misalignment angle between A1 and A2. F is the Faraday rotation ferromagnetic layer.

Of even greater importance is the realization of significant gain using periodic assemblies forming the so called DBE crystal. The fabrication of the DBE crystal can be done without magnetic materials and even more importantly using an arrangement or stacks of Frequency Selective Surfaces (FSS) surfaces as displayed in Fig. 8. In doing so, we mimicked the anisotropy in the dielectric layers by printing very thin conducting strips on low-loss Rogers RO4350 substrate and designed the DBE band structure with proper F-layer thicknesses and misalignment angles as shown in Fig. 8. The Bloch band structure is shown in Fig. 9(a). Using a Tx-Rx antenna pair and a network analyzer, our first experiment demonstrated the existence of the regular and degenerate band edges as plotted in Fig. 9(c).

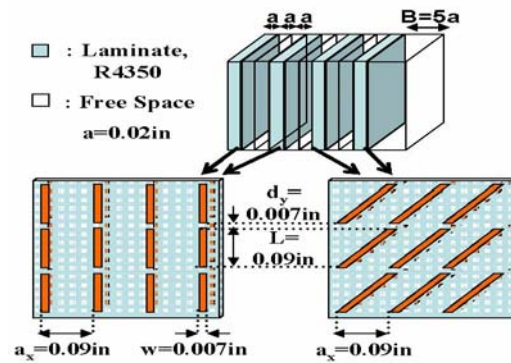


Fig. 8. DBE design using PCB technology.

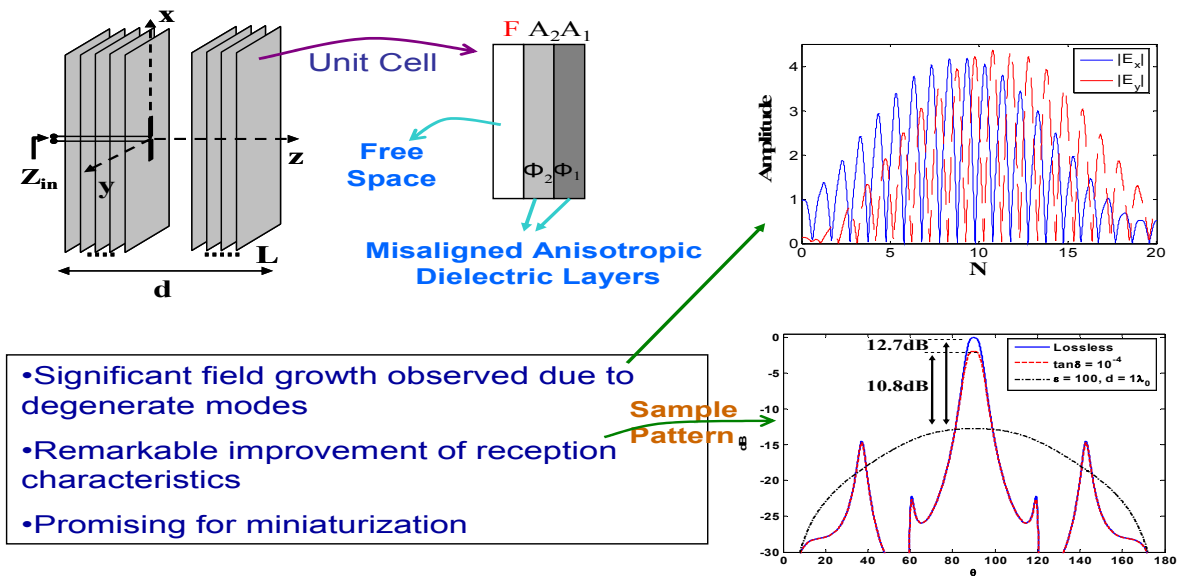


Fig. 7. Demonstration of the field amplitude growth and antenna gain realization using the non-magnetic DBE crystals (periodic assemblies).

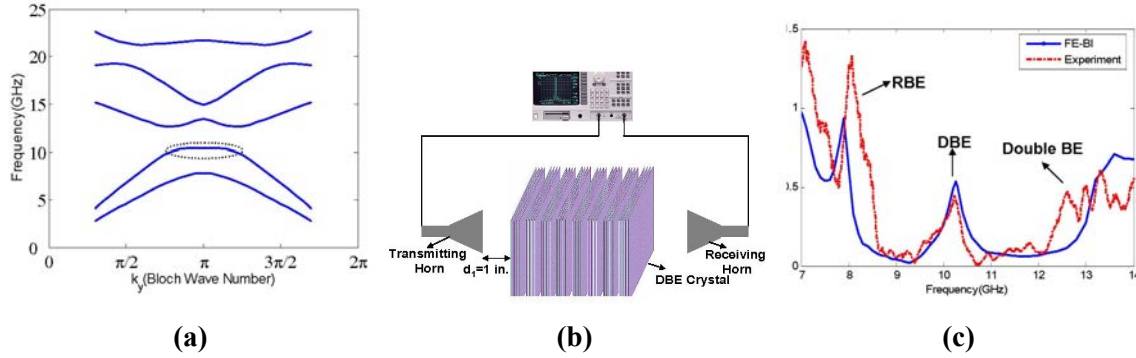


Fig. 9. Experimental verification of the field behavior within a DBE; (a) Designed band structure showing the DBE behavior, (b) Setup for polarimetric thru-transmission measurements using the Agilent E8362B, 10 MHz - 20 GHz PNA Series Network Analyzer, (c) Transmission through the crystal (different band edges are indicated).

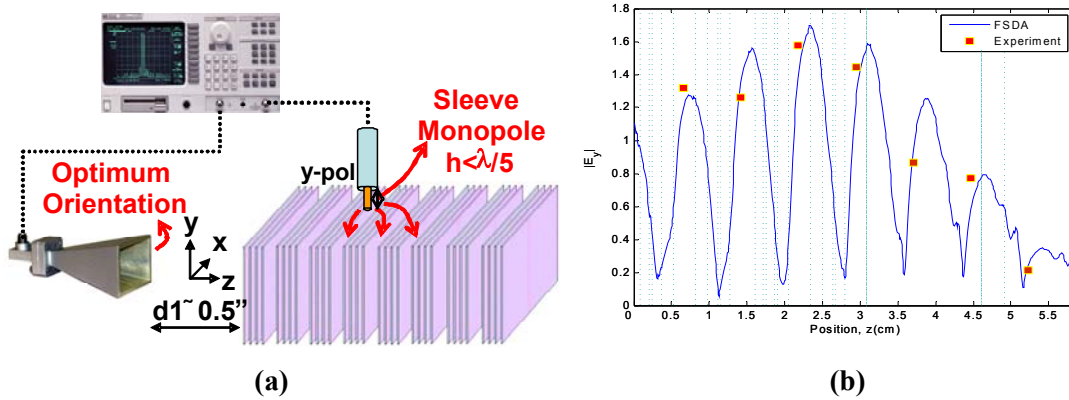


Fig. 10. Experimental verification of the DBE Field amplitude focusing: (a) Setup for field probing measurement using the Agilent E8362B, 10 MHz – 20 GHz PNA Series Network Analyzer, (b) Calculated vs. Measured electric field strength within the DBE crystal.

Further, we proceeded to demonstrate the focusing effect of the DBE crystal via probing of the field amplitudes within each free-space layer as shown in Fig. 10. These tests provided further verification of the field amplitude growth realization and possible miniaturization afforded by the proposed MPC and DBE materials. We are currently exploring the possibility of designing the anisotropic material layers via a careful combination of isotropic building blocks as outlined below.

IV. FABRICATING PERIODIC ASSEMBLIES OF DBES AND MPCS

Practical MPCs consist of 10-40 unit cells, with each cell composed of two “A” layers rotated with respect to each other and one “F” layer, as shown in Fig. 6. To realize the predicted gains, each layer needs to be made as a thin sheet, typically of dimensions $2'' \times 2'' \times 0.02''$, and a low dielectric loss $\tan\delta$, preferably $<10^{-5}$. Examples of possible sheet materials are rutile single crystals for the A

layers, and Ca, V-doped Yttrium Iron Garnet ceramics (CVGs) for the F layer. However the rutile crystals are not available with the desired $2'' \times 2''$ dimensions and their cost may prohibit practical realization. In addition, the measured losses of commercially available rutile crystals are $>10^{-4}$ while there is little opportunity to improve this number by modifying the composition. The properties of commercially available CVG materials are promising but are yet to be explored for this application and further developed. Little is also known about the compatibility and manufacturability of these materials into an operational device. These factors have inhibited the realization of a prototype. To overcome these issues we have been working with Prof. Verweij (Material Science Dept. at The Ohio State University)¹ on approaches as discussed below.

¹ Information on material properties and choices listed here are credited to Prof. Verweij’s group at the Ohio State Univ.

V. EXPLORATION OF STACKS FROM COMMERCIAL CERAMIC SHEETS

Recent investigations, carried out in close cooperation with Prof. Verweij have demonstrated that fully functional MPCs and DBEs may well be realized through advanced ceramic processing. It was found that use of anisotropic single crystals can be avoided by realizing artificial anisotropic dielectrics, exactly as in Fig. 11. The shown platelets consist of parallel arrangements of alternating ceramic beams. The ceramic route towards the manufacturing of A layers starts with stacking alternating layers of two different ceramics with low $\tan\delta$ and largely different dielectric constants, ϵ . After an adhesion treatment, the stacks are sliced in perpendicular direction to form the "striped" composite A layer (Fig. 12).

The two ceramic compositions chosen for the laminate were α - Al_2O_3 with reported best values of $\epsilon_r = 10$ and $\tan\delta = 2 \times 10^{-5}$ [19] and TiO_2 with reported best values of $\epsilon_r = 100$ and $\tan\delta = 6 \times 10^{-5}$ [20]. Dense-ceramic Al_2O_3 sheets are commercially available. But since this is not the case for TiO_2 , commercially available Ba-titanate (TD82) substrates were obtained that have a similar $\epsilon_r \sim 82$ but a higher loss of $\tan\delta = 3.7 \times 10^{-4}$ at 2.13 GHz. The stacks are shown in Fig. 12. Without adhesive, they were found to have an anisotropic dielectric constant as predicted from mean field theory, and a loss $\tan\delta \sim 9.3 \times 10^{-4}$ at 8.36 GHz. This higher loss is likely related to the presence of absorbed water on the individual layers and effects of the interfacial gaps due to less than perfect flatness of the platelets.

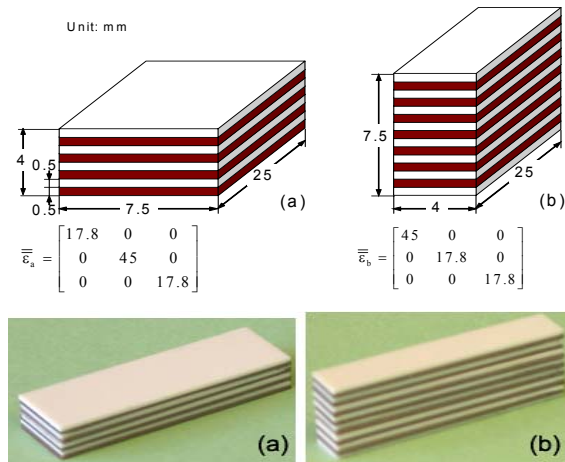


Fig. 11. *Upper*: geometry and theoretical dielectric tensor of two stacks, used for in-cavity dielectric measurements at the electro-science lab (ESL). The white and brown layers are Al_2O_3 and TD82 respectively. *Lower*: anisotropic dielectric laminates from commercial Al_2O_3 /TD82 substrates, stacked without adhesive, and the same dimensions.

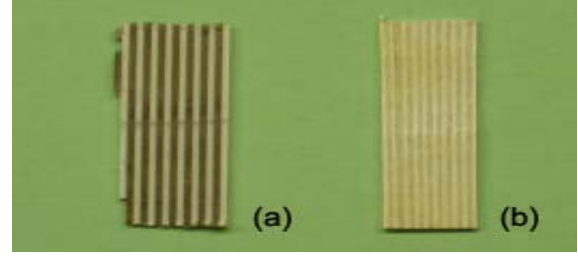


Fig. 12. 1 mm thick slices cut from (a) a commercial Al_2O_3 /TD82 stack with organic adhesion and (b) a homemade Al_2O_3 /TiO₂ stack with self-aligned, reactive adhesion.

The possibility to prepare striped layers was explored by Prof. Verweij's group using an organic polymer adhesive, followed by lamination. However, the organic adhesives were found to further increase the losses of the stacks to a $\tan\delta \sim 1.9 \times 10^{-3}$ for liquid adhesive (3M 4475) and 2.5×10^{-3} for double sided tape (3M 9492MP). The laminates were cut into 1 mm thick slices with a thin diamond blade using oil cooling. A first result is shown in Fig. 12a, but more focus is still necessary on avoiding deformation and in constructing materials that can exhibit loss tangents better than 10^{-5} .

VI. PRINTED CIRCUIT EMULATIONS OF ANISOTROPIC MATERIALS

Perhaps our most remarkable development in RF device miniaturization is the introduction of a novel pair of coupled printed microstrip lines (see Fig. 13) to emulate wave propagation within the usual DBE and MPC crystals. By adjusting the proximity of the microstrip lines or their width, emulation of the field growth and wave slow down can be done using standard of-the-shelf printed circuit technology. We have demonstrated this novel phenomenon using numerical tools and were able to show how small changes in parameters can be used to generate various k-w diagrams as shown in Fig. 14.

We can, thus, emulate propagation within crystals using a simple and easily realizable pair of transmission lines that may be allowed to couple with each other to generate the effects of the off-diagonal entries in the constituent permittivity tensors of the layered structure. This idea was demonstrated in [28] where we emulated a DBE dispersion diagram using the microstrip unit cell shown in Fig. 13. We demonstrated that by simply varying the width of one of the microstrip lines, various dispersion characteristics such as regular band edge (RBE) and double band edge (DbBE) crystals can be realized (See Fig. 14). The results in Fig. 14 were obtained using the analytical transfer matrices for coupled and uncoupled segments of the structure shown in Fig. 13

and enforcing the periodicity condition on the corresponding four ports of the structure.

The increase in field value within the coupled lines was demonstrated numerically as in Fig. 15 and can be exploited for high sensitivity antenna design. Two possible configurations are displayed in Fig. 16 and are the subject of future investigations.

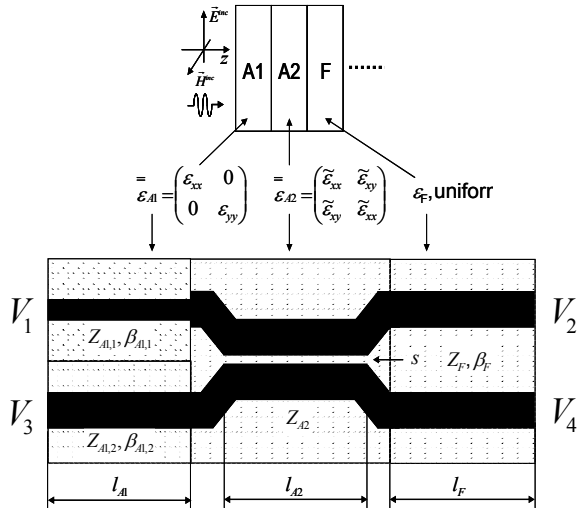


Fig. 13. A simple equivalent microstrip circuit for the three layers of the DBE and MPC crystals (patent pending).

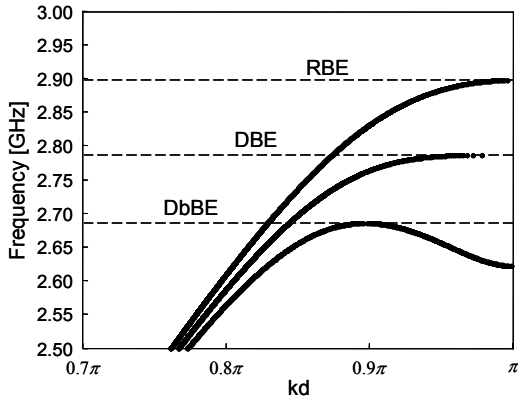


Fig. 14. Three distinct band edges can be realized by varying line #1 in Fig. 13.

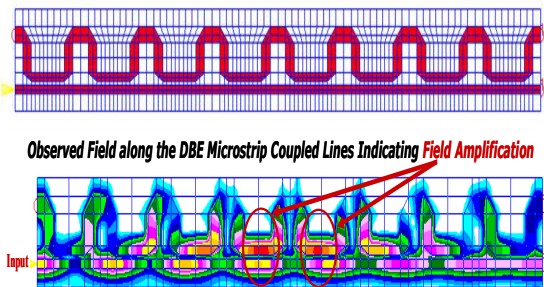


Fig. 15. Field distribution under the microstrip lines for an excitation at the DBE frequency.

DBE Printed Antenna Concept



Concept: Patch antenna modified with DBE Slots

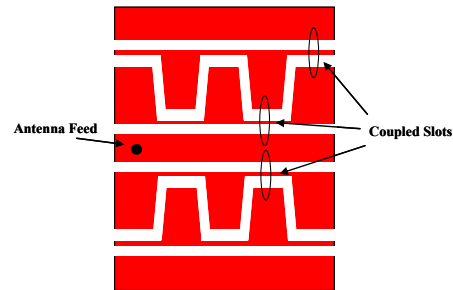


Fig. 16. DBE/MPC slot and patch antenna concepts.

VII. CONCLUSION

Material design capabilities offered by advances in dispersion engineering (including MPC/DBE crystals and negative index media) allow for unprecedented antenna and array designs possibilities. In this paper, we presented various avenues for antenna design using engineered materials. We specifically focused on MPCs and DBEs that support modes which can be harnessed to satisfy tight antenna design requirements. We summarized the properties of the frozen modes supported by these crystals and validated the existence of these modes with measurements. The paper concludes with the introduction of a simple coupled transmission line approach that emulates the dispersion and slow wave modes within the MPC and DBE crystals. Given the manufacturing simplicity of the printed coupled lines, the associated printed structures hold a great promise for realizing the advantages of the frozen modes.

ACKNOWLEDGEMENTS

This work was supported in part by the Air Force Office of Scientific Research under the MURI grant FA9550-04-1-0359 and the Office of Naval Research.

REFERENCES

- [1] *IEEE Transactions on Antennas and Propagation*, Special Issue on Metamaterials, vol. 51, Oct. 2003.
- [2] J. Joannopoulos, R. Meade, and J. Winn, "Photonic Crystals-Molding the Flow of Light," Princeton Univ. Press, 1995.

- [3] S.-Y. Lin, E. Chow, V. Hietala, P. R. Villeneuve, and J. D. Joannopoulos, "Experimental demonstration of guiding and bending of electromagnetic waves in a photonic crystal," *Science*, vol. 282, pp. 274–276, Oct. 1998.
- [4] H. Mosallaei and Y. Rahmat-Samii, "Periodic bandgap and effective dielectric materials in electromagnetics: Characterization and applications in nanocavities and waveguides," *IEEE Transactions on Antennas & Propagat.*, vol. 51, no. 3, pp. 549–563, Mar. 2003.
- [5] E. Yablonovich, "Photonic band-gap crystals," *J. of Physics: Condensed Matter*, vol. 5, no. 16, pp. 2443–2460, Apr. 1993.
- [6] D. R. Solli and J. M. Hickmann, "Photonic crystal based polarization control devices," *J. of Physics D: Applied Physics*, vol. 37, no. 24, pp. R263–R268, Dec. 2004.
- [7] B. Temelkuran, M. Bayindir, E. Ozbay, R. Biswas, M. M. Sigalas, G. Tuttle, and K. M. Ho, "Photonic crystal based resonant antenna with a very high directivity," *J. of Applied Physics*, vol. 87, no. 1, pp. 603–605, Jan. 2000.
- [8] R. Biswas, E. Ozbay, B. Temelkuran, M. Bayindir, M. M. Sigalas, and K. M. Ho, "Exceptionally directional sources with photonic-bandgap crystals," *J. of the Optical Society of America B*, vol. 18, no. 11, pp. 1684–1689, Nov. 2001.
- [9] A. Erentok, P.L.Luljak, and R. W. Ziolkowski, "Characterization of a volumetric metamaterial realization of an artificial magnetic conductor for antenna applications," *IEEE Trans. Antennas & Propagat.*, vol. 53, no. 1, pp. 160–172, Jan. 2005.
- [10] M. Antoniadis, F. Qureshi, and G. Eleftheriades, "Antenna Applications of Negative- Refractive-Index Transmission-Line Metamaterials," *2006 Int. Workshop on Antenna Technology, Conference Proceedings*, March 2006.
- [11] A. Figotin and I. Vitebskiy, "Nonreciprocal magnetic photonic crystals," *Physical Review E*, vol. 63, pp. 066–609, 1–20, May 2001.
- [12] A. Figotin and I. Vitebskiy, "Electromagnetic unidirectionality in magnetic photonic crystals," *Physical Review B*, vol. 67, pp. 165–210, 1–20, Apr. 2003.
- [13] G. Mumcu, K. Sertel, J.L. Volakis, A. Figotin and I. Vitebskiy, "RF propagation in finite thickness unidirectional magnetic photonic crystals," *IEEE T. Antenn. Propag.*, vol. 53, no. 12, pp. 4026–34, 2005.
- [14] G. Mumcu, K. Sertel, and J.L. Volakis, "Miniature Antennas and Arrays Embedded within Magnetic Photonic Crystals" *IEEE Antennas and Wireless Propagat. Letters*, vol. 5, pp. 168 – 171, 2006.
- [15] J. L. Volakis, C. C. Chen, M. Lee, and B. Kramer, "Miniaturization methods for narrowband and ultrawideband antennas," *IEEE international workshop on antenna Technology: Small Antennas and Novel Metamaterials*, Marina Mandarin, Singapore, Mar. 2005.
- [16] A. Figotin and I. Vitebskiy, "Slow light in photonic crystals," arXiv:physics/0504112 vol. 2, Apr. 2005. (Topical Review, submitted to "Waves in Random and Complex Media").
- [17] A. Figotin and I. Vitebskiy, "Electromagnetic unidirectionality and frozen modes in magnetic photonic crystals," *J. Magnetism and Magnetic Materials*, vol. 300, no. 1, pp. 117-121, May 2006.
- [18] S. Yarga, K. Sertel, and J. L. Volakis, "Degenerate Band Edge Crystals and Periodic Assemblies for High Gain Antennas," *submitted to IEEE Trans. Antennas & Propagat.* (see also paper by same authors in the 2006 IEEE Int. Symposium on Antennas and Propagat., Albuquerque, NM)
- [19] N. M. Alford and S. J. Penn, "Sintered alumina with low dielectric loss," *J. Appl. Phys.*, vol. 80, no. 10, pp. 5895-98, 1996.
- [20] A. Templeton, X. Wang, S. J. Penn, S. J. Webb, L. F. Cohen, and N. M. Alford, "Microwave dielectric loss of titanium oxide," *J. Am. Ceram. Soc.*, vol. 83, no. 1, pp. 95-100, 2000.
- [21] M. Lee, C-C. Chen, and J. L. Volakis, "Distributed Lumped Loads and Lossy Transmission Line Model for Wideband Spiral Antenna Miniaturization and Characterization," *IEEE Trans. Antennas and Propagat.* (Submitted)
- [22] B. A. Kramer, M. Lee, Chi-Chih Chen, and J. L. Volakis, "Design and Performance of an Ultra Wideband Ceramic-Loaded Slot Spiral," *IEEE Antennas and Propagat.* vol. 53, pp. 2193-2199, July 2005.
- [23] M. Lee, B. A. Kramer, C-C. Chen, and J. L. Volakis, "Broadband Spiral Antenna Miniaturization Limit," *2006 IEEE Antennas and Propagation Society International Symposium*, Albuquerque, NM
- [24] B. A. Kramer, C-C. Chen, and J. L. Volakis, "Miniature UWB Conformal Aperture via Volumetric Inductive Loading," *2006 IEEE Antennas and Propagation Society International Symposium*, Albuquerque, NM.
- [25] L. J. Chu, "Physical limitations of antenna Q," *J. Appl. Phys.*, vol. 19, pp. 1163–1175, 1948.
- [26] R. F. Harrington, "Effect of antenna size on gain, bandwidth, and efficiency," *J. Res. Nat. Bureau Stand.*, vol. 64D, pp. 1–12, Jan. 1960.
- [27] B. Kramer, S. Koulouridis, C-C. Chen, and J. L. Volakis, "A Novel Reflective Surface for an UHF Spiral Antenna" *IEEE Trans. Antennas and Propagat. Letters*, vol. 5, pp. 32 – 34, 2006.
- [28] C. Loecker, K. Sertel, and J. L. Volakis, "Emulation of Propagation in Layered Anisotropic Media with Equivalent Coupled Microstrip Lines," to appear in MWCL.



John L. Volakis was born on May 13, 1956 in Chios, Greece and immigrated to the U.S.A. in 1973. He obtained his B.E. Degree, summa cum laude, in 1978 from Youngstown State Univ., Youngstown, Ohio, the M.Sc. in 1979 from The Ohio State Univ., Columbus, Ohio and the Ph.D. degree in 1982, also from The Ohio

State Univ.

From 1982-1984 he was with Rockwell International, Aircraft Division (now Boeing Phantom Works), Lakewood, CA and during 1978-1982 he was a Graduate Research Associate at the Ohio State University ElectroScience Laboratory. From January 2003 he is the Roy and Lois Chope Chair Professor of Engineering at the Ohio State University, Columbus, Ohio and also serves as the Director of the ElectroScience Laboratory (with ~\$7M in research funding). Prior to moving to the Ohio State Univ, he was a Professor in the Electrical Engineering and Computer Science Dept. at the University of Michigan, Ann Arbor, MI. (1984-2003). He also served as the Director of the Radiation Laboratory from 1998 to 2000. His primary research deals with computational methods, electromagnetic compatibility and interference, design of new RF materials, multi-physics engineering and bioelectromagnetics. He has co-authored three books, 240 refereed journal papers, and over 340 conference papers. Dr. Volakis is listed by ISI among the top 250 most referenced authors (2004, 2005).

Dr. Volakis served as an Associate Editor of the *IEEE Transactions on Antennas and Propagation* from 1988-1992, and as an Associate Editor of *Radio Science* from 1994-97. He chaired the 1993 IEEE Antennas and Propagation Society Symposium and Radio Science Meeting, and co-chaired the same Symposium in 2003. Dr. Volakis was a member of the AdCom for the IEEE Antennas and Propagation Society from 1995 to 1998 and served as the 2004 President of the IEEE Antennas and Propagation Society. He also serves as an associate editor for the *J. Electromagnetic Waves and Applications*, the *IEEE Antennas and Propagation Society Magazine*, and the *URSI Bulletin*. He is a Fellow of the IEEE, and a member of Sigma Xi, Tau Beta Pi, Phi Kappa Phi, and Commission B of URSI. He is also listed in several Who's Who directories, including Who's Who in America.



Kubilay Sertel was born on June 27, 1973, in Tekirdag, Turkey. He received the B.S. degree from Middle East Technical University, Ankara, Turkey in 1995, the M.S. degree from Bilkent University, Ankara, Turkey in 1997, and the Ph.D. degree from the Electrical Engineering and Computer Science

Department at the University of Michigan, Ann Arbor, MI in 2003, respectively.

He is currently a Senior Research Associate at the ElectroScience Laboratory at the Ohio State University. His research areas include electromagnetic theory, computational electromagnetics, volume-surface integral equations and hybrid methods, fast and efficient methods for large-scale electromagnetics problems and parallel implementations of fast algorithms.



Chi-Chih Chen received his BSEE in 1988 from National Taiwan University in Taiwan, MSEE and PhD degrees in 1993 and 1997, respectively, from The Ohio State University. He has been with The Ohio State University ElectroScience Laboratory (ESL) since 1993 as a Postdoctoral Researcher (1997~1999),

Senior Research Associate (1999-2003) and Research Scientist in (2004~present). He is also an Adjunct Assistant Professor at The Ohio State University Electrical and Computer Engineering Department. Dr. Chen's research interests include ground penetrating radar technology, novel radar systems (vehicle obstacle detection, insect tracking, RFID, ...), buried target detection/classification, UWB antenna designs, UWB dual-polarization feed/probe antenna designs for antenna and RCS ranges, miniature antenna designs for communication and navigation systems.

Estimation of Blockage Effects of Complex Structures on the Performance of the Spacecraft Reflector Antennas by a Hybrid PO/NF-FF Method

Keyvan Bahadori and Yahya Rahmat-Samii

Antenna Research and Measurements Laboratory, Department of Electrical Engineering,
University of California, Los Angeles,
CA 90095 USA (e-mail: rahmat@ee.ucla.edu)

Abstract — A hybrid (PO/NF-FF) method is presented in this paper for estimating the blockage effects of complex structures on the performance of the spacecraft mounted reflector antennas. The method estimates the blockage effect based on null-field hypothesis. The main advantage of this method is its ease of implementation for different obstacle geometries. The accuracy and functionality of the method is demonstrated by comparing the results of this method with other methods such as Method of Moments (MoM) and Direct (PO). An alternative definition of beam efficiency is adopted when the radiated power is available only in the forward radiation region. As a case study, the method is used to evaluate the effects of side panels on the performance of a reflector antenna operating at K band. A new parameter is also defined to represent the effects of absorbed power by panels. This parameter may be used to estimate the contribution of absorbed power in increasing system noise temperature.

Index Terms — Blockage effect, FFT, Hybrid methods, near field, Physical Optics, Reflector antennas.

I. INTRODUCTION

Recent technology advances in building large and light reflector antennas with reduced launch mass and stowed volume allows scientists to envision the use of large reflector antennas for spaceborne applications. In many cases, the performance of the reflector can be affected by structures around the antenna which may potentially interfere with its radiated fields. The situation may be even more critical for high-frequency radiometer applications in which the beam efficiency of the antenna can be degraded by any blockage effects. Furthermore, in many applications, the blocking object can have varied signature before and after development on the platform. Therefore an initial assessment of these blockage effects in a reasonably fast fashion is essential for spaceborne platform designs.

In general, several conventional methods have been

considered for evaluating the effects of blocking objects on the performance of reflector antennas [1-4]. Using full-wave methods to analyze these effects can give accurate results. However, they are impractical due to very large dimensions of the antenna and blocking obstacles relative to the wavelength. Consequently, various types of approximations have been used to estimate the effect of large blocking objects. Induced field ratio (IFR) hypothesis has been invoked in [1] to study the effect of feed-support struts of symmetric paraboloidal reflectors. This hypothesis assumes that the currents at a point on the struts due to the plane-wave component of focal-region field are the same currents that would flow on an infinite, cylindrical structure of the same cross-section immersed in an infinite, free space plane wave with the same polarization and direction of incidence as the local geometrical ray incident upon that part of the struts as it emerges from the reflector. So this method is effective when the blocking obstacle is in ray-field regions and it is also limited to cylindrical strut structures. Another competitive method is observation-point-dependent shadowing technique which uses the null-field hypothesis [2, 3]. In this method, which is based on the GO approximation of the field, it is assumed that currents do not radiate in observation point directions which are shadowed by objects between the observer and the reflector. Thus, completely “dark” shadows are assumed to be contained within peripheries defined by geometrical rays. However, this method is restricted to some simple geometries and it is difficult to apply it for more complex structures. Another used method is to make the current zero in shadow regions caused by blocking objects [4]. This method is only useful when the blocking object is in front of the reflector and in the GO ray-field region.

Therefore, for the scenarios in which there are several blocking objects with different geometries and locations, the objective is to use a method which is applicable to large structures and can give fairly accurate results for obstacle in arbitrary locations in the forward region of the reflector (not only GO ray-field region). In

addition, since the shape of some of the obstacle may change during deployment on the platform, the method should be easily applied for arbitrary geometries.

This paper addresses a hybrid PO/NF-FF method using near-field to far-field transformation combined with null-fill hypothesis to estimate the effect of complex structures on the far-field pattern and beam efficiency of reflector antennas. A preliminary presentation of technique was documented in a recent conference paper [5]. The main advantage of this method is that it can be potentially used for any arbitrary shape of blockages. The accuracy of the method is verified by comparing the results with Method of Moments (MoM). To estimate the blockage effects on the beam efficiency, an alternative definition of beam efficiency will be introduced based on the total forward radiated power in the near-field plane. Finally, the results will be shown for a case study in which the blockage effects of side antenna panels, for an antenna configuration presented in [6], is estimated on the performance of the reflector antenna. A new parameter, “*Power Ratio*”, will be also defined to represent the effects of absorbed power by obstacle. This parameter can be used to estimate the contribution of absorbed power in increasing system noise temperature.

II. PO/NF-FF TRANSFORMATION METHOD

The evaluation of far-field pattern of an antenna from its near-field measurements by means of a near-field to far-field (NF-FF) transformation is well established and widely used [7]. There are several techniques for near-field measurements such as spherical, cylindrical, or planar measurements which have their own particular advantages depending upon the antenna and the measurement requirements. The method introduced in this paper is based on planar-rectangular near-field construction. Fig. 1 shows a schematic algorithm of this method. The field is calculated using Physical Optics (PO) on a finite rectangular plane through which the major portion of energy radiates. The near-field data is then used to construct the far-field pattern of the antenna using a fast Fourier transform FFT algorithm [8]. To evaluate the blockage effect, according to the null-field hypothesis, it is only required to make the field zero at the locations of conductor objects or their effective shadow regions which block the field. This can be done by post processing of the near-field data and use the modified near-field data to construct the affected far-field pattern. The important advantage is that once the near-field data is obtained it can be used for any arbitrary masking object geometry, and it is not necessary to modify algorithms for each case. This is clearly an approximation with reasonably useful results for engineering applications.

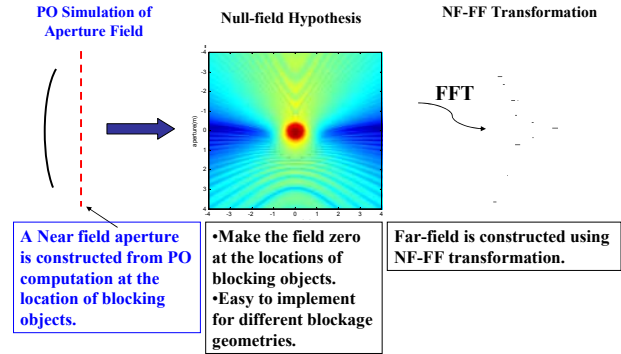


Fig. 1. Schematic algorithm of PO/NF-FF hybrid method to estimate the blockage effect of complex structures on the performance of the reflector antennas.

In general, this method can be used for any arbitrary object in GO field region by finding the projected shadow in the reference plane. For objects outside of GO field region the method is effective for planar structures by calculating the field at the location of the structure. For the cases where the objects are in different distances from the reflector, an iterative procedure can be invoked to estimate the effects of obstacles in different planes as shown in Fig. 2. The fields are nulled at the location of objects in the first plane and far-field is constructed. This far-field data is used to perform Inverse FFT to construct the near-field in the second plane. This near-field constructed data includes the effect of objects in the first plane. By nulling the field for objects in the second plane the far-field can be constructed and this iterative procedure can be performed until the effects of all objects in different planes are considered.

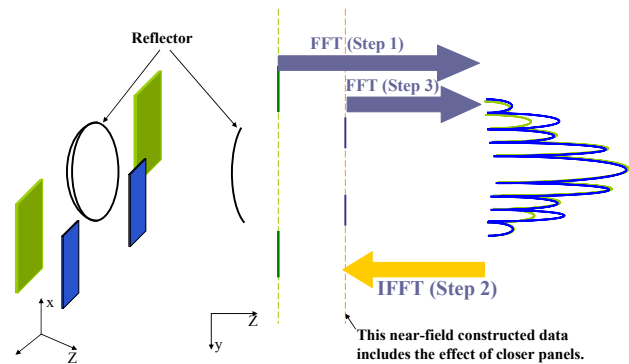


Fig. 2. An iterative procedure to evaluate the blockage effects of objects at different distances.

III. PO/NF-FF PERFORMANCE

A. Accuracy of PO Near-Field Data

To verify the accuracy of near-field data, the performance of a 2 m reflector fed by a dipole was simulated at 1.5 GHz using three different methods.

These dimensions allowed the problem to be solved by using Method of Moments. Fig. 3 shows the geometry of the reflector. The problem was first solved using the Method of Moments code [9] and the far-field was calculated from the current on the reflector. Then, a diffraction analysis code [10] was used to calculate the far-field pattern of the reflector. This code uses Physical Optics (PO) approximation of the current on the reflector and calculates the far-field directly from the PO current on the reflector. The third approach is the proposed PO/NF-FF method. The near-field data was simulated on a $30\lambda \times 30\lambda$ plane in front of the reflector (Fig. 3b) and far-field pattern was constructed by performing FFT calculation.

Fig. 4 shows the pattern of the reflector calculated by these three methods. A very good agreement is observed between all methods up to 40° . The discrepancy in sidelobe level after 40° is mainly due to the finite size of the near-field plane. It has to be also mentioned that for this configuration, the valid angle for the far-field pattern of PO/NF-FF method is 65° and the pattern cannot be relied on beyond this angle [11].

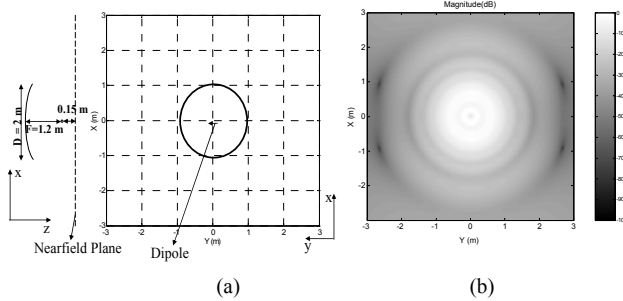


Fig. 3. (a) Geometry of a 2 m reflector fed by a dipole at 1.5 GHz and constructed near-field plane, (b) Constructed near field data.

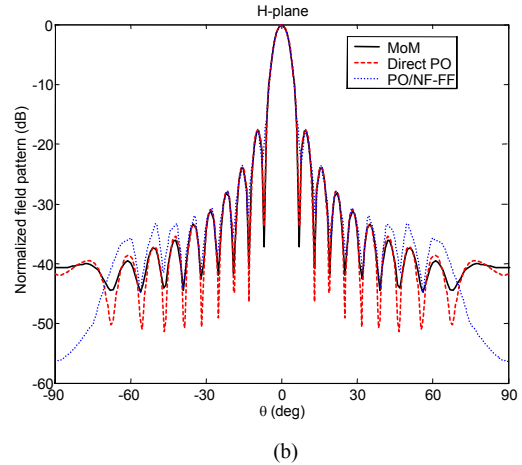
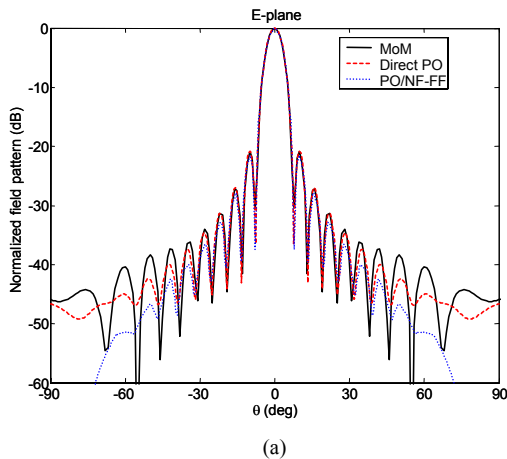


Fig. 4. Far-field pattern of a 2 m reflector fed by a dipole at 1.5 GHz using three different techniques, (a) E-plane, (b) H-plane.

B. Evaluation of Blockage Effect

A test scenario was also designed to evaluate the capability of the PO/NF-FF in predicting the effect of blocking objects. As shown in Fig. 5, a rectangular strip is assumed to block a 79 cm reflector operating at 18.7 GHz. The effect of this blockage is simulated by two methods: In the first method the PO currents in the shadow region of the reflector are made zero and then the far-field pattern is simulated directly from the modified current on the reflector. Since the blockage is in collimated field region of the reflector, the size of the shadowing region on the reflector was chosen to be equal to the actual size of the blockage. Secondly, PO/NF-FF method was used by constructing the near field data in a 8×8 meter window and nulling the field in the location of the strip and constructing the far-field from the modified near-field data. One can observe a good agreement between patterns in Fig. 6 and the main features of the patterns are very similar.

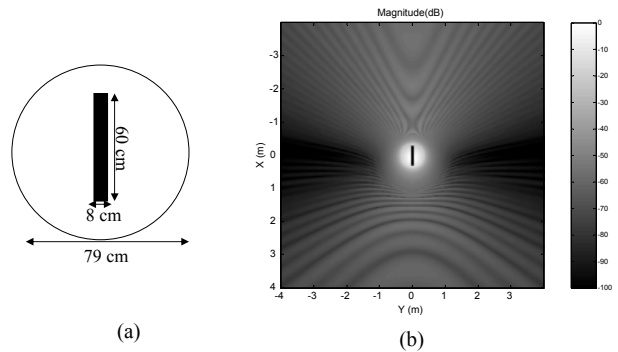


Fig. 5. (a) A 79 cm reflector antenna operating at 18.7 GHz blocked by a rectangular strip, (b) Near field data with blockage effect.

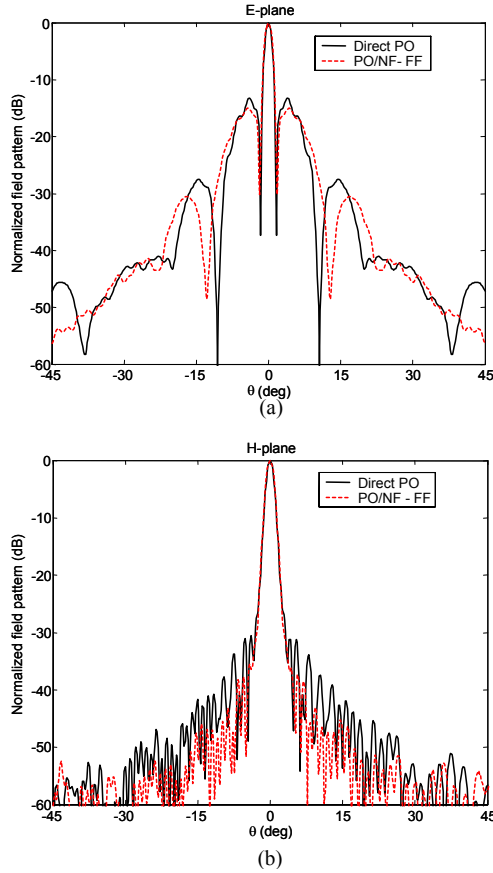


Fig. 6. Far-field pattern of the K band reflector blocked by the rectangular strip, (a) Direct PO method, (b) PO/NF-FF method.

IV. PO/NF-FF EVALUATION PARAMETERS

A. Beam Efficiency

Beam efficiency is one of the important parameters for characterizing the performance of reflector antennas used for radiometer applications. For a given power pattern of a reflector-antenna system the beam efficiency may be defined as [12],

$$BE = \frac{\text{Power radiated in the main beam}}{\text{Total radiated power}}$$

The total radiated power for a reflector can be calculated from the total power emitted from the feed including scattered field and feed spillover. However, in the NF-FF transformation method, although choosing a large enough near-field plane gives a reasonable accurate result for far-field pattern, the total measurable power is the “total forward radiated power” and there is always a fraction of power which is not considered due to plane truncation or back scattering. So, it is necessary to define beam efficiency based on this forward radiated power to have a proper criterion to estimate the effect of blockage.

Hence for this method, the beam efficiency is defined as

$$BE_{FFT} = \frac{\text{Power radiated in the main beam}}{\text{Total near field power captured in the front plane}}$$

For high edge taper and large enough near-field plane, this number is almost equal to the value calculated based on the original definition. This is verified by numerical examples in the following sections.

B. Power Ratio

In most practical cases, the field level is considerably low at the location of the blocking objects. Therefore no significant change is observed in far-field patterns. However the power absorbed by these panels can contribute to increase the system noise temperature. Hence, to consider the effect of this absorbed power, a parameter defined as “Power Ratio” is introduced,

$$\text{Power Ratio} = \frac{\text{Near field power at the location of blocking objects}}{\text{Total near field power captured in the front plane}}$$

It represents the ratio of the near field power at the location of blocking objects versus the total near field power captured in the front plane. It has been suggested that this parameter should signify the black body radiations of the blocked areas in front of the antenna which can potentially contribute to overall system noise temperature. An example of using this parameter will be demonstrated in the following sections.

V. A CASE STUDY: A K-BAND RADIOMETER REFLECTOR

The functionality of PO/NF-FF is demonstrated by calculating the effect of supporting struts and deployed side panels [6] on the performance of an offset parabolic radiometer reflector antenna. The antenna system configuration is shown in Fig. 7. The reflector has a diameter of 79 cm and the antenna operates at 18.7 GHz. The feed is Y polarized. The panels are dual polarized Ku band reflectarray for spaceborne radio altimeter.

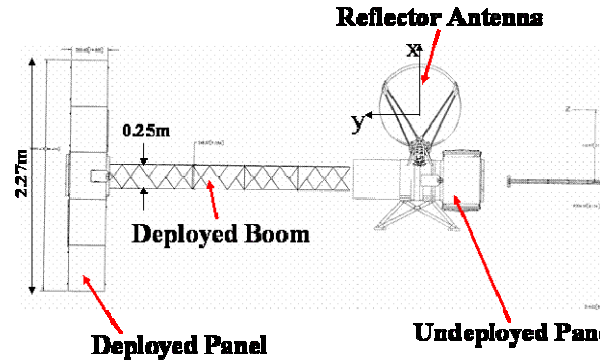


Fig. 7. Complex antenna system configuration operating at 18.7 GHz [6]. The panels are dual polarized Ku band reflectarray for spaceborne radio altimeter.

To verify the accuracy of the method, the far-field pattern is simulated using two methods. First, it was calculated directly using Physical Optics (PO) and second, it was calculated by simulating near-field data by Physical Optics and this data was then used to construct the far-field pattern (PO/NF-FF). In NF-FF transformation, to construct the far-field, near-field data was calculated in a rectangular aperture with dimensions of $500\lambda \times 500\lambda$. The aperture lies in the same plane as the deployable side panels. Shown in Fig. 8, the patterns are very similar in terms of directivity and side lobe profile. The beam efficiency values are calculated for both cases and as expected the values are similar. BE_{FFT} is 97.3% and it is slightly higher than BE (96.1%) due to the radiated field not captured in the near-field window and cause the total radiated power captured in the front window to be less than true total radiated power.

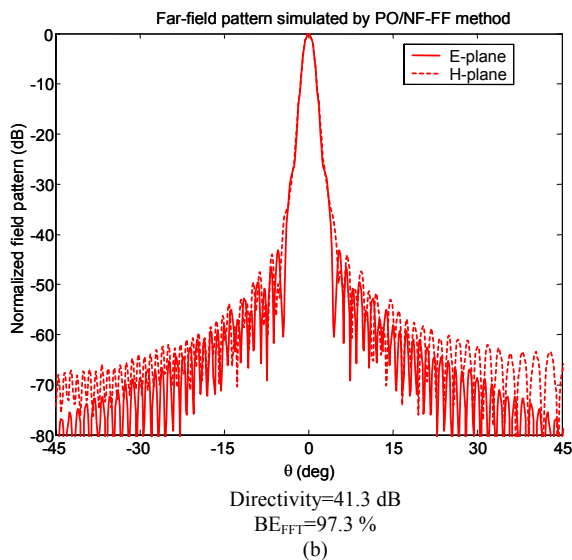
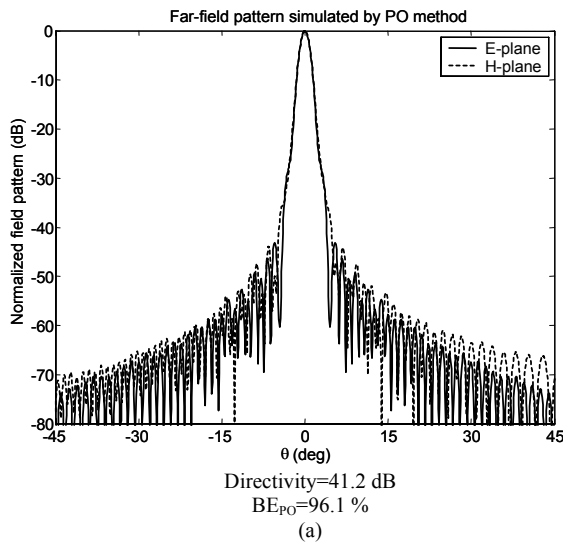


Fig. 8. (Far-field pattern of the reflector (without struts effect) (a) PO method, (b) PO/NF-FF method.

Next, the field is made zero at the location of supporting struts. The modified near-field pattern is shown in Fig. 9. The constructed far-field pattern from this near-field is now compared with measured far-field pattern in Fig. 10. The beam efficiency values are almost equal (94%) and the measured results confirm the performance of this method.

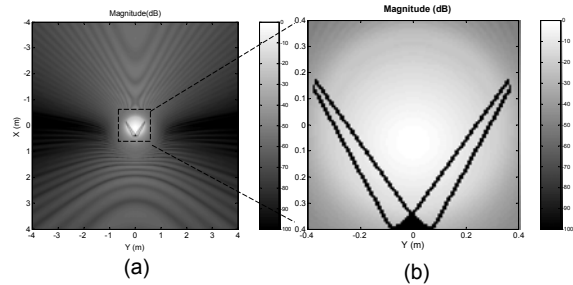


Fig. 9. (a) Near-field pattern of the reflector with strut blockage effect, (b) Enlarged center area.

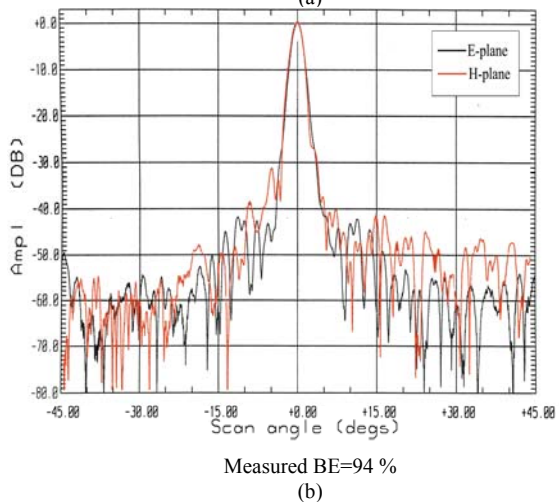
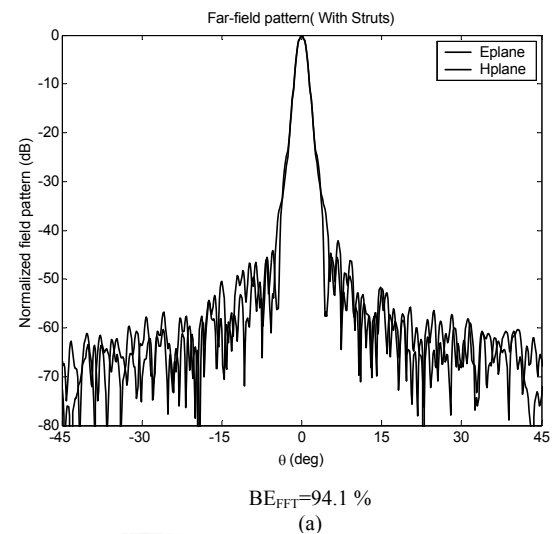


Fig. 10. Far-field pattern of the reflector with struts effect, (a) simulation results using PO/NF-FF method, (b) measured far-field result from an early JPL measurement.

The effect of undeployed and deployed booms and reflectarray panels were investigated. Fig. 11 shows the geometry of the deployed panels while Fig. 12 shows the modified near-field pattern and far-field pattern of the antenna. It should be noted that the near-field data with strut blockage effect were used for all these cases and it was modified for different blocking geometries.

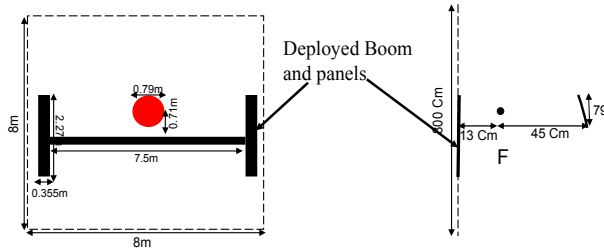


Fig. 11. Geometry of the deployed boom and panels on both sides of the reflector [6].

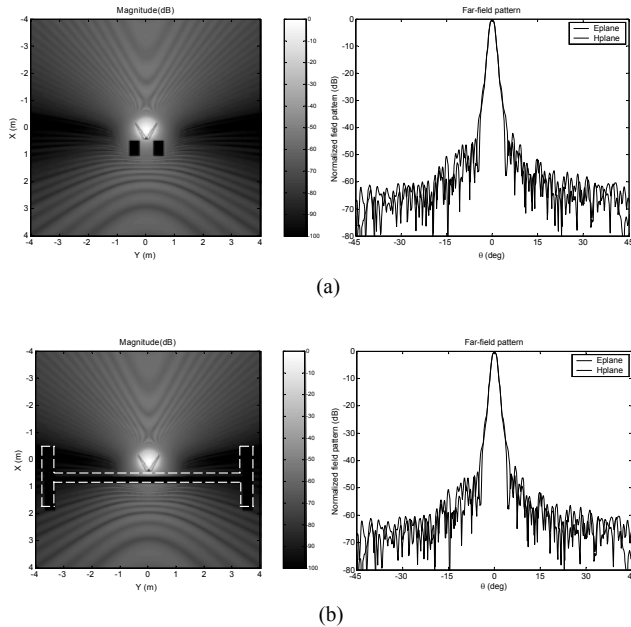


Fig. 12. Near-field and far-field simulated patterns of the reflector incorporating the effects of (a) Undeployed booms, (b) Deployed booms and panels.

No noticeable change is observed in far-field patterns due to blockage effects since the field level is very low at the location of blocking objects. This resulted to define the power ratio parameter, as discussed earlier, to indicate the contribution of absorbed power by blocking objects to overall system noise temperature. For this application, the power ratio was calculated with respect to the total power in (8 x 8) meter near field plane. The values for different cases are given in Table 1. For a given antenna system configuration it would be

the user's responsibility to determine what the accepted value for the power ratio should be in order to consider the blocking effects insignificant.

Table 1. Power Ratio for different blockage cases.

Case	Power Ratio
Undeployed Boom	4.1711e-5
Deployed Boom	3.8546e-5
Panels	3.4332e-8
Deployed Boom + Panels	3.8580e-5

VI. CONCLUSIONS

A Hybrid PO/NF-FF transformation method was utilized in this paper to provide an initial estimate of the effects of complex blockage structure on performance of reflector antennas. The method estimates the blockage effect based on the null-field hypothesis. The radiated near-field data of the reflector was simulated under PO approximation and the fields were made to zero in the location of blocking objects. An FFT routine was then used to construct the far-field from the modified near-field data. The advantage is that once the near-field data is constructed, the data can be post processed for any arbitrary shape blockage object. For obstacles in different distances, an iterative procedure can be used to incorporate the effect of all of them on the radiation performance. The accuracy of the PO near field data was verified when the far-field pattern constructed by this method was compared with the results from Method of Moments and direct Physical Optics method. An alternative definition of beam efficiency was adopted when the radiated power was available only in the forward region. To evaluate the functionality of the method, the effect of blocking of a strip in the center of the reflector was simulated by using PO/NF-FF and direct PO method. The result showed a very good agreement in main features.

Lastly, as a case study, the effects of deployed and undeployed reflectarray panels and booms on performance of an 80-cm reflector antenna were investigated. Since the panels were located in the low intensity field region, no significant changes were observed in the far-field. Therefore, a parameter called "power ratio" was defined to signify the effects of the blocking objects in front of the antenna on the overall system parameters. This parameter gives the ratio of the power absorbed in the location of blocking panels versus the total captured power in the front plane. This power may potentially contribute to increase the noise temperature of the antenna system.

This case study showed the capability and usefulness of this hybrid PO/NF-FF method in predicting

the blockage effects of arbitrary geometries, on the performance of reflector antennas with a fair accuracy and in a reasonably fast fashion. The method can be a viable tool in the initial design of spaceborne platforms for supporting reflector antennas. Preliminary results obtained using this method could then be verified using more sophisticated approaches.

REFERENCES

- [1] W. V. T. Rusch, O Sorensen and J. W. M. Baars, "Radiation cones from feed-support struts of symmetric paraboloidal antennas," *IEEE Transactions on Antennas and Propagation*, Vol. 30, No. 4, pp. 786-790, July 1982.
- [2] C. L. Gray, "Estimating the effect of feed support member blocking on antennas gain and sidelobe level" *Microwave Journal*, pp. 88-91, March 1964.
- [3] W. V. T. Rusch, and L. R. Welch, "Observation-point-dependent blocking shadows on a reflector antenna," *IEEE Transactions on Antennas and Propagation*, Vol. 37, No. 6, pp. 690-697, June 1989.
- [4] A. Moldsvor, and P. S. Kildal, "Analysis of aperture blockage in reflector antennas by using obstacle-located blockage currents," *IEEE Transactions on Antennas and Propagation*, Vol. 40, No. 1, pp. 100-102, January 1992.
- [5] K. Bahadori and Y. Rahmat-Samii, "A Hybrid PO/NF-FF Method to Estimate the Blockage Effects on the Performance of Spacecraft Mounted Reflector Antennas," *IEEE AP-S Int. Symp*, Washington DC, July 2005.
- [6] R. E. Hodges, and M. Zawadzki, "Design of a large dual polarized Ku band reflectarray for space borne radar altimeter," *IEEE AP-S Int. Symp*, Monterey, California, June 2004.
- [7] O. M. Bucci, G. D'Elia, and M. D. Migliore, "An effective near-field far-field transformation technique from truncated and inaccurate amplitude-only data," *IEEE Transactions on Antennas and Propagation*, Vol. 47, No. 9, pp. 1377-1385, September 1999.
- [8] M. S. Gatti, and Y. Rahmat-Samii, "FFT applications to plane-polar near-field antenna measurements," *IEEE Transactions on Antennas and Propagation*, Vol. 36, No. 6, pp.781-791, June 1995.
- [9] R. E. Hodges and Y. Rahmat-Samii, "An iterative current-based hybrid method for complex structures," *IEEE Transactions on Antennas and Propagation*, Vol. 45, No. 2, pp. 265-276, February 1997.
- [10] D. Duan and Y. Rahmat-Samii, "A generalized diffraction synthesis technique for high performance reflector antennas," *IEEE Transactions on Antennas and Propagation*, 43(1):27-40, January 1995.
- [11] Y. Rahmat-Samii, L. I. Williams, and R. G. Yaccarino, "The UCLA bi-polar planar-near-field antenna-measurement and diagnostics range," *IEEE Antenna and Propagation Magazine*, Vol. 37, pp. 16-35, December 1995.
- [12] Y. Rahmat-Samii, R. A. Hoferer, and H. Mosallaei, "Beam efficiency of reflector antennas: the simple formula," *IEEE Antenna and Propagation Magazine*, Vol. 40, pp. 82-87, October 1998.



Keyvan Bahadori (S'98) was born in Shiraz, IRAN, and grew up in Tehran. He received the BSEE degree from Sharif University of Technology in August, 2001. He received the MSEE from the University of California, Los Angeles with a thesis entitled "Ku/Ka Bands Spaceborne Precipitation Radar Antenna: Cylindrical Reflector Fed by Linear Array Feed," where he is currently working toward the Ph.D. degree.

He has worked in the Antenna Research, Analysis, and Measurement Laboratory at UCLA under the direction of Professor Yahya Rahmat-Samii since September of 2001. His research interests include novel designs of reflector antennas for spacecraft applications, high frequency hybrid methods, and ultra wideband (UWB) antennas for wireless communications.

Mr. Bahadori won a Silver medal in the 9th Iran National Physics Olympiad. He is also a member of IEEE in Antenna propagation and MTT societies, Iran young scholars club and Iran's Amateur Astronomer Society.



Yahya Rahmat-Samii (S'73-M'75-SM'79-F'85) received the M.S. and Ph.D. degrees in electrical engineering from the University of Illinois, Urbana-Champaign.

He is a Distinguished Professor and past Chairman of the Electrical Engineering Department, University of California, Los Angeles (UCLA). He was a Senior Research Scientist with the National Aeronautics and Space Administration (NASA) Jet Propulsion Laboratory (JPL), California Institute of Technology prior to joining UCLA in 1989. In summer 1986, he was a Guest Professor with the Technical University of Denmark (TUD). He has also been a consultant to numerous aerospace companies.

He has been editor and guest editor of numerous technical journals and books. He has authored and coauthored over 660 technical journal and conference papers and has written 20 book chapters. He coauthored *Implanted Antennas in Medical Wireless Communications*, (Morgan & Claypool Publishers, 2006), *Electromagnetic Optimization by Genetic Algorithms* (New York: Wiley, 1999) and *Impedance Boundary Conditions in Electromagnetics* (New York: Taylor & Francis, 1995). He also holds several patents. He has had pioneering research contributions in diverse areas of electromagnetics, antennas, measurement and diagnostics techniques, numerical and asymptotic methods, satellite and personal communications, human/antenna interactions, frequency selective surfaces, electromagnetic band-gap structures, applications of the genetic algorithms and particle swarm optimization, etc., (visit <http://www.ee.ucla.edu/antlab>). On several occasions, his research has made the cover of magazines and has been featured on several TV News casts. He is listed in Who's Who in America, Who's Who in Frontiers of Science and Technology and Who's Who in Engineering. Professor Rahmat-Samii is the designer of the IEEE Antennas and Propagation Society (IEEE AP-S) logo, which is displayed on all IEEE-AP-S publications.

Dr. Rahmat-Samii is a member of Commissions A, B, J and K of USNC/URSI, Antenna Measurement Techniques Association (AMTA), Sigma Xi, Eta Kappa Nu and the Electromagnetics Academy. He was elected vice-president and president of the IEEE Antennas and Propagation Society in 1994 and 1995, respectively. He was appointed an IEEE AP-S Distinguished Lecturer and presented lectures internationally. He was elected a Fellow of IEEE in 1985 and a Fellow of Institute of Advances in Engineering (IAE) in 1986. He was also a member of the Strategic Planning and Review Committee (SPARC) of the IEEE. He was the IEEE AP-S Los Angeles Chapter Chairman (1987-1989); his chapter won the best chapter awards in two consecutive years. He has been the plenary and millennium session speaker at numerous national and international symposia. He has been the organizer and presenter of many successful short courses worldwide. He was one of the directors and vice president of the Antennas Measurement AMTA for three years. He has also served as chairman and co-chairman of several national and international symposia. He was also a member of the University of California at Los Angeles (UCLA) Graduate council for three years.

For his contributions, Dr. Rahmat-Samii has received numerous NASA and JPL Certificates of Recognition. In 1984, Prof. Rahmat-Samii was the recipient of the coveted Henry Booker Award of International Union of Radio Science (URSI), which is given triennially to the most outstanding young radio scientist in North America.

Since 1987, he has been designated every three years as one of the Academy of Science's Research Council Representatives to the URSI General Assemblies held in various parts of the world. He was also invited speaker to address the URSI 75th anniversary in Belgium. In 1992 and 1995, he was the recipient of the Best Application Paper Prize Award (Wheeler Award) for papers published in 1991 and 1993 IEEE AP-S Transactions. From 1993 to 95, three of his Ph.D. students were named the Most Outstanding Ph.D. Students at the School of Engineering and Applied Science, UCLA. Ten others received various Student Paper Awards at the 1993-2004 IEEE AP-S/URSI Symposia. In 1999, he was the recipient of the University of Illinois ECE Distinguished Alumni Award. In 2000, Prof. Rahmat-Samii was the recipient of IEEE Third Millennium Medal and the AMTA Distinguished Achievement Award. In 2001, Rahmat-Samii was the recipient of the Honorary Doctorate in physics from the University of Santiago de Compostela, Spain. In 2001, he was elected as a Foreign Member of the Royal Flemish Academy of Belgium for Science and the Arts. In 2002, he received the Technical Excellence Award from JPL. He is the winner of the 2005 URSI Booker Gold Medal presented at the URSI General Assembly.

Enhanced Functionality for Hardware-Based FDTD Accelerators

Petersen F. Curt ¹, James P. Durbano ¹, Michael R. Bodnar ², Shouyuan Shi ²,
and Mark S. Mirotznik ³

¹ Accelerated Computing Division
EM Photonics, Inc., Newark, DE 19711, USA
pcurt@emphotonics.com, durbano@emphotonics.com

² Department of Electrical and Computer Engineering
University of Delaware, Newark, DE 19716, USA
bodnar@ee.udel.edu, sshi@ee.udel.edu

³ Department of Electrical Engineering and Computer Science
The Catholic University, Washington, DC, 20064, USA
mirotznik@cua.edu

Abstract — In this paper we present several architectural enhancements to our previously published hardware-based FDTD acceleration platform. This includes the addition of several new sources, including H-polarized point sources, voltage and current sources, Gaussian beams, and user-defined sources, such as waveguide mode profiles. We also discuss the recent support for extending objects into the absorbing boundary, which minimizes non-physical back reflections. With the addition of these features, the FDTD acceleration hardware has become a more robust and powerful tool, enabling the rapid simulation of a wider breadth of applications, including antennas, waveguides, and optics.

Keywords — Finite Difference Methods, Simulation, Hardware Acceleration, Electromagnetic Analysis, FPGA.

I. INTRODUCTION

Although the need for advanced electromagnetic analysis in a variety of applications is readily apparent, the long runtimes associated with these simulations frequently limit what can be realistically modeled. Consequently, designers are often forced to artificially limit the scope of their simulations in order to analyze problems within a reasonable time frame. Fortunately, with the advent of hardware-based FDTD solvers, many of these limitations have been overcome, resulting in more designers relying on acceleration hardware for

solutions to their computational needs. In [1, 2], we presented such a platform that demonstrated considerable improvements over software-based solutions in both speed and maximum problem size (Fig. 1). Although a significant achievement, this platform was limited in the types of problems it could solve. Specifically, the acceleration hardware was only capable of analyzing problems that incorporated either E-polarized point sources, uniform plane waves, or their temporally modulated variations. While this did allow a variety of simulations to be performed, a host of applications remained that could not be modeled, as they required more advanced source types. In this paper, we present our most recent architectural developments, which have focused on the incorporation of new source types. Notable platform additions include support for H-polarized point sources, voltage/current sources, and the introduction of a connecting boundary, which enables support for both Gaussian beams and also user-defined sources, such as waveguide mode profiles. We also discuss the recent support for extending objects into the absorbing boundary, which is vital to minimize non-physical back reflections associated with a variety of problems, including waveguides. Despite numerous publications on FDTD acceleration hardware, a fully 3D, hardware-based FDTD accelerator that encompasses such features has never been described until now [1-6].



Fig. 1. The FDTD hardware accelerator. This FPGA-based board provides the platform for the acceleration architecture. It includes the largest FPGA on the market and supports up to 16 GB DDR SDRAM. This platform has demonstrated performance comparable to 100-node PC clusters.

II. NEW SOURCE CONDITIONS

The original FDTD acceleration platform only supported two source types: single electric point sources and uniform plane waves. While the underlying hardware architecture was capable of quickly performing large simulations, the lack of support for more advanced source conditions prevented its application to numerous problems. For example, although the uniform plane wave source could be applied to many scattering problems, a spatially windowed plane wave (previously unsupported) was necessary to model “infinite” structures. Similarly, although a single point source (E polarized) was sufficient to model simple radiation patterns, the hardware accelerator did not support impedance-matched current sources and, thus, could not model many antenna structures. To expand the capabilities of the hardware accelerator, several new source conditions have been added to the architecture. In this section, we discuss four areas in which the hardware architecture has been enhanced, namely support for arbitrary magnitude and phase specification, magnetic field excitation, point source extensions, and the incorporation of a connecting boundary. These additions have directly enabled support for a wide range of sources, including magnetically polarized point sources, Gaussian beams, and guided mode profiles.

A. Arbitrary Magnitude and Phase Specification

Although the previous hardware design supported plane wave sources, their flexibility was limited. For example, it was not possible to specify an arbitrary magnitude (or phase) at the various points along the wavefront and, thus, the solver was limited to uniform plane waves. Although a temporal envelope function could be applied, spatially modulated waveforms, such as Gaussian beams, could not be implemented. Originally, uniform plane waves were supported because they were relatively easy to implement given that the magnitude along the phase front was constant.

However, it was clear that more advanced waveforms would be required to support a wider array of problems. Thus, the hardware solver was extended such that both the magnitude and phase of each point could be represented as a function of position.

Controlling the parameters of individual points was achieved by modifying the field update equations to incorporate both magnitude and phase terms in the source computation engine. Although this provided accurate answers, it also had the unfortunate consequence of doubling the memory requirements of the simulator and severely limiting performance. To remedy this, the incident field expressions were reformulated to use two new terms, dependant on the magnitude and phase, which have a limited range of [-1, 1]. To understand where these terms came from, assume that the incident electric and magnetic fields can be written as

$$\begin{aligned} E^{inc}(i, j, k, n) &= Source(i, j, n - 0.5) \\ H^{inc}(i, j, k, n) &= Source(i, j, n) \end{aligned}, \quad (1)$$

where:

$$\begin{aligned} Source(i, j, n) &= \\ A(i, j) f_{envelope}(n) &[\sin(\omega n \Delta t + \phi(i, j))] \end{aligned} \quad (2)$$

We can then expand the sine term in equation (2)

$$A(i, j) f_{envelope}(n) \begin{bmatrix} \sin(\omega n \Delta t) \cos(\phi(i, j)) + \\ \cos(\omega n \Delta t) \sin(\phi(i, j)) \end{bmatrix} \quad (3)$$

and rearrange to obtain

$$\begin{aligned} A(i, j) \cos(\phi(i, j)) &[f_{envelope}(n) \sin(\omega n \Delta t)] + \\ A(i, j) \sin(\phi(i, j)) &[f_{envelope}(n) \cos(\omega n \Delta t)] \end{aligned} \quad (4)$$

We can then rewrite equation (4) as

$$term1(i, j) f_{\cos}(n) + term2(i, j) f_{\sin}(n), \quad (5)$$

where

$$\begin{aligned} f_{\sin}(n) &= f_{envelope}(n) \sin(\omega n \Delta t), \\ f_{\cos}(n) &= f_{envelope}(n) \cos(\omega n \Delta t), \\ term1(i, j) &= A(i, j) \cos(\phi(i, j)), \\ term2(i, j) &= A(i, j) \sin(\phi(i, j)). \end{aligned} \quad (6)$$

By limiting the range to $[-1, 1]$, it was possible to compress the terms and store them in the same amount of memory as the previous architecture. Specifically, in the previous design, a 32-bit floating-point value was used to store the source information. In this updated design, the same memory footprint (32 bits) was used, but was subdivided into two 16-bit numbers (one for magnitude, one for phase). By limiting the range of these values, there was no need for an exponent field (as would be required by a floating-point number) and the 16 bits could be used to accurately represent a decimal value with minimal precision loss as compared to a true floating-point representation.

B. Magnetic Field Excitation

In the previous acceleration architecture, sources were introduced by adding the incident electric field to the appropriate mesh points, as determined by a lookup table. However, the hardware lookup table and associated computational logic did not support the direct excitation of magnetic field components. In the new architecture, this lookup table was expanded, as was the control and computational datapaths, to provide support for the introduction of magnetic incident fields (Table 1). This extension directly enabled support for two additional source conditions: a magnetic point source (H polarized) and a connecting boundary, consisting of both electric and magnetic source fields. These new source conditions, as well as other point source additions, are now described.

Table 1. Hardware Lookup Table. This table details the four coefficients (A-D) that must be stored for each material used in the simulation. Entries are included for both electric and magnetic fields. The newest lookup table entries, which support magnetic sources, are shaded.

	Mat #	A	B	C	D
E	0	Ae(0)	Be(0)	Ce(0)	De(0)
	1	Ae(1)	Be(1)	Ce(1)	De(1)
	...	Ae(...)	Be(...)	Ce(...)	De(...)
H	0	Ah(0)	Bh(0)	Ch(0)	Dh(0)
	1	Ah(1)	Bh(1)	Ch(1)	Dh(1)
	...	Ah(...)	Bh(...)	Ch(...)	Dh(...)

C. Point Source Extensions

With respect to point sources, recall that the previous acceleration architecture only provided support for a single E-polarized point source. In order to expand the capabilities of hardware platform, two primary point source extensions were incorporated, specifically, magnetically polarized point sources, as well as direct support for voltage and current sources.

When modeling simple radiators, a magnetically polarized point source is of little value, as a corresponding E-polarized source could be used (assuming the structure's impedance is known). However, the importance of such a source becomes readily apparent when simulating devices of higher complexity, where the electric and magnetic components of the source cannot necessarily be related by real impedance. For example, the characteristic impedance of active devices, such as power supplies, amplifiers, and transistors, may change over the duration of simulation. In these cases, it would be impossible to model an equivalent source without using mathematically complex approximations, which would complicate the overall design and reduce the accelerator's performance. To this end, the acceleration architecture was modified to generate H-polarized point sources.

Support for both E- and H-polarized sources was achieved by designing more generalized source computation engines that can be quickly switched to produce either electric or magnetic incident fields as needed. At the end of each half timestep, central control instructs the source computation engines to reconfigure themselves to perform the appropriate field update. This switch command is pipelined with the existing data and therefore does not impede the accelerator's performance.

After providing support for magnetic point sources, the hardware solver was then extended to provide direct support for voltage and current sources. By specifying the source impedance, in addition to the time-domain waveform, Thévenin and Norton equivalents could be constructed that made use of the underlying support of the E- and H-polarized point sources [4, 7]. This capability is useful for simulating the operation of circuits, microwave amplifiers, and custom antennas designed for a matched input impedance.

D. Connecting Boundary

A connecting boundary is the cornerstone of the FDTD total-field/scattered-field (TF/SF) formulation and is used to introduce a variety of incident source conditions, as well as easily detect scattering from an object [4]. These scattered results can then be analyzed

using post-processing techniques, such as Fourier transforms, near-to-far field transformations, and also radar cross-section calculations. Although the previous processing architecture supported a scattered-field formulation, which made determining the scattered fields quite easy, this formulation could not support extensions for more advanced sources, such as spatially modulated plane waves. Thus, it became necessary to implement a connecting boundary within the hardware solver.

The implementation of the hardware's connecting boundary was achieved by modifying the preprocessing performed on the host PC. Before a hardware simulation begins, the host analyzes the input parameters and loads the hardware accelerator's on-board memory with the appropriate runtime data. In this manner, the host can construct an effective connecting boundary by calculating the particular magnitude and phase required at every point along the boundary such that the incident wave propagates forward, and the associated backward traveling wave is cancelled. Specifically, two 32-bit floating-values are calculated along the connecting boundary before the simulation begins. These additional computations add minimal overhead and do not affect performance as the bulk of the computational time occurs while iteratively solving the solution space over many thousands of time steps.

By combining these updates with the recent addition of arbitrary magnitude and phase specification, the connecting boundary enabled support for a variety of additional source conditions, including Gaussian beams. Not only does this extend the capabilities of the accelerated solver, it can also lead to a reduction of problem size. For instance, applications such as optical filters, switches, and mode converters require the guiding of light from a waveguide onto another device. If the underlying platform cannot model the waveguide output directly (e.g., guided mode profile), it becomes necessary to simulate both the input waveguide along with the ultimate device under test. This leads to much larger mesh sizes, which results in longer simulation times, as well as increased numerical dispersion. However, if the guided mode profile can be entered directly, modeling the source waveguide along with the device under test is no longer necessary. Thus, by using the hardware's connecting boundary capability, the input waveguide problem can be solved separately, using the result to apply a known guided source profile directly at the device.

In this section we presented four areas in which the FDTD acceleration platform was extended, including arbitrary magnitude and phase specification, magnetic field excitation, point source extensions, and a

connecting boundary. The incorporation of these capabilities into the hardware solver enabled a much wider array of incident source conditions, such as voltage and current sources, Gaussian beams, and guided mode profiles, and thus directly provides support for a much broader application base, including advanced antenna and waveguide simulations. The next step in this process was to enhance the capabilities of the absorbing boundary conditions in order to further broaden the domain of the accelerated solver.

III. ADVANCED BOUNDARY CONDITION SUPPORT

When performing FDTD simulations, an appropriate absorbing boundary condition is necessary to prevent the non-physical reflection of outward-going waves back into the observation region. To this end, the original acceleration architecture incorporated Perfectly Matched Layer (PML) absorbing boundaries [8]. These boundaries "match" the outermost boundary layers to the background material of the computational space and then attenuate the outgoing fields. Unfortunately, if a material other than the background material were placed next to the boundary, such as the structure being simulated, the boundary nodes would no longer "match" the computational region and back reflections would occur. Additionally, if the device being simulated is part of a larger system, it may be necessary to extend a piece of the device into the boundary to give the appearance that it is part of a complete system. To resolve these issues, the hardware accelerator was modified to enable the extension of objects in the boundary layers. This capability was achieved by allowing mesh material information to be stored with both computation and boundary nodes. Previously, mesh material information was only stored for nodes inside the computation region. This was acceptable because nodes in the absorbing boundary were always assumed to be free space. Additional storage has been added in the new architecture to maintain information about material properties in the absorbing boundaries. Now, the acceleration engine can use this information to calculate the appropriate PML coefficients before they are used in the boundary updates.

The new architecture allows any dielectric structure to be extended into the boundary to create the appearance of an infinite space. Although an outward going wave may still be reflected after reaching the last absorbing layer, enough layers can be provided such that the magnitude of the reflection is inconsequential, as is the case in any software implementation. Specific

applications that benefit from this implementation include optical waveguides, periodic structures, and substrates with etched defects.

When coupled with the new source configuration, the extension of materials into the absorbing boundary enables much more efficient simulations for a variety of applications. In the next section, we present two such applications, the design of a coupled resonator optical waveguide (CROW) and a structure exhibiting left-handed behavior (LHM), and demonstrate the accuracy of the hardware accelerator.

IV. RESULTS

In order to verify the accuracy of these platform additions, a CROW structure was modeled and compared against published results [9]. A CROW structure is a common building block in many optical communication systems because of its ability to store/delay optical signals. Unfortunately, the exact behavior of CROW structures is difficult to determine analytically and, thus requires computational methods for their analysis. After extending the capabilities of the hardware platform, as described above, the accelerated solver could now be applied to such devices.

The following example uses a CROW as a delay element. The input and output waveguides run parallel to one another, but are separated by two ring resonators. This particular structure is made of silicon and placed in a free space environment. A 16 layer PML boundary surrounds the computational space. Because this structure is a component in a larger system, the input and output waveguides must be extended into the absorbing boundary. The input wave is introduced at one end of the left waveguide using the new connecting boundary source condition. The problem was simulated using a Gaussian modulated input pulse of bandwidth 0.2% for 200,000 timesteps, which is equivalent to about 20 ps. Fig. 2 shows the transient results at several points in the simulation.

The hardware accelerator was able to solve this 5.71 million node problem in 7.55 hours, corresponding to roughly 42 Mnps of sustained computational throughput (see [1, 2] for a detailed discussion of this performance measurement). Fig. 2 clearly shows how the input pulse is placed on the output after a delay of several picoseconds, which is in agreement with the two-dimensional simulation results presented in [9].

Next, we simulated a twenty-ring resonator structure, with a computational region size of 49.61 million FDTD nodes. This simulation was performed for 450,000 time steps and required 147.6 hours of

computation time. Previously, such a simulation would have been impossible in a standard desktop computing environment. The CROW achieved a delay of 15.78 ps delay (Fig. 3). In comparing these results against those of the two-ring structure, note that the resonant frequency is the same, but the overall transmission efficiency has decreased, which is due to the increased propagation losses associated with additional rings, including bending loss, roughness loss, and coupling loss. Furthermore, these simulations have revealed previously unknown scalability relationships that will simplify future CROW structure analyses [10]. A more thorough treatment of these results, including simulation data for five- and ten-ring structures, can be found in [10].

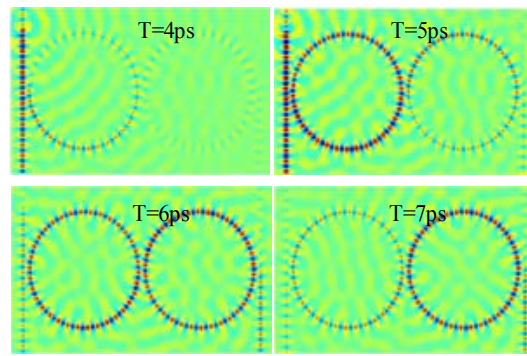


Fig. 2. Propagation through the 2-ring CROW structure. Here we see snapshots of the incident pulse as it travels through the ring resonators and, ultimately, to the output waveguide. The delay from input to output directly corresponds to previously published results.

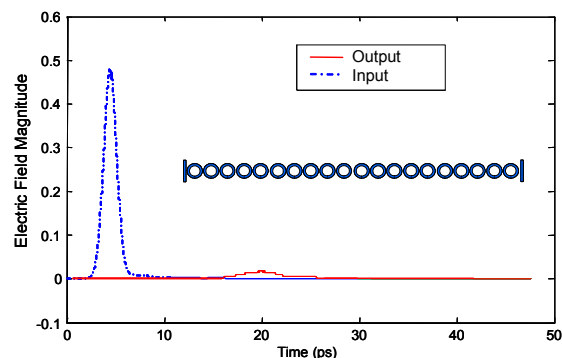


Fig. 3. Propagation through the 20-ring CROW structure. Here we see the input and output pulses associated with the 20-ring CROW. Note that the output pulse is a delayed (and attenuated) version of the input pulse.

Next, we modeled an LHM structure, which was composed of a periodic array of unit cells (Fig. 4).

Each unit cell consisted of an SRR structure patterned on one side of a dielectric substrate ($\epsilon_r = 3.4$) (Fig. 5) and a metallic wire ($0.5 \text{ mm} \times 1.0 \text{ mm} \times 20 \text{ mm}$) patterned on the other side of the substrate. The thickness of the SRR, the wire, and the substrate were chosen to be 0.5 mm . This unit cell, which measured $20 \text{ mm} \times 20 \text{ mm} \times 20 \text{ mm}$, was then replicated twenty times in the YZ plane, ten times in the XY plane, and three times in XZ plane to form an array of 600 SRR+wire pairs (lattice constant $a = 30 \text{ mm}$). This LHM structure was placed inside a two-dimensional waveguide formed by parallel, perfectly conducting plates, each 40.15 cm wide and 24 cm long, in order to provide vertical confinement and more accurately reflect a guided mode source.

Ultimately, the computational domain for this structure measured $24 \text{ cm} \times 40.15 \text{ cm} \times 5 \text{ cm}$, or $481 \times 803 \times 101$ cells (~ 40 million nodes), not including the PML absorbing boundary region. For an FDTD discretization of 0.5 mm , the corresponding timestep is $9.63 \times 10^{-4} \text{ ns}$. The 20,000 timestep simulation required less than 2 GB of memory and approximately 5.5 hours of computation time on the Celerity™ accelerator card [2]. However, because the acceleration platform contains 16 GB of RAM, an LHM structure consisting of up to 4,700 unit cells could be simulated.

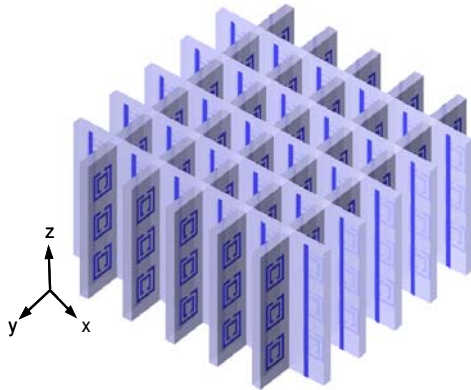


Fig. 4. LHM structure. This is a model (scaled down) of the LHM structure simulated on the hardware platform. From this model, it is easy to see both the SRRs and the wires.

To determine frequencies at which negative permittivity and permeability might exist, the transmission spectra of the LHM structure is measured to identify stopband frequency regions. Once these frequency regions are identified, a continuous wave is used to examine the steady-state behavior of the LHM structure. For this particular LHM structure, a broadband, z -polarized windowed plane wave, propagating along the x -direction, was used. A point detector was placed at the far end of the LHM structure in order to measure the

transmission spectra through the periodic array of SRRs. Specifically, the point detector recorded the time-varying electric and magnetic field amplitudes, which were then normalized to the source. The frequency response was then obtained by performing a Fast Fourier Transform (FFT) of the normalized data. Two simulations were performed: one with the SRRs alone (without wires) and one with both SRRs and wires. From these results, we see that the SRR structure, at resonance, has a stopband 38 dB down at 2.75 GHz (Fig. 6). For both wires and SRRs together, a small passband exists between 3.75 GHz and 4.25 GHz , near the resonance of the rings.

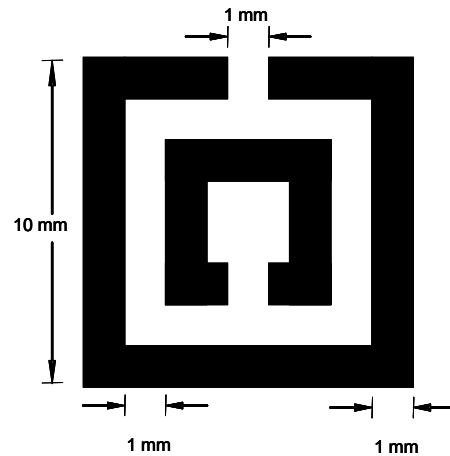


Fig. 5. A split-ring resonator. Here we see the SRR used in the LHM model. The length and width of each SRR were 10 mm , and the azimuthal inter-ring gaps were 1 mm .

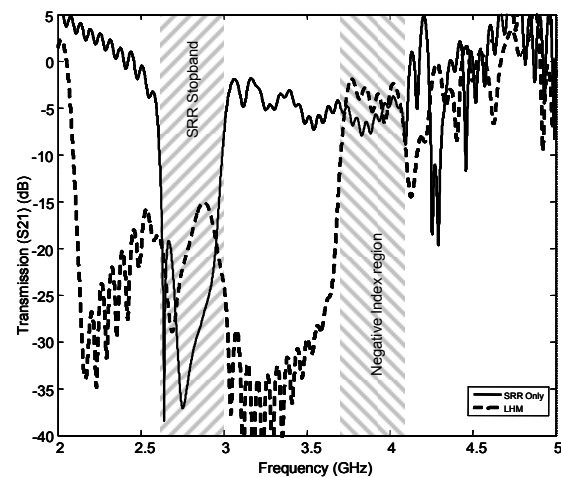


Fig. 6. Transmission Spectra of SRRs and SRRs + Wires (LHM). From these results, we see that the SRR structure, at resonance has a stopband 38 dB down at 2.75 GHz , with regions of positive and negative permeability on both sides. For both wires and SRRs together, a small passband exists between 3.75 GHz and 4.25 GHz , near the resonance of the rings.

To numerically demonstrate that the composite structure formed from the combination of SRRs and wires possesses a negative index of refraction, we constructed a 26° prism and embedded the LHM structure within it. By measuring the direction of the power leaving the prism, it is possible to calculate the index of refraction using Snell's Law.

The prism/LHM structure was simulated using a windowed plane wave source. The frequency of the incident beam was varied according to the transmission spectra results previously obtained (Fig. 6). Specifically, simulations were performed at frequencies of 2.88 GHz, 3.0 GHz, 3.8 GHz, and 3.9 GHz. The first frequency, 2.88 GHz, was chosen because it lies within the resonance band of the SRR structure. Such a frequency finds the structure to be highly attenuating, and a positive index of refraction was seen. Next, we shifted the frequency away from the resonance band of the SRRs to the edge of the stop band at 3.0 GHz. At this frequency, the overall LHM structure is highly dispersive, but it still possesses a positive index of refraction. The next frequency tested was 3.8 GHz, for which the structure is less dispersive and we note that the index of refraction has been slightly changed ($n = -1.4356$). Specifically, the wave front is now directed away from the surface of the prism, indicating a negative refraction index (Fig. 7). Finally, the structure was excited using a 3.9 GHz source, for which the structure is less dispersive but with a positive index of refraction.

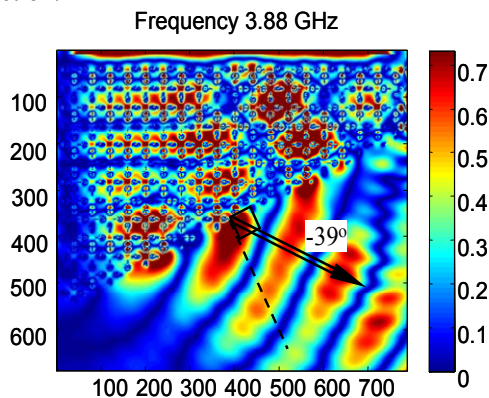


Fig. 7. Demonstrated Negative Refractive Index. Here we see the wave exiting the LHM/Prism structure. Notice that the wave front leaves the prism to the left of the normal, indicating negative refraction.

V. CONCLUSION

In this paper we presented several architectural additions to our previously published hardware-based FDTD acceleration platform, including H-polarized point sources, voltage and current sources, Gaussian

beams, spatially windowed plane waves, and user-defined sources, such as waveguide mode profiles. We also discussed the recent support for extending objects into the absorbing boundary, which minimizes non-physical back reflections. With the addition of these features, the FDTD acceleration hardware has become a more robust and powerful tool, enabling the rapid simulation of a wide breadth of applications, including antennas, waveguide structures, and optics. Ultimately, these features continue to demonstrate the capabilities of hardware-based acceleration tools for computational electromagnetics and prove, once again, the viability of such platforms for both academic and industrial applications.

REFERENCES

- [1] J. P. Durbano, F. E. Ortiz, J. R. Humphrey, D. W. Prather, and M. S. Mirotznik, "Hardware implementation of a three-dimensional Finite-Difference Time-Domain algorithm," *IEEE Antennas and Wireless Propagation Letters*, vol. 2, pp. 54-57, 2003.
- [2] J. P. Durbano, J. R. Humphrey, F. E. Ortiz, P. F. Curt, D. W. Prather, and M. S. Mirotznik, "Hardware Acceleration of the 3D Finite-Difference Time-Domain Method," presented at IEEE AP-S International Symposium on Antennas and Propagation, 2004.
- [3] W. Chen, P. Kosmas, M. Leeser, and C. Rappaport, "An FPGA Implementation of the Two-Dimensional Finite-Difference Time-Domain (FDTD) Algorithm," presented at The Twelfth ACM International Symposium on Field-Programmable Gate Arrays (FPGA), 2004.
- [4] A. Taflov and S. C. Hagness, *Computational Electrodynamics: The Finite-Difference Time-Domain Method*, 3rd ed. Norwood: Artech House, 2005.
- [5] L. Verducci, P. Placidi, G. Matrella, L. Roselli, F. Alimenti, P. Ciampolini, and A. Scorzoni, "A feasibility study about a custom hardware implementation of the FDTD algorithm," presented at The 27th General Assembly of the URSI, Maastricht, Netherlands, 2002.
- [6] R. N. Schneider, M. M. Okoniewski, and L. E. Turner, "A Software-Coupled 2D FDTD Hardware Accelerator," presented at IEEE AP-S International Symposium on Antennas and Propagation, Monterey, CA, 2004.
- [7] M. M. Mano, *Digital Design*, 3rd ed. Upper Saddle River: Prentice Hall, 2001.

- [8] J.-P. Berenger, "Three-Dimensional Perfectly Matched Layer for the Absorption of Electromagnetic Waves," *Journal of Computational Physics*, vol. 127, pp. 363-379, 1996.
- [9] J. K. S. Poon, J. Scheuer, S. Mookherjea, G. T. Paloczi, Y. Y. Huang, and A. Yariv, "Matrix analysis of microring coupled-resonator optical waveguides," *Optics Express*, vol. 12, pp. 90-103, 2004.
- [10] J. P. Durbano, A. S. Sharkawy, S. Shi, F. E. Ortiz, and P. F. Curt, "Accelerated Design Tools for Nanophotonic Devices and Applications," in *Handbook of Nanoscience, Engineering, and Technology*, D. Brenner, Ed., 2nd ed: CRC Press, 2006.



Petersen F. Curt is currently a Senior Engineer in the Accelerated Computing Division of EM Photonics, Inc. He received his B.Cp.E and M.E.E degrees from the University of Delaware in 2003, and 2005. Mr. Curt's research interests include hardware acceleration of

computationally-intense scientific algorithms and the study of reconfigurable logic in embedded systems.



James P. Durbano, Ph.D., is currently the Chief Hardware Architect of EM Photonics, Inc., Newark, DE and an Assistant Professor in the Computer and Information Sciences Department at the University of Delaware. He received the B.Cp.E., M.E.E., and Ph.D. degrees from the University of Delaware in 2000, 2002, and 2004, respectively. Dr. Durbano's research interests involve hardware-based acceleration of scientific computing using a variety of platforms, including field-programmable gate arrays (FPGAs), digital signal processors (DSPs), and graphics processing units (GPUs). Much of his work in this area has been focused on accelerating the Finite-Difference Time-Domain method.



Michael R. Bodnar is currently a M.S. student in the Electrical and Computer Engineering Department at the University of Delaware. He received a B.Cp.E. from the University of Delaware in 2005. Mr. Bodnar's research interests include hardware acceleration of computationally-intense scientific algorithms.



Shouyuan Shi, Ph.D., is currently an Associate Professor in the Department of Electrical and Computer Engineering, University of Delaware, Newark. He received the B.S., M.S., and Ph.D. degrees from Xidian University, Xi'an, China in 1991, 1994 and 1997 respectively, all in electrical engineering. His research interests include electromagnetic numerical modeling, electromagnetic imaging, antenna design, diffractive optical elements, RF microphotonic modulators, microdisk lasers, left-handed materials, and photonic crystals and their applications.



Mark S. Mirotznik, Ph.D, is currently an associate professor of Electrical Engineering and Computer Science at The Catholic University of America. He received a BSEE degree from Bradley University, Peoria Illinois, in 1988, MS degrees in Electrical Engineering and Biomedical Engineering from The University of Pennsylvania in 1991 and a Ph.D. in Biomedical Engineering from The University of Pennsylvania in 1992. Dr. Mirotznik's research interests include computational electromagnetics, biomedical instrumentation and micro/nano scale optical elements.

MoM Solution to Scattering from Three-Dimensional Inhomogeneous Magnetic and Dielectric Bodies

M. Hasanovic, C. Mei, J. R. Mautz, and E. Arvas

L. C. Smith College of Engineering and Computer Science
Syracuse University, Syracuse, NY 13244, USA
Email: mhasanov@syr.edu

Abstract — This paper presents a method of moments solution to scattering problems that involve inhomogeneous magnetic and dielectric bodies of arbitrary shapes. The volume equivalence principle was used to switch from an original problem that deals with an inhomogeneous magnetic and dielectric scatterer to a problem in free space with equivalent sources. The problem is described through a mixed potential formulation. The method of moments technique is then applied to achieve a numerical solution to the original problem. The volume of the scatterer is meshed by tetrahedral cells and face-based functions are applied to expand unknown quantities. Special attention is paid to the curl operation on vector potentials and corresponding volume integrals. The proposed formulation has been evaluated through some examples.

I. INTRODUCTION

The three-dimensional approach in solving particular electromagnetic scattering problems using the method of moments has been applied for the first time in the early 1980's. In 1984 Schaubert et al. [1] used tetrahedral cells to calculate electromagnetic scattering by arbitrarily shaped inhomogeneous dielectric bodies. This was the first time that three-dimensional cells and the volume formulation have been used in the computation of scattering involving the method of moments. They have basically opened a door to a new area of inhomogeneous scatterers. In 1986 Schaubert and Meaney have improved the calculations [2], especially in the domain of computation time. Singular integrals resulting from integration in the vicinity of sources have been evaluated by isolating the singularity in an infinitesimally small sphere and then using the analytical approach described in [3]. Recent work by Kulkarni et al. published in 2004 [4] compared face-based expansion functions used in [1] to the edge-based solenoidal basis functions used in [5], [6], and [7].

An extensive literature in this area shows a continuous interest in the method of moments technique in solving numerous theoretical and practical electromagnetic problems related to electromagnetic scattering. Many electromagnetic scattering problems have been solved using this approach. Most of them, however, deal with the two-dimensional meshing and expansion functions.

These problems usually involve homogeneous scatterers and the surface integral formulation [8]. Induced polarization currents, be them electric and/or magnetic, are located at the surface of the scatterer and can be represented through two-dimensional functions (pulse, rooftop, etc). There is not enough effort put in solving electromagnetic scattering from inhomogeneous scatterers. There are only a few papers that deal with inhomogeneous dielectrics. Usually they are related to some conventional geometries such as the sphere, the cube, and the cylinder. Most of them utilize symmetry of the shape in order to reach the final solution.

The main contribution of this paper is that it offers a generalized volume integral formulation for scatterers of arbitrary shape filled with an arbitrary magnetic and dielectric medium. The proposed formulation has been applied to numerous practical examples of scatterers illuminated by electromagnetic plane waves. Although this article presents data related to some symmetrical three dimensional scatterers, the approach is not limited to the shape of the scatterer in any sense. This is a significant generalization because previous work in this area dealt with scatterers of particular shapes. Furthermore, the developed solution does not put any limits on the geometrical assignment of material properties to the scatterer. It can be applied to multilayered scatterers, scatterers with materials assigned to different regions of the scatterer in a linear, exponential or any other fashion, etc.

II. FORMULATION

Assume that a source-free region containing an inhomogeneous magnetic and dielectric scatterer is illuminated by a plane electromagnetic wave. A magnetic and dielectric material is one that contains both magnetic and electric properties, i.e. both μ_r and ϵ_r of the material are not equal to 1. We can describe the electromagnetic behavior of the structure using Maxwell's equations

$$\nabla \times \mathbf{E}(\mathbf{r}) = -j\omega\mu_0\mu_r(\mathbf{r})\mathbf{H}(\mathbf{r}), \quad (1)$$

$$\nabla \times \mathbf{H}(\mathbf{r}) = j\omega\epsilon_0\epsilon_r(\mathbf{r})\mathbf{E}(\mathbf{r}), \quad (2)$$

$$\nabla \cdot [\epsilon_0\epsilon_r(\mathbf{r})\mathbf{E}(\mathbf{r})] = 0, \quad (3)$$

$$\nabla \cdot [\mu_0\mu_r(\mathbf{r})\mathbf{H}(\mathbf{r})] = 0 \quad (4)$$

where $\mathbf{E}(\mathbf{r})$ and $\mathbf{H}(\mathbf{r})$ are the complex valued phasors of the electric and magnetic fields respectively. We replace

the inhomogeneous scatterer by equivalent volume polarization currents $\mathbf{J}(\mathbf{r})$ and $\mathbf{M}(\mathbf{r})$ and charges $\rho_e(\mathbf{r})$ and $\rho_m(\mathbf{r})$ given by

$$\mathbf{J}(\mathbf{r}) = j\omega\epsilon_0[\epsilon_r(\mathbf{r}) - 1]\mathbf{E}(\mathbf{r}), \quad (5)$$

$$\mathbf{M}(\mathbf{r}) = j\omega\mu_0[\mu_r(\mathbf{r}) - 1]\mathbf{H}(\mathbf{r}), \quad (6)$$

$$\rho_e(\mathbf{r}) = \epsilon_0\epsilon_r(\mathbf{r})\mathbf{E}(\mathbf{r}) \cdot \nabla \left(\frac{1}{\epsilon_r(\mathbf{r})} \right), \quad (7)$$

$$\rho_m(\mathbf{r}) = \mu_0\mu_r(\mathbf{r})\mathbf{H}(\mathbf{r}) \cdot \nabla \left(\frac{1}{\mu_r(\mathbf{r})} \right) \quad (8)$$

and switch from the initial problem that involves inhomogeneity to a simpler problem that involves equivalent sources in free space. In (7) and (8), $\rho_e(\mathbf{r})$ and $\rho_m(\mathbf{r})$ were obtained by using the equations of continuity

$$\rho_e(\mathbf{r}) = -\frac{1}{j\omega} \nabla \cdot \mathbf{J}(\mathbf{r}) \quad (9)$$

$$\rho_m(\mathbf{r}) = -\frac{1}{j\omega} \nabla \cdot \mathbf{M}(\mathbf{r}). \quad (10)$$

The scattered field (\mathbf{E}^s , \mathbf{H}^s) can be obtained through the mixed potential formulation, which is

$$\mathbf{E}^s(\mathbf{r}) = -j\omega\mathbf{A}(\mathbf{r}) - \nabla V(\mathbf{r}) - \nabla \times \frac{\mathbf{F}(\mathbf{r})}{\epsilon_0}, \quad (11)$$

$$\mathbf{H}^s(\mathbf{r}) = -j\omega\mathbf{F}(\mathbf{r}) - \nabla U(\mathbf{r}) + \nabla \times \frac{\mathbf{A}(\mathbf{r})}{\mu_0} \quad (12)$$

where $\mathbf{A}(\mathbf{r})$ and $\mathbf{F}(\mathbf{r})$ are the vector potential functions and $U(\mathbf{r})$ and $V(\mathbf{r})$ are the scalar potential functions:

$$\mathbf{A}(\mathbf{r}) = \frac{\mu_0}{4\pi} \int_T \frac{\mathbf{J}(\mathbf{r}') \exp(-jk|\mathbf{r}-\mathbf{r}'|)}{|\mathbf{r}-\mathbf{r}'|} d\tau', \quad (13)$$

$$\mathbf{F}(\mathbf{r}) = \frac{\epsilon_0}{4\pi} \int_T \frac{\mathbf{M}(\mathbf{r}') \exp(-jk|\mathbf{r}-\mathbf{r}'|)}{|\mathbf{r}-\mathbf{r}'|} d\tau', \quad (14)$$

$$V(\mathbf{r}) = \frac{1}{4\pi\epsilon_0} \int_T \frac{\rho_e(\mathbf{r}') \exp(-jk|\mathbf{r}-\mathbf{r}'|)}{|\mathbf{r}-\mathbf{r}'|} d\tau', \quad (15)$$

$$U(\mathbf{r}) = \frac{1}{4\pi\mu_0} \int_T \frac{\rho_m(\mathbf{r}') \exp(-jk|\mathbf{r}-\mathbf{r}'|)}{|\mathbf{r}-\mathbf{r}'|} d\tau' \quad (16)$$

where T is the volume of the scatterer from the initial problem, $d\tau'$ is the differential element of volume at \mathbf{r}' , \mathbf{r}' is the position vector of the source point, and \mathbf{r} is the position vector of the observation point.

Replacing \mathbf{E} in (5) by $\mathbf{E}^s + \mathbf{E}^{inc}$, replacing \mathbf{H} in (6) by $\mathbf{H}^s + \mathbf{H}^{inc}$ where $(\mathbf{E}^{inc}, \mathbf{H}^{inc})$ is the incident field, substituting (11) and (12) into the resulting equations, and using

$$\mathbf{J}(\mathbf{r}) = j\omega \frac{\epsilon_r(\mathbf{r}) - 1}{\epsilon_r(\mathbf{r})} \mathbf{D}'(\mathbf{r}) \quad (17)$$

$$\mathbf{M}(\mathbf{r}) = j\omega \frac{\mu_r(\mathbf{r}) - 1}{\mu_r(\mathbf{r})} \mathbf{B}'(\mathbf{r}) \quad (18)$$

to eliminate $\mathbf{J}(\mathbf{r})$ and $\mathbf{M}(\mathbf{r})$ in favor of new unknowns \mathbf{D}' and \mathbf{B}' , we obtain

$$j\omega\mathbf{A} + \nabla V + \nabla \times \frac{\mathbf{F}}{\epsilon_0} + \frac{1}{\epsilon_0\epsilon_r} \mathbf{D}' = \mathbf{E}^{inc} \quad (19)$$

$$j\omega\mathbf{F} + \nabla U - \nabla \times \frac{\mathbf{A}}{\mu_0} + \frac{1}{\mu_0\mu_r} \mathbf{B}' = \mathbf{H}^{inc}. \quad (20)$$

As it is related to \mathbf{J} in (17), \mathbf{D}' reduces to the displacement vector $\mathbf{D} = \epsilon_0\epsilon_r\mathbf{E}$ when \mathbf{J} satisfies (19). Similarly, \mathbf{B}' reduces to the magnetic induction $\mathbf{B} = \mu_0\mu_r\mathbf{H}$ when \mathbf{H} satisfies (20).

III. APPLYING THE METHOD OF MOMENTS TECHNIQUE

Equations (19) and (20) are two equations that cannot be solved analytically. Expanding the unknown quantities $\mathbf{D}'(\mathbf{r})$ and $\mathbf{B}'(\mathbf{r})$ in terms of a set of face-based functions $\{\mathbf{f}_n(\mathbf{r})\}$ on a tetrahedral mesh as described in [1] and testing with $\{\mathbf{f}_m(\mathbf{r})\}$ as in Galerkin's method, (19) and (20) are transformed into the following set of equations:

$$j\omega \langle \mathbf{f}_m, \mathbf{A} \rangle + \langle \mathbf{f}_m, \nabla V \rangle + \left\langle \mathbf{f}_m, \nabla \times \frac{\mathbf{F}}{\epsilon_0} \right\rangle + \left\langle \mathbf{f}_m, \frac{1}{\epsilon_0\epsilon_r} \mathbf{D}' \right\rangle = \langle \mathbf{f}_m, \mathbf{E}^{inc} \rangle \quad (21)$$

$$j\omega \langle \mathbf{f}_m, \mathbf{F} \rangle + \langle \mathbf{f}_m, \nabla U \rangle - \left\langle \mathbf{f}_m, \nabla \times \frac{\mathbf{A}}{\mu_0} \right\rangle + \left\langle \mathbf{f}_m, \frac{1}{\mu_0\mu_r} \mathbf{B}' \right\rangle = \langle \mathbf{f}_m, \mathbf{H}^{inc} \rangle \quad (22)$$

where \mathbf{D}' and \mathbf{B}' are linear combinations of the \mathbf{f}_n 's containing unknown coefficients D_n and B_n and, for arbitrary \mathbf{A} and \mathbf{B} , $\langle \mathbf{A}, \mathbf{B} \rangle$ is the symmetric product of \mathbf{A} and \mathbf{B} defined to be the integral of their dot product over the volume of the scatterer. Equations (21) and (22) can be solved numerically for $\{D_n\}$ and $\{B_n\}$. All the kinds of terms in (21) and (22) except those involving the curls of vector potentials are treated in [1], [3], and [9].

Consider the term involving the curl of the magnetic vector potential in (22). The vector potential \mathbf{A} is given by (13) where \mathbf{J} is given by (17) with

$$\mathbf{D}'(\mathbf{r}) = \sum_{n=1}^N D_n \mathbf{f}_n(\mathbf{r}) \quad (23)$$

where

$$\mathbf{f}_n(\mathbf{r}) = \begin{cases} \frac{S_n}{3W_n^+} \boldsymbol{\rho}_n^+, & \mathbf{r} \in T_n^+ \\ \frac{S_n}{3W_n^-} \boldsymbol{\rho}_n^-, & \mathbf{r} \in T_n^- \end{cases} \quad (24)$$

In (24), T_n^+ and T_n^- are the two tetrahedrons that have the same face s_n , W_n^\pm is the volume of T_n^\pm , $\boldsymbol{\rho}_n^\pm$ is the vector

from the vertex of T_n^+ opposite s_n to \mathbf{r} , and $\boldsymbol{\rho}_n^-$ is the vector from \mathbf{r} to the vertex of T_n^- opposite s_n (Figure 1).

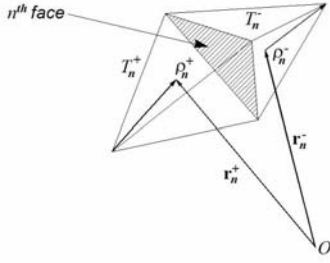


Fig. 1. Tetrahedral elements T_n^+ and T_n^- and notation.

Using (13), (17), (23), and (24), and assuming that ϵ_r is constant in each tetrahedron, we obtain

$$\begin{aligned} & \frac{1}{\mu_0} \nabla \times \mathbf{A}(\mathbf{r}) \\ &= j\omega \sum_{n=1}^N D_n \left[\frac{\beta_{1n}^+ s_n}{3} \nabla \times \mathbf{I}_{1n}^+(\mathbf{r}) + \frac{\beta_{1n}^- s_n}{3} \nabla \times \mathbf{I}_{1n}^-(\mathbf{r}) \right] \end{aligned} \quad (25)$$

where

$$\mathbf{I}_{1n}^\pm(\mathbf{r}) = \frac{1}{W_n^\pm} \int_{T_n^\pm} \boldsymbol{\rho}_n^\pm \frac{\exp(-jkR)}{4\pi R} d\tau' \quad (26)$$

and

$$\beta_{1n}^\pm = \frac{\epsilon_m^\pm - 1}{\epsilon_m^\pm} \quad (27)$$

where ϵ_m^\pm is ϵ_r in T_n^\pm . Testing (25) with the function $\mathbf{f}_m(\mathbf{r})$ yields

$$\begin{aligned} & \left\langle \mathbf{f}_m(\mathbf{r}), \nabla \times \frac{\mathbf{A}(\mathbf{r})}{\mu_0} \right\rangle = \int_{T_m^+} \mathbf{f}_m(\mathbf{r}) \cdot \left[\nabla \times \frac{\mathbf{A}(\mathbf{r})}{\mu_0} \right] d\tau \\ & + \int_{T_m^-} \mathbf{f}_m(\mathbf{r}) \cdot \left[\nabla \times \frac{\mathbf{A}(\mathbf{r})}{\mu_0} \right] d\tau \\ &= \frac{j\omega}{3} \sum_{n=1}^N s_n D_n \left[\beta_{1n}^+ I_{3n}(T_{m,n}^{++}) + \beta_{1n}^- I_{3n}(T_{m,n}^{+-}) \right] \\ & + \frac{j\omega}{3} \sum_{n=1}^N s_n D_n \left[\beta_{1n}^+ I_{3n}(T_{m,n}^{-+}) + \beta_{1n}^- I_{3n}(T_{m,n}^{--}) \right] \end{aligned} \quad (28)$$

where

$$I_{3n}(T_{m,n}^{++}) = \int_{T_m^+} \mathbf{f}_m(\mathbf{r}) \cdot \nabla \times \mathbf{I}_{1n}^+(\mathbf{r}) d\tau \quad (29)$$

$$I_{3n}(T_{m,n}^{+-}) = \int_{T_m^+} \mathbf{f}_m(\mathbf{r}) \cdot \nabla \times \mathbf{I}_{1n}^-(\mathbf{r}) d\tau. \quad (30)$$

A similar derivation can be obtained for the term involving the curl of electric vector \mathbf{F} .

Let us now consider one of the integrals in (29):

$$\begin{aligned} I_{3n}(T_{m,n}^{++}) &= - \int_{T_m^+} \nabla \cdot (\mathbf{f}_m \times \mathbf{I}_{1n}^+) d\tau + \int_{T_m^+} \mathbf{I}_{1n}^+ \cdot (\nabla \times \mathbf{f}_m) d\tau \\ &= - \sum_{i=1}^4 \int_{s_{m,i}^+} \mathbf{n}_{i}^+ \cdot (\mathbf{f}_m \times \mathbf{I}_{1n}^+) ds \\ &= - \frac{S_m}{3W_m^+} \sum_{i=1}^4 \int_{s_{m,i}^+} \mathbf{I}_{1n}^+ \cdot (\mathbf{n}_{i}^+ \times \boldsymbol{\rho}_{m,i}^+) ds \end{aligned} \quad (31)$$

where $s_{m,i}^+$, $i=1, \dots, 4$ are the four faces of the tetrahedron T_m^+ and \mathbf{n}_{i}^+ is the outward pointing unit normal vector to the face $s_{m,i}^+$.

If we now assume a fine mesh, then each of the four faces $s_{m,i}^+$, $i=1, \dots, 4$ is so small that the integral $\mathbf{I}_{1n}^+(\mathbf{r})$ for $\mathbf{r} \in s_{m,i}^+$ can be approximated by its value at the centroid of $s_{m,i}^+$ at $\mathbf{r} = \mathbf{r}_{m,i}^{c+}$. Hence, we can write

$$\begin{aligned} I_{3n}(T_{m,n}^{++}) &= - \frac{S_m}{3W_m^+} \sum_{i=1}^4 \int_{s_{m,i}^+} \mathbf{I}_{1n}^+ \cdot (\mathbf{n}_{i}^+ \times \boldsymbol{\rho}_{m,i}^+) ds \\ &= - \frac{S_m}{3W_m^+} \sum_{i=1}^4 \mathbf{I}_{1n}^+(\mathbf{r}_{m,i}^{c+}) \cdot \int_{s_{m,i}^+} (\mathbf{n}_{i}^+ \times \boldsymbol{\rho}_{m,i}^+) ds. \end{aligned} \quad (32)$$

Similar derivations can be performed for the other three integrals in (29) and (30).

Please note that the singularity resulting from $\mathbf{r}' = \mathbf{r}$ encountered in the evaluation of I_{3n} appears in expression (26) for \mathbf{I}_{1n}^\pm . So treating the singularity in expression (26) for \mathbf{I}_{1n}^\pm automatically takes care of it in the evaluation of I_{3n} .

IV. NUMERICAL RESULTS

Numerical data obtained through the MATLAB implementation of the proposed formulation is given here. We considered two shapes of scatterers - a sphere and a cube. These bodies are illuminated by a θ -polarized plane electromagnetic wave incident from the direction where $\theta=180^\circ$ and $\phi=0^\circ$ ($\mathbf{E}^{\text{inc}} = -\hat{\mathbf{a}}_x E^{\text{inc}} e^{-jkz}$). Results presented here are co-polarized and cross-polarized bistatic radar cross sections.

We first investigated an inhomogeneous two-layer magnetic and dielectric sphere of radius R with $k_0 R = k_0 R_2 = 0.408$ where k_0 is the free-space wave number. The radius of the core is half the radius of the whole sphere. The two layers of the sphere are assigned different material properties. As a first step in developing a mesh the entire outer surface of the sphere had been approximated by a grid of 72 triangles that served as a starting point for a tetrahedral mesh. Then a tetrahedral mesh has been grown from the outer triangular surface into the sphere producing a total of 256 tetrahedra and 548 faces. In order to achieve a better accuracy of the numerical results an additional refinement of the mesh in the close proximity to the outer surface has been undertaken, thus increasing the total number of tetrahedra to 520 and faces to 1184. Also, an additional refinement on the surface between the two layers with two different material properties has been performed. This surface contains surface charge and plays an extremely important

role in the way how this electromagnetic environment behaves. Refining the mesh in the close proximity to this surface resulted in a total of 928 tetrahedra and 2000 faces. Finally, the radius of the sphere has been so adjusted that the total volume of the tetrahedral approximation of the sphere is equal to the actual volume of the initial sphere. All computations have been performed on a regular PC machine with a 64bit CPU and 1024MB of RAM. It took about 2 hours to perform all necessary computations and about 80MB to store all data of interest.

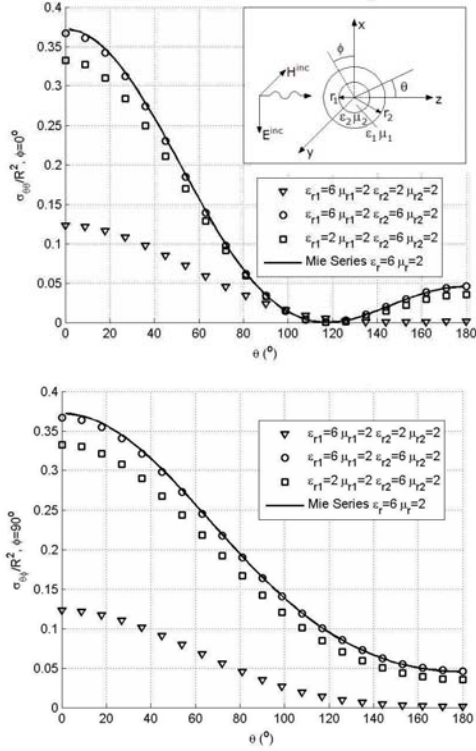


Fig. 2. Bistatic radar cross sections of an inhomogeneous two-layered dielectric and magnetic sphere for $k_0R=0.408$, various values of ϵ_r and μ_r , and number of tetrahedra=928.

Numerical results obtained for this scattering model are compared to results derived from the Mie series expansion and given in [10]. As observed in Figure 2, there is a good agreement between the numerical data and the Mie series solution. We have also performed a convergence test where we increased the number of tetrahedral mesh cells. It has been observed that an increase in the total number of meshing cells and decrease in the cell size increases the accuracy of the numerical solution and that MoM computation results converge to the exact results. We have varied relative permeabilities and permittivities of the two layers and investigated the scattering from this body. Please observe that a change in the relative permeability parameter generally affects the radar cross section of the magnetic and dielectric scatterer. The inner spherical layer plays a less important role in this effect, as it is partially shielded by the outer spherical shell and is electrically smaller than the outer layer [11].

We also investigated an inhomogeneous magnetic and dielectric cube assigned different electric and magnetic properties in a chess-like pattern (black cubical cells are

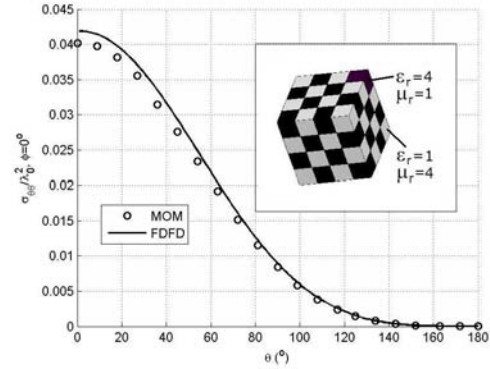


Fig. 3. Bistatic radar cross section $\sigma_{\theta\theta}$ of an inhomogeneous chess-like dielectric and magnetic cube (black inclusions $\epsilon_r=4$ and $\mu_r=1$ and white inclusions $\epsilon_r=1$ and $\mu_r=4$) for $d=0.2\lambda_0$ and number of tetrahedra=768.

filled by a dielectric with relative permeability $\epsilon_r=4$ and white cubical cells are filled by a magnetic with relative permittivity $\mu_r=4$). The length of a side of the cube is $d=0.2\lambda_0$ where $\lambda_0=2\pi k_0$. The center of the cube coincides with the origin of the coordinate system. Numerical results for this scattering model are given in Figure 3 and compared to the results obtained through the implementation of the FDFD formulation presented in [12]. As we can see there was a good agreement between our solution based on the MoM approach and results based on FDFD approach.

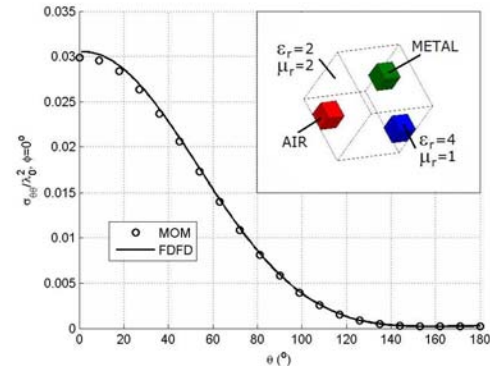


Fig. 4. Bistatic radar cross section $\sigma_{\theta\theta}$ of an inhomogeneous dielectric and magnetic cube with several inclusions (dielectric, air, metal) for $d=0.2\lambda_0$ and number of tetrahedra=768.

The proposed MoM formulation is then applied to calculate co-polarized and cross-polarized bistatic radar cross-sections of a magnetic and dielectric cube with several inclusions. Figure 4 presents numerical results obtained for the case of an inhomogeneous magnetic and dielectric cube ($\epsilon_r=2$, $\mu_r=2$) with the length of a side $d=0.2\lambda_0$ filled with several inclusions (metal, for $-0.05\lambda_0 < x < 0$, $0 < y < 0.05\lambda_0$, $0.05\lambda_0 < z < 0.1\lambda_0$; air, for $-0.05\lambda_0 < x < 0$, $-0.1 < y < -0.05\lambda_0$, $-0.1\lambda_0 < z < -0.05\lambda_0$; dielectric $\epsilon_r=4$, for $0.05\lambda_0 < x < 0.1\lambda_0$, $0.05\lambda_0 < y < 0.1\lambda_0$, $-0.05\lambda_0 < z < 0$). Results for cross-polarized bistatic radar cross

section of this scatterer have also been compared to results obtained through the implementation of [12] and a good agreement was observed.

V. CONCLUSION

This paper presents a numerical solution based on the method of moments for electromagnetic scattering from arbitrarily shaped three-dimensional inhomogeneous magnetic and dielectric scatterers. Cases that we studied here are a dielectric and magnetic sphere and a dielectric and magnetic cube. As observed, the radar cross sections change when the permittivity or permeability of the scatterer change.

As noted we have used the volume equivalence principle. There is also the surface equivalence theorem. Consequently, surface integral equations may be derived from the surface equivalence principle and volume integral equations may be derived from the volume equivalence principle. The volume equivalence principle and corresponding volume integral equations that we used in our work have a number of advantages including the applicability to inhomogeneous scatterers and a better accuracy at resonances (compared to the surface approach). The volume equivalence principle and volume integral equations are therefore mostly used in problems involving penetrable inhomogeneous scatterers. Inhomogeneity as an essential property of a scatterer can not be entirely described by sources on its surface. That is why we need to put equivalent induced current and charge sources inside the scatterer and not only on its surface. This way sources become volumetric in their nature. As it can be observed we move from an original problem involving inhomogeneity to a problem involving induced sources in free space. The latter problem is much easier to be solved. Therefore, as a conclusion, the advantage of using the volume approach and volume integral equations over the surface approach and surface integral equations is their more general property and ability to deal with scatterers that are not homogeneous.

The proposed solution is applicable to any shape of scatterer and to any kind of spatial dependence of material properties. However, it may suffer from a rapid growth of computational complexity in the case of electrically large objects with increased mesh resolution. This problem may be avoided by reducing the total number of unknowns through a choice of different basis functions. Edge-based expansion functions, often referred to as three-dimensional solenoidal expansion functions are first proposed by [5] as a solution to this problem. They have a better convergence rate and higher numerical stability according to [4]. Another way to improve the efficiency of the developed algorithm is to use some acceleration techniques such as those based on the fast Fourier transform [13]. Additional research with the objective of increasing the efficiency of the computer program through a reduction of memory and time requirements is definitely worthwhile.

REFERENCES

- [1] D. H. Schaubert, D. R. Wilton, and A. W. Glisson, "A tetrahedral modeling method for electromagnetic scattering by arbitrarily shaped inhomogeneous dielectric bodies," *IEEE Trans. Antennas Propagat.*, vol. AP-32, pp. 77–85, Jan. 1984.
- [2] D. H. Schaubert and P. M. Meaney, "Efficient computation of scattering by inhomogeneous dielectric bodies," *IEEE Trans. Antennas Propagat.*, vol. AP-34, pp. 587–592, Apr. 1986.
- [3] D. R. Wilton, S. M. Rao, A. W. Glisson, D. H. Schaubert, O. M. Al-Bundak, and C. M. Butler, "Potential integrals for uniform and linear source distributions on polygonal and polyhedral domains," *IEEE Trans. Antennas Propagat.*, vol. AP-32, pp. 276–281, Mar. 1984.
- [4] S. Kulkarni, R. Lemdiasov, R. Ludwig, and S. Makarov, "Comparison of two sets of low-order basis functions for tetrahedral VIE modeling," *IEEE Trans. Antennas Propagat.*, vol. 52, pp. 2789–2794, Oct. 2004.
- [5] L. S. Mendes and S. A. Carvalho, "Scattering of EM waves by homogeneous dielectrics with the use of the method of moments and 3D solenoidal basis functions," *Microwave and Optical Technology Letters*, vol. 12, no. 6, pp. 327–331, Aug. 1996.
- [6] S. A. Carvalho and L. S. Mendes, "Scattering of EM waves by inhomogeneous dielectrics with the use of the method of moments and 3-D solenoidal basis functions," *Microwave and Optical Technology Letters*, vol. 23, no. 1, pp. 42–46, Oct. 1999.
- [7] L. S. Mendes and E. Arvas, "Scattering of a TM wave by a chiral cylinder with the use of the method of moments and solenoidal basis functions," *Microwave and Optical Technology Letters*, vol. 14, no. 4, pp. 225–227, Mar. 1997.
- [8] N. Morita, N. Kumagai, and J. R. Mautz, *Integral Equation Methods for Electromagnetics*. Boston: Artech House, 1990.
- [9] R. D. Graglia, "Static and dynamic potential integrals for linearly varying source distributions in two- and three-dimensional problems," *IEEE Trans. Antennas Propagat.*, vol. AP-35, pp. 662–669, June 1987.
- [10] V. Demir, A. Elsherbeni, D. Worasawate, and E. Arvas, "A graphical user interface (GUI) for plane wave scattering from a conducting, dielectric or a chiral sphere," Software at ACES web site: <http://aces.ee.olemiss.edu>, Sept. 2004.
- [11] M. Hasanovic, "Electromagnetic scattering from an arbitrarily shaped three-dimensional inhomogeneous chiral body," Ph.D. Dissertation, Syracuse University, 2006.
- [12] L. Kuzu, V. Demir, A. Z. Elsherbeni, and E. Arvas "Electromagnetic scattering from arbitrarily shaped chiral objects using the finite difference frequency domain method," *Journal of Electromagnetic Waves and Applications (JEMWA)*, 2006. (Accepted for publication)
- [13] X. C. Nie, N. Yuan, L. W. Li, Y. B. Gan, and T. S. Yeo, "A fast combined field volume integral

equation solution to EM scattering by 3-D dielectric objects of arbitrary permittivity and permeability," *IEEE Trans. Antennas Propagat.*, vol. 54, pp. 961–969, Mar. 2006.



Moamer Hasanovic was born in Sarajevo, Bosnia-Herzegovina, in 1973. He received his B.S. from University of Sarajevo in 1997 and M.S. and Ph.D. degrees in electrical engineering from Syracuse University, Syracuse, NY, in 2002 and 2006, respectively.

He worked as an Electrical Engineer for BH Telecom Engineering, Sarajevo, and as a Teaching Assistant at Syracuse University. He is currently working as an RF Design Engineer at Anaren Microwave, Inc. in East Syracuse, NY. He has been awarded a German Academic Exchange Service Scholarship in 1997. His research interests are in the area of computational electromagnetics and microwave devices.

He is a member of the Applied Computational Electromagnetics Society (ACES).



Chong Mei received his B.S. and M.S. degrees in electrical engineering from Huazhong University of Science and Technology, Wuhan, China, in 1997 and 2000, respectively. He is currently pursuing his Ph.D. degree in electrical engineering at Syracuse

University, Syracuse, NY.

He has been with Anaren Microwave, Inc. in East Syracuse, NY since 2002, as an RF Design Engineer working on component design for the wireless market. His research interests are in computational electromagnetics and microwave devices.



Joseph R. Mautz was born in Syracuse, NY, in 1939. He received the B.S., M.S., and Ph.D. degrees in electrical engineering from Syracuse University, Syracuse, NY, in 1961, 1965, and 1969, respectively.

Until July 1993, he was a Research Associate in the Electrical Engineering and Computer Science Department, Syracuse University, where he worked on radiation and scattering problems. Currently, he is affiliated with the Electrical Engineering and Computer Science Department at the same university. His primary fields of interest are electromagnetic theory and applied mathematics.



Ercument Arvas received the B.S. and M.S. degrees from the Middle East Technical University, Ankara, Turkey, in 1976 and 1979, respectively, and the Ph.D. degree from Syracuse University, Syracuse, NY, in 1983, all in electrical engineering.

From 1984 to 1987, he was with the Electrical Engineering Department, Rochester Institute of Technology, Rochester, NY. In 1987, he joined the Electrical Engineering and Computer Science Department, Syracuse University, where he is currently a Professor in the Electrical Engineering and Computer Science Department. His research and teaching interests are in electromagnetic scattering and microwave devices.

Prof. Arvas is a Member of the Applied Computational Electromagnetics Society (ACES).

Surface Impedance Boundary Conditions of High Order of Approximation for the Finite Integration Technique

Luca Di Rienzo¹, Nathan Ida², and Sergey Yuferev³

⁽¹⁾ Dipartimento di Elettrotecnica, Politecnico di Milano, P.zza L. da Vinci, 32, 20133, Milano, Italy; luca.dirienzo@etec.polimi.it

⁽²⁾ Department of Electrical Engineering, The University of Akron, Akron, OH 44325-3904, USA; ida@uakron.edu

⁽³⁾ Nokia Corp., P.O. Box 1000, Tampere FIN-34101, Finland; sergey.yuferev@nokia.com

Abstract — Time domain Surface Impedance Boundary Conditions (SIBCs) of high order of approximation relating the electric field integral along the edge of the computational cell and the magnetic flux through its facet are derived and implemented into the Finite Integration Technique (FIT). It enables such effects as curvature of the conductor surface and variation of the electromagnetic field along the interface to be accurately described in the formulation. As a result, accuracy of numerical results is improved and the application area is expanded as compared with formulations employing classical low order Leontovich SIBCs. Numerical results obtained using low- and high-order FIT-SIBC formulations are compared with analytical results to demonstrate the advantages of the proposed approach.

Keywords — Surface Impedance Boundary Conditions, Finite Integration Technique, Time Domain Methods, Approximate Boundary Conditions.

I. INTRODUCTION

Although the surface impedance concept has the reputation of a sophisticated numerical technique, it is actually based on well-known assumption, namely: the electromagnetic field distribution in the conductor's skin layer can be described as a damped plane wave propagating in the bulk of the conductor normal to its surface. In other words, the behavior of the electromagnetic field in the conducting region may be assumed to be known *a priori*. The electromagnetic field is continuous across the real conductor's surface, so the intrinsic impedance of the wave remains the same at the interface. Therefore, the ratio E_x/H_y (*Surface Impedance*) at the xy -plane of a dielectric/conductor interface is assumed to be equal to the intrinsic impedance of the plane wave propagating in the conductor, in the positive z -direction

$$\left. \frac{E_x}{H_y} \right|_{\text{interface}} = \sqrt{\frac{j\omega_{\text{source}}\mu}{\sigma + j\omega_{\text{source}}\epsilon}} \Big|_{\sigma \gg \omega\epsilon} \approx \frac{1+j}{2} \omega_{\text{source}}\mu\delta, \quad (1)$$

$$\delta = \sqrt{\frac{2}{\omega_{\text{source}}\sigma\mu}}.$$

The *surface* relation in (1), taking into account parameters of the conductor's material and the source, contains all necessary information about the field distribution in the conductor's *volume*. Thus it may be used as a boundary condition to the governing equations for the dielectric space that excludes the conductor from the region of solution and reduces the computational space to be discretized. It can be represented in another form relating normal and tangential magnetic fields at the interface.

The relation in (1) is usually referred to as Leontovich's SIBC. Although it has been widely used in combination with most numerical methods, it does not take into account curvature of the interface and variation of the field along the surface. SIBCs of high order of approximation allowing for both mentioned effects have been developed in frequency domain [1-2] and time domain [3] to improve accuracy and expand the application area of the surface impedance concept.

In the present paper time domain SIBCs of high order of approximation are derived in the state variables of the Finite Integration Technique (FIT) [4]. It extends results obtained in [5] where a low order SIBC has been implemented into the FIT.

II. THE FINITE INTEGRATION TECHNIQUE

The FIT, first proposed in [4], is based on the discretization of Maxwell equations in their integral form on two different staggered grids, a primary and a dual grid [6-7]. An example of the orthogonal dual mesh used in FIT is shown in Fig. 1.

Let L_i , S_i , V_i be the edges, facets, and volumes of the primary grid G and \tilde{L}_i , \tilde{S}_i , \tilde{V}_i the edges, facets, and volumes of the dual grid \tilde{G} . Then, the state variables in FIT are defined as

$$\hat{e}_i = \int_{L_i} \vec{E} \cdot d\vec{l} \quad , \quad \hat{b}_i = \int_{S_i} \vec{B} \cdot d\vec{A} \quad , \quad (2)$$

$$\hat{h}_i = \int_{\tilde{L}_i} \vec{H} \cdot d\vec{l} \quad , \quad \hat{d}_i = \int_{\tilde{S}_i} \vec{D} \cdot d\vec{A} \quad , \quad (3)$$

while the current flux and the electric charge are defined as

$$\hat{j}_i = \int_{\tilde{S}_i} \vec{J} \cdot d\vec{A} \quad , \quad q_i = \int_{\tilde{V}_i} q \cdot dV \quad . \quad (4)$$

The discretized Maxwell equations are written in compact form in matrix notation as

$$\mathbf{C}\hat{\mathbf{e}} = -\frac{d}{dt}\hat{\mathbf{b}} \quad , \quad \tilde{\mathbf{C}}\hat{\mathbf{h}} = \frac{d}{dt}\hat{\mathbf{d}} + \hat{\mathbf{j}} \quad , \quad (5)$$

$$\hat{\mathbf{S}}\hat{\mathbf{b}} = 0 \quad , \quad \tilde{\mathbf{S}}\hat{\mathbf{d}} = \mathbf{q} \quad , \quad (6)$$

where \mathbf{C} and $\tilde{\mathbf{C}}$ are the discrete equivalent of the continuous curl operator and \mathbf{S} and $\tilde{\mathbf{S}}$ are the discrete equivalent of the continuous divergence operator.

Equations (5) and (6) constitute the so-called *Maxwell's Grid Equations*.

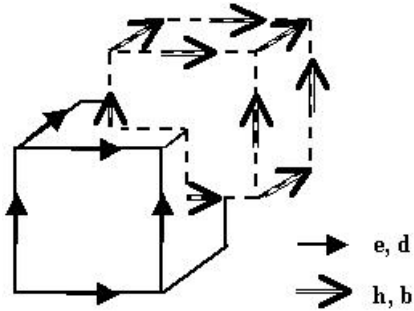


Fig. 1. One cell of the primary grid and one cell of the dual grid.

To complete the discrete system (5-6), the following three additional matrix operators (*material matrices*) must be introduced

$$\hat{\mathbf{d}} = \mathbf{M}_\varepsilon \hat{\mathbf{e}} \quad , \quad \hat{\mathbf{j}} = \mathbf{M}_k \hat{\mathbf{e}} \quad , \quad \hat{\mathbf{h}} = \mathbf{M}_{\mu^{-1}} \hat{\mathbf{b}} \quad . \quad (7)$$

In a dual-orthogonal grid system, the primary edges and dual facets (as well as the dual edges and primary facets) intersect at 90° . In this case the material matrices are diagonal with entries

$$\mathbf{M}_\varepsilon(i,i) = \frac{\varepsilon_{eff,i} \tilde{S}_i}{L_i} \quad , \quad \mathbf{M}_k(i,i) = \frac{\sigma_{eff,i} \tilde{S}_i}{L_i} \quad ,$$

$$\mathbf{M}_{\mu^{-1}}(i,i) = \frac{\tilde{L}_i}{\mu_{eff,i} S_i} \quad , \quad (8)$$

where $\varepsilon_{eff,i}$, $\sigma_{eff,i}$, and $\mu_{eff,i}$ are the material coefficients. These material relations are obtained introducing virtual field component \vec{E}^{virt} at the intersection point of the dual facet and the primary edge and \vec{B}^{virt} at the intersection point of primary facet and dual edge, so that

$$\hat{e}_i \cong E_i^{virt} \cdot L_i \quad , \quad \hat{d}_i \cong \varepsilon_{eff,i} E_i^{virt} \cdot \tilde{S}_i \quad ,$$

$$\hat{b}_i \cong B_i^{virt} \cdot S_i \quad , \quad \hat{h}_i \cong \mu_{eff,i}^{-1} B_i^{virt} \cdot \tilde{L}_i \quad . \quad (9)$$

Using a leap frog scheme, (5) are discretized in time as

$$\hat{\mathbf{e}}^{n+1/2} = \hat{\mathbf{e}}^{n-1/2} + \Delta t \left[\mathbf{M}_\varepsilon^{-1} \mathbf{C}^T \mathbf{M}_{\mu^{-1}} \hat{\mathbf{b}}^n \right] \quad ,$$

$$\hat{\mathbf{b}}^{n+1} = \hat{\mathbf{b}}^n - \Delta t \mathbf{C} \hat{\mathbf{e}}^{n+1/2} \quad . \quad (10)$$

III. SIBC OF HIGH ORDER OF APPROXIMATION IN TERMS OF FIT VARIABLES

In order to derive the SIBC of high order of approximation in the context of FIT, let us recall here that the approximate relation between the normal and tangential components of the magnetic flux density in the time domain can be written in the form [3]

$$B_\eta^s = \sum_{i=1}^2 \frac{\partial}{\partial \xi_i} \left\{ T_1 \times B_{\xi_i}^s + \frac{d_{3-i} - d_i}{2d_i d_{3-i}} T_2 \times B_{\xi_i}^s \right.$$

$$+ \frac{3d_{3-i}^2 - d_i^2 - 2d_i d_{3-i}}{8d_i^2 d_{3-i}^2} T_3 \times B_{\xi_i}^s$$

$$\left. + \frac{1}{2} T_3 \times \left(-\frac{\partial^2 B_{\xi_i}^s}{\partial \xi_{3-i}^2} + \frac{\partial^2 B_{\xi_i}^s}{\partial \xi_i^2} + 2 \frac{\partial^2 B_{\xi_{3-i}}^s}{\partial \xi_i \partial \xi_{3-i}} \right) \right\} \quad , \quad (11)$$

where the superscript “s” denotes quantities at the conductor surface, “*” denotes a time convolution product, d_k , $k=1,2$, are the local radii of curvature, and (ξ_1, ξ_2, η) are the principal curvature coordinates (Fig. 2).

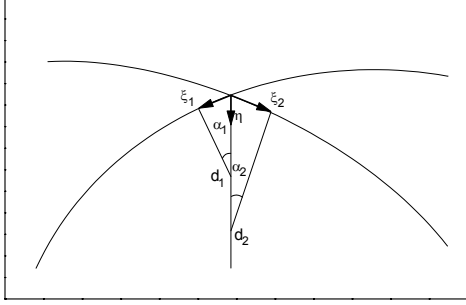


Fig. 2. Local orthogonal curvilinear coordinate systems related to the surface.

The time functions T_m , $m=1,2,3$ are defined as

$$T_1(t) = \sqrt{\frac{\mu_0}{\varepsilon_r \varepsilon_0}} I_0 \left(\frac{\sigma}{2\varepsilon_r \varepsilon_0} \right) \exp \left(-\frac{\sigma}{2\varepsilon_r \varepsilon_0} \right),$$

$$T_2(t) = \frac{1}{\sigma} \left[1 - \exp \left(-\frac{\sigma}{\varepsilon_r \varepsilon_0} \right) \right],$$

$$T_3(t) = \frac{2t}{\sigma \sqrt{\varepsilon_r \varepsilon_0 \mu_0}} I_1 \left(\frac{\sigma}{2\varepsilon_r \varepsilon_0} \right) \exp \left(-\frac{\sigma}{2\varepsilon_r \varepsilon_0} \right).$$

The first term in (11) gives the SIBC of Leontovich's order of approximation in which the body's surface is considered as a plane and the field is assumed to be penetrating into the conductor only in the direction normal to the body's surface. The second and third terms give corrections taking into account the curvature of the conductor surface. The last term allows for the electromagnetic field diffusion in directions tangential to the conductor's surface.

Let us analyze the expression in the last term of the right hand side of (11)

$$\begin{aligned} & \sum_{i=1}^2 \frac{\partial}{\partial \xi_i} \left(-\frac{\partial^2 B_{\xi_i}^s}{\partial \xi_{3-i}^2} + \frac{\partial^2 B_{\xi_i}^s}{\partial \xi_i^2} + 2 \frac{\partial^2 B_{\xi_{3-i}}^s}{\partial \xi_i \partial \xi_{3-i}} \right) = \\ & = \frac{\partial}{\partial \xi_1} \left(\frac{\partial^2 B_{\xi_1}^s}{\partial \xi_1^2} + \frac{\partial^2 B_{\xi_1}^s}{\partial \xi_2^2} \right) + \frac{\partial}{\partial \xi_2} \left(\frac{\partial^2 B_{\xi_2}^s}{\partial \xi_1^2} + \frac{\partial^2 B_{\xi_2}^s}{\partial \xi_2^2} \right) = \end{aligned}$$

$$\begin{aligned} & = \frac{\partial}{\partial \xi_1} \nabla^2 B_{\xi_1}^s + \frac{\partial}{\partial \xi_2} \nabla^2 B_{\xi_2}^s = \nabla \cdot \left[\left(\vec{n} \times \nabla^2 \vec{B}^s \right) \times \vec{n} \right] = \\ & = \vec{n} \cdot \nabla \times \left(\vec{n} \times \nabla^2 \vec{B}^s \right), \end{aligned} \quad (12)$$

where the unit normal vector \vec{n} is directed out of the body. Here the Laplacian operator of a vector field $\vec{f}(\xi_1, \xi_2)$ is defined as follows

$$\nabla^2 \vec{f} = \sum_{i=1}^3 \vec{a}_{\xi_i} \nabla^2 f_{\xi_i}.$$

The use of (12) allows (11) to be represented in the form:

$$\begin{aligned} B_{\eta}^s & = \sum_{i=1}^2 \frac{\partial B_{\xi_i}^s}{\partial \xi_i} \times T_1 + \sum_{i=1}^2 v_i \frac{\partial B_{\xi_i}^s}{\partial \xi_i} \times T_2 \\ & + \sum_{i=1}^2 w_i \frac{\partial B_{\xi_i}^s}{\partial \xi_i} \times T_3 + \frac{1}{2} \sum_{i=1}^2 \frac{\partial \nabla^2 B_{\xi_i}^s}{\partial \xi_i} \times T_3, \end{aligned} \quad (13)$$

where

$$v_i = \frac{d_{3-i} - d_i}{2d_i d_{3-i}}, \quad w_i = \frac{3d_{3-i}^2 - d_i^2 - 2d_i d_{3-i}}{8d_i^2 d_{3-i}^2}, \quad i=1,2. \quad (14)$$

Performing integration on both sides of (13) over the facet ABCD of the cell shown in Fig. 3, one obtains:

$$\begin{aligned} \hat{b}_0 & = \iint_{S_{b0}} B_{\eta}^s ds = \iint_{S_{b0}} \left(\sum_{i=1}^2 \frac{\partial B_{\xi_i}^s}{\partial \xi_i} \times T_1 + \sum_{i=1}^2 v_i \frac{\partial B_{\xi_i}^s}{\partial \xi_i} \times T_2 + \right. \\ & \left. + \sum_{i=1}^2 w_i \frac{\partial B_{\xi_i}^s}{\partial \xi_i} \times T_3 + \frac{1}{2} \sum_{i=1}^2 \frac{\partial \nabla^2 B_{\xi_i}^s}{\partial \xi_i} \times T \right) ds. \end{aligned} \quad (15)$$

Suppose the coordinates of points D and B in the $\xi_1 \xi_2$ -plane are (ξ_{10}, ξ_{20}) and $(\xi_{10} + \Delta \xi_1, \xi_{20} + \Delta \xi_2)$, respectively (here $\Delta \xi_1 = AB = CD$ and $\Delta \xi_2 = DA = BC$). Surface integrals appearing in (15) can be discretized as follows

$$\begin{aligned}
& \iint_{S_{b_0}} \sum_{i=1}^2 v_i \frac{\partial B_{\xi_i}^s}{\partial \xi_i} ds = \Delta \xi_1 \Delta \xi_2 \sum_{i=1}^2 v_i \frac{\partial B_{\xi_i}^s}{\partial \xi_i} = \\
& = v_1 \left[B_{\xi_1}^s(\xi_{10} + \Delta \xi_1) - B_{\xi_1}^s(\xi_{10}) \right] \Delta \xi_2 + \\
& + v_2 \left[B_{\xi_2}^s(\xi_{20} + \Delta \xi_2) - B_{\xi_2}^s(\xi_{20}) \right] \Delta \xi_1 = \\
& = v_1 B_1^{virt} L_{DA} + v_1 B_3^{virt} L_{BC} + v_2 B_2^{virt} L_{AB} + v_2 B_4^{virt} L_{CD} = \\
& = v_1 \hat{b}_1 \frac{L_{e_1}}{S_{b_1}} + v_1 \hat{b}_3 \frac{L_{e_3}}{S_{b_3}} + v_2 \hat{b}_2 \frac{L_{e_2}}{S_{b_2}} + v_2 \hat{b}_4 \frac{L_{e_4}}{S_{b_4}}, \quad (16)
\end{aligned}$$

where

$$L_{e_1} = DA, \quad L_{e_2} = AB, \quad L_{e_3} = BC, \quad L_{e_4} = CD,$$

$$S_{b_1} = S_{ADD'A'}, \quad S_{b_2} = S_{ABB'A'}, \quad S_{b_3} = S_{BCC'B'},$$

$$S_{b_4} = S_{CDD'C'}.$$

Performing the integration of the other terms in (15) in the same way, one obtains:

$$\begin{aligned}
\hat{b}_0 &= \iint_{S_{b_0}} B_{\eta}^s ds \\
&= \sum_{k=1}^4 \frac{L_{e_k}}{S_{b_k}} \left(\hat{b}_k \times T_1 + v_k \hat{b}_k \times T_2 + w_k \hat{b}_k \times T_3 + \frac{1}{2} \nabla^2 \hat{b}_k \times T_3 \right) \quad (17)
\end{aligned}$$

where $v_1 = v_3$, $v_2 = v_4$, $w_1 = w_3$, and $w_2 = w_4$.

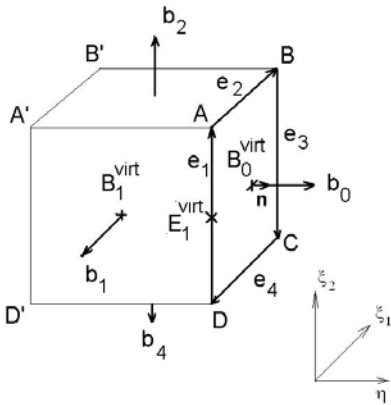


Fig. 3. Cartesian computational cell used in the FIT.

Substituting (17) into Faraday's law, we obtain the relation between $\hat{e}_k = \int_{L_{e_k}} \vec{E} \cdot d\vec{l}$ and $\hat{b}_k = \iint_{S_{b_k}} \vec{B} \cdot \vec{n} ds$,

$k=1,2,\dots,4$

$$\begin{aligned}
\hat{e}_k &= \frac{L_{e_k}}{S_{b_k}} \frac{\partial}{\partial t} \left(\hat{b}_k \times T_1 + v_k \hat{b}_k \times T_2 + w_k \hat{b}_k \times T_3 + \frac{1}{2} \nabla^2 \hat{b}_k \times T_3 \right) = \\
&= \frac{L_{e_k}}{S_{b_k}} \left(\hat{b}_k \times T_1' + v_k \hat{b}_k \times T_2' + w_k \hat{b}_k \times T_3' + \frac{1}{2} \nabla^2 \hat{b}_k \times T_3' \right) \quad (18)
\end{aligned}$$

where

$$\begin{aligned}
T_1'(t) &= \left(\frac{1}{\mu_0 \varepsilon_r \varepsilon_0} \right)^{1/2} \left\{ \delta(t) + \right. \\
&+ \left. \frac{\sigma}{2\varepsilon_r \varepsilon_0} \left[I_1 \left(\frac{\sigma t}{2\varepsilon_r \varepsilon_0} \right) - I_0 \left(\frac{\sigma t}{2\varepsilon_r \varepsilon_0} \right) \right] \exp \left(-\frac{\sigma t}{2\varepsilon_r \varepsilon_0} \right) \right\},
\end{aligned}$$

$$T_2'(t) = \frac{1}{\mu_0 \varepsilon_r \varepsilon_0} \exp \left(-\frac{\sigma t}{\varepsilon_r \varepsilon_0} \right),$$

$$\begin{aligned}
T_3'(t) &= \frac{t}{\mu_0 \varepsilon_r \varepsilon_0 \sqrt{\varepsilon_r \varepsilon_0 \mu_0}} \left[I_0 \left(\frac{\sigma t}{2\varepsilon_r \varepsilon_0} \right) - I_1 \left(\frac{\sigma t}{2\varepsilon_r \varepsilon_0} \right) \right] \\
&\times \exp \left(-\frac{\sigma t}{2\varepsilon_r \varepsilon_0} \right).
\end{aligned}$$

The third derivatives cannot be approximated within one computational cell shown in Fig. 3, so quantities defined in the surrounding cells of the computational grid must be used. Let p and q be ordinal numbers of the current cell in ξ_1 and ξ_2 directions, respectively. In the case of cartesian grid $L_{e_1} = L_{e_3}$ and $L_{e_2} = L_{e_4}$ so

$\nabla^2 \hat{b}_i^{p,q}$ can be approximated as follows:

$$\nabla^2 \hat{b}_1^{p,q} = \left(\hat{b}_1^{p+1,q} - 2\hat{b}_1^{p,q} + \hat{b}_1^{p-1,q} \right) / (L_{e_1})^2, \quad (19a)$$

$$\nabla^2 \hat{b}_2^{p,q} = \left(\hat{b}_2^{p,q+1} - 2\hat{b}_2^{p,q} + \hat{b}_2^{p,q-1} \right) / (L_{e_2})^2, \quad (19b)$$

$$\nabla^2 \hat{b}_3^{p,q} = \left(\hat{b}_3^{p+1,q} - 2\hat{b}_3^{p,q} + \hat{b}_3^{p-1,q} \right) / (L_{e_1})^2, \quad (19c)$$

$$\nabla^2 \hat{b}_4^{p,q} = \left(\hat{b}_4^{p,q+1} - 2\hat{b}_4^{p,q} + \hat{b}_4^{p,q-1} \right) / (L_{e_2})^2. \quad (19d)$$

Substitution of (19a-d) into (18) finally yields the relations between $\hat{e}_k^{p,q}$ and $\hat{b}_k^{p,q}$ for the current cell

$$\hat{e}_k^{p,q} = \left[\begin{array}{l} \hat{b}_k^{p,q} \times T'_1 + v_k \hat{b}_k^{p,q} \times T'_2 + w_k \hat{b}_k^{p,q} \times T'_3 \\ + \frac{L_{e_k}}{S_{b_k}} \frac{1}{2} \left(\hat{b}_k^{p+1,q} - 2\hat{b}_k^{p,q} + \hat{b}_k^{p-1,q} \right) / (L_{e_k})^2 \times T' \end{array} \right]. \quad (20)$$

The SIBC of low order of approximation derived in [5] is given only by the first term of the right hand side of (20)

$$\hat{e}_k^{p,q} = \frac{L_{e_k}}{S_{b_k}} \hat{b}_k^{p,q} \times T'. \quad (21)$$

IV. NUMERICAL EXAMPLE AND VALIDATION

A canonical 2D example is considered, for which the analytical solution is known [8]: a line current $I(t)$ placed at point $(0, y_s)$ radiating over a half-space (Fig. 4).

Although the high order SIBC accurately models the curvature of the surface, the test case has been chosen with planar surface in order not to introduce the typical error of FIT with cartesian grid known as the ‘‘staircase effect’’. As a matter of fact, the modeling of curved surfaces by means of high order SIBC and FIT would require a conformal scheme. In the proposed example the improvement in accuracy given by the SIBC of high order of approximation is only due to the modeling of the variation of the electromagnetic field along the surface, which is not accounted for by the low order SIBC of the Leontovich type. Hence, since the surface is planar, coefficients v_i and w_i in (18) are zero.

The computational domain (the dielectric half-space) is discretized into a 100×100 Cartesian grid made of one layer of 3D Yee cubic cells with side length $\Delta=0.015$ m. Mur’s first order absorbing boundary conditions are used at the other boundaries. Time convolutions in (18) are computed recursively applying the Prony’s method, as proposed in [9].

The following current pulse is considered

$$I(t) = \frac{t - \tau_0}{\tau} e^{-\left(\frac{t - \tau_0}{\tau}\right)^2}, \quad (22)$$

with $\tau = 40\Delta t$, $\tau_0 = 12\Delta t$, where the time step Δt was chosen as $\Delta t = \Delta x / 2c_0$. The electric field at point $(x_0, 0)$ is computed using the low order SIBC, the high order SIBC and the analytical solution (Fig. 5-6). As can be noted, at low values of conductivity ($\sigma = 0.1$ S/m) and when the filamentary source is near to the surface, the SIBC of low order does not give accurate results, while a better accuracy is reached by means of the present formulation. In the cases of higher values of conductivity ($\sigma = 1$ S/m, $\sigma = 10$ S/m), as shown in [4], the low order SIBC is accurate enough.

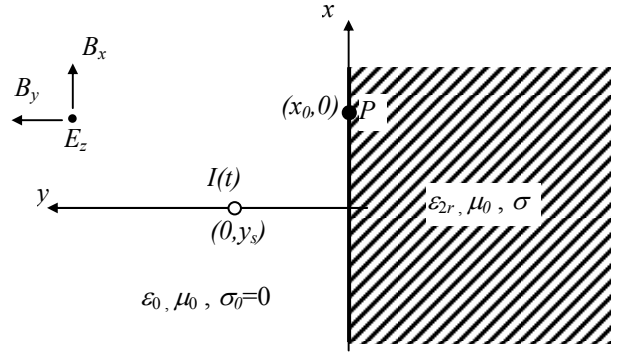


Fig. 4. Geometry of the test problem.

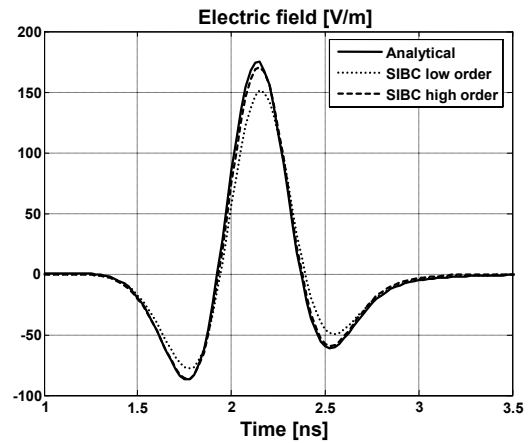


Fig. 5. Electric field at the observation point for $y_s = 10\Delta$; $x_s = 20\Delta$; $\sigma = 0.1$ S/m.

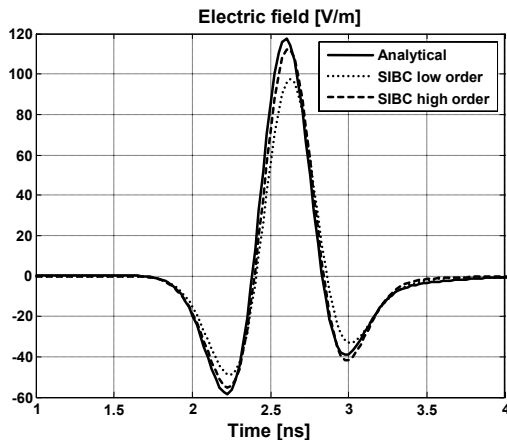


Fig. 6. Electric field at the observation point for $y_s=10\Delta$; $x_s=30\Delta$; $\sigma=0.1$ S/m.

V. CONCLUSIONS

The 2D numerical example has shown the improvement in accuracy of the proposed formulation compared to the corresponding formulation published in [5] employing low order SIBC. Even if FIT with Cartesian grid is computationally equivalent to FDTD, in the paper high order SIBCs have been expressed directly in FIT state variables and in future work they can be generalized to non cartesian grids and implemented in conformal schemes.

REFERENCES

- [1] S. M. Rytov, "Calculation of skin effect by perturbation method," *Zhurnal Experimental'noi i Teoreticheskoi Fiziki*, vol. 10, pp.180-189, 1940.
- [2] K. M. Mitzner, "An integral equation approach to scattering from a body of finite conductivity," *Radio Science*, vol. 2, pp. 1459-1470, 1967.
- [3] S. Yuferev and N. Ida, "Time domain surface impedance boundary conditions of high order of approximation," *IEEE Trans. on Magnetics*, vol. 34, no. 5, pp. 2605 – 2608, September 1998.
- [4] T. Weiland, "A discretization method for the solution of Maxwell's equations for six-component fields," *Electronic and Communication (AEÜ)*, vol. 31, pp. 116-120, 1977.
- [5] S. Yuferev, L. Di Rienzo, and N. Ida, "Surface impedance boundary conditions for the finite integration technique," *IEEE Trans. on Magnetics*, vol. 42, no. 4, pp. 823-826, April 2006.
- [6] T. Weiland, "Advances in FIT/FDTD modeling," *Proceedings of 18th Annual review of progress in applied computational electromagnetics*, pp. 1.1-1.14, 2002.

- [7] T. Weiland, "Time domain electromagnetic field computations with finite difference methods," *International Journal of Numerical Modelling: Electronic Networks, Devices and Fields*, vol. 9, pp. 295-319, 1996.
- [8] G. S. Smith, "On the skin effect approximation," *Am. J. Phys.*, vol. 58, no. 10, pp. 996-1002, 1990.
- [9] K. S. Oh and J. E. Schutt-Aine, "An efficient implementation of surface impedance boundary conditions for the finite-difference time-domain method," *IEEE Trans. Antennas Propagat.*, vol. 43, no. 7, pp. 660-666, 1995.



Luca Di Rienzo was born in Foggia, Italy, in 1971. He received the Laurea degree in 1996 and the Ph. D. degree in 2001, both in electrical engineering and from Politecnico di Milano, Milano, Italy.

He is currently assistant professor of electrical engineering with the

Dipartimento di Elettrotecnica of Politecnico di Milano. At present, his research interests are in the field of computational electromagnetics and include magnetic inverse problems and surface impedance boundary conditions. He is also involved in electromagnetic compatibility problems using commercial software packages.



Nathan Ida is currently Professor of electrical engineering at The University of Akron, Akron, Ohio, USA, where he has been since 1985. His current research interests are in the areas of numerical modeling

of electromagnetic fields, electromagnetic wave propagation, nondestructive testing of materials at low and microwave frequencies and in computer algorithms. Dr. Ida received his B.Sc. in 1977 and M.S.E.E. in 1979 from the Ben-Gurion University in Israel and his Ph.D. from Colorado State University in 1983.



Sergey Yuferev was born in St. Petersburg, Russia, in 1964. He received MSc degree in computational fluid mechanics from St. Petersburg Technical University in 1987 and PhD degree in computational electromagnetics from A.F.

Ioffe Institute in 1992. From 1987 to 1998 he was with Dense Plasma Dynamics Laboratory of A. F. Ioffe Institute. From 1999 to 2000 he was Visiting Associate Professor at The University of Akron, Ohio. Since 2000, he has been with Nokia Corp., Finland. His current research interests include numerical and analytical methods of computational electromagnetics and their application to EMC/EMI problems of mobile phones.

An Adaptive Basis Function Solution to the 1D and 2D Inverse Scattering Problems using the DBIM and the BIM

Ian Jeffrey, Vladimir I. Okhmatovski, Joe LoVetri, and Colin Gilmore

Department of Electrical and Computer Engineering
University of Manitoba, Winnipeg, MB, R3T 5V6, Canada
ijeffrey@ee.umanitoba.ca, okhmatov@ee.umanitoba.ca, lovetri@ee.umanitoba.ca

Abstract—We present the use of an adaptive set of basis functions used in conjunction with the MoM to solve the linearized scalar inverse electromagnetic scattering problem. The basis functions, which are whole-domain and harmonic, are selected to provide a perfectly conditioned solution under the first-order Born approximation when multiple frequency experiments are considered. In order to iteratively solve the full non-linear problem by the Distorted Born Iterative Method (DBIM) and/or the Born Iterative Method (BIM), we introduce a single parameter into the basis function expansion to demonstrate that it is possible to maintain a well-conditioned linearized inverse problem by selecting the parameter value that minimizes the condition number of the discrete matrix operator. The proposed technique eliminates the need for Tikhonov regularization or equivalent regularization schemes commonly applied to the single-frequency, pulse-basis formulation of the linearized inverse scattering problem.

Keywords—Inverse imaging, Distorted Born, Born, Iterative methods, regularization.

I. INTRODUCTION

It is well documented that the continuous, non-linear, time-harmonic, scalar inverse scattering problem in electromagnetics is ill-posed [1], [2]. In fact, using monochromatic interrogation and a first-order linearizing assumption such as the Born approximation [3], the linear inverse problem results in a Fredholm integral equation of the first kind that retains the ill-posedness of the full non-linear problem. As the resulting operator has a null-space, no unique solution exists and one must select one of an infinite number of solutions by imposing additional constraints, a process known as regularization [2], [4].

It is beneficial to examine the cause of the ill-posedness of the problem in order to choose a suitable regularization technique. In the linearized inverse

scattering problem, the smooth nature of the kernel tends to suppress the effects of high-frequency spatial variations of the unknown contrast function on the measured field values, thereby making the high-frequency contrast components irrecoverable from the field data [4]. Thus, a suitable regularization technique should, in some way, limit the high frequency components of the reconstructed contrast function.

A common way of solving the linearized inverse problem is to discretize the unknown contrast function in terms of a pulse basis expansion [5], [6] which, in itself, imposes no constraint on the maximum spatial frequency of the reconstructed contrast. Due to the ill-posedness of the continuous problem, the resulting discrete linear system is ill-conditioned [4] and, without regularization, directly solving the system yields a solution with little to no physical significance. Consequently, one of two types of regularization methods is commonly applied to the discrete system. The first, Tikhonov regularization, imposes a penalty constraint weighted by a regularization parameter. The parameter attempts to balance the error in the residual against the error inherent in the high spatial-frequency components [4-6]. Tikhonov regularization is capable of providing solutions that converge to the unknown contrast function when an iterative solution of the full-nonlinear problem is adopted [5], [6]. Unfortunately, the first-order approximation is often highly oscillatory depending on the type of penalty function selected (as shown in the numerical results of [5]) and gives little insight as to the physical nature of the true contrast.

The second popular regularization technique is the so-called truncated singular value decomposition method (TSVD) [4], [7]. As its name implies, this approach truncates the singular value reconstruction of the solution thereby constraining the high spatial-frequency components of the pulse-based solution. In fact, TSVD can be shown to be “*essentially equivalent to Tikhonov regularization when the penalty matrix is taken as the identity matrix*” [4]. Under this equivalence the

truncation order substitutes as a regularization parameter.

While for both Tikhonov regularization and TSVD there exist mathematical methods for determining a suitable value of the regularization parameter [4], [7], the solution is often quite sensitive to the parameter value and selecting an appropriate parameter can be both difficult and computationally expensive. The tools are, however, quite powerful and in cases when one has no choice but to regularize the problem by the aforementioned methods, they enable a meaningful solution to be obtained. The inverse scattering problem does not, however, necessarily require formal regularization provided that the problem is *formulated* carefully. Our approach is to select equations that arrive at a discrete system where only a single, meaningful solution is possible. Further, we wish to choose our equations in such a way that the Born Approximation remains a meaningful first-order solution *i.e.*, it is a smooth first-order approximation to the unknown contrast.

With this in mind, we note that in special cases the Born approximation is capable of annihilating the null-space of the discrete operator giving a unique first-order solution. Specifically, under plane-wave incidence, the measured field data may be identified as the spatial Fourier Transform of the unknown contrast function [3], [8]. Therefore, by applying an inverse Fourier Transform to the field data we may uniquely obtain the contrast up to some maximum spatial-frequency, a result that is sometimes referred to as Fourier Imaging. Thus, in Fourier Imaging, it is by multiple frequency experiments that we “regularize” the problem (in so far as we manage to make the solution both physical and unique). Essentially, we are adding information. Fourier techniques also have the advantage of a smooth, first-order approximation to the unknown contrast function [2].

In this paper, based on the idea that Fourier Imaging offers a well-conditioned first-order solution, we first derive a perfectly conditioned MoM formulation of the inverse problem by expanding the contrast function in terms of whole-domain complex exponential basis functions, *i.e.*, the Fourier series harmonics. Second, as the limitations of the Born approximation are well known, we present a parameterized set of harmonic basis functions suitable for iterative solution schemes for solving the full non-linear problem such as the Born Iterative Method (BIM) [5] and the Distorted Born Iterative Method (DBIM) [9].

As the focus of this paper is to illustrate the benefits of the proposed basis function expansion, we focus primarily on applying the basis functions to the (D)BIM solutions for the simple 1D, lossless, noise-free problem

which serves as a well documented benchmark for new inverse solution methods [1], [7]. To show that the theory can be extended to higher dimensions, we include a 2D formulation for the BIM. For both the 1D and 2D cases considered, we show successful reconstruction results.

What is presented herein is an elaboration of the work we have presented at various conferences during the past year [10-13]. We provide all details of the formulation and show results for both the BIM and the DBIM on the same problems.

II. THE MOM SOLUTION TO THE 1D SCATTERING PROBLEM UNDER THE BORN APPROXIMATION

Consider the 1D integral equation for electromagnetic scattering,

$$E(x) = E^{inc}(x) + k_0^2 \int_{-\infty}^{\infty} (\varepsilon(x') - 1)E(x')G(x, x')dx' \quad (1)$$

where $E(x)$ is the transverse component of the electric field, $E^{inc}(x)$ is the incident electric field, $\varepsilon(x)$ is the unknown relative permittivity as a function of position and where k_0 is the wavenumber of free space. Throughout this paper an $e^{i\omega t}$ time dependence is suppressed where $i = \sqrt{-1}$ and ω is the radial frequency of the electric field. The free-space Green's function $G(x, x')$ is,

$$G(x, x') = \frac{1}{2ik_0} e^{-ik_0|x-x'|} = \frac{1}{2ik_0} e^{-ik_0s(x-x')} \quad (2)$$

where $s = 1$ if $x > x'$ and $s = -1$ if $x < x'$. For the incident field, we consider plane waves propagating in either the positive or negative x direction *i.e.*,

$$E^{inc}(x) = e^{-ik_0s'x} \quad (3)$$

where the direction of propagation is negative for $s' = -1$ and positive for $s' = 1$. Assuming a permittivity contrast which is spatially bounded to a domain $D = [x_1, x_2]$, the infinite integral in (1) collapses to D . Applying the Born approximation, namely that scattering is weak and the field within the domain D may be approximated by the incident field, (1) becomes,

$$E(x; k_0, s, s') - e^{-ik_0s'x} = -\frac{ik_0}{2} e^{-ik_0sx} \int_{x_1}^{x_2} \delta\varepsilon(x') e^{-ik_0(s'-s)x'} dx' \quad (4)$$

Above, $\delta\varepsilon(x)$ is the contrast function used to denote the unknown relative permittivity contrast $\varepsilon(x) - 1$. To solve for the unknown contrast, we begin by expanding $\delta\varepsilon(x)$ in terms of $2L$ whole-domain complex exponential basis functions,

$$\delta\varepsilon(x) \approx \sum_{l=1}^L a_l e^{ik_l x} + \sum_{l=1}^L b_l e^{-ik_l x}. \quad (5)$$

For reasons which will be made clear, the spatial frequencies are selected as $k_l = l\Delta k - \Delta k/2$, for $l = 1, \dots, L$, where Δk is selected as $(2\pi)/(x_2 - x_1)$ i.e., the fundamental wavelength is selected as twice the size of imaging domain. *The $\Delta k/2$ shift is essential as it implicitly adds a DC component into each harmonic over the imaging domain.* As a result, we eliminate the need for an explicit DC basis function.

Upon substitution of (5) into (4) we obtain a single equation in $2L$ unknowns,

$$\frac{2i}{k_0} e^{ik_0 s x} (E(x; k_0, s, s') - e^{-ik_0 s' x}) = \sum_{l=1}^L a_l \int_{x_1}^{x_2} e^{-i(k_0(s' - s) - k_l)x'} dx' + \sum_{l=1}^L b_l \int_{x_1}^{x_2} e^{-i(k_0(s' - s) + k_l)x'} dx'. \quad (6)$$

While a typical approach to obtain a system of equations from (6) would be to test, or weight the equation by means of $2L$ different inner products on the domain D [14], we must take a different approach because the domain of the left-hand side of (6) does not coincide with D . Instead, we consider $2L$ independent scattering experiments. Using multiple scattering experiments is a typical way of creating a sufficient number of equations [6], [9], but normally (in higher dimensions) one has the ability to construct the different scattering experiments by taking different angles of incidence, rather than different frequencies. This freedom does not exist in the 1D problem. Instead, we construct L experiments with an incident field propagating in the positive x direction where the scattering amplitude is measured at a single location $x_a < x_1$ such that $s' - s = 2$. For each of these experiments the incident field wavenumber k_0 is selected as $k_m/2$ for $m = 1, \dots, L$. Next, we construct L experiments where the incident field propagates in the negative x direction (taking corresponding measurements at a single location $x_b > x_2$ such that $s' - s = -2$). Again we select the wavenumbers $k_0 = k_m/2$ for $m = 1, \dots, L$. For incidence in the positive x direction we obtain the following L algebraic equations:

$$\frac{2i}{k_0} e^{-i(k_m/2)x_a} (E(x_a; k_m/2) - e^{-i(k_m/2)x_a}) = \sum_{l=1}^L a_l \int_{x_1}^{x_2} e^{-i(k_m - k_l)x'} dx' + \sum_{l=1}^L b_l \int_{x_1}^{x_2} e^{-i(k_m + k_l)x'} dx' \quad (7)$$

while for propagation in the negative x direction we obtain,

$$\frac{2i}{k_0} e^{i(k_m/2)x_b} (E(x_b; k_m/2) - e^{i(k_m/2)x_b}) = \sum_{l=1}^L a_l \int_{x_1}^{x_2} e^{i(k_m + k_l)x'} dx' + \sum_{l=1}^L b_l \int_{x_1}^{x_2} e^{i(k_m - k_l)x'} dx'. \quad (8)$$

Due to our previous choices of k_l in the expansion (5), the functions $e^{ik_m x}$ are orthogonal over the imaging domain and the combined system of equations consisting of (7) and (8) is *perfectly conditioned*. We write the system as,

$$\begin{bmatrix} \mathbf{I} & \mathbf{0} \\ \mathbf{0} & \mathbf{I} \end{bmatrix} \cdot \begin{bmatrix} \mathbf{a} \\ \mathbf{b} \end{bmatrix} = \begin{bmatrix} \mathbf{f} \\ \mathbf{g} \end{bmatrix}, \quad (9)$$

where \mathbf{I} is the identity matrix, $\mathbf{a} = [a_1, a_2, \dots, a_L]^T$ and $\mathbf{b} = [b_1, b_2, \dots, b_L]^T$ are vectors of the unknown contrast expansion coefficients and \mathbf{f} and \mathbf{g} represent vectors of the left-hand side of (7) and (8), respectively, appropriately scaled by the width of the imaging domain. Clearly, this demonstrates that by using the proposed whole-domain basis functions and a multitude of scattering experiments we are able to produce a perfectly-conditioned system under the Born approximation. In fact, it can be shown that this result is equivalent to Fourier Imaging. Before presenting appropriate basis functions for iteratively solving the full non-linear problem, we summarize two common iterative techniques, namely the DBIM and BIM.

III. THE DISTORTED BORN ITERATIVE METHOD

The pertinent theory of the DBIM may be found in [9] and is summarized herein. As is common to many iterative techniques for solving the inverse scattering problem we consider equation (1) as two distinct equations used alternatively in a two-step updating procedure. At each iteration n , we identify from (1) the *data equation* when $x \notin D$. We assume an approximation to the fields within D (such as the Born approximation for the first iteration) and solve for the updated contrast function $\delta\varepsilon^{(n)}$. The key to the DBIM is that instead of computing $\delta\varepsilon^{(n)}$, we compute $\delta\varepsilon_b^{(n)}$

defined as the difference between $\delta\varepsilon^{(n)}$ and $\delta\varepsilon^{(n-1)}$. This is accomplished by numerically computed a Green's function $G_b^{(n-1)}$ from $\delta\varepsilon^{(n-1)}$ and the field values acquired at the $(n-1)^{th}$ iteration such that the distorted data equation becomes,

$$E(x) - E^{(n-1)}(x) = k_0^2 \int_{x_1}^{x_2} \delta\varepsilon_b^{(n)}(x') E^{(n-1)}(x') G_b^{(n-1)}(x, x') dx' \quad x \notin D \quad (10)$$

where $E(x)$ is simply the true total field which is a measurable quantity at $x \notin D$ and $E^{(n-1)}(x)$ is the total field produced by the contrast $\delta\varepsilon^{(n-1)}$.

To compute the numerical Green's function $G_b^{(n)}$, we use,

$$G_b^{(n)}(x, x') = G(x, x') + k_0^2 \int_{x_1}^{x_2} \delta\varepsilon^{(n)}(x'') G_b^{(n)}(x'', x') G(x, x'') dx'' \quad (11)$$

where we must first solve (11) for all source points $x' \in D$ when $x \in D$. We may then use (11) with $x \notin D$ to compute $G_b^{(n)}(x, x')$ at any location in space.

Next, the *domain equation* is used to update the field within the imaging region from the updated contrast $\delta\varepsilon^{(n)} = \delta\varepsilon_b^{(n)} + \delta\varepsilon^{(n-1)}$. Formally, we consider $x \in D$ and solve

$$E^{(n)}(x) = E^{inc}(x) + k_0^2 \int_{x_1}^{x_2} \delta\varepsilon^{(n)}(x') E^{(n)}(x') G(x, x') dx'. \quad (12)$$

We may solve the full non-linear inverse problem by repeating the following procedure beginning with $n = 1$:

- Solve for $\delta\varepsilon_b^{(n)}$ from (10) using the field computed from (12) at iteration $n-1$ and update $\delta\varepsilon^{(n)}$. In the case of $n = 1$ we approximate the field using the Born approximation, hence $\delta\varepsilon^{(0)} = 0$, $E^{(0)} = E^{inc}$ and $G_b^{(0)} = G$.
- Solve for the numerical Green's function at the observation points $x \notin D$ from equation (11) and solve for the updated field within the imaging domain from the current contrast function using (12). From the field solution within D , use (12) to directly compute $E^{(n)}$ at the observation point(s) $x \notin D$.

IV. THE BORN ITERATIVE METHOD

While the DBIM attempts to re-use information of the profile at each iteration by formulating the problem in terms of $\delta\varepsilon_b^{(n)}$, a simpler iterative scheme that simply computes $\delta\varepsilon^{(n)}$ at each iteration without computation of the numerical Green's function may be used. This method, namely the BIM is detailed in [5]. The BIM data equation may be obtained from (10) by setting $G_b^{(n-1)}(x, x') = G(x, x')$ and $\delta\varepsilon_b^{(n)} = \delta\varepsilon^{(n)}$ for all n . Also, it is necessary to set $E^{(n-1)}(x) = E^{inc}(x)$ on the left hand side of (10). The BIM domain equation is the same as that of the DBIM.

V. AN ADAPTIVE, WHOLE DOMAIN BASIS FORMULATION FOR THE DBIM/BIM

The iterative procedure summarized in the previous section makes use of two integral equations for iteratively solving the non-linear, scalar, electromagnetic inverse scattering problem under the linearizing assumption of the Born Approximation. The domain equation (12) (which has the same form as (11)) is a second-kind integral equation and is not ill-posed. For instance it can readily be solved by expanding the unknown field quantity into pulse basis functions and using point-matching. Consequently, the solution to equations (11) and (12) will not be discussed further. Conversely, the data equation, corresponding to a linearized inverse problem, is ill-posed as discussed in Section 1 and we must either use standard regularization techniques or formulate the problem carefully. We consider therefore, the basis function expansion for the unknown contrast presented in Section 2, which, despite the ill-posedness of the problem gave an ideally conditioned matrix. It is clear however, that the orthogonality property used to produce this ideally conditioned system will vanish at subsequent iterations if the basis function expansion (5) is used. Instead, for iterations $n > 1$ in the DBIM we expand the contrast in a parameterized set of basis functions,

$$\delta\varepsilon_b^{(n)}(x) \approx \sum_{l=1}^L a_l^{(n)} e^{i\alpha^{(n)} k_l x} + \sum_{l=1}^L b_l^{(n)} e^{-i\alpha^{(n)} k_l x} \quad (13)$$

where $\alpha^{(n)}$ is an iteration dependent, real-valued parameter used to dynamically modify the basis function expansion of the unknown contrast function with the sole purpose of minimizing the condition number of the discrete matrix. (A similar expansion is used for $\delta\varepsilon^{(n)}$ in the BIM.) The motivation for minimizing the condition number of the matrix is discussed in Section 7.

Specifically, if we substitute the expansion (13) into (10), making the dependence on the measurement location and incident field direction explicit via the parameters s and s' , (while dropping the explicit dependence on k_0 for brevity) we obtain,

$$\begin{aligned} (E(x, s, s') - E^{(n-1)}(x, s)) = & \\ & \sum_{l=1}^L a_l^{(n)} k_0^2 \int_{-\infty}^{\infty} e^{i\alpha^{(n)} k_x x'} E^{(n-1)}(x', s, s') G_b^{(n-1)}(x, x', s) dx' \\ & + \sum_{l=1}^L b_l^{(n)} k_0^2 \int_{-\infty}^{\infty} e^{-i\alpha^{(n)} k_x x'} E^{(n-1)}(x', s, s') G_b^{(n-1)}(x, x', s) dx'. \end{aligned} \quad (14)$$

Applying the same testing procedure as the one adopted for the first-order solution we obtain an iteration dependent linear system which we write in compact form as,

$$\begin{bmatrix} E_{11}^{(n-1)} & E_{12}^{(n-1)} \\ E_{21}^{(n-1)} & E_{22}^{(n-1)} \end{bmatrix} \cdot \begin{bmatrix} \mathbf{a}^{(n)} \\ \mathbf{b}^{(n)} \end{bmatrix} = \begin{bmatrix} \mathbf{f}^{(n-1)} \\ \mathbf{g}^{(n-1)} \end{bmatrix} \quad (15)$$

where $E_{11}^{(n-1)}$ and $E_{21}^{(n-1)}$ are matrix representations of those terms in (14) corresponding to the coefficients $\mathbf{a}^{(n)}$ while $E_{12}^{(n-1)}$ and $E_{22}^{(n-1)}$ correspond to the terms involving $\mathbf{b}^{(n)}$. Equation (15) reduces to equation (10) for $n = 1$ under the Born Approximation with $\alpha^{(1)} = 1$. In the case of the BIM, the right hand side is iteration independent.

The matrix in (15) will, in general, be dense and ‘‘poorly’’ conditioned if the parameter $\alpha^{(n)} = 1$ is selected. Therefore, we minimize the condition number $C^{(n)}$ of the matrix by performing an optimization over the parameter $\alpha^{(n)}$. Experience has shown that the function $C^{(n)}(\alpha^{(n)})$ is not unimodal as shown in Fig. 4 and hence a global optimization routine is required and is discussed in Section 7.

VI. EXTENSION TO THE BIM IN 2D

In 2D the time-harmonic, lossless, non-linear, scalar inverse scattering problem for transverse magnetic (TM) fields may be mathematically represented by the 2D version of the non-linear integral equation (1),

$$E_z^s(\hat{\rho}; \hat{k}) = k_0^2 \int_{-\infty}^{\infty} \int_{-\infty}^{\infty} \delta\varepsilon(\hat{\rho}') E_z(\hat{\rho}'; \hat{k}) G(\hat{\rho}, \hat{\rho}'; k_0) dx' dy' \quad (16)$$

where a cartesian coordinate system is assumed and the position vector is given by $\hat{\rho} = x\hat{x} + y\hat{y}$. $E_z^s(\hat{\rho}; \hat{k}) = E_z(\hat{\rho}; \hat{k}) - E_z^{\text{inc}}(\hat{\rho}; \hat{k})$ is the z -component of the scattered field defined as the difference between the total field $E_z(\hat{\rho}; \hat{k})$ and the incident field $E_z^{\text{inc}}(\hat{\rho}; \hat{k})$. The fields are parameterized by the wavevector $\hat{k} = k_x\hat{x} + k_y\hat{y}$, and the wavenumber k_0 is given by $k_0 = |\hat{k}|$. In (16), we assume the 2D, free-space Green’s function $G(\hat{\rho}, \hat{\rho}'; \hat{k})$,

$$G(\hat{\rho}, \hat{\rho}'; \hat{k}) = \frac{1}{4i} H_0^{(2)}(k_0 |\hat{\rho} - \hat{\rho}'|), \quad (17)$$

where $H_0^{(2)}(x)$ is the zeroth-order Hankel function of the second kind. In the far-field, this Green’s function may be replaced with its large argument approximation,

$$G(\hat{\rho}, \hat{\rho}'; \hat{k}) \approx \frac{i+1}{4i\sqrt{\pi}} \frac{e^{-ik_0 |\hat{\rho} - \hat{\rho}'|}}{\sqrt{k_0 |\hat{\rho} - \hat{\rho}'|}}. \quad (18)$$

Again, we consider incident plane waves now defined as,

$$E_z^{\text{inc}}(\hat{\rho}; \hat{k}) = e^{i\hat{k} \cdot \hat{\rho}}. \quad (19)$$

Under the assumption of a rectangularly bounded imaging domain $D = \{\hat{\rho}: \rho_x \in [x_1, x_2], \rho_y \in [y_1, y_2]\}$ such that the contrast function $\delta\varepsilon(\hat{\rho}) = 0 \quad \forall \hat{\rho} \notin D$, and under the Born approximation, the integral in (16) collapses to D and becomes,

$$E_z^s(\hat{\rho}) = \frac{k_0^2(i+1)}{4i\sqrt{\pi}\sqrt{k_0}} \int_{y_1}^{y_2} \int_{x_1}^{x_2} \delta\varepsilon(\hat{\rho}') e^{i\hat{k} \cdot \hat{\rho}'} \frac{e^{-ik_0 |\hat{\rho} - \hat{\rho}'|}}{\sqrt{|\hat{\rho} - \hat{\rho}'|}} dx' dy' \quad (20)$$

where the explicit parameterization by \hat{k} has been dropped for brevity. Now, making an additional far-field assumption we approximate the phase term as $|\hat{\rho} - \hat{\rho}'| \approx \rho - \hat{\rho} \cdot \hat{\rho}'$ where $\hat{\rho} = \rho\hat{\rho}$ and approximate the amplitude term by $\sqrt{|\hat{\rho} - \hat{\rho}'|} \approx \sqrt{\rho}$. Then, the integral equation becomes,

$$E_z^s(\hat{\rho}) = \frac{k_0^2(i+1)e^{-ik_0\rho}}{4i\sqrt{\pi}\sqrt{k_0}\sqrt{\rho}} \int_{y_1}^{y_2} \int_{x_1}^{x_2} \delta\varepsilon(\hat{\rho}') e^{i\hat{k} \cdot \hat{\rho}'} e^{ik_0\hat{\rho} \cdot \hat{\rho}'} dx' dy'. \quad (21)$$

By writing the incident field wavevector \hat{k} as $\hat{k} = k_0\hat{k}$ we may further reduce the integral equation to,

$$E_z^s(\vec{\rho}) = \beta(\vec{\rho}; k_0) \int_{y_1 x_1}^{y_2 x_2} \delta\varepsilon(\vec{\rho}') e^{i k_0(\hat{k} + \hat{\rho}) \cdot \vec{\rho}'} dx' dy' \quad (22)$$

where $\beta(\vec{\rho}; k_0)$ has been used to representing the leading terms in (21). Once again, we expand the unknown contrast function in terms of whole-domain, harmonic basis functions as,

$$\delta\varepsilon(\vec{\rho}) \approx \sum_{u=-(U-1)}^U \sum_{v=-(V-1)}^V a_{u,v} e^{i((k_{xu}\hat{k}_x + k_{yv}\hat{k}_y) \cdot \vec{\rho})} \quad (23)$$

where $k_{xu} = (u-1/2)\Delta k_x$, and $k_{yv} = (v-1/2)\Delta k_y$. The coefficients $a_{u,v}$ correspond to the unknown amplitude of the $(u, v)^{\text{th}}$ basis function, while U and V limit the number of basis functions selected. For convenience we now impose a natural ordering on the pairs (u, v) such that we may re-write the basis function expansion (23) as,

$$\delta\varepsilon(\vec{\rho}) \equiv \sum_{l=1}^L a_l e^{i(\vec{k}_l \cdot \vec{\rho})} \quad L = 1, 2, \dots, 4UV \quad (24)$$

where each l corresponds to a unique pair (u, v) and where \vec{k}_l is given by the corresponding value $k_{xu}\hat{k}_x + k_{yv}\hat{k}_y$.

Substitution of the basis function expansion into integral equation (22) yields,

$$\frac{E_z^s(\vec{\rho})}{\beta(\vec{\rho}; k_0)} = \sum_{l=1}^L a_l \int_{y_1 x_1}^{y_2 x_2} e^{i(\vec{k}_l \cdot \vec{\rho}') + i k_0(\hat{k} + \hat{\rho}) \cdot \vec{\rho}'} dx' dy'. \quad (25)$$

Thus, (25) represents a single equation in the $L = 4UV$ unknowns a_l . To obtain more equations we now considering multiple incident fields at different angles of incidence and various frequencies. Specifically, we note that if we take any incident field where $\hat{k} = \rho$, we obtain,

$$\frac{E_z^s(\vec{\rho})}{\beta(\vec{\rho}; k_0)} = \sum_{l=1}^L a_l \int_{y_1 x_1}^{y_2 x_2} e^{i(\vec{k}_l \cdot \vec{\rho}') + i(2\vec{k} \cdot \vec{\rho}')} dx' dy'. \quad (26)$$

To create a set of L equations in L unknowns we vary the incident field wavevector in a manner analogous to the 1D case *i.e.*, we let the physical wavevector $\vec{k} = \vec{k}_m/2$, for $m = 1, 2, \dots, L$. This results in,

$$\frac{E_z^s(\vec{\rho}_m)}{\beta(\vec{\rho}; k_m/2)} = \sum_{l=1}^L a_l \int_{y_1 x_1}^{y_2 x_2} e^{i(\vec{k}_l \cdot \vec{\rho}') + i(\vec{k}_m \cdot \vec{\rho}')} dx' dy'. \quad (27)$$

where we have taken a different measurement location $\vec{\rho}_m$ for each equation. Note that $\vec{\rho}_m$ must be both in the far field, and in the direction of \vec{k}_m to validate previous assumptions. Finally, we note that if we select $\Delta k_x = (2\pi)/(x_2 - x_1)$ and $\Delta k_y = (2\pi)/(y_2 - y_1)$ then the basis functions are orthogonal to the kernel of the integral operator over the domain D which reduces the inverse problem (27) to a perfectly conditioned linear system analogous to (9),

$$I \cdot \mathbf{a} = \mathbf{f}. \quad (28)$$

Again, like the 1D case, at subsequent iterations beyond the first-order Born Approximation, we use the basis function expansion,

$$\delta\varepsilon^{(n)}(\vec{\rho}') \approx \sum_{l=1}^L a_l e^{i\alpha^{(n)}(\vec{k}_l \cdot \vec{\rho}')} \quad L = 1, 2, \dots, 4UV \quad (29)$$

where, as discussed in Sections 5, the parameter $\alpha^{(n)}$ is used to minimize the condition number of the discrete operator.

VII. NUMERICAL RESULTS

The iterative procedure using the adaptive basis function expansion previously described was implemented and tested. Herein we show the 1D results for a relative permittivity contrast selected to be the positive cycle of sinusoid with period 0.4 m centered over the domain $x = [-0.1, 0.1]$ having an amplitude of 2 and a rectangular contrast of amplitude 1 existing over the same domain. Data was acquired at the locations $x = -0.4$ and $x = 0.4$ m while the imaging domain was restricted to $D = [-0.3, 0.3]$ m. The contrast was expanded using 20 basis functions *i.e.* $L = 10$ and a direct search of the parameter space was performed over the range $[1, 1.4]$. The results of the 1D-DBIM and BIM are shown in Figs. 1 and 2, respectively. As expected, the DBIM method converges faster than the BIM [5], [9]. Note that in Fig. 1, the Distorted Born reconstruction for the sinusoid converges at iteration 2 and therefore, the curve for iteration 6 lies on top of the curve for iteration 2. The profile error from iteration to iteration for both methods is shown in Fig. 3 while the

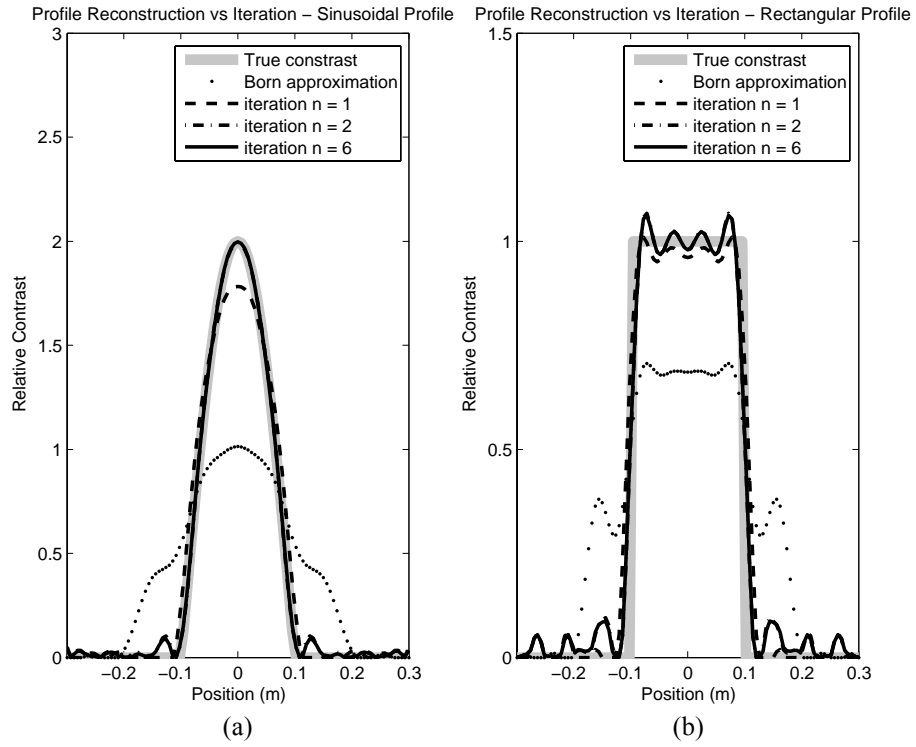


Fig. 1. 1D DBIM profile reconstruction results: sinusoidal (a), rectangular (b).

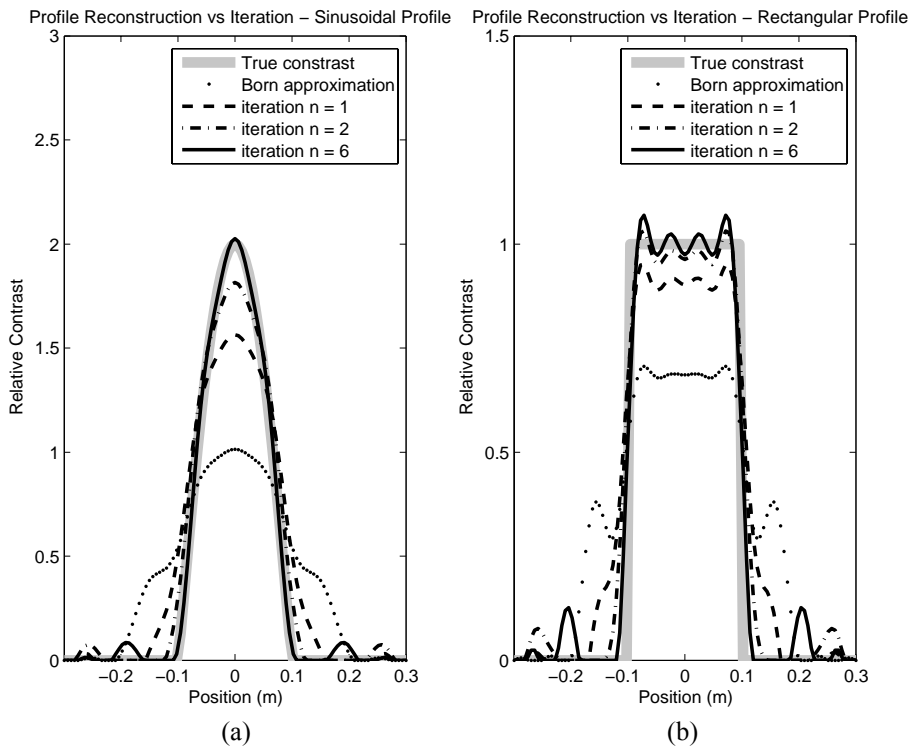


Fig. 2. 1D BIM profile reconstruction results: sinusoidal (a), rectangular (b).

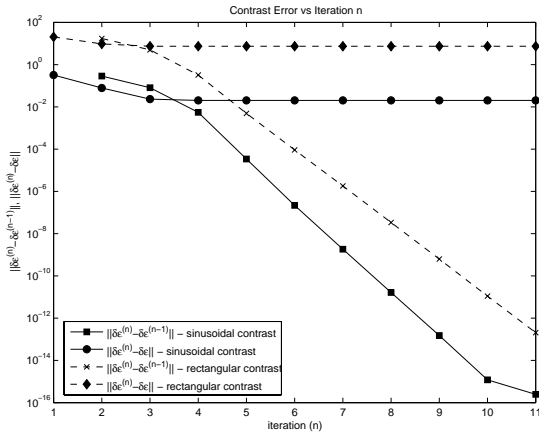
system condition number versus parameter value $\alpha^{(n)}$ are shown for the two methods in Fig. 4.

For the 2D case, we show the results of the BIM for a contrast function that consists of two Gaussian pulses, centered at $(x, y) = (0.2, 0.2)$ m and $(0.3, 0.3)$ m within a square imaging domain that extends in both dimensions from 0.0 to 0.5 m. The standard deviation of each pulse is 0.025 in both spatial dimensions. The pulse closer to the origin was given a maximum amplitude of 2 while the other, an amplitude of 1. To iteratively reproduce the contrasts we used 144 basis functions (selecting $U = V = 6$). Figure 5 shows the true contrast function and reconstructed profiles after the Born approximation and the sixth iteration.

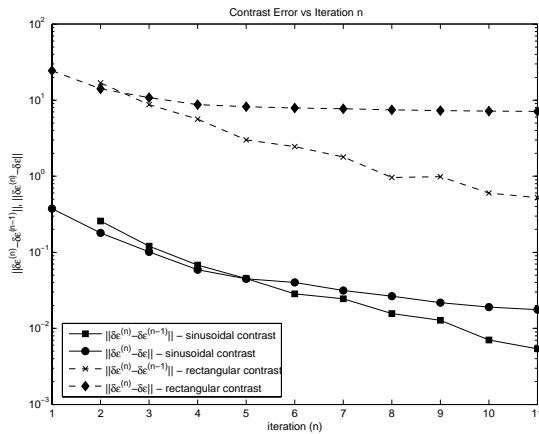
In all cases, the forward solution was obtained from a MoM formulation using a pulse basis over the imaging domain.

VIII. DISCUSSION

While a rigorous mathematical investigation of the effects of our parameterized basis function expansion is subject to ongoing research, we can suggest three immediate reasons why this technique is a good candidate for solving the linearized inverse scattering problem. First, the very nature of the basis function expansion limits the high frequency components of the reconstructed profile which, as discussed in Section 1, contributes to the ill-posedness of the original problem. Second, as the condition number is defined as the ratio of the largest to smallest singular values of the operator matrix, we are implicitly demanding that the solution to the discrete system, corresponding to the basis function coefficients, is not overwhelmed by unconstrained high frequencies. This can be seen by ordering the singular

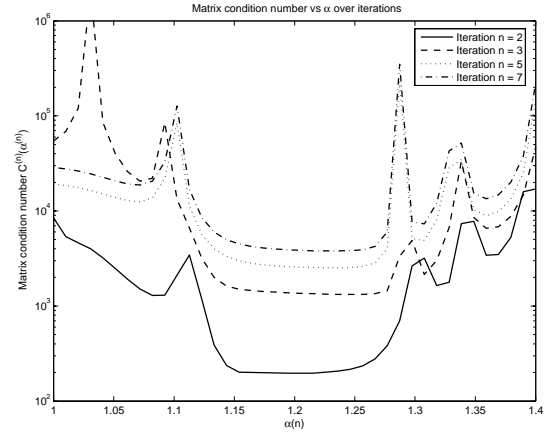


(a)

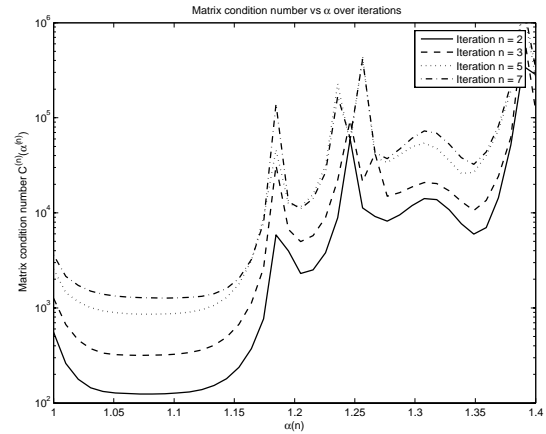


(b)

Fig. 3. 1D error convergence: DBIM (a), BIM (b). The values corresponding to the rectangular contrast have been increased by a factor of 100 for clarity.



(a)



(b)

Fig. 4. 1D condition number as a function of $\alpha^{(n)}$ for various iterations: DBIM (a), BIM (b). Condition number values have been increased by a factor of 10 times the iteration count for clarity.

values of the discrete operator in non-increasing order and noting that the corresponding singular vectors have a non-decreasing number of zero crossings. frequency [4]. Lastly, and perhaps most importantly, if we consider the multiple-frequency approach in conjunction with minimization of the condition number as a sort of regularization technique itself, the selection of the basis function parameter (which, in this context would double as the regularization parameter) is well-defined: we select the value of the regularization parameter which minimizes the condition number of the discrete operator.

Two comments should be made. First, at an arbitrary iteration n , the function $C^{(n)}(\alpha^{(n)})$ is not unimodal and an optimization technique is required to determine the optimal value of $\alpha^{(n)}$. For the results shown in this paper, as the optimization space is over a single parameter (for both the 1D and 2D formulations), we have used a direct search over the parameter space. Empirically, we have found that at each iteration, the condition number has a global minimum on the interval $\alpha^{(n)} \in [1, \alpha_{\max}^{(n)}]$ where,

$$\alpha_{\max}^{(n)} = \sqrt{\max(\text{Re}(\delta\varepsilon^{(n)}(x)) + 1)}. \quad (30)$$

The previous expression is motivated by the fact that the basis function parameter is present as a phase term in the basis function expansion and should therefore be in some way proportional to the field velocity in the medium. Fig. 4 shows typical behaviour of the condition number as a function of the regularization parameter.

Clearly, minimizing the condition number of the matrix involves the repetitive computation of the discrete operator for each $\alpha^{(n)} \in [1, \alpha_{\max}^{(n)}]$ and its condition number. Fortunately, the number of harmonic basis functions required to satisfactorily reproduce an unknown contrast function is generally much less than if a pulse basis expansion was considered. As a result, the condition number evaluation does not pose significant computational strain.

Second, in many cases the condition number of the operator matrix is not unreasonably large. Nevertheless, minimization of the condition number is *still required* to obtain a good solution. Thus, at each iteration, it is essential to pick $\alpha^{(n)}$ corresponding to the *minimal* condition number and not to one that appears “sufficiently small”.

IX. CONCLUSIONS

Herein we have shown that it is possible to avoid the use of common regularization techniques in the iterative solution to the inverse scattering problem by carefully formulating the experiments used to construct the

discrete linearized inverse problem. Specifically, adopting a multiple-frequency formulation with adaptive

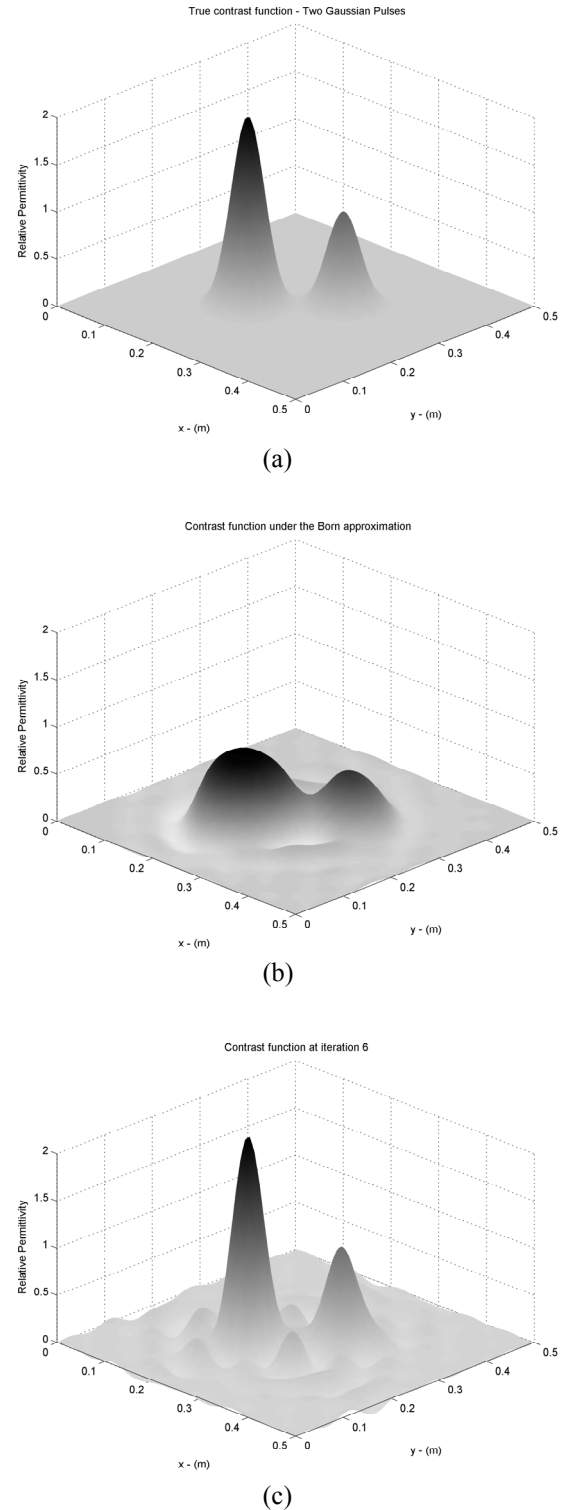


Fig. 5. 2D BIM profile reconstruction results: True contrast (a), first-order (b), and after six iterations (c).

basis functions and a global optimization over the basis parameter provides a well-conditioned matrix at each iteration. We have demonstrated the applicability of our adaptive basis functions to both the DBIM and BIM methods in 1D as well as to the BIM method in 2D (application to the 2D DBIM method poses no theoretical problems). Our current concerns are convergence to high-contrast profiles but this seems to be a problem which may be inherent in the Iterative Born techniques [2]. Even if this is the case, we plan on applying our approach of properly formulating the problem to other (possibly non-iterative) solution methods in order to determine exactly in what cases the usual regularization methods are avoidable. Future work will include a rigorous analysis of the ability of the proposed basis functions to reconstruct profiles in the presence of noisy field data. Also, we will consider an analysis for an optimum number of basis functions at each iteration.

ACKNOWLEDGEMENTS

The authors would like to acknowledge NSERC for supporting this research.

REFERENCES

- [1] W. C. Chew, *Waves and Fields in Inhomogeneous Media*, IEEE Press, 1990.
- [2] M. Oristaglio and H. Blok, "Wavefield Imaging and Inversion in Electromagnetics and Acoustics," *lecture notes*, Delft University, 2000.
- [3] M. Born and E. Wolf, *Principles of Optics*, 7th~ed, Cambridge University Press, 1999.
- [4] P. C. Hansen, "Numerical tools for analysis and solution of Fredholm integral equations of the first kind," *Inverse Problems* vol. 8, pp. 849-872, 1992.
- [5] Y. M. Wang and W. C. Chew, "An iterative solution of two-dimensional electromagnetic inverse scattering problem," *Int. J. Imaging Syst. Technol.*, vol. 1, no. 1, pp. 100-108, 1989.
- [6] Q. H. Liu *et al.*, "Active Microwave Imaging I - 2-D Forward and Inverse Scattering Methods", *IEEE Trans. Micro. Theo. and Tech.*, vol. 50, no. 1, pp. 123-133, 2002.
- [7] F. Soldovieri and R. Persico, "Reconstruction of an Embedded Slab from Multifrequency Scattered Field Data Under the Distorted Born Approximation," *IEEE Trans. Ant. and Propagat.*, vol. 52, no. 9, pp. 2348-2356, 2004.
- [8] A. J. Devaney, "Nonuniqueness in the inverse scattering problem," *J. Math. Phys.*, vol. 19, no. 7, pp. 1526-1531, 1978.
- [9] W. C. Chew and Y. M. Wang, "Reconstruction of two-dimensional permittivity distribution using the distorted born iterative method," *IEEE Trans. Med. Imag.*, vol. 9, pp. 218-25, June 1990.
- [10] V. I. Okhmatovski and J. LoVetri, "A Well-Conditioned Formulation of 1D Inverse Scattering Problem Under the Born Approximation," *ANTEM*, 2005.
- [11] I. Jeffrey, V. I. Okhmatovski, and J. LoVetri, "A Well-Conditioned Solution to the 1D Inverse Scattering Problem using the Distorted Born Iterative Method," *ACES 2006*, Miami Florida, 2006.

- [12] I. Jeffrey, V. I. Okhmatovski, and J. LoVetri, "A Modified Well-Conditioned Iterative Solution to the 1D Inverse Scattering Problem using the Born Iterative Method," *IEEE AP-S 2006*, Albuquerque, New Mexico, 2006.
- [13] C. Gilmore, I. Jeffrey, V. I. Okhmatovski, and J. LoVetri, "A Novel Multi-Frequency Regularization Method for the 2D Inverse Scattering Problem," *ANTEM 2006*, Montreal, Quebec, 2006.
- [14] R. F. Harrington, *Field Computation by Moment Methods*, New York: Maxmillan, 1968.



Ian Jeffrey received the B.Sc degree in Computer Engineering (with distinction) in 2002 and the M.Sc degree in Electrical and Computer Engineering in 2004 from the University of Manitoba, Winnipeg, Canada where he is currently working towards the Ph.D Degree in Electrical and Computer Engineering. His current research interests are in fast algorithms for computational electromagnetics, electromagnetic compatibility and inverse problems. Mr. Jeffrey held a Canadian NSERC Post-Graduate Scholarship A from 2002-2004 and currently holds an NSERC Post-Graduate Scholarship B.



Vladimir I. Okhmatovski was born in Moscow, Russia, in 1974. He received the M.S. (with distinction) and Candidate of Science (Ph.D.) degrees from the Moscow Power Engineering Institute, Russia, in 1996 and 1997, respectively. In 1997, he joined the Radio Engineering Department, Moscow Power Engineering Institute, as an Assistant Professor. From 1998 to 1999, he was a Post-Doctoral Research Associate with the National Technical University of Athens. From 1999 to 2003, he was a Post-Doctoral Research Associate with the University of Illinois at Urbana-Champaign. From 2003 to 2004, he was with the Department of Custom Integrated Circuits Advanced Research and Development, Cadence Design Systems Inc. He is currently an Assistant Professor with the Department of Electrical and Computer Engineering, University of Manitoba, Winnipeg, MB, Canada. His research interests are the fast algorithms of computational electromagnetics and modeling of high-speed digital circuits and mixed-signal components.



Joe LoVetri received the Ph.D. degree in electrical engineering from the University of Ottawa, ON, Canada, in 1991. From 1991 to 1999, he was an Associate Professor in the Department of Electrical and Computer Engineering, The University of Western Ontario, London, Ontario, Canada. He is currently a Professor in the Department of Electrical and Computer Engineering, and Associate Dean (Research) of the Faculty of Engineering, at University of Manitoba, Winnipeg, Canada. His main research interests are in time-domain CEM, modeling of EMC problems, GPR, and inverse imaging techniques.



Colin Gilmore received the B.Sc degree in Electrical Engineering (with distinction and winning the gold medal) in 2002 and the M.Sc Degree in Electrical Engineering in 2005 both from the University of Manitoba, Winnipeg, Canada where he is currently working towards the Ph.D Degree in Electrical Engineering. His current research interests are in the areas of GPR, signal processing, computational electromagnetics and inverse problems. Mr. Gilmore held a Canadian Natural Sciences and Engineering Research Council (NSERC) Post-Graduate Scholarship A from 2002-2004 and currently holds an NSERC Canada Graduate Scholarship.

High-Order FVTD on Unstructured Grids using an Object-Oriented Computational Engine

Dmitry Firsov¹, Joe LoVetri¹, Ian Jeffrey¹, Vladimir Okhmatovski¹, Colin Gilmore¹, and Walid Chamma²

¹Department of Electrical and Computer Engineering
University of Manitoba, Winnipeg, MB, Canada, R3T 5V6
firsovd@ee.umanitoba.ca, lovetri@ee.umanitoba.ca

²Radar Electronic Warfare Section
Defence R&D Canada - Ottawa, Department of National Defence
3701 Carling Avenue, Ottawa, Ontario, K1A 0Z4
Walid.Chamma@drdc-rddc.gc.ca

Abstract—An object-oriented implementation of a finite-volume time-domain (FVTD) engine for solving Maxwell’s equations is presented. The relevant aspects of the FVTD method are discussed from an object-oriented perspective and details of the object classes are given. Computational results obtained using the FVTD engine for solving Maxwell’s Equations on unstructured grids are also shown. The engine implements both MUSCL and polynomial interpolation methods to approximate the fluxes at the cell boundaries up to third-order accuracy. In addition, the engine has the capability of using a number of time-integration schemes. Results are presented for the transient scattering from a PEC sphere and a lossy dielectric cube. For the case of the sphere, almost perfect agreement with the analytic solution in the time-domain is achieved. The number of cells required as compared to FDTD is substantially reduced.

Keywords—Finite-volume time-domain, FVTD, Maxwell’s Equations, object-oriented design.

I. INTRODUCTION

The finite-difference time-domain (FDTD) algorithm is probably the most popular computational electromagnetics (CEM) technique in use today. The two main drawbacks of the *standard* FDTD method are that curved geometries must be approximated by “stair-stepping” the boundaries and that the electromagnetic field components are interlaced in space and time. These drawbacks require that a fine grid be used in order to resolve curved boundaries which increases the required computational resources. There have been several

successful investigations on modifying the method for non-rectangular boundaries but these are difficult to implement and use [1].

In recent years, the computational electromagnetic community has taken interest in the finite-volume time-domain (FVTD) algorithm as an alternative or companion to the simple and powerful FDTD algorithm for solving Maxwell’s equations [2, 3, 4]. The primary reason for this interest is that the basic formulation of FVTD does not require a structured spatial mesh and so its ability to solve electromagnetic problems involving complex geometries is not constrained by a lack of ability to accurately describe the physical problem.

The finite-volume technique is a standard technique used in Computational Fluid Dynamics (CFD) [5]. One of the first comprehensive implementations of the technique for CEM was reported by Shankar *et al.* in the early 1990’s [2]. Shankar’s method collocates all the field components at the center of each finite volume and is implemented on structured body-fitted curvilinear grids. It is a characteristic-based FVTD scheme which uses a two-step second-order upwinding scheme. A similar technique has also been presented by Shang [6]. Recently, two other groups have reported achieving excellent results using a characteristic-based FVTD technique [3, 4]. Both use a second-order accurate Monotone Upstream-centered Scheme for Conservation Laws (MUSCL) to interpolate the fluxes at the finite-volume facets.

In this paper we consider the FVTD method on unstructured grids and present the use of a higher-order flux-interpolatory method, developed by Ollivier-Gooch for fluid-dynamics problems [8], for our FVTD computational engine. In addition, as the implementation

of our computational engine was undertaken from an object-oriented perspective, this paper demonstrates the flexibility of such an implementation of the FVTD algorithm for handling a multitude of volumetric mesh descriptions, time-integration, and flux-integration approximations. Also, in order to facilitate an in-depth understanding of the method, we provide an outline of the class hierarchy and programming tactics used during implementation. Although our FVTD implementation is in C++, the object-oriented concepts we discuss are not language specific.

This paper is organized as follows: In Section 2, we discuss the object-oriented implementation of a discretized volumetric mesh. Section 3 presents a brief overview of the theory behind the FVTD method as it pertains to Maxwell's equations. In Section 4, we discuss some of the interpolatory techniques available for flux-integration, namely MUSCL and polynomial interpolation schemes. Section 5 overviews the time-integration schemes considered which retain the operator representation of the FVTD update equation as a matrix-vector-product. Finally, Section 6 validates the engine by comparing computational results using FDTD, FVTD with MUSCL interpolation, and FVTD with third-order interpolation against FDTD. The problems of transient scattering from a PEC sphere and from a lossy dielectric cube are considered.

II. OBJECT-ORIENTED MESH REPRESENTATION

The FVTD solution of Maxwell's equations requires a volumetric grid over a specified three-dimensional region of interest. The meshing software we use¹ is capable of producing unstructured meshes comprised of tetrahedrons, hexahedrons, prisms, or pyramids and so our FVTD engine has been designed to function using any of these volumetric elements. Any volumetric mesh consisting of polyhedral elements may be fully described as a collection of elements which are, in turn, described by vertices and facets. Thus the mesh description inherently includes a geometrical hierarchy. Using an object-oriented approach, our FVTD engine implements a volumetric mesh as an object consisting of instances of elements, vertices and facets each implemented as their own separate classes as depicted in Fig. 1. The mesh itself is an instance of the *cMesh* class and contains the geometrical description of the mesh via arrays of volumetric elements and vertices. A *cMesh* object is responsible for accessing the mesh description from file

1. A versatile mesh generator is *Gmsh* (www.geuz.org/gmsh/), a program available under the GNU license agreement that is capable of producing unstructured volumetric grids. It is our tool of choice for mesh generation.

and is additionally responsible for saving the mesh description in alternative formats compatible with various visualization tools². A brief discussion of the vertex, element and facet descriptions follows.

Each vertex in the mesh, represented by an instance of the *cPoint* class, contains three critical pieces of information: its spatial location, a unique identification tag corresponding to its location in the array of points in the *cMesh* object, and a list of pointers to all elements sharing it. The *cPoint* class also doubles as a general Euclidean vector class and is equipped with standard vector operators such as the cross-product.

Each element in the mesh, represented by an instance of the *cElement* class, is also given a unique identification tag and contains a list of pointers to *cPoint* objects (denoting the vertices of the element) as well as a list of the neighbouring elements. Storing neighbouring elements by their identification tag is essential for an efficient implementation. The element type is specified by a member in the *cElement* class. In addition, the *cElement* class is equipped with a set of utility functions used to compute various geometrical properties of a given instance of the class. The functions include the computation of the element volume and dynamic instantiation of element facets, as they are required throughout the FVTD algorithm, by means of the *cFacet* class. The different types of volumetric elements each require different functions for appropriately computing their geometrical properties. Because simple polyhedral computations can be easily coded inline, our implementation does not exploit inheritance to derive a specific element from a base element class. If, however, higher order elements were of interest (i.e., elements with curved boundaries) such inheritance would be beneficial for more complicated geometrical computations.

Although it is possible to pre-compute and store facet information for each element in the mesh, experience has shown that such a list significantly increases memory requirements. Therefore, as needed, element facets are generated via function calls in the *cElement* class which dynamically instantiate an instance of the *cFacet* class. A facet object is responsible for computing both the area and outward normal of the facet which it stores for use during the FVTD algorithm.

2. We often make use of *ParaView* (www.paraview.org) for visualizing vector fields.

III. FVTD FOR CONSERVATION LAWS AND MAXWELL'S EQUATIONS

The FVTD algorithm is usually applied to physical phenomena which are governed by a *conservation law*. For example, given a scalar quantity, denoted by $u(\mathbf{x}, t)$, a typical conservation law would be,

$$\partial_t u(\mathbf{x}, t) + \nabla \cdot \mathbf{f}(u(\mathbf{x}, t)) = S(\mathbf{x}, t) \quad (1)$$

where the flux vector \mathbf{f} is some function of u , and $S(\mathbf{x}, t)$ is a source term. Integrating the conservation law over an arbitrary volume, T_i , with boundary ∂T_i gives,

$$\int_{T_i} \partial_t u(\mathbf{x}, t) dV + \int_{\partial T_i} \mathbf{f}(u(\mathbf{x}, t)) \cdot d\mathbf{s} = \int_{T_i} S(\mathbf{x}, t) dV \quad (2)$$

where the divergence theorem has been applied to the second term and $d\mathbf{s} = \hat{\mathbf{n}} ds$ is the outward directed surface element vector. The FVTD method for solving electromagnetic problems considers all of the electric and magnetic field components as components of a solution vector $\mathbf{u} = [\mathbf{E} \ \mathbf{H}]^T$, and then casts Maxwell's equations into a form analogous to (1). Following a procedure similar to that given in [3], starting from Maxwell's two curl equations,

$$\begin{cases} \epsilon \partial_t \mathbf{E} - \nabla \times \mathbf{H} + \sigma \mathbf{E} = -\mathbf{J} \\ \mu \partial_t \mathbf{H} + \nabla \times \mathbf{E} = 0 \end{cases} \quad (3)$$

we employ the matrix operator,

$$\mathbf{S}(\mathbf{x})\mathbf{b} = \begin{bmatrix} 0 & -x_3 & x_2 \\ x_3 & 0 & -x_1 \\ -x_2 & x_1 & 0 \end{bmatrix} \begin{bmatrix} b_1 \\ b_2 \\ b_3 \end{bmatrix} = \mathbf{x} \times \mathbf{b} \quad (4)$$

by which the curl of a vector can be expressed in terms of the divergence of a matrix operating on the vector,

$$\nabla \times \mathbf{x} \equiv (\text{div} \mathbf{S}(\mathbf{x}))^T = \begin{bmatrix} \partial_2 x_3 - \partial_3 x_2 \\ -\partial_1 x_3 + \partial_3 x_1 \\ \partial_1 x_2 - \partial_2 x_1 \end{bmatrix}. \quad (5)$$

In terms of this new operator, Maxwell's equations can be written as

$$\begin{cases} \epsilon \partial_t \mathbf{E} - (\text{div} \mathbf{S}(\mathbf{H}))^T + \sigma \mathbf{E} = -\mathbf{J} \\ \mu \partial_t \mathbf{H} + (\text{div} \mathbf{S}(\mathbf{E}))^T = 0 \end{cases} \quad (6)$$

or, even more succinctly as

$$\partial_t \mathbf{u} + \alpha^{-1} \mathbf{K} \mathbf{u} = \alpha^{-1} (\mathbf{G} + \mathbf{B} \mathbf{u}), \quad (7)$$

where,

$$\alpha \triangleq \begin{bmatrix} \epsilon & \mathbf{0} \\ \mathbf{0} & \mu \end{bmatrix}, \mathbf{K} \mathbf{u} = \begin{bmatrix} -\nabla \times \mathbf{H} \\ \nabla \times \mathbf{E} \end{bmatrix}, \mathbf{B} \triangleq \begin{bmatrix} -\sigma & \mathbf{0} \\ \mathbf{0} & \mathbf{0} \end{bmatrix}, \mathbf{G} \triangleq \begin{bmatrix} -\mathbf{J} \\ \mathbf{0} \end{bmatrix}. \quad (8)$$

Integrating the curl equations (7) over an element denoted by T_i with boundary ∂T_i and using the

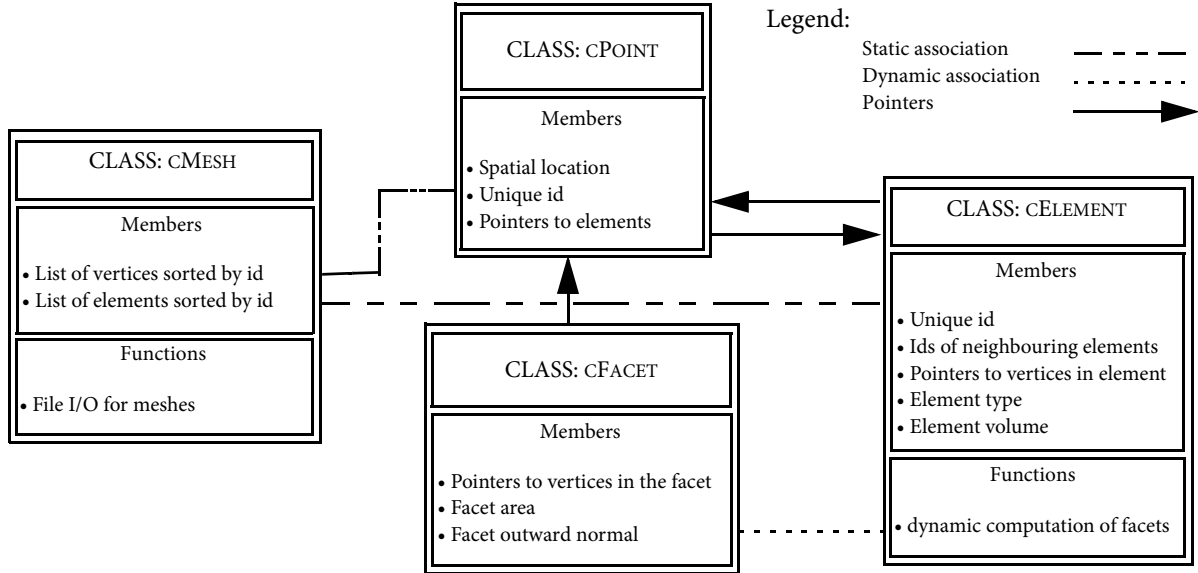


Fig. 1. Object-oriented mesh representation: class hierarchy.

divergence theorem to convert the integral over volume to integrals over the surface as in (2) we arrive at

$$\int_{T_i} \partial_i \mathbf{u} d\mathbf{x} + \int_{\partial T_i} \alpha^{-1} \mathbf{A}(\hat{\mathbf{n}}) \mathbf{u} ds = \int_{T_i} \alpha^{-1} \mathbf{G} d\mathbf{x} + \int_{T_i} \alpha^{-1} \mathbf{B} \mathbf{u} d\mathbf{x} \quad (9)$$

where matrix $\mathbf{A}(\hat{\mathbf{n}})$ is defined by,

$$\mathbf{A}(\hat{\mathbf{n}}) = \begin{bmatrix} \mathbf{0} & -\mathbf{S}(\hat{\mathbf{n}}) \\ \mathbf{S}(\hat{\mathbf{n}}) & \mathbf{0} \end{bmatrix}, \quad (10)$$

where $\hat{\mathbf{n}}$ denotes the outward normal to the volume surface ∂T_i . Analogous to (2), the value $\mathbf{A}(\hat{\mathbf{n}}) \mathbf{u}$ is referred to as the flux through the surface ∂T_i .

In order to discretize the electromagnetic problem of interest we associate with each cell a value of the generalized solution vector \mathbf{u}_i located at the barycentre \mathbf{x}_i of element T_i . This value is taken to represent the average of the generalized solution vector over the element T_i , i.e.,

$$\mathbf{u}_i = \frac{1}{\mu(T_i)} \int_{T_i} \mathbf{u}(\mathbf{x}) d\mathbf{x} = \mathbf{u}(\mathbf{x}_i) + O(\|\Delta \mathbf{x}^2\|) \quad (11)$$

where $\mu(T_i)$ is the volume of element T_i , and where $\Delta \mathbf{x}$ scales with the size of the element. Next, we define $\tilde{\mathbf{A}}(\hat{\mathbf{n}}) \triangleq \alpha^{-1} \mathbf{A}(\hat{\mathbf{n}})$ and decompose $\tilde{\mathbf{A}}(\hat{\mathbf{n}})$ as a sum of matrices with positive and negative eigenvalues (due to the symmetry of $\mathbf{A}(\hat{\mathbf{n}})$ the eigenvalues are real). Limiting each volumetric element to a homogeneous isotropic space described by material parameters $\boldsymbol{\varepsilon} = \text{diag}(\varepsilon, \varepsilon, \varepsilon)$ and $\boldsymbol{\mu} = \text{diag}(\mu, \mu, \mu)$, it can be shown that the matrix $\tilde{\mathbf{A}}(\hat{\mathbf{n}})$ has six eigenvalues given by $\Lambda = \text{diag}\{0, 0, v, v, -v, -v\}$ where $v = 1/\sqrt{\varepsilon\mu}$. To avoid inducing artificial numerical oscillations into the solution, it is beneficial to perform *flux-splitting* [3] by decomposing $\tilde{\mathbf{A}}(\hat{\mathbf{n}})$ into

$$\tilde{\mathbf{A}}(\hat{\mathbf{n}}) = \tilde{\mathbf{A}}(\hat{\mathbf{n}})^+ + \tilde{\mathbf{A}}(\hat{\mathbf{n}})^-, \quad (12)$$

where,

$$\tilde{\mathbf{A}}(\hat{\mathbf{n}})^+ = \frac{1}{2} \begin{bmatrix} -v\mathbf{S}(\hat{\mathbf{n}})^2 & -\varepsilon^{-1}\mathbf{S}(\hat{\mathbf{n}}) \\ \mu^{-1}\mathbf{S}(\hat{\mathbf{n}}) & -v\mathbf{S}(\hat{\mathbf{n}})^2 \end{bmatrix}$$

$$\tilde{\mathbf{A}}(\hat{\mathbf{n}})^- = \frac{1}{2} \begin{bmatrix} v\mathbf{S}(\hat{\mathbf{n}})^2 & -\varepsilon^{-1}\mathbf{S}(\hat{\mathbf{n}}) \\ \mu^{-1}\mathbf{S}(\hat{\mathbf{n}}) & v\mathbf{S}(\hat{\mathbf{n}})^2 \end{bmatrix}. \quad (13)$$

To compute the value of the surface integral in (9) we require knowledge of the flux $\mathbf{A}(\hat{\mathbf{n}}) \mathbf{u}$ on the boundary ∂T_i . To determine the flux, we let \mathbf{u}^* denote the solution vector on the inside part of the surface ∂T_i

while using \mathbf{u}^{**} to denote the solution vector on the outside part of ∂T_i . We can consider \mathbf{u}^* and \mathbf{u}^{**} as limits of the solution $\mathbf{u}(\mathbf{x})$ from the inside or outside of the element on to ∂T_i . The electromagnetic boundary conditions for the continuity of the tangential electric and magnetic field components across a boundary,

$$\begin{cases} \hat{\mathbf{n}} \times \mathbf{E}^* = \hat{\mathbf{n}} \times \mathbf{E}^{**} = \hat{\mathbf{n}} \times \mathbf{E} \\ \hat{\mathbf{n}} \times \mathbf{H}^* = \hat{\mathbf{n}} \times \mathbf{H}^{**} = \hat{\mathbf{n}} \times \mathbf{H} \end{cases}, \quad (14)$$

are used to express the flux at the surface ∂T_i in terms of the operator $\mathbf{A}(\hat{\mathbf{n}})$ as $\mathbf{A}(\hat{\mathbf{n}}) \mathbf{u} = \mathbf{A}(\hat{\mathbf{n}}) \mathbf{u}^* = \mathbf{A}(\hat{\mathbf{n}}) \mathbf{u}^{**}$. As \mathbf{u}^* and \mathbf{u}^{**} are not known explicitly they must be interpolated from the known values in the cell interior.

The flux at the boundary ∂T_i may be split by first calculating $\hat{\mathbf{n}} \times \mathbf{E}$ and $\hat{\mathbf{n}} \times \mathbf{H}$ at the cell boundary. Let us consider the top and bottom blocks of $\tilde{\mathbf{A}}(\hat{\mathbf{n}})^+ \mathbf{u}^*$ and $\tilde{\mathbf{A}}(\hat{\mathbf{n}})^- \mathbf{u}^{**}$ separately. The top block is

$$-\frac{1}{2} v_1 \mathbf{S}(\hat{\mathbf{n}})^2 \mathbf{E}^* - \frac{1}{2} \frac{\mathbf{S}(\hat{\mathbf{n}})}{\varepsilon_1} \mathbf{H}^* \quad \text{and}$$

$$\frac{1}{2} v_2 \mathbf{S}(\hat{\mathbf{n}})^2 \mathbf{E}^{**} - \frac{1}{2} \frac{\mathbf{S}(\hat{\mathbf{n}})}{\varepsilon_2} \mathbf{H}^{**}. \quad (15)$$

We multiply the first by ε_1 and the second by ε_2 to obtain

$$-\frac{1}{2} Y_1 \mathbf{S}(\hat{\mathbf{n}})^2 \mathbf{E}^* - \frac{1}{2} \mathbf{S}(\hat{\mathbf{n}}) \mathbf{H}^* \quad \text{and}$$

$$\frac{1}{2} Y_2 \mathbf{S}(\hat{\mathbf{n}})^2 \mathbf{E}^{**} - \frac{1}{2} \mathbf{S}(\hat{\mathbf{n}}) \mathbf{H}^{**} \quad (16)$$

where $Y_s = \varepsilon_s v_s = \sqrt{\varepsilon_s / \mu_s}$. Finally, a linear combination of these two gives the desired quantity,

$$\hat{\mathbf{n}} \times \mathbf{H} = \alpha \left(-\frac{1}{2} Y_1 \mathbf{S}(\hat{\mathbf{n}})^2 \mathbf{E}^* - \frac{1}{2} \mathbf{S}(\hat{\mathbf{n}}) \mathbf{H}^* \right) +$$

$$\beta \left(\frac{1}{2} Y_2 \mathbf{S}(\hat{\mathbf{n}})^2 \mathbf{E}^{**} - \frac{1}{2} \mathbf{S}(\hat{\mathbf{n}}) \mathbf{H}^{**} \right) \quad (17)$$

where $\alpha = 2Y_2 / (Y_1 + Y_2)$ and $\beta = 2Y_1 / (Y_1 + Y_2)$. A similar construction can be made for the bottom block of $\tilde{\mathbf{A}}(\hat{\mathbf{n}})^+ \mathbf{u}^*$ and $\tilde{\mathbf{A}}(\hat{\mathbf{n}})^- \mathbf{u}^{**}$ in order to obtain $\hat{\mathbf{n}} \times \mathbf{E}$.

Using these results, we come to a concise representation for the flux,

$$\mathbf{A}(\hat{\mathbf{n}}) \mathbf{u} = T_i \alpha_i \tilde{\mathbf{A}}(\hat{\mathbf{n}})^+ \mathbf{u}^* + T_k \alpha_k \tilde{\mathbf{A}}(\hat{\mathbf{n}})^- \mathbf{u}^{**} \quad (18)$$

where,

$$\begin{aligned}
 T_i &= 2 \begin{bmatrix} Y_k(Y_i + Y_k)^{-1} \mathbf{I} & 0 \\ 0 & Z_k(Z_i + Z_k)^{-1} \mathbf{I} \end{bmatrix} \text{ and} \\
 T_k &= \begin{bmatrix} Y_i(Y_i + Y_k)^{-1} \mathbf{I} & 0 \\ 0 & Z_i(Z_i + Z_k)^{-1} \mathbf{I} \end{bmatrix} \quad (19)
 \end{aligned}$$

and $\mathbf{I} \in \mathbb{R}^{3 \times 3}$ is the identity matrix, and $Z = Y^{-1}$ is the impedance.

At PEC boundaries zero tangential electric field and the image principle can be used to derive that the linear operation of $\tilde{\mathbf{A}}(\hat{\mathbf{n}})$ on \mathbf{u} becomes $\tilde{\mathbf{A}}(\hat{\mathbf{n}})\mathbf{u} = \alpha_i T^{\text{pc}} \tilde{\mathbf{A}}(\hat{\mathbf{n}})^+ \mathbf{u}^*$, where

$$T^{\text{pc}} = \begin{bmatrix} 2\mathbf{I} & 0 \\ 0 & 0 \end{bmatrix}. \quad (20)$$

Consequently, it can be shown that the scattered field formulation derived using the image principle results in,

$$\tilde{\mathbf{A}}(\hat{\mathbf{n}})\mathbf{u}^s = \alpha_i T^{\text{pc}} \tilde{\mathbf{A}}(\hat{\mathbf{n}})^+ \mathbf{u}^{s*} - 2\tilde{\mathbf{A}}(\hat{\mathbf{n}})^- \mathbf{G}^{s*}, \quad (21)$$

where $\mathbf{G}^{s*} = \begin{bmatrix} -\mathbf{E}^i & 0 \end{bmatrix}^{*\text{T}}$ is the source term for the scattered field formulation.

Finally, while a discussion of high-order mesh truncation schemes is beyond the scope of this paper, it is possible to obtain a simple mesh boundary condition by setting $\tilde{\mathbf{A}}(\hat{\mathbf{n}})^-$ to zero at the mesh boundary.

IV. FLUX INTEGRATION: MUSCL AND POLYNOMIAL INTERPOLATION

It is apparent from (9) and (18) that integration around the boundary of an element requires knowledge of the flux (or equivalently the solution values \mathbf{u}^* and \mathbf{u}^{**}) at both sides of the cell boundary. As we are only storing the solution at the barycentres of the elements, we require interpolation of these values to the element border in order to accurately integrate the flux. Two common techniques for interpolating the flux at the cell boundary are the so-called *upwind* and MUSCL schemes [3]. As upwinding provides only first-order accuracy and results in significant dissipation, we omit it from further consideration. For brevity, details of the MUSCL scheme are omitted, however the MUSCL scheme as detailed in [3] was implemented yielding second-order accurate results as will be shown in Section 6. Further, we have applied polynomial interpolation, for which we now summarize the required theory for computing the fluxes at the volumetric element boundaries.

IV.A The ENO Requirement

In any interpolatory technique used to compute the value of the solution \mathbf{u} at the boundary of a facet, we make use of a stencil comprised of the values \mathbf{u}_i located at the centers of some elements in the neighbourhood of the facet of interest. Although stencils for an arbitrarily high order of approximation are available, when they're applied to a solution with strong gradients, experience in CFD has shown that this could result in unwanted numerical oscillations [7]. The idea behind *essentially non-oscillatory* (ENO) interpolation schemes, used frequently in CFD for approximating the solution value at a given facet, is to use only neighbouring solution values that are *smoothly* connected to the solution at the facet in question. That is, the stencil that we use to approximate the facet values cannot cross points where the solution has steep gradients. Details can be found in several publications dealing with computational fluid dynamics (see, for example, [7, 8]) which deal with problems that involve the evolution of shocks.

Initially, we believed that maintaining ENO interpolation schemes would be critical to updating the solution inside the computational domain. We thought that material boundaries would require special care in selecting the interpolation stencil in an analogous manner to handling shocks in computational fluid dynamics. However, upon numerical experimentation, we found that such interpolatory stencil modifications at material boundaries were unnecessary and, due to the overhead required in computing the modified stencils, we no longer impose ENO requirements. To date, we have not encountered a problem of interest where such a scheme is required. We do however, acknowledge that for some problems, we may have to re-evaluate the importance of ENO schemes.

IV.B General Polynomial Interpolation

The work described herein closely follows the work of Ollivier-Gooch found in [8]. In describing the polynomial interpolation method of Ollivier-Gooch we consider a polynomial $P_i(\mathbf{x} - \mathbf{x}_i)$ which interpolates the field value solution $\mathbf{u}(\mathbf{x})$ around a point \mathbf{x}_i and require that the difference between this polynomial and the exact solution be of order $k + 1$, that is,

$$P_i(\mathbf{x} - \mathbf{x}_i) - \mathbf{u}(\mathbf{x}) = O(\|\mathbf{x} - \mathbf{x}_i\|^{k+1}). \quad (22)$$

IV.C Stencil Selection

We require a stencil such that the data we use to determine the coefficients of our polynomial are not too far from the control volume center, \mathbf{x}_i . A good way to collect finite volumes for the stencil around a finite

volume T_i is to use the first neighbouring elements around T_i , *i.e.*, those which share a common facet with T_i . Iterating this process and thereby adding new elements to our control volume, we will collect a large enough stencil to achieve the desired accuracy: enough points to determine the coefficients for our polynomial. The set of elements from which the stencil will be generated may be written as,

$$S_i^k = \{T_s : \exists T_n \in S_i^{k-1}, \partial T_s \cap \partial T_n \neq \emptyset\} \quad (23)$$

with $S_i^1 = \{T_i\}$. The intersection $\partial T_s \cap \partial T_n$ is assumed null if there is no common facet between elements T_s and T_n . The stencil S_i^k is then built by considering the center points of each element in S_i^{k-1} . Usually k will be the same as the maximal possible order of accuracy for the stencil [8].

IV.D Polynomial Interpolation Theory

According to the dimensions of our problem, we consider the function $\mathbf{u}(\mathbf{x}) : \mathbb{R}^3 \rightarrow \mathbb{R}^6$ and we write a general Taylor's expansion about the point \mathbf{x}_i . If the function is infinitely differentiable in the neighbourhood of \mathbf{x}_i , then we can write,

$$\mathbf{u}(\mathbf{x}) = \sum_{m=0}^k \frac{1}{m!} \sum_{m_1, m_2, m_3} \frac{\partial^m \mathbf{u}(\mathbf{x}_i)}{(\partial x_1)^{m_1} (\partial x_2)^{m_2} (\partial x_3)^{m_3}} \times \prod_{s=1}^3 (x_s - (x_i)_s)^{m_s} + O(\|\Delta \mathbf{x}\|^{k+1}) \quad (24)$$

which is a polynomial approximation for $\mathbf{u}(\mathbf{x})$ given by the truncated Taylor's expansion of degree k . In (24) $m_1 + m_2 + m_3 = m$. As the FVTD solution is in terms of cell-averaged values \mathbf{u}_i , we let the expansion point \mathbf{x}_i correspond to the barycentre of T_i and take a volumetric average of both sides of (24) over T_i to obtain,

$$\begin{aligned} \frac{1}{\mu(T_i)} \int_{T_i} \mathbf{u}(\mathbf{x}) d\mathbf{x} &\triangleq \mathbf{u}_i = \\ \sum_{m=0}^k \frac{1}{m!} \sum_{m_1, m_2, m_3} \frac{\partial^m \mathbf{u}(\mathbf{x}_i)}{(\partial x_1)^{m_1} (\partial x_2)^{m_2} (\partial x_3)^{m_3}} \times & \quad (25) \\ \frac{1}{\mu(T_i)} \int \prod_{T_i, s=1}^3 (x_s - (x_i)_s)^{m_s} d\mathbf{x} + \frac{1}{\mu(T_i)} \int O(\|\Delta \mathbf{x}\|^{k+1}) d\mathbf{x} & \end{aligned}$$

Now it is our desire to express $\mathbf{u}(\mathbf{x})$ in terms of the average values \mathbf{u}_i . We begin by extracting the first term of the summation in (25) which happens to be $\mathbf{u}(\mathbf{x}_i)$ and write it in terms of \mathbf{u}_i as,

$$\begin{aligned} \mathbf{u}(\mathbf{x}_i) &= \mathbf{u}_i - \\ \sum_{m=1}^k \frac{1}{m!} \sum_{m_1, m_2, m_3} \frac{\partial^m \mathbf{u}(\mathbf{x}_i)}{(\partial x_1)^{m_1} (\partial x_2)^{m_2} (\partial x_3)^{m_3}} \times & \quad (26) \\ \frac{1}{\mu(T_i)} \int \prod_{T_i, s=1}^3 (x_s - (x_i)_s)^{m_s} d\mathbf{x} - \frac{1}{\mu(T_i)} \int O(\|\Delta \mathbf{x}\|^{k+1}) d\mathbf{x} & \end{aligned}$$

Next, by extracting the first term of (24) we obtain

$$\begin{aligned} \mathbf{u}(\mathbf{x}) &= \mathbf{u}(\mathbf{x}_i) + \\ \sum_{m=1}^k \frac{1}{m!} \sum_{m_1, m_2, m_3} \frac{\partial^m \mathbf{u}(\mathbf{x}_i)}{(\partial x_1)^{m_1} (\partial x_2)^{m_2} (\partial x_3)^{m_3}} \times & \quad (27) \\ \prod_{s=1}^3 (x_s - (x_i)_s)^{m_s} + O(\|\Delta \mathbf{x}\|^{k+1}). & \end{aligned}$$

Finally, substitution for $\mathbf{u}(\mathbf{x}_i)$ from (26) into (27) gives,

$$\begin{aligned} \mathbf{u}(\mathbf{x}) &= \mathbf{u}_i + \sum_{m=1}^k \frac{1}{m!} \sum_{m_1, m_2, m_3} \frac{\partial^m \mathbf{u}(\mathbf{x}_i)}{(\partial x_1)^{m_1} (\partial x_2)^{m_2} (\partial x_3)^{m_3}} \times \\ \left[\prod_{s=1}^3 (x_s - (x_0)_s)^{m_s} - p_i(m_1, m_2, m_3) \right] & + O(\|\Delta \mathbf{x}\|^{k+1}) \quad (28) \\ - \frac{1}{\mu(T_i)} \int_{T_i} O(\|\Delta \mathbf{x}\|^{k+1}) d\mathbf{x} & \end{aligned}$$

where

$$p_i(m_1, m_2, m_3) \triangleq \frac{1}{\mu(T_i)} \int \prod_{T_i, s=1}^3 (x_s - (x_0)_s)^{m_s} d\mathbf{x} \quad (29)$$

define the element moments and where $\mathbf{P}_i(\mathbf{x} - \mathbf{x}_i)$ corresponds to the first two terms on the right hand side of (28) because the two error terms are of the same order. By the selected substitution method we have implicitly enforced that the average polynomial value over the element T_i is equal to the cell-averaged solution \mathbf{u}_i *i.e.*,

$$\frac{1}{\mu(T_i)} \int_{T_i} \mathbf{P}_i(\mathbf{x} - \mathbf{x}_i) d\mathbf{x} = \frac{1}{\mu(T_i)} \int_{T_i} \mathbf{u}(\mathbf{x}) d\mathbf{x} \triangleq \mathbf{u}_i, \quad (30)$$

due to the fact that, upon cell-averaging of (28), the error terms cancel. Finally, to determine the polynomial coefficients, corresponding to the partial derivatives in (28), we minimize,

$$\left\| \mathbf{u}_j - \frac{1}{\mu(T_j)} \int_{T_j} \mathbf{P}_i(\mathbf{x} - \mathbf{x}_j) d\mathbf{x} \right\| \quad \forall T_j \in S_i^k, \quad (31)$$

where details can be found in [8].

We note that expression (28) can be used to compute the true solution anywhere within the stencil from the cell-averaged value in each element. Therefore, this method enables us to convert the stored cell-average values into a high-order solution for \mathbf{u}^* and \mathbf{u}^{**} on element boundaries. It also allows us to output the true solution for electromagnetic problems of interest such as for scattering from a PEC sphere as shown in Section 6.

IV.E Object-Oriented Flux Interpolation

It is clear that an object-oriented approach to the implementation of an engine capable of various flux-interpolation schemes is possible. Further, one may be interested in adaptively applying different flux-integration techniques to save on computational resources in regions where high-order techniques are not required for adequate accuracy. Therefore, it is not desirable to derive a flux-interpolation method from a base class. Instead, our implementation uses a switch statement to select between the methods so that all methods are at our disposal during computation.

Using the above methods to approximate the flux at the boundaries *i.e.* \mathbf{u}^* and \mathbf{u}^{**} we substitute (18) into the second term of (9),

$$\begin{aligned} \frac{1}{\mu(T_i)} \int_{\partial T_i} \alpha^{-1} \mathbf{A}(\hat{\mathbf{n}}) \mathbf{u} ds \approx \\ M_i \\ \frac{1}{\mu(T_i)} \sum_{m=1} (T_i \alpha_i \tilde{\mathbf{A}}(\hat{\mathbf{n}}_m)^+ \tilde{\mathbf{u}}^* + T_{i_m} \alpha_{i_m} \tilde{\mathbf{A}}(\hat{\mathbf{n}}_m)^- \tilde{\mathbf{u}}^{**}) \end{aligned} \quad (32)$$

where M_i is the number of facets making up element T_i , i_m denotes the element neighbouring T_i via its m^{th} facet and $\hat{\mathbf{n}}_m$ denotes the outward normal to the m^{th} facet. Note that $\tilde{\mathbf{u}}^*$ and $\tilde{\mathbf{u}}^{**}$ are the integrals of the inner and outer solutions over facet m respectively which we compute analytically from the polynomial interpolation function up to third-order accuracy.

Finally, for a mesh comprising of N elements we define

$$\begin{bmatrix} \left(\frac{1}{V_1} \int_{\partial T_1} \alpha^{-1} \mathbf{A}(\hat{\mathbf{n}}) \mathbf{u} ds \right)^T \\ \vdots \\ \left(\frac{1}{V_N} \int_{\partial T_N} \alpha^{-1} \mathbf{A}(\hat{\mathbf{n}}) \mathbf{u} ds \right)^T \end{bmatrix} \triangleq \mathbf{L} \mathbf{U} \quad (33)$$

where $\mathbf{U} = [\mathbf{u}_1^T \ \mathbf{u}_2^T \ \dots \ \mathbf{u}_N^T]^T$ is the vector of all unknowns. Using the notation of (32) and (33) in (9) gives,

$$\partial_t \mathbf{U} + \mathbf{L} \mathbf{U} = \mathbf{F} \quad (34)$$

where the time-derivative is taken element by element over \mathbf{U} and where \mathbf{F} is a source term where each element of \mathbf{F} represents the right-hand-side of (9) at the i^{th} cell. It is of importance to note that under linear flux interpolation the result of the operator \mathbf{L} operating on \mathbf{U} can be viewed as a matrix-vector product.

V. TIME-INTEGRATION SCHEMES

Having organized the flux-integration into a matrix-vector product over the entire computational space, it remains to discretely approximate the time derivative in (34). We have considered forward-Euler, predictor-corrector, Runge-Kutta and Crank-Nicholson methods. These methods are explicit schemes, save Crank-Nicholson. For source-free media, the predictor-corrector scheme discretization of (34) using a time-step of Δt will give a system of equations of the form,

$$\mathbf{U}^{(n+1)} = \mathbf{U}^{(n)} - \Delta t \mathbf{L} \mathbf{U}^{(n)} + \frac{\Delta t^2}{2} \mathbf{L}^2 \mathbf{U}^{(n)} + O(\Delta t^3). \quad (35)$$

It is clear that this may be re-written as,

$$\mathbf{U}^{(n+1)} = \tilde{\mathbf{L}} \mathbf{U}^{(n)} \quad (36)$$

where, $\tilde{\mathbf{L}} = \mathbf{I} - \Delta t \mathbf{L} + (\Delta t^2/2) \mathbf{L}^2$ and $\mathbf{I} \in \mathbb{R}^{6N \times 6N}$. In fact, any explicit scheme can be formulated as a matrix-vector-product and so an explicit formulation of the FVTD method requires the one-time filling of the matrix $\tilde{\mathbf{L}}$, setting the initial value of the solution vector over the domain, followed by a simple matrix-vector product at each time-step. Implementation of this update scheme should make use of the matrix-vector product updating inherent in the algorithm. For this reason, we have used our matrix library, based on an underlying abstract matrix class, namely, *cAbstractMatrix*. The benefit is that this abstract class is compatible with various linear system solvers such as our own implementations of *GMRES*, *BCGStab*, etc. [9], so that in implicit schemes, when the operator shows up on the left-hand side of the update equation, our solvers can be used.

Unfortunately, storing the entire operator matrix will require substantial amounts of memory for large meshes. For example, in the case of a tetrahedral mesh using simple upwinding, each block of six rows of the matrix would contain five (corresponding to the element

in question and its four facets) 6×6 blocks. A mesh consisting of one million elements where 8 byte double precision values are used to store the matrix entries would require $6 \times 6 \times 5 \times 8 \times 10^6 = 1.44$ Gigabytes of RAM to store the matrix. The situation becomes worse when higher-order interpolatory schemes are considered (for example the MUSCL scheme would increase this requirement 5 times). With our current resources we are unable to store the entire matrix. Instead, we update the solution \mathbf{u}_j by dynamically computing the i^{th} six-row block of \mathbf{L} . Therefore, for explicit schemes, we have overloaded the *cAbstractMatrix* matrix-vector-product operator with this row-by-row method of multiplication. The matrix class we use to implement the *cAbstractMatrix* class for solving FVTD problems we call *cMaxwellApprox*. A depiction of the conceptual flow of the algorithm as well as the corresponding object-oriented design is shown in Fig. 2.

VI. NUMERICAL RESULTS AND DISCUSSION

VI.A Scattering from a PEC sphere

We present the FVTD results for scattering from a perfectly electrical conducting (PEC) sphere as an exact

series solution is available in the frequency domain [10], and a time domain solution may be easily obtained using the inverse Fourier transform. This problem was selected as a benchmark for the FVTD engine as the irregular surface of the sphere coincides with one of the primary reasons for developing finite-volume methods on irregular grids: eliminating the need for stair-stepping at arbitrarily shaped boundaries.

The finite-volume algorithm using the previously discussed flux- and time-integration methods was tested for a PEC sphere with a three metre radius centered at the origin of a Cartesian coordinate system. An x -polarized electric-field plane-wave transient pulse $\mathbf{E} = g(t)\hat{\mathbf{x}}$ incident in the z -direction and varying as the derivative of a Gaussian was selected where, for $t \geq 0$

$$g(t) = -2A(t - t_0)b^{-2}\exp(-b^{-2}(t - t_0)^2). \quad (37)$$

The parameters were selected as: $A = 1$, $b = 1.14 \times 10^{-8}$ s, and $t_0 = 4.0 \times 10^{-8}$ s giving a shortest free-space wavelength of about 3 metres resulting in significant energy in the resonance region of the sphere.

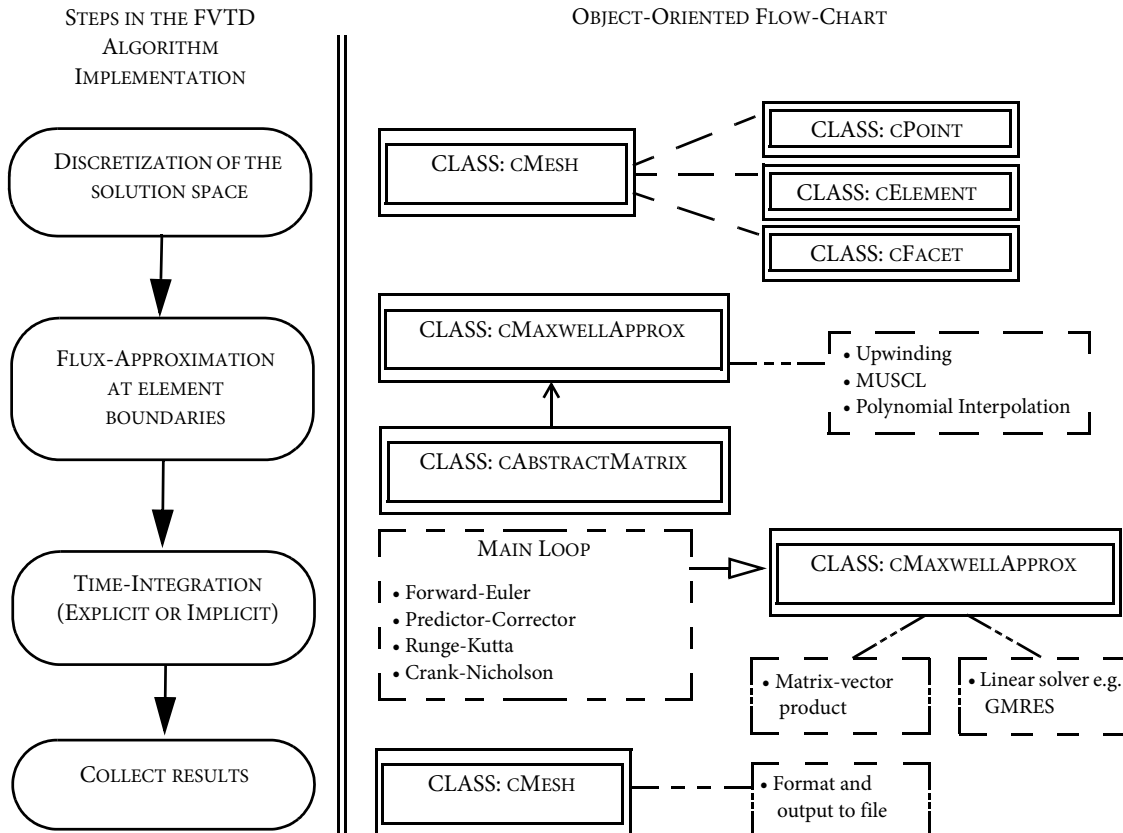


Fig. 2. Algorithm flow and associated class description for the FVTD engine.

Fig. 3 shows the computational results for the x -component of the scattered field at the back-scatter location $(0, 0, -7)$ (a), (c), (e), as well as at the side-scatter location $(-7, 0, 0)$ (b), (d), (f). For both measurement locations, the analytic solution is compared to solutions obtained using the MUSCL and polynomial interpolation finite-volume methods computed on a mesh with an average cell edge length of 0.75 m. All results shown use the second-order predictor-corrector time-integration scheme. In addition, FDTD results are presented for a cell edge length of 0.1 m. The figure shows that the FVTD results are in excellent agreement with the analytic solution.

To further test the FVTD engine, the same PEC sphere problem was solved for volumetric meshes with average element edge lengths of 0.6 and 0.5 m. The back-scattering results are summarized in Table 1. In the table, the L_2 error denotes the percent error between the computed solution and the analytic solution as measured by the L_2 norm. Clearly, for the same level of discretization polynomial interpolation is more accurate than MUSCL as expected due to the higher-order spatial approximations used in the polynomial interpolation scheme.

Comparing the FVTD results with the FDTD results we see that for the 0.1 m FDTD grid, the FVTD algorithm provides better accuracy using MUSCL on the 0.5 m mesh. Third-order polynomial interpolation provided more accurate results than FDTD even in the case of the 0.75 m mesh. The increased accuracy obtained for both the MUSCL and polynomial interpolation schemes comes at the cost of increased memory requirements needed to properly store the unstructured mesh as discussed in Section 2. For example, we require 203 Megabytes of RAM to store 700,000 mesh element solutions using the MUSCL scheme, while FDTD uses roughly the same amount of memory for 8 million grid point solutions. Fortunately,

the MUSCL solution at this level of discretization already out-performs the accuracy of FDTD for the simple case of the PEC sphere. For more complicated geometries, we feel that the benefits of any of the FVTD techniques will be even more prominent.

VI.B Scattering From a Dielectric cube

To test the FVTD implementation's ability to handle dielectric bodies and finite conductivities we show the scattering from a lossy, dielectric cube. As there is no known analytic solution for this problem we simply compare the results with the FDTD solution. The cube dimensions were selected as 6 m and the physical parameters were selected as: $\epsilon_r = 4$, $\mu_r = 1$, $\sigma = 0.01$ S/m. An x -polarized, z -incident, electric-field plane-wave Gaussian transient pulse $\mathbf{E} = f(t)\hat{\mathbf{x}}$ was selected such that for $t \geq 0$

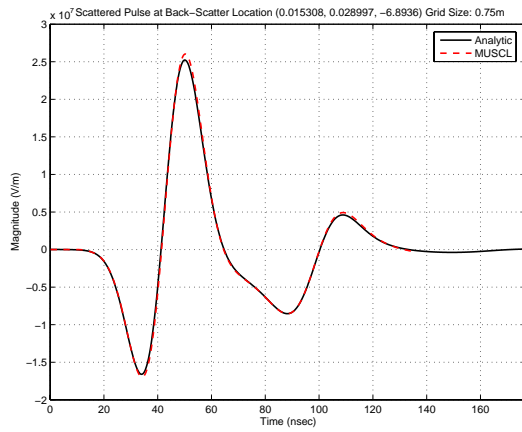
$$f(t) = A \exp(-b^2(t-t_0)^2) \quad (38)$$

with parameters $A = 1000$, $b = 1.14 \times 10^{-8}$ s, and $t_0 = 4.0 \times 10^{-8}$ s. Again, FVTD results were simulated on a volumetric mesh with an average element edge size of 0.75 m and were compared to FDTD results obtained from two regular grids: a 0.2 m regular grid and a 0.5 m regular grid. Results are shown in Fig. 4.

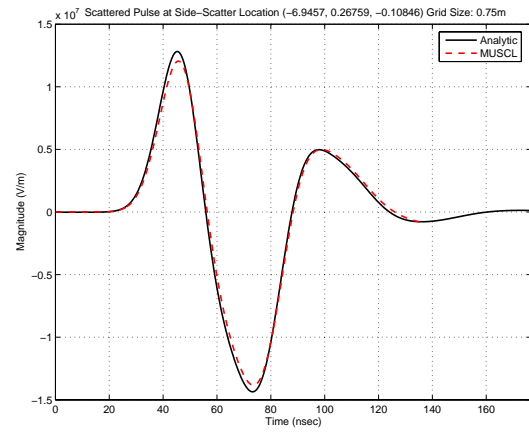
From the results, we can see that the FVTD solution to the lossy cube problem compares quite well with the FDTD solution. The largest difference in the plots is most likely due to differences in the dielectric modelling: FDTD assumes a diamond shaped stencil for imposed dielectric objects while FVTD is capable of imposing a constant dielectric within each finite volume, providing a more accurate physical model of the cube.

Table 1: Comparison of PEC sphere back-scattering results.

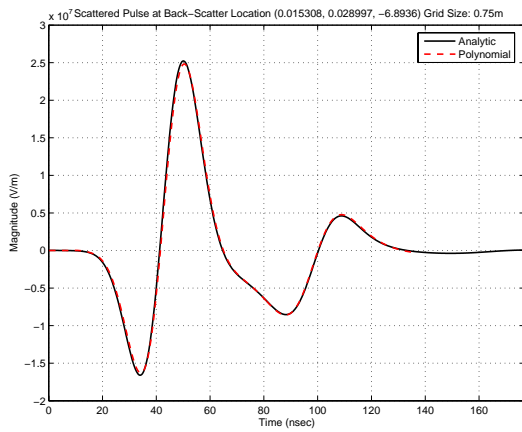
Solution method	Average Element dimension (m)	Number of mesh cells	Memory Requirements (Mb)	Number of time steps	L_2 Error of E_x
MUSCL	0.75	~200,000	62	~750	7.13%
MUSCL	0.6	~400,000	117	~900	7.40%
MUSCL	0.5	~700,000	203	~1100	2.87%
Polynomial-3	0.75	~200,000	131	~750	3.12%
Polynomial-3	0.6	~400,000	251	~900	1.70%
Polynomial-3	0.5	~700,000	435	~1100	1.69%
FDTD	0.1	~8,000,000	223	~2000	3.25%



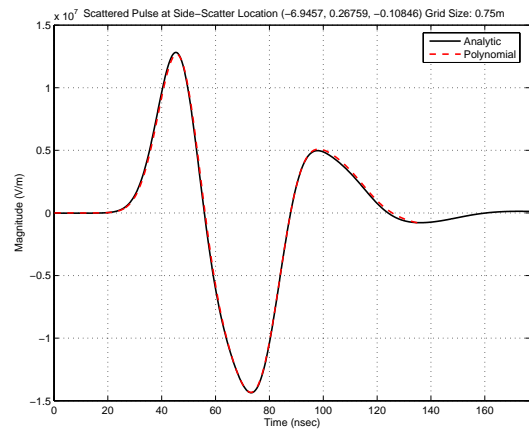
(a)



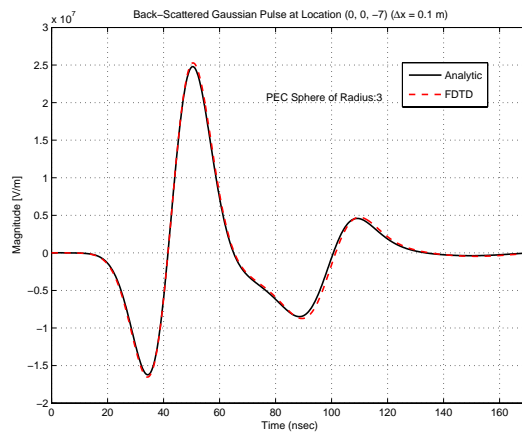
(b)



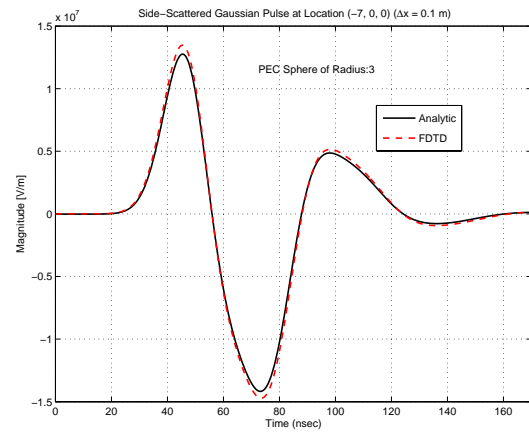
(c)



(d)



(e)



(f)

Fig. 3. Scattering from a 3 meter PEC sphere: Back-scattering (a), (c), (e); and Side-scattering (b), (d), (f); MUSCL (a), (b); Polynomial Interpolation (c), (d); FDTD (e), (f).

VII. CONCLUSIONS

The unstructured grid FVTD method using MUSCL or polynomial interpolated flux-integration, and second-order predictor-corrector time-integration, has given excellent results for all scattering problems tested thus far. The FVTD method has shown to yield more accurate results than FDTD solutions for the same level of discretization. This is due to a more accurate approximation of the geometry for curved scatterers in FVTD. In the case of the PEC sphere, to obtain the same level of accuracy using FDTD required a cubical cell-size 7 times smaller than the average cell edge-length in FVTD.

Although we have not included a comparison of the computational time required by FVTD and FDTD for the same numerical problem, we can say that compared to an un-optimized FDTD implementation, our un-optimized

FVTD engine ran substantially faster for the same level of accuracy. We did compare the performance of our engine against a fully optimized commercial FDTD package and found that our engine ran significantly slower. Consequently, we are currently working on optimizing our code and formulating a new criterion for obtaining the maximum time-step which satisfies stability conditions on an unstructured grid.

ACKNOWLEDGEMENTS

The authors would like to acknowledge Defence R&D Canada and NSERC for supporting this research.

REFERENCES

- [1] A. Taflove (editor), *Advances in Computational Electrodynamics: The Finite-Difference Time-Domain Method*, Artech House Inc, Boston, 1998.
- [2] V. Shankar, A. H. Mohammadian, and W. F. Hall, "A Time-Domain Finite-Volume Treatment for the Maxwell Equations," *Electromagnetics*, Vol. 10, No. 1-2, pp 127 - 145, 1990.
- [3] P. Bonnet, X. Ferrieres, B. L. Michielsen, P. Klotz, and J. L. Roumiguieres, "Finite-Volume Time Domain Method," in *Time Domain Electromagnetics*, S. M. Rao (editor), Academic Press, San Diego, 1999.
- [4] C. Fumeaux, D. Baumann, P. Leuchtmann, and R. Vahldieck, "A Generalized Local Time-Step Scheme for Efficient FVTD Simulations in Strongly Inhomogeneous Meshes," *IEEE Trans. on Microwave Theory and Techniques*, Vol. 52, No. 3, pp. 1067-1076, March 2004.
- [5] C. Hirsch, *Numerical Computation of Internal and External Flows, Vol. I: Fundamentals of Numerical Discretization*, John Wiley & Sons Ltd., New York, 1988.
- [6] J. S. Shang, "Characteristic-Based Algorithms for Solving the Maxwell's Equations in the Time Domain," *IEEE Antennas and Propagation Magazine*, Vol. 37, No. 3, pp. 15-25, June 1995.
- [7] X.-D. Liu, S. Osher, and T. Chan, "Weighted Essentially Non-oscillatory Schemes," *Journal of Computational Physics*, vol. 115, pp. 200-212, 1994.
- [8] C. F. Ollivier-Gooch, "Quasi-ENO Schemes for Unstructured Meshes Based on Unlimited Data-Dependent Least-Squares Reconstruction," *Journal of Computational Physics*, Vol. 133 (1), pp 6-17, 1997.
- [9] Y. Saad, *Iterative Methods for Sparse Linear Systems*, 2nd. Ed. SIAM, 2003.
- [10] R. F. Harrington, *Time-Harmonic Electromagnetic Fields*, McGraw-Hill, 1961.
- [11] D. K. Firsov, I. Jeffrey, J. LoVetri, and C. Gilmore, "An Object Oriented Finite-Volume Time-Domain Computational Engine", *ACES 2006, Miami Florida*.
- [12] D. Firsov, J. LoVetri, I. Jeffrey, V. Okhmatovski, and W. Chamma, "High-Order FVTD on Unstructured Grids", *ACES 2006, Miami Florida*.

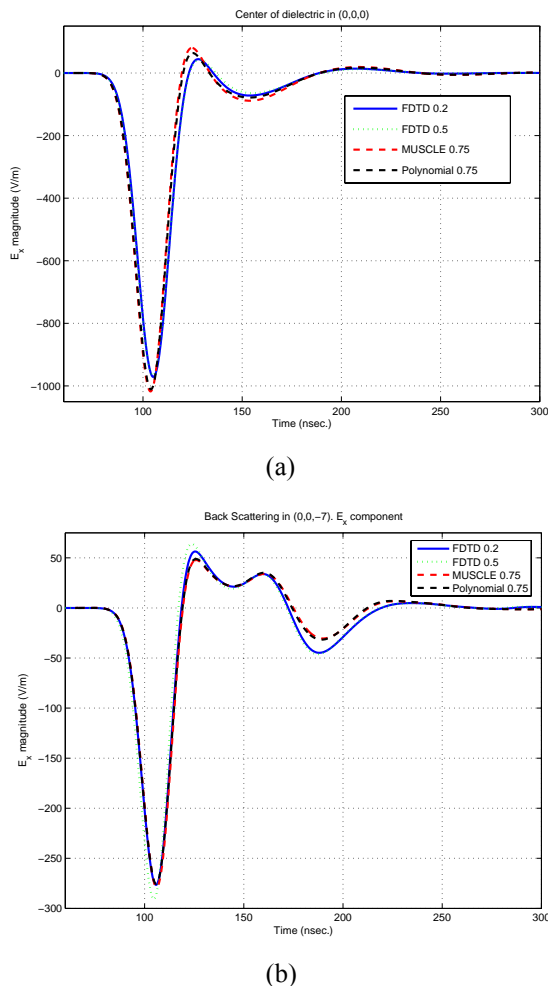


Fig. 4. FVTD and FDTD scattering from a dielectric cube with nonzero conductivity at: cube center (0, 0, 0) (a); back-scatter point (0, 0, -7) (b).



Dmitry K. Firsov received his diploma (with distinction) and Candidate of Science (Ph.D.) degrees in mathematics from Tomsk State University, Russia, in 1999 and 2002 respectively. In 2002 he was an Assistant Professor at Tomsk State University, Department of Theoretical Mechanics. From 2003-2005 he was a post-doctoral fellow with the Department of Mathematics at the University of Manitoba, Canada. Currently, Dmitry is a post-doctoral fellow with the Department of Electrical Engineering at the University of Manitoba. He is currently working in the area of numerical methods for partial differential equations.



Joe LoVetri received the Ph.D. degree in electrical engineering from the University of Ottawa, ON, Canada, in 1991. From 1991 to 1999, he was an Associate Professor in the Department of Electrical and Computer Engineering, University of Western Ontario, Canada. He is currently a Professor in the Department of Electrical and Computer Engineering, and Associate Dean (Research) of the Faculty of Engineering at University of Manitoba, Winnipeg, Canada. His main research interests are in time-domain CEM, modeling of EMC problems, GPR, and inverse imaging techniques.



Ian Jeffrey received the B.Sc degree in Computer Engineering (with distinction) in 2002 and the M.Sc degree in Electrical and Computer Engineering in 2004 from the University of Manitoba, Winnipeg, Canada where he is currently working towards the Ph.D Degree in Electrical and Computer Engineering. His current research interests are in fast algorithms for computational electromagnetics, electromagnetic compatibility and inverse problems.



Vladimir I. Okhmatovski received the M.S. (with distinction) and Candidate of Science (Ph.D.) degrees from the Moscow Power Engineering Institute, Russia, in 1996 and 1997, respectively. From 1998-1999, he was a Post-Doctoral Research Associate with the National Technical University of Athens. From 1999-2003, he was a Post-Doctoral Research Associate with the University of Illinois at Urbana-Champaign. From 2003-2004, he was with the Department of Custom Integrated Circuits Advanced Research and Development, Cadence Design Systems Inc. He is currently an Assistant Professor with the Department of Electrical and Computer Engineering, University of Manitoba, Winnipeg, MB, Canada. His research interests are the fast algorithms of computational electromagnetics and modeling of high-speed digital circuits and mixed-signal components.



Colin Gilmore received the B.Sc degree in Electrical Engineering (with distinction and winning the gold medal) in 2002 and the M.Sc Degree in Electrical Engineering in 2005 both from the University of Manitoba, Winnipeg, Canada where he is currently working towards the Ph.D Degree in Electrical Engineering. His current research interests are in the areas of GPR, signal processing, computational electromagnetics and inverse problems.



Walid Chamma was born in Saida, Lebanon, received the B.E. degree in electrical engineering from the American University of Beirut (AUB), Lebanon, in 1984, and the M. Sc. and Ph.D. degrees in electrical engineering from the University of Manitoba, Winnipeg, MB, Canada, in 1988 and 1993, respectively. From 1993-1998 he worked as a Research Engineer in the Antennas and Electromagnetic Group, InfoMagnetics Technologies (IMT) Corporation, Winnipeg, MB, Canada, where he participated in the design of several low-profile antennas for mobile satellite (MSAT) communications, as well as the development of a general-purpose finite-difference time-domain (FDTD) code for solving electromagnetic problems. In 1999, he joined the Radar Electronic Warfare (REW) section at Defence R&D Canada – Ottawa, as a Defence Scientist. His primary research interest is in applied electromagnetics, antenna design and new concepts in radar applications.

Improved Smart Antenna Design Using Displaced Sensor Array Configuration

Raed M. Shubair

Communication Engineering Department
Etisalat University College, P.O.Box 573, Sharjah, UAE
Tel: + 971 6 5611333, Fax: + 971 6 5611789
E-mail: rshubair@ece.ac.ae

Abstract—In this paper we propose a new sensor array configuration for improved smart antenna design. The new configuration involves two parallelly-displaced sensor arrays in the vertical plane. The proposed sensor array configuration avoids the problem of spatial aliasing encountered in largely spaced sensor arrays and reduces the effects of inter-element mutual coupling for closely spaced arrays. Moreover, the proposed sensor array configuration allows for doubling the number of array elements and, hence, increasing the system capacity, without significantly increasing the array aperture. This allows for a more accurate beam pattern to be generated especially in a radio environment with a large number of interference signals. Numerical results are presented to demonstrate the improved performance of direction-of-arrival estimation and adaptive beamforming algorithms when the proposed array configuration is used.

Index Terms—Smart antennas, adaptive array processing, direction-of-arrival estimation, adaptive beamforming.

I. INTRODUCTION

The main impairments in wireless communication are multipath fading, co-channel interference, and delay spread. Smart antenna systems overcome these impairments providing a wider coverage and a greater capacity. This promising technology has been incorporated in 3G and 4G wireless systems allowing for high data rate applications [1], [2].

A smart antenna system at the base station of a cellular mobile system is depicted in Fig. 1. It consists of a uniform linear antenna array for which the currents are adjusted by a set of complex weights using an adaptive beamforming algorithm. The adaptive beamforming algorithm optimizes the array output beam pattern such that maximum radiated power is produced in the directions of desired mobile users and deep nulls are generated in the directions of undesired signals representing co-channel interference from mobile users in adjacent cells [1]-[4]. Prior to adaptive beamforming, the directions of users and interferers must be obtained using a direction-of-arrival estimation algorithm [5], [6], shown in Fig. 1.

Most smart antenna systems utilize a uniform linear array (ULA) of N elements that are spaced apart by half-wavelength ($d = \lambda/2$). The inter-element spacing in a ULA is chosen to be $\lambda/2$ in order to reduce mutual coupling effects which deteriorate the performance of the direction-of-arrival estimation and adaptive beamforming algorithms as demonstrated in [2], [6]. If the inter-element spacing is chosen to be smaller than $\lambda/2$ the mutual coupling effects cannot be ignored and the beamforming algorithm fails to produce the actual beam pattern. On the other hand, increasing the inter-element spacing beyond $\lambda/2$ results in spatial aliasing which takes the form of unwanted peaks in the output beam pattern. It is therefore concluded that $d = \lambda/2$ represents the optimum value for the inter-element spacing in a ULA.

Due to practical considerations it is desirable to design smart antenna systems with smaller size. This can be done by employing a ULA with smaller aperture. Since the inter-element spacing in a ULA is maintained to $\lambda/2$ the array aperture can be reduced by decreasing the number of antennas in the array. This will, however, limit the array capability of handling more desired and interfering signals resulting in a reduction in the system capacity.

It is therefore desirable to design a smart antenna system which can handle more signals without increasing the array aperture significantly. This paper presents a new array configuration which consists of two parallelly-displaced arrays aligned in the vertical plane. The proposed array configuration has several advantages. First, it maintains almost the same radiation aperture as the conventional uniform linear array yet it can handle more signals from users and interferers. Second, the horizontal displacement between the two arrays in the proposed array configuration allows for resolving correlated signals encountered in multipath propagation environment without having to apply spatial smoothing techniques [5]. Moreover, the vertical displacement between the arrays allows for resolving signals arriving at grazing incidence (endfire direction) in the vertical plane.

The paper is organized as follows. Section II develops the signal model for the proposed array configuration. Sections III and IV present the theory of the direction-of-arrival estimation and adaptive beamforming algorithms, respectively. Section V presents results that demonstrate the improved performance of

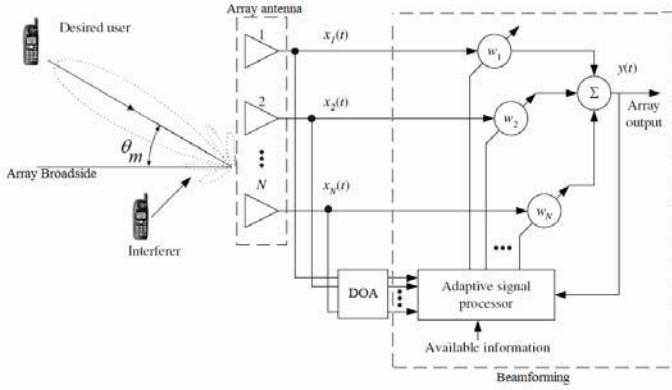


Fig. 1. A functional block diagram of a smart antenna system.

the smart antenna system employing the proposed array configuration when compared to the conventional ULA. Finally, conclusions are given in Section VI.

II. SIGNAL MODEL

Consider two parallel uniform linear arrays displaced by a horizontal distance $d = \lambda/4$ and vertical separation $s = \lambda/2$, as shown in Fig. 2. Each array consists of N linear equispaced omni-directional sensors with inter-element spacing $d = \lambda/2$ receiving M narrowband signals $s_m(t)$ incident with azimuth angles of arrival $\theta_m, 1 \leq m \leq M$. The two arrays are assumed to be located parallel to the x -axis and the azimuth angle θ_m is measured with respect to the z -axis. Following this coordinate system, the received data vector $\mathbf{x}(t)$ is given by

$$\mathbf{x}(t) = \sum_{m=1}^M [\mathbf{a}_1(\theta_m) + \mathbf{a}_2(\theta_m)] s_m(t) + \mathbf{n}(t) \quad (1)$$

where $\mathbf{n}(t)$ is a noise vector modeled as temporally white and zero-mean complex Gaussian process, $\mathbf{a}_1(\theta_m)$ and $\mathbf{a}_2(\theta_m)$ are the steering (or response) vectors for the two parallel arrays, corresponding to the DOA of the m^{th} signal. The steering vectors for the two subarrays are defined as

$$\mathbf{a}_1(\theta_m) = \left[e^{-j(n-1)2\pi\left(\frac{d}{\lambda}\right)\sin\theta_m} \right]^T, \quad 1 \leq n \leq N \quad (2)$$

$$\mathbf{a}_2(\theta_m) = \mathbf{a}_1(\theta_m) \cdot e^{-j2\pi\left(\frac{\Delta}{\lambda}\right)\sin\theta_m} \cdot e^{-j2\pi\left(\frac{s}{\lambda}\right)\cos\theta_m} \quad (3)$$

where $[\cdot]^T$ is the transpose operator, λ is the wavelength of the incident signals, and Δ is the horizontal displacement between the two arrays and is equal to $\lambda/4$ as illustrated in Fig. 2. The combination of all possible steering vectors forms the array manifold (or steering vector) matrices \mathbf{A}_1 and \mathbf{A}_2 . The received signal vector $\mathbf{x}(t)$ of (1) can then be re-written as

$$\mathbf{x}(t) = [\mathbf{A}_1 + \mathbf{A}_2] s(t) + \mathbf{n}(t) = \mathbf{A}s(t) + \mathbf{n}(t) \quad (4)$$

where the overall array manifold matrix $\mathbf{A} = \mathbf{A}_1 + \mathbf{A}_2$.

III. DIRECTION-OF-ARRIVAL ESTIMATION

A common direction-of-arrival estimation algorithm is MUSIC (Multiple Signal Classification) [5]. It starts by applying temporal averaging over K snapshots (or samples) taken from the signals incident on the sensor array. This averaging process leads to forming a spatial correlation (or covariance) matrix \mathbf{R} defined as

$$\mathbf{R} = \frac{1}{K} \sum_{t=1}^K \mathbf{x}(t)\mathbf{x}(t)^H \quad (5)$$

where $[\cdot]^H$ denotes the Hermitian operator. Substituting $\mathbf{x}(t)$ from (4) into (5) results in

$$\mathbf{R} = \frac{1}{K} \sum_{t=1}^K \mathbf{A}s(t)s(t)^H \mathbf{A}^H + \mathbf{n}(t) \mathbf{n}(t)^H \quad (6)$$

which can be expressed as

$$\mathbf{R} = \mathbf{A}\mathbf{R}_{ss}\mathbf{A}^H + \sigma_n^2 \mathbf{I} \quad (7)$$

where \mathbf{R}_{ss} is the signal covariance matrix, σ_n^2 is the noise variance, and \mathbf{I} is an identity matrix of size $N \times N$.

It can be shown [6] that the covariance matrix \mathbf{R} has M signal eigenvalues with corresponding eigenvectors $\mathbf{e}_1, \mathbf{e}_2, \dots, \mathbf{e}_M$. The remaining $N - M$ eigenvalues of the covariance matrix \mathbf{R} represent noise eigenvalues with corresponding eigenvectors $\mathbf{e}_{M+1}, \mathbf{e}_{M+2}, \dots, \mathbf{e}_N$. We form the signal subspace matrix \mathbf{E}_s for which the columns are the M signal eigenvectors of the covariance matrix \mathbf{R} , i.e., $\mathbf{E}_s = [\mathbf{e}_1 \mathbf{e}_2 \dots \mathbf{e}_M]^T$. Similarly, we form the noise subspace matrix \mathbf{E}_n for which the columns are the remaining $N - M$ noise eigenvectors of the covariance matrix \mathbf{R} , i.e., $\mathbf{E}_n = [\mathbf{e}_{M+1} \mathbf{e}_{M+2} \dots \mathbf{e}_N]^T$. The normalized MUSIC angular spectrum is then given by [1],

$$P(\theta) = \frac{\mathbf{A}^H \mathbf{A}}{\mathbf{A}^H \mathbf{E}_n \mathbf{E}_n^H \mathbf{A}} \quad (8)$$

By examining the denominator in (8), it is evident that peaks in the MUSIC angular spectrum occur whenever the overall array manifold (or steering vector) matrix \mathbf{A} is orthogonal to the noise subspace matrix \mathbf{E}_n . These angles θ at which the peaks occur define the directions-of-arrival of the signals impinging on the sensor array. The number of signals that can be detected is restricted by the number of elements in the sensor array. In [5] it was verified that an N -element sensor array can detect up to $N - 1$ uncorrelated signals. This number reduces to $N/2$ signals if they are correlated. A comprehensive performance evaluation of the MUSIC algorithm for DOA estimation can be found in [6] and [7].

IV. ADAPTIVE BEAMFORMING

An adaptive beamformer, shown in Fig. 3, consists of multiple antennas; complex weights, the function of which is to amplify (or attenuate) and delay the signals from each antenna element; and a summer to add all of the processed signals, in order to tune out the signals not of interest, while enhancing the signal of interest. Hence, beamforming is

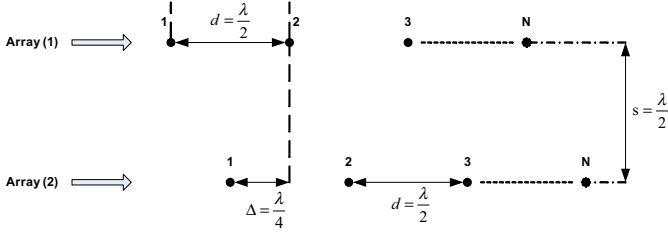


Fig. 2. Proposed array configuration consists of two parallelly-displaced arrays in the vertical plane displaced horizontally by a distance $\Delta = \lambda/4$ and separated vertically by a distance $s = \lambda/2$.

sometimes referred to as spatial filtering, since some incoming signals from certain spatial directions are filtered out, while others are amplified. The output response of the uniform linear array shown in (3) is given by

$$y(n) = \mathbf{w}^H \mathbf{x}(n), \quad (9)$$

where \mathbf{w} is the array weights vector and \mathbf{x} is the received signal vector given in (4).

The array weights vector \mathbf{w} in (9) are obtained using an adaptive beamforming algorithm. Adaptive beamforming algorithms are classified as either DOA-based, temporal-reference-based, or signal-structure-based. In DOA-based beamforming, the direction-of-arrival algorithm passes the DOA information to the beamformer, as illustrated in Fig. 1. The beamforming algorithm is used to design a radiation pattern with the main beam directed towards the signal of interest, and with nulls in the directions of the interferers.

On the other hand, temporal-reference beamformers use a known training sequence to adjust the weights, and to form a radiation pattern with a maximum towards the signal of interest and nulls towards the signals not of interest. Specifically, if $d(n)$ denotes the sequence of reference or training symbols known a priori at the receiver at time n , an error, $\epsilon(n)$ is formed as

$$\epsilon(n) = d(n) - \mathbf{w}^H \mathbf{x}(n). \quad (10)$$

This error signal ϵ is used by the beamformer to adaptively adjust the complex weights vector \mathbf{w} so that the mean-squared error (MSE) is minimized. The choice of weights that minimize the MSE is such that the radiation pattern has a beam in the direction of the source that is transmitting the reference signal, and that there are nulls in the radiation pattern in the directions of the interferers. Once the beamformer has locked onto the reference signal, then the complex weights are maintained as fixed, and transmission of the data packet begins. The array weights vector using the Least Mean Squares (LMS) algorithm can be expressed as [7],

$$\mathbf{w}(n+1) = \mathbf{w}(n) + \mu \mathbf{x}(n) \epsilon^*(n) \quad (11)$$

where $\mathbf{w}(n+1)$ denotes the weights vector to be computed at iteration $n+1$ and μ is the LMS step size which is related to the rate of convergence in other words, how fast the LMS algorithm reaches steady state. The smaller the step size the longer it takes the LMS algorithm to converge. This means that a longer reference or training sequence is needed, which

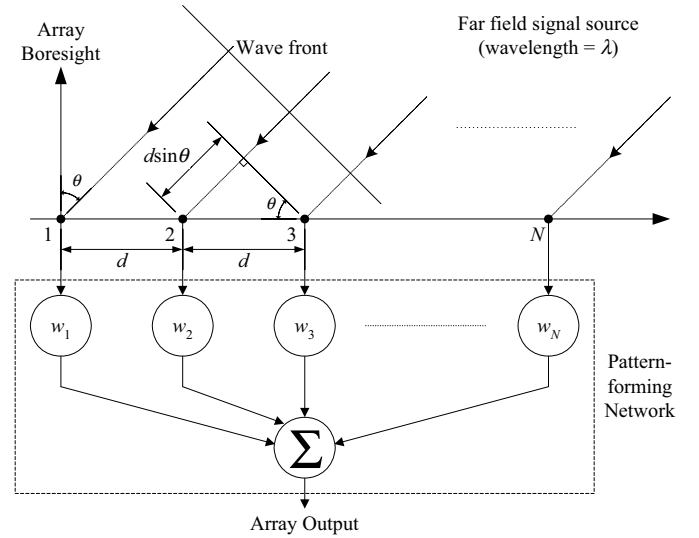


Fig. 3. Top view of a smart antenna system utilizing a uniform linear array (ULA) of N sensors.

would reduce the payload and, hence, the bandwidth available for transmitting data. In order to ensure the stability and convergence of the algorithm, the adaptive step size should be chosen within the range specified as

$$0 < \mu < \lambda_{\max}^{-1} \quad (12)$$

where λ is the maximum eigenvalue of the input covariance matrix \mathbf{R} obtained in (7).

V. RESULTS AND DISCUSSION

We have obtained the results for MUSIC direction-of-arrival estimation and LMS adaptive beamforming algorithms using both the conventional uniform linear array configuration with $N = 4$ elements in the array, and the proposed two parallelly-displaced array configuration with $N = 4$ elements in each array so that total number of elements used is $2N = 8$. Inter-element spacing of $d = \lambda/2$ is maintained in both configurations.

Simulation results for the MUSIC direction-of-arrival estimation algorithm are presented in Figs. 4 and 5. We have assumed a signal-to-noise ratio $SNR = 20$ dB and the number of snapshots $K = 1000$. The MUSIC algorithm is used to detect two incoming signals arriving at incidence angles $\theta_{m=1} = -60^\circ$ and $\theta_{m=2} = 60^\circ$. Figs. 4 and 5 show the MUSIC angular spectrum for the conventional uniform linear array configuration and proposed parallelly-displaced array configuration, respectively. It is evident from Fig. 5 that using the proposed array configuration results in a MUSIC spectrum with sharper peaks and lower noise floor. Hence, the MUSIC algorithm can better resolve incoming signals when the proposed array configuration is used.

Simulation results for the LMS adaptive beamforming algorithm are presented in Fig. 6. In this case, both the desired and interfering signals take the form of a simple complex sinusoidal-phase modulated signal. By doing so it can be shown in the simulations how interfering signals of the same

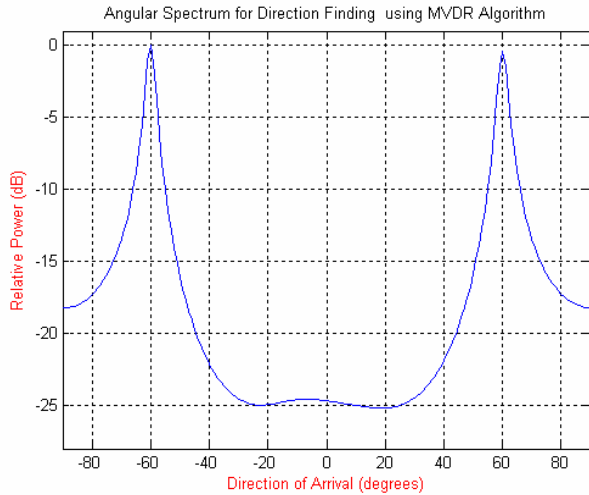


Fig. 4. MUSIC angular spectrum using conventional uniform linear array configuration with $N = 4$.

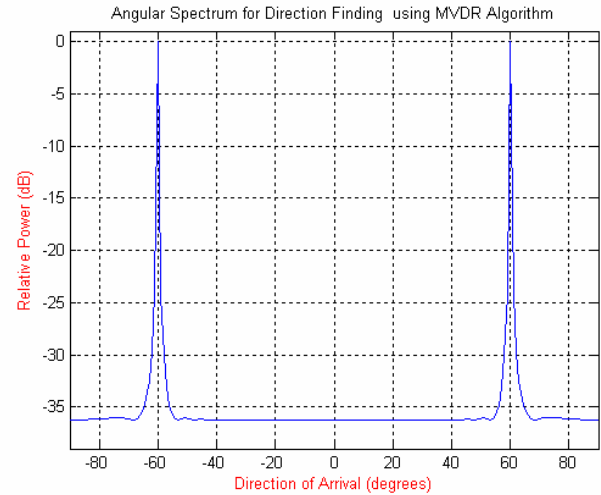


Fig. 5. MUSIC angular spectrum using proposed two parallel-displaced array configuration with $2N = 8$.

frequency as the desired signal can be separated to achieve rejection of co-channel interference. In the example provided here, the desired signal arrives at an angle $\theta_S = 20^\circ$ and interference signal arrives at an angle $\theta_I = -40^\circ$. The signal-to-noise ratio $SNR = 20$ dB and signal-to-interference ratio $SIR = -10$ dB. The LMS adaptive step size is $\mu = 0.001$ and the number of iterations is 1000. Fig. 6 shows the LMS beam pattern using both conventional and proposed array configurations. It is evident from Fig. 6 that using the proposed array configuration (solid line), the LMS beamformer is able to iteratively update the array weights to force a deep null in the direction of the interference signal $\theta_I = -40^\circ$. The null is -60 dB deep below the maximum. The proposed array configuration (solid line in Fig. 6) also allows the LMS beamformer to produce a maximum in the right direction toward the desired signal at $\theta_S = 20^\circ$. Hence, the performance of the LMS beamformer is superior when the proposed parallel-displaced array configuration is used.

VI. CONCLUSIONS

We have proposed a new sensor array configuration which improves the performance of smart antenna systems. The proposed configuration consists of two parallel-displaced sensor arrays aligned in the vertical plane. Performance results for both MUSIC direction-of-arrival estimation and LMS adaptive beamforming algorithms show significant improvement when the proposed array configuration is used. Besides the improved performance of the direction-of-arrival and adaptive beamforming algorithms, the proposed array configuration has several other advantages. First, it maintains almost the same radiation aperture as the conventional uniform linear array yet it can handle more signals from users and interferers because it has more array sensors when compared to the conventional uniform linear array. Second, the horizontal displacement in the proposed configuration between the two parallel arrays allows for resolving correlated signals encountered in multipath propagation environment without having to apply

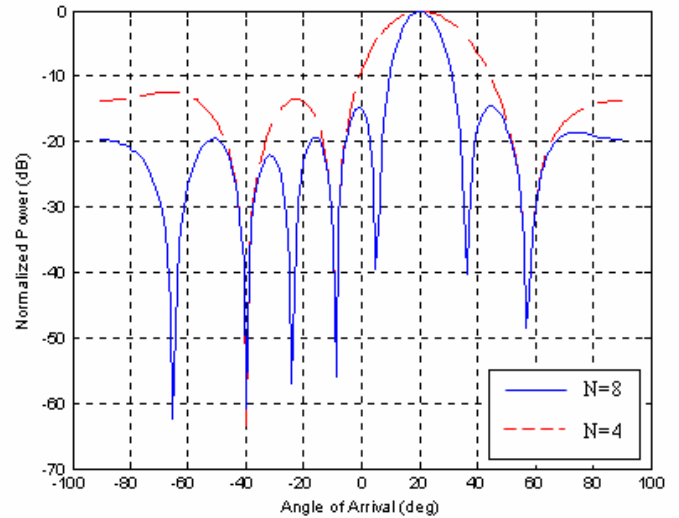


Fig. 6. LMS beam pattern using conventional uniform linear array configuration with $N = 4$ (dashed line), and proposed two parallel-displaced array configuration with $2N = 8$ (solid line).

spatial smoothing techniques. Moreover, the vertical separation between the two parallel arrays allows for resolving signals arriving at grazing incidence (endfire direction) in the vertical plane.

REFERENCES

- [1] R. M. Shubair and A. Al-Merri, "Convergence study of adaptive beamforming algorithms for spatial interference rejection," *Proc. of Int. Symp. Antenna Technology & Applied Electromagnetics (ANTEM'05)*, Saint-Malo, France, June 15-17, 2005.
- [2] R. M. Shubair and W. Al-Jessmi, "Performance analysis of SMI adaptive beamforming arrays for smart antenna systems," *Proc. of IEEE Int. Symp. Antennas & Propagation (AP-S'05)*, Washington, D.C., USA, pp. 311-314, July 3-8, 2005.
- [3] R. M. Shubair, A. Al-Merri, and W. Al-Jessmi, "Improved adaptive beamforming using a hybrid LMS/SMI approach," *Proc. of IEEE Int. Conf. Wireless and Optical Communications Networks (WOCN'05)*, Dubai, UAE, pp. 603-606, March 6-8, 2005.

- [4] R. M. Shubair and A. Al-Merri, "Robust algorithms for direction finding and adaptive beamforming performance and optimization," *Proc. of IEEE Int. Midwest Symp. Circuits & Systems (MWSCAS'04)*, Hiroshima, Japan, pp. 589–592, July 25–28, 2004.
- [5] E. M. Al-Ardi, R. M. Shubair, and M. E. Al-Mualla, "Computationally efficient DOA estimation in a multipath environment using covariance differencing and iterative spatial smoothing," *Proc. of IEEE Int. Symp. Circuits & Systems (ISCAS'05)*, Kobe, Japan, pp. 3805–3808, May 23–26, 2005.
- [6] E. M. Al-Ardi, R. M. Shubair, and M. E. Al-Mualla, "Investigation of high-resolution DOA estimation algorithms for optimal performance of smart antenna systems," *Proc. of 4th IEE Int. Conf. 3G Mobile Communications (3G'03)*, London, UK, pp. 460–464, June 5–7, 2003.
- [7] E. M. Al-Ardi, R. M. Shubair, and M. E. Al-Mualla, "Performance evaluation of direction finding algorithms for adaptive antenna arrays," *Proc. of 10th IEEE Int. Conf. Electronics, Circuits & Systems (ICECS'03)*, Sharjah, United Arab Emirates, Vol. 2, pp. 735–738, December 14–17, 2003.
- [8] S. Haykin, *Adaptive Filter Theory*. Prentice-Hall, 4th Ed., 2002.



Raed M. Shubair received his B.A.Sc. degree from Kuwait University, Kuwait, in June 1989 and his Ph.D. degree from the University of Waterloo, Canada, in February 1993, both in Electrical Engineering. From March 1993 to August 1993 he was a Postdoctoral Fellow at the Department of Electrical and Computer Engineering, University of Waterloo, Canada. In September 1993 he joined Etisalat University College, UAE, where he is currently an Associate Professor at the Communication Engineering Department and leader of the Communication &

Information Systems (CIS) research group. His current research interests include adaptive array processing, smart antennas and MIMO systems, as well as applied and computational electromagnetic modeling of RF and microwave circuits for wireless communications. Dr. Shubair has authored over 80 papers in refereed technical journals and international conferences. He has been a member of the technical program, organizing, and steering committees of numerous international conferences and workshops. Dr. Shubair organized and chaired a number of technical sessions in international conferences including IEEE Symposium on Antenna and Propagation (AP-S), IEEE Symposium on Electronics, Circuits and Systems (ICECS), Progress in Electromagnetics Research Symposium (PIERS), and Applied Computational Electromagnetics Symposium (ACES). Dr. Shubair is a Senior Member of the IEEE. He was also elected to the MIT Electromagnetics Academy in 2001. He has supervised a large number of research projects including *Adaptive Beamforming for Next-Generation Wireless Communications*, recipient of the 2004 IEE Award, as well as *Design of Optimum SMI Beamformers for Spatial Interference Rejection*, recipient of the 2005 IEE Award. Dr. Shubair is a founding member of the IEEE UAE Signal Processing and Communications Joint Societies Chapter. He is listed in *Who's Who in Electromagnetics* and in several editions of *Who's Who in Science and Engineering*.

Development of Wideband L-Probe Coupled Patch Antenna

Kwai Man Luk¹, Kai Fong Lee², and Hau Wah Lai¹

¹Department of Electronic Engineering, City University of Hong Kong

²School of Engineering, The University of Mississippi

Abstract — The patch antenna fed by an L-shaped probe was proposed in 1998. This feeding method, and its modified version, the meandering strip, has led to the development of a new class of wideband patch antennas which can be operated in linear, circular or dual polarization with excellent performance characteristics. L-probe coupled patch antennas are simple in structure and low in material and production costs. Moreover, it can be designed with dual wideband performance which is very attractive for modern mobile communications. This paper presents a review of the general designs for linearly and circularly polarized L-probe patch antennas. Comparisons between measured and simulated results are presented. Methods for gain enhancement and cross polarization suppression are also introduced. The designs and performances of two dual-band wideband L-probe fed patch antennas are also described.

I. INTRODUCTION

In the last two decades or so, many methods have been developed to broaden the bandwidth of microstrip patch antennas. One way is to use the L-probe coupled feeding method. Since its introduction some seven years ago, a number of developments have taken place, including the designs for dual-band, dual-polarized and circularly polarized wideband patch antennas. The objective of this paper is to give an account of these developments.

The paper begins with a description of the context in which the method was developed, followed by a summary of the characteristics of the basic L-probe fed patch antenna and the characteristics of a twin L-probe fed patch antenna. It proceeds to describe the more recent developments, including a derivation of the L-probe, called the meander or M-strip feeding method. The design of a dual-band dual-polarized antenna array is then presented. The paper ends with some concluding remarks.

II. BRIEF REVIEW OF BANDWIDTH BROADENING TECHNIQUES OF MICROSTRIP PATCH ANTENNAS

The basic structure of a microstrip patch antenna consists of an area of metallization supported above a

ground plane and fed against the ground at an appropriate location (Figure 1). The region between the metallic patch and the ground plane forms a resonant cavity. The patch geometry can take on a variety of shapes. Two common feeds are the coaxial probe and the microstrip line (Figure 2). The bandwidth of a patch antenna is governed by the impedance bandwidth, commonly defined as the range of frequencies for which the standing wave ratio (SWR) is less than or equal to 2. In general, for most frequencies of interest, the bandwidth increases with substrate thickness and also increases as the relative permittivity decreases. However, one cannot obtain wide bandwidth just by increasing the substrate thickness. For the coaxial fed case, the length of the probe is increased when the substrate thickness increases. The large inductance associated with a lengthy probe makes it impossible to match the antenna to the feedline. For the stripline fed case, the width of the line increases with substrate thickness, which increases the spurious radiation from the line and alters the resonant frequency of the antenna. Also, there is a lower bound on the value of the relative permittivity, namely, unity. The result is that narrow bandwidth (< 5%) is the major problem associated with the basic form of microstrip patch antennas fed by a coaxial probe or a microstrip line.

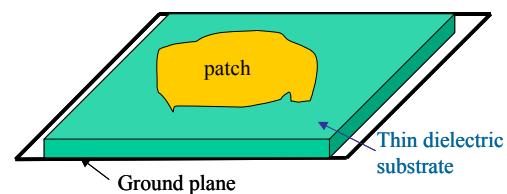


Fig. 1. Basic structure of a microstrip patch antenna.

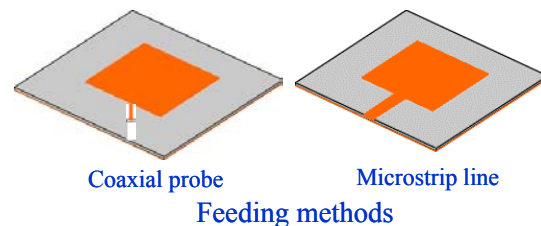


Fig. 2. Patch shapes and two common feeding methods.

In the last two decades or so, a number of bandwidth broadening techniques of microstrip antennas have been developed. Wideband designs use one or more of the following: (1) introduction of an additional resonance to the main patch resonance so that the overall response is broadband; (2) low permittivity substrates; (3) thick substrates and a scheme to overcome the mismatch problem.

Figure 3 shows three wideband coaxially fed patches. In Figures 3(a) and 3(b), parasitic patches are added either in the same layer (coplanar) or in another layer (stacked). The parasitic patches introduce an additional resonance. The coplanar design seldom exceeds 15% bandwidth, and it has the disadvantage of increasing the lateral size of the antenna [1]. The stacked geometry can achieve about 20% bandwidth [2]. Although it does not increase the lateral size, it introduces another layer.

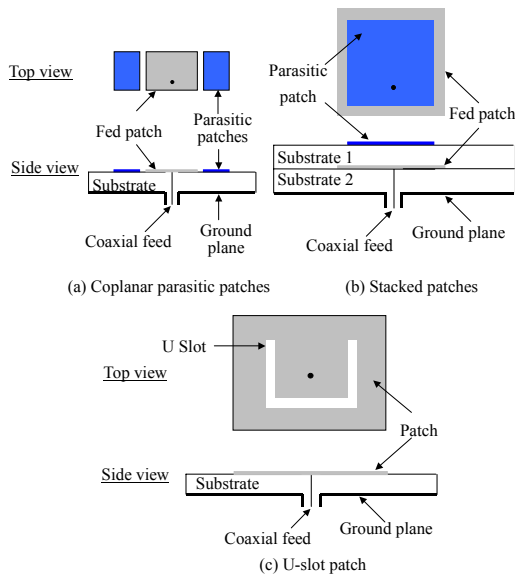


Fig. 3. Three broadband coaxial fed microstrip patch antennas.

Figure 3(c) shows a single-layer, single patch wideband microstrip antenna. In this design, a U-shaped slot is cut in the patch [3, 4]. The U-slot introduces a second resonance and provides a capacitance which tends to cancel the probe inductance, allowing the use of thick substrate. With a foam substrate thickness of about 0.08 free space wavelength, this antenna easily achieves 30% bandwidth. The main disadvantage is that the cross polarization radiation in the H-plane is quite high.

Another wideband design is feeding the patch by a microstrip line through an aperture (slot) [5] (Figure 4a). If the resonant frequency of the aperture (slot) is near the resonance of the patch, the effective bandwidth will be increased. Bandwidth of 10% can be

achieved using a single patch. If a stacked patch geometry is used [6] (Figure 4b), 50% bandwidth has been reported. However, there is significant backlobe radiation due to the resonant slot.

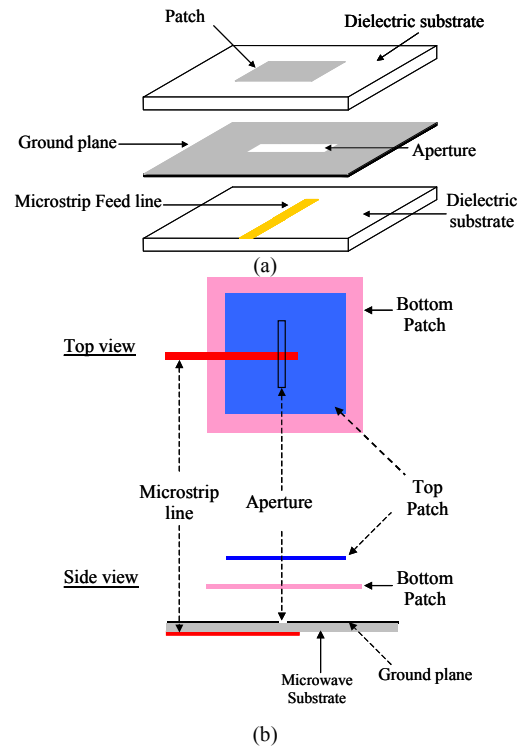


Fig. 4. (a) Aperture coupled patch, (b) Aperture coupled stacked patches.

III. THE L-SHAPED PROBE FEEDING MECHANISM

Shortly after the publication of the first paper on the U-slot single layer single patch wideband patch antenna, another wideband single layer single patch antenna was introduced. This design achieves wide band operation using an L-shaped probe feeding method. The geometry is shown in Figure 5 and a prototype of this antenna is shown in Figure 6. This design uses low permittivity substrate (air or foam) of thickness about 0.1 free space wavelength. The feed is a modified version of the coaxial probe. Instead of the center conductor extending vertically to the patch and connected to it, a portion of it is bent in the horizontal direction. The horizontal arm of the probe is approximately a quarter of a wavelength long. It provides a capacitance to counteract the inductance due to the vertical part. This design has only one patch and one layer but it achieves 30% or more bandwidth. This feeding method for patch antennas was first discussed in [7, 8].

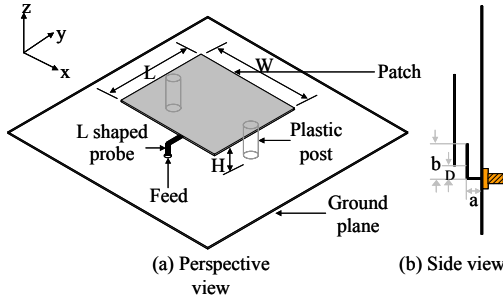


Fig. 5. Geometry of the L-probe coupled patch antenna.



Fig. 6. Prototype of the L-probe coupled patch antenna.

To illustrate the characteristics of the basic L-probe proximity coupled patch antenna, consider a design with the dimensions given in the caption of Figure 7.

Figure 7 shows the simulated gain and SWR versus frequency for this antenna. The simulated radiation patterns are shown in Figure 8. It is seen that this antenna has an impedance bandwidth of 36%, an average gain of about 8.5 dB across the matching bandwidth, with stable broadside patterns. However, the cross polarization level at the edges of the band is high, due to radiation from the vertical arm of the probe. These characteristics are similar to the U-slot patch antenna.

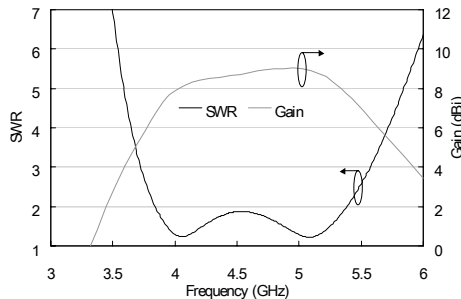


Fig. 7. Simulated SWR and gain versus frequency of the L-probe coupled antenna of Figure 6 with the following dimensions: $W=30$ mm, $L=25$ mm, $H=6.6$ mm, $a=5.5$ mm, $b=10.5$ mm, $d=2$ mm.

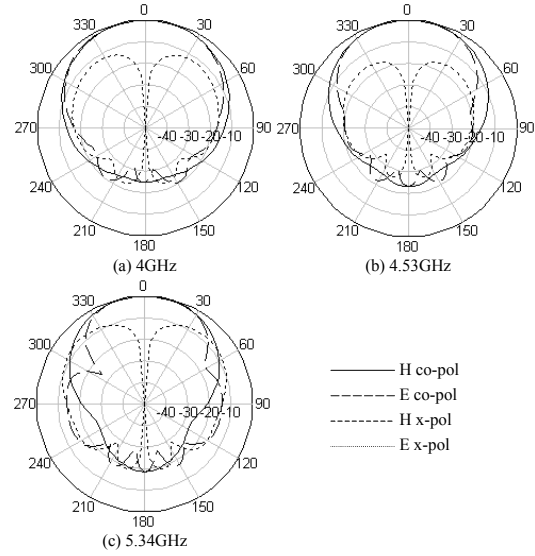


Fig. 8. Simulated radiation patterns of the L-probe coupled antenna with the dimensions shown in the caption of Figure 7.

In what follows, we describe various recent developments which show that the L-probe feeding method can be used to achieve a variety of performance characteristics.

IV. TWIN-L-PROBE FEEDING MECHANISM

By feeding the patch with twin L probes, the gain of the antenna is enhanced, accompanied by a reduction in the cross polarization radiation. The geometry is shown in Figure 9 [9]. The separation of the two L-probes is about half a wavelength and the width W of the patch is about 0.7 wavelength. The measured SWR and gain of this antenna are shown in Figure 10. The case of a single L-probe is also included. It is seen that the bandwidth for the twin L-probe is slightly smaller than the single L-probe, but the gain of the antenna is about 10 dBi for most of the passband. The maximum gain of the single L-probe is about 8 dB but it drops off rapidly in the upper half of the pass band. Figure 11 shows the measured radiation patterns. It is seen that the beamwidth is narrower than the single L-probe case. The cross polarization levels at the edges of the pass band are significantly reduced.

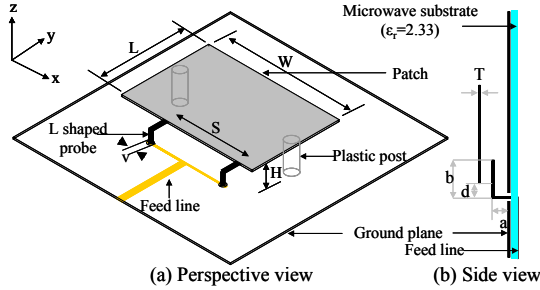


Fig. 9. Geometry of the twin-L-probe fed patch antenna.

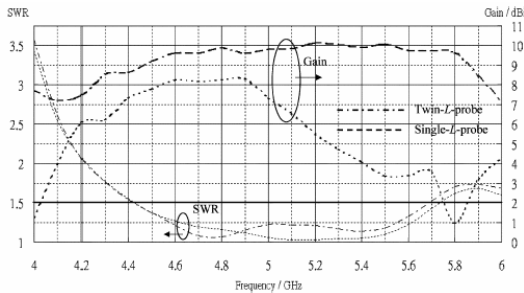


Fig. 10. Measured SWR and gain of the twin-L-probe coupled patch of Figure 9 with the following dimensions: $L=22$ (0.367λ), $H=6$ (0.1λ), $W=44$ (0.733λ), $T=0.3$ (0.005λ), $a=4.5$ (0.075λ), $b=12$ (0.2λ), $v=2$ (0.033λ), $d=0$ (0λ), $s=28.6$ (0.477λ). The case of single L-probe coupled patch is also shown for comparison. (From Mak et. al. [9], c 2005 IEEE)

V. WIDEBAND DUAL FREQUENCY L-PROBE FED PATCH ANTENNA

There are many applications in wireless communications that involve two or more distinct frequencies. It is sometimes possible that a broadband microstrip antenna can cover the frequencies of interest. However, the disadvantage of using a broadband antenna is that it also receives undesired frequencies unless some kind of filtering network is introduced to reject such frequencies. On the other hand, the advantage of a dual-frequency design is that it focuses only on the frequencies of interest and is thus more desirable. Dual-frequency microstrip antennas can be designed by using a single-element, stacked patches, patch with reactive loading, or patches with slots. When these are fed by the conventional coaxial probe, the resulting bandwidths are narrow. The bandwidths in the two bands can be considerably enhanced by means of L-probes. Two designs are described below.

A. Dual-Band Patch Antenna Fed by Two Separate L-Probes

One such design is shown in Figure 12 [10]. It consists of two stacked patches, with the smaller one on the top layer. Each patch is fed by a L-probe. Figure 13 shows the simulation and measurement results of the return loss and antenna gain at the lower and upper bands. It appeared that the simulation results missed two high Q resonances in the lower band and one high Q resonance in the upper hand. The impedance bandwidth is 26.6% and 42.2%, respectively, at the lower and upper bands, while the peak gains are 8.4 dBi and 8 dBi within these two bands. The simulated and measured radiation patterns at 0.89 GHz and 2.4 GHz, respectively, are shown in Figures 14 and 15, respectively. All simulations in this paper are performed with the Zeland IE3D software.

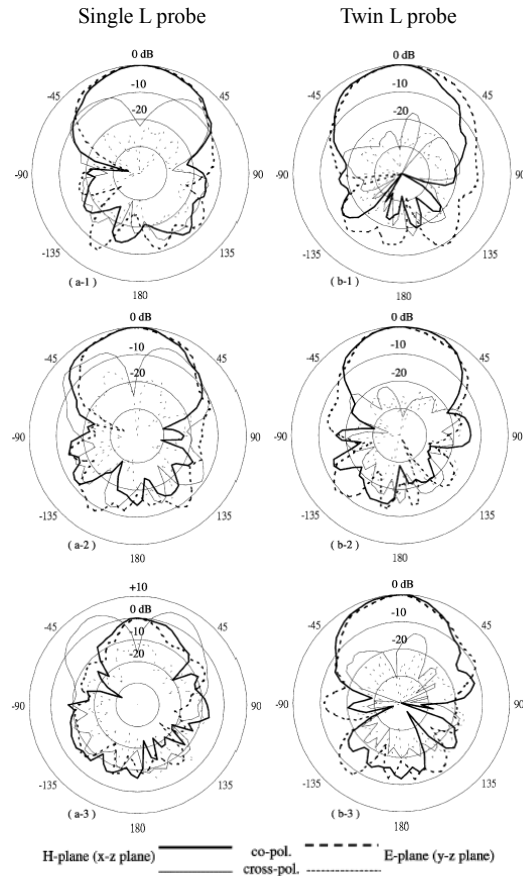


Fig. 11. Measured radiation patterns of the single L-probe and twin-L-probe coupled patch antennas. (From Mak et. al. [9], c 2005 IEEE)

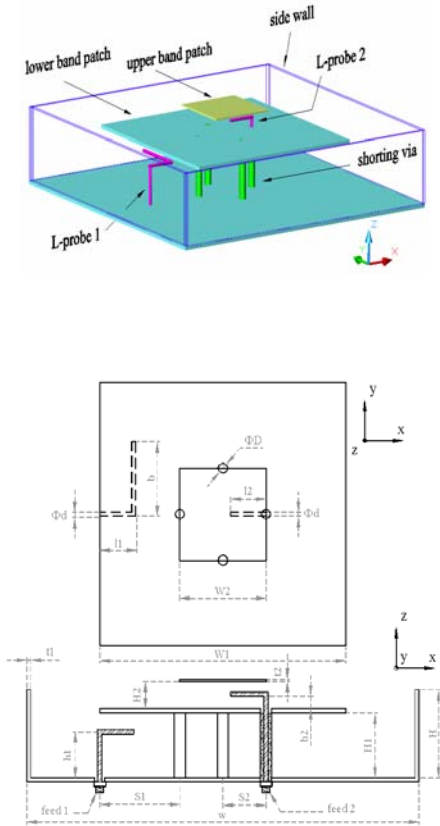
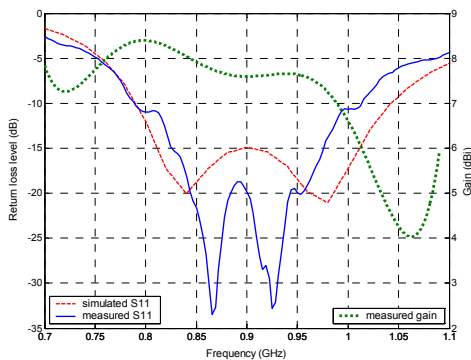
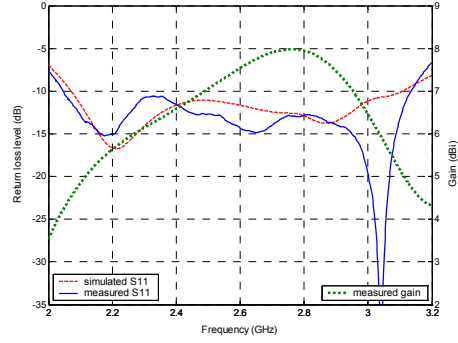


Fig. 12. Geometry of the two-layer dual-band L-probe coupled patch antenna. $W=243.6$ mm ($0.72\lambda_1$), $H=47$ mm ($0.139\lambda_1$), $W1=125.6$ mm ($0.37\lambda_1$), $H1=33$ mm ($0.098\lambda_1$), $l1=20.5$ mm ($0.061\lambda_1$), $h1=24.8$ mm ($0.074\lambda_1$), $b=33.5$ mm ($0.1\lambda_1$), $W2=44$ mm ($0.36\lambda_2$), $H2=13$ mm ($0.106\lambda_2$), $l2=19$ mm ($0.155\lambda_2$), $h2=9.5$ mm ($0.077\lambda_2$), $t1=2$ mm, $t2=1$ mm, $D=4.6$ mm, $d=2$ mm, $S1=62.8$ mm, $S2=22$ mm. (From Li et. al. [10], c 2005 IEEE)



(a) Lower band



(b) Upper band

Fig. 13. Simulated and measured return loss and gain of the antenna in Figure 12 at the lower and upper frequency bands. (From Li et. al. [10], c 2005 IEEE)

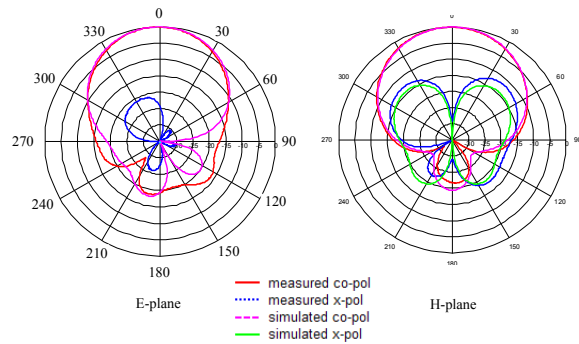


Fig. 14. Simulated and measured radiation patterns at 0.89 GHz of the antenna in Figure 12. (From Li et. al. [10], c 2005 IEEE)

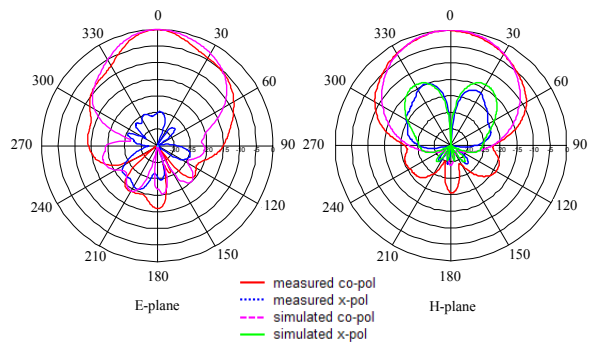


Fig. 15. Simulated and measured radiation patterns at 2.45 GHz of the antenna in Figure 13. (From Li et. al. [10], c 2005 IEEE)

B. Dual-Band Patch Antenna Fed by Two Combined L-Probes

Another design of dual-band patch antenna [11] fed by L-probes is shown in Figure 16. Instead of using two distinctly different feeds, as in the case shown in Figure 12, the two probes are combined together to form a single feed structure. Two slots are etched from the radiation edge of the lower-band patch to suppress the excitation of the TM_{20} mode that would influence the upper-band radiation pattern. The performance of the antenna is simulated by IE3D ver. 10. Figure 17 shows the simulated return loss for the antenna of Figure 16, with dimensions shown in the captions. The antenna operates at 900 MHz (λ_1 , lower-band operation) and 1.8 GHz (λ_2 , upper-band operation). The impedance bandwidth of 21% and 11% was found for the lower and upper bands, respectively. It is wide enough to cover GSM 900 and 1800 cellular phone systems. The maximum gain of 8.7 dBi was found in the upper band. The simulated radiation patterns are shown in Figures 18 and 19. The 3 dB beamwidths of lower and upper bands are 71° and 83° in the H-plane and are 51° and 57.5° in the E-plane. The cross polarizations is -10 dB and -13 dB in the lower and upper bands, respectively. The measured results agree with the simulation. Results can be found in [11].

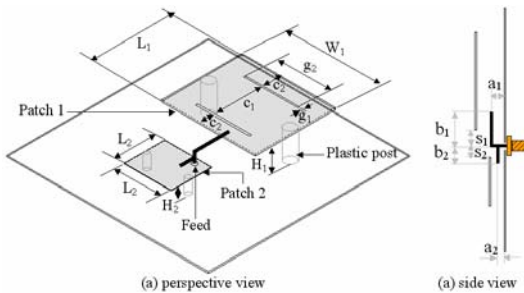


Fig. 16. Geometry of the dual-band patch antenna with combined dual L-probe feed.

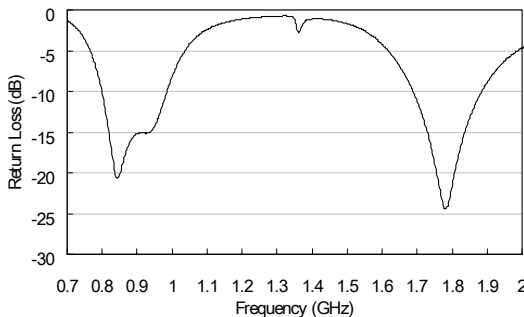


Fig. 17. Simulated return loss of the antenna shown in Figure 16 with the following dimensions: $L_1 = W_1 = 102$ mm ($0.324\lambda_1$), $H_1 = 45.5$ mm ($0.145\lambda_1$), $b_1 = 51$ mm ($0.162\lambda_1$), $a_1 = 31$ mm ($0.098\lambda_1$), $S_1 = 4$ mm ($0.0127\lambda_1$), $g_1 = 2$ mm ($0.0064\lambda_1$), $g_2 = 90$ mm ($0.286\lambda_1$), $c_2 = 25.5$

mm ($0.081\lambda_1$) $L_2 = 37$ mm ($0.22\lambda_2$), $H_2 = 24$ mm ($0.128\lambda_2$), $b_2 = 31$ mm ($0.184\lambda_2$), $a_2 = 13$ mm ($0.077\lambda_2$), $S_2 = 4$ mm ($0.0238\lambda_2$).

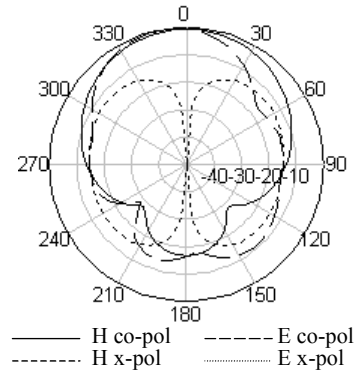


Fig. 18. Simulated radiation pattern of lower band at 953 of the antenna shown in Figure 16, with the dimensions given in the caption of Figure 17.

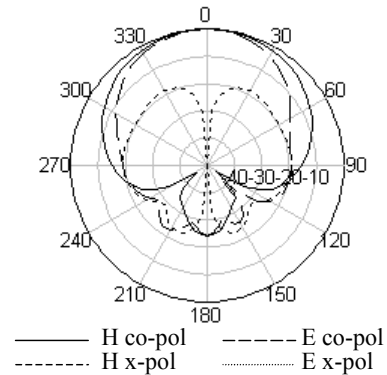


Fig. 19. Simulated radiation pattern of the higher band at 1.786 GHz of the antenna shown in Figure 16, with the dimensions given in the caption of Figure 17.

VI. MEANDERING STRIP FED PATCH ANTENNA

The L-probe patch antenna has a cross-polarization level of about -15 dBi which may be too high in some applications. Phase cancellation technique can be employed to suppress the cross-polarization as described in [12]. This method can suppress the cross-polarization effectively but it requires a wideband matching network to feed the two oppositely oriented probes which are 180 degrees out of phase with each other, thereby increasing the complexity of the antenna structure. In addition, the E-plane pattern of the L-probe patch antenna is not symmetrical with respect to the broadside direction. This may affect the performance in antenna array design.

As a modification of the L-probe patch antenna technique, a patch antenna fed by a meandering strip

has been invented recently [13]. As shown in Figure 20, the L-shaped probe is replaced by a strip feed which has a meandering form. The strip looks like a combination of one L-shaped probe and one inverted L-shaped probe. It is formed by bending a metal strip so that it has 3 portions normal to the ground plane and patch, and 2 portions parallel to the ground plane and patch. For an appropriate length of the strip, the phases of the current in the vertical portions of the strip are such that their radiations in the far-zone cancel, resulting in the suppression of cross polarization.

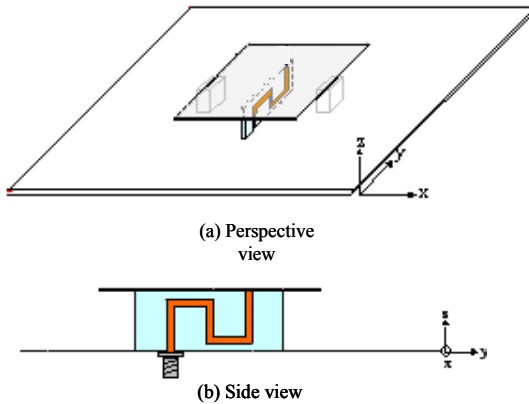


Fig. 20. Geometry of the printed meandering strip fed patch antenna.

For ease of fabrication, the meandering strip can be printed on a printed circuit board. For a typical design, the impedance bandwidth is similar to the L-probe patch antenna, while the cross-polarization is lower than -20 dBi over the operating band. Very symmetrical radiation patterns in the E-plane and H-plane are observed. Due to the suppression of cross-polarization, a higher gain of about 8.5 dBi can be achieved, which is about 1 dBi higher than the L-probe patch antenna.

It was discovered that the impedance bandwidth of the meandering strip patch antenna can be increased to over 60% with acceptable performance in other electrical parameters. This is achieved by increasing the width of the meandering strip to about 0.25λ . This antenna represents the state-of-the-art wideband patch antenna technology.

VII. CIRCULARLY POLARIZED STACKED PATCH ANTENNA FED BY A MEANDERING PROBE

Both the L-probe and the meandering strip feeding method can be used for circularly polarized patch antenna. Figure 21 shows one such design using two truncated stacked patches fed by a meandering strip.

This arrangement generates two pairs of orthogonal modes, resulting in wide impedance bandwidth (34%, $SWR < 2$) as well as wide 3 dB axial ratio bandwidth (14%). The simulated results are shown in Figure 22.

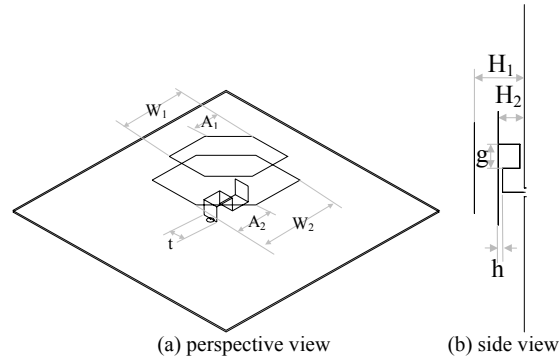


Fig. 21. Geometry of the meandering strip fed stacked patches with truncated corners for circular polarization.

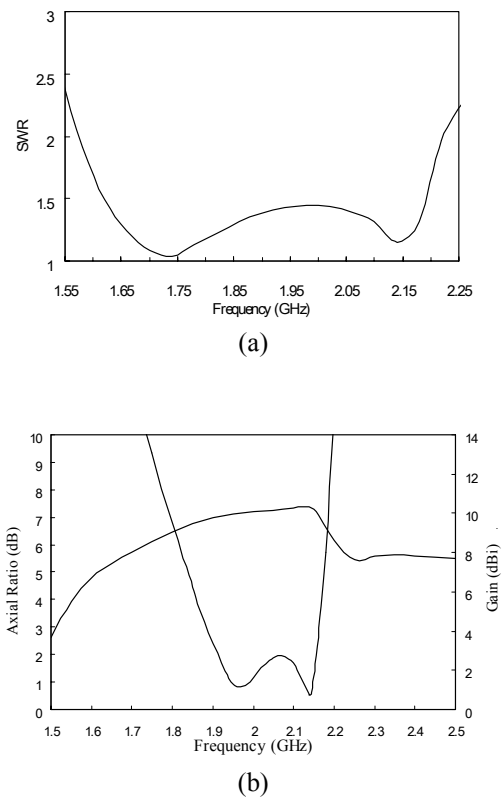


Fig. 22. (a) Simulated SWR (b) simulated AR and gain of the antenna shown in Figure 21 with the following dimensions: $W_1=56$ mm ($0.378\lambda_0$), $W_2=66$ mm ($0.445\lambda_0$), $A_1=17$ mm ($0.115\lambda_0$), $A_2=23.5$ mm ($0.159\lambda_0$), $H_1=18.5$ mm ($0.125\lambda_0$), $H_2=11.5$ mm ($0.078\lambda_0$), $t=16$ mm ($0.108\lambda_0$), $g=1.45$ mm ($0.01\lambda_0$), $h=9.3$ mm ($0.063\lambda_0$).

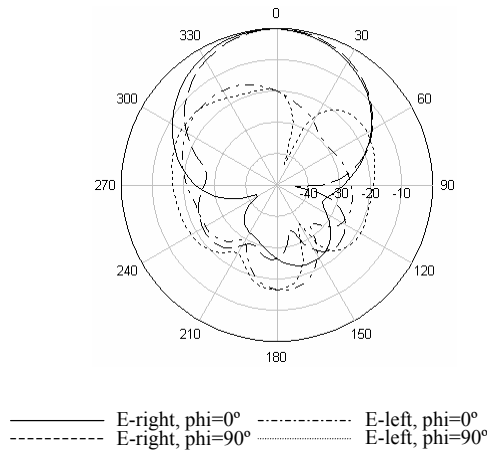


Fig. 23. Simulated radiation pattern of the higher band at 2.036 GHz of the antenna shown in Figure 21, with the dimensions given in the caption of Figure 22.

VIII. CONCLUDING REMARKS

In conclusion, a class of wideband patch antennas, in the form of L-probe and the M-strip proximity coupled patch antennas, have been described. These antennas can be designed to yield wide bandwidth, high gain, and low back radiation. They can also be designed for dual-band and/or dual-polarized applications. It is relatively simple in structure and low in production cost.

ACKNOWLEDGMENT

The authors acknowledge the contributions of the following Ph.D. students: K F Tong, C L Mak, Y X Guo, R Chair, K L Lau, H Wong, P Li, T P Wong, S L Yang.

REFERENCES

[1] W. Chen, K. F. Lee, and R. Q. Lee, "Spectral-domain moment method analysis of coplanar microstrip parasitic subarrays," *Microw. Opt. Technol. Lett.*, Vol. 6, No. 3, pp. 157-163, 1993.

[2] R. Q. Lee, K. F. Lee, and J. Bobinchak, "Characteristics of a two-layer electromagnetically coupled rectangular patch antenna," *Electron. Lett.* Vol. 23, No. 20, pp. 1070-1072, 1987.

[3] T. Huynh and K. F. Lee, "Single-layer single-patch wideband microstrip antenna," *Electron. Lett.*, Vol. 31, No. 16, pp. 1310-1312, 1995.

[4] K. F. Lee, K. M. Luk, K. F. Tong, S. M. Shum, T. Huynh and R. Q. Lee, "Experimental and simulation studies of the coaxially fed U-slot rectangular patch antenna," *IEE*

Proc.-Microw.,Antennas, Propagat., Vol. 144, pp. 354-358, 1997.

[5] D. M. Pozar, "A reciprocity method of analysis for printed slot and slot-coupled microstrip antennas," *IEEE Trans. Antennas Propagat.*, AP-34, pp. 1439-1446, 1986.

[6] S. D. Targonski, R. B. Waterhouse and D. M. Pozar, "Design of wide-band aperture-stacked patch microstrip antennas," *IEEE Trans on Antennas Propagat.*, Vol. 46, pp. 1245-1251, 1998.

[7] K. M. Luk, C. L. Mak, Y. L. Chow and K. F. Lee, "Broadband microstrip patch antenna," *Electron. Lett.*, Vol. 34, pp. 1442-1443, 1998.

[8] C. L. Mak, K. M. Luk, K. F. Lee, and Y. L. Chow, "Experimental study of a microstrip patch antenna with an L-shaped probe," *IEEE Trans. Antennas Propagat.*, AP-48, No. 5, pp. 777-783, 2000.

[9] C. L. Mak, H. Wong, and K. M. Luk, "High-gain and wide-band single-layer patch antenna for wireless communications," *IEEE Trans. Vehicular Technology*, Vol. 54, No. 1, pp. 33-40, 2005.

[10] P. Li, K. M. Luk, and K. L. Lau, "A Dual-Feed Dual-Band L-Probe Patch Antenna," *IEEE Trans on Antennas Propagat.*, Vol. 53, pp. 2321-2323, 2005.

[11] K. M. Luk, C. H. Lai, and K. F. Lee, "Wideband L-probe-feed patch antenna with dual-band operation for GSM/PCS base stations," *Electron. Lett.*, Vol. 35, pp. 1123-1124, 1999.

[12] S. H. Chiou, and J. H. Lu, "Cross-polarization level reduction of broadband triangular patch antenna with dual L-strip Lines," *Microw. Opt. Technol. Lett.*, Vol. 33, No. 4, pp. 300-303, 2002.

[13] H. W. Lai, and K. M. Luk, "Wideband patch antenna with low cross-polarisation," *Electronics Lett.*, Vol. 41, No. 6, pp. 297-298, March 2005.



Kwai-Man Luk was born and educated in Hong Kong. He received the B.Sc.(Eng.) and Ph.D. degrees in electrical engineering from The University of Hong Kong in 1981 and 1985, respectively. He joined the Department of Electronic Engineering at City University of Hong Kong in 1985 as a Lecturer. Two years later, he moved to the Department of Electronic Engineering at The Chinese University of Hong Kong where he spent four years. Professor Luk returned to the City University of Hong Kong in 1992, and he is currently a Head and Chair Professor of Electronic Engineering Department. His recent research interests include design of patch, planar and dielectric resonator antennas, microwave and antenna measurements, and

computational electromagnetics. He is the author of 1 edited book, 7 research book chapters, over 235 journal papers and 180 conference papers. He was awarded two US patent and 9 PRC patents on the design of a wideband patch antenna with an L-shaped probe recently.

Professor Luk is the General Chairman of the 2006 IEEE Region 10 Conference (TENCON) to be held in Hong Kong in October 2006. He was the Technical Program Chairperson of the Progress in Electromagnetics Research Symposium (PIERS 1997) held in Hong Kong in January 1997, and the General Vice-Chairperson of the 1997 Asia-Pacific Microwave Conference held in Hong Kong in December 1997. He has successfully supervised over 10 Ph.D. students. Most of them have achieved their distinguished careers in Hong Kong, Singapore, Japan, UK and the USA.

Professor Luk received an international best paper award, the Japan Microwave Prize, at the 1994 Asia Pacific Microwave Conference held in Chiba, Japan in December 1994. He awarded the very competitive Croucher Foundation Senior Research Fellow in Hong Kong in 2000. He received the Applied Research Excellence Award in City University of Hong Kong in 2001. Professor Luk is a Fellow of the Institute of Electrical and Electronics Engineers, Inc., a Fellow of the Chinese Institute of Electronics, PRC, a Fellow of the Institution of Electrical Engineers, UK, and a Member of the Electromagnetics Academy, USA.



Kai-Fong Lee received his B.Sc. and M.Sc. degrees from Queen's University, Canada and his Ph.D. degree from Cornell University, all in electrical engineering. In his career, Dr. Lee has held research, teaching and administrative positions at a number of institutions

in the U.S. and abroad, including University of California, San Diego, National Center for Atmospheric Research, National Oceanic and Atmospheric Administration, UCLA, NASA, the Catholic University of America, The Chinese University of Hong Kong, The University of Akron, the University of Toledo, and the University of Missouri-Columbia. He was the founding Head of the Department of Electronic Engineering at the City University of Hong Kong. He served as Chairman of the Department of Electrical Engineering at The University of Toledo and Chairman and of the Department of Electrical Engineering at the University of Missouri-Columbia. Since January 2001, he has been Dean of Engineering and Professor of Electrical Engineering at the University of Mississippi.

Professor Lee worked on plasma waves and instabilities from 1965-1980 and on antennas since 1981. His publications include a textbook (PRINCIPLES OF ANTENNA THEORY, WILEY 1984), an edited book (ADVANCES IN MICROSTRIP AND PRINTED ANTENNAS, WILEY-INTERSCIENCE 1997), ten invited book chapters on microstrip antennas, 180 Journal Articles and 137 conference papers. He is a Fellow of IEEE and a Fellow of IEE.



Hau-Wah Lai was born and educated in Hong Kong. He received the B.Eng. and Ph.D. degrees in electronic engineering from the City University of Hong Kong in 2001 and 2005, respectively.

He was a Research Assistant with the Department of Electronic Engineering, City University of Hong Kong in 2004. Since 2005, he has been a Senior Research Assistant with the Wireless Communications Research Centre in the same University, and has been responsible for antenna designs, consultations and research. He has authored over 20 technical papers in international journals and conferences. He was awarded one US patent on the design of a wideband patch antenna with a meandering strip feed recently. He is also the team leader of a project.

Doctor Lai has been listed in Marquis Who's Who in the Science and Engineering 2006/2007 and Marquis Who's Who in Asia 2006/2007 (first edition). He received the outstanding presentation award in 2002 Postgraduate Research Expo presented by the City University of Hong Kong. His research interests include the design of microstrip patch antennas, RFID communication system and applied electromagnetics.

Novel Broadband Dielectric Resonator Antennas Fed Through Double-Bowtie-Slot Excitation Scheme

G. Almpanis, C. Fumeaux, and R. Vahldieck

Swiss Federal Institute of Technology (ETH Zurich)
 Laboratory for Electromagnetic Fields & Microwave Electronics (IFH)
 E-mail: almpanis@ifh.ee.ethz.ch

Abstract — This paper discusses the concept and the realization of novel wideband dielectric resonator antennas (DRAs), in which a dielectric cylinder or parallelepiped are fed from a microstrip line through two parallel bowtie-slots. The concept of partial independence of the slot modes from the dielectric resonator mode is exploited in such a way that the resonances of the slot modes and of the DRA are designed to occur at different frequencies. As a result, the bandwidth of the DRA is significantly improved, while stability in the radiation patterns and low cross-polarization are maintained. Finally, a study is performed concerning the influence of the gap between the dielectric resonator and the ground plane upon the overall performance of the DRA. Comparison of the results from a commercial software tool (HFSS[®]) and from the Finite-Volume Time-Domain (FVTD) method is made.

Index Terms — Dielectric resonator antenna, slot-coupling, wideband antennas, bowtie slots, gap, FVTD.

I. INTRODUCTION

The demand for wireless communications in the lower GHz range is rising dramatically due to the public's need for mobility and internet connectivity at flexible locations. Dielectric resonator antennas (DRAs) [1] are very attractive candidates for such applications, because of their high radiation efficiency, low dissipation loss and small size. Other inherent advantages include the ease of excitation, the low fabrication cost and the large bandwidth compared to a patch antenna. For instance, a DRA of dielectric permittivity $\epsilon_r = 10$ has an impedance bandwidth of around 10%, which is wide enough for a number of applications. However, for multiband applications wider bandwidths are always of interest and therefore various bandwidth enhancement techniques have been the focus of many DRA investigations.

Most of the bandwidth enhancement techniques involve complicated structures for the dielectric resonator such as stacked DRAs [2], [3], [4], parasitic elements [5], [6], or non-canonical geometries [7], [8]. In most of these cases the manufacturing difficulty and hence the cost increases. To eliminate this problem, this paper

introduces a simple but effective method to broaden the DRA bandwidth without adding manufacturing difficulties. In this solution, a microstrip line couples energy to a dielectric resonator through two parallel bowtie-slots. The advantage of the design proposed in Figure 1 lies in the weak coupling of the dielectric resonator mode to the slot modes [9]. Therefore, the modes can be independently designed in such a way, that the resonant frequencies are sufficiently separated from one another and, as a result, the impedance bandwidth increases. Moreover, the polarization and the radiation patterns of the DRA are maintained, since the slot modes and the fundamental modes of either the cylindrical or the rectangular dielectric resonator have similar radiation characteristics.

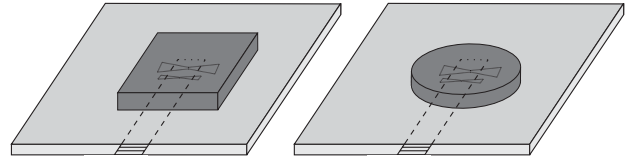


Fig. 1. Proposed antenna geometry.

The design procedure for a double-bowtie-slot-coupled DRA is described in Section II. The validity and repeatability of the design process are demonstrated in Sections III and IV, where two individual cases are considered. The first case involves a simple cylindrical dielectric resonator (DR) that is fed by the double-bowtie-slot excitation scheme, while in the second case the disc is replaced by a dielectric parallelepiped. Simulation and experimental results are shown, in order to prove the initial hypothesis. Finally, a discussion is made in Section V about the effect of a gap. Simulation and experimental results are shown, in order to prove the initial hypothesis. Finally, a discussion is made in Section V about the effect of a gap between the dielectric resonator and the ground plane of the microstrip line.

II. DESIGN CONCEPT

The design of a dielectric resonator fed from a microstrip line through two parallel bowtie-slots is a straightforward procedure, if the concept of the partial independence of the DR mode from the slot modes is taken into consideration. Therefore, the design process can be separated into three main steps.

In the first step, the two bowtie slots are designed to be resonant at nearby frequencies f_1 and f_2 . To that end, the structure depicted in Figure 2 is simulated assuming a flat dielectric superstrate structure (permittivity ϵ_{rd}). To that end, the structure depicted in Figure 2 is simulated assuming a flat dielectric superstrate structure (permittivity ϵ_{rd} and height h) on top of the slots and infinitely extended in the x-y direction. This allows the computationally efficient use of the commercial software tool Ansoft Designer[®] (Method of Moments). The bowtie slots with lengths L_{s1} , L_{s2} and widths W_{s1} , W_{s2} are etched into the groundplane of a microstrip line, which is a 50 Ω line of width W_m . The distances from the centers of the two slots to the open end of the microstrip line are P_1 and P_2 , respectively, so that good impedance matching can be ensured.

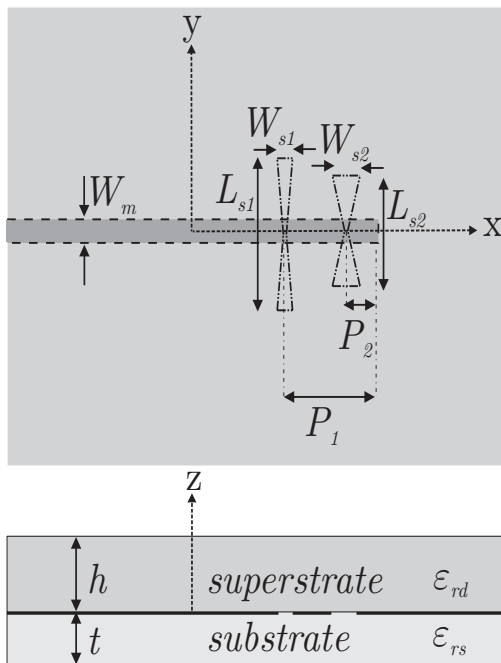


Fig. 2. Schematic of the structure with the bowtie-slots between a sub- and a superstrate.

With reference to Figure 2, the parameters that determine the frequency of resonance for the bowtie-slots are primarily the permittivity of sub- and superstrate, ϵ_{rs} and ϵ_{rd} , respectively, as well as the slot lengths L_{s1} and L_{s2} . The widths W_{s1} and W_{s2} (or the flare angles of the

bowties) are primarily used as matching parameters for the two slots, as well as to further increase their bandwidth [10].

The second step involves the design of the dielectric resonator. For dielectric resonators of a canonical shape like a cylinder or a parallelepiped, the literature offers us closed-form expressions for the resonant frequency of their fundamental modes [11]. Therefore, for a DR of the same permittivity ϵ_{rd} and height h as that of the superstrate in Figure 2, the other dimensions (radius for the cylinder, length and width for the parallelepiped) are tuned in order to achieve a resonant frequency f_3 for the DR, which is nearby, but larger than the frequencies f_1 and f_2 .

In the third step, the feeding scheme from the first step is combined with the DR designed in the second step. To do so, the feed design of Figure 2 is kept unchanged, but the lateral substrate dimensions are made finite and the superstrate is replaced by the DR, whose dimensions and permittivity were determined during the second step. The final structure, which is depicted in Figure 1, is fine-tuned, so that its impedance bandwidth is further enhanced. This optimization involves primarily the stub lengths P_1 and P_2 , the flare angles of the bowties as well as the position of the dielectric resonator center relative to the center line of the feeding microstrip. Since the structure is no longer infinitely extended in x- and y-direction, all the simulations in this last step are performed with Ansoft HFSS[®] (Finite Elements Method).

It should be emphasized that the mutual coupling of the two slots in parallel configuration may affect the radiation patterns of the DRA. The two slots in parallel point the beam at an angle different from the broadside direction. To achieve a broadside radiation pattern of the DRA, two methods can be used. First, the distance between the two slots can be further decreased with respect to the wavelength of operation. Second, shifting the center of the DR along the line connecting the slot centers does not only influence the matching, but can also affect the direction of maximum radiation. Obviously, the dielectric resonator serves as a dielectric loading for higher front-to-back ratio, but most importantly, it helps form the radiation patterns generated by the feed.

III. DOUBLE BOWTIE-SLOT-COUPLED CYLINDRICAL DRA

For operation of the DRA in the 5.0 GHz – 6.5 GHz range using a simple dielectric cylinder, the aforementioned procedure results in an antenna geometry, as illustrated in Fig. 3. The cylindrical DRA is made from Rogers TMM[®] 10i laminate, with dielectric permittivity $\epsilon_{rd} = 9.8$, height $h = 4.5$ mm, and radius $r = 12$ mm. The dielectric disc lies on top of the two bowtie slots, which have dimensions $L_{s1} = 7.9$ mm, $L_{s2} = 6$ mm, $W_{s1} = 0.58$

mm, $W_{s2} = 2.02$ mm, while their width at the center is $W_{c1} = W_{c2} = 0.3$ mm. The center of the cylindrical DR is placed at a position $P = 3.1$ mm from the open end of the microstrip line. The width of the microstrip line is $W_m = 2.4$ mm and its open end is at distances $P_1 = 4.1$ mm and $P_2 = 2.7$ mm from the slot centers. Finally, the Duroid substrate's permittivity is $\epsilon_{rs} = 2.2$, its thickness is $t = 0.7874$ mm and its dimensions are $100 \text{ mm} \times 100 \text{ mm}$.

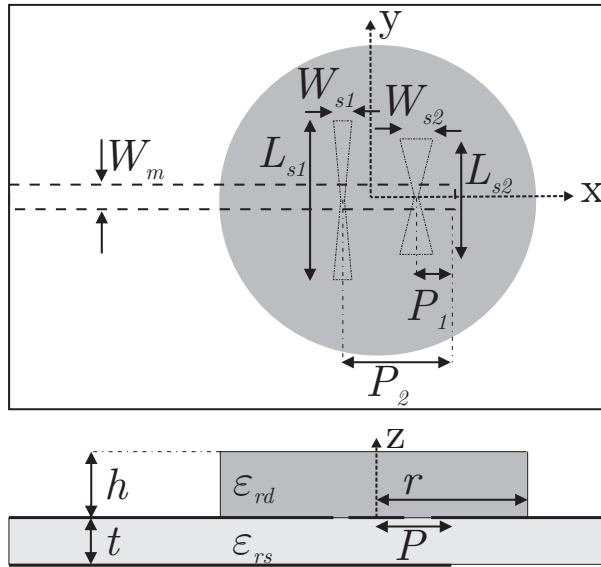


Fig. 3. Schematic of the double-bowtie-slot-coupled cylindrical DRA.

According to the specifications given above, an antenna prototype was manufactured and measured. The measured and simulated return loss of the double-bowtie-slot-coupled DRA is illustrated in Figure 4. An experimental impedance bandwidth of 33 per cent is obtained, a very satisfying value for a structure with a single cylindrical DRA. The small discrepancy between simulated and measured results is most probably caused by the gap between the ground plane and the DR. A more extensive discussion on this subject is made in Section V.

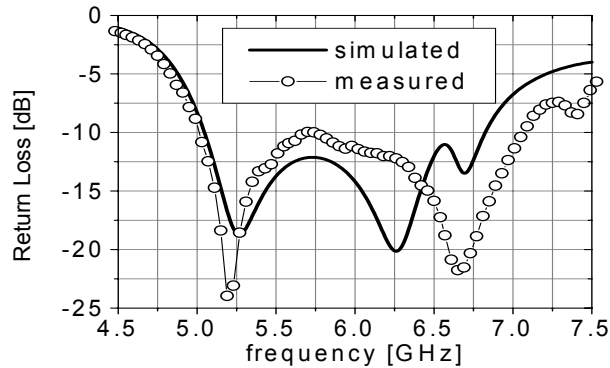


Fig. 4. Measured and simulated Return Loss of the cylindrical DRA as a function of frequency.

To further illustrate the excitation of the three modes in the proposed scheme, the simulated real and imaginary parts of the impedance are depicted in Figure 5. The two slot modes are excited at 5.6 GHz and 6.5 GHz, while the fundamental HEM_{110} mode of the cylindrical DR is at 6.75 GHz. This statement can be further substantiated by looking at the real and imaginary parts of the input impedance (Figure 6) of the infinitely extended superstrate structure depicted in Figure 2. In this case, the infinite superstrate plays the role of a dielectric loading but does not excite any resonant modes. Therefore, only the two slot modes are excited, while the presence of the dielectric loading improves the front-to-back ratio. Figure 6 proves the aforementioned hypothesis, since only two modes are observed: one at 5.65 GHz and one at 6.7 GHz. A comparison between Figures 5 and 6 clearly associates the third mode (indicated by the local maximum of the real part of the impedance) in Fig. 5 with the DR mode. It is worth mentioning that according to the simulations performed, the replacement of the superstrate by the DR slightly shifts the resonant slot modes to lower frequencies, due to the lowering of the effective permittivity ϵ_{eff} for the slots.

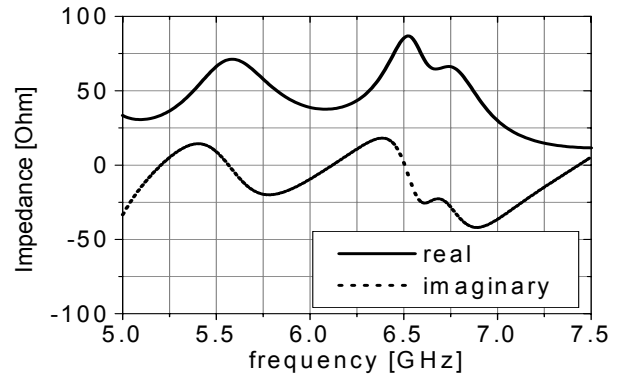


Fig. 5. Real and imaginary impedance of the structure with two bowtie-slots and the cylindrical DRA on top.

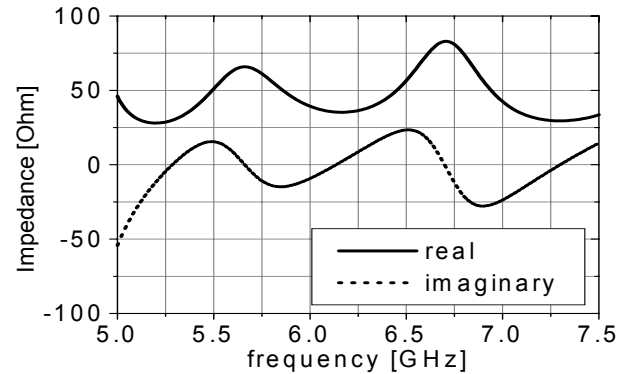


Fig. 6. Real and imaginary impedance of the structure with two bowtie-slots and a superstrate (no DRA).

The measured radiation patterns (parallel and cross polarization) are depicted in Figures 7, 8, 9 at frequencies 5.2 GHz, 6.25 GHz, and 6.7 GHz, respectively. As expected, the polarization remains reasonably pure for a wide angle range and the gain in the broadside direction is stable at around 3.5 dBi. In addition to that, the shift of directivity to an off-broadside angle, caused by the slot array, has been cancelled through the optimization of the distance between the slots and the position of the center of the dielectric disc. Therefore, stable radiation patterns are achieved.

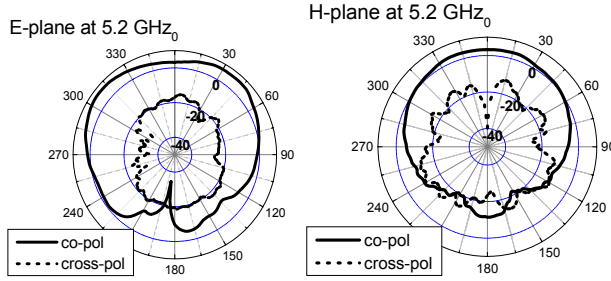


Fig. 7. Measured radiation patterns of the cylindrical DRA at 5.2 GHz.

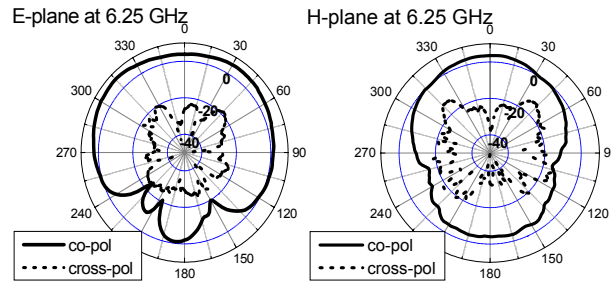


Fig. 8. Measured radiation patterns of the cylindrical DRA at 6.25 GHz.

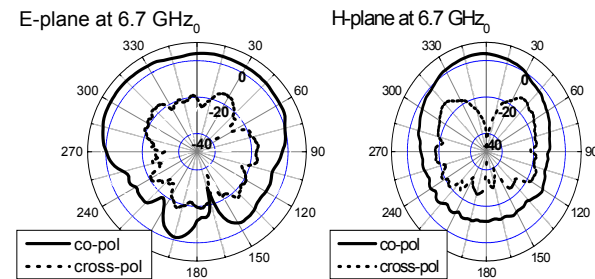


Fig. 9. Measured radiation patterns of the cylindrical DRA at 6.7 GHz.

IV. DOUBLE BOWTIE-SLOT-COUPLED RECTANGULAR DRA

The general validity of the proposed design procedure is further substantiated by the application of the same concept to the case of a rectangular DR fed by two

parallel bowtie slots. It should be noted that the choice of the cylindrical and the rectangular dielectric resonator was made based on two criteria: the presence of closed formed expressions for the determination of the frequencies of the resonant modes and the ease of fabrication.

For the same frequency range of operation, the feed geometry and the dimensions of the various components are kept unchanged from the cylindrical DRA configuration. The sole difference is obviously the dielectric resonator, which is now a parallelepiped made from Rogers TMM[®] 10i laminate of dielectric permittivity. The sole difference is obviously the dielectric resonator, which is now a parallelepiped made from Rogers TMM[®] 10i laminate of dielectric permittivity $\epsilon_{rd} = 9.8$ with dimensions $a = d = 20.5$ mm and $h = 4.5$ mm. For better matching and radiation patterns, the rectangular DR is centered at a distance $P' = 3.6$ mm from the open end of the microstrip line, and displaced by distance $\Delta y = 1.2$ mm from the microstrip's center line.

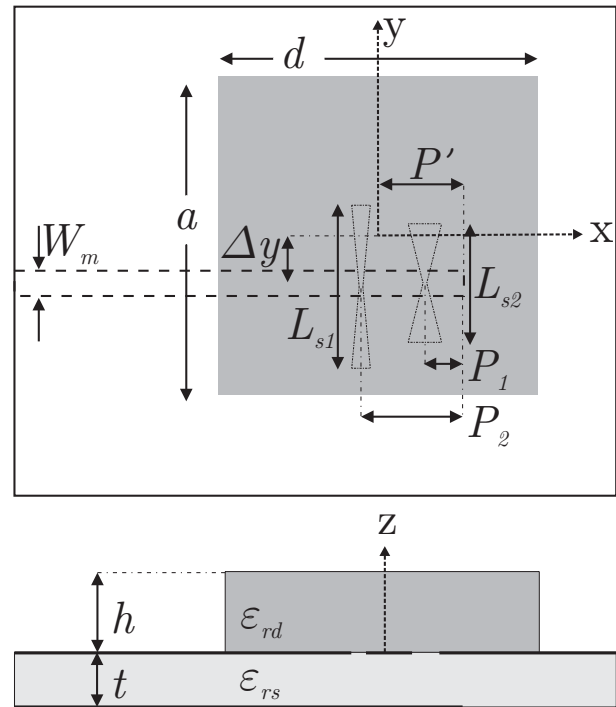


Fig. 10. Schematic of the double-bowtie-slot-coupled rectangular DRA.

The DRA was manufactured according to the geometry depicted in Figure 10. Figure 11 shows the resulting return loss and a measured bandwidth of more than 37%. Good agreement is obtained between simulation and experiment.

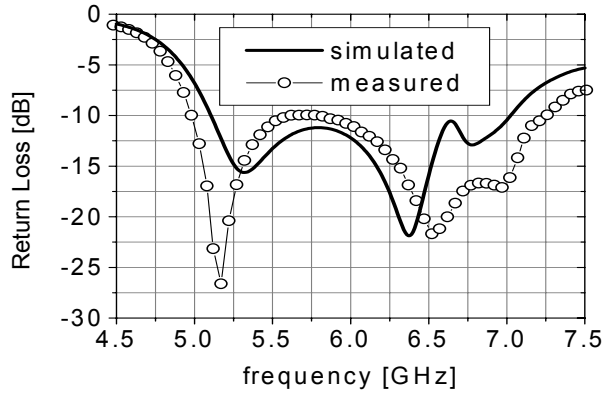


Fig. 11. Measured and simulated Return Loss of the rectangular DRA as a function of frequency.

Finally, the radiation patterns (parallel and cross polarization) of the rectangular DRA are shown in Figures 12, 13, 14 at frequencies 5.15 GHz, 6.5 GHz, and 6.95 GHz, respectively. Just like in the cylindrical configuration, stable radiation patterns are achieved. It is important to note here that if a rectangular (not a square) DR had been used ($a \neq d$ in Figure 10), the polarization purity would have been improved. This is due to the fact that the TE_{111}^x mode would be resonant at a different frequency compared to the TE_{111}^y mode and therefore the polarization at the frequency of the TE_{111}^y mode would not be distorted by the orthogonal resonant mode.

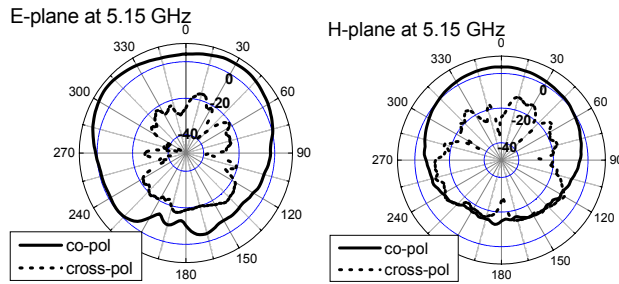


Fig. 12. Measured radiation patterns of the rectangular DRA at 5.15 GHz.

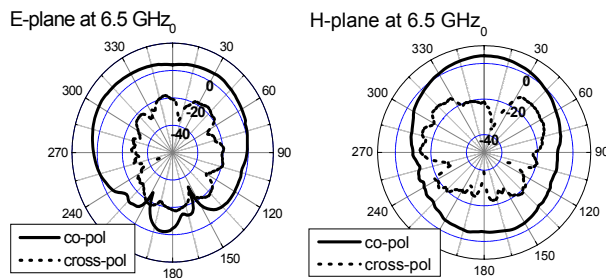


Fig. 13. Measured radiation patterns of the rectangular DRA at 6.5 GHz.

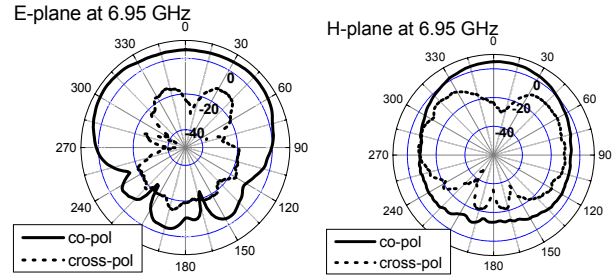


Fig. 14. Measured radiation patterns of the rectangular DRA at 6.95 GHz.

V. EFFECT OF THE GAP BETWEEN THE GROUNDPLANE AND THE DIELECTRIC RESONATOR

The comparison between the HFSS simulations and the measured data for the return loss of the fabricated DRAs reveals a reasonably good agreement (Figures 4 and 11). It demonstrates an accurate numerical design of the operational bandwidth, despite the fact that observed S11 resonances are slightly shifted. The discrepancies between simulations and measurements can be partly explained by imperfections of the realized prototypes. Fabrication imperfections relevant to probe-fed DRAs have been discussed in [12] and [13]. In the present case of a slot-fed DRA, a major physical source of error consists in a gap between the dielectric resonator and the metallic ground plane. For the prototypes fabricated in the frame of the present investigations, the dielectric resonator adheres to the ground plane using a thin layer of Vaseline (Fig. 15). This allows easy variation of the relative location of the DR with respect to the feed circuit, for testing purposes. In addition, this way of attaching the DR presented the advantage of allowing a convenient reuse of the same feeding circuit with various dielectric resonators. This adhesion layer might be replaced by dielectric glue in future fabrication runs.

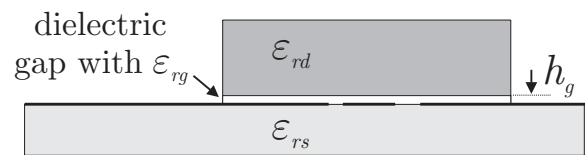


Fig. 15. Schematic showing the characteristics of dielectric gap between the DR and the ground plane.

The present section presents a numerical study of the effect of this Vaseline-filled gap for the case of the double-bow-tie slot fed cylindrical DRA. A full simulation of the device including the dielectric gap faces two main difficulties:

First, the thickness h_g of the gap is not well known. A constant gap thickness h_g of a few tens of microns is assumed. More precise information is not available, neither in the form of an average gap size, nor regarding typical gap variations under the surface of the DR. The dielectric permittivity ϵ_{rg} of the Vaseline is estimated to take a value between 2 and 3.

Second, simulating a gap with a thickness below 50 μm in the lower GHz frequency range is a very challenging task for general-purpose electromagnetic simulation tools, since the gap thickness is in the order of $\lambda_0 / 500$ or smaller.

The latter problem is best solved by using a strongly inhomogeneous mesh to resolve the gap. This has been done with the commercial code HFSS[®] and, for comparison, also with an in-house written code based on the Finite-Volume Time-Domain method. Both methods make use of tetrahedral meshes, which permit rapid variations in cell sizes to accommodate fine structural details equally well as the free space surrounding the DR. Apart from this common feature, the two methods differ greatly, and some characteristics relevant to the present simulation are shortly described in the following:

a) HFSS is based on the Finite-Element method in the frequency domain. The resolution of the gap requires a dramatic increase in the number of cells. The limitation in the capability to solve the present problem arises since the memory load increases faster than linearly with the number of unknowns, leading to an explosion of the memory costs. In the present study, the resolution of thin dielectric gaps in HFSS simulations required at times more than 10 GB of memory.

b) The FVTD method [14], [15] is a time-domain method that can be used in any polyhedral discretization. It is therefore characterized by a large geometrical flexibility, e.g., when applied in a tetrahedral mesh. Applications of the method to DRAs have been presented previously in [13] and [16]. The second of those references in particular shows the simulation of a slot-fed DRA. In the present case (as for HFSS), the resolution of the dielectric gap between the ground plane and the DR also increases dramatically the number of cells in the tetrahedral mesh. However, because of only a linear increase of the memory with the number of unknowns, the memory cost remains at a level around 1 GB, compatible for use on a standard PC. The limitation in the capability of the program to solve the dielectric gap problem is more due to the CPU time required to achieve convergence of the results in this resonant structure. Even when using a local-time stepping technique [17], the efficiency of the scheme is not dramatically increased, since tiny cells, which are required for the gap resolution, represent a very large percentage of the total number of cells. Therefore, simulations of a DRA in the presence of

very thin gaps requires several days of computations, limiting the simulation capabilities.

Because of the incomplete knowledge of the gap properties, and because of the limitation of both tools chosen for the numerical simulation, the present analysis must be interpreted in a qualitative manner, as a demonstration of the potential effects of a gap between the dielectric and the ground plane. Several configurations of Vaseline-filled gaps have been tested with both tools in the case of the cylindrical DR fed by double bow-tie slots (presented in Sect. III). The results are shown in Figure 16 for HFSS and Figure 17 for FVTD. In both cases, the dielectric gap is of height $h_g = 30 \mu\text{m}$ and of dielectric permittivity $\epsilon_{rg} = 2.7$. Both figures include the simulated return loss with and without dielectric gap, as well as the measured data for comparison. From those graphs, it is observed that without the gap, both simulation tools represent the -10 dB bandwidth of operation with reasonable accuracy, although slight differences occur. In addition, it is observed that the introduction of a thin dielectric gap between the DR and the ground plane has a sensible effect on the simulated performance. This effect is qualitatively very similar for both numerical tools and supports our assumption about the effect of the small gaps on the return loss. A more precise match to simulation is not expected, considering that the modeling of the dielectric gap is at the limit of the capabilities of both tools and that the real characteristics of the dielectric gap are unknown.

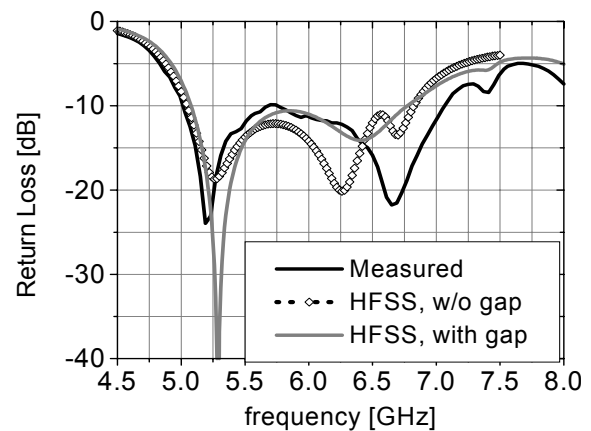


Fig. 16. HFSS simulations of the return loss for the cylindrical DRA with and without dielectric gap (thickness $h_g = 30 \mu\text{m}$, $\epsilon_{rg} = 2.7$). The curves are compared to measured data.

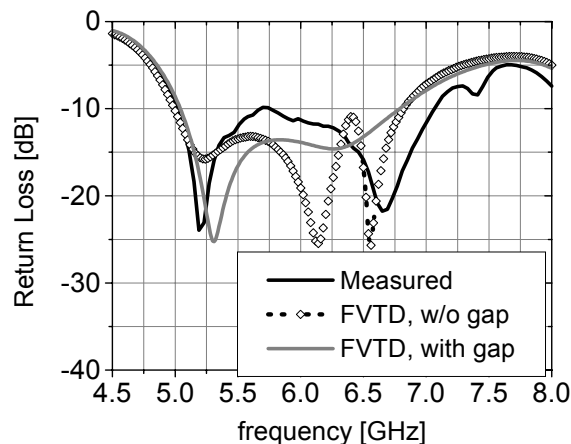


Fig. 17. FVTD simulations of the return loss for the cylindrical DRA with and without dielectric gap (thickness h_g). FVTD simulations of the return loss for the cylindrical DRA with and without dielectric gap (thickness $h_g = 30 \mu\text{m}$, $\epsilon_{rg} = 2.7$). The curves are compared to measured data.

VI. CONCLUSION

It was shown that the resonances of a 2-element array of bowtie-slots and a dielectric resonator can be combined for bandwidth enlargement. Novel double-bowtie-slot-coupled DRA designs were proposed with more than 30 % bandwidth, 3.5 dBi gain in the broadside direction, and stable radiation patterns and polarization. The effect of the gap between the dielectric resonator and the ground plane of the microstrip line has been discussed.

ACKNOWLEDGMENT

The authors would like to acknowledge the valuable support from H.-R. Benedickter. The authors are also grateful to M. Lanz for fabricating the feeding structure. This work was supported by ETH Research Grant TH-38/04-1.

REFERENCES

[1] S. A. Long, M. W. McAllister, and L. C. Shen, "The resonant cylindrical dielectric cavity antenna," *IEEE Trans. Antennas Propagation*, Vol. 31, No. 3, pp. 406 - 412, May 1983.

[2] A. Petosa, A. Ittipiboon, Y. M. M. Antar, D. Roscoe, and M. Cuhaci, "Recent advances in dielectric-resonator antenna technology," *IEEE Antennas and Propagation Magazine*, Vol. 40, No. 3, pp. 35 - 48, June 1998.

[3] A. A. Kishk, B. Ahn and D. Kajfez, "Broadband stacked dielectric resonator antennas," *Electronics Letters*, Vol. 25, No. 18, pp. 1232 - 1233, Aug. 1989.

[4] K. W. Leung, K.Y. Chow, K.M. Luk, and E. K. N. Yung, "Offset dual-disk dielectric resonator antenna of very high permittivity," *Electronics Letters*, Vol. 32, No. 22, pp. 2038 - 2039, Oct. 1996.

[5] A. Laisne, R. Gillard and G. Piton, "Circularly polarized dielectric resonator antenna with metallic strip," *Electronics Letters*, Vol. 38, No. 3, pp. 106 - 107, Jan. 2002.

[6] B. Li and K. W. Leung, "Strip-Fed Rectangular Dielectric Resonator Antennas With/Without a Parasitic Patch," *IEEE Trans. Antennas Propagation*, Vol. 53, No. 7, pp. 2200 - 2207, July 2005.

[7] A. A. Kishk, Y. Yan, A. W. Glisson, "Conical dielectric resonator antennas for wide-band applications," *IEEE Trans. Antennas Propagation*, Vol. 50, No. 4, pp. 469 - 474, April 2002.

[8] A. Ittipiboon, A. Petosa, D. Roscoe and M. Cuhaci, "An Investigation of a Novel Broadband Dielectric Resonator Antenna," *IEEE International Symposium on Antennas and Propagation Digest*, Baltimore, MA, pp.2038-2041, June 1996.

[9] A. Buerkle, K. Sarabandi and H. Mosallaei, "Compact Slot and Dielectric Resonator Antenna With Dual-Resonance, Broadband Characteristics," *IEEE Trans. Antennas Propagation*, Vol. 53, No. 3, pp. 1020 - 1027, March 2005.

[10] G. Almpanis, C. Fumeaux, and R. Vahldieck, "Double-Bowtie-Slot-Coupled DRA for Enhanced Bandwidth," *22nd Annual Review of Progress in Applied Computational Electromagnetics*, ACES, Miami, FL, USA, pp. 812-818, March 2006.

[11] K. M. Luk and K. W. Leung, "Dielectric Resonator Antennas", Research Studies Press, Baldock, England, 2003.

[12] G.P. Junker, A.A. Kishk, A.W. Glisson and D. Kajfez, "Effect of fabrication imperfections for ground-plane-backed dielectric-resonator antennas," *IEEE Trans. Antennas Propagation*, Vol. 37, No. 1, pp. 40-47, Feb. 1995.

[13] C. Fumeaux, D. Baumann and R. Vahldieck, "Advanced FVTD simulation of dielectric resonator antennas and feed structures," *ACES Journal*, Vol. 19, No. 3, pp. 155-164, Nov. 2004.

[14] V. Shankar, A.H. Mohammadian and W.F. Hall, "A time-domain, finite-volume treatment for the Maxwell equations," *Electromagnetics*, Vol. 10, pp. 127-145, 1990.

[15] P. Bonnet, X. Ferrieres, B.L. Michielsen, P. Klotz and J.L. Roumigières, "Finite-Volume Time Domain Method", Chapter 9 in *Time domain electromagnetics*, edited by S.M. Rao, Academic Press, San Diego, 1999.

- [16] D. Baumann, C. Fumeaux, G. Almpanis and R. Vahldieck, "Microstrip port definition in FVTD and application to slot-fed dielectric resonator antennas," *22nd Annual Review of Progress in Applied Computational Electromagnetics, ACES*, Miami, FL, USA, pp. 787-794, March 2006.
- [17] C. Fumeaux, D. Baumann, P. Leuchtmann and R. Vahldieck, "A generalized local time-step scheme for efficient FVTD simulations in strongly inhomogeneous meshes," *IEEE Trans. Microwave Theory and Techniques*, Vol. 52, No. 3, pp. 1067-1076, March 2004.



Georgios Almpanis received the Dipl. Ing. degree in electrical and computer engineering from the National Technical University of Athens, Greece, in 2003, the M.Sc degree in Optics and Photonics from CREOL & FPCE, UCF, Florida, USA in 2004 and is currently working toward the Ph.D. degree at the Swiss Federal Institute of Technology (ETH)

Zürich, Zürich, Switzerland.

In the Summer of 2002 he did an internship in the Norwegian University of Science and Technology (NTNU), in Trondheim, Norway. From March to August 2003, he was a Research Scientist with the Greek Telecommunications Company, working on the field of antenna engineering. In January 2005, he joined the ETH Zürich, where he is currently with the Laboratory for Electromagnetic Field Theory and Microwave Electronics (IFH). His main research interests include dielectric resonator antennas and ultra-wideband communication systems.

Mr. Almpanis was a 3rd prize winner at the 6th European Union Contest for Young Scientists in Helsinki, Finland, in 1996. He was a recipient of a scholarship from the Fulbright Foundation for the academic year 2003-2004 and from the Gerondelis Foundation for the academic year 2004-2005.



Christophe Fumeaux received the Diploma and Ph.D. degrees in physics from the Swiss Federal Institute of Technology (ETH), Zurich, Switzerland, in 1992 and 1997, respectively. From 1998 to 2000, he was a Post-Doctoral Researcher involved in infrared technology with the School of Optics, University of Central Florida, Orlando. In

2000, he joined the Swiss Federal Office of Metrology, Bern, Switzerland, as a Scientific Staff Member. Since 2001, he has been a Research Associate with the Laboratory for Electromagnetic Fields and Microwave Electronics (IFH), ETH, Zürich, Switzerland. During the Fall of 2005, he was a Visiting Scientist with the Laboratory of Sciences and Materials for Electronics, and of Automatic (LASMEA), University Blaise Pascal, Clermont-Ferrand, France. His current main research

interest concerns computational electromagnetics in the time domain for numerical analysis of microwave circuits and antennas.

Dr. Fumeaux has been the chairman of the IEEE Swiss Joint Chapter on Microwave Theory and Techniques, Antennas and Propagation, and EMC since January 2006. He was the recipient of the ETH Silver Medal of Excellence for his doctoral dissertation. He was the recipient of the outstanding paper award of the Applied Computational Electromagnetics Society (ACES) in 2004.



Ruediger Vahldieck received the Dipl.-Ing. and the Dr.-Ing. degrees in electrical engineering from the University of Bremen, Germany, in 1980 and 1983, respectively.

He was a Postdoctoral Fellow with the University of Ottawa, Ottawa, ON, Canada, until 1986. In 1986, he joined the Department of Electrical and Computer

Engineering, University of Victoria, BC, Canada, where he became a Full Professor in 1991. During Fall and Spring of 1992 to 1993 he was a Visiting Scientist at the "Ferdinand-Braun-Institute für Hochfrequenztechnik", Berlin, Germany. In 1997, he was appointed Professor for electromagnetic field theory at the Swiss Federal Institute of Technology, Zurich, and became head of the Laboratory for Electromagnetic Fields and Microwave Electronics (IFH) in 2003. In 2005, he became President of the Research Foundation for Mobile Communications and was elected Head of the Department of Information Technology and Electrical Engineering (D-ITET), ETH Zurich. Since 1981 he has published more than 300 technical papers in books, journals and conferences. His research interests include computational electromagnetics in the general area of EMC and in particular for computer-aided design of microwave, millimeter wave and optoelectronic integrated circuits.

Dr. Vahldieck received the Outstanding Publication Award of the Institution of Electronic and Radio Engineers in 1983, the K.J. Mitra Award of the IETE (in 1996) for the best research paper in 1995, and the ACES Outstanding Paper Award in 2004. He is the Past-President of the IEEE 2000 International Zurich Seminar on Broadband Communications (IZS'2000) and since 2003 President and General Chairman of the international Zurich Symposium on Electromagnetic Compatibility (EMC Zurich). He is a member of the editorial board of the IEEE TRANSACTIONS ON MICROWAVE THEORY AND TECHNIQUES. From 2000 until 2003 he served as Associate Editor for the IEEE MICROWAVE AND WIRELESS COMPONENTS LETTERS and from July 2003 until the end of 2005 as the Editor-in Chief. Since 1992, he has been on the Technical Program Committee of the IEEE International Microwave Symposium, the MTT-S Technical Committee on Microwave Field Theory, and in 1999 on the TPC of the European Microwave Conference. From 1998 until 2003 Professor Vahldieck was the Chapter Chairman of the IEEE Swiss Joint Chapter on MTT, AP, and EMC.

Approximated Method Neglecting Coupling for Conformal Array

François Chauvet¹, Régis Guinvarc'h¹ and Marc Hélier²

¹ SONDRA, Supélec

3 rue Joliot-Curie, 91190 Gif-sur-Yvette France

francois.chauvet@supelec.fr, regis.guinvarch@supelec.fr

² Université Pierre et Marie Curie-Paris 6 /LISIF

3 rue Galilée, 94200 Ivry-sur-Seine France

marc.helier@upmc.fr

Abstract — Full modeling of large conformal array can be time and memory consuming. An approximated method that takes into account the vectorial nature of the radiated field is presented. The radiation characteristic of the array is obtained by means of the vectorial sum of each element radiation characteristic, rotated according to the orientation of the element. The coupling between elements will be evaluated in the case of interest: a conformal array on an inflatable structure. In the approximated method, coupling will be neglected in such a case. To illustrate the approach, a spiral antenna will be chosen and modeled with MoM. Finally, array radiation patterns obtained by the approximated method will be compared with a full wave MoM to validate our method, in the case of a simplified 1D circular array.

Keywords — Spiral antenna, coupling, wideband array, conformal antennas.

I. INTRODUCTION

A high altitude airship (HAA) offers great potential as a host platform for low frequency antenna array [1]. The main advantage is the large surface available, allowing good performances for applications like radar tracking and telecommunications at lower cost than satellites. The antenna array has to be conformed to the ellipsoidal shape of the airship hull and must fill wideband, low weight, low power, low profile conditions. The array lies on the side of the airship and must achieve a bandwidth centered on 500 MHz as well as digital beamforming capability. The unusual configuration of our array must be pointed out since we assume that no ground plane will be used because of low profile condition and because we assume that the equipment must lie outside the hull.

The usual modeling tool (FEKO) based on method of moments (MoM) is no longer appropriate to study such a

large array. Indeed, the number of antennas is too high and modeling becomes time and memory consuming.

However, it is possible to obtain the radiation characteristic of the array if the coupling between elements is low by making the sum of each element contributions [2]. Thus, only one radiation characteristic of an isolated element has to be computed by the MoM, reducing the computation time consequently.

Therefore, after presenting the approximated method based on rotation of the radiation characteristic and phase shift according to the position of each element. The choice of a radiating element will be explained and results of FEKO simulations of this antenna will be described.

Then coupling between array elements will be examined in the chosen frequency range at different array curvatures in order to quantify the effect of coupling.

Finally, considering a small array, radiation patterns obtained with exact method and computed with neglected coupling by the approximated method will be compared. Influence of the frequency and curvature will be investigated.

II. APPROXIMATED METHOD

In order to avoid the modeling of the full array, we assume that the radiated far field of the conformal array is the sum of the radiated far fields of each antenna element as it is usually assumed for classical planar array [3]. This assumption involves neglecting the coupling between elements. Thus, this method can be applied for any radiating element, as long as the coupling between elements of the array is low. This approach is expected to noticeably reduce the time consuming issue, since it is only necessary to model only one antenna element with an exact method before doing the sum of all elements of the array. The antenna must be modeled in its own environment in order to define its radiation characteristic.

First, phase shift between elements due to the distance from the phase reference are taken into account. Each element at position m is characterized by a translation vector δ_m (Fig. 1). Thus the components (E_θ , E_φ) of the array total far field \mathbf{E}^{tot} in the main coordinate system (\mathbf{e}_r , \mathbf{e}_θ , \mathbf{e}_φ) (Figure 2) can be expressed as a function of the \mathbf{E}_m far field radiated by element m , expressed in the main coordinate system as well,

$$\mathbf{E}^{\text{tot}}(\theta, \varphi) = \sum_{m=1}^N \exp(jk \vec{e}_r \cdot \vec{\delta}_m) \mathbf{E}_m(\theta, \varphi). \quad (1)$$

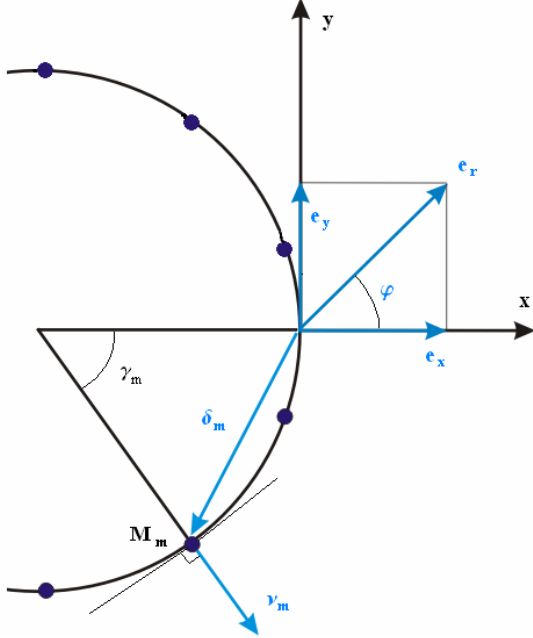


Fig. 1. Circular 1D conformal array configuration.

In order to obtain \mathbf{E}_m , the orientation of each antenna element has to be taken into account as it changes, in a given direction, magnitude, phase and polarization properties of the isolated element. FEKO gives far field results as (E'_θ , E'_φ) components of the element antenna far field \mathbf{E}' [4], at discrete values (θ' , φ') in the local coordinate system of an isolated element (\mathbf{e}'_r , \mathbf{e}'_θ , \mathbf{e}'_φ). The radiation characteristic \mathbf{E}' has to be expressed in the main coordinate system (\mathbf{e}_r , \mathbf{e}_θ , \mathbf{e}_φ). The orientation of each element is taken into account by means of a rotation matrix \mathbf{R} (see figure 2).

A general rotation \mathbf{R} can be written in terms of successive rotation matrix \mathbf{R}_z , \mathbf{R}_ξ , and $\mathbf{R}_{z'}$ [5], with the three rotation Euler angles γ , β , ψ , (see figure 3),

$$\mathbf{R} = \mathbf{R}_{z'}(\psi) \mathbf{R}_\xi(\beta) \mathbf{R}_z(\gamma). \quad (2)$$

To obtain the rotated radiation characteristic, we apply eq. (3), where \mathbf{E}_m has its components in the main coordinate system (\mathbf{e}_r , \mathbf{e}_θ , \mathbf{e}_φ)

$$\mathbf{E}_m(\theta, \varphi) = \mathbf{T}_2 \mathbf{R}_m \mathbf{T}_1 \mathbf{E}'(\theta', \varphi'). \quad (3)$$

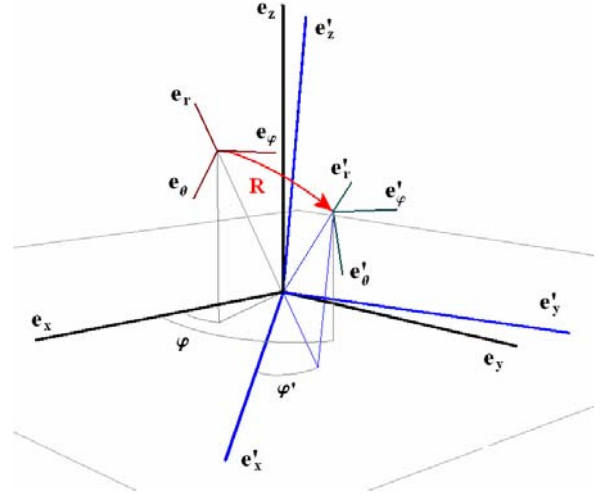


Fig. 2. Local coordinate system of an isolated element (\mathbf{e}'_r , \mathbf{e}'_θ , \mathbf{e}'_φ) and main coordinate system (\mathbf{e}_r , \mathbf{e}_θ , \mathbf{e}_φ) rotated by a rotation matrix \mathbf{R} .

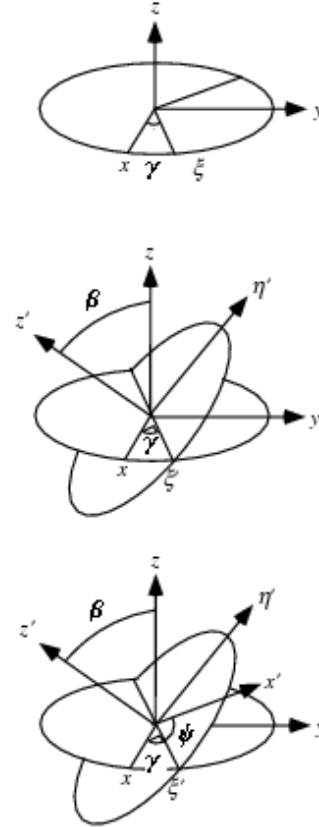


Fig. 3. Successive rotation matrix \mathbf{R}_z , \mathbf{R}_ξ , and $\mathbf{R}_{z'}$, with the three rotation Euler angles γ , β , ψ .

As rotation matrix, \mathbf{R}_m must be used in a cartesian coordinate system. Transformation matrix \mathbf{T}_1 from spherical to cartesian coordinate system and transformation matrix \mathbf{T}_2 from cartesian to spherical are required and given below

$$\mathbf{T}_1 = \begin{bmatrix} \sin \theta' \cos \varphi' & \cos \theta' \cos \varphi' & -\sin \varphi' \\ \sin \theta' \sin \varphi' & \cos \theta' \sin \varphi' & \cos \varphi' \\ \cos \theta' & -\sin \theta' & 0 \end{bmatrix}, \quad (4)$$

$$\mathbf{T}_2 = \begin{bmatrix} \cos \varphi \sin \theta & \sin \varphi \sin \theta & \cos \theta \\ -\sin \varphi & \cos \varphi & 0 \\ \cos \varphi \cos \theta & \sin \varphi \cos \theta & -\sin \theta \end{bmatrix}. \quad (5)$$

\mathbf{T}_2 is not equal to \mathbf{T}_1^{-1} since the angles (θ, φ) used in \mathbf{T}_2 can be expressed as function of (θ', φ') as follows

$$\theta = \arccos \left(\frac{a_x(\theta', \varphi')}{\sqrt{a_x^2(\theta', \varphi') + a_y^2(\theta', \varphi') + a_z^2(\theta', \varphi')}} \right)$$

$$\varphi = \arccos \left(\frac{a_x(\theta', \varphi')}{\sqrt{a_x^2(\theta', \varphi') + a_y^2(\theta', \varphi')}} \right) \quad (6)$$

with the unit vector \mathbf{a} , given by

$$\begin{bmatrix} a_x(\theta', \varphi') \\ a_y(\theta', \varphi') \\ a_z(\theta', \varphi') \end{bmatrix} = \mathbf{R}_m \begin{bmatrix} \sin \theta' \cos \varphi' \\ \sin \theta' \sin \varphi' \\ \cos \theta' \end{bmatrix}. \quad (7)$$

It must also be noticed that the spherical coordinates angles (θ', φ') of the requested far field calculated by FEKO takes discrete values. The new coordinate angles (θ, φ) in the main coordinate system $(\mathbf{e}_x, \mathbf{e}_y, \mathbf{e}_z)$ do not necessary match. For that reason an interpolation method will be required (see figure 4).

III. CHOICE OF THE ANTENN ELEMENT

We have seen before that the approximated method relies on the antenna element radiation characteristics that are taken into account in the array radiation characteristic. The method can be applied if the coupling between elements is low, thus an element that fulfills our design requirement has to be chosen to illustrate the approach. In our configuration, the choice of the antenna element is determined by different parameters. First limitations are resulting from the platform itself. The

antenna must radiate broadside, must be flat and must still radiate without ground plane. This prohibits all the antennas fed with a reference to a ground plane. Secondly, wideband performances of the array are limited by the size of the antenna since the elements must be half wavelength spaced. Finally, the conformation of the array leads to polarization and magnitude changes due to the various orientations of the elements. The choice of the antenna must be done after exploring these points.

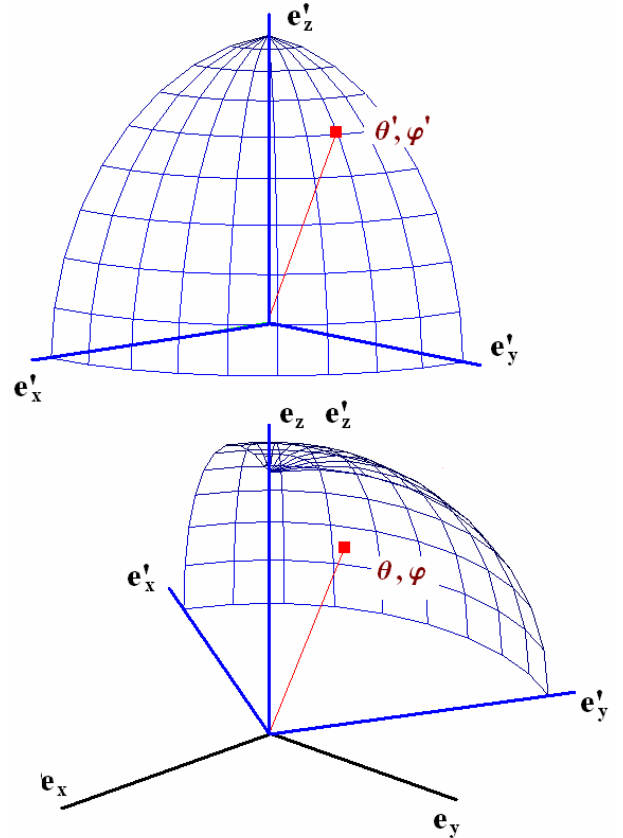


Fig. 4. Discretization of the spherical coordinate angles (θ', φ') in the (θ, φ) coordinate system of reference do not necessary match with the discretization of the main coordinate system.

Many designs exist for wideband and ultra wideband antenna [6], [7]. Some of them are low profile and research has been done recently to improve their performances. Archimedean spiral is a good candidate for wideband applications and has been chosen for our goal. It is usually not considered for phased array due to its size requirement [8]. Indeed, it radiates if its diameter D is larger or equal to λ_{\max}/π (with λ_{\max} the largest wavelength in the band). In addition, distance between array elements center to center, must be lower than half of the smallest wavelength of the bandwidth to avoid grating lobes when scanning. This leads to an element size less than or equal to $\lambda/2$. In consequence, condition

$2D \leq \lambda \leq \pi D$ must be fulfilled and the bandwidth is limited approximately to 1.5:1. Thus we can expect good functioning between 400 MHz and 600 MHz.

VSWR of a 0.27 m diameter spiral modeled with commercial software FEKO, calculated with a 200 Ω reference impedance, is plotted in figure 5. It can be observed that this antenna can radiate efficiently above 400 MHz. Its size corresponds to a distance between array elements center to center of 0.25 m, thanks to the curvature. Therefore, scanning can be obtained till the upper frequency, 600 MHz.

In a conformal configuration, all the elements do not radiate with the same field in a given direction because on their own radiation characteristic. Indeed the orientation of the elements depends on their position on the surface. Thus, it is required to know what is the radiation characteristic of the antenna element before including it in the approximated method in order to calculate the array radiation pattern.

Far field of the considered antenna is right hand circularly polarized (RHC) above the plane of the antenna and left hand circularly polarized (LHC) below (see figure 6). It has also the great advantage to radiate the same polarization over 180° (figure 6). That implies that the polarization characteristic of the conformal array will not be too much influenced by the orientations of the antenna elements.

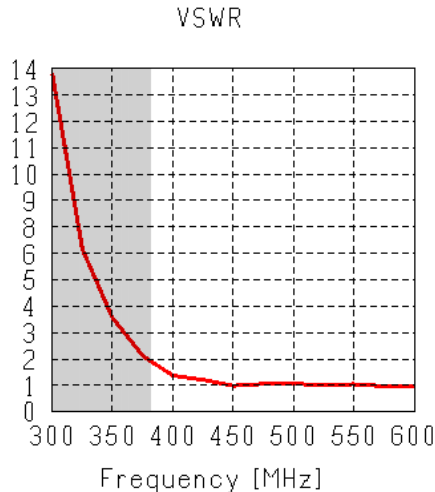


Fig. 5. VSWR of a spiral antenna with diameter of 0.27 m, calculated with 200 Ω reference impedance.

Gain in RHC polarization is plotted according to the φ angle in figure 7, at various frequencies. It can be seen that the more the frequency increases, the more the RHC polarized radiated field decreases, in the inward direction φ = 180°.

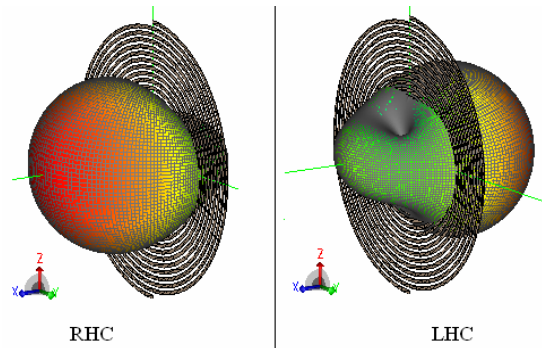


Fig. 6. 3D radiation pattern of spiral antenna. RHC polarized (right part) and LHC polarized (right part).

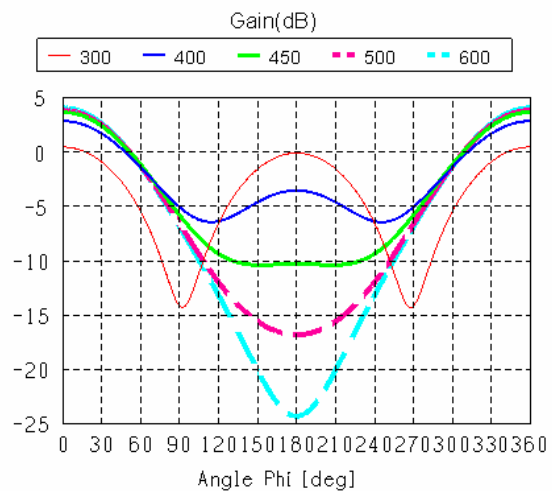


Fig. 7. Gain of RHC polarized component of the far field versus φ angle, at θ=90°, at various frequencies.

IV. STUDY OF COUPLING BETWEEN ARRAY ELEMENTS

Before using the approximated method, it is necessary to evaluate coupling between array elements, which have neglected in our approach. A circular 1D array with angle of curvature α and identical antennas (co-polar configuration) is considered (see figure 8). Only an eight-antenna array has been modeled with MoM, as it is time consuming. Coupling effects have been investigated based on the computation of the S parameters between spiral antenna ports.

The influence of the frequency within a range of 300 MHz to 600 MHz as well as the curvature effect has been studied.

The S parameters for the planar case (0° of curvature) are shown in figure 9, whereas those for the conformal case (10° of curvature) are plotted in figure 10. Both figures show results for eight identical antennas radiating a RHC polarized far field in the outward direction. Angle of curvature α is the angle seen between

the element centers of two successive antennas from to the origin of the coordinate system.

It can be clearly noticed two different behaviors for the S parameters according to the frequency. The coupling between the element 1 (see figure 8) and an element close to it, i.e. S_{12} and S_{14} , roughly decreasing with the frequency, whereas an increase can be observed concerning the elements located in the opposite part of the array i.e. S_{16} and S_{18} . The rise appends at 450 MHz, where the distribution of the current along the two spiral arms exhibits also higher values.

When comparing the planar (figure 9) and the 10° conformal (figure 10) cases, few differences can be distinguished. We can conclude that a small angle of curvature like 10° , almost do not change radically the coupling between elements. The effect of curvature is clearer for the far element coupling S_{16} and S_{18} .

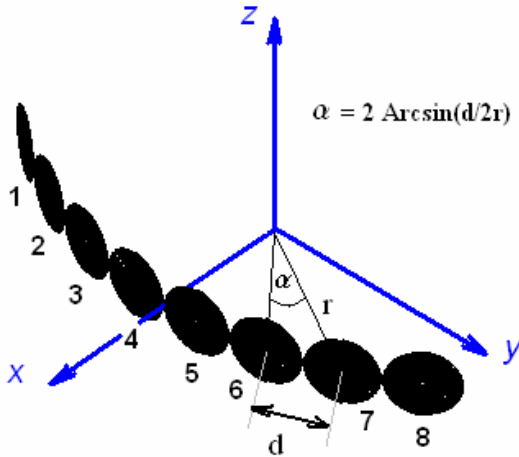


Fig. 8. Circular 1D conformal array configuration considered for the simulation. The 8 antennas are equally spaced. Angle of curvature α can vary.

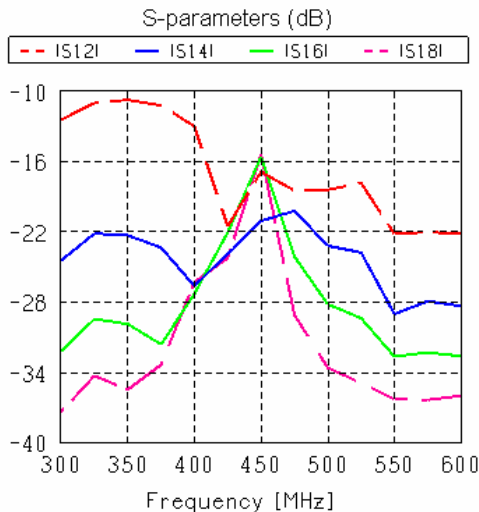


Fig. 9. S-parameters versus frequency. For the planar case $\alpha = 0^\circ$.

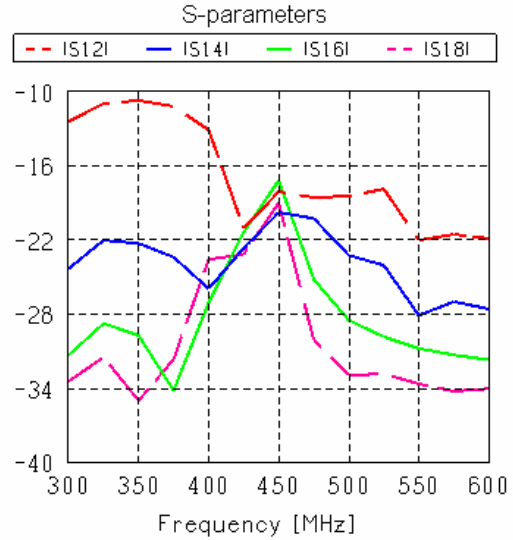


Fig. 10. S-parameters versus frequency. For the conformal case $\alpha = 10^\circ$.

V. COMPARISON OF METHODS

Radiation patterns obtained by the approximated method and FEKO are now compared for different frequencies and different angles of curvature in order to validate the approach. Figure 11 shows an example of radiation pattern plotted for RHC electric far field, at 450 MHz, with a curvature of 10° . On the upper part, can be seen the effects of the rotation of radiation pattern. Each radiation pattern corresponds to an antenna element that has been rotated according to its orientation, in the $\theta = 90^\circ$ plane.

The middle part depicts conformal array radiation pattern that corresponds to a uniformly excited array with omnidirectional sources. It emphasizes the effects due to the geometry of the conformal array itself. Those effects are combined in the radiation pattern, given by the approximated method, using equations (1) and (3), and can be observed in the lower part of figure 11, which shows the comparison between the two methods. It can be observed that the radiation pattern due to point sources has been reshaped by each antenna element radiation characteristic to give the final radiation pattern.

The two methods have been compared for frequencies within the range of 400 MHz to 600 MHz and for 0° , 5° , and 10° of curvature. Some examples are given below. Figures 12 and 13 show the comparison of two methods for the planar case, at 400 MHz and 600 MHz, respectively. Figures 14 and 15 show the results for the 10° conformal case, at 400 MHz and 600 MHz, respectively.

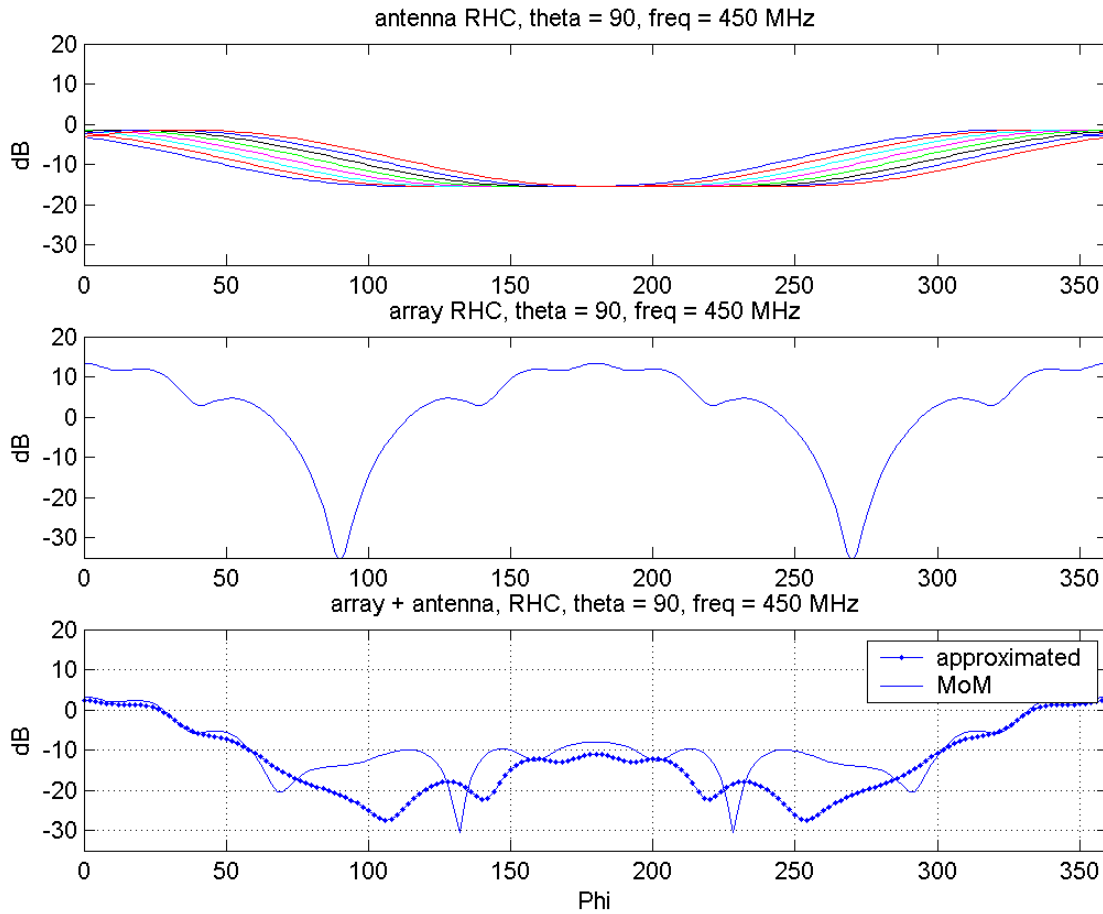


Fig. 11. RHC electric far field at 450 MHz with curvature of 10° . Top: 8 antenna rotated radiation patterns. Middle: uniformly excited conformal array with omni-directional sources. Bottom: comparison between the two methods.

As it can be seen in figures 12 to 15, reconstruction of the main lobe at $\varphi=0^\circ$, is fulfilled for frequencies within the band 400 MHz to 600 MHz. Inward lobe, at $\varphi=180^\circ$, exhibits more important differences between the two methods, especially when the radiation of the isolated element in this direction is particularly low. When comparing the planar case with the conformal case, it can be noticed that this difference for the inward lobe happens in both cases. Moreover, both cases exhibit higher differences at 600 MHz. Therefore we can conclude that this effect comes from the radiation characteristic of the isolated element itself when used in the approximated method.

We highlight before that at 450 MHz behavior of coupling strongly changes. Nevertheless, no specific effect has been noticed concerning the differences between exact method and approximated method (see figure 11), except that stronger differences can be distinguished around $\varphi=90^\circ$ and $\varphi=270^\circ$ corresponding to the lowest radiation direction of the antenna element (endfire direction). So, for the considered array of eight spiral antennas, in the conformal case as in the planar

case, it is possible to obtain the shape and level of the main lobe simply by summing the contribution of each antenna element, including the orientation of each one.

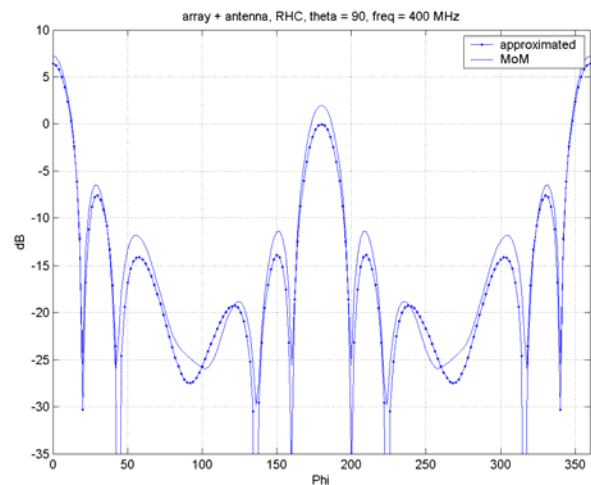


Fig. 12. Two methods comparison for 0° curvature (planar case) at 400 MHz.

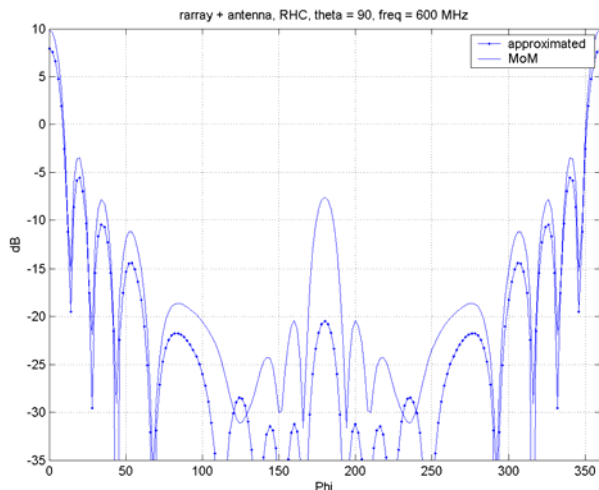


Fig. 13. Two methods comparison for 0° curvature (planar case) at 600 MHz.

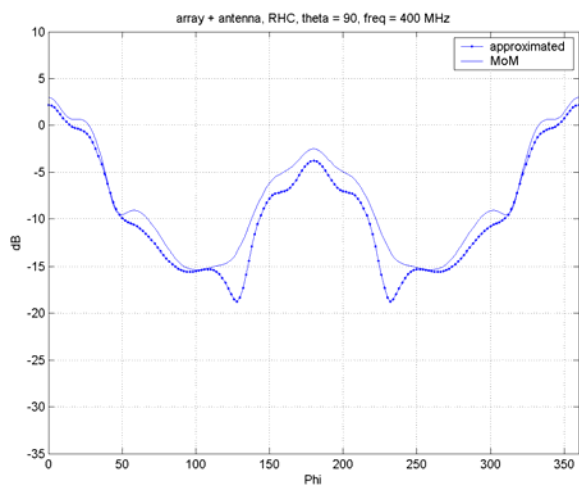


Fig. 14. Two methods comparison for 10° curvature (conformal case) at 400 MHz.

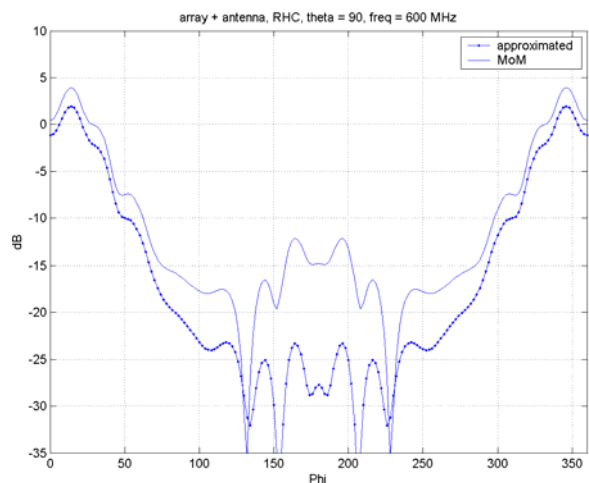


Fig. 15. Two methods comparison for 10° curvature (conformal case) at 600 MHz.

VI. CONCLUSIONS

An approximated method has been presented to solve the time consuming issue of a large array modeled with MoM. It has been illustrated with a specific configuration: a conformal spiral antenna array that achieves wideband performances on an inflatable structure. The approximated method neglects the coupling and is based on the summation that includes the rotation of each element radiation characteristic. It has the advantage of taking into account the vectorial nature of the array radiation characteristic. For the chosen design, coupling between elements has been studied, and the curvature of the array seems to not influence significantly its value. Finally, validation of the radiation patterns obtained by the approximated method has been performed by comparing with a full wave method. It has shown that main lobe reconstruction is fulfilled, but differences still remain for the inward lobe because of low levels in that direction. However, this method allows to predict the shape of array radiation pattern in a very simple and general way. It provides also an interesting tool that can be used as a first approximation for conformal array analysis.

REFERENCES

- [1] Integrated Sensor Is Structure, "Proposer information pamphlet", DARPA, Sept. 2003
- [2] C. A. Balanis, *Antenna theory, analysis and design*, Wiley; 2 Edition, ISBN: 0471592684, May 1996.
- [3] R. C. Hansen, *Microwave Scanning Antennas*, Vol. II, Academic Press, New York and London, 1966.
- [4] EM Software & Systems-S.A., *FEKO User's Manual*, 32 Techno Lane, Technopark, Stellenbosch, 7600 South Africa, June 2004.
- [5] A. Gray, *A Treatise on Gyrostatics and Rotational Motion*, MacMillan, London, 1918.
- [6] S. - Y. Suh, "A comprehensive investigation of new planar wideband antennas", PhD thesis in Electrical Engineering, Virginia Polytechnic Institute and State University, July 2002.
- [7] E. Caswell, "Design and analysis of star spiral with application to wideband arrays with variable element sizes", PhD thesis in Electrical engineering, Virginia Polytechnic institute and state University, Dec., 2001.
- [8] H. Steykal, J. Ramprecht, and H. Holter, "Spiral element broad band phased array", *IEEE Trans. Antennas Propagation*, Vol. 53, No. 8, pp. 2558-2562, August 2005.

Two Element Phased Array Dipole Antenna

Mitsuo Taguchi¹, Kotaro Era², and Kazumasa Tanaka³

¹ mtaguchi@nagasaki-u.ac.jp

^{1,3} Department of Electrical and Electronic Engineering, Nagasaki University
1-14 Bunkyo-machi, Nagasaki-shi, 852-8521 JAPAN

² Presently, Murata Manufacturing Company Ltd.
10-1 Higashikotari 1-chome, Nagaokakyo-shi, Kyoto 617-8555 JAPAN

Abstract — Two element array of dipole antennas with 90 degree phase difference feed is proposed for directional antenna applications. In the numerical analysis, the electromagnetic simulator WIPL-D based on the method of moment is used. At first, the distance between the two elements is fixed to be a quarter wavelengths at the design frequency of 2.45 GHz. The front-to-back ratio is calculated. Then, by adjusting the length of the two elements and the distance between the two elements, a front-to-back ratio of 15.3 dB is obtained. The relation between the front-to-back ratio of this antenna and the feed point currents is discussed. The measured input impedance with 90 degree hybrid phase shifter agrees with the calculated result.

I. INTRODUCTION

For the short-range wireless communication, a small antenna with unidirectional radiation characteristics is desired. As the directional antenna composed of wire elements, the Yagi-Uda antenna and the Electronically Steerable Passive Radiator (ESPAR) antenna are well known [1], [2]. These antennas consist of single driven element and some parasitic elements. In the Yagi-Uda antenna, the induced currents on the parasitic elements are controlled by adjusting the length of the parasitic elements and the distance between the elements [1]. In the ESPAR antenna, the current of the parasitic elements are controlled by adjusting the reactance loaded at the feed point of them [2]. These antennas are spatially phase controlled antennas. Since only one element is excited in these antennas, the current distribution on each element can be easily controlled by changing the distance between elements or loaded reactance at parasitic elements.

In this paper, two element array of dipole antennas with 90° phase difference feed is proposed for the directional antenna [3]. At first, the distance between two dipole elements is fixed to be a quarter wavelength at the design frequency of 2.45 GHz, and the length of two elements are changed to obtain high front-to-back

ratio. This antenna array configuration is numerically and experimentally analyzed. In the numerical analysis, the electromagnetic simulator WIPL-D based on the method of moment is used [4]. Next, the distance between the two dipole elements and the length of two elements are adjusted in order to obtain highest front-to-back ratio. Finally, the relation between the front-to-back ratio and the feed point current on each element is discussed.

II. ANALYTICAL AND EXPERIMENTAL MODEL

Figure 1 shows the structure of the two element phased array dipole antenna. The antenna elements are fed with 90° phase difference. The distance between the two elements is d . The length of the antenna elements #1 and #2 are $L1$ and $L2$, respectively. The radius of each element is $a = 1$ mm. In the numerical analysis by WIPL-D, antenna elements are excited by the delta-gap generators. The design frequency is 2.45 GHz.

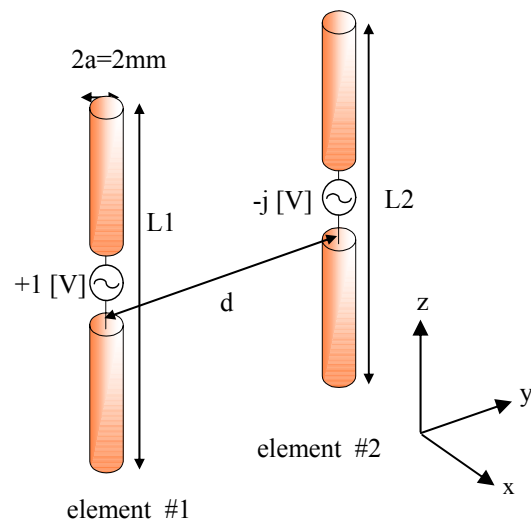


Fig. 1. Structure of proposed antenna.

Figure 2 shows the experimental model. Two monopole elements are mounted on a ground plane of dimensions 87 cm by 87 cm. This antenna is driven through the 90 degree hybrid phase shifter. The reflection coefficient Γ at the input port of the hybrid phase shifter is expressed in terms of the reflection coefficients Γ_2 and Γ_3 seen from ports 2 and 3 toward the load [5].

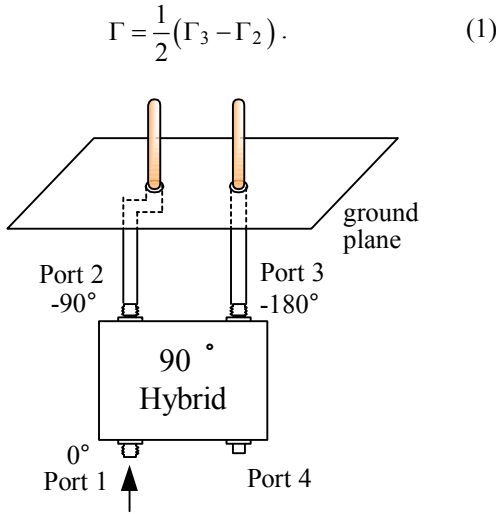


Fig. 2. Experimental model.

III. RESULTS AND DISCUSSION

A. Case I: $d = 0.25 \lambda_c$

At first, the distance between two dipole elements d is fixed to be $30.6 \text{ mm} = 0.25 \lambda_c$, where λ_c is the wavelength at the design frequency 2.45 GHz . Figure 3 shows the calculated input impedances at feed points of each element for $L_1 = L_2 = 61.2 \text{ mm} = 0.5 \lambda_c$. At the frequencies less than 2.1 GHz , the input resistance on the element #1 becomes small compared with the single dipole antenna. This phenomenon is similar to the horizontal dipole located above the infinite ground plane. The difference of impedances between two elements at higher frequencies is observed from 2.45 GHz [6]. Since each element is excited with 90 degree phase difference, the mutual coupling is different at each element. Therefore this difference occurs.

Figure 4 shows the front-to-back ratio characteristics. The front-to-back ratio is 4.8 dB at 2.45 GHz and becomes highest at 1.9 GHz . Figure 5 shows the maximum front-to-back ratio calculated in the frequency band from 1 GHz to 3 GHz . Figure 6 shows L_2 and the frequency when the maximum front-to-back

ratio is obtained. The maximum front-to-back ratio is obtained for the ratio of L_2 to L_1 from 0.93 to 0.95 .

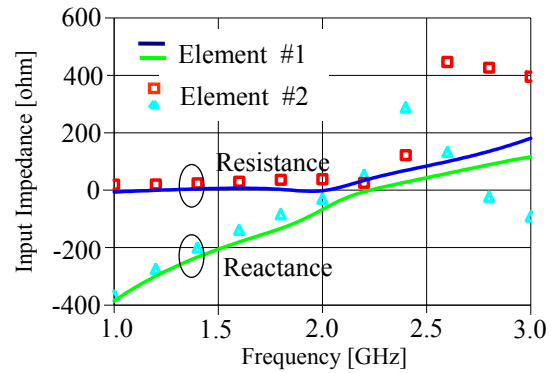


Fig. 3. Calculated input impedance at feed point of each element, $d=30.6 \text{ mm}$, $L_1=L_2=61.2 \text{ mm}$.

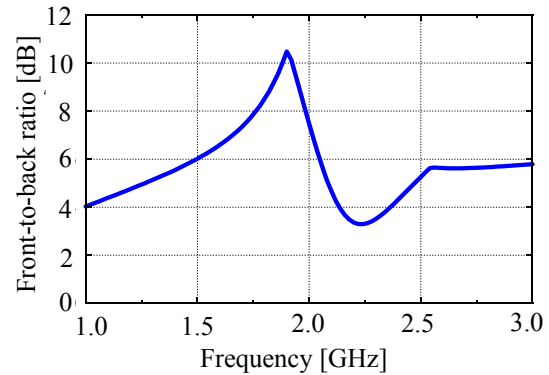


Fig. 4. Calculated front-to-back ratio characteristics, $d=30.6 \text{ mm}$, $L_1=L_2=61.2 \text{ mm}$.

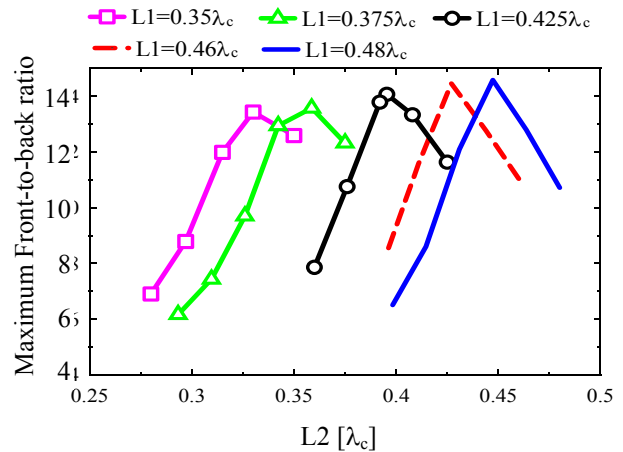


Fig. 5. Calculated maximum front-to-back ratio.

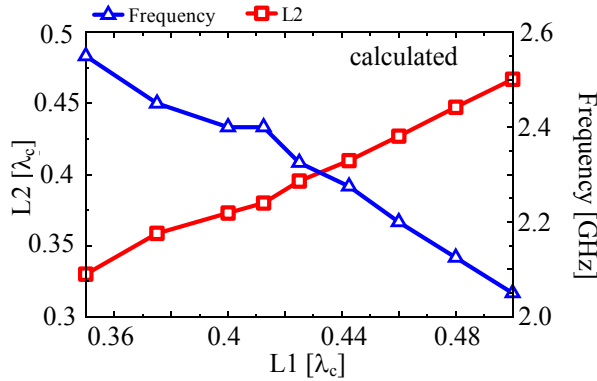


Fig. 6. L2 for maximum front-to-back ratio and its frequency.

B. Case II: $d \neq 0.25\lambda_c$

By adjusting the distance between both elements d and the length of two elements $L1$ and $L2$, the maximum front-to-back ratio is obtained at the design frequency 2.45 GHz. The maximum front-to-back ratio of 15.3dB is obtained in the case of $d = 20.6$ mm, $L1 = 54.6$ mm, and $L2 = 50.2$ mm.

Figures 7 and 8 show the electric field radiation pattern in xy plane at 2.45GHz, the input impedance characteristics at the feed point of each element in this case, respectively. In Figure 7, the electric field radiation pattern in the Case I is also shown for comparison.

Figure 9 shows the calculated and measured input impedance characteristics at the input port of the 90° hybrid phase shifter. In the calculation, the attenuation and the phase delay in the coaxial cable between the phase shifter and the antenna element is considered. Figure 10 shows the VSWR characteristics of this antenna. The VSWR less than 3 is obtained near the design frequency 2.45 GHz.

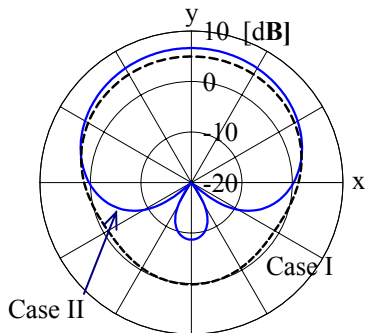


Fig. 7. Calculated electric field radiation patterns in xy plane (vertical polarization) at 2.45 GHz, Case I: $d = 30.6$ mm, $L1 = L2 = 61.2$ mm, Case II: $d = 20.6$ mm, $L1 = 54.6$ mm, $L2 = 50.2$ mm.

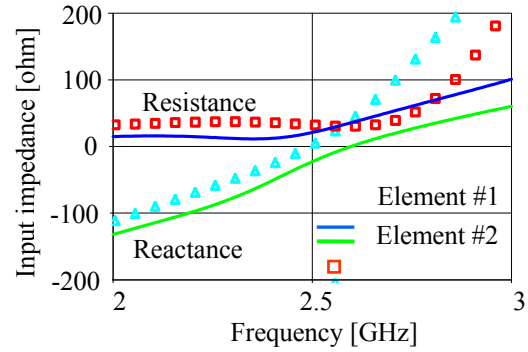


Fig. 8. Calculated input impedance at feed point of each element, $d = 20.6$ mm, $L1 = 54.6$ mm, $L2 = 50.2$ mm.

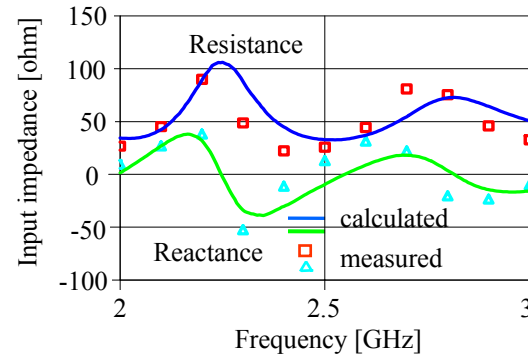


Fig. 9. Input impedance characteristics at input port of 90° hybrid phase shifter, $d = 20.6$ mm, $L1 = 54.6$ mm, $L2 = 50.2$ mm.

C. Discussion

The front-to-back ratio of the antenna is 4.8 dB at 2.45 GHz in the case I of $d = 30.6$ mm, and $L1 = L2 = 61.2$ mm. On the other hand, the front-to-back ratio becomes maximum (15.3 dB) in the case II of $d = 20.6$ mm, $L1 = 54.6$ mm, and $L2 = 50.2$ mm. The radiation characteristics are determined by the current distribution on each element. Here, the synthesized feed point current vectors including the spatial phase delay between two elements are shown in order to discuss why the front-to-back ratio is different in case I and II. Figure 11 shows the feed point current of each element and the synthesized currents in the $+y$ and $-y$ direction in case I of $d = 30.6$ mm, $L1 = L2 = 61.2$ mm. The distance between two elements $d = 30.6$ mm corresponds to the spatial phase delay of 90° at 2.45 GHz. Without considering the attenuation along the propagation, the current on the element #2 added by the current #1 with 90° phase delay contributes to the radiation toward $+y$ direction. The current on the

element #1 added by the current #2 with 90° phase delay contributes to the radiation toward $-y$ direction. The amplitude of feed point current on the element #2 is too small compared with that on the element #1, and the phase difference of currents is not equal to the excitation phase difference of 90° because of the mutual coupling. Therefore the current on the element #1 does not cancel out the current on the element #2 with 90° phase delay. As the result, the amplitude of synthesized current toward $-y$ direction does not become small. Therefore the front-to-back ratio becomes low.

Figure 12 shows the feed point current of each element and the synthesized currents in the $+y$ and $-y$ directions in case II of optimized model ($d = 20.6$ mm, $L1 = 54.6$ mm, $L2 = 50.2$ mm). The distance between the two elements $d = 20.6$ mm corresponds to about 60 degrees of the spatial phase delay at 2.45 GHz. There is a large difference between the amplitudes of the two synthesized current vectors. Therefore, the front-to-back ratio becomes high.

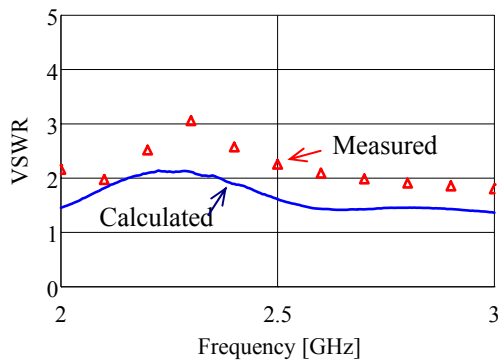


Fig. 10. VSWR characteristics at input port of 90° hybrid phase shifter, $d=20.6$ mm, $L1=54.6$ mm, $L2=50.2$ mm.

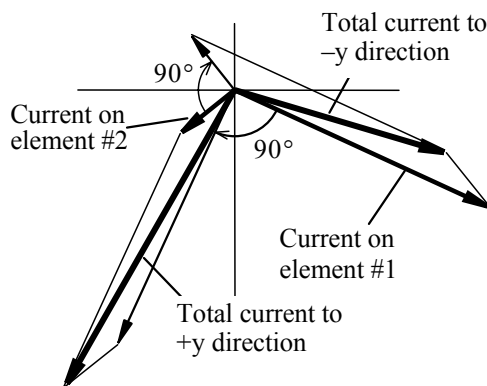


Fig. 11. Current on each element and synthesized currents toward $+y$ and y directions at 2.45 GHz, $d=30.6$ mm, $L1=L2=61.2$ mm, FB ratio = 4.8 dB.

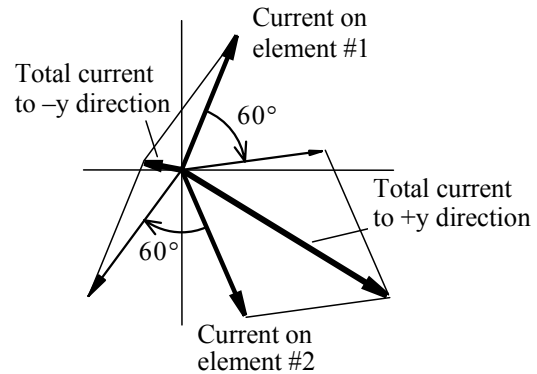


Fig. 12. Current on each element and synthesized currents toward $+y$ and $-y$ directions at 2.45 GHz, $d=20.6$ mm, $L1=54.6$ mm, $L2=50.2$ mm, FB ratio = 15.3 dB.

IV. CONCLUSION

Two element phase array of dipole antennas with 90° phase difference feed has been analyzed numerically and experimentally. In the spatially phase controlled antennas such as Yagi-Uda antenna and ESPAR antenna, the feed point current on each element is easily controlled. However, it is difficult in the proposed antenna due to the mutual coupling between two elements. By adjusting the length of each element and the distance between the two elements, the front-to-back ratio of 15.3 dB have been obtained.

Although the proposed antenna has a simple structure, it has the unidirectional radiation characteristics. This antenna array configuration can be a promising element antenna for base station antennas of short-range wireless communication systems.

REFERENCES

- [1] H. Yagi, "Beam transmission of ultra-short waves," *Proc. IRE*, vol. 16, p. 715, 1928.
- [2] T. Ohira and K. Gyoda, "Electronically steerable passive array radiator antennas for low-cost analog adaptive beam-forming," *Proc. IEEE International Conference on Phased Array Systems and Technology*, pp. 101-104, May 2000.
- [3] M. Taguchi, K. Era, and K. Tanaka, "Two element phased array dipole antenna," *Proc. on the 22th Annual Review of Progress in Applied Computational Electromagnetics*, 15-5, March 2006.
- [4] "WIPL-D Pro v5.1 User's Manual," WIPL Ltd., 2004.

- [5] R. J. Weber: “*Introduction to Microwave Circuits*”, pp.322-324, IEEE Press, 2001.
- [6] K. Era, K. Tanaka, and M. Taguchi, “2 Element phased array dipole antenna,” *ITE Technical Report*, BCT2005-131, Oct. 2005 (*in Japanese*).



Mitsuo Taguchi received his B. E. and M. E. degrees from Saga University, Japan in 1975 and 1977, respectively, and a Dr. Eng. Degree from Kyushu University Japan in 1986. From 1977 to 1987, he was a Research Associate at Saga University.

Since 1987 he has been an Associate Professor at Nagasaki University. In 1996 he was a visiting researcher at the Department of Electrical Engineering at the University of California, Los Angeles. His research interests are the small antenna for mobile communication and UWB antennas. Dr. Taguchi is a member of ACES, IEEE, the Institute of Electronics, Information and Communication Engineers of Japan, the Institute of Electrical Engineers of Japan and the Institute of Image Information and Television Engineers of Japan.



Kotaro Era received his B. E. and M. E. degrees from Nagasaki University, Japan in 2004 and 2006. From 2004 to 2006, he has studied on the directional antenna in the Graduate School of Science and Technology, Nagasaki University. Since 2006, he joined Murata Manufacturing Company, Ltd, Nagaokakyo, Japan.



Kazumasa Tanaka received his B. S., M. S. and Dr. E. degrees in Electronic Communication Engineering, in 1965, 1967, and 1975, respectively, all from Kyushu University, Japan. Since 1981, he has been a professor at Nagasaki University. His main areas of interest are the diffraction of optical beams, the detection of optical signals, and optical engineering. Dr. Tanaka is a member of the Japan Society of Applied Physics and Optical Society of America and the Institute of Electronics, Information and Communication Engineers of Japan.

Mixed Order Tangential Vector Finite Elements (TVFEs) for Tetrahedra and Applications to Multi-Functional Automotive Antenna Design

Tutku Karacolak and Erdem Topsakal

Department of Electrical and Computer Engineering
Mississippi State University,
Mississippi State, MS 39762, USA

Abstract — Mixed order tangential vector finite elements (TVFEs) of order 0.5, 1.5, and 2.5 for tetrahedra are presented and used in conjunction with an exact Finite Element-Boundary Integral (FE-BI) formulation. The main advantage of using mixed order elements is to reduce the computational complexity when solving large problems. As an illustrative example, a wide band antenna is designed and placed on an automobile. Results regarding the antenna return loss, far field pattern, axial ratio, and gain are presented.

I. INTRODUCTION

Printed microstrip patch antennas are widely used in wireless communications because they are low profile, low cost, and can easily be integrated with other circuitry. However, conventional patches find very few applications due to their narrow bandwidth. In the past, techniques have been proposed to overcome this bandwidth problem by using parasitic patches, stacked patches, and thick substrates [1]-[2]. Despite the advantages, these methods enlarge the antenna size either in the antenna plane or in the antenna height. Some other patch antennas investigated include E-shaped, spiral, tapered slot, and bow-tie [3]-[6]. E-shaped and square slot antennas are preferred for wideband and multi-band operations. They have been used in mobile and satellite communications, remote sensing, electronic warfare, and radar systems [7]-[10].

Another important application area is the design of multi-functional automotive antennas. Nowadays, satellite radio, navigation, and personal communication systems are standard features in many automobiles. These applications require a compact circularly polarized wideband antenna with decent gain and omni-directional characteristics. In this study, we propose the design of such antenna by using a square slot with an E-shaped tuning stub. The antenna has less than -10 dB return loss in the 0.8 GHz -3.35 GHz band and can be used for GPS, XM, GSM, and PCS systems. FE-BI software is used for simulations. Initial antenna results are validated with Ansoft's HFSS. In addition, the antenna is placed on the

automobile and simulations are carried out to observe the changes in the antenna parameters in the presence of the automobile.

II. FORMULATION

The finite element method boundary integral method (FE-BI) is known to be very accurate when analyzing antennas with fine geometrical details [11]. Using tetrahedral elements offers higher flexibility when simulating complex structures, and mixed-order tangential vector finite elements (TVFEs) guarantee tangential field continuity across element boundaries and suppress spurious modes [12].

In the past, mixed order TVFEs are proposed up to 1.5th order for a patch antenna backed by a dielectric filled rectangular cavity recessed in infinite ground plane [13]. Formulation used in [13] omits the edge effects and determines the unknown magnetic currents on the boundary and the electric fields inside the finite element domain. It is obvious that for a general radiation problem involving a complex structure such formulation will easily fail. An alternative exact formulation was introduced in [14]. In this formulation the FE-BI system is of the form

$$\begin{bmatrix} E_{vv} & E_{vs} & 0 \\ E_{sv} & E_{ss} & S \\ 0 & K & L \end{bmatrix} \begin{bmatrix} E_v \\ E_s \\ J \end{bmatrix} = \begin{bmatrix} V_v \\ V_s \\ V_j \end{bmatrix} \quad (1)$$

where E_v refers to the electric fields in the interior volume of the antenna and E_s is the sub-column for the surface fields. The J sub-column of unknowns contains the current density unknowns on the large metallic surface of the sub-structure. In the given system, the sub-matrices E_{ss} , E_{vv} , E_{sv} , and E_{vs} are sparse and can thus be treated efficiently in the context of an iterative solver. Their explicit form is known [14]. The time harmonic electric field is related to the time-dependent electric field by $E(x, y, z; t) = \Re\{\bar{E}(x, y, z)e^{j\omega t}\}$ where $j = \sqrt{-1}$. They are extracted by discretizing the functional

$$F(\mathbf{E}) = \frac{1}{2} \int_v \left[\frac{1}{\mu_r} (\nabla \times \vec{E}) \cdot (\nabla \times \vec{E}) - k_0^2 \epsilon_r \vec{E} \cdot \vec{E} \right] dv. \quad (2)$$

For Magnetic Field Integral Equation (MFIE) formulation, the elements of the matrix in (1) are obtained from the operators

$$L = \int_s ds \vec{t}(\vec{r}) \cdot \left[\int_s ds' \vec{G}(\vec{r}, \vec{r}') \cdot \vec{M}(\vec{r}') \right] \quad (3)$$

$$K = \int_s ds \vec{t}(\vec{r}) \cdot \left[\frac{1}{2} \vec{J}(\vec{r}) + \int_s ds' \vec{J}(\vec{r}') \times \nabla g(\vec{r}, \vec{r}') \right] \quad (4)$$

where

$$\vec{G}(\vec{r}, \vec{r}') = \left(\vec{I} + \frac{1}{k_0^2} \nabla \nabla' \right) g(\vec{r}, \vec{r}') \quad (5)$$

and

$$g(\vec{r}, \vec{r}') = \frac{e^{-jk_0|\vec{r}-\vec{r}'|}}{|\vec{r}-\vec{r}'|}. \quad (6)$$

Finally, the elements of the coupling matrix are obtained from

$$S = -ik_0 \int_s (\vec{E} \times \vec{H}) \cdot \hat{n} ds. \quad (7)$$

Elements and Basis Functions

We consider a tetrahedral element with nodes 1, 2, 3, and 4. The volume of the tetrahedron is denoted by V . The simplex coordinates ξ_1, ξ_2, ξ_3 , and ξ_4 at a point P are defined in the usual manner, where V_n denotes the volume of the tetrahedron formed by P and the nodes of the triangular face opposite to node n (Fig. 1).

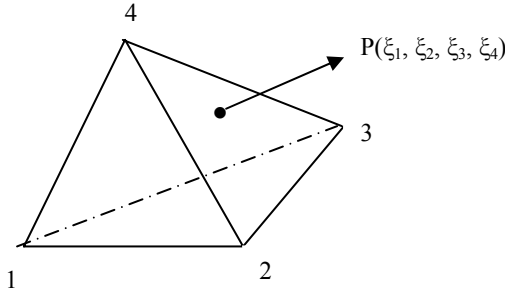


Fig. 1. Geometry of a tetrahedral element.

A mixed-order TVFE of order 0.5 is characterized by six linearly independent vector basis functions which are expressed as

$$\xi_i \nabla \xi_j - \xi_j \nabla \xi_i, i < j. \quad (8)$$

A mixed order TVFE of order 1.5 is characterized by 20 linearly independent vector basis functions in a hierarchical fashion. In addition to the six edge-based vector functions (8), it is characterized by the six edge-based vector basis functions

$$(\xi_i - \xi_j)(\xi_i \nabla \xi_j - \xi_j \nabla \xi_i), i < j \quad (9)$$

and the eight face-based vector basis functions

$$\xi_k (\xi_i \nabla \xi_j - \xi_j \nabla \xi_i), i < j < k \quad (10)$$

$$\xi_j (\xi_k \nabla \xi_i - \xi_i \nabla \xi_k), i < j < k. \quad (11)$$

A mixed order TVFE of order 2.5 is characterized by 45 linearly independent vector basis functions in a hierarchical fashion. In addition to the 12 edge-based vector functions (8)-(9) and eight face-based vector functions (10)-(11), it is characterized by the six edge-based vector basis functions

$$(\xi_i - \xi_j)^2 (\xi_i \nabla \xi_j - \xi_j \nabla \xi_i), i < j \quad (12)$$

16 face-based vector basis functions

$$\nabla (\xi_i \xi_j \xi_k), i < j < k \quad (13)$$

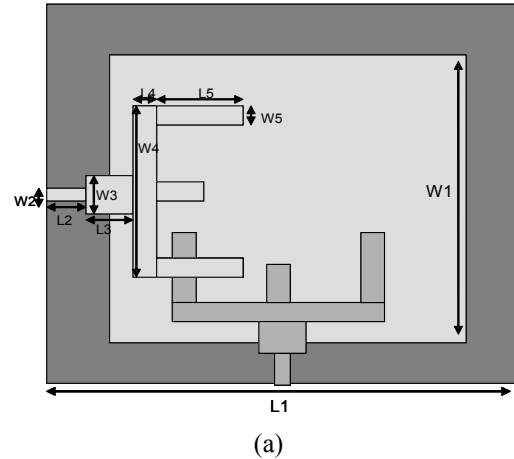
$$\xi_k^2 (\xi_i \nabla \xi_j - \xi_j \nabla \xi_i), i < j, i \neq j \neq k \neq i \quad (14)$$

and the three cell-based vector basis functions

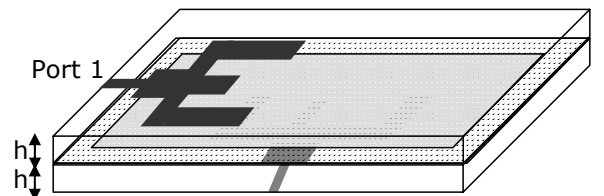
$$\xi_j \xi_k (\xi_i \nabla \xi_i - \xi_i \nabla \xi_i), i, j, k > 1, i \neq j \neq k \neq i, j < k. \quad (15)$$

III. ANTENNA GEOMETRY

The top and side views of the antenna are shown in Fig. 2a and Fig. 2b, respectively. The antenna consists of a square slot placed between two substrates of the same material.



(a)



(b)

Fig. 2. a) Top and b) Side view of the antenna.

Two E-shaped patches are printed orthogonally (one on the top and one on the bottom of the antenna) and connected to two orthogonal microstrip feed lines. Through proper selection of the parameters of the E-shaped tuning stub, it is expected that the coupling between the microstrip line and the printed wide slot can be controlled more effectively. When dimensions of the E-shaped tuning stub change, the coupling changes and the antenna has different resonance characteristics.

The design maintains a high degree of polarization isolation and employs a symmetric feeding structure. The antenna is a bi-directional radiator, and the radiation patterns on both sides are approximately the same. Moreover, circular polarization is obtained by simultaneous excitation. Neltec NH 9300 ($\epsilon_r=3$, $\tan\delta=0.0023$) with a thickness of 1.27 mm is used for the substrate material. The dimensions of the antenna and the antenna specifications are given in Table 1 and Table 2, respectively. Antenna was designed using a trial-and-error approach.

Table 1. The dimensions of the designed antenna.

	Antenna Dimensions
L1	75 mm
L2	6 mm
L3	8.5 mm
L4	3 mm
L5	12 mm
L6	6 mm
W1	57 mm
W2	1.18 mm
W3	5 mm
W4	33 mm
W5	3 mm
h	1.27 mm

IV. NUMERICAL RESULTS

A. Square Slot Antenna

The return loss comparison of the antenna between FE-BI method and HFSS for Port 1 is shown in Fig. 3. Both simulations have very similar characteristics. The HFSS simulation show that the antenna operates in the band 0.8 GHz – 3.35 GHz with a 10 dB bandwidth of 123%. Similarly, according to FE-BI result the band extends from 0.74 GHz to 3.02 GHz with a bandwidth of 121%. Thus, it can be used for GPS (1.227 GHz and 1.575 GHz), XM (2.332 GHz-2.345 GHz), GSM (890 MHz-915 MHz and 935 MHz-960 MHz), and PCS (1.85 GHz-1.99

GHz and 2.18 GHz-2.20 GHz) bands. All FE-BI simulations are done by using 1.5 and 2.5 order elements throughout the entire finite element domain.

Table 2. Square slot antenna specifications.

	Antenna Specifications
Frequency Range	0.8 GHz–3.35 GHz
Impedance	50 ohms
Return Loss	Less than -10 dB
Polarization	Circular
Axial Ratio	Less than 3 dB
Gain	2 dB
VSWR(min performance)	Less than 2:1 Nominal

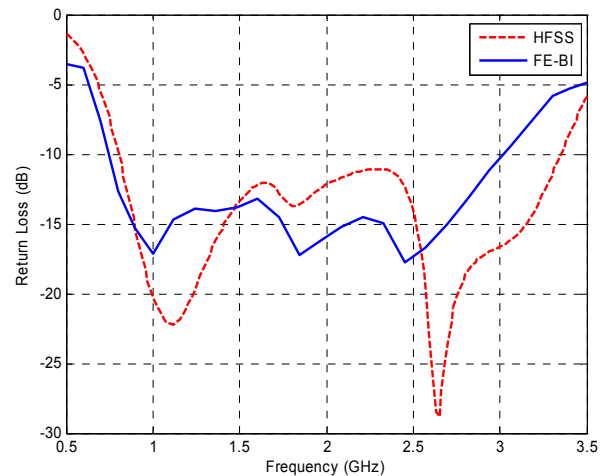


Fig. 3. Return loss of the antenna for Port 1.

S11 and S22 are also very similar due to the symmetry of the ports as shown in Fig. 4. The VSWR and the peak gain of the antenna when only Port 1 is excited are shown in Fig. 5 and Fig. 6. The VSWR level is below “2” throughout the entire band, and reasonable gain flatness around 2 dB is obtained until 2.8 GHz.

Figure 7 shows the calculated axial ratio of the antenna. The antenna provides circular polarization in two bands of 0.8 GHz - 1.9 GHz and 2.8 GHz - 3.35 GHz with 3 dB bandwidths of 95% and 25%, respectively. Axial ratios computed on the x-z and y-z planes at GPS frequencies

(1.227 GHz and 1.575 GHz) are shown in Fig. 8a and Fig. 8b. The axial ratio is less than 3 dB around the z-axis which is the main direction of radiation.

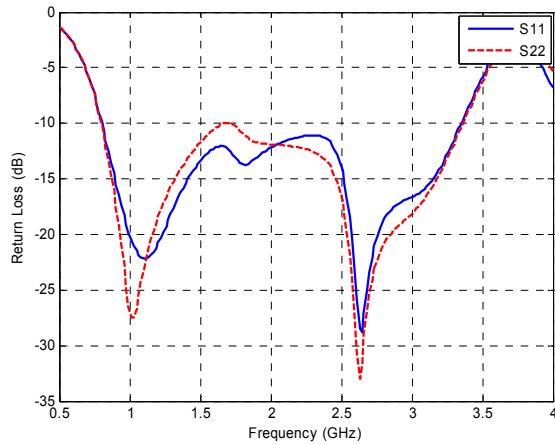


Fig. 4. S11 and S22.

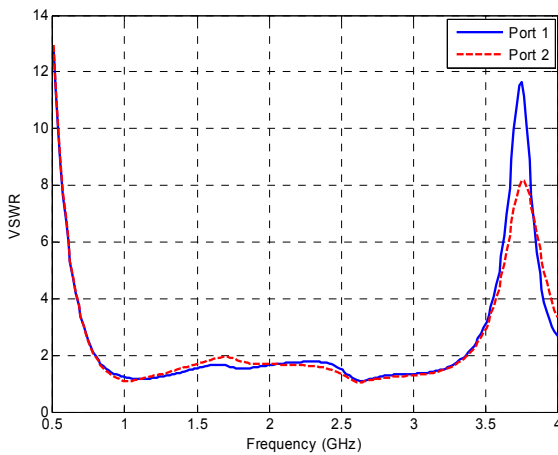


Fig. 5. VSWR for both ports.

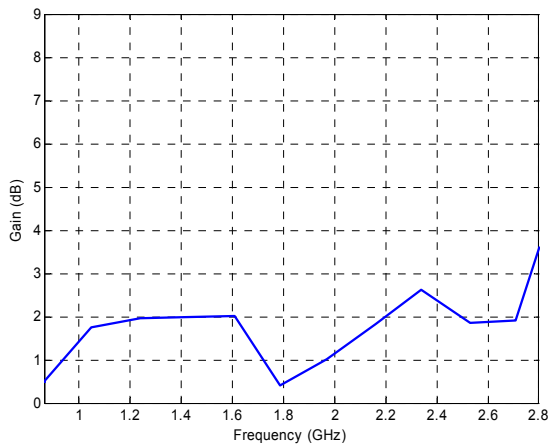


Fig. 6. Peak gain when only Port 1 is excited.

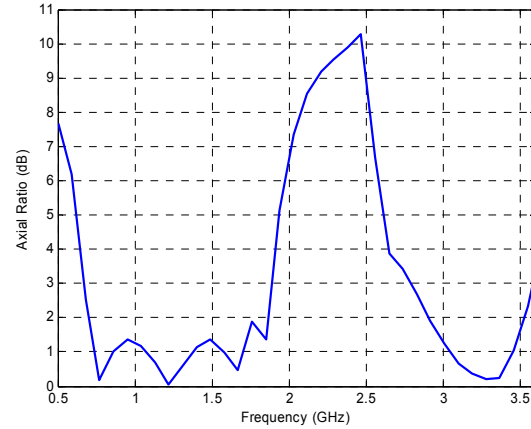
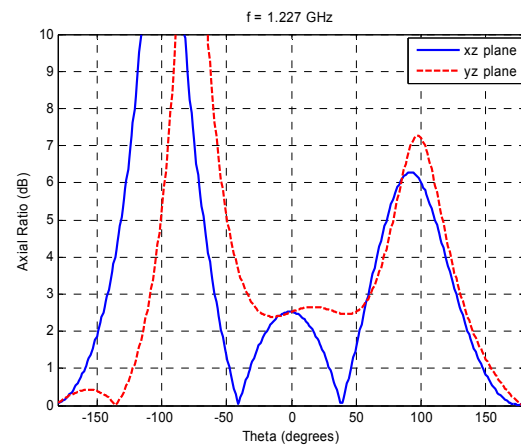
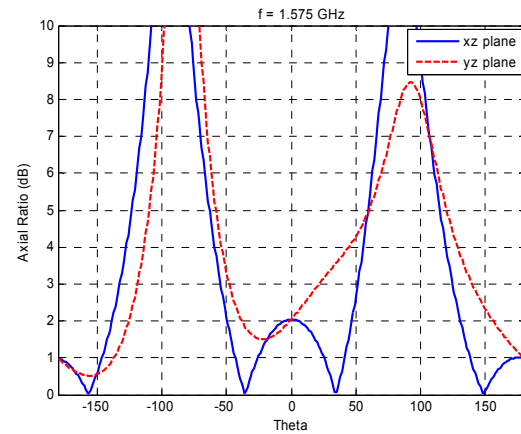


Fig. 7. Axial ratio.



(a)



(b)

Fig. 8. Axial ratio on (x-z) and (y-z) planes at a) 1.227 GHz and b) 1.575 GHz.

Figure 9 shows the far field radiation patterns of the antenna on the x-z and y-z planes. E-phi and E-theta components for both planes are calculated at 0.8 GHz, 1.575 GHz, 2.34 GHz, and 3 GHz. It is apparent from the plots that the antenna has omni-directional radiation

characteristics. The cross polarized fields deteriorate as the frequency increases.

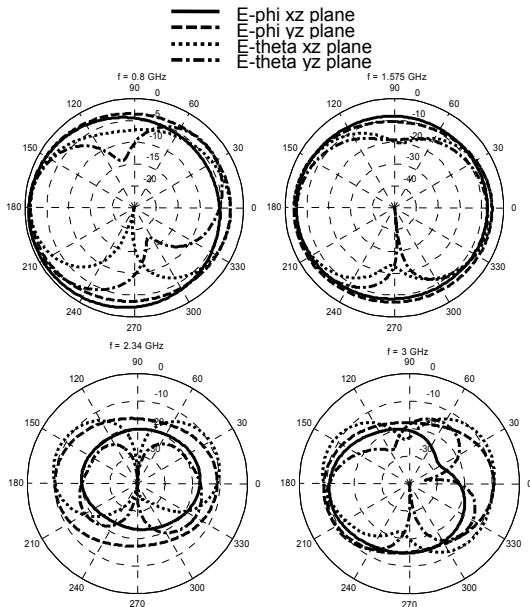


Fig. 9. Radiation patterns of the antenna shown in Fig. 2 on x-z and y-z planes at 0.8 GHz, 1.575 GHz, 2.34 GHz, and 3 GHz.

B. Automotive Applications

Figure 10a, Fig. 10b, Fig. 10c, and Fig. 10d show the antenna on the roof, trunk, 4-door automobile, and convertible automobile meshes, respectively. The length, width, and height of the problems at 3 GHz are also given. In order to reduce the number of unknowns 0.5 order elements are used for the regions further away from the antenna while 1.5 and 2.5 order elements are employed in the vicinity of the antenna.

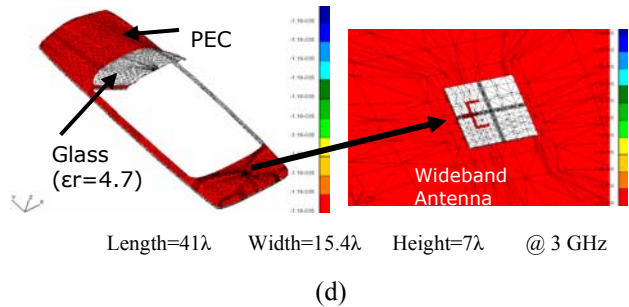
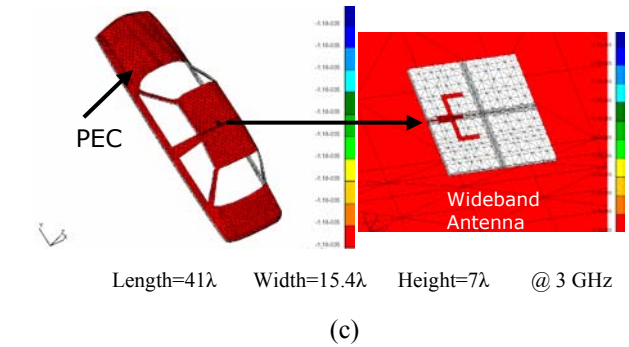
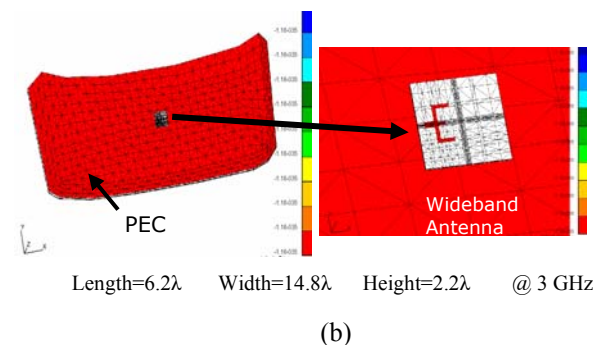
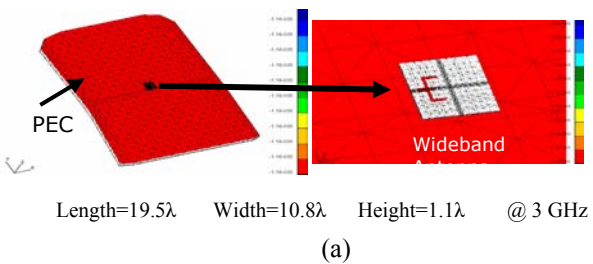


Fig. 10. Square slot antenna on the a) Roof, b) Trunk, c) Whole 4-Door Automobile, and d) Whole Convertible Automobile.

Table 3 shows the number of FE and BI unknowns and total solution time for each problem when combination of 0.5 and 2.5 order elements, and 2.5 order elements alone, are used. The residual error is kept constant for both solutions. BICGSTAB (*l*) algorithm is used for the iterative solver which is superior to other solvers for antenna analysis [15]. As clearly seen from Table 3, mixed order elements improve the solution time and reduces the memory. In BICGSTAB (*l*) algorithm *l*=4 is used for the simulations. In addition, the convergence characteristics of each problem are shown in Fig. 11, Fig. 12, Fig. 13, and Fig. 14, respectively.

Table 3. The number of FE and BI unknowns and total solution time for each problem.

	Total FE Unknowns	Total BI Unknowns	Total Solution Time (sec)
Roof	5473 (0.5+2.5) 37,825 (2.5)	4880 (0.5+2.5) 14,362 (2.5)	2,664 52,872
Trunk	4,721(0.5+2.5) 30,523(2.5)	3,860 (0.5+2.5) 11,312(2.5)	9,636 73,467
4-Door Automobile	9,756(0.5+2.5) 67,312(2.5)	11,400(0.5+2.5) 33,113(2.5)	4,3450 123,543
Convertible Automobile	10688(0.5+2.5) 74,561(2.5)	10980(0.5+2.5) 32,452(2.5)	24,491 137,687

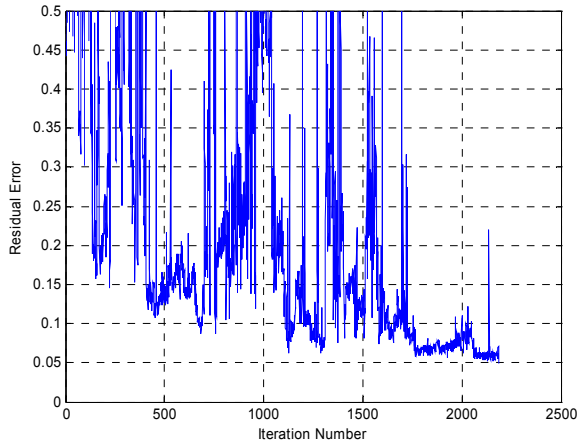


Fig. 11. Convergence behavior of the antenna on the roof.

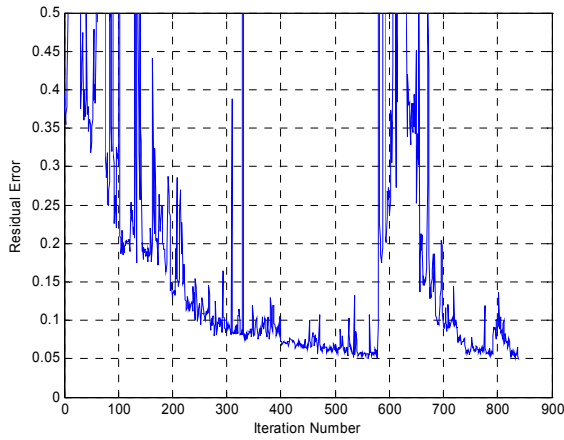


Fig. 12. Convergence behavior of the antenna on the trunk.

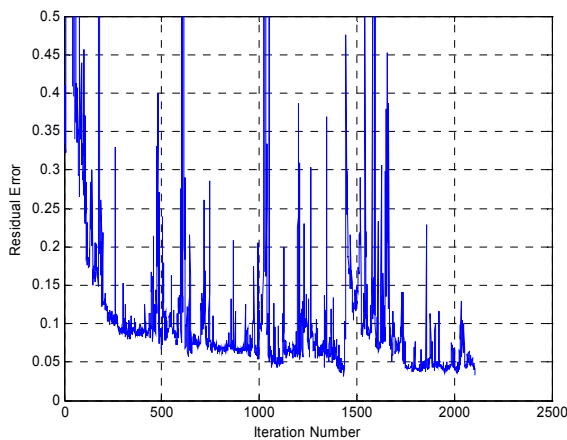


Fig. 13. Convergence behavior of the antenna on the 4-Door automobile.

polarization levels for the antenna on the roof and trunk are lower than the antenna alone, the difference is very small around the main direction of radiation (z-axis). Moreover, the cross polarization levels of the antenna on the trunk are lower than the antenna.

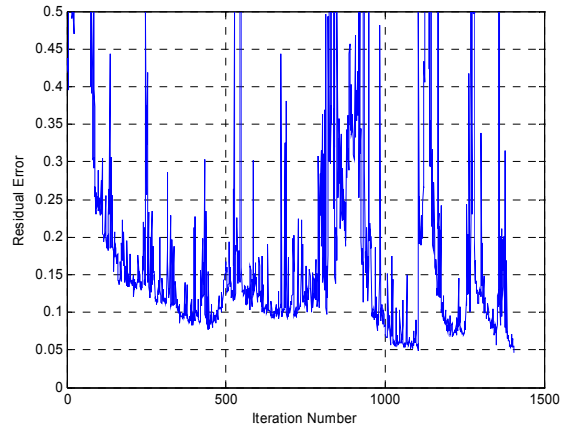


Fig. 14. Convergence behavior of the antenna on the convertible automobile.

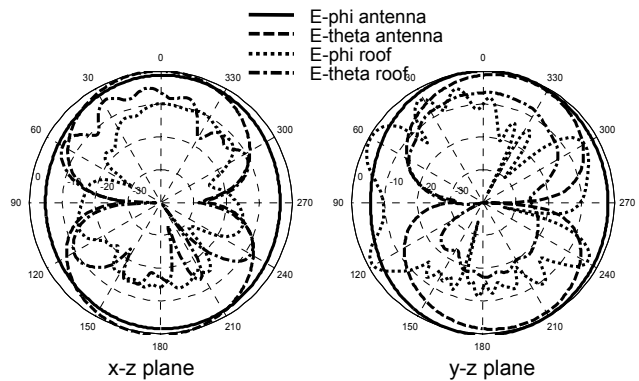


Fig. 15. Radiation pattern comparison of the antenna alone and the antenna on the roof at GPS.

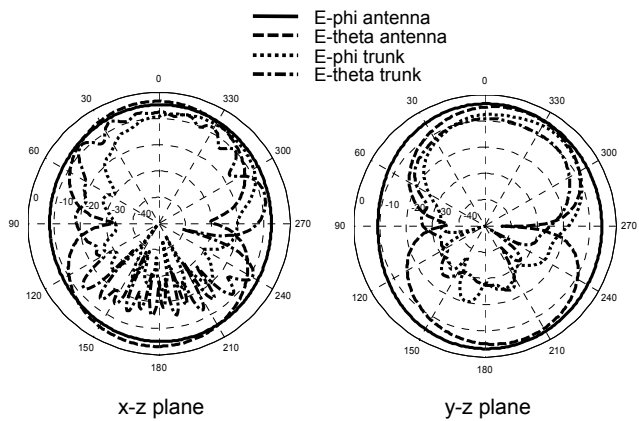


Fig. 16. Radiation pattern comparison of the antenna alone and the antenna on the trunk at GPS.

Figure 15 and Fig. 16 show the similar radiation characteristics of the antenna and the antenna on the roof and on the trunk at GPS, respectively. Although the co-

Figure 17 and Fig. 18 show the radiation pattern comparisons of the antenna and the antenna on the 4-Door and convertible automobiles. The co-polarization patterns are very similar in both cases. Especially, E-phi patterns on the y-z plane have very close values. The saw-like pattern for the automobiles is actually an expected case. Besides that, the y-z plane is wider than the x-z plane and the automobiles have more deteriorated cross-polarization patterns.

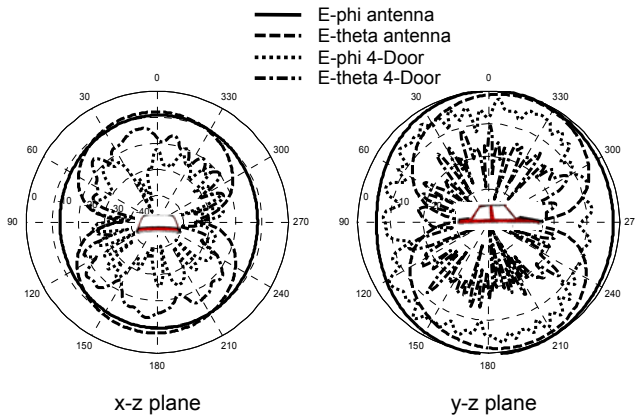


Fig. 17. Radiation pattern comparison of the antenna alone and the antenna on the 4-Door automobile at GPS.

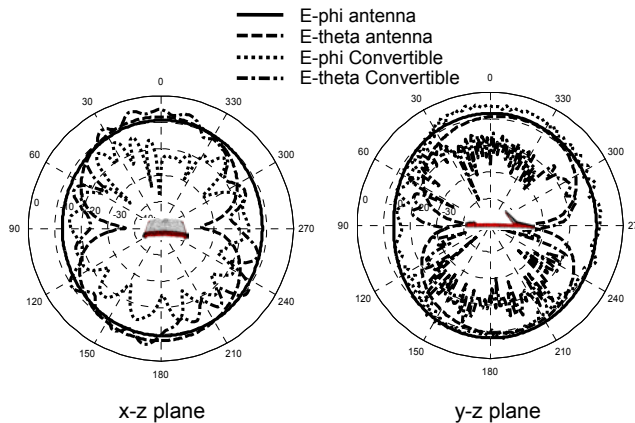


Fig. 18. Radiation pattern comparison of the antenna alone and the antenna on the convertible automobile at GPS.

V. CONCLUSION

A set of hierarchical mixed-order TVFEs for tetrahedral elements up to and including 2.5 order are proposed. A wide band square slot antenna with an E-shaped tuning stub is designed using FE-BI method that employs the presented mixed order TVFEs. The antenna operates in the band 0.8 GHz – 3.35 GHz. The antenna has an average gain of 2 dB and provides circular polarization.

ACKNOWLEDGMENT

The work reported herein was funded in part by the High Performance Computing Visualization Initiative under a contract from the Department of Defense.

REFERENCES

- [1] G. Kumar and K. C. Gupta, "Directly coupled multiple resonator wide-band microstrip antenna," *IEEE Trans. Antennas Propagat.*, vol. AP-33, pp. 588-593, June 1985.
- [2] D. M. Pozar, "Microstrip antenna coupled to a microstrip-line," *Electron. Lett.*, vol. 21, no. 2, pp. 49-50, Jan. 1985.
- [3] J. Gong and J. L. Volakis, "Parametric study and design of slot-spiral antennas using an FE-BI antenna code," *Antennas and Propagation Society International Symposium*, vol. 3, pp. 2046 – 2049, 21-26 July 1996.
- [4] Q. Shen, B. L. Ooi, and M. S. Leong, "A novel E-shaped broadband microstrip patch antenna," *Piers2000 Proceedings*, pp. 621, July 5th – July 14th, 2000, Boston, USA.
- [5] J. Thaysen, K. B. Jakobsen, and H. R. Lenler-Eriksen, "Wideband cavity backed spiral antenna for stepped frequency ground penetrating radar," *Antennas and Propagation Society International Symposium*, vol. 1B, pp. 418 – 421, 3-8 July 2005.
- [6] E. Gschwendtner, J. Parlebas, and W. Wiesbeck, "Spiral antenna with frequency-independent coplanar feed for mobile communication systems," *Antennas and Propagation Society International Symposium*, vol. 1, pp. 560 – 563, 11-16 July 1999.
- [7] F. Yang, X. X. Zhang, X. Ye, and Y. Rahmat-Samii, "Wide-band E-shaped patch antennas for wireless communications," *IEEE Trans. Antennas Propagat.*, vol. 49, no. 7, pp. 1094-1100, July 2001.
- [8] Y. Ge, K. P. Esselle, and T. S. Bird, "Broadband E-shaped patch antennas for 5-6 GHz wireless computer networks," *IEEE Antennas Propagat. Soc. Int. Symp. Dig.*, Columbus, OH, USA, June 2003, pp. II: 942-945.
- [9] A. A. Eldek, A. Z. Elsherbeni, and C. E. Smith, "Dual-Wideband Square Slot Antenna with a U-Shaped Printed Tuning Stub for Personal Wireless Communication Systems," *Progress in Electromagnetics Research*, vol. 53, pp. 319-333, 2005.
- [10] J. Y. Sze and K. L. Wong, "Bandwidth Enhancement of a Microstrip-Line-Fed Printed Wide-Slot Antenna," *IEEE Trans. Antennas Propagat.*, vol. 49, no. 7, pp. 1020-1024, July 2001.
- [11] J. L. Volakis, A. Chatterjee and L. Kempel, "Finite Element Methods for Electromagnetics," *IEEE Press*, 1998.

- [12] T. Karacolak and E. Topsakal, "Hierarchical Tangential Vector Finite Elements for Tetrahedra," *IEEE AP-S International Symposium and USNC/URSI Meeting*, 3-8 July 2005.
- [13] L. S. Andersen and J. L. Volakis, "Accurate and efficient simulation of antennas using hierarchical mixed-order tangential vector finite elements for tetrahedral," *IEEE Trans. Antenna Propagat.*, vol. 47, pp. 1240-1243, August 1999.
- [14] R. X. Q. Sheng, J. M. Jin, J. M. Song, C. C. Lu, and W. C. Chew, "On the formulation of hybrid finite-element and boundary-integral method for 3D scattering," *IEEE Trans. Antennas Propagat.*, vol. 46, no. 3, pp. 303-311, March 1998.
- [15] E. Topsakal, R. Kindt, K. Sertel, and J. Volakis, "Evaluation of the BICGSTAB(l) Algorithm for the Finite Element Boundary Integral Method," *IEEE Antennas Propagat. Magazine*, vol. 43, no. 6, pp. 124-131, December 2001.



Tutku Karacolak received the B.S. degree in electrical and electronics engineering from Bilkent University, Ankara, Turkey, in 2004, the M.S. degree in electrical engineering from Mississippi State University, Starkville, MS, in 2006, and is currently working toward the Ph.D. degree in electrical engineering at the Mississippi State University. His research interests are implantable antennas, numerical methods, antenna analysis and design.



Erdem Topsakal was born in Istanbul, Turkey in 1971. He received his BSc. degree in 1991, M.Sc. degree in 1993 and PhD degree in 1996 all in Electronics and Communication Engineering from Istanbul Technical University. He worked as an Assistant Professor in Electrical and Electronics Engineering Department at Istanbul Technical University between 1997 and 1998. He was a post doctoral fellow from 1998 to 2001 and an assistant research scientist from 2001 to July 2003 in Electrical Engineering and Computer Science Department of the University of Michigan. In August 2003, he joined the Electrical and Computer Engineering Department of James Worth Bagley College of Engineering at Mississippi State University as an Assistant Professor. His research areas include implantable antennas, electromagnetic theory, numerical methods, fast methods, antenna analysis and design, frequency selective surfaces/volumes, electromagnetic coupling and interference, direct and inverse scattering. He has published over 70 journal and conference papers in these areas. He received the URSI young scientist award in 1996 and NATO fellowship in 1997. He is a senior member of IEEE and an elected member of the URSI commissions B and K. He currently serves as the Vice Chair of the Mississippi Academy of Sciences and Associate Editor in Chief of the ACES journal.

Modeling and Analysis of a Dual-Band Dual-Polarization Radiator Using FEKO

Amir I. Zaghoul¹, C. Babu Ravipati², and M. T. Kawser¹

¹Bradley Department of Electrical and Computer Engineering
Virginia Polytechnic Institute and State University, ARI, Arlington, VA 22203
amirz@vt.edu, mkawser@vt.edu

²Applied EM, Inc., Hampton, VA 23666
babu@appliedem.com

Abstract — A dual-band hybrid antenna element comprising of microstrip and waveguide radiating elements is theoretically investigated through computer simulations. The low band radiator is a Shorted Annular Ring (SAR) microstrip antenna and the high band antenna is an open ended circular waveguide. First, the characteristics of a SAR patch antenna are presented and reviewed. Then the dual-band antenna configuration is described, which is realized by forming a waveguide radiator in the shorted region of the SAR microstrip antenna. Modeling and analysis of the SAR patch antenna and the hybrid element are investigated using the method-of-moment-based software package FEKO. The analysis includes return loss computations showing the element bandwidth at different frequency bands and the radiation patterns in the E- and H- planes. Feeding the element in phase quadrature produces circular polarizations (CP). The radiation patterns of the CP dual-band element are also analyzed using FEKO and the axial ratio performance is subsequently assessed.

I. INTRODUCTION

Dual-band antennas operating from a single aperture are desired in several modern communications, satellite communications, remote sensing, and multi-function radar systems. Providing multiple antennas to handle multiple frequencies and polarizations becomes especially difficult if the available space is limited (as with airborne platforms and submarine periscopes). Few techniques are currently available to achieve such dual band operation with microstrip antennas [1]. A rectangular patch can be operated at dual bands using the first resonance of the two orthogonal dimensions of the rectangular patch, which are the TM_{100} and TM_{010} modes. The frequency ratio is roughly equal to the ratio between the two orthogonal sides of the patch. Multiple radiation elements are also used for operation

at dual bands. A third popular approach is the introduction of reactive loading to a single patch.

The orthogonal mode patch can have simultaneous matching of the input impedance at the two frequencies with a single feed structure. But then it gives two orthogonal polarizations from the two frequencies. A probe-fed patch can be used to accomplish this approach where the location of the probe is displaced from the two principal axes of the patch. Slot coupling can also be used to implement single feed dual matching.

The dual band operation can also be achieved using multiple radiating elements. In this case, each of the radiating elements supports strong currents and radiation at its resonance frequency. This category includes multilayer stacked patches. This approach can also be used to broaden the bandwidth of a single band antenna when the two frequencies are forced to be closely spaced. Multi-band antennas can also be obtained by printing more resonators on the same substrate.

Another popular technique for obtaining a dual band operation is the use of reactively loaded patch. A stub can be connected to one radiating edge of the patch so as to create a further resonant length for another operating frequency. The radiating edge can also be loaded with an inset or a spur-line. However, if a higher value of the frequency ratio is intended then shorting vias or lumped capacitors can be used between the patch and the ground plane. Etching slots on the patch can also introduce reactive loading.

A dual band element is presented in this paper and uses a hybrid of microstrip and waveguide radiators each resonating at a different frequency [2]. The hybrid antenna is realized by forming an open ended waveguide in the shorted region of a Shorted Annular Ring (SAR) microstrip antenna [3]. The SAR microstrip antenna acts as the low band radiator and the open ended waveguide acts as the high band radiator.

The upper to lower frequency ratio can be controlled by the proper choice of various dimensions and dielectric material. Operation in both linear and circular polarization is possible in either band. Moreover, both broadside and conical beams can be generated in either band from this antenna element. The following sections present a modeling and analysis of this dual band antenna element using the moment-based software package FEKO [4].

II. MODELING OF SHORTED ANNULAR RING (SAR) PATCH ANTENNAS

Annular ring and rectangular or square ring are popular geometries for microstrip antennas. They have one more design variable than the conventional circular patch, which is the inner dimension. Both inner and outer dimensions can be used to control the resonant frequency of the patch. They also generally offer greater impedance bandwidth. If the patch is shorted at the inner radius of the annular ring, the element is called Shorted Annular Ring (SAR) patch and it can offer some special advantages. Similar shorting at the inner dimension of the rectangular or square ring produces the same properties. The configurations of the circular and square versions of the SAR element are shown in Figure 1.

The SAR microstrip antenna was first investigated by Goto's group [5-6] for dual frequency use and subsequently as a circular polarization self-diplexing antenna [7] for mobile communications. Lin and Shafai [8] have used cavity method to analyze the characteristics of TM_{11} as well as TM_{21} modes of SAR patch antenna. Iwasaki and Suzuki investigated an electromagnetically coupled shorted patch antenna [9] and Boccia, et al. reported GPS application of elliptical annular microstrip antenna [10].

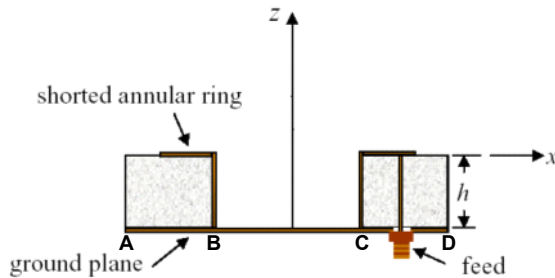


Fig. 1. Shorted annular ring (SAR) microstrip antenna.

To reduce the mutual coupling between the SAR in array environments, the surface waves propagating along the array structure has to be reduced. Jackson, et al. [3] showed that reduced surface wave excitation can be achieved by proper choice of the inner and outer radii of a SAR microstrip antenna. Therefore, if SAR

microstrip antenna is designed accordingly, it is then called Shorted Annular Ring Reduced Surface Wave (SAR-RSW) microstrip antenna. The relationship between the outer radius a and inner radius b at resonance is

$$J'_n(ka)Y_n(kb) - J_n(kb)Y'_n(ka) = 0 \quad (1)$$

where J_n and Y_n are the Bessel functions of the first and second kind. If the values of a , b , and the substrate dielectric constant ϵ_r are given, the frequency can be varied and a number of roots can be determined for $n = 0, 1, 2, \dots$. This gives the different resonant modes of operation of the SAR microstrip antenna.

Table 1. Resonant frequency using FEKO and equation (1).

Inner/Outer radius	Res. freq. (GHz) from FEKO	Res. freq. (GHz) from equation 1
0	2.82	2.77
0.1	2.87	2.82
0.2	3.02	2.98
0.3	3.29	3.25
0.4	3.68	3.66
0.5	4.29	4.28

A simulation of the SAR element was performed using FEKO for $\epsilon_r = 2.5$, $h = 1.5$ mm, and $a = 19.2$ mm. Table 1 compares the resonant frequency results using FEKO and equation (1). The broadside radiation patterns in the E- and H-planes were also computed using FEKO and the results are shown in Figure 2 for different inner/outer radius ratios.

Another interesting feature of the SAR antenna is that the lowest order mode produces a conical radiation pattern unlike the conventional microstrip antennas. This result was first reported by Goto [6] for use as a planar conical beam antenna, but this feature has not received attention. With suitable choice of outer and inner radii, a single feed antenna design, which produces conical pattern at lower frequency and broadside pattern at higher frequency, can be realized. Figures 3 and 4 present the return loss and radiation patterns, respectively, calculated using the full-wave MoM simulation FEKO for an optimized SAR antenna producing conical (at 3.85 GHz) and broadside (at 5.0 GHz) patterns from a single point feed. The peak directivity of the monopole-like pattern is 3.0 dB at about 15° from the horizon and that of the broadside mode is 8.0 dB. The bandwidth (in terms of -10 dB return loss) is about 2% and 3%, respectively, for conical and broadside modes.

Conical patterns are typically generated using higher order mode excited circular microstrip antennas [11-12]. A TM_{21} excited circular microstrip resonating at 3.85 GHz requires a radius of 20 mm. On the other hand, the radius of SAR patch antenna resonating at the same frequency is 13.7 mm, which is 25% less in size. A comparative study of compact circular microstrip antennas producing conical patterns was presented in [12].

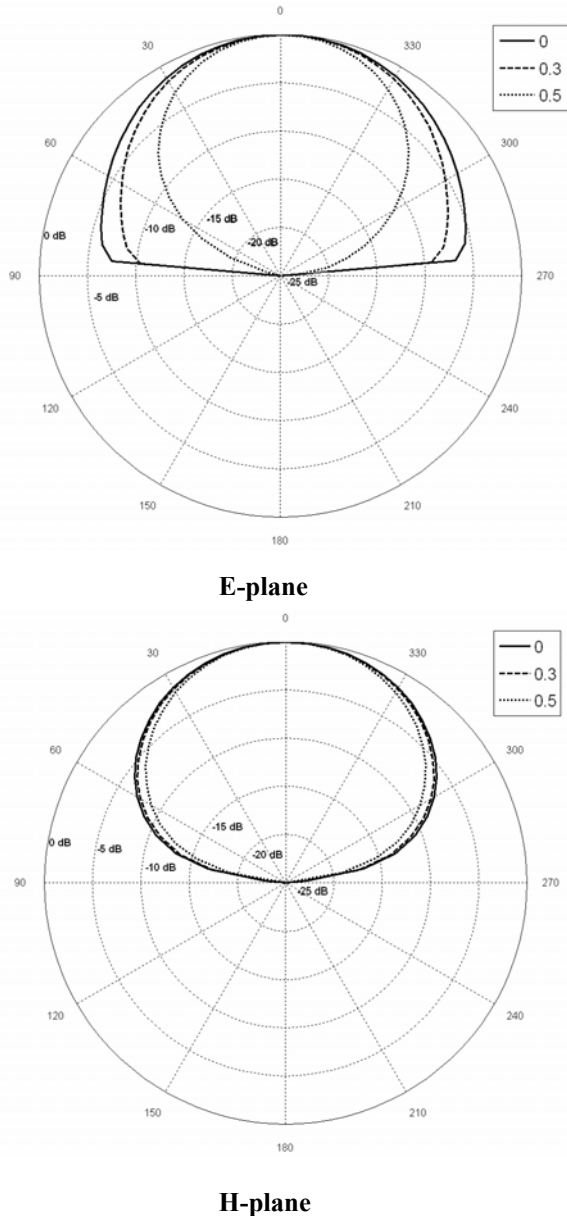


Fig. 2. E- and H- plane patterns of SAR element for different inner/outer radius ratios.

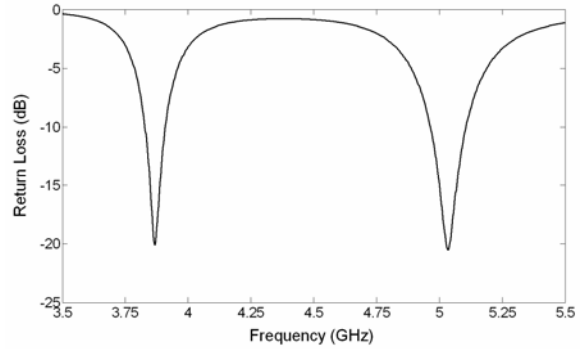


Fig. 3. Computed return loss of optimized SAR antenna; Parameters: $a=13.4$ mm, $b=4.7$ mm, $h=1.5$ mm, $\epsilon_r=2.35$.

III. MODELING OF LINEARLY POLARIZED HYBRID DUAL BAND RADIATOR

The hybrid dual band element uses the annular or square ring as the low-frequency radiator in consistence with the SAR-RSW patch design. Figure 5 shows circular and square configurations for the hybrid dual-band element. The ground plane in its shorted annular region at the center creates an aperture that can be used as an open-ended waveguide radiator and can be designed to operate at the higher frequency band. The dimensions and dielectric materials of the SAR patch antenna and the waveguide radiator are appropriately chosen for the required dual band operation. The cut-off frequency of the dominant mode for the waveguide defines its higher band frequency. In general, the cut-off frequency of the dominant mode is far above the lower band frequency. Thus, the waveguide acts as a high pass filter in the lower band and yields good isolation between the ports. Although the dimension of waveguide is fixed, the higher band frequency can be reduced by dielectric loading the waveguide. The cut-off frequency can be changed to a desired value by loading of the waveguide with dielectric material of appropriate permittivity.

As in the SAR element, the hybrid antenna can be operated for a conical radiation pattern in either band. The lowest resonant mode of the SAR microstrip antenna is TM_{01} , which produces a conical radiation pattern. If the SAR microstrip antenna dimension is designed such that the resonant frequency in TM_{01} mode becomes the desired frequency, the antenna will produce a conical beam in the lower band. In order to generate a conical radiation pattern in the higher band, an appropriate feed design in the waveguide is required to generate higher order modes, which will produce conical radiation patterns.

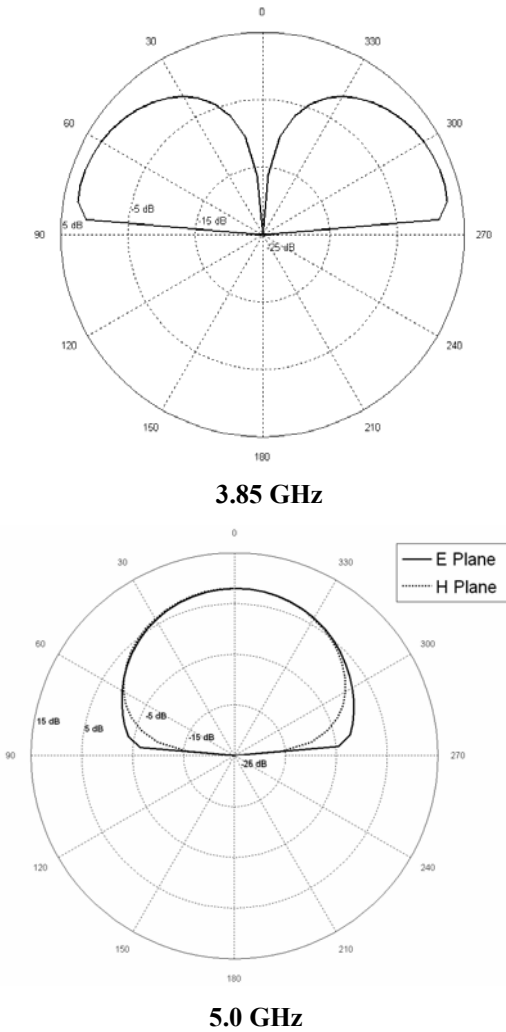


Fig. 4. Computed radiation pattern at 3.85 GHz and 5.0 GHz; Parameters: $a=13.4$ mm, $b=4.7$ mm, $h=1.5$ mm, $\epsilon_r=2.35$.

The circular hybrid element, comprising of an annular ring and a circular open-ended waveguide, was simulated using FEKO for insertion losses, radiation patterns, and port-to-port isolation at the two frequency bands. The simulation model is shown in Figure 6. The return loss at the lower frequency band is shown in Figure 7 indicating a -10 dB return loss of 3%. Figures 8 shows radiation patterns at the lower and higher frequencies of 3.0 GHz and 7.3 GHz for a circular element of parameters: $a = 27.8$ mm, $b = 13.9$ mm, $\epsilon_r = 2.2$, and $h = 2.54$ mm. At 3 GHz, the calculated peak directivity is 8.8 dB and the 3 dB beam widths are 55° and 63° in the E- and H- planes, respectively. The dual-band antenna produces a peak directivity of 9.5 dB and beam widths of 33° (E-plane) and 48° (H-plane) at 7.3 GHz. The higher frequency represents a margin of 16% over the cut-off frequency of 6.3 GHz for the air-filled circular waveguide.

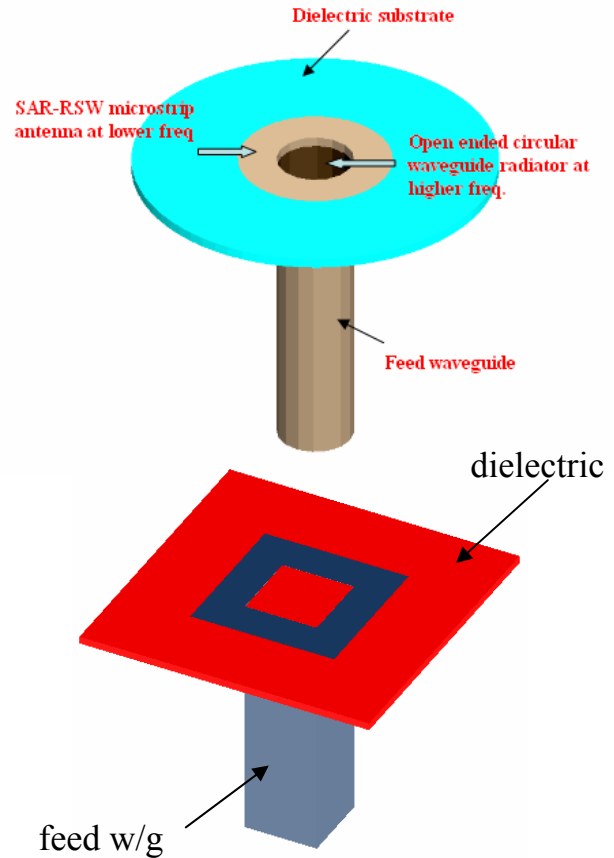


Fig. 5. Circular and square configurations for the hybrid dual-band element.

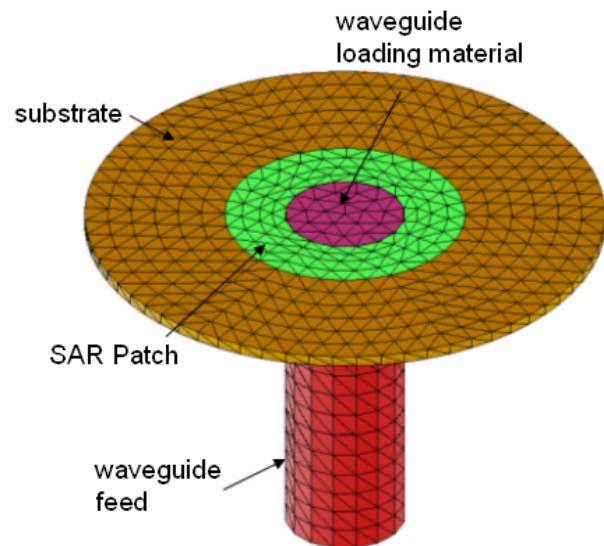


Fig. 6. Modeled dual-band antenna using FEKO.

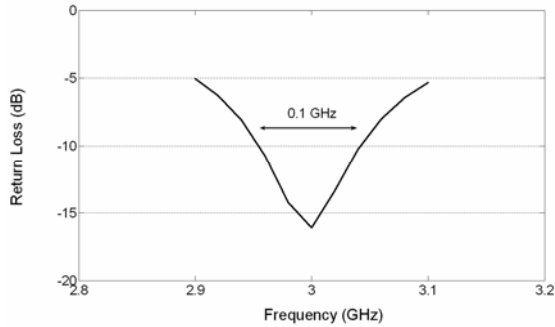


Fig. 7. Computed return loss of dual-band antenna at lower frequency; Parameters: $a=27.8$ mm, $b=13.9$ mm, $h=2.54$ mm, $\epsilon_r=2.2$.

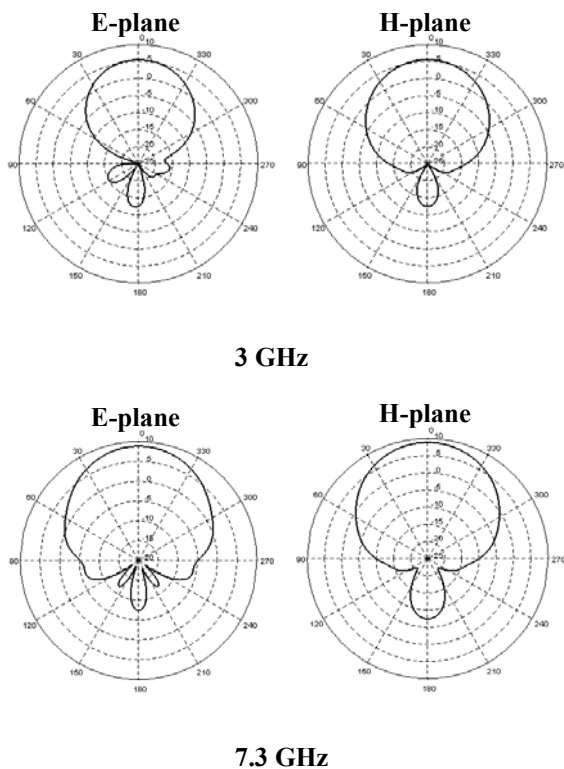


Fig. 8. E- and H- plane radiation patterns of the hybrid dual-band element.

One of the features of this dual-band configuration is the good inherent port-to-port isolation at lower frequency. For low frequency signals, the circular waveguide acts as a high-pass filter and good isolation between the ports is achieved in the low frequency band. In other words, the length of the waveguide feed section determines the isolation between the ports. The computed isolation data at the two bands are shown in Figure 9. Isolations in excess of 85 dB at the lower frequency band and 31 dB at the higher frequency band were calculated.

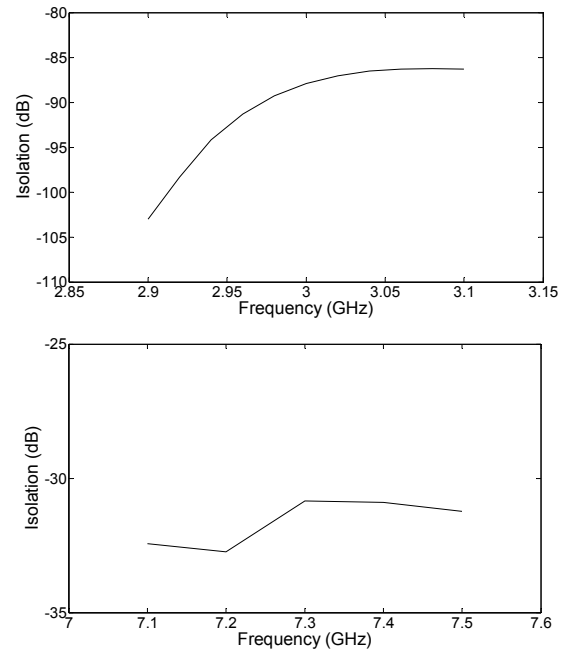


Fig. 9. Port-to-port isolation at the two frequency bands of the hybrid element.

Another parameter to control one of the operating frequencies is the permittivity of the dielectric material inside the waveguide. The higher frequency can be reduced by dielectric loading of the waveguide. The present work considers only the dominant mode excitation in the circular waveguide, which produces broadside patterns. Higher order modes, for example TM_{01} mode, can be made possible with an appropriate waveguide feed design and will generate conical patterns. An example is shown in Figure 10 for the radiation patterns of a dielectric loaded waveguide radiating element with a dielectric constant of 3.0. The upper frequency is reduced to 4.2 GHz. The lower frequency characteristics remain almost unaffected except for the isolation between the ports, which depends on the separation between the operating and waveguide cut-off frequencies. The increase in beam width and the reduction in directivity are due to the decrease in the size of the radiating element.

IV. MODELING OF CIRCULARLY POLARIZED HYBRID DUAL BAND RADIATOR

Feeding the radiators within the hybrid element at two orthogonal points with equal amplitudes and in phase quadrature produces circular polarization. The feeding can be such that dual circular polarizations are produced. Feeding at four points with sequential 90-degree phase shifts will produce lower axial ratios. This was simulated using FEKO for the hybrid element

at the two frequency bands of operation. The models for dual and quad feeding of the shorted annular ring are shown in Figure 11. All design parameters required in simulation such as, inner and outer radii, feed position, dielectric constant, substrate height, ground plane size, and operating frequency were the same as used in linear polarization of the hybrid antenna.

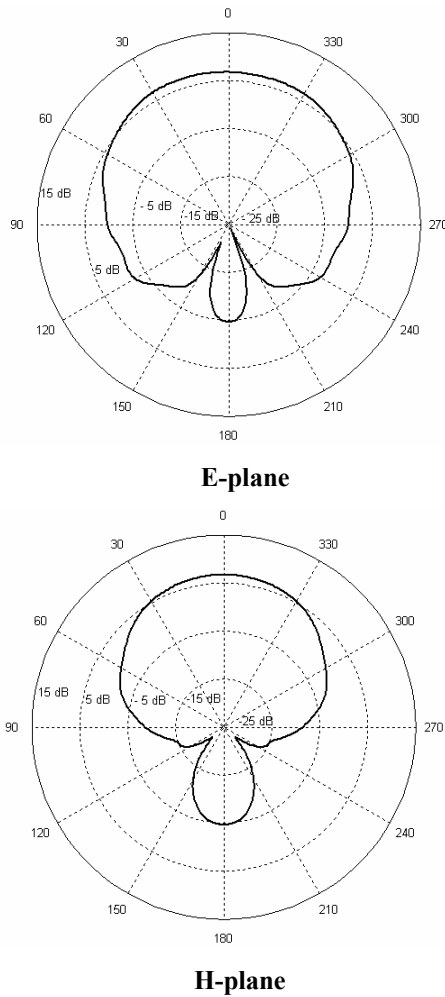


Fig. 10. Computed E- and H- plane patterns at 4.2 GHz for dielectric-loaded waveguide.

Simulation results at the lower frequency band for the circular hybrid antenna are shown in Figures 12 and 13 for the dual-fed element and in Figures 14 and 15 for the quad-fed element. The results of the simulation indicated that low axial ratios can be obtained on axis over a bandwidth greater than the impedance bandwidth. Quad feeding produced broader impedance bandwidth and perfect axial ratio on axis. It also produced larger beamwidth over which the axial ratio is below certain level, e.g. 3 dB. Resulting radiation patterns were almost identical in the E- and H-planes, supporting the low axial ratio results.

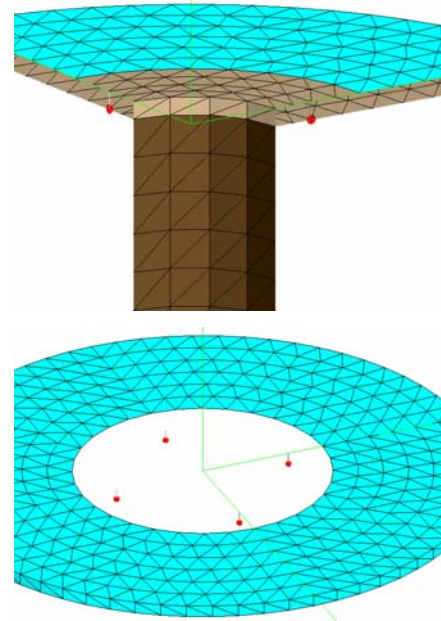


Fig. 11. FEKO model for dual and quad feeding of hybrid element for circular polarization.

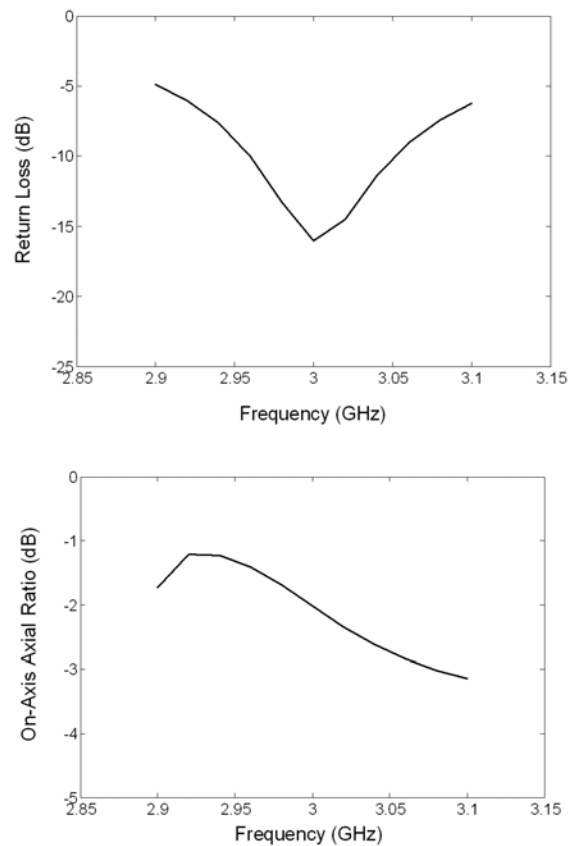
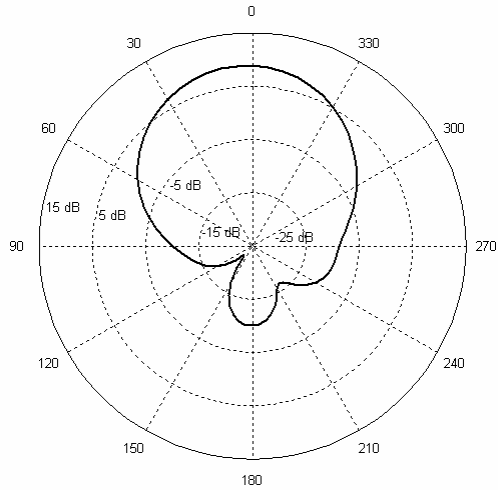
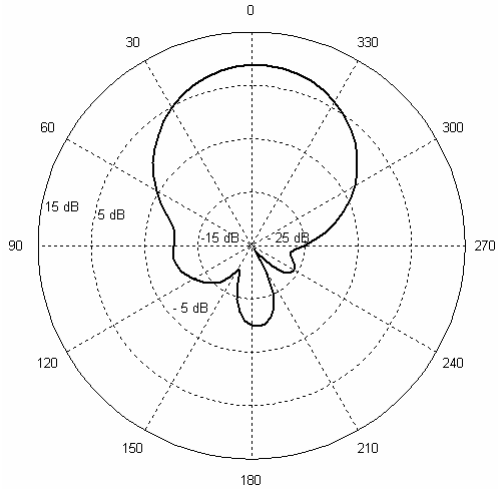


Fig. 12. Return loss and on-axis axial ratio at lower band for circular hybrid element with dual-fed circularly polarized SAR.



(a)



(b)

Fig. 13. Radiation patterns at 3 GHz for circular hybrid element with dual-fed circularly polarized SAR: (a) $\phi = 0^\circ$ plane and (b) $\phi = 90^\circ$ plane.

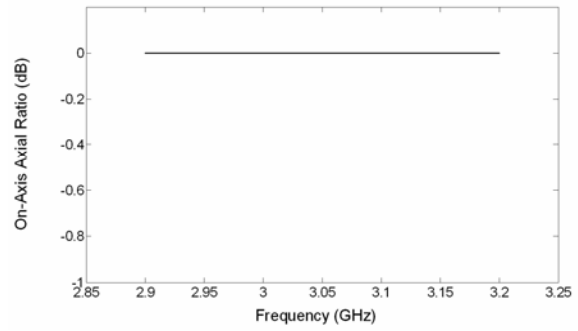
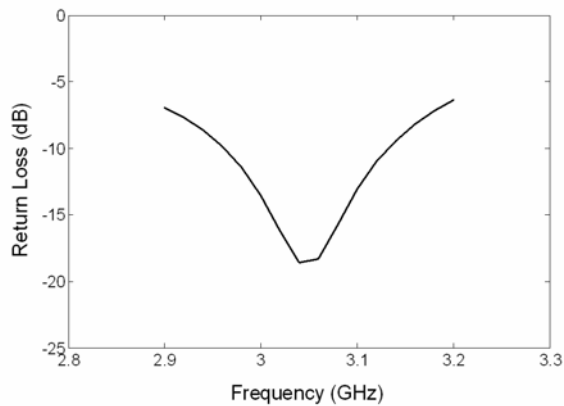
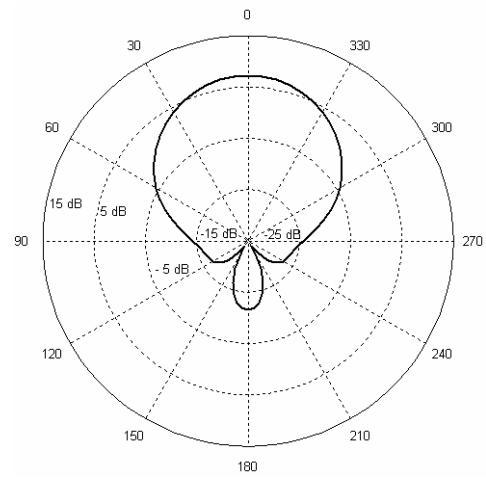
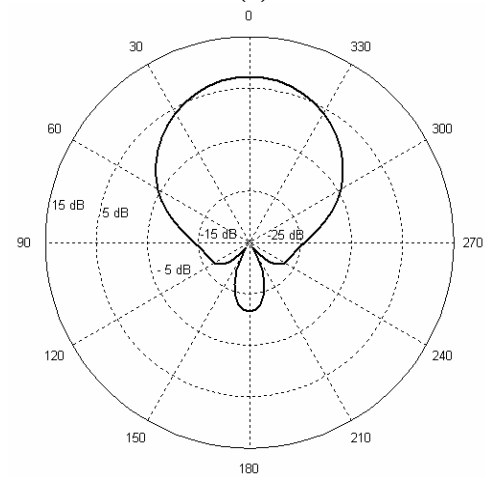


Fig. 14. Return loss and on-axis axial ratio at lower band for circular hybrid element with quad-fed circularly polarized SAR.



(a)



(b)

Fig. 15. Radiation patterns at 3 GHz for circular hybrid element with quad-fed circularly polarized SAR: (a) $\phi = 0^\circ$ plane and (b) $\phi = 90^\circ$ plane.

V. CONCLUSIONS

A dual-band dual polarization radiating element was modeled using the electromagnetic software package FEKO. Return loss, radiation patterns, and port-to-port isolations were calculated. The program was also used to design and optimize the element parameters in order to achieve the dual-band operation at the desired frequencies. Circular polarization operation was simulated by feeding the element at two orthogonal points in phase quadrature or at four points in sequential phase progression.

REFERENCES

- [1] S. Maci and G. B. Gentili, "Dual-Frequency Patch Antennas," *IEEE Antennas and Propagation Magazine*, vol. 39, no. 6, pp. 13 - 20, December 1991.
- [2] C. B. Ravipati and A. I. Zaghoul, "A Hybrid Antenna Element for Dual-Band Applications," *IEEE Antennas and Propagation Society International Symposium Digest*, Monterey, CA, vol. 4, pp. 3412-3415, June 2004.
- [3] D. R. Jackson, J. T. Williams, A. K. Bhattacharyya, R. L. Smith, S. J. Buchheit and S. A. Long, "Microstrip Patch Designs That Do Not Excite Surface Waves," *IEEE Transactions on Antennas and Propagation*, vol. 41, no. 8, pp. 1026 - 1037, August 1993.
- [4] FEKO Suite 4.1, EM Software and Systems www.feko.info, 2003.
- [5] M. Kuribayashi and N. Goto, "A dual frequency element," *National Convention of IECE*, Japan, no. 643, March 1982.
- [6] N. Goto and K. Kaneta, "Ring patch antennas for Dual frequency use," *1987 IEEE Antennas and Propagation Society International Symposium Digest*, vol. 25, pp. 944 - 947, June 1987.
- [7] M. Nakano, H. Arai, W. Chujo, M. Fujise and N. Goto, "Feed circuits of double-layered self-diplexing antenna for mobile satellite communications," *IEEE Transactions on Antennas and Propagation*, vol. 40, no. 10, pp.1269-1271, October 1992.
- [8] Y. Lin and L. Shafai, "Characteristics of concentrically shorted circular patch microstrip antennas," *IEE Proceedings*, vol. 137, Pt. H, no. 1, February 1990.
- [9] D. H. Iwasaki and Y. Suzuki, "Electromagnetically coupled circular-patch antenna consisting of multilayered configuration," *IEEE Transactions on Antennas and Propagation*, vol. 44, no. 6, pp. 777 - 780, June 1996.
- [10] L. Boccia, G. Amendola, G. Di Massa and L. Giulicchi, "Shorted annular patch antennas for multi-path rejection in GPS-based attitude determination," *Microwave and Optical Technology Letters*, January 2001.
- [11] J. Q. Howell, "Microstrip antennas," *IEEE Transactions on Antennas and Propagation*, vol. 23, no.1, pp. 90 - 93, January 1975.
- [12] C. B. Ravipati, "Compact circular microstrip antennas for conical patterns," *IEEE Antennas and Propagation Society International Symposium Digest*, Monterey, CA, vol. 4, pp. 3820-3822, June 2004.

Amir I. Zaghoul received the Ph.D. and M.A.Sc. degrees from the University of Waterloo, Canada in 1973 and 1970, respectively, and the B.Sc. degree (Honors) from Cairo University, Egypt in 1965, all in electrical engineering. In 2001 he joined Virginia Polytechnic Institute and State University (Virginia Tech) as Professor in the Bradley Department of Electrical and Computer Engineering. Prior to Virginia Tech, he was at COMSAT Laboratories for 24 years performing and directing R&D efforts on satellite communications and antennas, where he received several research and patent awards, including the Exceptional Patent Award. He held positions at the University of Waterloo, Canada (1968-1978), University of Toronto, Canada (1973-74), Aalborg University, Denmark (1976) and Johns Hopkins University, Maryland (1984-2001). He is a Fellow of the IEEE and the recipient of the 1986 Wheeler Prize Award for Best Application Paper in the IEEE Transactions on Antennas and Propagation. He is also an Associate Fellow for The American Institute of Aeronautics and Astronautics (AIAA), a Member of Commissions A & B of the International Union of Radio Science (URSI), member of the IEEE Committee on Communications and Information Policy (CCIP), member of the IEEE Publication Services and Products Board (PSPB), and member of the Administrative Committee of the IEEE Antennas Propagation Society.

C. Babu Ravipati received his Ph.D. in Electrical Engineering from the Indian Institute of Technology, Kanpur, India in 1996. He worked as a post-doctoral fellow at the University of Manitoba, Winnipeg, Canada during 1996-1998. He was involved with the design and development of satellite antennas at EMS Technologies Canada, Ste-Anne-de-Bellevue, Quebec during 1998-2003. Since June 2003, he has been with Applied EM Inc. Hampton as a Senior Research Engineer.

Mohammad T. Kawser received M.S. degree from Virginia Tech in 2005 and B.S. degree from Bangladesh University of Engineering and Technology, Bangladesh in 1999, both in Electrical Engineering. He has been with WirelessLogix, Texas since March, 2006 as a RF and Tools Engineer. His work experience also includes Qualcomm and Islamic University of Technology. His research activities involve microstrip/waveguide hybrid antenna elements and multiple band multiple polarization radiators.

Polymorphic Time Domain Computational Electromagnetics

Poman P.M. So

University of Victoria, Victoria, BC, Canada

Abstract — CEM methods such as FDTD and TLM are the de-facto standard for general purpose EM field modeling in the time domain. On the other hand, the Microsoft .NET Framework and the associated C# programming language have become the de-facto standard for software development on Windows. This paper presents the technique for building a time domain CEM object library in C#. This approach could be the basis for creating an open-source standard CEM library.

Index Terms — CEM, FDTD, TLM, time domain analysis, object-oriented approach.

I. INTRODUCTION

Traditional computational electromagnetics (CEM) research does not place sufficient emphasis on object-oriented design and implementation. Classic and recent CEM books [1] – [8] do not address the importance of object orientation at all. As a result, software packages developed by CEM practitioners usually cannot be maintained outside of their respective research institutions. It is hard to imagine engineers around the world would have to re-invent the basic string and math functions before they could start writing codes to solve their design problems. However, when it comes to developing new programs for CEM applications most CEM practitioners have to start from scratch because there is no standard CEM library at their disposal. Using free packages such as NEC [9], TLM3D [10], YatPac [11], and MEEP [12] to solve EM problems is one thing; building new programs base on these packages is a completely different challenge.

In the author's opinion, general purpose CEM methods such as MOM, FEM, FDTD and TLM are mature enough to be placed in an open source standard CEM library. The existence of such a library would not pose unwanted competition to the CEM software industry because the role of CEM industry should be in optimizing the well known modeling methods with proprietary features, in customizing the software with industrial strength graphical user interface front-end, and in interconnecting the field modeling engines to CAD/CAE packages.

Object-oriented paradigm is the key for implementing a standard CEM library. However, Object orientation is not equivalent to programming in Java, C++, and C#. In fact, it is not difficult to find procedure-oriented spaghetti code written in these languages. A truly object-oriented program makes good use of encapsulation, inheritance, and polymorphism. Stroustrup discusses the concept in great details in his authoritative C++ book [13].

The author has illustrated the advantages of an OOP CEM framework in an earlier paper [14]; in order to build a standard CEM library in a reasonably short period of time, existing procedure-oriented CEM codes should be leveraged as much as possible. This paper thus spells out the details of converting a procedure-oriented program to an object-oriented implementation. Since the Microsoft .NET Framework and its associated C# programming language have become the de-facto standard for the Windows software industry, this paper makes use of the C# programming language to apply the OOP techniques to computational electromagnetics.

II. IMPLEMENTATION OF TLM IN C#

The theory of TLM is well described in the literature [1], [4], [15] and [16]. Procedure-oriented implementation of the method can be found in [1] and [10]; a package written in C/C++ has been recently released by Russer *et al.* [11]. These TLM source codes are invaluable resources for CEM researchers who are interested in the TLM method. However, these computer codes are based on legacy modules that are not object-oriented. To illustrate the idea of object-oriented implementation, this paper describes the software technology for converting the TLM_INHO Pascal program in [1] to a reusable class object in C#; the source codes presented in this paper can be downloaded at the CERL website [17].

C# is not the only programming language that is suitable for implementing polymorphic CEM programs. Many CEM professionals may prefer C++ and Java to C# because of the maturity of the two older languages as well as the general availability of third party numerical libraries [18] and [19]. C# is used in this paper because it supports multi-dimensional arrays in a

way that is similar to Pascal and FORTRAN. Furthermore, C# supports C++ style operator overloading which is a crucial feature for implementing a complex mathematic library. Finally, C# can leverage the computing power of library modules written in C/C++, Pascal and FORTRAN via the .NET Framework InteropServices. Hence, C# is a serious programming language that CEM researchers may not want to ignore.

The first step to convert the TLM_INHO.PAS program to C# is to map the Pascal data types to the equivalent C# data objects. Pascal's numeric data types such as `integer` and `single` can be translated in a straightforward manner to the C#'s `int` and `float` data types. In both languages, double precision floating point numbers are called `double`.

```
{----- Pascal Code Segment -----}
nx, ny : integer; {mesh dimension }
d1, d2 : single;  {normalized freq.}
header :string[80]; {temp. storage }

//----- C# Code Segment -----
int nx, ny;      // mesh dimension
float d1, d2;   //normalized freq
string header;  //temporary storage
```

Listing 1. Code segment using simple data types to illustrate the equivalence of data types between Pascal and C#.

The string types between these two languages are quite different. In Pascal, string is an array of characters; the characters in a string can be manipulated at run-time. In C#, string is an immutable built-in type; a new string must be created if any characters in the old string are to be changed. In addition to that, the C# string is a reference type. When the value of a string variable is assigned to another string variable, only the reference to the string is assigned to the new variable; both variables will refer to the same character string. The code segments in Listing 1 and 2 illustrate the said concepts. When the content of a string is no longer referred by a string variable, the memory location occupied by the defunct string will be recovered by the .NET Framework's garbage collection utility. This garbage collection concept applies to all built-in and user defined reference data types.

Arrays in Pascal and C# are quite similar but the differences have to be noted. In Pascal, array lower bounds can be easily specified. In C#, arrays have a default lower bound of zero; arrays with user specified lower bounds can be created with the static

`CreateInstance` class method. In the original TLM_INHO.PAS program, the three-dimensional array for storing voltage impulses is declared as:

```
v:array[1..5,1..12,1..12] of single;
```

A three-dimensional C# array that allows indices to span through [1..5, 1..12, 1..12] would be:

```
float[, ,] v = new float[6,13,13];
```

The above three-dimensional C# array in fact has 1×13×13 extra entries. To avoid wasting storage, one may use the following statement:

```
float[, ,] v = (float[, ,])
    Array.CreateInstance(
        typeof(float),
        new int[] { 5,12,12 },
        new int[] { 1, 1, 1 });

string a, b; // string variables
a = "abc"; // assign address of "abc"
b = a;     // to a and b. a and b now
           // refer to the same string
a = "def" // a refer to a new string.
b = a;    // a and b now refer to
           // "def", "abc" becomes
           // inaccessible.
```

Listing 2. Code segment illustrates the reference characteristic of the C# string; the unreferenced "abc" string will eventually be garbage collected by the .NET Framework.

Instead of typing the declaration statement above repetitively in a source file, one may define the following generic static method to create three dimensional arrays:

```
public static T[, ,] Array3D<T>
    (int x1, int x2, int y1,
     int y2, int z1, int z2){
int[] dim={x2-x1+1, y2-y1+1, z2-z1+1};
int[] lower={x1, y1, z1};
return (T[, ,])Array.CreateInstance(
        typeof(T), dim, lower);
}
```

Using this generic method, a three dimensional array of storage for the voltage impulses can be created via the following simple statement:

```
float[, ,] v =
    Array3D<float>(1,5,1,12,1,12);
```

The same technique can be employed to create two-dimensional arrays of any type; the generic method in this case would be:

```
public static T[,] Array2D<T>
(int x1, int x2, int y1, int y2){
    int[] dim = { x2-x1+1, y2-y1+1 };
    int[] lower = { x1, y1 };
    return (T[,])Array.CreateInstance(
        typeof(T), dim, lower);
}
```

Hence, non-zero lower bound two-dimensional arrays of type char, int and float can be declared like:

```
char[,] a =
Array2D<char>(1, 5, 1, 120);
int[,] b =
Array2D<int>(1, 5, 1, 120);
float[,] c =
Array2D<float>(1, 5, 1, 120);
```

One would expect this technique to work for one-dimensional arrays as well. However, the version 2.0 C# compiler does not allow one-dimensional System.Array to be typecast to T[]. This compiler deficiency, or bug, can be overcome by using the following simple Array1D<T> class.

```
namespace TLM
{
    public class SrStream : StreamReader...
    public class SwStream : StreamWriter...
    public class Base
    {
        Protected Math Methods
        Data
        Protected IO Methods

        public class Array1D<T>
        {
            public Array1D(int x1, int x2)...
            public T this[int i]...
            public Array a;
        }

        #region Public Methods
        //=====
        public static T[,] Array2D<T>(int x1, in
        public static T[, ,] Array3D<T>(int x1,
```

Fig.1. Helper classes for a new TLM_INHO object.

```
public class Array1D<T>{
    public Array1D(int x1, int x2){
        int[] dim = { x2 - x1 + 1 };
        int[] lower = { x1 };
        a = Array.CreateInstance(
            typeof(T), dim, lower);
    }
}
```

```
public T this[int i]{
    get { return (T)a.GetValue(i);
    }
    set { a.SetValue(value,i); }
}
public Array a;
}
```

Besides demonstrating C#'s generic class definition, this implementation also illustrates the use of C#'s indexer, [], as well as the accessor (get) and mutator (set) property methods. With these array creation methods and the Array1D<T> class, it is straightforward to transform the TLM_INHO Pascal program to a C# program — all data and procedures crucial to the TLM simulation are placed inside a main C# class; supporting data and utility functions are placed in other general purpose helper classes. A screen shot of the module that contains the immediate helper classes for a new TLM_INHO object is shown in Figure 1. SrStream and SwStream are text based file IO classes whereas the TheBase consists of the previously mentioned static array creation methods and the Array1D<T> helper class.

Figure 2 shows the private variables of an inhomogeneous medium TLM class, InHo. Since InHo is derived from TheBase, InHo inherits all the data and methods of TheBase. As a result, InHo can make use of the array creation methods and the one-dimensional array class, TheBase, without using the <class>.<method> notation. Besides the private data shown in the figure, InHo has a number of public methods for data I/O, field simulation, and data processing. Figure 3 shows a main program that makes use of the InHo class to implement a single-thread TLM simulation algorithm identical to the original

```
public class InHo : TheBase
{
    #region Private Data
    //=====
    int nx, ny; // number of nodes in mesh
    int io, it, jo, ni; // output point (io,jo), or
    int kb, kc, kd, ke; // number of boundaries, cor

    float[, ,] v = Array3D<float>(1, 5, 1, 12, 1, 12);
    float[,] data = Array2D<float>(1, 101, 1, 2);
    char[,] outc = Array2D<char>(1, 101, 1, 70);
    Array1D<float> rc = new Array1D<float>(1, 10);
    Array1D<float> rd = new Array1D<float>(1, 10);
    Array1D<float> va = new Array1D<float>(1, 6);
    Array1D<float> eh = new Array1D<float>(0, 300);
    Array1D<float> r = new Array1D<float>(1, 12);
    int[,] ib = Array2D<int>(1, 12, 1, 8);
    int[,] ibd = Array2D<int>(1, 10, 1, 8); // waveguid
    int[,] ie = Array2D<int>(1, 5, 1, 7); // excitat:
    int[,] ia = Array2D<int>(1, 8, 1, 4); // computat

    float ehre, ehim, d; // field ma
```

Fig.2. The class structure of TLM_IHNO in C#.

```

class Program
{
    static void Main(string[] args)
    {
        InHo tlm = new InHo(@"..\..\TLM_INHO_INP.txt",
                           @"..\..\TLM_INHO_OUT.txt");
        if (tlm.OpenFiles())
        {
            tlm.ReadData();
            tlm.Iterate(false);
            tlm.Fourier();
            tlm.CurveFit();
            tlm.Correct();
            tlm.PrintReport();
            tlm.PlotGraph();
            tlm.CloseFiles();
        }
    }
}
    
```

Fig.3. A C# program that employs the TLM_INHO class library.

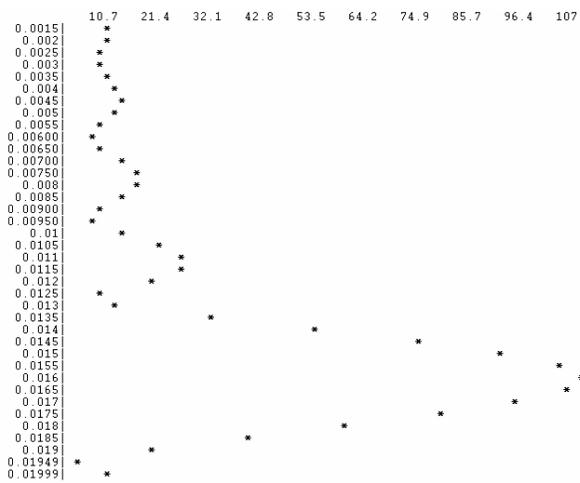


Fig.4. The output of the TLM program in figure 3.

```

        virtual public void PlotGraph()...
        public void Run(bool bShowProgress)...
        public void Work()...
    }

    public class InHo_2 : InHo
    {
        public InHo_2(String ifs, String ofs) : base(
            override public void PlotGraph()...
        )
    }
    
```

Fig.5. InHo_2, a new class derived from InHo.

Pascal program. The false argument passed to the Iterate method informs the tlm object it is not necessary to send output to the console during the field simulation process. The original Output (renamed PlotGraph) procedure has been made virtual to support polymorphism.

The new program has been used to analysis the rectangular resonator associated with the original Pascal TLM_INHO program. The output from the current C# implementation, which is identical to the output of the original program, is shown in Figure 4.

The above computation has validated that the Program, InHo, and TheBase classes have been properly implemented in C# using the object-oriented paradigm. The helper classes and array creation methods are general purpose utilities for converting codes in other programming languages to C#.

One of the advantages of object-oriented implementation is the ease of leveraging computing power of existing software modules via object inheritance and polymorphism. If the PlotGraph method of InHo is made virtual, a new class, say InHo_2, can be derived from InHo with a new pixel-based graphical PlotGraph method that overrides the original string-based implementation. The code structure of such an implementation is shown in Figure 5. Inheritance and polymorphism are powerful features that do not exist in the traditional procedure-oriented programming paradigm.

Another advantage of object-oriented implementation is the feasibility of instantiating multiple copies of the InHo objects in the Main method. A multiple-engine TLM program can be easily created using the InHo class library; Figure 6 depicts the code segment of a dual-engine simulation program. On a multi-processor computer, the engines will run simultaneously. In order to illustrate the concurrent behaviour of the dual-engine implementation, a true argument is passed to the iterate method so that the tlm objects would print the name of the input file and the iteration number to the console during the field computation process. The screen image in Figure 7 shows interspersed outputs from the two concurrent threads in Figure 6.

```

#region Multi-Thread TLM_InHo
//=====
InHo tlm_1 = new InHo(@"..\..\TLM_INHO_INP_1.txt",
                    @"..\..\TLM_INHO_OUT_1.txt");
InHo tlm_2 = new InHo(@"..\..\TLM_INHO_INP_2.txt",
                    @"..\..\TLM_INHO_OUT_2.txt");
ThreadStart delegate_1 = new ThreadStart(tlm_1.Work);
ThreadStart delegate_2 = new ThreadStart(tlm_2.Work);
Thread thread_1 = new Thread(delegate_1);
Thread thread_2 = new Thread(delegate_2);
thread_1.Start();
thread_2.Start();
#endregion
    
```

Fig.6. A multi-thread TLM_INHO code segment in C#.

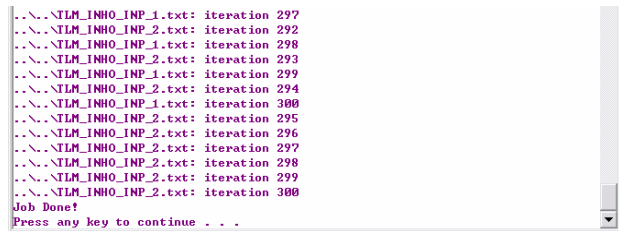


Fig.7. A screen image consists of interspersed outputs from the two execution threads in Fig 5.

Recently released CEM codes, [9] and [12], are mostly implemented in C++. However, as the author has mentioned earlier, programs implemented in C++ are not necessarily object-oriented programs. Programs that do not take advantage of object inheritance and polymorphism are merely class oriented programs. More applications of object-oriented programming paradigm to computational electromagnetics can be found in [20]-[25]. Details about polymorphism and concurrent programming in C# can be found in [26] and [27].

III. CONCLUSION

A C# implementation of the classical two-dimensional TLM algorithm by Hoefler has been presented. Object-oriented features such as encapsulation, inheritance and polymorphism have been demonstrated. The object-oriented paradigm presented in this paper can be used to convert most legacy procedure-oriented CEM programs to modern object-oriented library modules. The technique presented in this paper is equally applicable in the Java environment, or in the C++ world with other operating systems. The author is advocating placing commonly used CEM engines, such as MoM, FEM, FDTD and TLM, in an open source standard CEM library to benefit the EM community at large.

ACKNOWLEDGEMENT

The author wishes to acknowledge the financial support of the National Science and Engineering Research Council of Canada.

REFERENCES

- [1] W. J. R. Hoefler (editor T. Itoh), *Numerical Techniques for Microwave and Millimeter-Wave Passive Structures*, Chapter 8, John Wiley & Sons, 1989.
- [2] P.P. Silvester and R.L. Ferrari, *Finite Elements for Electrical Engineers*, Second Edition, Cambridge University Press, 1990.
- [3] R.C. Booton Jr., *Computational Methods for Electromagnetics and Microwaves*, John Wiley & Sons, 1992.
- [4] C. Christopoulos, *The Transmission-Line Modeling Method*, IEEE Press / Oxford University Press, 1995.
- [5] T. Itoh, C. Pelosi, and P.P. Silvester, *Finite Element Software for Microwave Engineering*, John Wiley & Sons, 1996.
- [6] M.N.O. Sadiku, *Numerical Techniques in Electromagnetics*, Second Edition, CRC Press, 2001.
- [7] D.B. Davidson, *Computational Electromagnetics for RF and Microwave Engineering*, Cambridge University Press, 2005.
- [8] A. Taflove and S.C. Hagness, *Computational Electrodynamics, The Finite-Differences Time-Domain Method*, Third Edition, Artech House, 2005.
- [9] NEC, <http://www.si-list.org/swindex2.html>.
- [10] W.J.R. Hoefler, <http://www.cerl.ece.uvic.ca/wjrh/tlm/prog-fortran.html>.
- [11] P. Russer, <http://www.hft.ei.tum.de/php/resYATSIM2.php> and <http://www.yatpac.org/index.php>.
- [12] MEEP, <http://ab-initio.mit.edu/wiki/index.php/Meep>.
- [13] B. Stroustrup, *The C++ Programming Language*, Special Edition, Addison-Wesley, 2000.
- [14] P.P.M. So, "An Object-oriented Framework for Computational Electromagnetics," *22nd Annual Review of Progress in Applied Computational Electromagnetics*, pp. 219-224, March 12-16, 2006.
- [15] P. B. Johns and R. L. Beurle, "Numerical solution of two-dimensional scattering problems using a transmission-line matrix," *Proc. IEE*, Vol. 118, No. 12, pp. 1203-1208, 1971.
- [16] W. J. R. Hoefler, "Time domain electromagnetic simulation for microwave CAD applications," *IEEE Trans. MTT*, Vol. 40, No. 7, pp. 1517-1527, 1992.
- [17] CERL at UVic, www.cerl.ece.uvic.ca
- [18] W.H. Press, S.A. Teukolsky, W.T. Vetterling, and B.P. Flannery, *Numerical Recipes in C++*, *The Art of Scientific Computing*, Second Edition, Cambridge University Press, 2002.
- [19] JMSL, <http://www.vni.com/products/ims/jmsl/jmsl.html>.
- [20] D. Kurumbalapatiya and S.R.H. Hoole, "An Object-oriented Representation of Electromagnetic Knowledge," *IEEE Trans. On Magnetics*, Vol. 29, No. 2, pp. 1939-1942, March 1993.
- [21] E.J. Silva and R.C. Mesquita, "Data Management in Finite Element Analysis Programs Using Object-oriented Techniques," *IEEE Trans. on Magnetics*, Vol. 32, No. 3, pp. 445-1448, May 1996.

- [22] E.Z. Zhou, "Object-oriented Programming, C++ and Power System Simulation," *IEEE Trans. on Power Systems*, Vol. 11, No. 1, pp. 206 – 215, February 1996.
- [23] L. Baduel, F. Baude, D. Caromel, C. Delbe, N. Gama, S. El Kasmi, and S. Lanteri, "A Parallel Object-oriented Application for 3D Electromagnetism," *Proceedings of the 18th International Parallel and Distributed Processing Symposium (IPDPS'04)*.
- [24] C. G. Biniaris, A. I. Kostaridis, D. I. Kaklamani, and I. S. Venieris, "Implementing Distributed FDTD Codes with Java Mobile Agents," *IEEE Trans. Antenna and Propagation Magazine*, Vol. 44, No. 6, pp. 115 – 119, December 2002.
- [25] D. G. Lympopoulos, D. Logothetis, P. Atlamazoglou, and D. I. Kakalamani, "Using Object-oriented and Literate-Programming Techniques for the Development of a Computational Electromagnetics Library," *IEEE Antennas and Propagation Magazine*, Vol. 47, No. 3, pp. 31–38, June 2005.
- [26] A. Troelsen, *Pro C# 2005 and the .NET 2.0 Platform*, APress, 2005.
- [27] J. Richter, *CLR Via C#*, 2ED, Microsoft Press, 2006.



Poman P. M. So received the B.Sc. degree in Computer Science and Physics from the University of Toronto, Canada, in 1985. He received his degrees in Electrical Engineering from the University of Ottawa (B.A.Sc. and M.A.Sc.) and the University of Victoria (Ph.D.) in 1987, 1989 and 1996, respectively.

From April 1997 to June 1998, he was a senior antenna engineer at MDS Space Mission (Ste-Anne-de-Bellevue, Quebec, Canada), formerly known as Spar Aerospace Ltd. His work included high frequency (10 to 40 GHz) antennas and feed components design for commercial satellite systems as well as Ka-band active antenna CAD software development. In October 1993, he was invited to the Ferdinand-Braun-Institut für Höchstfrequenztechnik Berlin, Berlin, Germany, as a research scientist. From August 1990 to February 1991, he was a visiting researcher at the University of Rome in Rome, Italy, and the Laboratoire d'Electronique in Sophia Antipolis, France.

Dr. Poman So joined the Department of Electrical and Computer Engineering at the University of Victoria as an Assistant Professor in 2005. He is a Senior Member of IEEE and a registered Professional Engineer in the Province of British Columbia, Canada. He has twenty years of research and industrial experience in object-oriented computational electromagnetics. He is a co-founder of the Faustus Scientific Corporation and is the creator of the company's MEFiSTo line of electromagnetic modeling software.

IV. APPENDIX

THEBASE.CS: AN OBJECT-ORIENTED TLM LIBRARY IN C#

```

using System;           using System.Collections.Generic;
using System.Text;     using System.IO;
namespace TLM{
public class SrStream : StreamReader{
    public SrStream(String ifs) : base(ifs){}
    public String ReadString(){
        char a = ' '; do{ a = (char)Read();} while (char.IsWhiteSpace(a));
        string buffer = "";
        do{ buffer += a; a = (char)Read();} while (!char.IsWhiteSpace(a));
        return buffer;
    }
    public float ReadFloat() { return float.Parse(ReadString()); }
    public int ReadInt() { return int.Parse(ReadString()); }
}
public class SwStream : StreamWriter{
    public SwStream(String ofs) : base(ofs){ }
    public string Format<T>(T v, int pl){
        string str = v.ToString().PadLeft(pl, ' ');
        return str.Substring(0, pl);
    }
}
public class TheBase{

    // Protected Math Methods
    //=====
    protected double atan(double v) { return Math.Atan(v); }
    protected double exp(double v) { return Math.Exp(v); }
    protected double cos(double v) { return Math.Cos(v); }
    protected double sin(double v) { return Math.Sin(v); }
    protected double sqrt(double v) { return Math.Sqrt(v); }
    protected double floor(double v) { return Math.Floor(v); }
    // Data
    //=====
    public SrStream sr;
    public SwStream sw;
    public String input_file, output_file;
    // Protected IO Methods
    //=====
    protected string Format<T>(T v, int pl) { return sw.Format<T>(v, pl); }
    protected float ReadFloat() { return sr.ReadFloat(); }
    protected int ReadInt() { return sr.ReadInt(); }
    public class Array1D<T>{
        public Array1D(int x1, int x2){
            int[] dim={ x2 - x1 + 1 }; int[] lower={ x1 };
            a = Array.CreateInstance(typeof(T), dim, lower);
        }
        public T this[int i]{
            get { return (T)a.GetValue(i); }
            set { a.SetValue(value, i); }
        }
        public Array a;
    }
    // Public Methods
    //=====
    public TheBase(String ifs, String ofs){
        input_file = ifs;

```

```

        output_file= ofs;
    }
    public bool OpenFiles(){
        try{
            sr = new SrStream(input_file);
            sw = new SwStream(output_file);
            return true;
        }
        catch (Exception e){
            Console.WriteLine("An error occurred: '{0}'", e);
            CloseFiles();    return false;
        }
    }
    public void CloseFiles(){
        if (sr != null) sr.Close();
        if (sw != null) sw.Close();
    }
    public static T[,] Array2D<T>(int x1, int x2, int y1, int y2){
        int[] dim={ x2 - x1 + 1, y2 - y1 + 1 };
        int[] lower={ x1, y1 };
        return (T[,])Array.CreateInstance(typeof(T), dim, lower);
    }
    public static T[,,] Array3D<T>(int x1,int x2,int y1,int y2,int z1,int z2){
        int[] dim={ x2 - x1 + 1, y2 - y1 + 1, z2 - z1 + 1 };
        int[] lower={ x1, y1, z1 };
        return (T[,,])Array.CreateInstance(typeof(T), dim, lower);
    }
} }
TLM_INHO.CS: An object-oriented TLM Library in C#
using System;
using System.Text;
using System.Threading;
using System.Collections.Generic;
using System.IO;

namespace TLM{
public class InHo : TheBase{
    int nx, ny;           // number of nodes in mesh
    int io, it, jo, ni;  // output point (io,jo), output type & num of iters
    int kb, kc, kd, ke;  // number of boundaries,computational boxes,dielectric
                        // boundaries & excitation points or lines
    float[, ,] v = Array3D<float>(1, 5, 1, 12, 1, 12); // voltage buffer
    float[,] data = Array2D<float>(1, 101, 1, 2);
    char[,] outc = Array2D<char>(1, 101, 1, 70);
    Array1D<float> rc = new Array1D<float>(1, 10); // reflection coef
    Array1D<float> rd = new Array1D<float>(1, 10); // relative permittivity
    Array1D<float> va = new Array1D<float>(1, 6); // initial values
    Array1D<float> eh = new Array1D<float>(0, 300); // storage for results
    Array1D<float> r = new Array1D<float>(1, 12);
    int[,] ib = Array2D<int>(1, 12, 1, 8);
    int[,] ibd = Array2D<int>(1, 10, 1, 8); // waveguide, boundaries & codes
    int[,] ie = Array2D<int>(1, 5, 1, 7); // excitation points and code (115)
    int[,] ia = Array2D<int>(1, 8, 1, 4); // computation boxes
    float ehre, ehim, d; // field magnitudes and normalized frequencies
    float pcf, cf, d1, d2, ds; // normalized frequencies & step size
    float peak, a, cs, max, yo;
    int npt, l, j, m, i, ic, pt, ptp, ptm, nn; // iteration counters}

void ReadHeader(){ String header;
    header = sr.ReadLine(); sw.WriteLine(header);
    header = sr.ReadLine(); sw.WriteLine(header);
}
}

```

```

void ReadNxNy(){ ReadHeader(); nx = sr.ReadInt();
ny = sr.ReadInt(); sr.ReadLine();
sw.WriteLine("{0} {1}", Format<int>(nx, 4), Format<int>(ny, 4));
}
void ReadBound(){ ReadHeader(); kb = 0;
do{ kb = kb + 1;
for (m = 1; m <= 8; m++){ ib[kb, m] = ReadInt();
sw.WriteLine("{0}", ib[kb, m].ToString().PadLeft(4, ' '));
if (m == 4) sw.WriteLine(" ");
}
r[kb] = ReadFloat(); it = ReadInt(); sr.ReadLine();
sw.WriteLine("{0}{1}", Format<float>(r[kb], 16), Format<int>(it, 10));
} while (it > 0);
}
void ReadDielBound(){ ReadHeader(); kd = 0;
do{ kd = kd + 1;
for (m = 1; m <= 8; m++){ ibd[kd, m] = ReadInt();
sw.WriteLine("{0}", Format<int>(ibd[kd, m], 4));
if (m == 4) sw.WriteLine(" ");
}
rc[kd] = ReadFloat(); it = ReadInt(); sr.ReadLine();
sw.WriteLine("{0}{1}", Format<float>(rc[kd], 18), Format<int>(it, 10));
} while (it > 0);
}
void ReadCompBox(){ ReadHeader(); kc = 0;
do{ kc = kc + 1;
for (m = 1; m <= 4; m++){ ia[kc, m] = ReadInt();
sw.WriteLine("{0}", Format<int>(ia[kc, m], 4));
}
rd[kc] = ReadFloat(); it = ReadInt(); sr.ReadLine();
sw.WriteLine("{0}{1}", Format<float>(rd[kc], 22), Format<int>(it, 22));
} while (it > 0);
}
void ReadExcitation(){ ReadHeader(); ke = 0;
do{ ke = ke + 1;
for (m = 1; m <= 7; m++){ ie[ke, m] = ReadInt();
sw.WriteLine("{0}", Format<int>(ie[ke, m], 4));
if (m == 4) sw.WriteLine(" ");
}
va[ke] = ReadFloat(); it = ReadInt(); sr.ReadLine();
sw.WriteLine("{0}{1}", Format<float>(va[ke], 16), Format<int>(it, 17));
} while (it > 0);
}
void ReadFreq(){
sr.ReadLine(); sr.ReadLine(); d1 = ReadFloat();
d2 = ReadFloat(); ds = ReadFloat(); sr.ReadLine();
sr.ReadLine(); sr.ReadLine(); io = ReadInt();
jo = ReadInt(); l = ReadInt(); ni = ReadInt();
yo = ReadFloat(); sr.ReadLine();
sw.WriteLine("Output point is ({0},{1})",
Format<int>(io, 4), Format<int>(jo, 4));
sw.WriteLine("Number of iterations is {0}", ni);
sw.WriteLine("Permittivity stub admittance is {0}", yo);
sw.WriteLine(" D1 D2 Step Size");
sw.WriteLine("{0}{1}{2}", Format<float>(d1, 8), Format<float>(d2, 8),
Format<float>(ds, 18));
}
public InHo(String ifs, String ofs) : base(ifs, ofs) { }
public void ReadData(){
ReadNxNy(); ReadBound(); ReadDielBound();
}

```

```

    ReadCompBox();          ReadExcitation();          ReadFreq();
}
public void Iterate(bool bShowProgress){
    if (bShowProgress){
        Console.WriteLine("Finished reading input.");
    }
    float a, vx, vy, vxy;
    // CLEAR WORKING SPACE
    for (j = 1; j <= ny; j++){
        for (i = 1; i <= nx; i++){
            for (m = 1; m <= 5; m++){
                v[m, i, j] = 0;
            } } }
    // INITIALIZE EXCITATION POINTS
    for (nn = 1; nn <= ke; nn++){
        for (j = ie[nn, 3]; j <= ie[nn, 4]; j++){
            for (i = ie[nn, 1]; i <= ie[nn, 2]; i++){
                m = ie[nn, 5];
                while (m <= ie[nn, 7]){
                    v[m, i, j] = va[nn];          m = m + ie[nn, 6];
                } v[5, i, j] = va[nn];
            } } }
    // Sample Output at time zero }
    switch (1){
        case 3: eh[0] = 2 * (v[1, io, jo] + v[2, io, jo] + v[3, io, jo] +
            v[4, io, jo] + yo * v[5, io, jo]) / (4 + yo); break;
        case 2: eh[0] = yo * (v[3, io, jo] - v[1, io, jo]); break;
        case 1: eh[0] = yo * (v[4, io, jo] - v[2, io, jo]); break;
    }
    for (ic = 1; ic <= ni; ic++){
        // INHOMOGENEOUS SHUNT NODE SCATTERING PROCEDURE
        for (nn = 1; nn <= kc; nn++){
            for (j = ia[nn, 3]; j <= ia[nn, 4]; j++){
                for (i = ia[nn, 1]; i <= ia[nn, 2]; i++){
                    a = (v[1, i, j] + v[2, i, j] + v[3, i, j] + v[4, i, j]
                        + v[5, i, j] * rd[nn]) * 2 / (rd[nn] + 4);
                    v[1, i, j] = a - v[1, i, j];          v[2, i, j] = a - v[2, i, j];
                    v[3, i, j] = a - v[3, i, j];          v[4, i, j] = a - v[4, i, j];
                    v[5, i, j] = a - v[5, i, j];
                } } }
            // SET UP BOUNDARY CONDITIONS
            for (nn = 1; nn <= kb; nn++){
                for (j = ib[nn, 3]; j <= ib[nn, 4]; j++){
                    for (i = ib[nn, 1]; i <= ib[nn, 2]; i++){
                        vxy = v[ib[nn, 6], i, j];
                        v[ib[nn, 6], i, j] = r[nn] * v[ib[nn, 5], i
                            + ib[nn, 8], j + ib[nn, 7]];
                        v[ib[nn, 5], i + ib[nn, 8], j + ib[nn, 7]] =
                            r[nn] * vxy;
                    } } }
            // PERFORM IMPEDANCE MODIFICATIONS AT AIR-DIELECTRIC BOUNDARIES
            if (ibd[1, 1] != 0){
                for (nn = 1; nn <= kd; nn++){
                    for (j = ibd[nn, 3]; j <= ibd[nn, 4]; j++){
                        for (i = ibd[nn, 1]; i <= ibd[nn, 2]; i++){
                            vx = v[ibd[nn, 6], i, j];
                            vy = v[ibd[nn, 5], i + ibd[nn, 8], j + ibd[nn, 7]];
                            v[ibd[nn, 6], i, j]
                                = -rc[nn] * vy + (1 + rc[nn]) * vx;
                            v[ibd[nn, 5], i + ibd[nn, 8], j + ibd[nn, 7]]

```

```

        = rc[nn] * vx + (1 - rc[nn]) * vy;
    } } } }
    // INTERCHANGE IMPULSES AMOUNG NODES
    for (nn = 1; nn <= kc; nn++){
        for (j = ia[nn, 3]; j <= ia[nn, 4]; j++){
            for (i = ia[nn, 1]; i <= ia[nn, 2]; i++){
                a = v[3, i, j];          v[3, i, j] = v[1, i, j + 1];
                v[1, i, j + 1]          v[4, i, j] = v[2, i + 1, j];
                v[2, i + 1, j] = a;
            } } }
    // Sample Output
    switch (1){
        case 3: eh[ic] = 2 * (v[1,io,j0] + v[2,io,j0] + v[3,io,j0] +
            v[4, io, j0] + yo * v[5, io, j0]) / (4 + yo); break;
        case 2: eh[ic] = yo * (v[3, io, j0] - v[1, io, j0]); break;
        case 1: eh[ic] = yo * (v[4, io, j0] - v[2, io, j0]); break;
    }
    if (bShowProgress){
        Console.WriteLine("{0}: iteration {1}", input_file, ic);
        Thread.Sleep(1);
    } } }
public void Fourier(){
    float ra, rb, cs, u, uk, ehre, ehim, ehmod, d;
    npt = 0; max = 0; ra = 0; rb = 6.283184f; d = d1;
    while (d <= d2){
        ehre = 0; ehim = 0; uk = (float)exp(-d * ra); u = uk;
        for (ic = 0; ic <= ni; ic++){
            cs = ic * rb * d;
            ehre = (float)(ehre + (eh[ic] * cos(cs) * uk));
            ehim = (float)(ehim - (eh[ic] * sin(cs) * uk));
            uk = uk * u;
        }
        ehmod = (float)(sqrt(ehre * ehre + ehim * ehim));
        npt = npt + 1; data[npt, 1] = d;
        data[npt, 2] = ehmod; d = d + ds;
    }
    for (j = 1; j <= npt; j++){
        if (data[j, 2] > max){
            max = data[j, 2]; peak = data[j, 1]; pt = j;
        }
    }
}
public void CurveFit(){
    float ai, bmax;
    if (pt > 1 && pt < npt){ ptp = pt + 1; ptm = pt - 1;
        ai = ((data[ptm,2]-max)*(data[ptm,1]-data[ptp,1])-(data[ptm, 2]-
            data[ptp, 2]) * (data[ptm, 1] - data[pt, 1]));
        ai = ai / ((data[ptm,1] - data[pt,1])*(data[pt,1]-data[ptp,1]) *
            (data[ptm, 1] - data[ptp, 1]));
        bmax = (data[ptm,2]-max)/(data[ptm,1]-data[pt,1])-ai*(data[ptm,1]
            + data[pt, 1]);
        peak = -bmax / (2 * ai);
    }
}
public void Correct(){
    float a, p;
    // VELOCITY ERROR CORRECTION
    p = (float)(3.14592653 * peak);
    cf = (float)(p / atan(sqrt(2.0) * sin(p)));
    pcf = peak / cf;
}
public void PrintReport(){
    sw.WriteLine();
}

```

```

        sw.WriteLine("          RESULTS");
        sw.WriteLine("          -----");
        sw.WriteLine("{0} points plotted.", Format<int>(npt, 4));
        sw.WriteLine("  Maximum plotted field magnitude:");
        sw.WriteLine("{0}", Format<float>(max, 14));
        cf = 1 / cf;
        sw.WriteLine("  The velocity correction factor (Do/D) is {0}", cf);
        sw.WriteLine(
            "  MESH SIZE/MESH WAVELENGTH      MESH SIZE/FREE SPACE      FIELD
(EHMOD) MAGNITUDE");
        sw.WriteLine("          (D)          (Do)          WAVELENGTH");
        sw.WriteLine(
            "  -----");
        for (j = 1; j <= npt; j++){
            sw.WriteLine("          {0}          {1}          {2}",
                Format<float>(data[j, 1], 8),
                Format<float>(data[j, 1] * cf, 8),
                Format<float>(data[j, 2], 8));
        }
        sw.WriteLine();
        sw.WriteLine("Maximum field value at D = {0}", peak);
        sw.WriteLine("  corresponding to Do = {0} <=== FINAL RESULT", pcf);
    }
    public void PlotGraph(){
        float u;
        sw.WriteLine("          Graph of EHMOD vs. D");
        sw.WriteLine("  D          EHMOD");
        u = max / 70;
        if (u == 0)
            Console.WriteLine("No plot generated - all values equal zero.");
        else{
            sw.WriteLine("          ");
            for (j=7; j<=63; j+=7) sw.WriteLine("  {0}", Format<float>(j*u, 4));
            sw.WriteLine("  {0}", Format<float>(max, 4));
            for (j = 1; j <= npt; j++){
                data[j, 2] = data[j, 2] / max;
                data[j, 2] = (float)(floor(70 * data[j, 2]));
                for (i = 1; i <= 70; i++){
                    outc[j, i] = ' ';
                    if (data[j, 2] == i) outc[j, i] = '*';
                }
                sw.WriteLine(" {0}|", Format<float>(data[j, 1], 7));
                for (i = 1; i <= 70; i++){ sw.WriteLine(outc[j, i]); }
            }
            sw.WriteLine();
        }
    }
    public void Run(bool bShowProgress){
        ReadData();          Iterate(bShowProgress);          Fourier();
        CurveFit();          Correct();          PrintReport();
        PlotGraph();
    }
    public void Work(){
        if (OpenFiles()){ Run(true); CloseFiles();
        }
    }
}
}

```

TLM.CS: An object-oriented TLM Program in C#

```

using System;          using System.Text;          using System.Threading;
using System.Collections.Generic;          using TLM;

```

```
namespace CS_TLM{ // This is the main program to test out the TLM class
class Program{
    static void Main(string[] args){
        // Single Thread TLM_InHo
        //=====
        InHo tlm = new InHo(@"../../TLM_INHO_INP.txt",
                           @"../../TLM_INHO_OUT.txt");
        if (tlm.OpenFiles()){
            tlm.Run(false);    tlm.CloseFiles();
        }
        // Multi-Thread TLM_InHo
        //=====
        InHo tlm_1 = new InHo(@"../../TLM_INHO_INP_1.txt",
                              @"../../TLM_INHO_OUT_1.txt");
        InHo tlm_2 = new InHo(@"../../TLM_INHO_INP_2.txt",
                              @"../../TLM_INHO_OUT_2.txt");
        ThreadStart delegate_1 = new ThreadStart(tlm_1.Work);
        ThreadStart delegate_2 = new ThreadStart(tlm_2.Work);
        Thread thread_1 = new Thread(delegate_1);
        Thread thread_2 = new Thread(delegate_2);
        thread_1.Start();    thread_2.Start();
        while (thread_1.IsAlive || thread_2.IsAlive){ Thread.Sleep(1); }
        Console.WriteLine("Job Done!");
    }
}
```

Simulation of Non Linear Circuits by the Use of a State Variable Approach in the Wavelet Domain

S. Barmada, A. Musolino, and M. Raugi

Department of Electrical Systems and Automation
University of Pisa, Via Diotisalvi 2, 56126 Pisa, Italy
sami.barmada@dsea.unipi.it

Abstract — A method for the simulation of complex circuits with nonlinear elements is proposed. The method is based on wavelet expansion of the state variable description, and leads to a compact representation of the nonlinear problem which is characterized by accuracy and computational efficiency.

Keywords — Circuit Simulation, Nonlinear Loads, Wavelet Expansion.

I. INTRODUCTION

The most common approach to design and optimize microwave devices is to represent them through equivalent circuits, which are in general composed by linear, non linear, lumped, and distributed elements.

The main difficulty of the problem is the mixed nature between linear components (best treated in the frequency domain) and nonlinear components (best treated in the time domain). Some authors proposed the impulse response and convolution (IRC) technique [1] – [3], in which a great computational effort is dedicated to the process of recording and convolving the quantities related to the nonlinear elements. A different approach consists of approximating the frequency response by a Padè approximation, so called asymptotic waveform evaluation method, and has been used for both linear and nonlinear circuits [4] – [6]; the main drawback of the method is the sometimes low approximation (due to the reduction in the number of poles) in case of very complex circuits. In [7] a further approach is presented: the numerical inversion of Laplace transform technique, which is characterized by several advantages with respect to IRC and AWE, but suffers from the series approximations and the nonlinear iterations involved.

Recently wavelet based techniques have been proposed also for the analysis of nonlinear circuits (in transient or steady state mode), showing good potential [8], [9]. A basis of Daubechies wavelets on the interval is here used to expand the unknown quantities and the circuit equations are obtained by the application of the modified nodal analysis. The nonlinearities are treated by the use of the substitution theorem, and the problem is solved by the application of a standard Newton –

Raphson algorithm with an analytical calculation of the Jacobian.

This particular formulation makes the method efficient from a computational point of view, since the matrices involved in the calculation are sparse (i.e. characterized by a small number of non zero elements), hence the number of multiplications required in the solution is low. Furthermore the characteristics of the chosen wavelet basis reduce the size of the matrix.

The method has been tested in several cases, here is reported the calculation of voltages and currents in a complex circuit, and the results are compared with the results coming from a SPICE simulation.

II. MATHEMATICAL FORMULATION

A. Modified Nodal Analysis in the Wavelet Domain

Let us consider a complex circuit, composed by a set of lumped and distributed parameters, connected to independent voltage generators and linear loads. It is possible to divide the circuit into two interconnected parts: a subnetwork φ composed by lumped linear and nonlinear elements, for which we are interested in the calculation of voltages and currents, and a linear subnetwork π , composed by lumped and/or distributed elements, seen as a multiple port circuit. By the used of the MNA it is possible to write the circuit equations in the Laplace domain in the following form [10]

$$\mathbf{W}_\varphi s \mathbf{x}_\varphi(s) + \mathbf{G}_\varphi \mathbf{x}_\varphi(s) + \mathbf{L}_\pi(s) \mathbf{i}_\pi(s) = \mathbf{b}(s) \quad (1)$$

where \mathbf{x}_φ is the vector of unknowns (nodal voltages, whose dimension is the total number of MNA variables); \mathbf{W}_φ and \mathbf{G}_φ are constant matrices describing the lumped elements of the network φ and \mathbf{b} is a constant vectors whose entries are the independent voltage and current sources (together with the initial condition sources, if present). \mathbf{L}_π is a matrix whose entries are zeroes or ones, mapping the vector $\mathbf{i}_\pi(s)$ of currents entering the linear subnetwork π into the node space of

the network φ . The linear multiterminal subnetwork π can be described by the standard approach as

$$\mathbf{Y}_\pi(s)\mathbf{V}_\pi(s)=\mathbf{i}_\pi(s) \quad (2)$$

where $\mathbf{Y}_\pi(s)$ is the y parameter matrix and $\mathbf{V}_\pi(s)$ is the vector of terminal voltage nodes connecting the subnetwork to the network φ . By substituting (2) in (1) it is possible to write

$$\tilde{\mathbf{W}}_\varphi s\mathbf{x}_\varphi(s)+\tilde{\mathbf{G}}_\varphi\mathbf{x}_\varphi(s)=\mathbf{b}(s) \quad (3)$$

where $\tilde{\mathbf{G}}_\varphi$ and \mathbf{W}_φ take also into account the contribution of the matrix $\mathbf{Y}_\pi(s)$.

As an example, we apply the MNA to the simple network represented in Fig. 1.

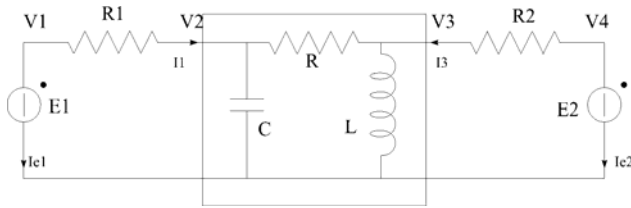


Fig. 1. Simple network for MNA analysis.

In this case equations (1) and (2) respectively become

$$\begin{bmatrix} G_1 & -G_1 & 0 & 0 & 1 & 0 \\ -G_1 & G_1 & 0 & 0 & 0 & 0 \\ 0 & 0 & G_2 & -G_2 & 0 & 0 \\ 0 & 0 & -G_2 & G_2 & 0 & 1 \\ 1 & 0 & 0 & 0 & 0 & 0 \\ 0 & 0 & 0 & 1 & 0 & 0 \end{bmatrix} \begin{bmatrix} v_1 \\ v_2 \\ v_3 \\ v_4 \\ i_{e1} \\ i_{e2} \end{bmatrix} + \begin{bmatrix} 0 & 0 \\ 1 & 0 \\ 0 & 1 \\ 0 & 0 \\ 0 & 0 \\ 0 & 0 \end{bmatrix} \begin{bmatrix} i_1 \\ i_3 \end{bmatrix} = \begin{bmatrix} 0 \\ 0 \\ 0 \\ 0 \\ E_1 \\ E_2 \end{bmatrix} \quad (4)$$

$$\begin{bmatrix} i_1 \\ i_3 \end{bmatrix} = \begin{bmatrix} sC & -(sC+G) \\ -(1/sL+G) & 1/sL \end{bmatrix} \begin{bmatrix} v_2 \\ v_3 \end{bmatrix}. \quad (5)$$

We now consider a wavelet basis $\mathbf{b}(t)=[b_1(t), \dots, b_n(t)]$ on the interval $[0, T_m]$; by performing the Wavelet Expansion (WE) of a generic function $f(t)$, we obtain a vector of coefficients of dimension n ; the notation used is the following: $f(t)=\mathbf{b}\mathbf{f}=\sum_j b_j(t)f_j$, where $\mathbf{f}=[f_1, \dots, f_n]^T$ is the vector of the wavelet coefficients. By using the

differential operator \mathbf{D} and the integral operator \mathbf{I} in the wavelet domain (for wavelets on the interval, introduced in [11]) the differentiation (or integration) of a function is simply performed by a matrix – vector product, i.e.,

$$h(t)=\frac{df(t)}{dt} \Rightarrow \mathbf{h}=\mathbf{D}\mathbf{f}. \text{ Formally this means that it is}$$

possible to obtain the equation in the wavelet domain by simply using the Laplace domain equations and substitute the variables with the vectors of coefficients and the operator s with the differential matrix \mathbf{D} . According to this, equation (3) can be expressed as

$$(\tilde{\mathbf{W}}_\varphi + \tilde{\mathbf{G}}_\varphi)\mathbf{x}_\varphi = \mathbf{T}\mathbf{x}_\varphi = \mathbf{b} \quad (6)$$

i.e., an algebraic systems of the form $\mathbf{T}\mathbf{x}_\varphi = \mathbf{b}$ in which the matrix \mathbf{T} is straightforwardly calculated, the vector \mathbf{b} contains the WE of the independent generators and \mathbf{x}_φ is the vector of unknowns (the wavelet coefficients of the expansion of the unknown voltages).

For the example of Fig. 1 we obtain for the matrix

$$\tilde{\mathbf{W}}_\varphi + \tilde{\mathbf{G}}_\varphi = \mathbf{T} \quad \begin{bmatrix} G_1\mathbf{U} & -G_1\mathbf{U} & 0 & 0 & \mathbf{U} & 0 \\ -G_1\mathbf{U} & G_1\mathbf{U} + \mathbf{C}\mathbf{D} & -\mathbf{C}\mathbf{D} - G_2\mathbf{U} & 0 & 0 & 0 \\ 0 & -\mathbf{I}/L - G_2\mathbf{U} & \mathbf{I}/L + G_2\mathbf{U} & -G_2\mathbf{U} & 0 & 0 \\ 0 & 0 & -G_2\mathbf{U} & G_2\mathbf{U} & 0 & \mathbf{U} \\ \mathbf{U} & 0 & 0 & 0 & 0 & 0 \\ 0 & 0 & 0 & \mathbf{U} & 0 & 0 \end{bmatrix} \quad (7)$$

where \mathbf{U} is the identity matrix of the proper dimension. As it can be easily seen the matrix \mathbf{T} is sparse and the system can be easily and conveniently solved by an iterative technique, requiring a low CPU time consumption.

B. Treatment of the Nonlinearities

The presence of nonlinearities (connected at the output ports) leads to an additional term in equation (1)

$$\mathbf{W}_\varphi s\mathbf{x}_\varphi(s)+\mathbf{G}_\varphi\mathbf{x}_\varphi(s)+\mathbf{L}_\pi(s)\mathbf{i}_\pi(s)+\mathbf{L}[\mathbf{F}(\mathbf{x}_\varphi(t))]=\mathbf{b}(s) \quad (8)$$

where $\mathbf{F}(\mathbf{x}_\varphi(t))$ represents the above mentioned nonlinearities.

For the sake of simplicity we here refer to a simple two port network, represented in Fig. 2a, where one port is connected to an independent generator, while the other port is connected to a nonlinear load, whose constitutive

relation is $i = f(v)$. The extension to a more complex circuit (i.e. characterized by several ports, connected to generators, linear and nonlinear loads) is straightforward.



Fig. 2a. Circuit with a nonlinear load.



Fig. 2b. Application of the substitution's theorem.

It is possible to substitute the nonlinear load with a voltage generator imposing the unknown voltage $v_{NL}(t)$, as shown in Fig. 2b. Let us suppose that we are interested in calculating the current i_{NL} flowing through the nonlinear load. By applying the superposition effect (once the substitution has been performed the circuit is linear) we can write

$$i_{NL} = i_{NL}^a + i_{NL}^b \quad (9)$$

where the first term i_{NL}^a is related only to the presence of the independent generator E and can be calculated by simply solving a linear problem (of the kind reported in equation (6)), while i_{NL}^b is the current related to the effect of the unknown voltage generator and needs of course to be calculated. Under these assumptions we can write in the wavelet domain

$$\mathbf{i}_{NL} = \mathbf{i}_{NL}^a + \mathbf{i}_{NL}^b = \mathbf{i}_{NL}^a + \mathbf{T}\mathbf{v}_{NL} \quad (10)$$

where the vectors represent the WE of the currents, the matrix \mathbf{T} is the matrix solving the linear problem (see equation (6)), and \mathbf{v}_{NL} is the wavelet expansion of the unknown voltage source. At this stage equation (10) is characterized by two vectors of unknowns: \mathbf{i}_{NL} and \mathbf{v}_{NL} . The additional equation needed to solve the problem is the constitutive equation of the nonlinear load and it is enforced as follows.

By inverse transforming (10) we obtain the following time domain expression of the unknown current

$$i_{NL}(t) = i_{NL}^a(t) + \sum_k \sum_j T_{kj} v_{NL,j} b_k(t) \quad (11)$$

where the terms $b_k(t)$ are the function of the wavelet basis, $v_{NL,j}$ are the entries of the vector \mathbf{v}_{NL} , while the terms T_{kj} are the entries of the square matrix \mathbf{T} . Equation (11) must satisfy the constitutive equation of the nonlinear load $i = f(v)$; in order to enforce it we impose the collocation at the discrete times t_n , n equally spaced points in the interval $[0, T_m]$ (the ones which are characteristic of the definition of the wavelet functions [12]) obtaining a set of nonlinear equations in the unknown coefficients $v_{NL,j}$.

The constitutive equation of the nonlinear load $i - f(v) = 0$ can be written as

$$i_{NL}^a(t) + \sum_k \sum_j T_{kj} v_{NL,j} b_k(t) - f\left(\sum_j v_{NL,j} b_j(t)\right) = 0 \quad (12)$$

i.e., $F(\mathbf{v}_{NL}) = 0$ in which we underline that the unknowns are the coefficients $v_{NL,j}$. The analytical evaluation of the Jacobian is straightforwardly written as follows

$$\frac{\partial F}{\partial v_{NL}} = \sum_k T_{kj} b_k(t_n) - \frac{\partial f}{\partial v} b_j(t_n). \quad (13)$$

The solution of the system is performed by adopting a Newton – Raphson algorithm, with an analytical evaluation of the Jacobian. The convenience of the proposed method, in terms of low CPU time consumption in the presence of nonlinear loads, stands in the availability of the analytical form of the Jacobian; as a matter of fact its knowledge allows us to use a sparsification procedure which results in a reduction of the CPU time employed for the solution, as explained in the next section.

C. Computational Cost of the Proposed Method

The main advantage in using a wavelet basis stands in the fact that it is possible to represent very complex waveforms (typical of fast electrical transients, like the ones in microwave circuits) by a small number of wavelet functions (hence by a small number of coefficients). This leads to a reduced dimension of the matrices involved in the simulations, with respect to other standard techniques.

Furthermore it is well known that wavelets tend to concentrate in time zones where approximation needs to be high and have a reduced weight (low wavelet coefficients) in the other zones, a property known in the literature as self adaptive zooming. According to this observation, the use of a thresholding procedure is a common practice to reduce the computational cost [12], [13]. The coefficients of the wavelet matrix that are smaller than a fraction (typically a few thousandths) of the maximum are forced to zero.

This procedure does not significantly affect the accuracy of the computations (when reasonable values of the threshold are used) and produces sparse matrices that can be efficiently stored and computed. In particular in [12] it is shown that for diagonal dominant matrices it is possible to obtain a percentage of non-zero elements of the order between 5% and 15% with solutions that are affected by extremely low error. The sparsification procedure is convenient because the number of multiplications required for the simulation is considerably lower with respect to the full matrix, leading to a significant CPU time reduction and a lower storage memory.

It is noteworthy that a lower approximation in the evaluation of the Jacobian (which is exactly calculated by the analytical computation as in (13) and post processed by the sparsification procedure) does not affect the correctness of the solution, and may have effects only on the number of iterations necessary to reach convergence.

In the evaluation of the overall computation time reduction we have to consider the weight of the wavelet transform of the input quantities and the inverse wavelet transform of the results. These operations are efficiently performed via matrix vector products characterized by sparse matrices [14]. As a consequence the reduction of the time needed to perform the matrix vector product obtained with the threshold procedure has a strong impact on the overall computation cost, as it involves the most time consuming activity.

III. NUMERICAL APPLICATION

As an example of application of the proposed technique we considered the circuit schematically shown in Fig. 3. It is composed by four Multiconductor Transmission Lines (three conductors and ground each) represented by blocks B, C, E, and F and by the blocks A and D constituted by three longitudinally disposed resistors of 0.1Ω each. The per unit length parameters of the lines are the same for each line and are here reported

$$R = \begin{bmatrix} 351.63 & 0 & 0 \\ 0 & 366.11 & 0 \\ 0 & 0 & 351.63 \end{bmatrix} \Omega/\text{m}$$

$$L = \begin{bmatrix} 4.3698 \cdot 10^{-7} & 7.675 \cdot 10^{-8} & 1.57 \cdot 10^{-8} \\ 7.675 \cdot 10^{-8} & 4.35 \cdot 10^{-7} & 7.675 \cdot 10^{-8} \\ 1.57 \cdot 10^{-8} & 7.675 \cdot 10^{-8} & 4.3698 \cdot 10^{-7} \end{bmatrix} \text{H/m}$$

$$G = \begin{bmatrix} 7.5 \cdot 10^{-4} & 0 & 0 \\ 0 & 7.5 \cdot 10^{-4} & 0 \\ 0 & 0 & 7.5 \cdot 10^{-4} \end{bmatrix} \Omega^{-1}/\text{m}$$

$$C = \begin{bmatrix} 1.082 \cdot 10^{-10} & -0.197 \cdot 10^{-10} & -0.006 \cdot 10^{-10} \\ -0.197 \cdot 10^{-10} & 1.124 \cdot 10^{-10} & -0.197 \cdot 10^{-10} \\ -0.006 \cdot 10^{-10} & -0.197 \cdot 10^{-10} & 1.082 \cdot 10^{-10} \end{bmatrix} \text{F/m}$$

The lines in B and C are respectively long 10 and 5 cm, while those in E and F have the same length of 15 cm.

A voltage generator of waveform

$$e_1(t) = 10 \cdot e^{-\left(\frac{t-2T}{T}\right)^2} \cdot \sin[2\pi f(t-2T)] V$$

is applied to terminal #1, with $T = 0.11 \text{ ns}$, $f = 2.8 \text{ GHz}$ and characterized by an internal resistive impedance $R_1 = 10 \Omega$.

The amplitude of the waveform $e_1(t)$ shown in Fig. 4, has been chosen in order to strongly evidence the nonlinear effects.

Terminals 2, 3, 5, 6, 8, 9, 11, and 12 are connected to 50Ω termination resistances.

Terminal # 4 is terminated on the series connection of a 15Ω resistance and of a nonlinearity described by the following characteristic

$$v_4(t) = 10^5 \cdot i_4^3(t).$$

Terminals 7 and 10 are terminated on series connection between a 20Ω resistance and a diode of characteristic

$$i_{4,7}(t) = I_0 \cdot \left(e^{v_{4,7}(t)/v_r} - 1 \right)$$

where $I_0 = 1 \text{ pA}$ and $v_r = 0.025865 \text{ V}$.

The system has been simulated by using a basis of 128 Daubechies wavelet with 6 vanishing moments.

The same system has also been simulated with SPICE and the results have been compared with those obtained by the approach here presented.

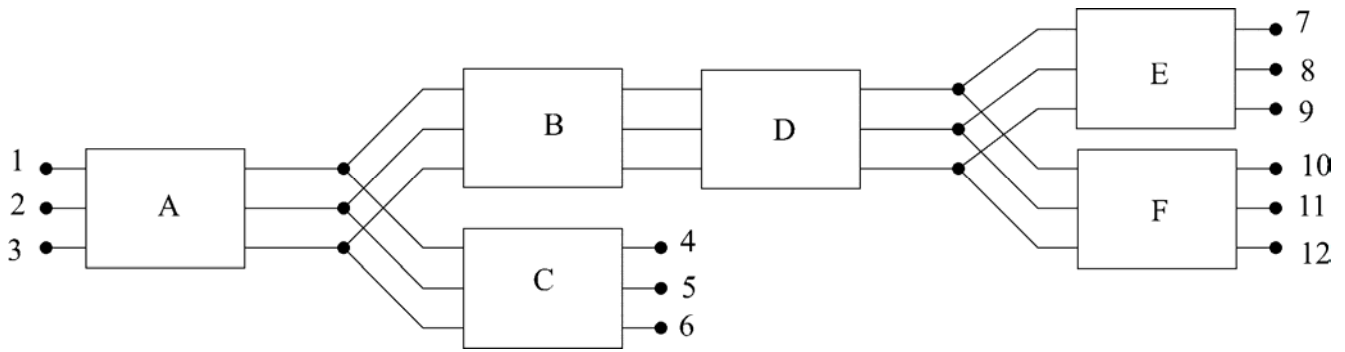


Fig.3. Analysed circuit.

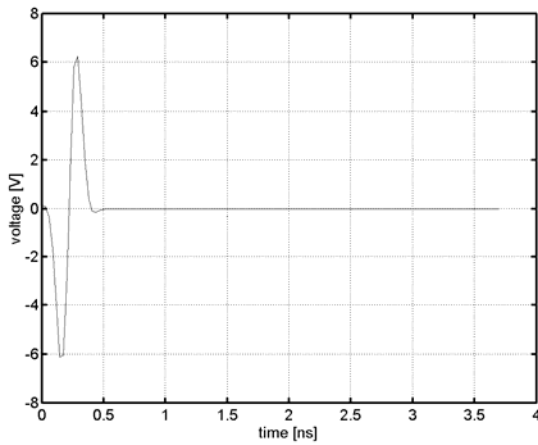


Fig. 4. Input voltage at terminal #1.

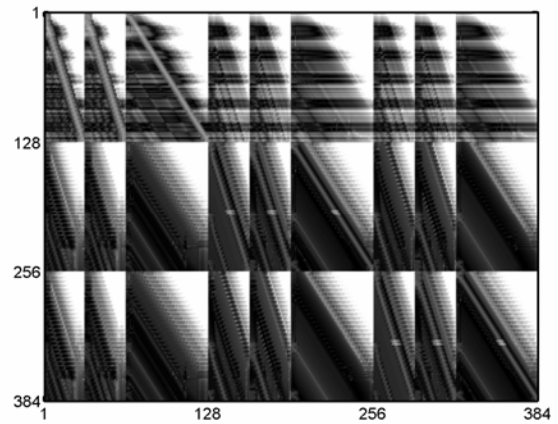


Fig. 6. Typical sparsity pattern of the Jacobian matrix in the version that uses original full matrices.

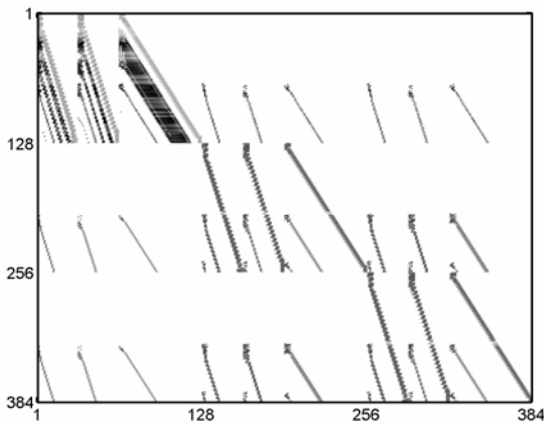


Fig. 5. Typical sparsity pattern of the Jacobian matrix in the version that uses sparse matrices.

Two versions of the proposed method have been implemented: the first one which performs the sparsification in order to take advantage of the available numerical routines for treatment of sparse matrices while the other uses the original full matrices.

The comparison has been performed by considering the Jacobian matrices related to comparable deviation of $F(v_{NL})$ from zero in the cases of solution of the sparsified and original system.

Figures 5 and 6, respectively, show the Jacobian used in Newton-Raphson scheme with and without sparsification.

Figures 7 and 8, respectively, show the voltage and the current on the cubic nonlinearity.

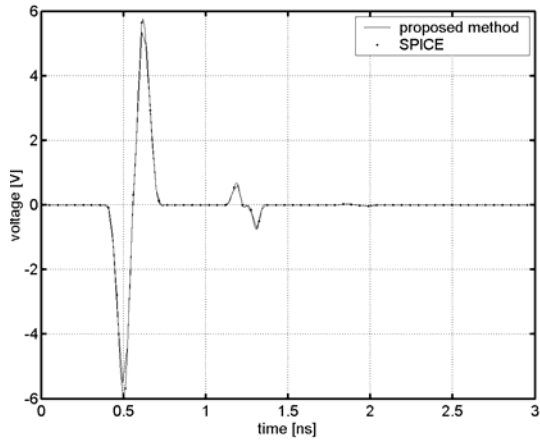


Fig. 7. Comparison between the voltages on the cubic nonlinearity obtained by the proposed approach and by SPICE.

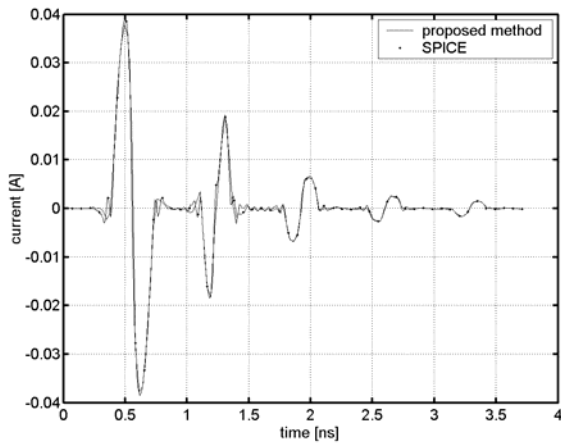


Fig. 8. Comparison between the currents on the cubic nonlinearity obtained by the proposed approach and by SPICE.

The waveforms obtained by the two approaches are practically indistinguishable. In order to appreciate the good agreement between the results a zoom on the voltages is shown in Fig. 9.

Figures 10 and 11 show the voltage and the current on the diodes. As expected the current on the diode is unidirectional and the voltage on the diode does not exceed the value of 0.65 V that approximately represents the direct bias voltage of a silicon diode.

The first procedure has required 23 iterations while the second one 35. The solution of the linear system obtained after the thresholding procedure was about five times faster than that in the other one. The total CPU time (2.8 sec) required to solve the nonlinear problem by using sparse matrices using the standard Newton-Raphson was three times shorter than the modified Newton-Raphson

with full matrices (9.3 sec). The used threshold was 5% of the maximum element of each column.

As for the SPICE simulation the CPU time was about 4 seconds.

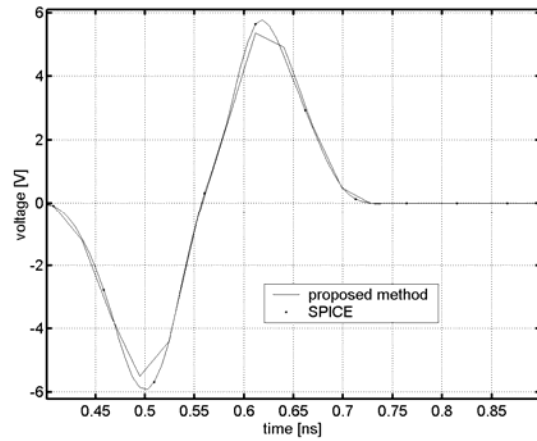


Fig. 9. Enlarged portion of Fig. 7.

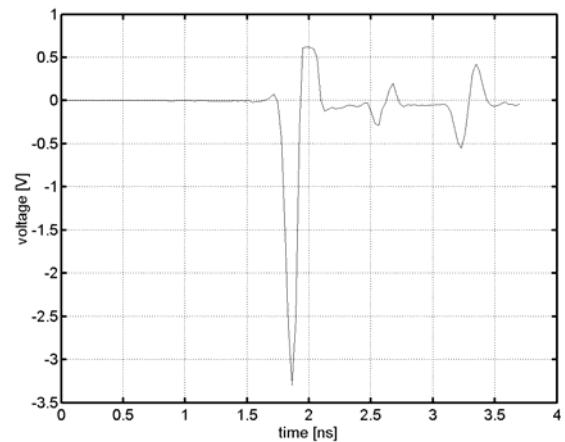


Fig. 10. Voltage on the diodes on terminals #7 and #10.

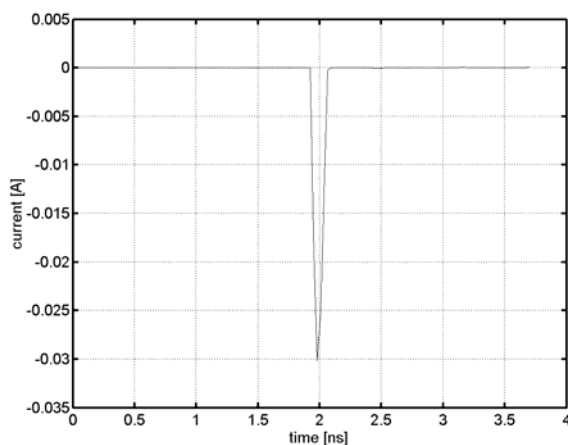


Fig. 11. Current across the diodes on terminals #7 and #10.

IV. CONCLUSIONS

A method for the simulation of complex circuits, in presence of nonlinear elements is here proposed. The method is based on wavelet expansion and a special treatment of the nonlinearity. The method allows a fast computation, together with the required accuracy and low memory consumption.

ACKNOWLEDGMENTS

This work is supported in part by the Italian Ministry of University (MIUR) under a Program for the Development of Research of National Interest (PRIN grant # 2004093025).

REFERENCES

- [1] A. R. Djordjevic and T. K. Sarkar, "Analysis of Time Response of Lossy Multiconductor Transmission Line Networks," *IEEE Trans. Microwave Theory Tech.*, vol 43, pp. 314 – 323, Oct. 1987.
- [2] J. E. Schutt-Aine and R. Mittra, "Nonlinear Transient Analysis of Coupled Transmission Lines," *IEEE Trans. Circuits Syst.*, vol 36, pp. 959 – 967, July 1989.
- [3] P. Stenius, P. Heikkila, and M. Valtonen, "Transient Analysis of Circuits Including Frequency Dependent Components Using Transgyrator and Convolution," *Proc. 11th European Conf. Circuit Theory Design pt. III*, pp. 1299 – 1304, 1993.
- [4] R. Achar, M. S. Nakhla, and Q. J. Zhang, "Full Wave Analysis of High Speed Interconnects Using Complex Frequency Hopping," *IEEE Trans. Computer Aided Design*, vol. 17, pp. 997 – 1010, Oct. 1998.
- [5] E. Chiprout and M. Nakhla, "Fast Nonlinear Waveform Estimation for Large Distributed Networks," *IEEE MTT-S Int. Microwave Symp. Dig.*, vol. 3, pp. 1341 – 1344, June 1992.
- [6] R. J. Trihy and R. A. Rohrer "AWE Macromodels for Nonlinear Circuits," *Proc. 36th Midwest Circuits Syst. Symp*, vol 1., pp. 633 – 636, Aug. 1993.
- [7] R. Griffith and M. S. Nakhla "Mixed Frequency/Time Domain Analysis of Nonlinear Circuits," *IEEE Trans. Computer Aided Design*, vol 11, pp. 1032 – 1043, Aug. 1992.
- [8] N. Soveiko and M. S. Nakhla, "Steady State Analysis of Multitone Nonlinear Circuits in Wavelet Domain," *IEEE Trans. Microwave Theory Tech.*, vol. 52, no. 3, pp. 75 – 797, March 2004.
- [9] D. Zhou, W. Cai, and X. Zeng, "An Adaptive Wavelet Method for Nonlinear Circuit Simulation,"

IEEE Trans. Circuit Systems I, vol. 46, no. 8, pp. 931 – 938, Aug. 1999.

- [10] R. Achar and M. S. Nakhla, "Simulation of High Speed Interconnects," *Proc. of The IEEE*, vol. 89, no. 5, pp. 693 728, May 2001.
- [11] S. Barmada and M. Raugi, "A General Tool for Circuit Analysis Based on Wavelet Transform," *Int. J. of Circuit Theory and Applications*, vol. 28, no. 5, pp. 461 – 480, 2000.
- [12] T. K. Sarkar and M. Salazar – Palma, M. C. Wicks, *Wavelet Applications in Engineering Electromagnetics*. Artech House, 2002.
- [13] R. L. Wagner and W. C. Chew, "A Study of Wavelets for the Solution of Electromagnetic Integral Equations," *IEEE Trans. On Antenna and Prop.*, vol. 43, no. 8 pp. 802-810, Aug. 1995.
- [14] T. Palenius and J. Roos, "Comparison of Reduced-Order Interconnect Macromodels for Time Domain Simulation," *IEEE Trans. Microwave Theory Tech.*, vol. 52, no. 9, pp. 2240-2250, Sept. 2004.
- [15] T. K. Sarkar, C. Su, R. Adve, M. Salazar Palma, L. Garcia Castillo, and R. R. Boix, "A Tutorial on Wavelets from an Electrical Engineering Perspective, Part 1: Discrete Wavelet Techniques," *IEEE Antenna and Propagation Magazine*, vol. 40, no. 5, pp. 49-70, Oct. 1998.



Sami Barmada was born in Livorno, Italy, on November 18, 1970. He received the Master and Ph.D. degrees in electrical engineering from the University of Pisa, Pisa, Italy, in 1995 and 2001, respectively.

From 1995 to 1997, he was with ABB Teknologi, Oslo, Norway, where he was involved with distribution network analysis and optimization. He is currently an Associate Professor with the Department of Electrical System and Automation, University of Pisa, where he is involved with numerical computation of electromagnetic fields, particularly on the modeling of multiconductor transmission lines and to the application of wavelet expansion to computational electromagnetics.

Dr. Barmada was the technical chairman of the Progress In Electromagnetic Research Symposium (PIERS), Pisa, Italy, 2004 and the General Chair of the ACES 2007 Conference, Verona, Italy.

He was the recipient of the 2003 J F Alcock Memorial Prize, presented by The Institution of Mechanical Engineering, Railway Division, for the best paper in technical innovation.



Antonino Musolino was born in Reggio Calabria on January the 7th 1964. He received the Master degree in Electronic Engineering and the Ph. D degree in Electrical Engineering from the University of Pisa in 1990 and 1995 respectively.

He is currently an Associate Professor of electrical engineering with the Department of Electrical Systems and Automation, University of Pisa. His main research activities are the numerical methods for the analysis of electromagnetic fields in linear and nonlinear media, the design of special electrical machines and the application of the WE to computational electromagnetics.



Marco Raugi received the Electronic Engineering degree and Ph.D. degree in electrical engineering from the University of Pisa, Pisa, Italy, in 1985, and 1990, respectively.

He is currently a Full Professor of electrical engineering with the Department of Electrical Systems and Automation, University of Pisa. His research concerns numerical methods for the analysis of electromagnetic fields in linear and nonlinear media. His main applications have been devoted to nondestructive testing, electromagnetic compatibility in TLLs, and electromagnetic launchers. He has authored or coauthored approximately 100 papers in international journals and conferences. He has served as chairman for various Editorial Boards.

Dr. Raugi was the general chairman of the Progress In Electromagnetic Research Symposium (PIERS), Pisa, Italy, 2004. He has served as chairman and session organizer of international conferences.

He was the recipient of the 2002 IEEE Industry Application Society Melcher Prize Paper Award.

Monochromatic Scattering from Three-Dimensional Gyrotropic Bodies Using the TLM Method

Ahmet F. Yagli¹, Jay K. Lee², and Ercument Arvas²

(1) Turksat A.S.

Konya Yolu 40.km Golbasi, Ankara, Turkey
afyagli@turksat.com.tr

(2) Department of Electrical Engineering and Computer Science
Syracuse University, Syracuse, NY 13244, USA
leejk@syr.edu, earvas@syr.edu

Abstract – A three-dimensional scattering field Transmission Line Modeling (TLM) algorithm is established to obtain bistatic radar cross sections of gyroelectric and gyromagnetic objects at a single frequency. Although gyrotropic material properties are highly frequency dependent, their permittivity and permeability tensors are made of complex constants at a given frequency. For verification, the results for gyrotropic spheres are compared with those from previous studies, in which an analytical approach and the Method of Moments along with Conjugant Gradient Fast Fourier Transform method were used.

Index terms – Gyrotropic material, Scattering, Transmission Line Modeling (TLM).

I. INTRODUCTION

Obtaining the electromagnetic scattering of three dimensional homogeneous gyrotropic objects is the main goal of this paper. Previously, there have been some studies regarding the radar cross sections of two dimensional or three dimensional anisotropic materials. An analytical solution of electromagnetic fields in homogeneous plasma anisotropic media is given by Geng et al. [1]. They displayed some numerical results of scattering from gyroelectric spheres. Geng and Wu [2] showed an analytical solution of the scattering fields of a ferrite sphere by a plane wave using spherical vector-wave function. They compare some of their numerical results for radar cross sections of gyromagnetic spheres with MoM CG-FFT simulation results of Zhu et al. [3].

Differential time domain methods such as the finite difference time domain (FDTD) method [4] or the transmission line modeling (TLM) method [5] are widely used for modeling electromagnetic problems consisting

of complex materials with arbitrarily shaped structures. The main difference between the two techniques is the layout of the unit cell and the time-stepping process [6,7]. In this paper, we derive a scattering field 3D TLM formulation from Paul's algorithm discussed in Reference [6]. Paul's TLM algorithm is a total field formulation, in which it was difficult to generate a perfect plane wave as our incident wave. We needed to obtain the scattering field formulation, where the incident wave is analytically injected to the computation space. Since our TLM computation space is truncated, a near field to far field transformation method is also used to obtain the far field scattering [8,9].

We describe the TLM algorithm used for modeling 3D gyrotropic objects in this study. Then the simulation results of gyrotropic spheres, cubes, and finite cylinders are demonstrated. Our TLM simulation results for gyrotropic spheres are validated by the currently available alternative methods.

II. GYROTROPIC MEDIA

Gyrotropic media have been an important research topic because of their anisotropic and nonreciprocal behavior. When subjected to a constant magnetic field, both plasmas and ferrites, which exist in nature, exhibit anisotropic constitutive parameters. Plasmas and ferrites under the influence of the applied magnetic field, are generally called magnetized plasmas (or magnetoplasmas) and magnetized ferrites respectively. For magnetized plasmas the anisotropy is described by using a permittivity tensor instead of a scalar permittivity, because of their rich free electron content. On the other hand, magnetized ferrites are characterized by a permeability tensor in place of a scalar permeability value. In ferrites, the anisotropic behavior is due to the magnetic dipole moments, which form the structure of the material.

A good example for magnetized plasmas is the earth's ionosphere layer, where the free electrons and charged ions are greatly affected by the earth's magnetic field between the two poles. We can see the ionosphere as a free electron gas around a huge magnet. There is a wide variety of usage for ferrite devices, from telecommunication to military applications.

A gyrotropic medium is called *electrically gyrotropic* or *gyroelectric* if the medium is characterized by a relative permittivity tensor and a constant permeability value. If we write the constant magnetic field as $\vec{B}_0 = \hat{b}_0 B_0$, where the unit vector \hat{b}_0 shows the direction of the field vector, the relative permittivity and permeability tensors of a gyroelectric medium can be expressed in the following dyadic form

$$\vec{\bar{\epsilon}} = \epsilon_1 (\vec{\bar{I}} - \hat{b}_0 \hat{b}_0) - j\epsilon_2 (\hat{b}_0 \times \vec{\bar{I}}) + \epsilon_3 \hat{b}_0 \hat{b}_0, \quad \vec{\bar{\mu}} = \mu \vec{\bar{I}}. \quad (1)$$

In this equation $\vec{\bar{I}}$ is the unit matrix, which has value of 1 at diagonal elements and 0 at off-diagonal elements, and j is $\sqrt{-1}$. In this study the time variation of field components is taken as $e^{j\omega t}$.

When a medium is characterized by a relative permeability tensor and a constant permittivity value, the medium is called *magnetically gyrotropic* or *gyromagnetic*. The relative permittivity and permeability tensors of a gyromagnetic medium can be expressed in the following dyadic form

$$\vec{\bar{\mu}} = \mu_1 (\vec{\bar{I}} - \hat{b}_0 \hat{b}_0) - j\mu_2 (\hat{b}_0 \times \vec{\bar{I}}) + \mu_3 \hat{b}_0 \hat{b}_0, \quad \vec{\bar{\epsilon}} = \epsilon \vec{\bar{I}}. \quad (2)$$

Reference [10] discusses dyadic tensor and vector operations in detail.

In the Cartesian coordinate system, if $\vec{B}_0 = \hat{z} B_0$, the relative permittivity and permeability tensors can be obtained as

$$\vec{\bar{\epsilon}} = \begin{bmatrix} \epsilon_1 & j\epsilon_2 & 0 \\ -j\epsilon_2 & \epsilon_1 & 0 \\ 0 & 0 & \epsilon_3 \end{bmatrix} \quad (3)$$

and

$$\vec{\bar{\mu}} = \begin{bmatrix} \mu_1 & j\mu_2 & 0 \\ -j\mu_2 & \mu_1 & 0 \\ 0 & 0 & \mu_3 \end{bmatrix}. \quad (4)$$

For example, if the medium is a magnetoplasma, which is a gyroelectric medium, then the permittivity tensor parameters are given by [11]

$$\epsilon_1 = 1 - \frac{\omega_p^2 (\omega - j\nu_c)}{\omega [(\omega - j\nu_c)^2 - \omega_b^2]}, \quad (5a)$$

$$\epsilon_2 = -\frac{\omega_p^2 \omega_b}{\omega [(\omega - j\nu_c)^2 - \omega_b^2]}, \quad (5b)$$

$$\epsilon_3 = 1 - \frac{\omega_p^2}{\omega^2 - j\omega\nu_c} \quad (5c)$$

where ω_b is the gyrofrequency or cyclotron frequency, ω_p is the plasma frequency, and ν_c is the electron collision frequency representing the loss mechanism. (ω is the angular frequency and equal to $2\pi f$.) The cyclotron frequency represents the effect of the applied magnetic field, and is proportional to this static magnetic field

$$\omega_b = -\frac{eB_0}{m}. \quad (6)$$

Here m denotes the mass of each electron with charge e , which is a negative number. The positive number $-e/m$ is called the gyromagnetic ratio.

The plasma frequency can be formulated as

$$\omega_p = \sqrt{\frac{N_0 e^2}{m \epsilon_0}} \quad (7)$$

where N_0 is the number of free electrons per unit volume.

The effect of collisions, which leads to the absorption of energy, is taken into account by adding the collision frequency into the formulation. These collisions are mainly due to thermal motions. For *cold* plasma, thermal motions are generally neglected, since the distance traversed by an electron is shorter. With $\nu_c = 0$, the parameters of the permittivity tensor of the cold plasma can be written as follows

$$\epsilon_1 = 1 - \frac{\omega_p^2}{\omega^2 - \omega_b^2}, \quad (8a)$$

$$\epsilon_2 = -\frac{\omega_p^2 \omega_b}{\omega(\omega^2 - \omega_b^2)}, \quad (8b)$$

$$\epsilon_3 = 1 - \frac{\omega_p^2}{\omega^2}. \quad (8c)$$

The derivations of these parameters are given in [12].

On the other hand if the medium is a magnetized ferrite which is a gyromagnetic medium, then the permeability parameters are defined as [10]

$$\mu_1 = 1 + \frac{\omega_0 \omega_m}{\omega_0^2 - \omega^2}, \quad (9a)$$

$$\mu_2 = \frac{\omega \omega_m}{\omega_0^2 - \omega^2}, \quad (9b)$$

$$\mu_3 = 1 \quad (9c)$$

where ω_m is the saturation magnetization frequency, and ω_0 is the Larmor precessional frequency.

III. SCATTERING FIELD 3D TLM MODELING OF GYROTROPIC MEDIA

In his Ph.D dissertation [6] and his paper [7], Paul established a new TLM formulation starting from Maxwell's equations. In his method, the governing field update equation in Laplace domain is

$$2\overline{F}^e = 4\overline{F} + \overline{\sigma} \overline{F} + s\Delta t 2\overline{M} \overline{F} \quad (10)$$

where $\overline{\sigma}$ and \overline{M} are the conductivity and the susceptibility matrices, respectively ($s = j2\pi f$). \overline{F}^e (in Paul's dissertation it is represented as \overline{F}^r and called the vector of reflected fields) is the node excitation vector and \overline{F} is the vector of total normalized fields. s is the Laplace variable and Δt stands for the time step duration. Starting from the total field TLM formulation's governing field update equation (10), we can derive the scattering field TLM formulation, which has a field update equation in the form of

$$2\overline{F}_{scat}^e = 4\overline{F}_{scat} + \overline{\sigma} \overline{F}_{scat} + s\Delta t 2\overline{M} \overline{F}_{scat} + \overline{\sigma} \overline{F}_{inc} + s\Delta t 2\overline{M} \overline{F}_{inc} \quad (11)$$

where \overline{F}_{scat} and \overline{F}_{inc} are the normalized scattered and incident field vectors [13,14].

In our computations, the conductivity matrix $\overline{\sigma}$ will be taken as zero. The susceptibility matrix \overline{M} has both real and imaginary elements.

Since we assume an applied static magnetic field in z direction, the relative permittivity tensor of the gyroelectric materials has the following form

$$\overline{\epsilon} = \begin{bmatrix} \epsilon_1 & j\epsilon_2 & 0 \\ -j\epsilon_2 & \epsilon_1 & 0 \\ 0 & 0 & \epsilon_3 \end{bmatrix} \quad (12)$$

which means an electric susceptibility matrix of

$$\overline{\chi}_e = \begin{bmatrix} \chi_{e1} & \chi_{e2} & 0 \\ -\chi_{e2} & \chi_{e1} & 0 \\ 0 & 0 & \chi_{e3} \end{bmatrix} = \begin{bmatrix} \epsilon_1 - 1 & j\epsilon_2 & 0 \\ -j\epsilon_2 & \epsilon_1 - 1 & 0 \\ 0 & 0 & \epsilon_3 - 1 \end{bmatrix}. \quad (13)$$

Similarly, for gyromagnetic materials, the relative permeability tensor will be given by

$$\overline{\mu} = \begin{bmatrix} \mu_1 & j\mu_2 & 0 \\ -j\mu_2 & \mu_1 & 0 \\ 0 & 0 & \mu_3 \end{bmatrix} \quad (14)$$

which implies a magnetic susceptibility matrix of

$$\overline{\chi}_m = \begin{bmatrix} \chi_{m1} & \chi_{m2} & 0 \\ -\chi_{m2} & \chi_{m1} & 0 \\ 0 & 0 & \chi_{m3} \end{bmatrix} = \begin{bmatrix} \mu_1 - 1 & j\mu_2 & 0 \\ -j\mu_2 & \mu_1 - 1 & 0 \\ 0 & 0 & \mu_3 - 1 \end{bmatrix}. \quad (15)$$

For single frequency formulation, the tensor elements will be constant values. Thus, \overline{M} matrix consists of constant elements which have real and imaginary parts. For gyroelectric medium we have

$$\overline{M} = \begin{bmatrix} \chi_{e1} & \chi_{e2} & & & & \\ -\chi_{e2} & \chi_{e1} & & & & \\ & & \chi_{e3} & & & \\ & & & \chi_m & & \\ & & & & \chi_m & \\ & & & & & \chi_m \end{bmatrix} \quad (16)$$

where χ_m is the magnetic susceptibility value. The matrix elements, which are not shown, have a value of zero. For gyromagnetic case the matrix \overline{M} has the form

$$\overline{M} = \begin{bmatrix} \chi_e & & & & & \\ & \chi_e & & & & \\ & & \chi_e & & & \\ & & & \chi_{m1} & \chi_{m2} & \\ & & & -\chi_{m2} & \chi_{m1} & \\ & & & & & \chi_{m3} \end{bmatrix} \quad (17)$$

where χ_e is the electric susceptibility value. χ_m and χ_e are assumed to be real quantities.

In the field update equation

$$2\overline{F}_{scat}^e = 4\overline{F}_{scat} + s\Delta t 2\overline{M} \overline{F}_{scat} + s\Delta t 2\overline{M} \overline{F}_{inc} \quad (18)$$

when we multiply the matrix elements with $s\Delta t$ term, we will have

$$s\Delta t \chi_{e1} = s\Delta t \Re[\epsilon_1] + js\Delta t \Im[\epsilon_1] = s\Delta t \Re[\epsilon_1] - \omega\Delta t \Im[\epsilon_1], \quad (19)$$

$$s\Delta t \chi_{m1} = s\Delta t \Re[\mu_1] + js\Delta t \Im[\mu_1] = s\Delta t \Re[\mu_1] - \omega\Delta t \Im[\mu_1], \quad (20)$$

$$s\Delta t \chi_{e2} = -s\Delta t \Im[\epsilon_2] + js\Delta t \Re[\epsilon_2] = -s\Delta t \Im[\epsilon_2] - \omega\Delta t \Re[\epsilon_2], \quad (21)$$

$$s\Delta t \chi_{m2} = -s\Delta t \Im[\mu_2] + js\Delta t \Re[\mu_2] = -s\Delta t \Im[\mu_2] - \omega\Delta t \Re[\mu_2], \quad (22)$$

$$s\Delta t \chi_{e3} = s\Delta t \Re[\epsilon_3] + js\Delta t \Im[\epsilon_3] = s\Delta t \Re[\epsilon_3] - \omega\Delta t \Im[\epsilon_3], \quad (23)$$

$$s\Delta t \chi_{m3} = s\Delta t \Re[\mu_3] + js\Delta t \Im[\mu_3] = s\Delta t \Re[\mu_3] - \omega\Delta t \Im[\mu_3] \quad (24)$$

where $\Re[\cdot]$ and $\Im[\cdot]$ denote the real and imaginary parts of $[\cdot]$, respectively. According to the derivations shown above, the term $s\Delta t 2\overline{M}$ can be decomposed into two parts as

$$s\Delta t 2\overline{M} = s\Delta t 2\overline{X}_1 + 2\overline{X}_2 \quad (25)$$

where both \overline{X}_1 and \overline{X}_2 matrices have real valued elements and can be shown in explicit form for gyroelectric

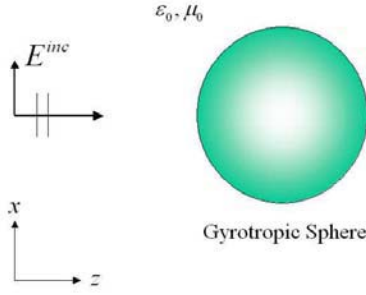


Fig. 1. Incidence of a plane wave to a gyrotropic sphere in free space.

where

$$V_{inc} = i_{inc} = -\Delta l \sin(2\pi f(n\Delta t - \frac{1}{c}z\Delta l)) \quad (39)$$

n is the time step index and z is the z coordinate index of the cell. We have $-\Delta l$ in the front, since these quantities are normalized fields. V_{inc} in (38) denotes the E field in x direction, while i_{inc} represents the H field in y direction.

The results of bistatic RCS (radar cross section) calculations of gyrotropic spheres obtained by Geng et al. [1,2] and Zhu et al. [3], were reproduced using the TLM algorithm discussed before. Zhu et al. used the Method of Moments (MoM) speeded up with the Conjugate-Gradient Fast Fourier Transform (CG-FFT) approach. In [1] and [2], Geng et al. derived the scattering fields of eigenfunction representation in spectral domain, using the expansion of plane wave factors with the spherical vector wave function in isotropic media, and the Fourier Transformation. Since the results of the previous studies are for the total RCS (summation of co-polarization scattering and cross-polarization scattering) on E plane (the plane which is parallel to E^{inc}) and on H plane, which is perpendicular to the E plane, here we calculate the RCS of the same type in order to compare with the previous results.

First, we will examine a gyroelectric sphere, where the electrical dimension is chosen as $k_0 a = 0.5$ (k_0 is the free space wavenumber). Discretized space step Δl is set to be $a/20$ in our simulation. The time step Δt is equal to $\Delta l/2c$ for 3D TLM simulations, where c is the speed of light in free space, because the transmission lines connecting the nodes have an inductance per unit length of $\mu_0/2$ and a capacitance per unit length of $\epsilon_0/2$. Thus, the velocity of propagation inside the transmission lines is $2c$. The relative permittivity tensor elements are assumed to be $\epsilon_1 = 5$, $\epsilon_2 = 1$, $\epsilon_3 = 7$. On the other hand, the relative permeability of the sphere is assumed

to be 1. Our simulation results are compared with those of Geng et al. in Fig. 2. The E plane is the xz plane, while the H plane is the yz plane. The results agree well with each other.

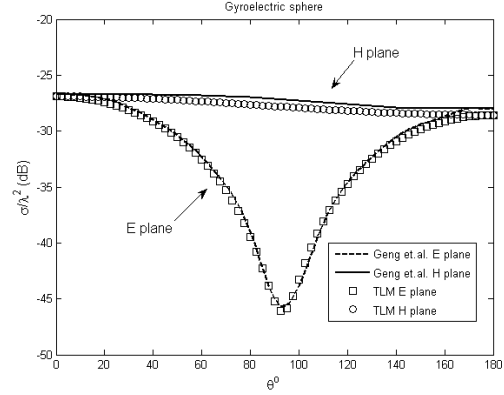


Fig. 2. Radar cross sections versus scattering angle θ . The results of TLM algorithm are shown along with the results of Geng et al. [1]. $k_0 a = 0.5$, $\epsilon_1 = 5$, $\epsilon_2 = 1$, $\epsilon_3 = 7$ ($\Delta l = a/20$)

Another gyroelectric sphere with $k_0 a = \pi$ is considered. The relative permeability value is chosen to be 1, while the relative permittivity tensor elements are $\epsilon_1 = 5.3495$, $\epsilon_2 = -2$, $\epsilon_3 = 7$. This example is also taken from the paper of Geng et al. [1]. The simulation was run with $\Delta l = \lambda/50$ (λ is free space wavelength). The agreement between the RCS results, which are plotted in Fig. 3, is reasonably good.

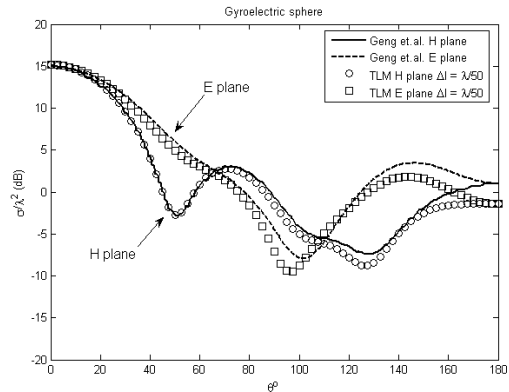


Fig. 3. Radar cross sections versus scattering angle θ . The results of TLM algorithm are shown along with the results of Geng et al. [1]. $k_0 a = \pi$, $\epsilon_1 = 5.3495$, $\epsilon_2 = -2$, $\epsilon_3 = 7$ ($\Delta l = \lambda/50$)

Our next simulation case is a gyromagnetic sphere, where $k_0 a = 0.2\pi$. The discretized space step Δl is chosen to be $a/20$, and $\Delta t = \Delta l/2c$. The relative

permeability tensor elements are $\mu_1 = 5$, $\mu_2 = -1$, and $\mu_3 = 7$. Although, $\mu_3 = 7$ does not represent the ferrite material, we chose it to compare with the results of Geng et al.[2]. We assumed the relative permittivity of the sphere as 1. Fig. 4 shows the comparison of our simulation results with those of Geng et al.[2].

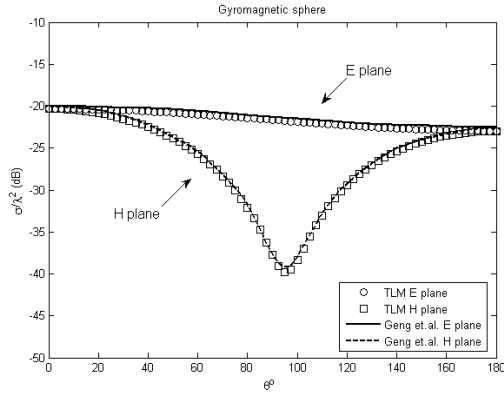


Fig. 4. Radar cross sections versus scattering angle θ . The results of TLM algorithm are shown along with the results of Geng et al. [2]. $k_0a = 0.2\pi$, $\mu_1 = 5$, $\mu_2 = -1$, $\mu_3 = 7$

As another simulation example, we modeled a gyromagnetic sphere with $k_0a = 2$, whose RCS was computed by Zhu et al. previously [3]. Similar to our previous sphere examples, we assumed a relative permittivity of 1. The relative permeability tensor elements are $\mu_1 = 1$, $\mu_2 = -1$ and $\mu_3 = 1$. $\Delta l = a/20$ and $\Delta t = \Delta l/2c$. Our RCS results agree well with the results obtained by Zhu et al. as shown in Fig. 5.

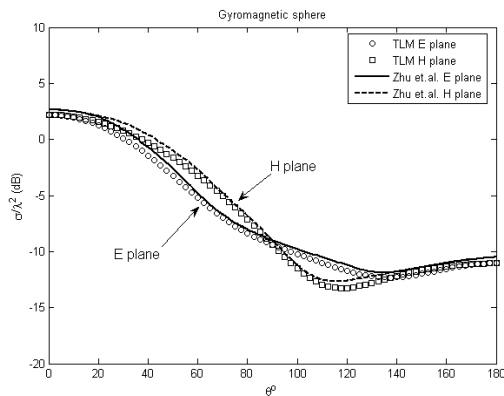


Fig. 5. Radar cross sections versus scattering angle θ . The results of TLM algorithm are shown along with the results of Zhu et al. [3]. $k_0a = 2$, $\mu_1 = 1$, $\mu_2 = -1$, $\mu_3 = 1$

It has been shown that our bistatic RCS results for

gyrotropic spheres modeled using TLM algorithm agree well with the analytic bistatic RCS results of Geng et al. and MoM CG-FFT results of Zhu et al. As an advantage, our method is capable of simulating arbitrarily shaped, inhomogeneous objects. The radiation problems are also easy to implement with our technique.

Next, we will demonstrate the simulation of a gyroelectric cube. The incident field is x polarized plane wave traveling in z direction as shown in Fig. 6. In our computations the center of the cube coincides with the origin of the coordinate system. The length d of one side of the cube, is set to be 1.2λ , where λ is the wave length of the incident field.

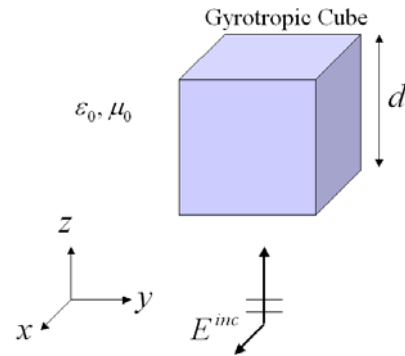


Fig. 6. Incidence of a plane wave on a gyrotropic cube in free space.

In our simulation $\Delta l = \lambda/30$ and $\Delta t = \Delta l/2c$. The permeability of the gyroelectric material is 1, while the permittivity tensor values are $\epsilon_1 = 1$, $\epsilon_2 = 1$ and $\epsilon_3 = 1$. The bistatic RCS of the cube is given in Fig. 7.

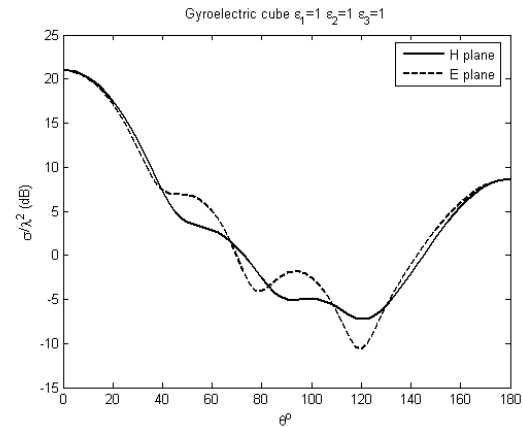


Fig. 7. Bistatic radar cross sections of the gyroelectric cube versus scattering angle θ . $d = 1.2\lambda$, $\epsilon_1 = 1$, $\epsilon_2 = 1$, and $\epsilon_3 = 1$.

Keeping the dimensions of the cube as same as

gyroelectric case, we modeled a gyromagnetic cube, with a relative permittivity of 1. The relative permeability tensor elements are assumed as $\mu_1 = 1$, $\mu_2 = 1$ and $\mu_3 = 1$. The discrete time-step and space-step values are kept the same as gyroelectric cube case. Fig. 8 exhibits the bistatic RCS results of our TLM simulation for this gyromagnetic cube.

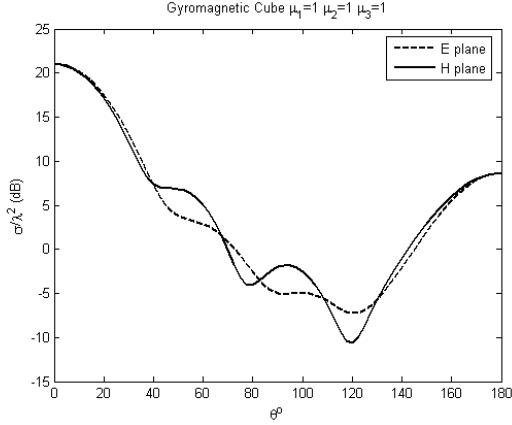


Fig. 8. Bistatic radar cross sections of the gyromagnetic cube versus scattering angle θ . $d = 1.2\lambda$, $\mu_1 = 1$, $\mu_2 = 1$, and $\mu_3 = 1$.

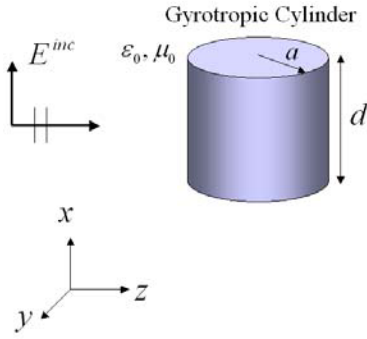


Fig. 9. Incidence of a plane wave on a gyrotropic finite cylinder in free space.

The finite circular cylinder is another special case in investigating the electromagnetic scattering of three dimensional gyrotropic objects. In our TLM simulations, we placed the gyrotropic cylinder as in Fig. 9, where the circular cross section is in y - z plane. An x polarized incident plane wave is traveling in z direction. The radius of the cylinder is denoted as a , while the height is represented by d .

We first modeled a gyroelectric cylinder, which has a height of $d = 1.2\lambda$ and a radius of $a = d/2$. We set $\Delta l = \lambda/30$ and $\Delta t = \Delta l/2c$. Our gyroelectric

cylinder has a relative permeability of 1, while the relative permittivity tensor elements are $\varepsilon_1 = 1$, $\varepsilon_2 = 1$ and $\varepsilon_3 = 1$. The bistatic RCS of the cylinder is given in Fig. 10.

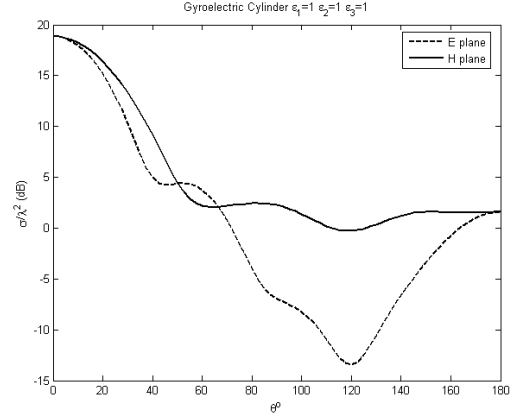


Fig. 10. Bistatic radar cross sections of the gyroelectric finite cylinder versus scattering angle θ . $d = 1.2\lambda$, $a = d/2$, $\varepsilon_1 = 1$, $\varepsilon_2 = 1$, and $\varepsilon_3 = 1$.

A gyromagnetic cylinder was simulated next, with the same discrete space-step and time-step as in gyroelectric cylinder case. The material has a relative permittivity value of 1. The relative permeability tensor elements are set as $\mu_1 = 1$, $\mu_2 = 1$ and $\mu_3 = 1$. The bistatic RCS of this cylinder is given in Fig. 11.

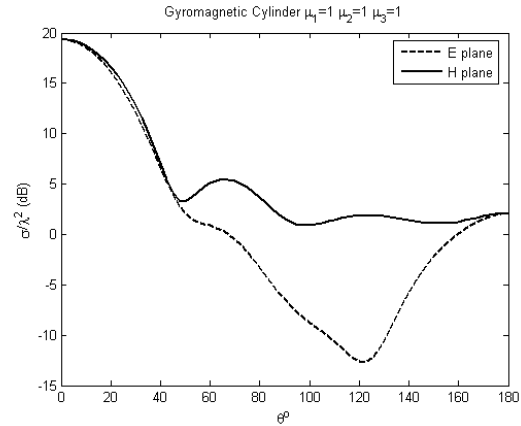


Fig. 11. Bistatic radar cross sections of the gyromagnetic finite cylinder versus scattering angle θ . $d = 1.2\lambda$, $a = d/2$, $\mu_1 = 1$, $\mu_2 = 1$, and $\mu_3 = 1$.

V. CONCLUSIONS

In this paper, the scattering field formulation of 3D TLM algorithm is derived starting from Paul's total field formulation TLM algorithm discussed in the [6]. Then

the gyrotropic material modeling for single frequency is explained. Moreover the near field to far field transformation with the notion of radar cross section is adapted to our TLM algorithm. The usage of this method is exhibited by modeling some gyrotropic spheres, cubes, and finite cylinders and computing the bistatic radar cross sections of these three dimensional scatterers. The TLM simulation results are validated by the results of the currently available methods used by Geng et al. [1,2] and Zhu et al. [3]. Using our method, it is easier to simulate arbitrarily shaped inhomogeneous gyrotropic objects.

ACKNOWLEDGMENTS

The authors wish to thank Dr. Atef Elsherbeni and Dr. Veysel Demir, for the valuable discussions on time domain electromagnetic computations.

REFERENCES

- [1] Y. Geng, X. Wu, and L. W. Li, "Analysis of electromagnetic scattering by a plasma anisotropic sphere," *Radio Science*, vol. 38, no. 6, pp. 12/1–12/12, December 2003.
- [2] Y. L. Geng and X. B. Wu, "A plane electromagnetic wave scattering by a ferrite sphere," *J. of Electromagn. Waves and Appl.*, vol. 18, no. 2, pp. 161–179, 2004.
- [3] X. Q. Zhu, Y. L. Geng, and X. B. Wu, "Calculation of electromagnetic scattering from three-dimensional anisotropic objects (in Chinese)," *Chin. J. Radio Sci.*, vol. 17, pp. 209–215, 2002.
- [4] K. S. Kunz and R. J. Luebbers, *The Finite Difference Time Domain Method for Electromagnetics*. CRC Press, 1993.
- [5] C. Christopoulos, *The Transmission Line Modelling Method TLM*. IEEE Press, 1995.
- [6] J. Paul, "Modelling of general electromagnetic material properties in tlm," Ph.D. dissertation, University of Nottingham, 1998.
- [7] J. Paul, C. Christopoulos, and D. W. P. Thomas, "Generalized Material Models in TLM – Part2: Materials with Anisotropic Properties," *IEEE Trans. on Antennas and Propagation*, vol. 47, no. 10, pp. 1535–1542, October 1999.
- [8] V. Demir, "Electromagnetic scattering from three-dimensional chiral objects using the fdtd method," Ph.D. dissertation, Syracuse University, 2004.
- [9] V. Demir, A. Z. Elsherbeni, D. Worasawate, and E. Arvas, "A graphical user interface (GUI) for plane wave scattering from a conducting, dielectric or a chiral sphere," *IEEE Antennas and Propagation Magazine*, vol. 46, no. 5, pp. 94–99, October 2004.
- [10] H. C. Chen, *Theory of Electromagnetic Waves, Coordinate Free Approach*. McGraw Hill, 1983.
- [11] V. L. Ginzburg, *The Propagation of Electromagnetic Waves in Plasmas*, 2nd ed. Pergamon Press, 1970.
- [12] A. Eroglu, "Electromagnetic wave propagation and radiation in a gyrotropic medium," Ph.D. dissertation, Syracuse University, 2004.
- [13] A. F. Yagli, E. Arvas, and J. K. Lee, "Electromagnetic Scattering From Three-Dimensional Gyrotropic Objects at Single Frequency Using The TLM Method," *ACES Conference*, pp. 642–648, March 12–16 2006.
- [14] H. H. Erkut, A. F. Yagli, and E. Arvas, "Electromagnetic scattering from a three-dimensional chiral body using the TLM method," *ACES Conference*, pp. 649–654, March 12–16 2006.



Ahmet Fazil Yagli was born in Kirikkale, Turkey, in 1979. He received the B.S. degree in Electrical and Electronics Engineering from Middle East Technical University, Ankara, Turkey in 2001, and the M.S. and Ph.D. degrees in Electrical Engineering from Syracuse University, Syracuse, NY in 2005 and 2006, respectively.

He served as a teaching assistant from August 2001 to May 2002, and as a research assistant from May 2002 to May 2006 in the Electrical Engineering and Computer Science Department of Syracuse University, Syracuse, NY. He is currently working for Turksat AS, Turkish Satellite Operator, in Ankara, Turkey. His research interests are in areas of computational methods for electromagnetics, radar cross section computation, and design and implementation of microwave devices.

Dr. Yagli is a member of ACES.



Jay Kyoon Lee was born in Sam-Chuk, Korea. He received the B.S. degree in Electronics Engineering from the Seoul National University, Seoul, Korea in 1976 and the S.M. and Ph.D. degrees in Electrical Engineering from the Massachusetts Institute of Technology (MIT), Cambridge, Massachusetts, in 1981 and 1985, respectively.

From 1976 to 1978, he served as an Operation Officer in the Air Defense Artillery Battalion of the Korean Army. He was employed by the Nam and Nam World Patent Office in Seoul, Korea in 1978-79. He was a Postdoctoral Research Associate at Research Laboratory of Electronics at MIT in 1985 and then joined the faculty of the Department of Electrical and Computer Engineering at Syracuse University in Syracuse, New York, where he is now Program Director of Electrical Engineering. He worked on the SAR imaging problem at Naval Air Development Center in Warminster, PA during summers of 1987 and 1988 and was a Visiting Professor at Rome Air Development Center in Rome, NY in 1990. He also worked at Naval Research Laboratory, Washington, DC during summer of 1993 and was an Invited Visiting Professor at Seoul National University in Seoul, Korea in 2000. His teaching and research interests include electromagnetic fields and waves, microwave remote sensing, waves in anisotropic

and gyrotropic media, antennas and propagation, microwave engineering, and radar clutter modeling. He has published numerous journal articles, book chapters and conference papers.

Dr. Lee is a Senior Member of the IEEE and a member of the American Geophysical Union, the Electromagnetics Academy and the Korean-American Scientists and Engineers Association (KSEA) in America. He has been on the International Editorial Board of Journal of Electromagnetic Waves and Applications since 1993. He has received the Eta Kappa Nu Outstanding Undergraduate Teacher Award from Syracuse University in 1999, the IEEE Third Millennium Medal in 2000, the College Educator of the Year Award from the Technology Alliance of Central New York in 2002 and the IEEE Region 1 Award in 2003. He has served as President of the Upstate New York Chapter of the KSEA in 1990-91, as Faculty Advisor of Korean Student Association at Syracuse University since 1993, as Chair of IEEE Syracuse Section in 1995-96, as Student Activities Committee Chair of IEEE Region 1 in 1996-2000, and as Faculty Advisor of IEEE Student Branch of Syracuse University since 1996.



Ercument Arvas received the B.S. and M.S. degrees from the Middle East Technical University, Ankara, Turkey, in 1976 and 1979 respectively, and PhD degree from Syracuse University, Syracuse, NY, in 1983, all in electrical engineering.

From 1984 to 1987, he was with the EE Department of Rochester Institute of Technology, Rochester, NY. In 1987, he joined the Electrical Engineering and Computer Science Department of Syracuse University, where he is currently a Professor. His research and teaching interests are in electromagnetic scattering and microwave devices.

He is a member of ACES and a Fellow of IEEE.

High Frequency Phase Variable Model of Electric Machines from Electromagnetic Field Computation

O. A. Mohammed, S. Ganu, N. Abed, S. Liu, and Z. Liu

Department of Electrical and Computer Engineering
Energy Systems Laboratory
Florida International University, Miami, FL 33174, USA

Abstract — This paper presents a high frequency phase variable model of electric machines obtained using finite element (FE) analysis. The model consists of the low frequency phase variable model in parallel with a high frequency winding branch. The resistance and inductance of individual winding turns are calculated by magnetodynamic FE analysis while capacitance is calculated by electrostatic FE analysis. With the obtained parameters, a distributed model was formed based on the winding arrangement. The order of the distributed winding model is reduced using the Kron reduction technique to form the lumped parameter high frequency winding branch. A Permanent Magnet synchronous motor (PMSM) with its operating inverter is used as an example. The developed model is then used to evaluate the motor-inverter interaction. The results show the ability of the developed model to represent the motor's high frequency behavior under different operating conditions.

Index Terms — FE, high frequency, PM synchronous motor, Kron reduction, phase variable model, lumped parameters, distributed parameters

I. INTRODUCTION

Many efforts have been devoted to develop the high frequency induction motor models based on experiments. Using these models, the overvoltage at the machine terminals, electromagnetic interference, and voltage distribution among the winding turns have been reported [1, 2]. A conventional direct-quadrature (dq) axis model of PMSM has also been developed using an experimental approach [3]. The model can represent the motor's low and high frequency behaviors.

In this paper, an FE based physical motor model of randomly wound PMSM is developed. The developed model can be used to test, improve, and optimize the motor design. This model consists of a high frequency branch connected in parallel with a low frequency phase variable model. The low frequency phase variable model represents the

motor's low frequency behavior while the high frequency winding branch represents the high frequency behavior. A change in the winding arrangement will affect only the high frequency winding branch parameters and will not affect the low frequency phase variable model parameters.

The FE based approach is used to calculate the high frequency model parameters. The developed model is used to evaluate the integrated motor drive high frequency behavior. This includes the motor terminal overvoltage, effect of switching frequencies on the motor currents and output torque. The simulation results show the ability of the developed model to represent the motor low and high frequency behavior under various dynamic operating conditions.

II. HIGH FREQUENCY WINDING BRANCH PARAMETER CALCULATION USING FE

A 2-hp, 6-poles, 36-slots, random wound winding arrangement, with 128 amp-turns per half slot motor was used as an example. Due to the symmetry, a one pole of the motor's geometry is used considering the individual turns in each half slot as shown in Fig. 1. Each slot contains 18 turns with 9 turns in each half slot. Each turn utilizes #14 gauge wire with diameter of 1.6281 mm. Diameter of insulation is 1.73 mm. The same positioning of the turns within the other slots is maintained. To consider the geometry effects on the inductance and capacitance, all the slots in one pole of the motor's geometry were modeled. The winding resistance, inductance and capacitance values are function of the operating frequency. The resistance increases with the increase in the supply frequency due to the skin and proximity effects. The skin effect is the tendency of the current to remain at the surface region of the conductor while the proximity effect is the action of the magnetic field of adjacent conductors on the current density distribution inside the given

conductor. The inductance value decreases with the increase of the frequency. The change in the capacitance values with the change in the frequency is minimal and can be ignored in the considered frequency range. The capacitances are distributed between turn to turn and turn to ground. The capacitance provides an easy path for high frequency current components to flow between the turns and to ground.

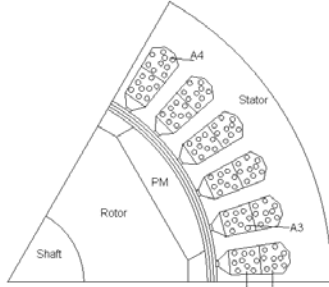


Fig. 1. One pole motor geometry with individual winding turns.

A 2-D magnetodynamic FE analysis is performed to obtain resistances and inductances of the different winding turns. This analysis is a steady state time harmonic form of diffusion equation [4]. First a geometry description is set up by assigning the proper material properties to the different parts of the one pole geometry. The rotor and stator iron are composed of nonlinear magnetic material with linear resistivity. The turn conductors are assigned with unit permeability and resistivity. Assignment of resistivity is required to include the eddy current effects. The motor magnets are assumed to be linear. The shaft, fixing wedge and insulation inside the slots were assigned with air. The meshing is selected in coordination with the skin depth. The size of the mesh elements inside each turn is kept less than the skin depth. The skin depth is calculated according to the rise time of the pulse width modulation (PWM) pulses. The rise time of the PWM pulse is $1\ \mu\text{s}$ which corresponds to the frequency component of 1-MHz. The skin depth at 1-MHz frequency is $6.6\ \text{e-}5\ \text{m}$. The meshing details inside the one pole model are shown in Fig. 2. The

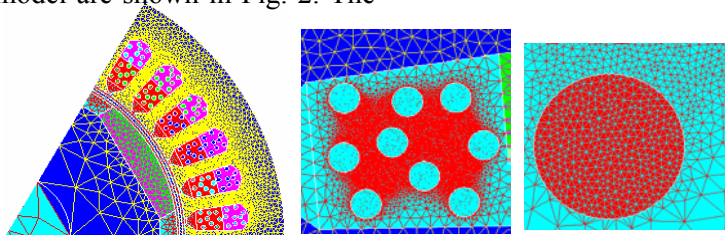


Fig. 2. Mesh details inside one pole model, inside slot and inside turn.

mesh contains 7937 line elements and 179692 surface elements.

Periodic boundary conditions are assigned to the wedge shaped pole structure while the homogeneous Dirichlet boundary conditions are applied to the outer stator surface. The FE-circuit coupling allows us to simulate the exact operating conditions with real voltage supply connection. The field and circuit equations are coupled and solved simultaneously [5]. The magnetic field inside the motor is governed by the following partial differential equation

$$\nabla \times H = J_s + J_e \quad (1)$$

where, J_s is the source current density, J_e is the induced current density, and H is the field intensity. In general, the current in the circuit domain with m loops can be represented by the following set of equations

$$[E_m] = [R_m][I_m] + [L_m] \frac{d}{dt}[I_m] + \left[\frac{1}{C_m} \right] \int I_m dt + [\gamma_m] \quad (2)$$

where, R_m represents the matrix of resistances, L_m is the matrix of inductances, C_m is the matrix of capacitances, γ_m is the matrix of non-linear voltage drops, I_m is the matrix of currents, and E_m is the matrix of voltages. More details about the formulation can be found in [5].

The inductance and resistance frequency response of the different turns were obtained by solving the magnetodynamic problem for various supply frequencies. The frequency range used is from 10-kHz to 1-MHz. Usually the PWM switching frequencies are in the range of tens of kHz. The upper limit of the frequency range is selected to include harmonics up to 1-MHz.

The computation took 4 hours to solve the magnetodynamic problem on a Pentium P4, 3-GHz machine. During the simulation all the turns were connected in series. After solving the coupled field circuit problem, the resistances and inductances as functions of frequency were obtained.

The variation of the resistance and the inductance versus the frequency for different turns in the first half slot of phase A are shown in Figs. 3 and 4, respectively.

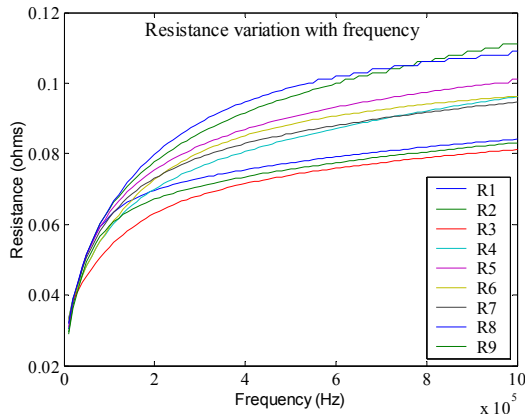


Fig. 3. Resistance variation with frequency.

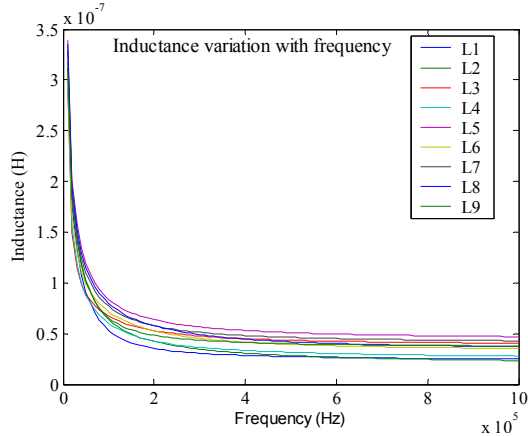


Fig. 4. Inductance variation with frequency.

In Figs. 3 and 4, R_1, R_2, \dots and L_1, L_2, \dots correspond to the resistance and the inductance of the different turns in the first half slot of phase A respectively. It is difficult to point out each individual turn in Figs. 3 and 4, since all the curves are very close to each other. Therefore, the figures are just meant to show

the trend of variation of resistance and inductance with frequency. It should be noted that the slope of the resistance curve becomes smaller and also the slope of inductance curve becomes constant in the higher frequency region. The inductance obtained by this method is apparent global inductance. Since simultaneous excitation of all the turns in a given half slot is performed, the inductance value contains both self and mutual inductance terms. The skin effect inside the iron is more pronounced compared to the turn conductors. As a result, the flux lines do not penetrate the iron region but remain confined inside the slot. Figure 5(a) shows flux plot at 30 kHz frequency while Fig. 5(b) shows the flux plot at 1-MHz frequency. The flux plots are at steady state. These figures clearly show the fact that the stator iron acts as a flux barrier due to the increased eddy currents at high frequency. The position and numbering of turns in the first slot is also shown in Fig. 5(b). Similar calculations were repeated for each half slot.

The capacitances were calculated from FE electrostatic analysis since capacitances are function of the motor geometry and not the supply frequency. The electric field is assumed to be linear in this case and it is proportional to the applied voltage. The analysis determines the electric scalar potential distribution due to the applied voltage [6]. The turn conductors were treated as perfect conductors and hence are not meshed. The insulation in the slot and surrounding of the conductor is finely meshed. The mesh details in the slot and the insulation is shown in Fig. 6(a-c). The capacitance calculation is based on the energy principle. By applying voltage on the conductors, the ground capacitance matrix was calculated from the stored static energy. The electric potential distribution inside the motor is governed by the following partial differential equation,

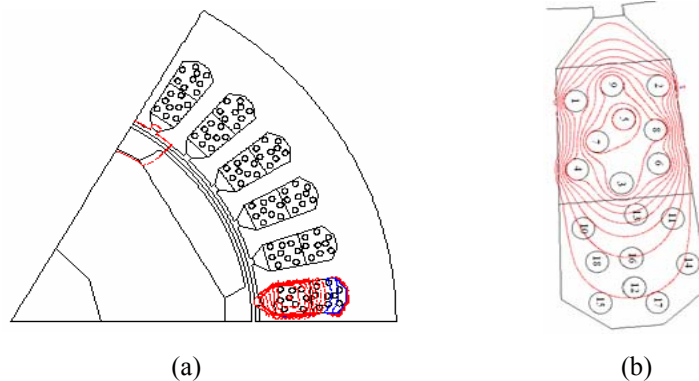


Fig. 5.(a) Flux lines in one pole machine at 30 kHz, (b) In the slot at 1 MHz.

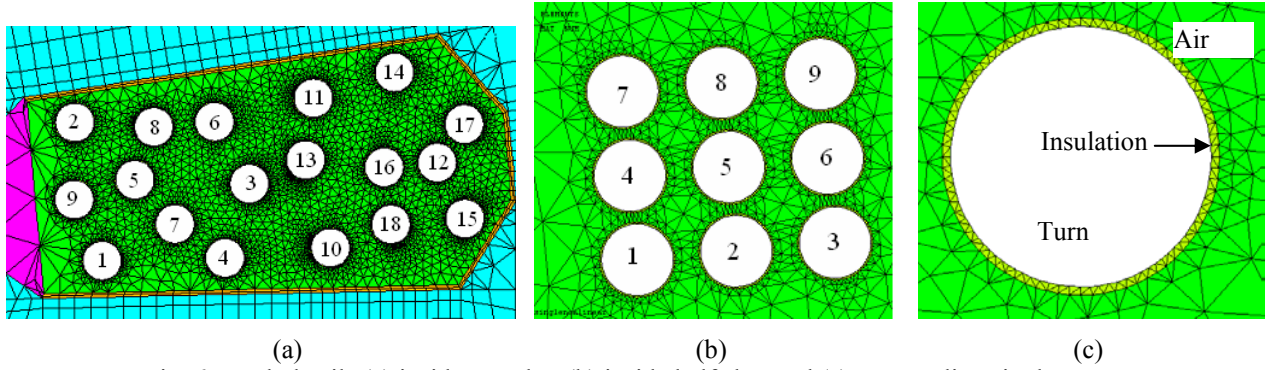


Fig. 6. Mesh details (a) inside one slot, (b) inside half slot, and (c) surrounding single turn.

$$\nabla \cdot (\epsilon_r \epsilon_0 \nabla V) = -\rho \quad (3)$$

where, ρ is surface charge density, ϵ_r is relative permittivity, ϵ_0 is air permittivity, and V is electric scalar potential.

To calculate the lumped capacitance matrix, charges are related to the potential differences. Similar capacitance calculations were repeated for each half slot. The mutual capacitances were calculated between turns within each half slot. All capacitances were multiplied by the mean length of the turn as the calculated capacitances are per unit length. The self capacitance is the addition of the ground capacitance and mutual capacitances with other turns.

III. DISTRIBUTED PARAMETER MODEL AND ITS REDUCTION

The distributed parameter winding model is shown in Fig. 7. The model is formed using the high frequency parameters obtained from the FE analysis. The distributed model consists of the resistance of each turn, the global inductance of each turn, the capacitance to ground for each turn and the mutual capacitances with other turns inside the half slot. The used motor has 216 turns per phase. All the turns in a given phase are connected in series thus forming 217 nodes. The parameters of the first turn are between nodes 1 and 2; the parameters of the second turn are between nodes 2

and 3 and so on. The ground capacitance is equally distributed between the two ends of the turn. Here, C_{12} is the mutual capacitance between turns 1 and 2; R_1 and L_1 are the resistance and global inductance of the first turn, respectively. Also, C_{1g} is the capacitance to the ground of the first turn and so on. The resistance and inductance values used in the model are the average values over the considered frequency range.

The order of the distributed parameter winding model obtained above is reduced by using Kron reduction technique [7]. This reduction is performed in order to reduce the simulation time so that a global solution of the combined low and high frequency phenomena of PWM motor-inverter interaction can be obtained at much faster speeds. PWM is the modulation technique to obtain inverter output voltage control. The nodal method is used to form the admittance matrix of the distributed winding model. In this algorithm, all the nodes other than the terminal nodes are eliminated. To eliminate the internal nodes, the admittance matrix is partitioned such that the nodes to be removed are represented in the upper rows. The partitioned matrices are shown below in (4). In equation (4), i and j are terminal nodes and n is the number of turns. The reduced admittance matrix is obtained from (4) using matrix transformation formula given in (5),

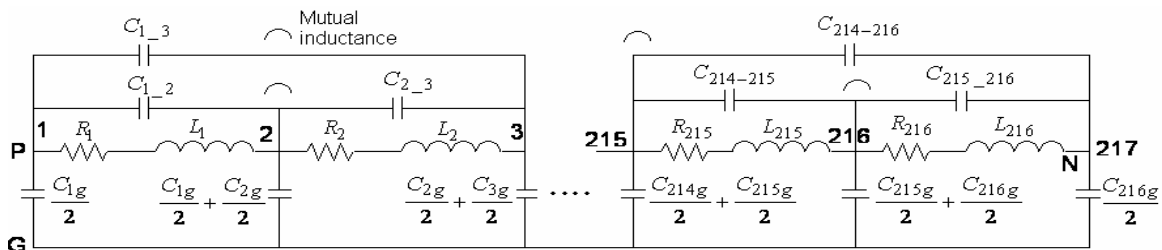


Fig. 7. Distributed parameter winding circuit obtained from FE analysis.

$$\begin{aligned}
 \text{B1} & \begin{bmatrix} Y_{11} & \dots & Y_{1,(n-1)} \\ \vdots & \dots & \vdots \\ Y_{(n-1),1} & \dots & Y_{(n-1),(n-1)} \end{bmatrix} & \begin{bmatrix} Y_{1i} & Y_{1j} \\ \vdots & \vdots \\ Y_{(n-1),i} & Y_{(n-1),j} \end{bmatrix} & \text{B3} \\
 \text{B2} & \begin{bmatrix} Y_{i1} & \dots & Y_{i,(n-1)} \\ Y_{j1} & \dots & Y_{j,(n-1)} \end{bmatrix} & \begin{bmatrix} Y_{ii} & 0 \\ 0 & Y_{jj} \end{bmatrix} & \text{B4}
 \end{aligned} \quad (4)$$

$$Y_{node}^{red} = B_4 - B_3 B_1^{-1} B_2 = \begin{bmatrix} y_{11} & y_{12} \\ y_{21} & y_{22} \end{bmatrix}. \quad (5)$$

In (5), Y_{node}^{red} is the reduced (2×2) admittance matrix. The π -network model shown in Fig. 8 (a), is used to represent the resultant matrix (5) using the principle of two port circuit [8]. The obtained π -network is symmetrical with equal diagonal elements. From the π -network model parameters, the high frequency branch parameters R, L, and C_g are obtained. The lumped equivalent circuit for the high frequency branch is shown in Fig. 8 (b).

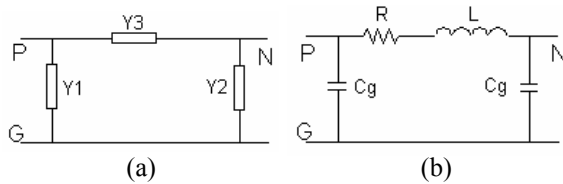


Fig. 8. (a) π -network model, (b) Reduced order high frequency winding branch.

The high frequency phase variable model is shown in Fig. 9. This model consists of the low frequency phase variable model in parallel with the high frequency winding branch. The low frequency phase variable model was previously developed by the authors [9]. A filter is connected in series with the high frequency winding branch to filter out the fundamental (60 Hz) frequency components [10]. The lumped parameter values at various switching frequencies are given in Table 1. It should be observed that there is slight change in the values of the parameters by changing the winding arrangement from a form wound winding type to random wound winding type for same number of turns. Further details on the parameters of form wound winding type motor can be found in [11].

IV. SIMULATION AND RESULTS

The high frequency phase variable motor model is tested in an integrated motor drive system as shown in Fig.10. A vector control algorithm is used to drive the motor. The motor drive system consists of a PWM inverter, cable and the

developed motor block model. The load torque is set to its rated value of 12 N.m.

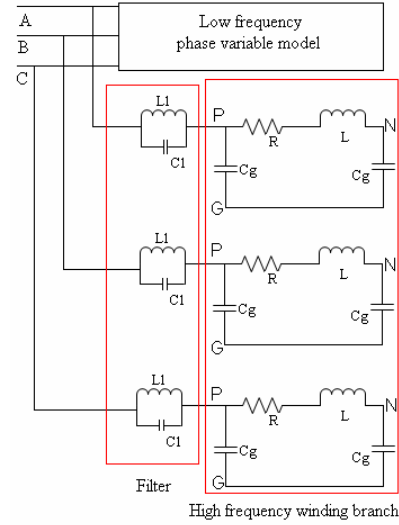


Fig. 9. High frequency phase variable model.

Table 1. Lumped parameters at different frequencies.

Per phase	10 kHz	20 kHz	30 kHz
Resistance R (Ω)	6.66	8.08	9.02
Inductance L (μ H)	67.37	38.46	29.97
Capacitance C_g (nF)	1.42	1.42	1.42

As shown in Fig. 10, there are two cascaded control loops to control the motor. The inner loop controls the motor's stator currents. The outer loop controls the motor's speed. A high frequency cable model was used to connect motor to the inverter [12]. The simulation was performed at various switching frequencies namely, 10-kHz, 20-kHz, and 30-kHz. For PWM switching operation, the simulation time step should be in the range of nanoseconds in order to capture the spikes in the various waveforms. Figure 11 shows the three phase current profiles at different switching frequencies. The pulsations in the current waveform are due to PWM switching action. The spikes in the current waveform are due to high voltage edge rates of converter elements and cable parameters. The high frequency branch enables us to include these spikes. These spikes are clearly visible in 10-kHz current waveform results. At 20-kHz and 30-kHz frequency, there is an increase in

the number of current spikes since the spikes are formed at each transition point. Since the capacitance values are constant for all cases, the increase in the magnitude of current spikes is marginal. The spikes in phase A current are clearly shown in Fig. 12. Typical torque waveform is shown in Fig. 13 at various switching frequencies. The pulsations in the torque are due to the PWM switching action. The frequencies in the simulations are approximate values since the motor is working under the hysteresis current controller. Therefore the captions of Fig. 11 to Fig. 14 are annotated with (approx.) label. The spikes are also visible in the ground current which is shown in Fig. 14. This current is the current passing to the ground through high frequency winding branch. This current produces electromagnetic interference with other electrical equipments connected to the ground. The motor model is also tested for the overvoltage phenomenon when connected through a long cable to the PWM inverter. Due to the impedance mismatch between the cable impedance and the motor input impedance, the voltage builds up at motor's terminal and can reach a peak value of double the DC supply voltage. This can damage the motor's insulation. Predicting this overvoltage magnitude is very crucial in the insulation design

and selection process. To investigate the effect of cable length on the motor overvoltage, the motor model is connected to a cable of different lengths. The overvoltage at 10-kHz switching frequency is shown in Fig. 15. As the length of the cable increases, the amplitude of the voltage increases and the frequency of oscillations decrease. The simulation results show that the developed model can predict motor-inverter interaction at faster speeds than full FE model. The developed model can be used to evaluate EMI issues during the design and development process numerically.

V. CONCLUSION

A high frequency phase variable electric machines model is developed using FE analysis. This was done numerically rather than experiments. This approach will allow us to evaluate the motor high frequency behavior during the design process. The winding arrangement changes show a little difference in the parameter values for equal number of turns. The model can predict motor high frequency behavior such as motor current spikes, terminal overvoltage as well as the ground currents at fast computation speed. The model can be utilized in design optimization and insulation selection for motors during design process as well as in the evaluation of EMI issues.

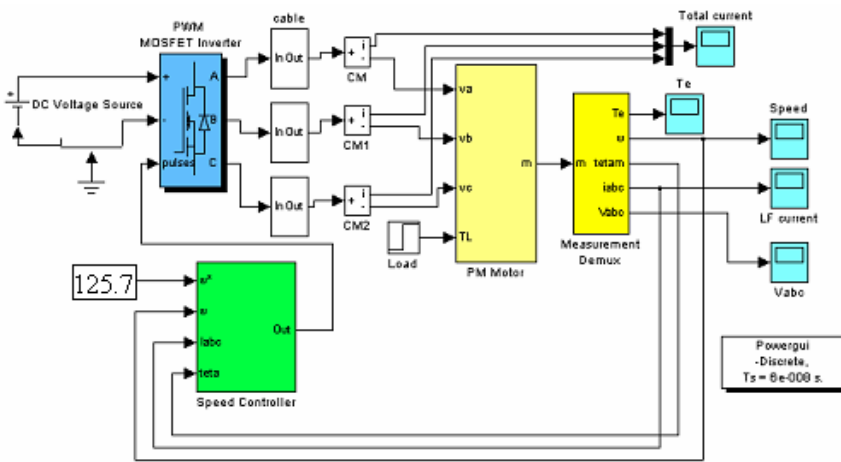


Fig. 10. Integrated motor drive system.

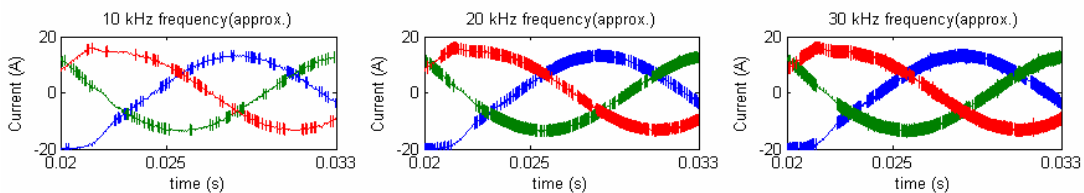


Fig. 11. Three phase steady state current waveform at different switching frequencies.

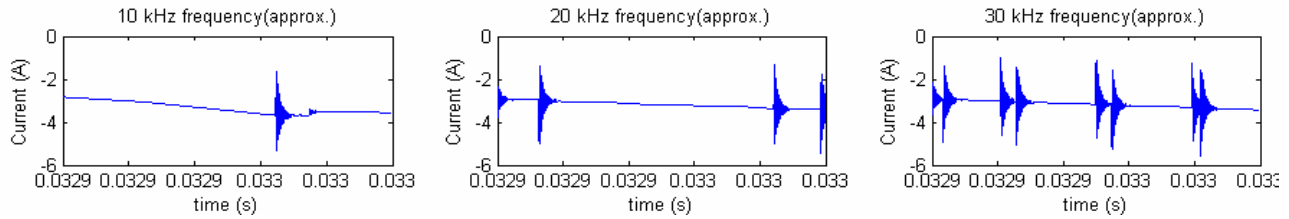


Fig. 12. Phase A steady state current waveform at different switching frequencies.

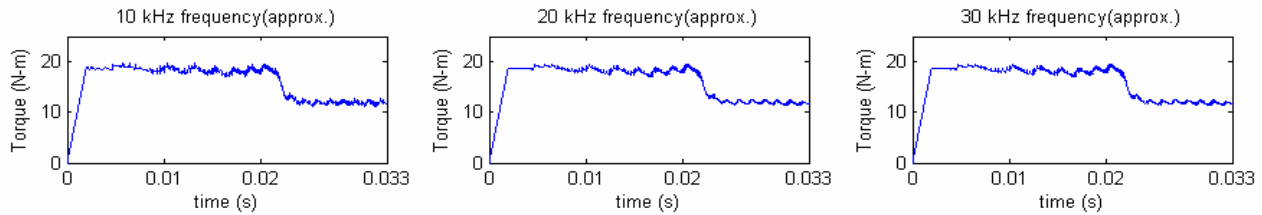


Fig. 13. Torque profile at different switching frequencies.

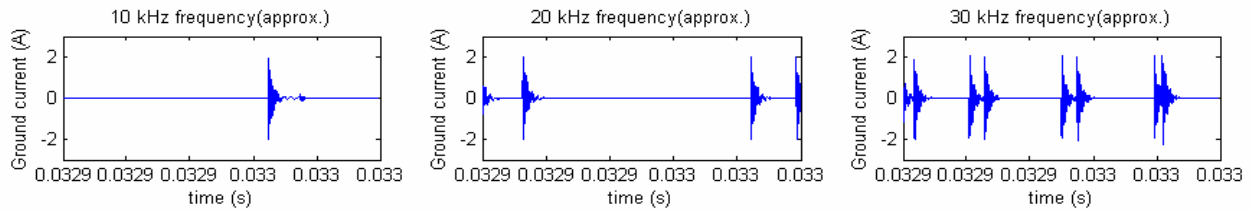


Fig. 14. Grounding current at different switching frequencies.

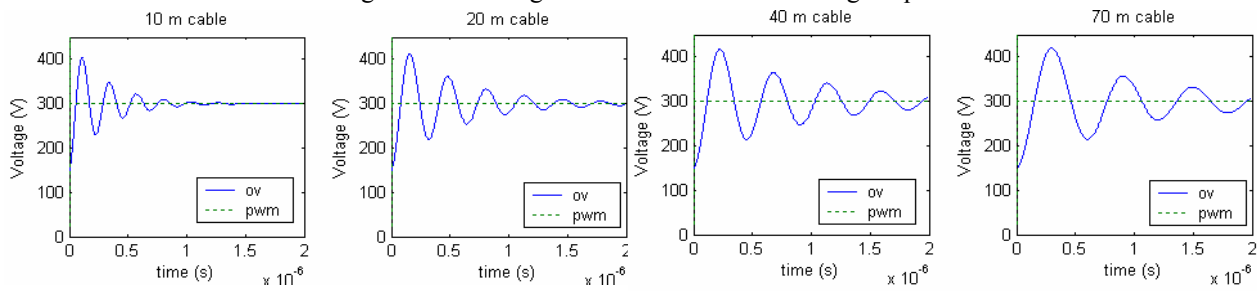


Fig. 15. Overvoltage profile for different cable lengths.

REFERENCES

[1] A. Boglietti, E. Carpaneto, "Induction Motor High Frequency Model" conf. Rec. IEEE IAS annual meeting, pp.1551-1558, 1999.

[2] H. A. Toliyat, G. Suresh, and A. Abur, "Estimation Of Voltage Distribution On The Inverter Fed Random Wound Induction Motor Windings Supplied Through Feeder Cable," IEEE Transactions on EC, Vol. 14, No. 4, pp. 976-981, Dec. 1999.

[3] S. D. Sudhoff, J. Tichenor, J. Drewniak, "Wide Bandwidth Multi-Resolutional Analysis of A Surface Mounted PMSM," IEEE Transactions on EC, Vol. 14, No. 4, pp. 976-981, Dec. 1999.

[4] S. J. Salon, "Finite Element Analysis of Electrical Machines," Kluwer academic publishers, 1995.

[5] F. Piriou and A. Razek, "Finite Element Analysis in Electromagnetic Systems Accounting for Electric Circuits," IEEE Transactions on Magnetics, Vol. 29, No. 2, pp. 1669-1675, March 1993.

[6] A. Hieke, Siemens and IBM, "ANSYS APDL for Capacitance", Proceedings from 'Second International Conference on Modeling and Simulation of Microsystems, Semiconductors, Sensors and Actuators' San Juan, Puerto Rico, pp. 172, (1999).

[7] G. Kron, "Tensor Analysis of Networks," John Willey and Sons, 1939.

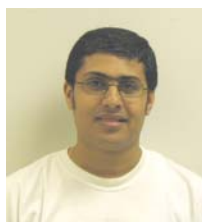
[8] Leonard Bobrow, "Elementary Linear Circuit Analysis," pp. 575-577.

- [9] O. A. Mohammed, S. Liu and Z. Liu, "Physical Modeling Of PM Synchronous Motors For Integrated Coupling With Machine Drives," IEEE Transactions on Magnetics, Vol. 41, No. 5, pp. 1628-1631, May 2005.
- [10] L. Ran, S. Gokani, J. Clare, K. J. Bradley, and C. Christopoulos, "Conducted Electromagnetic Emissions in Induction Motor Drive Systems Part I- Time Domain Analysis And Identification Of Dominant Modes," IEEE Transaction on Power Electronics, Vol. 13, No. 4, pp. 757-767, July 1998.
- [11] O. A. Mohammed, S. Ganu, N. Abed, S. Liu and Z. Liu, "High Frequency PM Synchronous Motor Model Determined By FE Analysis," IEEE Transactions on Magnetics, pp. 1291-1294, April 2006.
- [12] A. Moreira, T. A. Lipo, G. Venkataramanan, S. Bernet, "High Frequency Modeling For Cable And Induction Motor Overvoltage Studies In Long Cable Drives," IAS Transactions, Vol. 38, No. 5, pp. 1297-1306, Sept. 2002.



Osama A. MOHAMMED.

Dr. Mohammed received his M.S. and Ph.D. degrees in Electrical Engineering from Virginia Polytechnic Institute and State University. He has many years of teaching, curriculum development, research and industrial consulting experience. He authored and co-authored more than 300 technical papers in the archival literature as well as in National and International Conference records in addition to additional numerous technical and project reports and monographs. He specializes in Electrical Power Systems, design optimization of electromagnetic devices, Artificial Intelligence Applications to Energy Systems as well as Electromagnetic Field Computations in Nonlinear Systems. He has current interest in Shipboard power systems and integrated motor drive systems. Dr. Mohammed is a fellow of IEEE and is the current president of ACES. He is editor of IEEE Transactions on Magnetics and COMPEL Journal.



Shreerang GANU. Mr. Ganu received his Bachelor degree in Electrical Engineering from Pune University, India in 1998, M.S. degree in Electrical Engineering from Florida International University Miami,

USA in 2002. Currently he is working towards his Ph.D. degree in Electrical Engineering at Florida International University. His research includes computational electromagnetics applied to electrical machines, motor drives and power systems.



Nagy ABED. Mr. Abed is a Student Member of IEEE since 1997. He received the B.S. and M.S. degrees in electrical engineering from Mansoura University, Egypt, in 1996 and 1999, respectively. He is currently a Graduate Student in the Ph.D. program at Florida

International University. His current academic and research interests include power systems, Finite element, Power electronics, power quality, and computer aided design of electromagnetic devices in low and high frequencies.



Dr. Shuo LIU. Dr. Liu received her Ph.D. from Hebei University of Technology, Tianjin, China in 2001. In 2001, she joined Energy Systems Laboratory at the Department of Electrical and Computer Engineering of Florida International University, Miami, FL USA as a

postdoctoral researcher. Her research interests are in the area of electromagnetic field numerical calculation and modeling of electric machines. She has 7 journal and 30 conference publications. She became a senior IEEE member in 2004.



Dr. Zhiqiang LIU. Dr. Liu received his Ph.D. from Tianjin University, China in 2002. He was an associate professor at the Department of Industrial Engineering and Automation at Hebei University of Technology, Tianjin, China. Currently he is working in the

Energy Systems Laboratory at Florida International University, Miami, FL USA as a visiting researcher. His research interests are in the areas of power electronics and motor drive.

Cascading Optical Negative Index Metamaterials

Alexander V. Kildishev and Uday K. Chettiar

Birck Nanotechnology Center, School of Electrical and Computer Engineering
Purdue University, IN 47907 USA (e-mail: a.v.kildishev@ieee.org)

Abstract — We use a spatial harmonic analysis (SHA) method to homogenize optical metamaterials with a negative refractive index; the method provides a more general approach than other methods for estimating the effective index of materials arranged of cascaded elementary layers. The approach is validated for a single layer and a triple layer two dimensional metal grating.

Index Terms — Negative Index Metamaterial, Spatial Harmonic Analysis (SHA), Homogenization.

I. INTRODUCTION

The refractive index ($n = n' + in''$) is the key parameter in the interaction of light with matter. While n' has generally been considered to be positive, the condition $n' < 0$ does not violate any fundamental physical law, and materials with negative index have some remarkable properties. Such materials are called negative-index materials (NIMs), and in these materials the phase velocity is directed against the flow of energy. There are no known naturally-occurring optical NIMs. Optical properties of such media have been considered in early papers by Mandel'shtam [1] and Veselago [2]. Proof-of-principle experiments [3] have shown that artificially designed materials (metamaterials) consisting of split ring resonators (SRRs) and metal wires can act as NIMs at microwave wavelengths. NIMs drew a large amount of attention after Pendry predicted that NIMs can act as a superlens allowing for an imaging resolution which is limited not by the wavelength but rather by material quality [4].

A. Homogenization of an Elementary Layer

A possible approach to designing negative index materials is a periodic array of elementary coupled metal-dielectric resonators. This work takes a closer look at approaches which simultaneously provide fast calculation of the field inside a given metamaterial arranged of elementary periodic layers and calculation of its effective parameters.

First we review an established approach to homogenization of a thin layer of NIM. For a given monochromatic incident light, it is possible to measure the complex reflectance and transmittance coefficients (r and t) and then unambiguously retrieve the refractive index of the NIM sample. This effective parameter can be conveniently obtained from the characteristic matrix of a homogeneous film at normal incidence [5].

Here we consider an effective layer of NIM over a homogeneous thick substrate with a refractive index n_2 , as shown in Fig. 1. The conservation of the tangential electric and magnetic fields at the first interface gives the standard boundary conditions (BCs), $H_0 = H_1$, $E_0 = E_1$. Then, using the definitions of the complex reflection and transmission coefficients ($\bar{r}_0 = E_{0,r}/E_i$, $\bar{t}_1 = E_{1,t}/E_i$, and $\bar{r}_1 = E_{1,r}/E_i$), we have

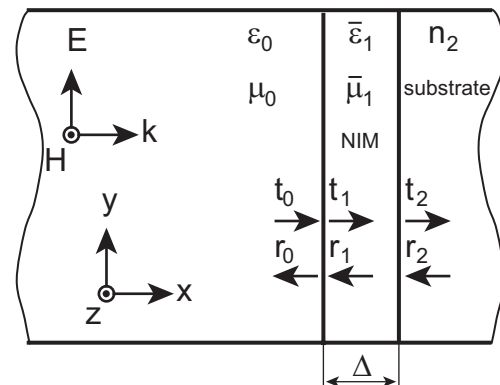
$$\mathbf{V} \begin{pmatrix} 1 \\ \bar{r}_0 \end{pmatrix} = \mathbf{D}_1 \mathbf{V} \begin{pmatrix} \bar{t}_1 \\ \bar{r}_1 \end{pmatrix}, \quad (1)$$


Fig. 1. Simplified approach to the homogenization of a thin equivalent layer of NIM on top of a thick substrate with a refractive index n_2 . The equivalent layer is characterized by the effective permittivity and permeability. Note that $r_2 = 0$, provided that the layer is not illuminated.

where \mathbf{V} is a rotation matrix.

$$\mathbf{V} = \begin{pmatrix} 1 & -1 \\ 1 & 1 \end{pmatrix}, \quad (2)$$

and

$$\mathbf{D}_1 = \begin{pmatrix} \bar{\eta}_1^{-1} & 0 \\ 0 & 1 \end{pmatrix}, \quad (3)$$

where $\bar{\eta}_1 = \sqrt{\bar{\mu}_1/\bar{\epsilon}_1}$ is the effective impedance of the NIM layer with effective permeability $\bar{\mu}_1$ and effective permittivity $\bar{\epsilon}_1$.

Then, using the scaled thickness of the layer, $\delta_1 = 2\pi \Delta_1/\lambda$, with the transport matrix

$$\mathbf{A}_1 = \begin{pmatrix} e^{-i\bar{\eta}_1\delta_1} & 0 \\ 0 & e^{i\bar{\eta}_1\delta_1} \end{pmatrix}, \quad (4)$$

i.e., backpropagating \bar{r}_1 and propagating \bar{t}_1 up to the second interface we arrive at the equation

$$\mathbf{D}_1 \mathbf{V} \mathbf{A}_1^{-1} \begin{pmatrix} \bar{t}_1 \\ \bar{r}_1 \end{pmatrix} = \begin{pmatrix} n_2 \bar{t}_2 \\ \bar{t}_2 \end{pmatrix}. \quad (5)$$

Combining (1) and (5) gives the following form

$$\begin{pmatrix} 1 - \bar{r}_0 \\ 1 + \bar{r}_0 \end{pmatrix} = \mathbf{D}_1 \mathbf{V} \mathbf{A}_1 \mathbf{V}^{-1} \mathbf{D}_1^{-1} \begin{pmatrix} n_2 \bar{t}_2 \\ \bar{t}_2 \end{pmatrix}. \quad (6)$$

From the above we have

$$\mathbf{V}^{-1} \mathbf{D}_1^{-1} \begin{pmatrix} 1 - \bar{r}_0 \\ 1 + \bar{r}_0 \end{pmatrix} = \mathbf{A}_1 \mathbf{V}^{-1} \mathbf{D}_1^{-1} \begin{pmatrix} n_2 \bar{t}_2 \\ \bar{t}_2 \end{pmatrix} \quad (7)$$

or

$$\begin{pmatrix} \frac{1 + \bar{r}_0 + (1 - \bar{r}_0) \bar{\eta}_1}{\bar{t}_2 (1 + n_2 \bar{\eta}_1)} \\ \frac{1 + \bar{r}_0 - (1 - \bar{r}_0) \bar{\eta}_1}{\bar{t}_2 (1 - n_2 \bar{\eta}_1)} \end{pmatrix} = \begin{pmatrix} e^{-i\bar{\eta}_1\delta_1} \\ e^{i\bar{\eta}_1\delta_1} \end{pmatrix}. \quad (8)$$

Then, multiplying the components of each vector from both sides we arrive at

$$\bar{\eta}_1 = \pm \sqrt{\frac{(1 + \bar{r}_0)^2 - \bar{t}_2^2}{(1 - \bar{r}_0)^2 - \bar{t}_2^2 n_2^2}}, \quad (9)$$

while summing up the components and using (9) gives

$$\cos \bar{\eta}_1 \delta_1 = \frac{1 - \bar{r}_0^2 + n_2 \bar{t}_2^2}{[(1 + \bar{r}_0) n_2 + 1 - \bar{r}_0] \bar{t}_2}. \quad (10)$$

Equation (6) can be written in another manner as

$$\mathbf{Q}_0 = \mathbf{M}_1 \mathbf{Q}_2, \quad (11)$$

using $\mathbf{Q}_0 = \begin{pmatrix} t_0 \\ r_0 \end{pmatrix}$, $\mathbf{Q}_2 = \begin{pmatrix} t_2 \\ r_2 \end{pmatrix}$, and $\mathbf{M}_1 = \mathbf{S}_1 \mathbf{A}_1 \mathbf{S}_1^{-1}$,

where \mathbf{S}_1 is the symmetric matrix, $\mathbf{S}_1 = \mathbf{V}^{-1} \mathbf{D}_1 \mathbf{V}$. Note that for a single layer on a substrate, $r_2 = 0$ and t_0 is the incident field.

B. Nomenclature of Matrix Functions

To simplify the notations (and further programming), nomenclature for matrix functions is defined in parallel with direct matrix notation. First, we introduce a general 2×2 matrix partitioning function (\mathbf{w}) with partitions comprised of four different $\hat{m} \times \hat{m}$ square matrices ($w^{0,0}, w^{0,1}, w^{1,0}, w^{1,1}$):

$$\mathbf{w}(w^{0,0}, w^{0,1}, w^{1,0}, w^{1,1}) = \begin{pmatrix} w^{0,0} & w^{0,1} \\ w^{1,0} & w^{1,1} \end{pmatrix}. \quad (12)$$

Second, using (12) we add a partitioning function (\mathbf{s}) for arranging four bi-diagonally symmetric partitions combined of two $\hat{m} \times \hat{m}$ matrices (s_0 and s_1):

$$\mathbf{s}(s_0, s_1) = \mathbf{w}(s_0, s_1, s_1, s_0) = \begin{pmatrix} s_0 & s_1 \\ s_1 & s_0 \end{pmatrix}. \quad (13)$$

Then, using (12) and a $\hat{m} \times \hat{m}$ null matrix (\circ) we suggest to define another function (\mathbf{d}) for making a diagonally partitioned matrix of two $\hat{m} \times \hat{m}$ matrices (b_0 and b_1) as

$$\mathbf{d}(b_0, b_1) = \mathbf{w}(b_0, \circ, \circ, b_1) = \begin{pmatrix} b_0 & \circ \\ \circ & b_1 \end{pmatrix}. \quad (14)$$

In addition, the following constant rotation matrix arranged of $2\hat{m} \times 2\hat{m}$ identity matrices (\mathbf{i}) is used

$$\mathbf{i} = \mathbf{w}(i, -i, i, i) = \begin{pmatrix} i & | & -i \\ \hline -i & | & i \end{pmatrix}. \quad (15)$$

Finally, a stacking function (\mathbf{c}) is defined for a stacked vector made of two equal vectors (v_1, v_2) with \hat{m} components as

$$\mathbf{c}(v_1, v_2) = \begin{pmatrix} v_1 \\ v_2 \end{pmatrix}. \quad (16)$$

Thus for example, (2)-(4) and (11) can be rewritten using (12)-(16) for $\hat{m} = 1$ as

$$\mathbf{Q}_0 = \mathbf{c}(t_0, r_0), \quad \mathbf{Q}_2 = \mathbf{c}(t_2, r_2), \quad (17)$$

$$\mathbf{A}_1 = \mathbf{d}(e^{-i\hat{m}_1\delta}, e^{i\hat{m}_1\delta}), \quad \mathbf{D}_1 = \mathbf{d}(\eta_1^{-1}, 1), \quad \mathbf{V} = \mathbf{i}. \quad (18)$$

C. Basics of SHA in Cascaded NIM Layers

Equations (9) and (10) provide an easy approach to the characterization of thin metamaterials. With this simple assumption it is thought that a cascaded bulk material can be arranged using a stack of q equivalent layers with an effective transformation matrix $\mathbf{M}^q = \mathbf{S}\mathbf{A}^q\mathbf{S}^{-1}$. In general, this straightforward approach assumes that the spatial harmonics of each layer interact only with the same harmonics of other layers in the stack. In essence, this loose assumption ignores any transformation of a given incident harmonic into the spatial harmonics of different order, which are either reflected or transmitted. To illustrate this issue, consider another approach to obtaining effective parameters of a multilayer NIM arranged of thin infinite elementary layers with periodic distribution of elementary materials. Essentially, the enhanced method follows the recipe for a classical case of stratified media (see for example, [6]-[11]).

We note that a variety of rigorous algorithms have been based on SHA for diffraction gratings. After the publications of Burckhardt [7], Kaspar [8], and Knop [9], a very similar method was introduced by Moharam and Gaylord [10]-[12]. Analytical approaches to the problem were shown by Botten and McPhedran [13]-[15]. An alternative to Botten's method was discussed by Tayeb and Petit [16]-[18]. Due to space constrains, here we only give a brief list of early publication; a larger review will be published elsewhere.

We start with monochromatic Maxwell's equations $\nabla \times \vec{E} = i\omega\vec{D}$, $\nabla \times \vec{H} = -i\omega\vec{D}$ arriving at

$$\begin{aligned} k^2 n^2 \vec{H} &= \nabla \times \nabla \times \vec{H} - \nabla \ln \varepsilon \times \nabla \times \vec{H}, \\ k^2 n^2 \vec{E} &= \nabla \times \nabla \times \vec{E} - \nabla \ln \mu \times \nabla \times \vec{E}. \end{aligned} \quad (19)$$

In addition, using $\nabla \cdot \vec{B} = 0$ and $\nabla \cdot \vec{D} = 0$ we have

$$\begin{aligned} \nabla \cdot \vec{H} &= -\nabla \ln \mu \cdot \vec{H}, \\ \nabla \cdot \vec{E} &= -\nabla \ln \varepsilon \cdot \vec{E}, \end{aligned} \quad (20)$$

and finally

$$\begin{aligned} k^2 n^2 \vec{H} + \nabla^2 \vec{H} &= -\nabla (\nabla \ln \mu \cdot \vec{H}) \\ &\quad - \nabla \ln \varepsilon \times \nabla \times \vec{H}, \\ k^2 n^2 \vec{E} + \nabla^2 \vec{E} &= -\nabla (\nabla \ln \varepsilon \cdot \vec{E}) \\ &\quad - \nabla \ln \mu \times \nabla \times \vec{E}. \end{aligned} \quad (21)$$

D. Bloch-Floquet Waves in Cascaded 2D Layers

A simpler 2D example is used here to illustrate the approach because derivations for the spatial harmonic analysis (SHA) in 2D are less difficult. Consider a single period (l) of an infinite interface of a free-space domain with the domain of a material characterized by a set of step-wise continuous permittivity values ($\varepsilon_{1,1}, \varepsilon_{2,1}, \dots$), as shown in Fig. 2a.

Provided that a TM ($\vec{H} = \hat{z} \cdot h$) boundary-value problem is taken, then only the tangential components of the H and E field distributions over l are required in this case. A local coordinate system is introduced, with a unit normal (\hat{x}), a unit transverse vector (\hat{z}) and a tangent unit vector (\hat{y}). Then, consider two scalar fields (h and d) as the distribution of the transverse magnetic field ($h = \hat{z} \cdot \vec{H}$) over l and the distribution the electric field ($d = \varepsilon \hat{y} \cdot \vec{E}$). A monochromatic Maxwell equation $\hat{y} \cdot (\nabla h \times \hat{z}) = -i\omega d$ couples the fields

$$d = (i\omega)^{-1} h', \quad (22)$$

where the normal derivative of h is denoted $h' = \hat{x} \cdot \nabla h$.

The core of any SHA approach is the transformation of the fields from a physical space to spatial spectral space using available proper functions (g^m). Provided that h and g^m are sets of discrete values obtained at a uniform grid on l , these sets are considered as two vec-

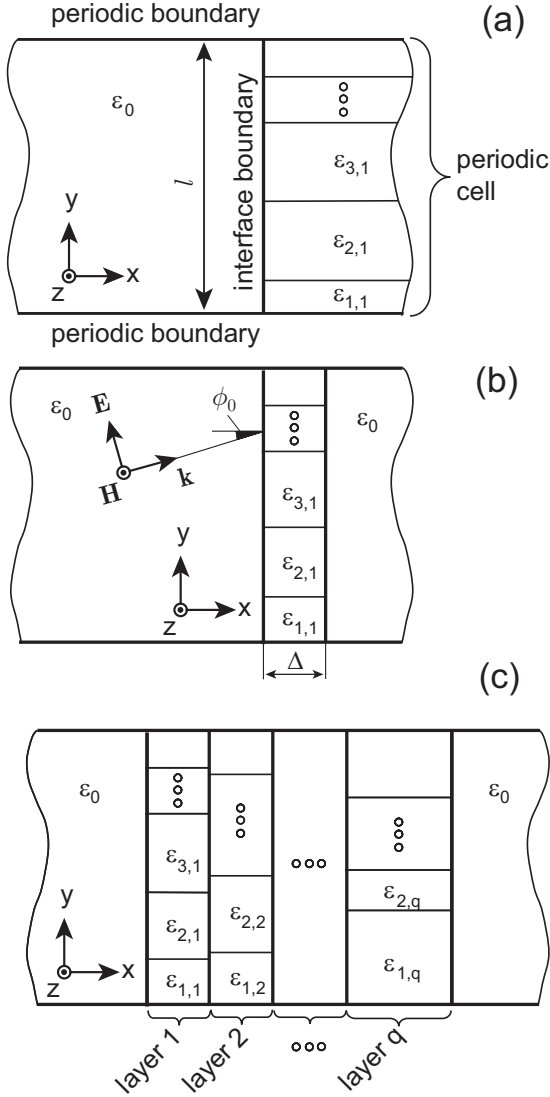


Fig. 2. (a) Interface of an elementary layer of NIM with free space; (b) an isolated elementary layer; (c) a cascaded multilayer NIM.

tors (h and g^m). The sum $\sum_{p=-p_{\max}}^{p_{\max}} g_p^{\nu*} g_p^m$ is considered here as a scalar product of two vectors $(g^\nu, g^m)_l$, where p is a point of the grid on l arranged of $\hat{p} = 2p_{\max} + 1$ points. Note that the proper functions g^m are orthonormal on l , i.e. $(g^\nu, g^m)_l = \delta(m - \nu)$.

Let us isolate the first elementary layer, for example, as shown in Fig. 2b. The magnetic field is defined by $h_1 = \sum_{m=-\infty}^{\infty} g_t^m c_{t,1}^m + g_r^m c_{r,1}^m$, where g_t^m and g_r^m are transmitted and reflected elementary fields of order m . In essence, the field h_1 is decomposed into elementary fields (the Bloch-Floquet waves), which are orthonormal on l . In a truncated approximation, $|m| \leq m_{\max}$,

the vectors g^m can form a $\hat{p} \times \hat{m}$ matrix g , $\hat{m} = 2m_{\max} + 1$ and the complex magnitudes of the reflected and transmitted fields ($c_{r,1}^m$ and $c_{t,1}^m$) can be taken as the components of two different \hat{m} -dimensional vectors $c_{r,1}$ and $c_{t,1}$. Then, the magnetic field in matrix form is defined by $h_1 = g_{t,1} c_{t,1} + g_{r,1} c_{r,1}$.

The Bloch-Floquet theorem allows for the separation of variables, $g_t = v_1 u_1$ and $g_r = v_1 u_1^{-1}$, where u is an $\hat{m} \times \hat{m}$ matrix exponential, $u_1 = \exp \iota k_{x,1} kx$, of a proper values matrix, $k_{x,1}^m$; and v_1 is a $\hat{p} \times \hat{m}$ matrix constructed of orthogonal vectors v_1^m . For the free-space case, indices in u , v , and k_x^m are dropped, and the proper functions u are defined through $k_x^m = \sqrt{1 - (k_y^m)^2}$, where $k_y^m = m\lambda l^{-1} + \sin \phi_0$ and ϕ_0 is the angle of incidence (shown in Fig. 2b). The wavefront $v^m = \hat{p}^{-1/2} \exp \iota k_y^m ky$ is just an orthonormal Fourier component of the m^{th} order.

1) Eigenvalue Problem

To obtain both $k_{x,1}$ and a_1 for a given elementary layer, where the permittivity of elementary materials (a piece-wise continuous function ϵ_1) is periodic in the y direction but constant in the x direction, it is necessary to attain an eigenvalue problem formulation. In this case,

$$k^2 \epsilon_1 h_1 + \nabla^2 h_1 - f_1 \partial_y h_1 = 0, \quad (23)$$

where f is the logarithmic derivative, $f_1 = \partial_y \ln \epsilon_1$, ϵ_1 and ϵ_1^{-1} are $\hat{p} \times \hat{p}$ diagonal matrices, and k^2 is a scalar.

The above equation can then be rewritten using $h_1 = v_1 (u_1 c_{t,1} - u_1^{-1} c_{r,1})$. Next, introducing a_1 as an $\hat{m} \times \hat{m}$ matrix mapping an orthogonal basis v_1 into the free-space basis v , ($v_1 = v a_1$), substituting $\iota (v^{-1} f_1 v) k_y$ with $\iota (k_y v^{-1} \epsilon_1 v - v^{-1} \epsilon_1 v k_y) \iota v^{-1} \epsilon_1^{-1} v k_y$ and using γ_1 for $v^{-1} \epsilon_1 v$, $\tilde{\gamma}_1$ for $v^{-1} \epsilon_1^{-1} v$ and i for the $\hat{m} \times \hat{m}$ identity matrix, (23) is further simplified as

$$a_1 k_{x,1}^2 a_1^{-1} = \gamma_1 (i - k_y \tilde{\gamma}_1 k_y). \quad (24)$$

The transform a_1 is required because in contrast with the free-space case, each wavefront v_1^m in an elementary inhomogeneous layer is not a single Fourier com-

ponent anymore; however, as a ‘physical function’* it still can be expressed as a superposition of Fourier components. Note that equation (24) is written in an eigenvalue form since $k_{x,1}^2$ is a diagonal matrix. The equation can be solved either numerically or analytically for both $k_{x,1}^2$ and a_1 , provided that γ_1 and k_y are known.

2) Mixed Boundary-Value Problem

Transverse field continuity together with the conservation of the tangential electric field on l gives the standard boundary conditions (BCs), $h_0 = h_1$, $\varepsilon_1 h'_0 = h'_1$, where the pairs h , h' represent the magnetic field and its normal derivative just before and after the interface; ε_1 are the values of permittivity at the collocation points on l .

After using the definitions of the fields $h_0 = v(u c_{t,0} - u^{-1} c_{r,0})$, $h_1 = v a_1 (u_1 c_{t,1} - u_1^{-1} c_{r,1})$ and taking the normal derivatives, a spectral form of the BC is

$$c_0 = s_1 c_1. \quad (25)$$

Here,

$$c_0 = \mathbf{d}(u, u^{-1}) \mathbf{c}(c_{t,0}, c_{r,0}), \quad c_1 = \mathbf{d}(u_1, u_1^{-1}) \mathbf{c}(c_{t,1}, c_{r,1}),$$

$$\text{and } s_1 = \mathbf{i}^{-1} \mathbf{d}(a_1, k_x^{-1} \gamma_1^{-1} a_1 k_{x,1}) \mathbf{i}.$$

At the second interface (as shown in Fig. 2b), the equation for the elementary layer is given by

$$b_1 c_1 = s_1^{-1} c_2, \quad (26)$$

where $b_1 = \mathbf{d}(\beta_1, \beta_1^{-1})$; the matrix exponential $\beta_1 = \exp \iota k_{x,1} \delta_1$ adjusts the phases for the scaled thickness of the layer ($\delta_1 = 2\pi \Delta_1 / \lambda$).

Combining (25) and (26) gives the following form

$$c_0 = s_1 b_1^{-1} s_1^{-1} c_2. \quad (27)$$

Since k_x is given as a common matrix for all layers, a possible alternative is to employ a normalization ($\mathbf{c}_0 = \mathbf{i} c_0$ and $\mathbf{c}_2 = \mathbf{i} c_2$), where the upper and lower partitions of \mathbf{c}_0 and \mathbf{c}_2 correspond to a magnetic component and a normalized electric component, respectively. These Fourier components are both continuous across any interlayer interface and form the basis for

wave matching. Then, (27) is simplified to

$$\mathbf{c}_0 = \mathbf{d}_1 \mathbf{b}_1^{-1} \mathbf{d}_1^{-1} \mathbf{c}_2, \quad (28)$$

where the linear operators $\mathbf{d}_1 = \mathbf{d}(a_1, k_x^{-1} \gamma_1^{-1} a_1 k_{x,1})$ and $\mathbf{b}_1 = \mathbf{i} b_1 \mathbf{i}^{-1}$ are unique for each layer with a given distribution of elementary materials (γ_1), defined matrices of the proper values $k_{x,1}$ and the proper vectors a_1 .

For the trivial case of a uniform slab with a permittivity $\bar{\varepsilon}_1$, $a_1 = \mathbf{i}$, $\gamma_1 = \bar{\varepsilon}_1 \mathbf{i}$ and a generalized analog of (6) is

$$\begin{pmatrix} \tilde{h}_0 \\ \tilde{h}'_0 \end{pmatrix} = \begin{pmatrix} \mathbf{i} & \mathbf{o} \\ \mathbf{o} & \eta_1 \end{pmatrix} \mathbf{i} \begin{pmatrix} \beta_1^{-1} & \mathbf{o} \\ \mathbf{o} & \beta_1 \end{pmatrix} \mathbf{i}^{-1} \begin{pmatrix} \mathbf{i} & \mathbf{o} \\ \mathbf{o} & \eta_1^{-1} \end{pmatrix} \begin{pmatrix} \tilde{h}_2 \\ \tilde{h}'_2 \end{pmatrix}, \quad (29)$$

where the tangential fields are the corresponding matrices of the Fourier transforms, $\tilde{h} = v^{-1} h$, $\tilde{h}' = (\iota k v)^{-1} h'$; $\eta_1 = \text{diag}(\bar{\varepsilon}_1^{-1} k_x^m)$ (from (24), $k_{x,1}^2 = \bar{\varepsilon}_1 \mathbf{i} - k_y^2$, and $k_{x,1}^m = \sqrt{\bar{\varepsilon}_1 - (k_y^m)^2}$). Then for example, validation of (29) for a plane wave at normal incidence gives a familiar result, shown earlier in (11).

From (28) we also note that in general, the following identity holds

$$\begin{pmatrix} \tilde{h}_0 \\ \tilde{h}'_0 \end{pmatrix} = \begin{pmatrix} a_1 & \mathbf{o} \\ \mathbf{o} & k_x^{-1} \gamma_1^{-1} a_1 k_{x,1} \end{pmatrix} \times \begin{pmatrix} \cos k_{x,1} \delta_1 & -\iota \sin k_{x,1} \delta_1 \\ -\iota \sin k_{x,1} \delta_1 & \cos k_{x,1} \delta_1 \end{pmatrix} \times \begin{pmatrix} a_1^{-1} & \mathbf{o} \\ \mathbf{o} & k_{x,1}^{-1} a_1^{-1} \gamma_1 k_x \end{pmatrix} \begin{pmatrix} \tilde{h}_2 \\ \tilde{h}'_2 \end{pmatrix}, \quad (30)$$

with $\cos k_{x,1} \delta_1$ and $\sin k_{x,1} \delta_1$ being arranged of adequate matrix exponentials.

II. SHA IN BI-PERIODIC NIM LAYERS

As yet there has been no mention of how to handle bi-periodic structures with generally different periods in z and y directions (denoted here as l_y and l_z respectively, as shown in Fig. 3). In contrast to the previous example, essentially there are two difficulties to overcome. First, there are a dramatically larger number of spatial harmonics (\bar{m}^2 in bi-periodic structures, versus \bar{m} in the single-periodic NIMs of Fig. 2a). This volume could be quite demanding for pure numerical solvers. On top of that, the already large number of basis spatial

* i.e., a piecewise continuous function with a limited variation on l .

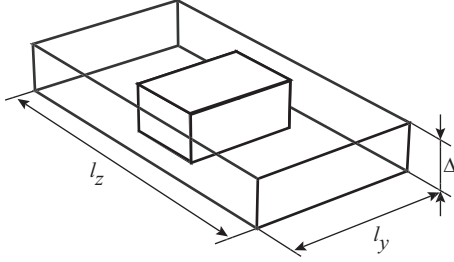


Fig. 3. Sketch of an example 3D periodic cell.

harmonics in which the fields is expressed should be increased even further to ensure convergence of the eigenvalues. A simple example of a bi-periodic layer of a binary material is shown in Fig. 3, where the layer is arranged of a metallic rectangular block which is immersed in a dielectric host. Certainly in real life applications each elementary layer (cross-section) could be much more involved. The electromagnetic field components inside a bi-periodic structure also should be bi-periodic with periods being the same as the length (l_y) and width (l_z) of the unit cell.

Then, each field component (e.g., $\vec{H} = (h_x, h_y, h_z)$) can be expressed as

$$h_i = \tilde{v}_i \tilde{u} c_i, \quad i = x, y, z, \quad (31)$$

where each field component is written as the product of a cell periodic part $\tilde{v} = \tilde{v}(y, z)$ and a wavelike part $\tilde{u} = \exp(i\tilde{k}_x x)$, as a consequence of Bloch's theorem.

As usual, we start with Maxwell's equations $\nabla \times \vec{E} = i\omega \vec{B}$, $\nabla \times \vec{H} = -i\omega \vec{D}$, and since $\nabla \cdot \vec{H} = 0$, i.e. $\nabla \times \nabla \times \vec{H} = -\nabla^2 \vec{H}$, we arrive at

$$-\nabla^2 \vec{H} = \varepsilon_r^{-1} \nabla \varepsilon_r \times (\nabla \times \vec{H}) + k^2 \varepsilon_r \vec{H}. \quad (32)$$

Introducing a tangent field $\vec{h}_\tau = \hat{y} h_y + \hat{z} h_z$, we note that

$$-\nabla^2 \vec{h}_\tau = \omega^2 \varepsilon \mu \vec{h}_\tau + \varepsilon^{-1} \begin{pmatrix} \hat{y} \partial_z \varepsilon (\partial_y h_z - \partial_z h_y) \\ -\hat{z} \partial_y \varepsilon (\partial_x h_z - \partial_z h_y) \end{pmatrix}. \quad (33)$$

After splitting the components of \vec{h}_τ , (33) yields

$$\begin{aligned} -\nabla^2 h_y &= \omega^2 \varepsilon \mu h_y + \varepsilon^{-1} \partial_z \varepsilon (\partial_y h_z - \partial_z h_y), \\ -\nabla^2 h_z &= \omega^2 \varepsilon \mu h_z + \varepsilon^{-1} \partial_y \varepsilon (\partial_x h_z - \partial_z h_y). \end{aligned} \quad (34)$$

Then, using separation of variables (31) in matrix

form, $\vec{h}_\tau = \tilde{v} \tilde{u} \vec{c}$, where $\tilde{v} = \tilde{v}(x, y)$, $\tilde{u} = \tilde{u}(z)$, the above is rewritten as

$$\begin{aligned} (a_y k_x^2 a_y^{-1}) a_y \tilde{u} c_y &= \begin{pmatrix} v^{-1} \varepsilon v - (k_y^2 + k_z^2) \\ -i v^{-1} \varepsilon^{-1} \partial_z \varepsilon v k_z \end{pmatrix} a_y \tilde{u} c_y \\ &\quad + i v^{-1} \varepsilon^{-1} \partial_y \varepsilon v k_y a_z \tilde{u} c_z, \\ (a_z k_x^2 a_z^{-1}) a_z \tilde{u} c_z &= \begin{pmatrix} v^{-1} \varepsilon v - (k_y^2 + k_z^2) \\ -i v^{-1} \varepsilon_r^{-1} \partial_y \varepsilon_r v k_y \end{pmatrix} a_z \tilde{u} c_z \\ &\quad + i v^{-1} \varepsilon^{-1} \partial_y \varepsilon v k_z a_z \tilde{u} c_y, \end{aligned} \quad (35)$$

where

$$\begin{aligned} k_z &= \alpha_z \hat{i} + \text{diag}[m_z \lambda / l_z], \quad k_y = \alpha_y \hat{i} + \text{diag}[m_y \lambda / l_y], \\ \alpha_y \hat{y} + \alpha_z \hat{z} &= \vec{k}_0 - (\vec{k}_0 \cdot \hat{x}) \hat{x}, \quad \text{and } \vec{k}_0 = \vec{k} / |\vec{k}| \text{ is a unit} \\ &\text{vector defined by the wavevector } (\vec{k}) \text{ of the incident} \\ &\text{field.} \end{aligned}$$

The latter is further simplified with the aid of the following identities for the partial logarithmic derivatives

$$\begin{aligned} i v^{-1} \varepsilon^{-1} \partial_z \varepsilon v &= \gamma k_z \gamma^{-1} - k_z, \\ i v^{-1} \varepsilon^{-1} \partial_y \varepsilon v &= \gamma k_y \gamma^{-1} - k_y, \end{aligned} \quad (36)$$

where $\gamma = v^{-1} \varepsilon v$. Then we arrive at

$$\begin{aligned} (a_y k_x^2 a_y^{-1}) a_y \tilde{u} c_y &= (\gamma - k_y^2 - \gamma k_z \gamma^{-1} k_z) a_y \tilde{u} c_y \\ &\quad + (\gamma k_z \gamma^{-1} k_y - k_z k_y) a_z \tilde{u} c_z, \\ (a_z k_x^2 a_z^{-1}) a_z \tilde{u} c_z &= (\gamma k_y \gamma^{-1} k_z - k_y k_z) a_y \tilde{u} c_y \\ &\quad + (\gamma - k_z^2 - \gamma k_y \gamma^{-1} k_y) a_z \tilde{u} c_z. \end{aligned} \quad (37)$$

The second term in the right side of both equations in (37) corresponds to the cross polarization. For a symmetric grating we can show that both $(\gamma k_z \gamma^{-1} k_y - k_z k_y)$ and $(\gamma - k_z^2 - \gamma k_y \gamma^{-1} k_y)$ are equal to zero and consequently we have no cross polarization for symmetric gratings. This simplification yields two decoupled eigenvalue equations as shown below

$$\begin{aligned} a_y k_x^2 a_y^{-1} &= \gamma (i - k_z \gamma^{-1} k_z) - k_y^2 \\ a_z k_x^2 a_z^{-1} &= \gamma (i - k_y \gamma^{-1} k_y) - k_z^2. \end{aligned} \quad (38)$$

For an asymmetric grating the two eigenvalue equations would be coupled via the cross polarizations term.

A 2D TM case ($c_y = k_z = 0$, i.e. the structure is periodic in the y direction only, there is no magnetic field

along the direction of periodicity) gives ($\tilde{\gamma}_y = v^{-1}\varepsilon_r(y)v$)

$$a_z k_x^2 a_z^{-1} = \gamma_y (i - k_y \gamma_y^{-1} k_y), \quad (39)$$

while a 2D TE case ($c_y = k_y = 0$, i.e. the structure is periodic in z -direction only, there is no electric field along the direction of periodicity and $\gamma_z = v^{-1}\varepsilon(z)v$) is

$$a_z k_x^2 a_z^{-1} = \gamma_z - k_z^2. \quad (40)$$

Note that equations (39)-(40) also provide a solution for structures with interleaving single-period layers with 90-degree rotation of their periodicity directions.

III. CASCADING THE ELEMENTARY LAYERS

Cascading a set of q elementary layers (depicted in Fig. 2c) gives

$$c_0 = w_1 c_1. \quad (41)$$

Here, $w_1 = \prod_{\nu=1}^q \tilde{w}_\nu$ and $\tilde{w}_\nu = s_\nu b_\nu^{-1} s_\nu^{-1}$ is an elementary transform due to ν -th layer.

Provided that each subset of q elementary layers is again stacked m times, then the matrix power $w_0^m = [w_0]^m$ is used with the following transformation

$$c_0 = w_0^m c_1. \quad (42)$$

Transformations equivalent to (27) - (42) can be written as

$$\begin{pmatrix} c_i \\ c_r \end{pmatrix} = \begin{pmatrix} w_{0,0} & w_{0,1} \\ w_{1,0} & w_{1,1} \end{pmatrix} \begin{pmatrix} c_t \\ 0 \end{pmatrix}, \quad (43)$$

where c_i are the spatial harmonic coefficients of the source, c_r is a set of the spatial harmonic coefficients of reflected light, and c_t are the harmonic coefficients of transmitted light.

A. Reflection and Transmission Coefficients

The major work-load in the above method falls on the calculation of the proper values and vectors ($k_{x,\nu}$ and a_ν) for each elementary layer. Once the values are obtained, the characteristic matrices of each layer are arranged as $s_\nu b_\nu^{-1} s_\nu^{-1}$.

Introducing the transformations $\rho_\nu c_{t,\nu} = c_{r,\nu}$, $\tau_\nu c_{t,\nu} = c_{i,\nu}$ (with initial values given by $\tau_q = i$, and $\rho_q = 0$), the matrices of spatial spectral reflectance and transmittance are defined as

$$\begin{aligned} \rho_{\nu-1} &= (w_\nu^{1,0} + w_\nu^{1,1} \rho_\nu) (w_\nu^{0,0} + w_\nu^{0,1} \rho_\nu)^{-1}, \\ \tau_{\nu-1} &= \tau_\nu (w_\nu^{0,0} + w_\nu^{0,1} \rho_\nu)^{-1}, \end{aligned} \quad (44)$$

where the characteristic matrix is partitioned as

$$\tilde{w}_\nu = \begin{pmatrix} w_\nu^{0,0} & | & w_\nu^{0,1} \\ \hline w_\nu^{1,0} & | & w_\nu^{1,1} \end{pmatrix}. \quad \text{The partitions are calculated using } s_\nu,$$

which is a matrix with symmetrical partitions,

$$\begin{aligned} s_\nu &= \mathbf{s}(s_\nu^0, s_\nu^1) \quad \text{with} \quad s_\nu^0 = \frac{1}{2}(k_x^{-1} \gamma_\nu^{-1} a_\nu k_{x,\nu} + a_\nu) \quad \text{and} \\ s_\nu^1 &= \frac{1}{2}(k_x^{-1} \gamma_\nu^{-1} a_\nu k_{x,\nu} - a_\nu) \quad \text{and a similar matrix} \\ s_\nu^{-1} &= \mathbf{s}(\tilde{s}_\nu^0, \tilde{s}_\nu^1) \quad \text{with} \quad \tilde{s}_\nu^0 = \frac{1}{2}(k_{x,\nu}^{-1} a_\nu^{-1} \gamma_\nu k_x + a_\nu^{-1}) \quad \text{and} \\ \tilde{s}_\nu^1 &= \frac{1}{2}(k_{x,\nu}^{-1} a_\nu^{-1} \gamma_\nu k_x - a_\nu^{-1}), \quad \text{then} \end{aligned}$$

$$\begin{aligned} w_\nu^{0,0} &= s_\nu^0 \beta_\nu^{-1} \tilde{s}_\nu^0 + s_\nu^1 \beta_\nu \tilde{s}_\nu^1, & w_\nu^{0,1} &= s_\nu^0 \beta_\nu^{-1} \tilde{s}_\nu^1 + s_\nu^1 \beta_\nu \tilde{s}_\nu^0, \\ w_\nu^{1,0} &= s_\nu^1 \beta_\nu^{-1} \tilde{s}_\nu^0 + s_\nu^0 \beta_\nu \tilde{s}_\nu^1, & w_\nu^{1,1} &= s_\nu^1 \beta_\nu^{-1} \tilde{s}_\nu^1 + s_\nu^0 \beta_\nu \tilde{s}_\nu^0. \end{aligned} \quad (45)$$

Thus, for example, a single-layer structure is calculated as follows: $\tau_0 = (w_1^{0,0})^{-1}$, $\rho_0 = w_1^{1,0} (w_1^{0,0})^{-1}$. Then, the transmitted and reflected Bloch-Floquet waves are

$$c_{t,1} = \tau_0 c_i, \quad c_{r,0} = \rho_0 c_i. \quad (46)$$

B. A Simple Validation Test

A simplified 2D single-layer model for validating the simulation method is shown in Fig. 4a. The sample structure is intentionally made of a very thin metallic grating (with 10-nm thickness). The grating is arranged of 400-nm gold strips separated by narrow strips of silica, the period of the structure is 480 nm. The large aspect ratio of the metallic strips and a large electric resonance at a wavelength of about 1.2 micron are among the main challenges of the test model. To obtain a good set of reference data, the structure was simulated using a commercial software package with 5th-order finite elements. The validity of the FEM solution was verified by using the same model with different levels of additional meshing refinement and an adaptive solver. The results were stable upon the use of 41,000 degrees of freedom (field variables), where the bulk of the resources had been spent for the free-space buffer, non-reflecting lay-

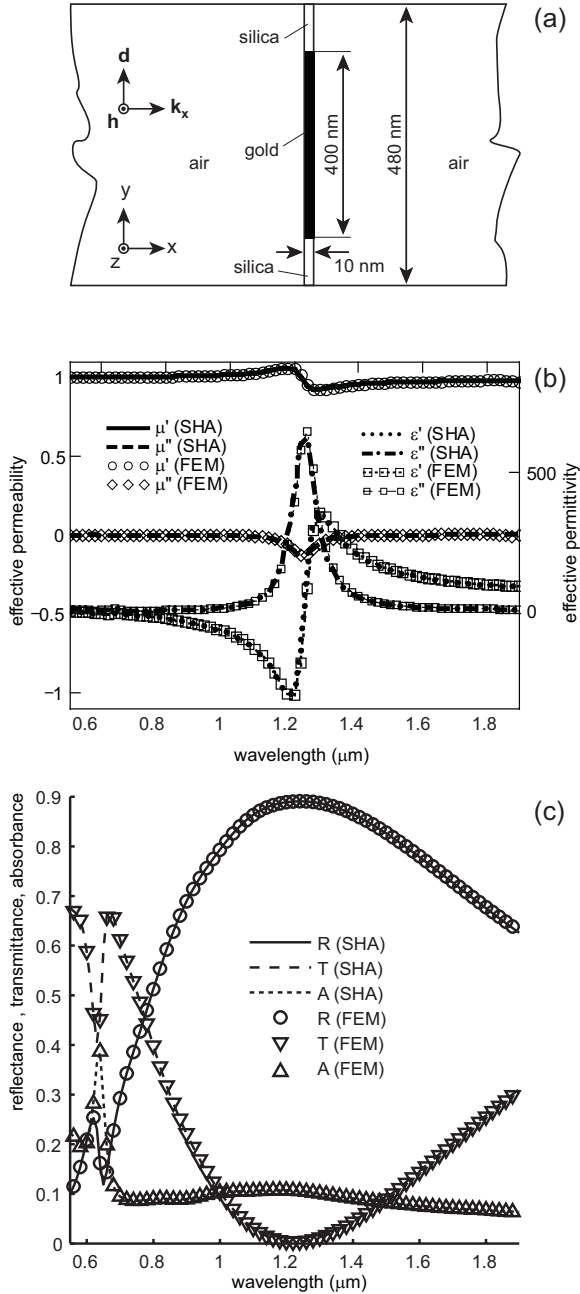


Fig. 4. (a) Geometry sketch of a resonant elementary layer; (b) effective permeability and permittivity obtained for the elementary layer using FEM and SHA (using 11 eigenvalues); (c) comparison of the reflection, transmission, and absorption spectra obtained in simulations using FEM and SHA (11 eigenvalues).

ers and adequate meshing at the corners.

In contrast to FEM, the spatial harmonic analysis method appeared much more efficient. The problem was stabilized after the use of 11 eigenvalues with a calculation time of about 100 times less versus the FEM solver with the same number of wavelength points and

the same computational hardware. It should be noted that the amount of simulation time using SHA is approximately proportional to the total number of elementary layers and scales approximately as the square (or cube) of the total number of eigenvalues in 2D (or 3D) problems, while the performance of FEM solvers decreases very moderately with increasing layers. Both models appeared to be quite sensitive to the material properties of the metal. In both cases, the interpolated complex refractive index was based on the experimental table of Johnson and Christy [19]. In addition to simple validation of the modeling approach, the test model of Fig. 4a reveals all typical features of the periodic structures with localized plasmonic resonances, e.g. at the same wavelength the electric resonance is always accompanied by a satellite magnetic antiresonance and vice versa.

As has been discussed in [5] and shown in equations (10) and (11), the effective refractive index \bar{n}_1 and its effective impedance $\bar{\eta}_1$ of a given elementary layer can be uniquely determined either experimentally or from simulations. Rewriting (10) as

$$\bar{n}_1 = \frac{1}{\delta_1} \left(\arccos \frac{1 - \bar{r}^2 + n_2 \bar{t}^2}{[1 + n_s - (1 - n_2) \bar{r}] \bar{t}} \right), \quad (47)$$

$$\nu = 0, 1, 2, \dots$$

we can determine \bar{n}_1 , where n_2 is the refractive index of the thick substrate beyond the elementary layer, and \bar{r} and \bar{t} are the complex reflection and transmission coefficients of the propagating plane wave mode. In simulations \bar{r} and \bar{t} can be obtained from

$$\bar{t} = (\tau_0)_{0,0}, \quad \bar{r} = (\rho_0)_{0,0}, \quad (48)$$

i.e., in essence by taking only the central terms of the transmission and reflection matrices. Then, the effective permittivity and the effective permeability are given by

$$\bar{\mu}_1 = \bar{n}_1 \bar{\eta}_1, \quad \bar{\epsilon}_1 = \bar{n}_1 / \bar{\eta}_1. \quad (49)$$

C. Implementation Details for the 2D Case

Although the process of solving (24) is relatively simple for dielectric sub-wavelength gratings, a direct treatment of metallic sub-wavelength gratings is more difficult because of the much higher contrast in permittivity within the optical wavelength range.

The following steps are taken to alleviate the problem:

1) The Fourier transform of inverted permittivity

First, we take the following modification of (23)

$$k^2 h_1 + \varepsilon_1^{-1} \partial_x^2 h_1 + \partial_y (\varepsilon_1^{-1} \partial_y h_1) = 0. \quad (50)$$

Using $h_1 = v a_1 (u_1 c_{t,1} - u_1^{-1} c_{r,1})$ and $\varepsilon_1^{-1} = v \tilde{\gamma}_1 v^{-1}$ we have

$$v - v \tilde{\gamma}_1 a_1 k_x^2 a_1^{-1} + (\partial_y v) v \tilde{\gamma}_1 k_x = 0, \quad (51)$$

or

$$i - k_y \tilde{\gamma}_1 k_y = \tilde{\gamma}_1 a_1 k_x^2 a_1^{-1}. \quad (52)$$

Finally, we can use the following version of (24)

$$a_1 k_x^2 a_1^{-1} = \tilde{\gamma}_1^{-1} (i - k_y \tilde{\gamma}_1 k_y), \quad (53)$$

which provides stable convergence in the presence of metallic elements.

Moreover, in accord with (53) the Fourier transform of the inverted permittivity $\tilde{\gamma}_1$ and its inverse $\tilde{\gamma}_1^{-1}$ is used respectively in (28) and (30) instead of γ_1^{-1} and γ_1 .

2) Analytical calculation of the Fourier transform

In addition, along with the use of the inverted permittivity, the Fourier transformation $\tilde{\gamma}_1$ in (25) is calculated analytically provided that $\varepsilon_1(y)$ over the period l is a combination of homogeneous segments. Indeed, for any $m > 0$ $l^{-1} \int e^{-ik_y^m y} dy = e^{-ik_y^m y} / (ik_y^m)$, thus for example, a term $\tilde{\gamma}_1^{p,m}$ (at row p and column m) of the square matrix $\tilde{\gamma}_1$ for the elementary layer in Fig. 4a, is given by

$$\left(\varepsilon_g^{-1} + \varepsilon_s^{-1} \right) \frac{\sin[\kappa\pi(p-m)]}{\pi(p-m)} \quad \text{if } p \neq m, \quad (54)$$

$$\kappa\varepsilon_g^{-1} + (1-\kappa)\varepsilon_s^{-1} \quad \text{otherwise}$$

where $\kappa = w/l$ is the metal filling factor and ε_g and ε_s is the permittivity of gold and silica, respectively.

IV. DISCUSSIONS

Both remedies built on (53) and (54) work well with metallic structures. For example, Fig. 5 shows the real and imaginary parts of the effective refractive index that is restored using the complex transmission and reflection

coefficients at normal incidence [5]. (The geometry of the layer has been already shown in Fig. 4a.) Both real and imaginary parts of the refractive index are converging rapidly. Small features around 650 nm are suppressed only for $m_{\max} = 1$, and both curves are quickly converging to their limits; starting from $m_{\max} = 9$ the corresponding curves with larger m_{\max} are overlapping.

In contrast, a direct application of the initial formulation (24) is of limited utility to the problem. We note that the transmission and reflection spectra demonstrate much slower convergence and substantial artifacts. For example, Fig. 6 depicts the results obtained from the problem of Fig. 4a using the initial eigenvalue formulation (24).

It is important to note that a convergence control should be implemented for the entire multilayer structure; otherwise insignificant modes of an elementary layer could be considerably enhanced due to additional resonances of coupled elementary layers.

Consider for example the real part of the refractive index, n' , shown in Fig. 7a. The values of n' are restored from \bar{r} and \bar{t} , which are calculated for a single

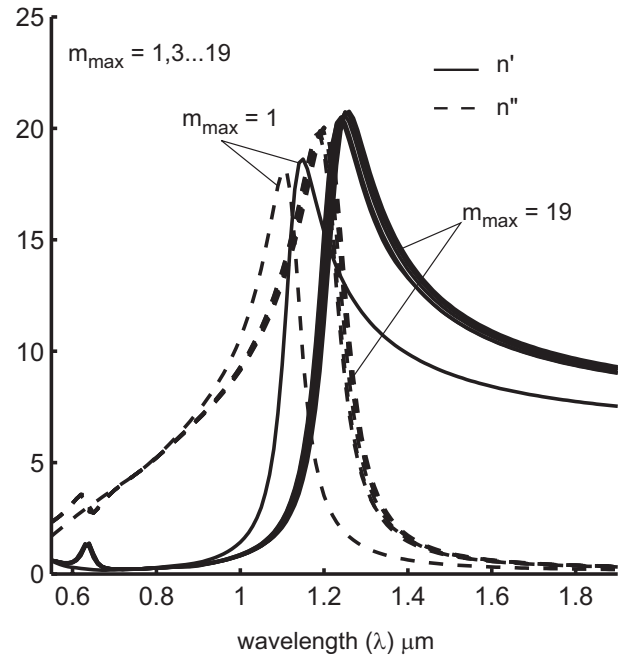


Fig. 5. Real and imaginary part of the refractive index (n' and n'') vs. wavelength calculated with a different number of spatial harmonics ($m_{\max} = 1, 3, 19$). Starting from $m_{\max} = 9$ the difference in the results is almost indiscernible.

layer depicted in the inset of Fig. 7a. There is no resonance within the selected 300-nm wavelength segment,

and the values of n' converge quickly starting from $m_{\max} = 6$.

Now we take a triple-layer structure arranged of two identical elementary layers of Fig. 7a separated by a uniform 100-nm layer of silica. The structure exhibits an additional magnetic resonance within the selected wavelength range. As expected, this resonance, which appears due to additional near-field coupling between the metallic strips, requires taking into account an increased number of modes. The same level of relative error is now achieved starting from $m_{\max} > 10$.

As a result, additional care is required for the accurate calculation of stacked substructures arranged of elementary layers and cascaded materials integrating different or identical multilayer substructures. It also follows from the analysis of equations (27)-(45) that:

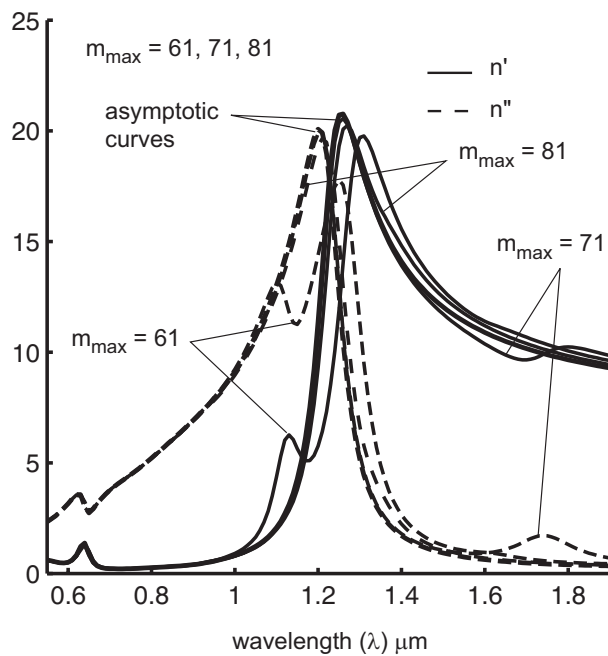


Fig. 6. Real and imaginary part of the refractive index (n' and n'') vs. wavelength calculated using (24) for $m_{\max} = 61, 71, 81$. Starting only from $m_{\max} = 71$ the difference in the results are converging well to the asymptotic curves obtained using (53).

(i) None of asymmetric multilayer composites can be effectively described either by the simplified homogenization approach (9)-(11), or through its generalized analog (30). (A multilayer composite is asymmetric if it contains an odd number of elementary layers and the layers are not mirror-symmetric relative to the central layer; all structures with an even number of distinct layers are always asymmetric).

(ii) Effective optical parameters (including an effective negative refractive index) obtained in a single symmetric sub-set of elementary layers may not guarantee the same effective parameters in a bulk material arranged of identical subsets, not merely because of absorptive losses but also due to new interactions of near-field waves introduced by the use of cascading.

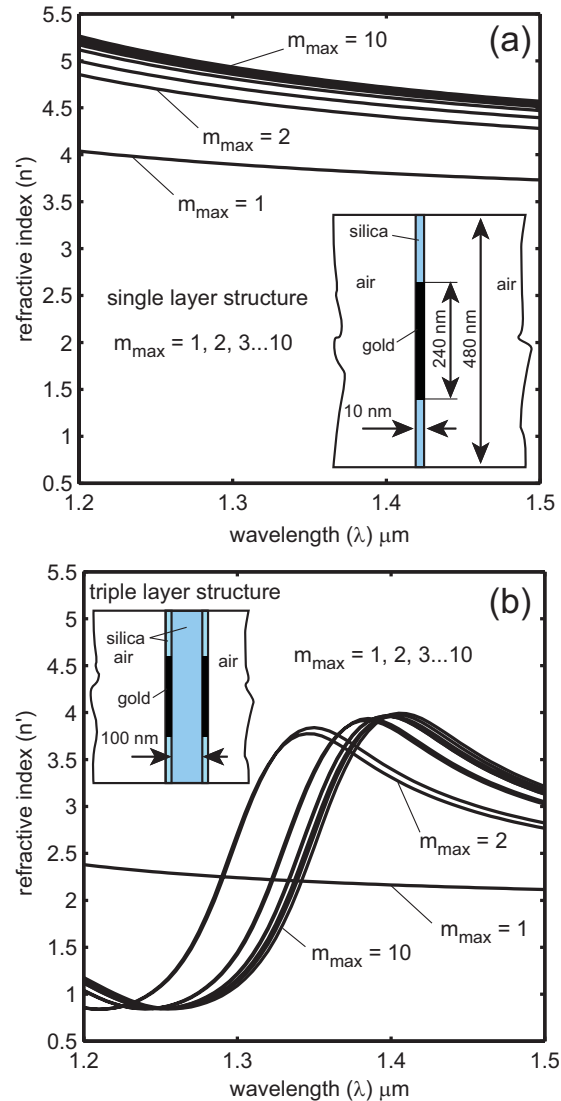


Fig. 7. The real part of the refractive index (n') vs. wavelength. (a) n' calculated for a single layer structure shown in the inset for $m_{\max} = 1, 2 \dots 10$. Starting from $m_{\max} = 6$ there is almost no difference in the curves, (b) n' calculated for a triple layer structure arranged from two identical layers of diagram (a) separated by a 100-nm uniform layer of silica. The inset depicts the triple-layer structure. Convergence to the same level of error begins starting from $m_{\max} = 10$. Slower convergence is caused by an additional resonance due to strong near-field coupling between the layers.

To illustrate (i) consider a classical example of a sub-set structure with two homogeneous lossless layers [[20], p. 72]. The characteristic matrix of two layers with thicknesses Δ_1 and Δ_2 , and indices n_1 and n_2 , is computed as $\mathbf{w}_2 = \tilde{\mathbf{w}}_1 \tilde{\mathbf{w}}_2$, with $\tilde{\mathbf{w}}_1 = \mathbf{d}_1 \mathbf{b}_1^{-1} \mathbf{d}_1^{-1}$ and $\tilde{\mathbf{w}}_2 = \mathbf{d}_2 \mathbf{b}_2^{-1} \mathbf{d}_2^{-1}$. The effective characteristic matrix (\mathbf{w}_{eff}) of an equivalent single layer, which is defined as

$$\mathbf{w}_{eff} = \begin{pmatrix} \mathbf{w}_{eff}^{0,0} & | & \mathbf{w}_{eff}^{0,1} \\ \hline \mathbf{w}_{eff}^{1,0} & | & \mathbf{w}_{eff}^{1,1} \end{pmatrix} \quad (55)$$

$$= \begin{pmatrix} \cos n_{eff} k_x \delta & -i n_{eff} \sin n_{eff} k_x \delta \\ -i n_{eff}^{-1} \sin n_{eff} k_x \delta & \cos n_{eff} k_x \delta \end{pmatrix},$$

(using a scaled thickness, $\delta = k(\Delta_1 + \Delta_2)$ and the effective index, n_{eff}), should be equal to the characteristic matrix of the double-layer \mathbf{w}_2 . To be equivalent to \mathbf{w}_{eff} , the product $\mathbf{w}_2 = \tilde{\mathbf{w}}_1 \tilde{\mathbf{w}}_2$ must have identical diagonal partitions since $\mathbf{w}_{eff}^{0,0} = \mathbf{w}_{eff}^{1,1}$ in (55). This is true only if the product commutes, i.e. $\tilde{\mathbf{w}}_1 \tilde{\mathbf{w}}_2 = \tilde{\mathbf{w}}_2 \tilde{\mathbf{w}}_1$, leaving the only trivial case of $n_1 = n_2$ possible. Therefore, even a simple stack of two distinct lossless films cannot be adequately modeled by a single effective layer. Physically, the condition $\tilde{\mathbf{w}}_1 \tilde{\mathbf{w}}_2 = \tilde{\mathbf{w}}_2 \tilde{\mathbf{w}}_1$ means that the effective parameters of a multilayer NIM should not depend on which side is chosen for illumination, i.e. its structure should be symmetric.

Note that although $\tilde{\mathbf{w}}_1 \tilde{\mathbf{w}}_2 \tilde{\mathbf{w}}_3 = \tilde{\mathbf{w}}_3 \tilde{\mathbf{w}}_2 \tilde{\mathbf{w}}_1$ is always true for any triple-layered structure, since the first and the last layers are equal ($\tilde{\mathbf{w}}_1 = \tilde{\mathbf{w}}_3$), the homogenization of $\mathbf{w}_3 = \mathbf{d}_1 (\mathbf{b}_1^{-1} \mathbf{d}_{12} \mathbf{b}_2^{-1} \mathbf{d}_{12}^{-1} \mathbf{b}_1^{-1}) \mathbf{d}_1^{-1}$ is not very simple even for the structure with homogeneous elementary layers.

Now to exemplify (ii) consider a cascaded structure arranged of identical symmetric substructures, then $w_3 = s_1 b_1^{-1} s_{12} b_2^{-1} s_{12}^{-1} b_1^{-1} s_1^{-1}$, where $s_{12} = s_1^{-1} s_2 = \mathbf{i}^{-1} \mathbf{d}_1^{-1} \mathbf{d}_2 \mathbf{i}$. The diagonally partitioned matrix $\mathbf{d}_1^{-1} \mathbf{d}_2$ is responsible for interactions between the layers. Cascading p triple-layer substructures suggests taking the p -th power of the characteristic matrix w_3 . Although the result is straightforward since $(w_3)^p = s_1 (b_1^{-1} s_{12} b_2^{-1} s_{12}^{-1} b_1^{-1})^p s_1^{-1}$, it is clear that new interactions of near-field waves introduced by cascading will change the effective properties of the cascaded structure in comparison to those of the initial three-layer sub-structure, unless it is possible to write w_3 as

$w_3 = s_{eff} b_{eff} s_{eff}^{-1}$, where b_{eff} is a diagonal matrix of effective eigenvalues and s_{eff} is a matrix of effective eigenvectors.

ACKNOWLEDGMENT

We would like to cite fruitful teamwork with V. Drachev, T. Klar, V. Shalaev, W. Cai, Z. Liu, and H.-K. Yuan. The authors also acknowledge important discussions with D. Werner.

This work was supported in part by ARO grant W911NF-04-1-0350, NSF-NIRT award ECS-0210445 and ARO MURI grant.

REFERENCES

- [1] L. I. Mandel'shtam, "Group velocity in crystal lattice," *JETP*, vol. 15, pp. 475, 1945.
- [2] V. G. Veselago, "The electrodynamics of substances with simultaneously negative values of ϵ and μ ," *Soviet Physics Uspekhi*, vol. 10, pp. 509–514, 1968.
- [3] R. A. Shelby, D. R. Smith, and S. Schultz, "Experimental verification of a negative index of refraction," *Science*, vol. 292, pp. 77–79, Apr. 2001.
- [4] J. B. Pendry, "Negative refraction makes a perfect lens," *Phys. Rev. Lett.*, vol. 85, no. 18, pp. 3966–3969, Oct. 2000.
- [5] A. V. Kildishev, W. Cai, U. K. Chettiar, H. K. Yuan, A. K. Sarychev, V. P. Drachev, and V. M. Shalaev, "Negative refractive index in optics of metal-dielectric composites," *J. of Opt. Soc. Am. B*, vol. 23, no. 3, pp. 423–433, Mar. 2006.
- [6] J. D. Vacchione and R. Mittra, "Cascading of Multiscreen Frequency Selective Surfaces," in *Frequency Selective Surface and Grid Array*, T. K. Wu, Ed. John Wiley & Sons, 1995.
- [7] C. B. Burkhart, "Diffraction of a Plane Wave at a Sinusoidally Stratified Dielectric Grating," *J. Opt. Soc. Am.*, vol. 56, no. 11, pp. 1502–1509, Nov. 1966.
- [8] F. G. Kaspar, "Diffraction by thick, periodically stratified gratings with complex dielectric constant," *J. Opt. Soc. Am.*, vol. 63, no. 1, pp. 37–45, Jan. 1973.
- [9] K. Knop, "Rigorous diffraction theory for transmission phase gratings with deep rectangular grooves," *J. Opt. Soc. Am.*, vol. 68, no. 9, pp. 1206–1210, Sept. 1978.
- [10] M. G. Moharam and T. K. Gaylord, "Rigorous coupled-wave analysis of planar-grating diffraction," *J. Opt. Soc. Am.*, vol. 71, no. 7, pp. 811–818, July 1981.
- [11] M. G. Moharam and T. K. Gaylord, "Rigorous coupled-wave analysis of grating diffraction – E-mode

- polarization and losses,” *J. Opt. Soc. Am.*, vol. 73, no. 4, pp. 451–455, Apr. 1983.
- [12] M. G. Moharam and T. K. Gaylord, “Three-dimensional vector coupled-wave analysis of planar-grating diffraction,” *J. Opt. Soc. Am.*, vol. 73, no. 9, pp. 1105–1112, Sept. 1983.
- [13] L. C. Botten, M. S. Craig, R. C. McPhedran, J. L. Adams, and J. R. Andrewartha, “The dielectric lamellar diffraction grating,” *Opt. Acta*, vol. 28, no. 3, pp. 413–428, 1981.
- [14] L. C. Botten, M. S. Craig, R. C. McPhedran, J. L. Adams, and J. R. Andrewartha, “The finitely conducting lamellar diffraction grating,” *Opt. Acta*, vol. 28, no. 8, pp. 1087–1102, 1981.
- [15] L. C. Botten, M. S. Craig, and R. C. McPhedran, “Highly conducting lamellar diffraction gratings,” *Opt. Acta*, vol. 28, no. 8, pp. 1103–1106, 1981.
- [16] G. Tayeb and R. Petit, “On the numerical study of deep conducting lamellar diffraction gratings,” *Optica Acta*, vol. 31, no. 12, pp. 1361–1365, 1984.
- [17] R. Petit and G. Tayeb, “Numerical study of the symmetrical strip-grating-loaded slab,” *J. Opt. Soc. Am. A*, vol. 7, no. 3, pp. 373–378, Mar. 1990.
- [18] S. E. Sandström, G. Tayeb, and R. Petit, “Lossy multistep lamellar gratings in conical diffraction mountings – an exact eigenfunction solution,” *J. of Electromagnetic Waves and Applications*, vol. 7, pp. 631–649, 1993.
- [19] P. Johnson and R. W. Christy, “Optical Constants of the Noble Metals,” *Phys. Rev. B*, vol. 6, no. 12, pp. 4370–4379, Dec. 1972.
- [20] M. Born and E. Wolf, *Principles of Optics*, Cambridge, 1964.



Alex V. Kildishev received the M.Sc., and Ph.D. degrees in electrical engineering from the Kharkov State Polytechnical University in the Ukraine. He has worked as a Senior Scientist at the Institute of Electrodynamics, Academy of Sciences, Ukraine. Since 1998 he has been a member

of the School of ECE, Purdue University, where he is currently a Principal Research Scientist at the PSL, Birk Nano-technology Center. His primary research interest is in the development of advanced computational methods for the spatial harmonic/modal analysis in general radiation and scattering problems in applied electromagnetics and optics. Other research interests include optimization of plasmonic metamaterials, MRI electromagnetics, and magnetic silencing. He has published over sixty journal articles in these areas; he is a coauthor of four book chapters and four patents. Dr. Kildishev is a Senior Member of the IEEE, and is a member of ACES and ICS.



Uday K. Chettiar received a bachelor degree in electrical engineering from Indian Institute of Technology, Mumbai, India in 2003. He is currently working towards his Ph.D. degree at Prof. Shalaev’s Photonics and Spectroscopy Laboratory (PSL), Purdue University, USA. He was a

gold medalist in the Indian National Physics Olympiad and a recipient of Benjamin Franklin-Meissner fellowship at Purdue. He has published four papers in peer-reviewed journals and has given four talks at international scientific conferences. Uday Chettiar is a member of OSA. His current research interests include simulation and analysis of optical metamaterials.

Characterizing Infrared Frequency Selective Surfaces on Dispersive Media

James Ginn¹, Brian Lail², David Shelton¹, Jeffrey Tharp¹, William Folks¹, and Glenn Boreman¹

¹ CREOL - College of Optics and Photonics
University of Central Florida, Orlando, FL 32816, USA

² Department of Electrical and Computer Engineering
Florida Institute of Technology, Melbourne, FL 32901, USA

Abstract — With the emergence of frequency selective surfaces (FSS) and other passive planar antenna devices at infrared frequencies, the increasing need for accurate characterization using numerical modeling prior to device fabrication has exposed limitations in the traditional modeling procedures used for lower frequency FSS designs. To improve full-wave FSS models at IR, a procedure to measure and integrate dispersive material properties in modeling is described. Measured and modeled results are provided as verification demonstrating the need to account for material dispersion in infrared FSS design.

Keywords — Frequency Selective Surfaces, Nanoscale device modeling.

I. INTRODUCTION

A Frequency Selective Surface, or FSS, is made up of a periodic arrangement of resonant structures for the purpose of spectral modification of reflected, transmitted, or emitted radiation. The resonant properties of these structures depend both upon the FSS layout (dimensions and periodicity) and the properties of the materials used in the construction. Thus, by varying the FSS layout and material properties, it is possible to tune the FSS resonance to meet specific design requirements.

Since the 1960s, FSS structures have been successfully designed and implemented for use in radio frequency (RF) applications. With growing interest in adapting low-frequency antenna layouts for infrared (IR) applications, several FSS designs have been fabricated and tested including designs using dipoles [1], crosses [2], and square loops [3]. To limit the need for repetitive fabrication and testing, commercially available numerical electromagnetic solvers have been successfully used to model and characterize FSS designs at IR [4]. One of the greatest limiting factors of IR FSS modeling, however, has been the assumption that materials at IR exhibit electromagnetic properties

independent of frequency. Traditionally a valid assumption at RF, the majority of materials utilized in FSS fabrication exhibit measurable frequency dependent (FD) optical properties at IR. This measurable material dispersion can have a significant impact on the measured performance of the fabricated FSS and will degrade agreement between measured and modeled results when assuming static material properties. Furthermore, a large number of commercial electromagnetic solvers used in FSS characterization were developed specifically for RF application and, thus, allow only frequency independent material definitions, or provide only a limited means to account for dispersive materials.

To overcome this limitation, this paper presents a procedure to account for FD material properties in IR FSS modeling. Frequency-dependent IR material measurement using an IR ellipsometer, and the integration of dispersive materials into existing commercially available full wave modeling packages is discussed. In addition, this paper includes analysis showing significant improvements in agreement between modeled and measured results.

II. FREQUENCY-DEPENDENT IR MATERIAL CHARACTERIZATION

Before modeling an IR FSS design, materials used for fabrication must be first characterized for their dispersive optical properties. While FD properties for many materials have been previously characterized and published, inconsistency in measurement approaches limit the utility of such results. Published material studies frequently characterize materials only in ideal situations, such as within a vacuum or as a bulk composition [5] or using mathematical models [6]. In addition, even if the material is studied in a similar configuration as the FSS to be modeled, variability in deposition techniques, layer intermixing, atmospheric conditions, material composition, and handling can render prior measured data inaccurate for modeling.

Clearly, for the highest possible accuracy when modeling FSS on dispersive materials, IR material properties must be characterized directly using the as-deposited materials or actual substrates.

Specifically, a J. A. Woollam Infrared Variable-Angle Spectroscopic Ellipsometer (IR-VASE) (Fig.1) was utilized to measure the IR properties of each material used in fabrication of the FSS over the wavelength range from 2 μm to 14 μm . For metals, deposition of the metal at a thickness greater than the skin depth on a known substrate, such as silicon, is recommended for accurate characterization of near bulk material properties. This is consistent with the metal thicknesses typically used in FSS designs; however, deposition at the exact fabricated metal thickness allow for representative results. To characterize dielectric stand-off layers, it is recommended to make measurements on the actual layer of material used in fabrication, before the application of electron resist. This facilitates both the determination of IR properties and the accurate measurement of the dielectric's thickness. The characteristics of each material are measured from samples, analyzed and fit to an oscillator model using software provided by the manufacturer, and stored in a shared network library as a spreadsheet file. Because most commercially available modeling software programs only accept material property definitions as complex dielectric constants, and not index of refraction, the measured data from the ellipsometer can also be converted for direct utilization by using the relationship

$$\tilde{n}(\lambda) = \sqrt{\tilde{\epsilon}_r(\lambda)}. \quad (1)$$

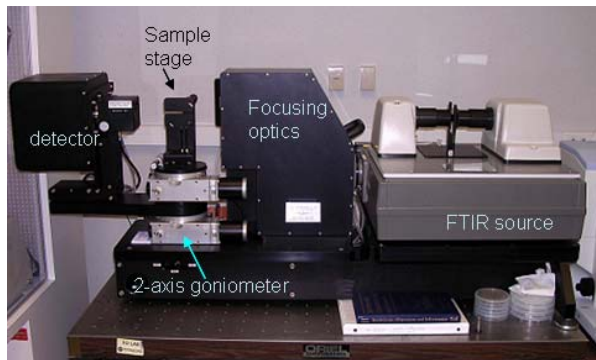


Fig. 1. IR-VASE.

As with any measurement apparatus, the IR-VASE is susceptible to both measurement and post processing errors. One of the capabilities of the IR-VASE analysis software is the ability to automatically determine both the standard deviation of the measured material response and material model errors. From these values and with proper deposition and analysis, optical properties from simple dispersive dielectrics and metals

should be within $\pm 5\%$ of their actual values. As material model complexity increases, error will also increase.

III. IMPLEMENTATION

To carry out modeling, a MATLAB function was created to utilize the measured FD material properties. The MATLAB function consists of three major components – User Interface (UI), Solver Independent Code (SIC), and Solver Specific Code (SSC). The UI component of the code provides the interface necessary for user input and real time presentation of results. The SIC component interprets the users input, reads FD material properties from the shared network library, and creates result files and directories. The SSC component provides functionality to interface with a specific external electromagnetic solver and to interpret the results generated by the solver. The function's layered approach is desirable as it allows for easy integration of multiple electromagnetic solvers without changing the UI or SIC. Currently, Ohio State University's Periodic Method of Moments (PMM) and Ansoft Designer, both Method of Moments solvers, are supported.

Solutions for frequency dependent material designs are realized using frequency point by point simulation. To improve performance, programs are provided with a template specifying initial geometry. Step modeling is achieved by populating the desired template with material properties at each frequency step and calling the necessary solver. In the function's current implementation, PMM setup files, written in FORTRAN, are directly modified at each step, whereas Designer setup files require modification using VBScript to directly interface with the modeling program. Results are then stored for each frequency step in a spreadsheet and the UI is updated in real-time. A summary of the program is provided in Fig. 2.

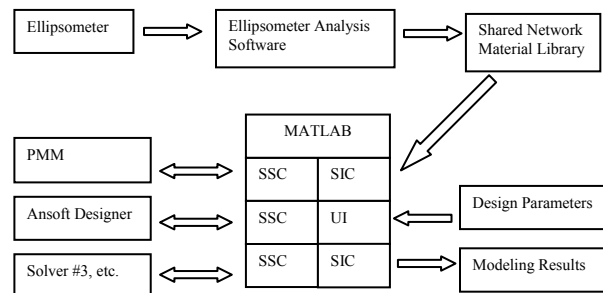


Fig. 2. Implementation of frequency-dependent modeling.

In addition to support for FD materials, the developed MATLAB function further enhances all of the solvers by adding new capabilities. Most significant of this new functionality, especially from the standpoint of the user,

is the fact that parameter input, user interfaces, and results are all presented identically regardless of the chosen solver. Neutral presentation is desirable to lower the learning curve necessary for modeling, such as the need to learn FORTRAN for PMM or the Ansoft product UI for Designer, and improves post processing and sharing of data between solvers. The function also facilitates the process of design optimization by adding the ability to specify variable parametric sweeps and by allowing auto-rendering of the design in 3-D. This functionality is not available in some commercially available solvers, including PMM.

IV. EXAMPLE RESULTS: SQUARE-LOOP FSS ON ZIRCONIUM

For verification of the need to account for FD material properties in FSS modeling, a Manganese square-loop FSS on Zirconium (ZrO_2) with a Gold ground plane (Fig. 3) was fabricated and tested using a $3\ \mu\text{m}$ to $14\ \mu\text{m}$ spectroradiometer manufactured by Infrared Systems Development Corporation. The radiometer measures the surface emissivity directly [4]. In addition, the same design was modeled using PMM assuming frequency independent materials ($\epsilon_r = 3.0272$, $\tan\delta = 0.023$, $R_s = 40\ \Omega$) and the developed MATLAB function following the process outlined in the previous sections with frequency dependent material properties. In addition, based on a $\pm 5\%$ variation in material properties, the maximum and minimum emissivity limits was calculated. Modeled results from Designer demonstrated acceptable agreement with results from PMM and, thus, are omitted. Fig. 4 is a plot of the modeled and measured emissivity of the square loop FSS. Neither PMM nor Designer support the calculation of emissivity directly, however, the developed MATLAB function calculates emissivity using the conservation of energy relationship

$$\alpha(\lambda) + \tau(\lambda) + \rho(\lambda) = 1. \quad (2)$$

With transmission τ set to zero due to the presence of the groundplane and with absorption α (unity minus reflection ρ) set equal to emissivity as a consequence of Kirchhoff's law. From the figure, the FD model provides an improved indication of the device's measured behavior over the frequency independent model including a better bandwidth match from $3\ \mu\text{m}$ to $6\ \mu\text{m}$, accurate prediction of the device's emissivity peak around $7\ \mu\text{m}$, and improved agreement of curve shape from $8\ \mu\text{m}$ to $14\ \mu\text{m}$. Even with the inclusion of errors in the material measurements, the FD model demonstrates reasonable agreement with measured results.

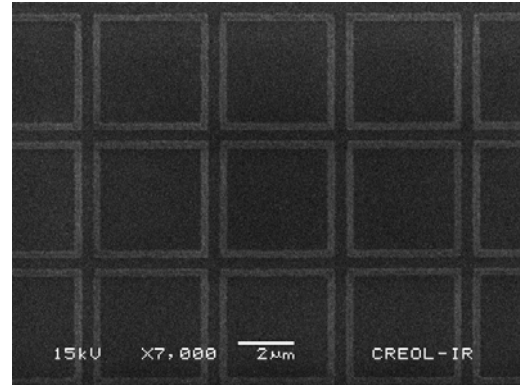


Fig. 3. SEM image of fabricated Square-Loop FSS on ZrO_2 .

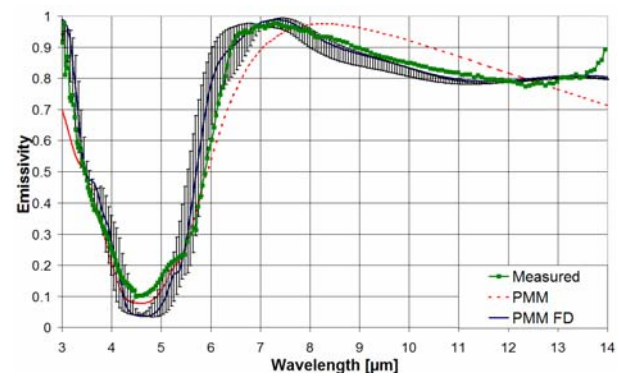


Fig. 4. Measured, frequency independent PMM, and frequency-dependent PMM results for square-loop FSS on ZrO_2 . Error bars represent total emissivity variation with material error.

In addition to modeling results, run time data for the model from Fig. 3 was also collected for each program and summarized in Table 1. As expected, the use of frequency dependent materials facilitated by a MATLAB function has resulted in an overall increase of run time. The increase can largely be attributed to additional time required to copy the measured permittivity values from the shared drive, extract the results, save the results to a spreadsheet file, generate of the function's GUI, and launch and close the desired solver. Overall, the longer runtime is acceptable due to the increase in model accuracy and additional program functionality.

Table 1. Comparison of runtime for a square-loop FSS using 100 frequency points.

	Frequency Independent	Frequency Dependent
Runtime	177s	552s

V. EXAMPLE RESULTS: SQUARE-LOOP FSS ON POLYMER

From the standpoint of mass production of an IR FSS, non-traditional stand-off layers, such as polymers, would be highly desirable for future designs to lower fabrication costs, reduce fabrication time, and allow for flexible substrates. Due to their composition, most polymers will exhibit significant frequency dependence and numerous loss bands at infrared. To evaluate FSS behavior on a polymer dielectric, another square loop FSS was modeled (Fig. 5) using both a fixed, lossless permittivity dielectric ($\epsilon_r = 1.5$, $\tan\delta = 0$) and the complex permittivity of PC0G46GL measured from the IR-VASE (Fig. 6). PC0G46GL is a fluoropolymer based on polycarbonate and represents a potential plastic substrate candidate. While deposition of a PC0G46GL substrate is feasible, development of THE PROCESS capability requires considerable investment of engineering time and has not yet been implemented. With the modeling capabilities developed; however, it is now reasonable to predict the behavior of PC0G46GL both for design optimization and benefit evaluation prior to development of fabrication capabilities.

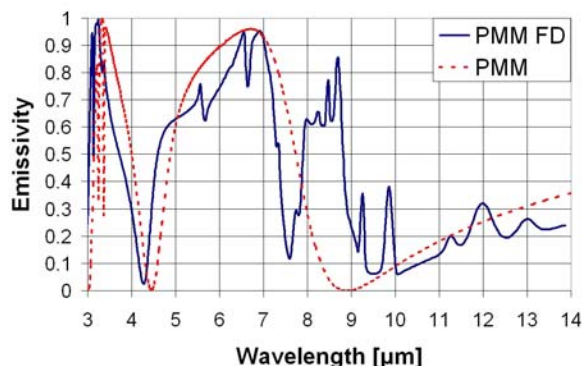


Fig. 5. Frequency independent PMM and frequency dependent PMM results for square loop on plastic.

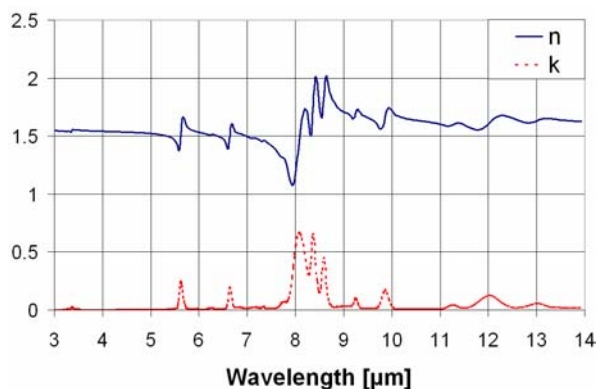


Fig. 6. Frequency dependent index of refraction (n,k) of PC0G46GL from ellipsometer.

When assuming a fixed permittivity dielectric, the square loop FSS was easily optimized for high emissivity from 5 μm to 8 μm simply by scaling existing designs and models. Running the same models using the developed MATLAB function and accounting for the frequency dependence of the plastic, the FSS retains some of its original behavior with the introduction of a high emissivity band between 8 μm to 9 μm and a sharp dip in emissivity around 7.5 μm . From a design standpoint, this new behavior can significantly change the potential applications of the FSS by effectively expanding the device's emissivity band and introducing an undesired dip in the middle of that band. Even with the measured IR properties, predicting these new trends before testing is clearly problematic when using only a frequency-independent model. By including material frequency dependence, further design optimization can occur with a reasonable expectation of accuracy and, thus, a reduction in the need of costly fabrication and measurement and investment risk.

VI. CONCLUSIONS

A procedure for the accurate characterization of a frequency selective surface design for use at infrared frequencies has been developed using dispersive materials. The procedure requires the use of material characterization and a custom MATLAB function to interface with commercially available electromagnetic solvers. Comparison of modeled and measured data for FSS designs on ZrO_2 and plastic substrates illustrate the significance of accurately modeling frequency-dependent material properties in performance predictions.

REFERENCES

- [1] W. L. Schaich, G. Schider, J. R. Krenn, A. Leitner, F. R. Aussenegg, I. Puscasu, B. Monacelli, and G. Boreman, "Optical resonances in periodic surface arrays of metallic patches," *Applied Optics*, vol. 42, no. 28, pp. 5714-5721, 2003.
- [2] K. D. Möller, J. B. Warren, J. B. Heaney, and C. Kotecki, "Cross-shaped bandpass filters for the near- and mid-infrared wavelength regions," *Applied Optics*, vol. 35, no. 31, pp. 6210-6215, Nov. 1996.
- [3] B. Monacelli, J. Pryor, B. A. Munk, D. Kotter, and G. D. Boreman, "Infrared frequency selective surfaces: design, fabrication and measurement," *Proc. SPIE*, vol. 5406, pp. 879-886, 2004.
- [4] B. Monacelli, J. Pryor, B. A. Munk, D. Kotter, and G. D. Boreman, "Infrared frequency selective

surface based on circuit-analog square loop design,” *IEEE Transactions on Antennas and Propagation*, vol. 53, no. 2, pp. 745-752, February 2005.

- [5] J. E. Raynolds, B. A. Munk, J. B. Pryor, and R. J. Marhefka, “Ohmic loss in frequency-selective surfaces,” *Journal of Applied Physics*, vol. 93, no. 9, pp. 5346- 5358, May 2003.
- [6] E. Topsakal, J. Volakis, “On the properties of materials for designing filters at optical frequencies” *2003 IEEE Antennas and Propagation Society International Symposium*, vol. 4, pp. 635 – 638, 22-27 June 2003.



James C. Ginn received a BS and MS in Electrical Engineering from the University of Central Florida in 2004 and 2006. He is currently pursuing his PhD in Electrical Engineering at the University of Central Florida and is a member of the Infrared Systems Research group at CREOL. His current research interests include infrared reflectarray design and high frequency computational electromagnetics.



Brian A. Lail received the BS in physics from Furman University, MS in physics and electrical engineering and PhD in electrical engineering from New Mexico State University. From 2002 to 2005 he was with the Department of Electrical and Computer Engineering at the University of Central Florida. Since 2005 he has been an Assistant Professor in the Department of Electrical and Computer Engineering at Florida Institute of Technology, Melbourne, FL, teaching and conducting research in applied and computational electromagnetics.



David J. Shelton received a BS in Physics from the University of Evansville in 2005. He is currently pursuing his PhD in Optics from CREOL at the University of Central Florida and is a member of the Infrared Systems Research group. David is an NSF IGERT fellow. His current research interests include tunable nanoscale FSS design and fabrication as well as flexible substrate FSS fabrication.



Jeffrey S. Tharp received a BS in Physics from the University of North Carolina at Asheville and an MS in Optical Science and Engineering from the University of North Carolina at Charlotte in 2002 and 2004, respectively. He is currently pursuing his PhD in Optics at the University of Central Florida, CREOL: College of Optics and Photonics and he is a member of the Infrared Systems Research group. His current research interests include polarization modification using infrared frequency selective surfaces.



William R. Folks is a researcher at the University of Central Florida in Orlando. He received his BS from Eastern Michigan University in 1989 and the Ph.D. in physics from Kent State University in 1995. His research interests are in liquid crystal displays, infrared optics, terahertz applications, and optical engineering.



Glenn D. Boreman received the B.S. degree in optics from the University of Rochester, Rochester, NY, in 1978 and the Ph.D. in optical sciences from the University of Arizona, Tucson, in 1984. Since 1984, he has been on the faculty of the University of Central Florida in Orlando, where he is currently Trustee Chair Professor of Optics, Physics, and Electrical Engineering. He is coauthor of *Infrared Detectors and Systems* (New York: Wiley, 1996), author of *Basic Electro-Optics for Electrical Engineers* (Bellingham, WA: SPIE, 1998) and *Modulation Transfer Function in Optical and Electro-Optical Systems* (Bellingham, WA: SPIE, 2001). His research interests include infrared and millimeter-wave sensing, and the transition of radiofrequency concepts such as antennas and frequency-selective surfaces to optical frequencies using electron-beam lithography.

Prof. Boreman is a Fellow of the Optical Society of America (OSA) and of the Society of Photo-Optical Instrumentation Engineers (SPIE). He served six years as Editor-in-Chief of OSA’s journal *Applied Optics*, and is a past member of the SPIE Board of Directors. Along with his students, he received the 1995 Kingslake Medal from SPIE.

2007 INSTITUTIONAL MEMBERS

AUSTRALIAN DEFENCE LIBRARY
Northcott Drive
Canberra, A.C.T. 2600 Australia

BAE SYSTEMS
W. Hanningfield Road
Technology Center Library
Great Baddow, Chelmsford
UK CM2 8HN

BEIJING BOOK COMPANY, INC
701 E Lindon Ave.
Linden, NJ 07036-2495

DARTMOUTH COLL-FELDBERG LIB
6193 Murdough Center
Hanover, NH 03755-3560

DSTO-DSTORL EDINBURGH
Jets AU/33851-99, PO Box 562
Milsons Point, NSW
Australia 1565

DTIC-OCP/LIBRARY
8725 John J. Kingman Rd. Ste 0944
Ft. Belvoir, VA 22060-6218

ELSEVIER
Bibliographic Databases
PO Box 2227
Amsterdam, Netherlands 1000 CE

ENGINEERING INFORMATION, INC
PO Box 543
Amsterdam, Netherlands 1000 Am

ETSE TELECOMUNICACION
Biblioteca, Campus Lagoas
Vigo, 36200 Spain

FGAN-FHR
Neuenahrerstrasse 20
Wachtberg, Germany 53343

FLORIDA INTERNATIONAL UNIV
10555 W. Flagler Street
Miami, FL 33174

GEORGIA TECH LIBRARY
225 North Avenue, NW
Atlanta, GA 30332-0001

HANYANG UNIVERSITY
Paiknam Academic Info. Ctr Library
17 Haengdang-Dong
Seongdong-Ku
Seoul, South Korea 133-791

HRL LABS, RESEARCH LIBRARY
3011 Malibu Canyon
Malibu, CA 90265

IEE INSPEC/Acquisitions Section
Michael Faraday House
6 Hills Way
Stevenage, Herts UK SG1 2AY

INSTITUTE FOR SCIENTIFIC INFO.
Publication Processing Dept.
3501 Market St.
Philadelphia, PA 19104-3302

LEMA-EPFL
ELB-ECUBLEMS
Lausanne, Switzerland
CH-1020

LIBRARY – DRDC OTTAWA
3701 Carling Avenue
Ottawa, Ontario, Canada K1A 0Z4

LIBRARY of CONGRESS
Reg. Of Copyrights
Attn: 40T Deposits
Washington DC, 20559

LINDA HALL LIBRARY
5109 Cherry Street
Kansas City, MO 64110-2498

MISSISSIPPI STATE UNIV LIBRARY
PO Box 9570 Mississippi State, MS
39762

MIT LINCOLN LABORATORY
Periodicals Library
244 Wood Street
Lexington, MA 02420

NAVAL POSTGRADUATE SCHOOL
Attn: J. Rozdal/411 Dyer Rd./ Rm 111
Monterey, CA 93943-5101

NAVAL RESEARCH LABORATORY
Code 3516
4555 Overlook Avenue SW
Washington, DC 20375-5334

NDL KAGAKU
C/O KWE-ACCESS
PO Box 300613 (JFK A/P)
Jamaica, NY 11430-0613

OHIO STATE UNIVERSITY
1320 Kinnear Road
Columbus, OH 43212

OVIEDO LIBRARY
PO BOX 830679
Birmingham, AL 35283

PENN STATE UNIVERSITY
126 Paterno Library
University Park, PA 16802-1808

PHILIPS RESEARCH LABORATORY
Cross Oak Lane, Stella Cox
Salfords, Redhill
UK RH1 5HA

RENTON TECH LIBRARY/BOEING
PO BOX 3707
SEATTLE, WA 98124-2207

SOUTHWEST RESEARCH
INSTITUTE
6220 Culebra Road
San Antonio, TX 78238

SWETS INFORMATION SERVICES
160 Ninth Avenue, Suite A
Runnemede, NJ 08078

TECHNISCHE UNIV. DELFT
Mekelweg 4, Delft, Holland, 2628 CD
Netherlands

TELSTRA
TRL/M2/770 Blackburn Road
Clayton, Victoria, Australia 3168

TIB & UNIV. BIB. HANNOVER
DE/5100/G1/0001
Welfengarten 1B
Hannover, Germany 30167

TU DARMSTADT
Schlossgartenstrasse 8
Darmstadt, Hessen
Germany D-64289

UNIV OF CENTRAL FLORIDA LIB.
4000 Central Florida Boulevard
Orlando, FL 32816-8005

UNIV OF COLORADO LIBRARY
Campus Box 184
Boulder, CO 80309-0184

UNIVERSITY OF MISSISSIPPI
John Davis Williams Library
PO Box 1848
University, MS 38677-1848

UNIV OF MISSOURI-ROLLA LIB.
1870 Miner Circle
Rolla, MO 65409-0001

USAE ENG. RES. & DEV. CENTER
Attn: Library/Journals
72 Lyme Road
Hanover, NH 03755-1290

ACES COPYRIGHT FORM

This form is intended for original, previously unpublished manuscripts submitted to ACES periodicals and conference publications. The signed form, appropriately completed, MUST ACCOMPANY any paper in order to be published by ACES. PLEASE READ REVERSE SIDE OF THIS FORM FOR FURTHER DETAILS.

TITLE OF PAPER:

RETURN FORM TO:

Dr. Atef Z. Elsherbeni
University of Mississippi
Dept. of Electrical Engineering
Anderson Hall Box 13
University, MS 38677 USA

AUTHORS(S)

PUBLICATION TITLE/DATE:

PART A - COPYRIGHT TRANSFER FORM

(NOTE: Company or other forms may not be substituted for this form. U.S. Government employees whose work is not subject to copyright may so certify by signing Part B below. Authors whose work is subject to Crown Copyright may sign Part C overleaf).

The undersigned, desiring to publish the above paper in a publication of ACES, hereby transfer their copyrights in the above paper to The Applied Computational Electromagnetics Society (ACES). The undersigned hereby represents and warrants that the paper is original and that he/she is the author of the paper or otherwise has the power and authority to make and execute this assignment.

Returned Rights: In return for these rights, ACES hereby grants to the above authors, and the employers for whom the work was performed, royalty-free permission to:

1. Retain all proprietary rights other than copyright, such as patent rights.
2. Reuse all or portions of the above paper in other works.

3. Reproduce, or have reproduced, the above paper for the author's personal use or for internal company use provided that (a) the source and ACES copyright are indicated, (b) the copies are not used in a way that implies ACES endorsement of a product or service of an employer, and (c) the copies per se are not offered for sale.

4. Make limited distribution of all or portions of the above paper prior to publication.

5. In the case of work performed under U.S. Government contract, ACES grants the U.S. Government royalty-free permission to reproduce all or portions of the above paper, and to authorize others to do so, for U.S. Government purposes only.

ACES Obligations: In exercising its rights under copyright, ACES will make all reasonable efforts to act in the interests of the authors and employers as well as in its own interest. In particular, ACES REQUIRES that:

1. The consent of the first-named author be sought as a condition in granting re-publication permission to others.
2. The consent of the undersigned employer be obtained as a condition in granting permission to others to reuse all or portions of the paper for promotion or marketing purposes.

In the event the above paper is not accepted and published by ACES or is withdrawn by the author(s) before acceptance by ACES, this agreement becomes null and void.

AUTHORIZED SIGNATURE

TITLE (IF NOT AUTHOR)

EMPLOYER FOR WHOM WORK WAS PERFORMED

DATE FORM SIGNED

Part B - U.S. GOVERNMENT EMPLOYEE CERTIFICATION

(NOTE: if your work was performed under Government contract but you are not a Government employee, sign transfer form above and see item 5 under Returned Rights).

This certifies that all authors of the above paper are employees of the U.S. Government and performed this work as part of their employment and that the paper is therefor not subject to U.S. copyright protection.

AUTHORIZED SIGNATURE

TITLE (IF NOT AUTHOR)

NAME OF GOVERNMENT ORGANIZATION

DATE FORM SIGNED

PART C - CROWN COPYRIGHT

(NOTE: ACES recognizes and will honor Crown Copyright as it does U.S. Copyright. It is understood that, in asserting Crown Copyright, ACES in no way diminishes its rights as publisher. Sign only if ALL authors are subject to Crown Copyright).

This certifies that all authors of the above Paper are subject to Crown Copyright. (Appropriate documentation and instructions regarding form of Crown Copyright notice may be attached).

AUTHORIZED SIGNATURE

TITLE OF SIGNEE

NAME OF GOVERNMENT BRANCH

DATE FORM SIGNED

Information to Authors

ACES POLICY

ACES distributes its technical publications throughout the world, and it may be necessary to translate and abstract its publications, and articles contained therein, for inclusion in various compendiums and similar publications, etc. When an article is submitted for publication by ACES, acceptance of the article implies that ACES has the rights to do all of the things it normally does with such an article.

In connection with its publishing activities, it is the policy of ACES to own the copyrights in its technical publications, and to the contributions contained therein, in order to protect the interests of ACES, its authors and their employers, and at the same time to facilitate the appropriate re-use of this material by others.

The new United States copyright law requires that the transfer of copyrights in each contribution from the author to ACES be confirmed in writing. It is therefore necessary that you execute either Part A-Copyright Transfer Form or Part B-U.S. Government Employee Certification or Part C-Crown Copyright on this sheet and return it to the Managing Editor (or person who supplied this sheet) as promptly as possible.

CLEARANCE OF PAPERS

ACES must of necessity assume that materials presented at its meetings or submitted to its publications is properly available for general dissemination to the audiences these activities are organized to serve. It is the responsibility of the authors, not ACES, to determine whether disclosure of their material requires the prior consent of other parties and if so, to obtain it. Furthermore, ACES must assume that, if an author uses within his/her article previously published and/or copyrighted material that permission has been obtained for such use and that any required credit lines, copyright notices, etc. are duly noted.

AUTHOR/COMPANY RIGHTS

If you are employed and you prepared your paper as a part of your job, the rights to your paper initially rest with your employer. In that case, when you sign the copyright form, we assume you are authorized to do so by your employer and that your employer has consented to all of the terms and conditions of this form. If not, it should be signed by someone so authorized.

NOTE RE RETURNED RIGHTS: Just as ACES now requires a signed copyright transfer form in order to do "business as usual", it is the intent of this form to return rights to the author and employer so that they too may do "business as usual". If further clarification is required, please contact: The Managing Editor, R. W. Adler, Naval Postgraduate School, Code EC/AB, Monterey, CA, 93943, USA (408)656-2352.

Please note that, although authors are permitted to re-use all or portions of their ACES copyrighted material in other works, this does not include granting third party requests for reprinting, republishing, or other types of re-use.

JOINT AUTHORSHIP

For jointly authored papers, only one signature is required, but we assume all authors have been advised and have consented to the terms of this form.

U.S. GOVERNMENT EMPLOYEES

Authors who are U.S. Government employees are not required to sign the Copyright Transfer Form (Part A), but any co-authors outside the Government are.

Part B of the form is to be used instead of Part A only if all authors are U.S. Government employees and prepared the paper as part of their job.

NOTE RE GOVERNMENT CONTRACT WORK: Authors whose work was performed under a U.S. Government contract but who are not Government employees are required so sign Part A-Copyright Transfer Form. However, item 5 of the form returns reproduction rights to the U. S. Government when required, even though ACES copyright policy is in effect with respect to the reuse of material by the general public.

January 2002

INFORMATION FOR AUTHORS

PUBLICATION CRITERIA

Each paper is required to manifest some relation to applied computational electromagnetics. **Papers may address general issues in applied computational electromagnetics, or they may focus on specific applications, techniques, codes, or computational issues.** While the following list is not exhaustive, each paper will generally relate to at least one of these areas:

- 1. Code validation.** This is done using internal checks or experimental, analytical or other computational data. Measured data of potential utility to code validation efforts will also be considered for publication.
- 2. Code performance analysis.** This usually involves identification of numerical accuracy or other limitations, solution convergence, numerical and physical modeling error, and parameter tradeoffs. However, it is also permissible to address issues such as ease-of-use, set-up time, run time, special outputs, or other special features.
- 3. Computational studies of basic physics.** This involves using a code, algorithm, or computational technique to simulate reality in such a way that better, or new physical insight or understanding, is achieved.
- 4. New computational techniques,** or new applications for existing computational techniques or codes.
- 5. “Tricks of the trade”** in selecting and applying codes and techniques.
- 6. New codes, algorithms, code enhancement, and code fixes.** This category is self-explanatory, but includes significant changes to existing codes, such as applicability extensions, algorithm optimization, problem correction, limitation removal, or other performance improvement. **Note: Code (or algorithm) capability descriptions are not acceptable, unless they contain sufficient technical material to justify consideration.**
- 7. Code input/output issues.** This normally involves innovations in input (such as input geometry standardization, automatic mesh generation, or computer-aided design) or in output (whether it be tabular, graphical, statistical, Fourier-transformed, or otherwise signal-processed). Material dealing with input/output database management, output interpretation, or other input/output issues will also be considered for publication.
- 8. Computer hardware issues.** This is the category for analysis of hardware capabilities and limitations of various types of electromagnetics computational requirements. Vector and parallel computational techniques and implementation are of particular interest.

Applications of interest include, but are not limited to, antennas (and their electromagnetic environments), networks, static fields, radar cross section, shielding, radiation hazards, biological effects, electromagnetic pulse (EMP), electromagnetic interference (EMI), electromagnetic compatibility (EMC), power transmission, charge transport, dielectric, magnetic and nonlinear materials, microwave components, MEMS technology, MMIC technology, remote sensing and geometrical and physical optics, radar and communications systems, fiber optics, plasmas, particle accelerators, generators and motors, electromagnetic wave propagation, non-destructive evaluation, eddy currents, and inverse scattering.

Techniques of interest include frequency-domain and time-domain techniques, integral equation and differential equation techniques, diffraction theories, physical optics, moment methods, finite differences and finite element techniques, modal expansions, perturbation methods, and hybrid methods. This list is not exhaustive.

A unique feature of the Journal is the publication of unsuccessful efforts in applied computational electromagnetics. Publication of such material provides a means to discuss problem areas in electromagnetic modeling. Material representing an unsuccessful application or negative results in computational electromagnetics will be considered for publication only if a reasonable expectation of success (and a reasonable effort) are reflected. Moreover, such material must represent a problem area of potential interest to the ACES membership.

Where possible and appropriate, authors are required to provide statements of quantitative accuracy for measured and/or computed data. This issue is discussed in “Accuracy & Publication: Requiring, quantitative accuracy statements to accompany data,” by E. K. Miller, *ACES Newsletter*, Vol. 9, No. 3, pp. 23-29, 1994, ISBN 1056-9170.

EDITORIAL REVIEW

In order to ensure an appropriate level of quality control, papers are peer reviewed. They are reviewed both for technical correctness and for adherence to the listed guidelines regarding information content.

JOURNAL CAMERA-READY SUBMISSION DATES

March issue	deadline 8 January
July issue	deadline 20 May
November issue	deadline 20 September

Uploading an acceptable camera-ready article after the deadlines will result in a delay in publishing this article.

STYLE FOR CAMERA-READY COPY

The ACES Journal is flexible, within reason, in regard to style. However, certain requirements are in effect:

1. The paper title should NOT be placed on a separate page. The title, author(s), abstract, and (space permitting) beginning of the paper itself should all be on the first page. The title, author(s), and author affiliations should be centered (center-justified) on the first page.
2. An abstract is REQUIRED. The abstract should be a brief summary of the work described in the paper. It should state the computer codes, computational techniques, and applications discussed in the paper (as applicable) and should otherwise be usable by technical abstracting and indexing services.
3. Either British English or American English spellings may be used, provided that each word is spelled consistently throughout the paper.
4. Any commonly-accepted format for referencing is permitted, provided that internal consistency of format is maintained. As a guideline for authors who have no other preference, we recommend that references be given by author(s) name and year in the body of the paper (with alphabetical listing of all references at the end of the paper). Titles of Journals, monographs, and similar publications should be in italic font or should be underlined. Titles of papers or articles should be in quotation marks.
5. Internal consistency shall also be maintained for other elements of style, such as equation numbering. As a guideline for authors who have no other preference, we suggest that equation numbers be placed in parentheses at the right column margin.
6. The intent and meaning of all text must be clear. For authors who are NOT masters of the English language, the ACES Editorial Staff will provide assistance with grammar (subject to clarity of intent and meaning).
7. Unused space should be minimized. Sections and subsections should not normally begin on a new page.

PAPER FORMAT

The preferred format for initial submission and camera-ready manuscripts is 12 point Times Roman font, single line spacing and double column format, similar to that used here, with top, bottom, left, and right 1 inch margins. Manuscripts should be prepared on standard 8.5x11 inch paper.

Only camera-ready electronic files are accepted for publication. The term “**camera-ready**” means that the material is neat, legible, and reproducible. Full details can be found on ACES site, Journal section.

ACES reserves the right to edit any uploaded material, however, this is not generally done. It is the author(s)

responsibility to provide acceptable camera-ready pdf files. Incompatible or incomplete pdf files will not be processed, and authors will be requested to re-upload a revised acceptable version.

SUBMITTAL PROCEDURE

All submissions should be uploaded to ACES server through ACES web site (<http://aces.ee.olemiss.edu>) by using the upload button, journal section. Only pdf files are accepted for submission. The file size should not be larger than 5MB, otherwise permission from the Editor-in-Chief should be obtained first. The Editor-in-Chief will acknowledge the electronic submission after the upload process is successfully completed.

COPYRIGHTS AND RELEASES

Each primary author must sign a copyright form and obtain a release from his/her organization vesting the copyright with ACES. Copyright forms are available at ACES, web site (<http://aces.ee.olemiss.edu>). To shorten the review process time, the executed copyright form should be forwarded to the Editor-in-Chief immediately after the completion of the upload (electronic submission) process. Both the author and his/her organization are allowed to use the copyrighted material freely for their own private purposes.

Permission is granted to quote short passages and reproduce figures and tables from and ACES Journal issue provided the source is cited. Copies of ACES Journal articles may be made in accordance with usage permitted by Sections 107 or 108 of the U.S. Copyright Law. This consent does not extend to other kinds of copying, such as for general distribution, for advertising or promotional purposes, for creating new collective works, or for resale. The reproduction of multiple copies and the use of articles or extracts for commercial purposes require the consent of the author and specific permission from ACES. Institutional members are allowed to copy any ACES Journal issue for their internal distribution only.

PUBLICATION CHARGES

ACES members are allowed 12 printed pages per paper without charge; non-members are allowed 8 printed pages per paper without charge. Mandatory page charges of \$75 a page apply to all pages in excess of 12 for members or 8 for non-members. Voluntary page charges are requested for the free (12 or 8) pages, but are NOT mandatory or required for publication. A priority courtesy guideline, which favors members, applies to paper backlogs. Authors are entitled to 15 free reprints of their articles and must request these from the Managing Editor. Additional reprints are available to authors, and reprints available to non-authors, for a nominal fee.

ACES Journal is abstracted in INSPEC, in Engineering Index, DTIC, Science Citation Index Expanded, the Research Alert, and to Current Contents/Engineering, Computing & Technology.